# International Conference on Aerospace and Mechanical Engineering

# ICAME ’15

## 14–16 December 2015

# International Conference on Aerospace and Mechanical Engineering

# ICAME '15

## 14–16 December 2015

*Organized by*

**Department of Mechanical Engineering**

**T.K.M. College of Engineering, Kollam-691005, Kerala, India**

***Sponsored by***

Technical Education Quality Improvement Programme (TEQIP-II)

***Co sponsored by***

Vikram Sarabhai Space Centre (VSSC), ISRO

TKM College Trust

Institution of Engineers (India), Kollam Local Centre


**McGraw Hill Education (India) Private Limited**

NEW DELHI

*McGraw Hill Education Offices*

**New Delhi** New York St Louis San Francisco Auckland Bogotá Caracas
Kuala Lumpur Lisbon London Madrid Mexico City Milan Montreal
San Juan Santiago Singapore Sydney Tokyo Toronto

**McGraw Hill Education (India) Private Limited**

Published by McGraw Hill Education (India) Private Limited,
P-24, Green Park Extension, New Delhi 110 016.

**International Conference on Aerospace and Mechanical Engineering, ICAME '15**



ISBN (13): 978-93-85965-16-6
ISBN (10): 93-85965-16-6

Managing Director: *Kaushik Bellani*
Director—Products (Higher Ed. & Professional): *Vibha Mahajan*

Sr. Researcher—Product Development: *Navneet Mehra*
Coordinator—Product Development: *Naveenta Bisht*
Head—Production (Higher Ed. & Professional): *Satinder S Baveja*
Manager—Production: *Sohan Gaur*

General Manager—Production: *Rajender P Ghansela*
Manager—Production: *Reji Kumar*



Typeset at Text-o-Graphics, B-1/56, Aravali Apartment, Sector-34, Noida 201 301, and printed at

Cover Printer:

Cover Designer: Kapil Gupta

Visit us at: www.mheducation.co.in

# ABOUT THE INSTITUTION

Thangal Kunju Musaliar College of Engineering (TKMCE) was established in the year 1958 in the state of Kerala by late Janab A. Thangal Kunju Musaliar, a leading industrialist and philanthropist. TKM College of Engineering, the very first Government-aided Engineering College in Kerala is situated in the cashew hub of Kerala, Kollam. The foundation stone of the college was laid in the year 1956 by Dr. Rajendra Prasad, the first President of Independent India. The college was formally inaugurated by Prof. Humayun Kabir, the then Minister for Scientific and Cultural Affairs, Govt. of India, on 3rd July, 1958. Spanning over an area of more than 25 acres, it is located in Karikode, by the side of the Kollam-Madurai(NH 208) road, about 5 kilometres from the heart of the Kollam city. The campus, a distinctive landmark that cuts above the rest is built in the aesthetic Mughal architectural style. The college is the major institution for technical education, run by the TKM educational trust, headed by Janab Shahal Hassan Musaliar. The college is affiliated to the University of Kerala and has eleven academic departments offering undergraduate and postgraduate programmes.

# ABOUT THE DEPARTMENT

The Mechanical Engineering Department has carved a niche for itself by offering the most competent instructional programmes to the students. In addition to the two Under Graduate Programmes (Mechanical Engineering. and Production Engineering), the department is conducting a Post graduate programme in Industrial Refrigeration and Cryogenic Engineering. The department is an approved research centre of University of Kerala and is a QIP(Quality Improvement Programme) centre approved by MHRD for Doctoral programme. The faculty of the department investigate a broad range of research in about a dozen thrust areas. Some of the specific areas include thermal management of electronic systems, nanomaterials and nanofluids, super conductivity, cryogenic heat transfer, heat and mass transfer in multiphase and single phase systems, food preservation, cryocoolers for space applications, computational combustion, fracture mechanics, micro structural studies, biomechanics, rapid prototyping. Much of the research is conducted within the department, but many projects are carried out in collaboration with other reputed institutions, Research and Development (R&D) organisations and laboratories within the country and abroad. The Department receives funding from agencies such as Ministry of Human Resource Development (MHRD), Department of Science and Technology (DST), Indian Space Research Organisation (ISRO) and other Government bodies and industries. The faculty members render assistance to R&D organisations and industries through technical advice and consultancy services.

# STEERING COMMITTEE

**Chief Patron**
Sri. T.K. Shahal Hassan Musaliar
President
TKM Trust & Chairman, BoG, TEQIP II, TKMCE

**Patrons**
Sri. T.K. Jalaluddin Musaliar
Treasurer, TKM Trust

Sri. T.K. Abdul Karim Musaliar
Member, TKM Trust

Sri.Haroon M
Member, TKM Trust

**Chairman**
Dr. S. Ayoob
Principal, TKMCE,Kollam

**Advisory Committee**
- Dr. Luigi Serio, CERN, Geneva, Switzerland
- Prof. Manfred Groll, University of Stuttgart, Germany
- Prof. D. Yogi Goswami, University of South Florida, USA
- Prof. Volodymyr A. Yartys, Institute for Energy Technology, NTNU, Norway
- Dr. Arend Nijhuis, University of Twente, Netherlands
- Dr. Chua Kian Jon Ernest, National University of Singapore, Singapore
- Prof. Maciej Chorowski, Wroclaw University of Technology, Poland
- Dr. Udo Althaler, RUAG space, Vienna, Austria
- Dr. Jung Kyung Kim, School of Mechanical Systems Engineering, Kookmin University, Seoul, South Korea
- Dr. Ramalingam Rajini, Karlsruhe Institute of Technology, Germany
- Dr. Aditi Oza, Air Liquide, USA
- Dr. Aswin T. R, University of Warwick, United Kingdom
- Dr. M.C. Dathan, Former Director, Vikram Sarabhai Space Centre(VSSC), ISRO, Thiruvananthapuram, India
- Dr. K Sivan, Director Vikram Sarabhai Space Centre(VSSC), ISRO, Thiruvananthapuram, India
- Sri. S. Anantha Narayanan, Director, NPOL, DRDO, Kochi, India

- Dr. Kuncheria P. Isaac, Vice Chancellor, Kerala Technological University, Thiruvananthapuram, India
- Dr.K.Vijayakumar, Director, Technical Education, Govt. of Kerala, India
- Prof. S. Srinivasa Murthy, Interdisciplinary Center for Energy Research (ICER), IISc, Bangalore, India
- Prof. Kanchan Chowdhury, Indian Institute of Technology Kharagpur, India
- Prof. Pradip Dutta, Indian Institute of Science, Bangalore, India
- Sri. S. Somanath, Director, Liquid Propulsion Systems Centre(LPSC), ISRO, Thiruvananthapuram, India
- Dr. Premachandran. B, Indian Institute of Technology, Delhi, India
- Dr. A. Ajayaghosh, NIIST, Thiruvananthapuram, India
- Prof.Muthukumar, Indian Institute of Technology, Guwahati, India
- Prof. Pratibha Sharma, Indian Institute of Technology Bombay, Mumbai, India
- Dr. Gopakumar V, Director, SPFU, Government of Kerala, India
- Prof. Parthasarathi Ghosh, Indian Institute of Technology, Kharagpur, India
- Prof. Sarith P Sathian, Indian Institute of Technology Madras, Chennai, India
- Prof. A. Sameen, Indian Institute of Technology Madras, Chennai, India
- Dr.T.M.Amarunnishad, Former Principal, TKMCE
- Prof. S. Parameswaran, Former Head, Department Mechanical Engineering, TKMCE

## Organizing Committee

**Chair**
Dr. J. Nazar
Professor and Head, Department of Mechanical Engineering, TKMCE, Kollam

**Co-Chairs**
Prof. P. Mohamed Iqbal
Professor, Department of Mechanical Engineering, TKMCE, Kollam
Dr. D. Roshankumar
Professor, Department of Mechanical Engineering, TKMCE, Kollam

**Organizing Secretary**
Dr. Jose Prakash M
Professor, Department of Mechanical Engineering, TKMCE, Kollam

**Joint Secretaries**
Dr. K.E. Reby Roy
Assistant Professor, Department of Mechanical Engineering, TKMCE, Kollam
Dr. Rijo Jacob Thomas
Assistant Professor, Department of Mechanical Engineering, TKMCE, Kollam

**Technical Support**
Mr. Arun M
Research Scholar (QIP), Department of Mechanical Engineering, TKMCE, Kollam
Mr. Sanukrishna S.S
Research Scholar (QIP), Department of Mechanical Engineering, TKMCE, Kollam

# PREFACE

The International Conference on Aerospace and Mechanical Engineering, ICAME'15 organized by the Department of Mechanical Engineering, Thangal Kunju Musaliar College of Engineering (TKMCE), Kollam, Kerala, India is held during 14-16 December 2015 in the college. This conference is sponsored by TEQIP-II and cosponsored by Vikram Sarabhai Space Centre (VSSC), Indian Space Research Organization (ISRO), Thiruvananthapuram, TKM Trust and Institution of Engineers (India), Kollam local Centre. The theme of ICAME'15 is '*Facing the Future –Growth through Sustainability*'. The conference is a platform for presenting advances in the fields of Aerospace and Mechanical Engineering and is a notable event which brings together academia, researchers, engineers and students in the field of Aerospace and Mechanical Engineering making the conference a perfect platform to share experience, foster collaborations across industry and academia, and evaluate emerging technologies across the globe.

The conference received papers from various fields under seven different tracks; i) Advances in Aerospace Technology ii) Advanced Manufacturing iii) Thermal and Fluids Engineering iv) Materials and Nanotechnology v) Engineering Design vi) Cryogenics and vii) Energy Conversion and Management. The conference has solicited and gathered about 100 technical research submissions related to all the topics that closely align to the conference theme. These papers are received and processed through EasyChair online conference management tool. After the rigorous peer-review by experts consisting of academicians and scientists from leading institutes, depending on the originality, significance, and clarity on their subject matter, 70 paper are selected for oral presentations.

The keynote speaker of the conference is Dr. Luigi Serio, Scientist, CERN, Switzerland. The invited speakers include Dr. Arend Nijhuis (University of Twente, Netherlands), Dr. Jung Kyung Kim (Kookmin University, South Korea), Dr. Rajinikumar Ramalingam (Karlsruhe Institute of Technology, Germany) and Dr. P. Muthukumar (Indian Institute of Technology, IIT Guwahati). Additional highlight of this conference is the unique 'Space Technology' workshop conducted by the scientists from ISRO. As a part of the work shop special lectures are arranged on topics such as ISRO's programmes- an over view, cryogenic and semicryogenic propulsion systems, structural technologies for space systems and solid propulsion system-end to end capability. An exhibition showcasing various rocket propulsion and space systems is also arranged.

As the editors, it is a great pleasure to present this volume of the proceedings on behalf of the organizing committee. This conference proceedings contain the keynote address, invited talks as well as contributed papers. The moment of writing this page reminds us of the helps and support of many; it is indeed a privilege to reminisce those most valuable ones while serving as the Organizers. The support of the Chairman and Members of the TKM college trust is gratefully acknowledged. Our Principal has been the major source of inspiration for this conference. We thank all the faculty and staff members of the department of Mechanical Engineering for their whole hearted support and encouragement.

On behalf of the organizing committee, we would like to thank all who have contributed to the conference especially the authors who have responded to our call for papers, the members of the advisory board, the most valued invited speakers and our own colleagues in the organizing committee. We also would like to place on record the services rendered by all the reviewers for the valuable time they spent on providing us the feedbacks and that too in a very short time. We thank the technical committee that helped us in selecting quality papers for presentation in the conference. On behalf of the organizing committee, we would like to acknowledge the valuable support extended to us by the Chairman of ISRO, Directors of VSSC and LPSC and their scientists in making this event a great success. We also acknowledge the support from top administrative officials of various industries, Directors of research organizations and the heads of different academic institutions in providing advices and also sponsoring delegates to this conference. We offer our sincere thanks for everyone who supported us throughout the planning and execution of this conference. The support rendered by Research Scholars (QIP) and post graduate students of the Department is acknowledged.

We also gratefully acknowledge the different organizations and agencies who have financially supported us. TEQIP -II has been the major financial supporter and we thank the Director, SPFU and the TEQIP Coordinator and his team in the college. We thank Institution of Engineers (India) Kollam local Centre for providing financial support. We thank McGraw Hill Education for publishing proceedings.

We hope that this conference will help all the delegates to operate more effectively by building co-operative and supportive collaborations thereby helping to inform the proper directions of current and future research. We wish all the delegates to have a great time during the conference.

With warmest regards
**Organizing Team**

## THANGAL KUNJU MUSALIAR COLLEGE OF ENGINEERING
KOLLAM-691005, KERALA

**Shahal Hassan Musaliar**
Chairman, Governing Body

**MESSAGE**

20 November 2015

It gives me immense pleasure to know that the Department of Mechanical Engineering is organising an **International Conference on Aerospace and Mechanical Engineering, ICAME'15** from 14-16 December 2015.

I hope that ICAME'15 would be a notable event which brings together academia, researchers, engineers and students in the field of Aerospace and Mechanical Engineering. It would be a great platform to share experience, foster collaborations across industry and academia, and evaluate emerging technologies across the globe.

I anticipate that the conference will bring out the latest developments in various fields under the different tracks such as Aerospace Technology, Advanced Manufacturing, Thermal and Fluids Engineering, Materials and Nanotechnology, Engineering Design, Cryogenics, Energy conversion and Management, Engineering Management etc. Such an experience is what our students and engineers need and I hope that this would motivate them to take up relevant and more meaningful research works which would bring up positive changes and developments to the society. Such exposure also will equip our Engineers to deal with problems that span across various fields and disciplines.

The theme of the conference, ***'Facing the Future - Growth through Sustainability'*** is highly relevant and I hope that this conference would serve as a platform where all are encouraged to provide sustainable solutions without harming the nature and its inhabitants.

Being conducted in technical collaboration with **VSSC, ISRO**, it is noteworthy to mention that it would be a great opportunity for all the conference delegates to interact and develop contacts with one of the most professionally successful team of Engineers and Scientists of India. I personally feel that the special workshop on 'Space Technology' by the Scientists from ISRO will provide hands-on experience as well as a closer look on the latest developments in our space missions.

I am happy to note that several experts of premier institutes from within the country and overseas are associating as well as attending this conference. I am sure that all the delegates would be looking forward to meet and interact with scientists from various parts of the globe especially from **CERN.** The presence of many delegates from different Government research organisations within India like **ISRO, NIIST (CSIR), DRDO,** etc**.** would provide the delegates a great exposure in those three days.

I know that the success of the conference depends ultimately on the people who have worked behind it and congratulate the organising team for their outstanding job. I convey my greetings to all the faculty and staff members of the department of Mechanical Engineering for their great effort and support.

I express my very best wishes for an effective, successful and productive ICAME'15.

**Shahal Hassan Musaliar**

# THANGAL KUNJU MUSALIAR COLLEGE OF ENGINEERING

KOLLAM-691005, KERALA

**Dr. S. Ayoob**
Principal

**MESSAGE**

20 November 2015

I am pleased to note that the department of Mechanical engineering our college is organizing an International Conference on Aerospace and Mechanical Engineering (ICAME'15) from 14–16 December 2015.

For the development of our country, it is imperative that we become self-reliant in science and technology through research and development. It is commendable that our Mechanical engineering Department is consistently taking up newer research activities and also collaborating with different external agencies in India and abroad. This conference organised by them would definitely help to promote and carry out more research and developmental activities in Aerospace and Mechanical Engineering and in their allied areas.

ICAME'15 will also facilitate in exchange of scientific information among industry, researchers and academia. I hope that this conference would facilitate the global exploration on the recent advances in the exciting research pursued in the field of Aerospace and Mechanical Engineering around the world.

'**Facing the Future –Growth through Sustainability**', which is the theme of the conference, is very much relevant today and I hope that this conference would serve in bringing out sustainable solutions. The technical collaboration with ISRO is noteworthy to mention that it would give the conference delegates an ideal platform to interact and network with the Engineers and Scientists of ISRO.

I congratulate the organisers for organising this conference and my best wishes for a grand success of this event.

I wish ICAME'15 be enjoyable, memorable and productive for participants.

**Dr. S. Ayoob**

## THANGAL KUNJU MUSALIAR COLLEGE OF ENGINEERING
KOLLAM-691005, KERALA

**Dr. J. Nazar**
Professor & Head
Dept. of Mechanical Engineering

**MESSAGE**

20 November 2015

It is indeed my pleasure and an honour that our department is organizing an International Conference on Aerospace and Mechanical Engineering ICAME'15 from 14–16 December 2015

The purpose of this conference is to bring together researchers, teachers from academic institutions and experts from industry to meet, exchange information and ideas in developments in the field. It brings together the newest developments in related technologies, engineering solutions, industry practices and academic research results on the same platform. The conference program has been designed to provide ample opportunities to researchers to network and to share ideas and information.

I hope that ICAME'15 would certainly help everyone to have the latest updates to have a better understanding to contribute more in the field of Aerospace and Mechanical Engineering.

I hope this conference ICAME'15 will be enjoyable, memorable, and productive for the delegates and looking forward to the technological innovations that result from their networking and discussions.

I wish all the best to all the delegates.

**Dr. J. Nazar**

# CONTENTS

# KEYNOTE AND INVITED LECTURES

# The Winding Road from Superconducting Wire to High Current Cables

A. Nijhuis[1], K.A. Yagotintsev[1], W.A.J. Wessel[1], T. Bagni[1], M. Dijkstra[1], J. Huang[1], M. Dhalle[1], P. Gao[1], K. Ilin[1], C. Zhou[1,2], A. Vostner[2], A. Devred[2], D. Bessette[2], Y. Wu[3], J. Qin[3], Y. Nabara[4], T. Boutboul[5], V. Tronza[6], S.-H. Park[7], N. Martovetsky[8], S. Pradhan[9], R. Wesche[10], D Uglietti[10], W. Goldacker[11], A. Kario[11], L. Muzzi[12], A. Della Corte[12], V.A. Anvar[13], R.J. Thomas[13], M.D. Sumption[14], M. Tomsic[15], M. Rindfleisch[15], M.S.A. Hossain[16], T.J. Haugan[17], D.C. van der Laan[18]

*[1] University of Twente, Faculty of Science & Technology, Enschede, The Netherlands*

*[2] ITER International Organization, Route de Vinon-sur-Verdon, Saint-Paul-lez-Durance, France*

*[3] Institute of Plasma Physics, Chinese Academy of Science (ASIPP), Hefei, People's Republic of China*

*[4] Japan Atomic Energy Agency, 801-1, Muko-yama, Naka-shi, Ibaraki, 311-0193 Japan*

*[5] Fusion for Energy (F4E), ITER Department. Magnet Project Team, 08019 Barcelona, Spain*

*[6] ITER-Center, 1 bld. 3 Kurchatov sq., 123182 Moscow, Russian Federation*

*[7] National Fusion Research Institute, 169-148 Gwahak-Ro, Yuseong-Gu, Daejeon 305-333, Korea*

*[8] Oak Ridge National Laboratory, 1 Bethel Valley Rd, Oak Ridge, TN 37831, USA*

*[9] Institute for Plasma Research, Gujarat, India*

*[10] SPC, Villigen, Switzerland*

*[11] KIT, Karlsruhe, Germany*

*[12] ENEA, Frascati Research Center, Frascati, Italy*

*[13] TKM College of Engineering, Department of Mechanical Engineering, Kollam, Kerala, India*

*[14] Ohio State University, Columbus, Ohio*

*[15] Hyper Tech Research, Inc. Columbus, Ohio*

*[16] University of Wollongong, Wollongong, Australia*

*[17] US Air Force Research Laboratory, Wright Patterson AFB, OH 45433, USA*

*[18] Advanced Conductor Technologies and University of Colorado, Boulder CO 80301, USA*

***Abstract***— For fast-pulsed magnets, like in nuclear fusion reactors for sustainable electricity generation, high current cables need to be developed to reduce the number of windings and thus the coil self-induction. For this reason, a large number of wires need to be assembled in a cable. The superconducting properties of the wires are restricted by critical values of temperature, magnetic field, current and strain and are different depending on the used materials. When the cables are subjected to fast changing magnetic fields in the order of 1 T/s, the wires in the cables are exposed to internal heating by induced currents. This causes an increase of temperature that needs to be well controlled. The large electromagnetic forces associated with high magnet fields up to 13 T and currents in the order of 50 to 100 kA, introduce torsion, axial and transverse loading of the wires. The various materials presently commercially available, i.e. NbTi, Nb3Sn, MgB2, REBCO and BSCCO, each have their specific properties and require a careful design optimization to guarantee reliable and economic operation. Here we present an overview of the activities at the University of Twente in the framework of collaborations specifically addressing the conductor research and design for nuclear fusion superconductors. The past decade developments, modeling and measurement methods concerning electromagnetic and mechanical properties are summarized.

# CERN: The Organization and its Facilities, the Research and Development Activities, the Large Hadron Collider and the Perspective for the Future

L. Serio

*Technology Department, CERN, 1211 Geneva 23, Switzerland*
luigi.serio@cern.ch

***Abstract*—**CERN, the European Organization for Nuclear Research, was founded in 1954 with the mandate of establishing a world-class fundamental physics research organization in Europe. Since then the Organization has evolved to become not only a laboratory for basic science research but also an incubator of ideas and developments for everyday life applications, a model of scientific cooperation and an international source of technical expertise.

CERN uses the world's largest and most complex scientific instruments to study the basic constituents of matter – the fundamental particles. The particles are made to collide together at close to the speed of light. The process gives the physicists clues about how the particles interact, and provides insights into the fundamental laws of nature.

The facilities are purpose-built particle accelerators and detectors. Accelerators boost beams of particles to high energies before the beams are made to collide with each other or with stationary targets. Detectors observe and record the results of these collisions.

The flagship installation at CERN is the Large Hadron Collider (LHC), the world's largest and most powerful particle accelerator which started operation in 2008. The LHC consists of a 27-kilometre ring of superconducting magnets with a number of accelerating RF superconducting cavities to boost the energy of the particles along the way. Inside the accelerator, two high-energy particle beams travel at close to the speed of light before they are made to collide. The beams travel in opposite directions in separate beam pipes – two tubes kept at ultrahigh vacuum. They are guided around the accelerator ring by a strong magnetic field maintained by superconducting electromagnets. The electromagnets are built from coils of special electric cable that operates in a superconducting state, efficiently conducting electricity without resistance or loss of energy. This requires a large cryogenic system to cool the magnets to -271.3°C.

Today CERN not only design, construct and operate world class machines such as the LHC for basic science research but by doing so it establishes models for multicultural and multidisciplinary organizations bringing together people from all over the world. In order to achieve the required performances CERN physicist and engineers have to push the limit of the available technologies and invent new. The results of this work is development of applied science and everyday life application spin offs such as the World Wide Web, PET (Positron Emission Tomography) and MRI (Magnetic Resonance Imaging), all of which came out of basic science conducted at CERN.

After the discovery at the LHC of the Higgs particle in 2012 allowing the award of the Nobel prize for physics for its theorization, CERN is collecting further data to study in detail the Higgs particle and its interactions while preparing for a planned machine upgrade to increase further the luminosity and therefore the performances of the accelerator. To complement these activities and pave the road to new physics and discoveries CERN has also started to work within international collaborations for future larger and more powerful machines.

# Cryogenics at CERN: Past, Present and Future Developments

L. Serio

*Technology Department, CERN, 1211 Geneva 23, Switzerland*

luigi.serio@cern.ch

***Abstract*—**CERN is the European Organization for Nuclear Research located on the French-Swiss border near Geneva. Its mission is to enable international collaboration in the field of high-energy particle physics research and to this end it designs, builds and operates particle accelerators, the associated experimental areas and various test facilities for the main components. The flagship of this complex is the Large Hadron Collider (LHC).

Particle accelerators, detectors, experimental areas and test facilities are largely based on superconducting technology and therefore require significant - in size and complexity - cryogenic systems to produce and distribute efficiently and reliably the cooling power required to maintain superconducting devices at their nominal operating temperatures and rapidly recover from any disturbances.

CERN has been designing, constructing and operating cryogenic installations for several decades and continuously adapted and improved their efficiency and performances.

CERN's installations are located on the ground and in underground caverns and tunnels and distributed over a radius of about 4 km centered on one of the two main sites and over the French - Swiss border.

The cryogenic installations and equipment are mainly based on state-of-the art industrial components developed with industry over the years and older installations consolidated and upgraded as required according to the physics and research program evolution. The installations comprise also very specific low temperature components and operate with various cryogenic fluids (LHe, LN2, LAr, LKr). The main installations provide cooling to the following cryogenic users: the LHC accelerator and its detectors, other accelerators and detectors, the test areas infrastructures and the central helium liquefier to distribute liquid helium to site users. The present total helium cryogenic refrigeration capacity well exceed 160 kW @ 4.5 K and more than 20 kW @ 1.9 K, distributed over a total integrated length of about 30 km.

The largest installation and equipment can be found in the LHC complex to provide cooling of 27 km of superconducting magnets operating at 8.3 T in a superfluid helium bath at 1.9 K. It consists of eight pairs of cryogenic plants of 18 kW @ 4.5 K and 2.4 kW @ 1.9 K serving each 3.3 km long sectors via compound cryogenic distribution lines as well as the associated infrastructure to manage an inventory of more than 150 t of helium and a distribution of more than 10'000 t of nitrogen per year. The LHC has also two large superconducting magnets detectors, ATLAS and CMS, with 3 dedicated helium refrigerators for a total capacity of 10.3 kW @ 4.5 K as well as a nitrogen refrigerator.

Today CERN cryogenic group is not only continuously operating the installations to serve the Organization research program but also preparing the design for the performance increase of the LHC machine and performing studies to prepare the conceptual design of new future and more powerful particle accelerators.

# Fiber Bragg Grating Sensors for Cryogenics and Superconducting Magnet Applications

Rajinikumar Ramalingam

*Institute of Technical Physics, Cryogenics Division, Karlsruhe Institute of Technology, Campus North, Germany.*
rajini-kumar.ramalingam@kit.edu

***Abstract***—The ability to provide real time information of superconducting (SC) magnets is an important diagnostic process for effective design, construction and protection of the SC magnet. There are many parameters like current density, magnetic flux, critical temperature, problems of buoyancy effects, transverse temperature gradients, and stress distributions which are involved in an optimised SC magnet design. Knowing the temperature and stress distribution (TSD) inside the SC magnets could help the magnet designer to identify the exact location of the hotspot generated and its direction of propagation, magnitude of the Lorentz force developed in the winding of the SC magnets. Based on this information, the magnet designer can improve the design of the SC magnet by modifying the material, routing the cooling channel in the required place, improve the winding to reduce the stress and so on.

A considerable theoretical effort was dedicated to understand the complex physical phenomenon associated with SC magnets. Even though the theoretical analysis seems to be very promising, experimental validations to support the theoretical investigations were missing, and hence, could not give the exact behavior of the thermodynamic parameters inside the SC magnet. The problem in validating the thermodynamic parameters experimentally is due to the unavailability of the suitable sensors that could be integrated in the SC magnets for accurate and reliable measurements.

Electrical strain gauge (ESG), diodes and many other conventional electro mechanical sensor systems that could be employed for the above said problems, are susceptible to the electromagnetic interference (EMI). In addition, the number of sensors required for long SC cable in conduit (CICC) will be more to get the signal TSD. Also, the risk involved in introducing electrical wires inside the SC magnets makes them unsuitable candidate for the needed measurement system.

Use of Fiber Bragg Grating (FBG) sensors is very appealing for sensing the TSD in superconducting magnets because of their miniature size and the possibility of having many sensors in a single fiber by wavelength division multiplexing (WDM) scheme. In this talk, I specify the design and technology requirements to adapt the FBG sensor concept for low temperature and superconducting magnet applications. Initial experiments, which demonstrate the properties of glass FBG at low temperatures, are reported along with some applications.

# Metal Hydride Based Thermal Management Systems

P. Muthukumar

*Indian Institute of Technology, Guwahati,India*
pmkumar@iitg.ernet.in

***Abstract*—**Dry (solid) sorption systems are attractive competitors to wet (liquid) sorption systems in providing useful cooling and heating outputs. Among the dry sorption systems, those based on the absorption/desorption of hydrogen to/from metal alloys offer several advantages such as low grade thermal utilization, energy efficient, environment friendliness, noise free and vibration less operation, compact in construction, etc.. In recent years many attempts have been made to develop metal hydride based heating and cooling systems. Major applications are seen in air-conditioning for buildings and automobiles, thermal storage, thermal up gradation, etc. In this paper, an overall view of research and development works on metal hydride based thermal management systems carried out at IIT Guwahati over a decade is presented.

The performances of metal hydride based thermal management systems depends mainly on the rate at which hydrogen is absorbed / desorbed to/from metal hydride reactors. Generally thermal models are employed to predict the rate of hydrogen absorption and desorption characteristics. Predicted the performances of metal hydride based simple and advance cooling systems employing coupled heat and mass transfer models. Based on the thermal models, optimized reactors designs for several applications have been designed and developed. Fabricated several pre-industrial scale prototypes of hydrogen storage reactor of about 100-200 g hydrogen storage capacity for automobile application and their performance have been tested at different operating conditions. Developed several prototypes of metal hydride based hydrogen compressor and heat transformer. Using a single-stage heat transformer, a heat input of 120 °C has been upgraded up to 170 °C. With double – stage heat transformer, the same heat input was upgraded up to 210 °C. Developed the several prototypes of metal hydride based single and double-stage hydrogen compressors and achieved a maximum compression ratio of 14 utilizing the heat input in the order 120-140°C. Recently, a working prototype of compressor driven metal hydride based cooling systems have been built and tested. At the operating conditions of 15 °C refrigeration temperature, the reported maximum COP was 2.7.

# Structural Technologies for Space Systems

A.K.Asraff

*Liquid Propulsion Systems Centre, ISRO, Trivandrum,India*

akasraff@yahoo.com

***Abstract***—The Liquid Propulsion Systems Centre is responsible of developing and delivering liquid, semi-cryogenic and cryogenic propulsion systems viz. stages and engines for the launch vehicle programmes of ISRO. The Structural Dynamics & Analysis Group takes care of all CAD modeling, structural analysis/simulation/material modeling and slosh engineering related activities of the Centre to support the above goals. Some of the challenging structural technologies implemented/developed/being developed at SDAG are briefly discussed below:

**Computer Aided Design:** SDAG has a well-equipped CAD facility consisting of a number of high power graphic workstations running SIEMENS-NX solid modelling software. The facility caters to semi-cryogenic and cryogenic engine/and stage modeling activities. These models serve the purpose of (i) preparation of fabrication drawings (ii) evaluation of mass properties of various subsystems of the stage viz. weight, mass moment of inertia, centre of gravity etc. (iii) design of routing of pipelines and their clamps/fixtures/brackets (iv) positioning of various subsystems (v) visualization etc.

**Structural Analysis:** The team handles all structural analysis activities of the Center and takes part actively in ensuring the structural integrity of various subsystems of the stage such as liquid propellant tanks, high pressure gas bottles, engines, thrust transfer structures, gas generators, thrust chambers, nozzles, preburners, turbines, turbopumps, control components, electronic boxes, pipelines, clamps, fixtures, brackets, bolted & welded connections etc.

Structural simulations are being done using ANSYS and ABAQUS finite element analysis codes implemented in high speed workstations and a server. Computational Fluid Dynamic studies are also being performed using the CFX code. Analysis support is provided at all stages of development viz. during preliminary design, design of subscale versions of different products, preliminary design verification tests, structural tests at the nominal and uprated/downrated regimes of operation, acceptance and qualification tests, margin demonstrations tests etc. Design optimization is also being done regularly to reduce weight of structures. Current analysis types being handled are: (i) linear and nonlinear structural analysis (ii) thermo-structural analysis (iii) material nonlinear analysis (iv) natural frequency analysis, harmonic response analysis, random vibrations, transient dynamics, shock response spectrum analysis (v) CFD analysis (vi) linear & nonlinear buckling analysis (vii) fracture & fatigue analysis etc.

**Material modeling:** The Group has recently established a high temperature Creep-Fatigue laboratory to evaluate the tensile, creep and low cycle fatigue properties of different metallic and non-metallic materials being used in engines and stages. Tests are being done at ambient and elevated temperatures as high as $1500^{o}$C. An environmental chamber enables testing in vacuum or flowing argon in order to eliminate high temperature oxidations of metals. Many tests have been completed for ferrous and non-ferrous metals and the results used for their constitutive modeling in tension, fatigue and creep.

**Slosh engineering:** A full-fledged slosh laboratory has been functioning under the Group for more than two decades. Vibration tests are done on scaled down models of propellant tanks made using a transparent material like Perspex to experimentally determine the forces, moments due to sloshing of propellants observed in partially filled tanks. Wall damping can also be evaluated by these tests. Equipment available are (i) a single DOF slosh test rig (ii) a two DOF slosh test rig (iii) Pitch/Yaw moment of inertia test rig (iv) Roll moment of inertia test rig etc. Apart from this activity, numerical evaluation of different slosh parameters for liquid propellant tanks/satellite tanks of all launch vehicle missions are also being done on a routine basis and passed on to the respective mission teams to incorporate in their On-Board Computer logic. Design of antislosh baffles is also done wherever necessary in order to impart additional slosh suppression.

**Product development:** Structural analysis/design/optimization support for the development of complex/special products is also extended by the team. Examples are (i) design, development, qualification and acceptance of a new kind of polymeric material called Polyimide for cryogenic pipe lines of rocket stages, (ii) structural design of a Carbon-Carbon fibre reinforced composite nozzle for one of the cryogenic engine thrust chambers.

# ISRO's Programme – An Overview

Shajiha M

*Liquid Propulsion Systems Centre, ISRO, Trivandrum, India*

m_shajiha@lpsc.gov.in

***Abstract***—ISRO's vision envisages harnessing space technology for national development, while pursuing space science research and planetary exploration. Over the years, Indian space programme made outstanding progress in mastering critical technologies and witnessed significant milestones in space exploration. This lecture provides glimpses of Indian space programme with highlights of launch vehicles (PSLV, GSLV & LVM3) and satellite missions for communication, navigation, earth observation and space science studies including India's maiden venture beyond earth orbit in its Chandrayaan 1 and Mars Orbiter mission. Critical technology demonstration missions like space capsule recovery experiment and crew module recovery experiment for future human space flight, reusable technology demonstrator etc. is also touched upon. Future plan for development of heavy lift launchers and advanced science missions such as lunar lander, ground based infrastructure, space industry, academia and international cooperation etc. is also included in this lecture.

# Solid Propulsion System: End To End Capability

S.S Vinod

*Vikram Sarabhai Space Centre (VSSC), ISRO, Trivandrum, India*
ss_vinod@vssc.gov.in

***Abstract***—Ever since the first flight of the sounding rocket from Thumba, solid motors has been synonymous with the progression of propulsion technology in ISRO. The progressive development made in the realms of solid propulsion during SLV and ASLV phases, made solid motors the obvious choice as propulsion units for PSLV and GSLV. Host of propulsion and other technologies were developed during the PSLV programme in the solid propulsion area and efforts were also made to indigenously develop materials and processing capabilities within ISRO and also with the support of industries and R&D institutions. Complementing the efforts in design and development, the analysis capabilities and non destructive testing capabilities also witnessed considerable development during this phase. Major infrastructure and facilities were established for processing the subsystems, to realise the motors, for carrying out the assembly operations and also for carrying out evaluation tests like structural tests, ground firing etc.. Efforts are also undertaken to improve the existing propulsion modules in terms of ballistic performance, mass fraction, reliability and cost. Thus today, ISRO has established end to end capabilities for designing, developing and realising Solid Propulsion Systems capable of performing as specified by any launch vehicle mission.

# Surface-tension-driven Cell Migration: A New Mechanism of Force Generation for Cell Propulsion

Jung Kyung Kim[#1]

[#]*Associate Professor, Department of Mechanical Engineering, Kookmin University*
*Seoul 02707, Republic of Korea*
[1]jkkim@kookmin.ac.kr

***Abstract—*** Although advancement in molecular biology during past decades enables us to elucidate the dynamic characteristics of biological systems at the molecular level, dynamic behaviors of physical or mechanical properties have not been fully addressed. As the systems approaches are actively adopted in biology, studies for revealing the link between physical dynamics and corresponding molecular mechanism will be crucial to better understanding of the inherent complexity and dynamics of biological phenomena. From the fluid dynamics point of view, it presents an opportunity to expand the definition of biofluid dynamics to study not only macroscopic flow in cardiovascular or respiratory system, but also molecular transport at the cellular or subcellular level. Surface tension is a dominant force in small scale. There have been some evidences which suggest the regulating role of surface tension in cellular machinery. My current aim is to find the role of surface tension in spreading and self-propulsion during cell migration by applying fluid dynamics approaches to describing the motion of droplets and thin films on substrates. Cell migration involves transient formation of membrane protrusions (lamellipodia, filopodia, blebs) at the leading edge of the cell that are thought to require rapid local changes in ion fluxes and cell volume, likely accompanied by rapid transmembrane water movement. Although previous studies found that surface tension is a regulating factor in cell migration, we still need a generalized explanation of the force generation mechanism. Various cells use surface tension gradient as a self-propulsion mechanism. Surface-tension-gradient-driven motion can give a foundation of the unifying theory for cell migration and other phenomena relating to cell motility, such as cytokinesis, intracellular vesicle transport, and bacterial colony dynamics.

# CONTRIBUTED PAPERS

# Development of a 100 N Liquid Bipropellant Thruster for Crew Module Atmospheric Re-entry Experiment (CARE) Mission

Ajith B.[1], M. Ponnuswamy[2], C. Rajeev Senan[3], P. Arunkumar[4]

*Spacecraft Engines Division, Liquid Propulsion Systems Centre, Indian Space Research Organisation, Valiamala, Trivandrum-695 547, India*

[1]b_ajith@lpsc.gov.in

[2]m_ponnuswamy@lpsc.gov.in

[3]c_rajeevsenan@lpsc.gov.in

[4]p_arunkumar@lpsc.gov.in

***Abstract* - Low thrust level engines which can deliver small impulse bit are very much essential to provide better controllability of spacecraft. A 100 N liquid bipropellant thruster with Nitrogen tetroxide (NTO) and Mono-methyl hydrazine (MMH) has been developed by Liquid Propulsion Systems Centre (LPSC) of Indian Space Research Organisation (ISRO) to have inflight control of the body rates for crew module during atmospheric re-entry. The thruster comprises of a coaxial swirl type injector, ablative cooled nozzle with a solenoid operated flow control valve. Thrusters were qualified to meet the extreme conditions. At normal supply pressures it delivers a specific impulse more than 220 s and has performed successfully in the recent CARE mission flight**

***Key words* – ISP, Minimum impulse bit**

## I. INTRODUCTION

Crew module Atmospheric Re-entry Experiment (CARE) was the first step towards the Human Space-flight Programme (HSP), which is one of the most ambitious missions of the Indian Space Research Organization (ISRO). Mission studies have projected the need for an active reaction control system for successful descent flight of the module. As part of this mission, the task of design and development of 100N bipropellant thrusters was taken up by LPSC.

LPSC of ISRO is responsible for the development of liquid bi-propellant thrusters for ISRO's launch vehicle and spacecraft programme. It has successfully developed and qualified Liquid Apogee Motor (LAM) and Attitude and Orbit Control System (AOCS) thrusters for its geostationary satellite (GEOSAT) programme.

As stated earlier, these 100N thrusters are designed for the Reaction Control System (RCS) of the Crew Module. The Reaction Control System is used for the back angle control of the Crew Module (CM) during atmospheric re-entry and provides damping effect against the induced pitch and yaw instabilities. The roll of the vehicle is controlled by altering the lift factor of the vehicle. Numerous missions similar to HSP have been attempted by various other space agencies and the requirement of the RCS for the CM varies from 100N to 440N.

Various propellant combinations such as $H_2O_2$ (mono-propellant), Hydrazine (mono-propellant), GOX-liquid ethanol (bi-propellant), NTO-MMH (bi-propellant) had been used globally depending upon the mission, weight of the CM, and propellant mass budget. In this mission NTO/MMH bipropellant combination is employed. This paper briefly describes the development, qualification and mission performance of 100N thrusters.

## II. MISSION REQUIREMENTS

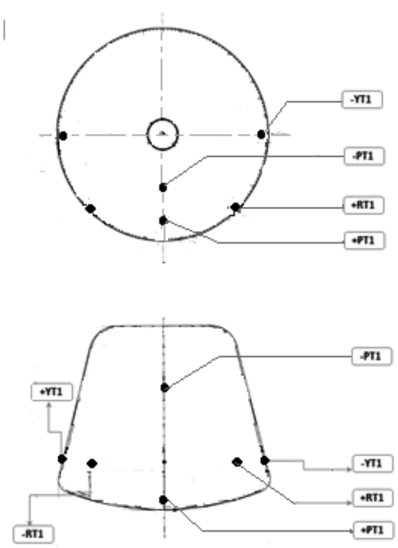


Figure 1 Thruster position in mission

The thrusters will be aiding the three axis control of the module during atmospheric re-entry which will be at an altitude of ~120km. It will be operational till 80km altitude in both continuous and pulse mode of operation based on Navigation Guidance & Control (NGC) commands. The thrusters are to be placed between the outer wall of the CM and inner pressurized chamber.

Two thrusters each for pitch, yaw and roll control were mounted on to the module as given in figure 1.

## III. THRUSTER DESCRIPTION

The 100 N thruster developed is a pressure fed bi propellant thruster with Nitrogen tetroxide /Mono Methyl Hydrazine propellant combination. This thruster comprises of a single element coaxial swirl type injector made of stainless alloy connected to the thrust chamber through a bolted joint. The flow to the thruster is controlled by a pair of thruster control valves mounted on the injector.

As the thrusters are in submerged configuration, cooling of the chamber has to be met with ablative liners encompassed in a stainless steel casing. Film cooling by virtue of swirl design of the injector also aids in thrust chamber cooling to a greater extent. The thermodynamic properties of the propellant at the mixture ratio is derived from generic software[1] Using these thermodynamic properties the thrust chamber dimensions were arrived at from first principles [2-3].

The injector flow dimensions for obtaining the required flow were finalised based on experience gained from the development of similar small thrust bipropellant thrusters and empirical relations as mentioned by Lefebvre et.al [4]. As most of the mission operations planned was in pulse mode, the thrusters have to operate at a faster response and should deliver better impulse repeatability at lower electrical pulse widths. This is attained by controlling the injector manifold volume down-stream of thruster control valve. The thruster operation is carried out at altitude of 90-100km and hence the nozzle expansion ratio was limited to 5.85:1.

Three different versions of thruster with three nozzle extension ducts were developed to suit the requirements of pitch, yaw and roll separately. The pitch and yaw ducts were normal while the roll thruster was scarfed to match the profile of the structure. The different types of thrusters are given in figure 2-3.


Figure 2 Pitch and Yaw thruster assembly

Figure 3 Roll thruster assemblies

The thruster specification is given in table-1.

TABLE 1
SPECIFICATION

| | |
|---|---|
| Thrust (Vacuum), N | 100 +/- 5% |
| Propellant combination | NTO/MMH |
| Mixture ratio by weight (O/F) | 1.65 +/- 0.05 |
| Specific impulse, seconds (minimum) | 225 (steady state)<br>200 (for >100ms EPW) |
| Minimum impulse bit for 100ms EPW, Ns | 9 |
| Weight (max), kg | 5.3 |
| ON response, ms | 130 |
| OFF response, ms | 170 |

## IV. DEVELOPMENT AND QUALIFICATION

100 N thruster development programme was carried out in a fast track mode within a period of 6 months. These thrusters were proposed to be used as reaction control thrusters. The development tests were carried out in two phases.

1. Sea level development tests
2. High altitude development tests

Sea level development tests itself were carried out in two different phases. The first phase consisted of testing the injector with a heat sink chamber and second phase tests were carried out with an ablative chamber. Both the chambers were of bolted flanged version. The first phase tests were done for a cumulative duration of 71s. The second phase tests were done on two injectors for a cumulative duration of 59s and 81srespectively to meet the approved qualification test matrix requirement.

The major objectives of qualification were to demonstrate the performance characteristics over a wide range of operating conditions.

First phase of qualification was done in a combined mode comprising continuous and pulse mode in a single shot. The detailed qualification test matrix is given in table 2.

TABLE 2
PHASE 1 QUALIFICATION TEST MATRIX

| **Test no** | **Pulse duration, s** | **No of pulses** | **Remarks** |
|---|---|---|---|
| **1** | 12 | 1 | Continuous |
| **2** | 4 | 1 | |
| **3** | 3 | 1 | |
| **4** | 1s ON / 1s OFF | 5 | 50% duty cycle pulsing |
| **5** | 0.25s ON/ 0.25s OFF | 4 | |
| **6** | 0.1s ON/ 0.1s OFF | 10 | |

In phase 2 qualification, extended duration test at nominal injection pressure as well as at lower and higher supply pressures were done. The details of the qualification matrix are given in table 3. All tests were done with mixture ratio maintained at 1.65

TABLE 3
PHASE 2 QUALIFICATION TEST MATRIX

| **Test** | **Duration s** | **Remarks** |
|---|---|---|
| **1** | 10 | Lower injection pressure |
| **2** | 10 | Higher injection pressure |
| **3** | 18 | Nominal injection pressure |

The qualification firing in simulated high altitude condition includes test with extended scarfed nozzle attached. Due to scarfing of the nozzle the thrust developed in the thrust axis is reduced by around 50%.

The major tests in the flight acceptance matrix are steady state firing for 12s, three pulse trains of 5 pulses each in three critical ON modulation pulse widths.

**Performance Characteristics**

The 100 N thruster operates at a nominal supply pressure of 1.15 MPa. The variation in thrust with supply pressure is shown in figure 4.

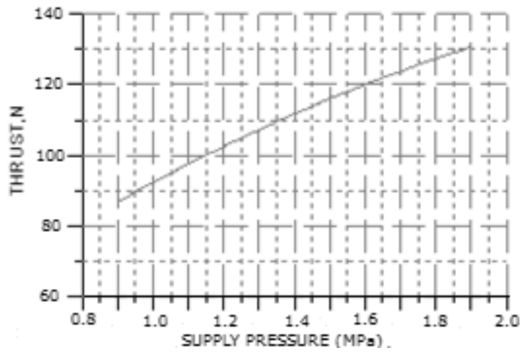


Figure 4 Thrust variation with pressure

The steady state specific impulse (ISP) achieved in qualification hardware at different supply pressures is shown in figure 5.

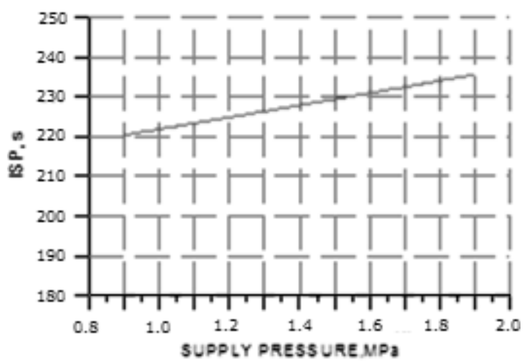


Figure 5 ISP variation with pressure

As feed pressure increases, the specific impulse also increases. This increase is due to better atomization of propellants at higher supply pressures.

The demonstrated specific impulse at rated supply pressure for 12 hardware realized are shown in figure 6.

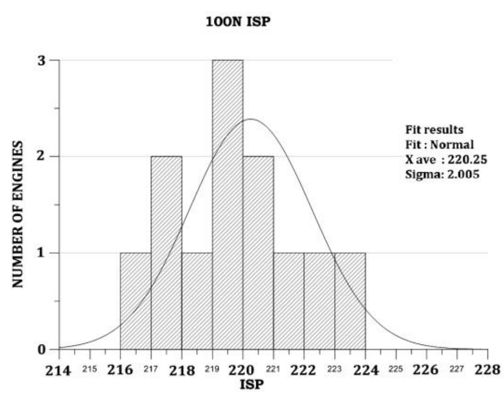


Figure 6 ISP of realised engines

A standard deviation of 2sec is observed of the whole spread of thrusters which is about 1% and is well below the specification of ± 5%.

The minimum impulse bit for 100ms Electrical pulse width (EPW), at rated supply pressure, for the realised engines is given in figure 7. It is observed that the average minimum impulse bit (MIBT) was 8.74Ns with a standard deviation of 0.88 which is also well within the acceptable specification limit.

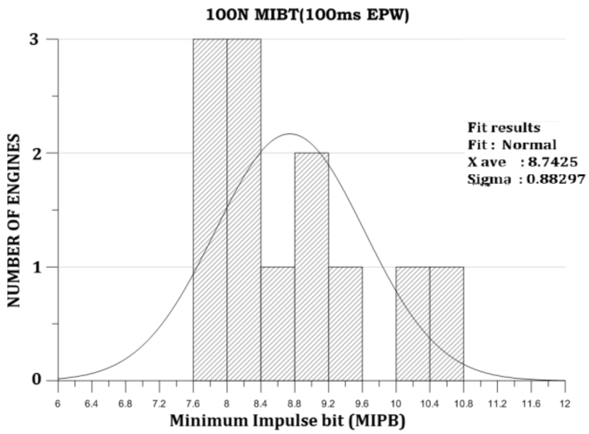


Figure 7 MIBT spread of realised engines

The spread in ISP is due to the sensitivity of flow passages to surface finish and dimensional tolerances. This affects the vaporisation of the propellants and combustion and ultimately on ISP.

Proper instrumentation was made to measure the temperatures at six locations on the hardware at six locations on the hardware as shown in figure 8.

The chamber skin temperature measured in the long duration test was 38$^0$C in both qualification hardware, showing the effectiveness of the silica phenolic ablative lining provided for cooling in the chamber. Thus the stringent requirement of keeping the casing below 40$^0$C for human space programme is met. A typical plot of the chamber temperature measurement is given in figure 9.

The pulse mode tests were carried out with different electrical pulse widths (EPW) with a duty cycle of 50%. The variation of impulse bit at different EPW at normal supply pressures is given in figure 10.This shows a behaviour delivering higher MIBT for longer ON pulse width as expected.

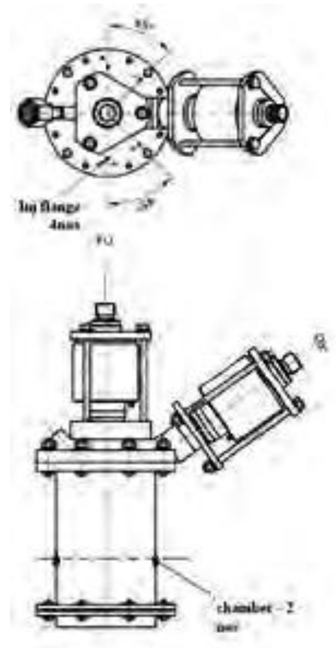

Figure 8 Temperature measurement location

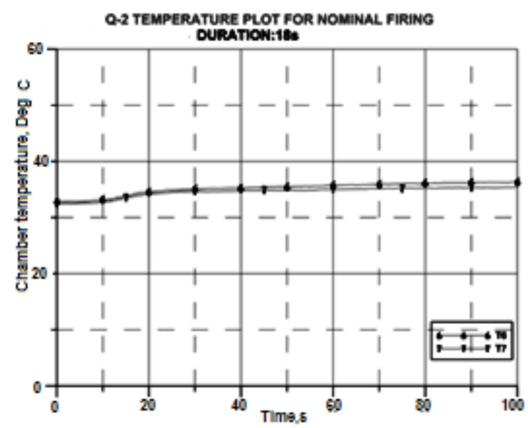


Figure 9 Temperature plot of 1000s firing

Thrust per pulse width has shown a variation as given in figure 11. At lower pulse width, due to insufficient supply of the propellant for combustion, low thrust is developed while at higher pulse width of 100ms and above, the thrust variation is almost negligible.

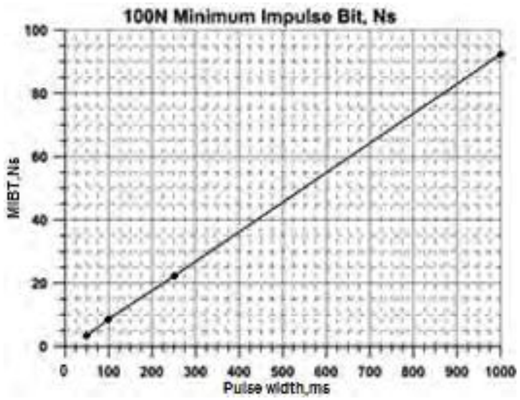


Figure 10 MIBT variations w.r.t EPW

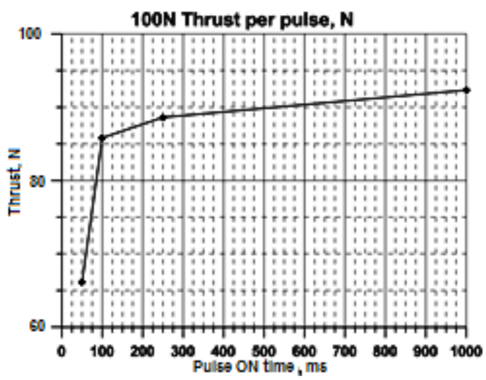


Figure 11 Thrust per pulse width variation

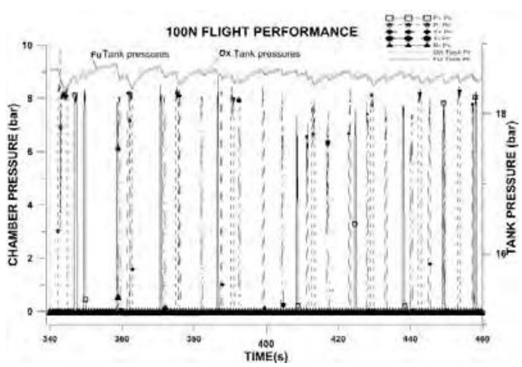


Figure 12 Thruster performances in mission

## V. MISSION PERFORMANCE:

After successful completion of development and qualification, 100 N thrusters were used in the CARE mission.

The performance and hardware temperatures experienced on board are comparable to that of ground test values and the thruster performance was normal.

The chamber pressure measured during the mission for the entire duration is given in figure 12.

## VI. CONCLUSION

LPSC/ISRO has successfully developed a 100N thruster for Human Space-flight Programme. The capability of this thruster to perform in extreme condition on board was demonstrated by the qualification tests.

Performance mapping of thrusters were carried out over a wide range of parameters. At nominal operating condition of 1.65 MPa it delivers a specific impulse more than 220s in continuous mode. Pulse mode tests were carried out over a spectrum of duty cycles and temperatures were within the acceptable limits. Six thrusters were realised and delivered to the project. On board performance of all the thrusters are normal.

## ACKNOWLEDGEMENT

The authors gratefully acknowledge the encouragement and support given by Shri. Somanath S, Director, LPSC and wish to thank Shri. Shajimon A Cherian, GD, ESEG for unceasing support in the development of 100N thrusters. The authors also thank all the personnel involved in the fabrication, and testing at various stages for their invaluable support given for the development of this thruster.

## REFERENCES

[1] Gordon Sanford and Mcbride, *Computer programme for calculation of complex chemical equilibrium compositions, rocket performance, incident and reflected shocks and Chapman- Jouguet Detonations*, NASA SP 273, Vol 1, October 1994

[2] Dieter k. Huzel and David Huang , *Design of Liquid Propellant Rocket Engine* NASA SP 125, NASA, 1967

[3] George P. Sutton, *Rocket Propulsion Elements*, Wiley Publications, 8th edition, January 2010

[4] Arthur H. Lefebvre , *Atomisation and Sprays*, Hemisphere, Newyork, 1989

# High Performance Thermal Protection Ablative Composites for Solid Rocket Motors

Mohankumar.L[#1], Anandapadmanabhan.E.N[#2], Chakravarthy.P[*3]

[#]*Composites Entity, Vikram Sarabhai Space Centre, ISRO*

*Thiruvananthapuram-695013, Kerala, India*

[1]l_mohankumar@vssc.gov.in

[2]en_anandapadmanabhan@vssc.gov.in

[*]*Department of Aerospace Engineering*

*Indian Institute of Space Science and Technology (IIST), ISRO,*

*Valiamala, Thiruvananthapuram, Kerala, India*

[3]p_chakravarthy@iist.ac.in

***Abstract*— Solid rocket motor nozzles encounter extremely hostile conditions during the motor operation. The high temperature, pressure, velocity of hot exhaust gases, heat flux, particle impingement of the solid propellant particles etc. contribute to harsh environment inside the nozzle. High temperature resistant metals or alloys alone cannot survive the operating conditions in a solid rocket motor. While the metallic structure provides the necessary structural capability, high performance composite materials are required for thermal protection. The property of ablation of certain high performance composites is utilised to protect the metallic backup structure from thermal degradation during the firing of the solid rocket motor. Ablative composites generally use Carbon or Silica as the reinforcement and phenolic resin as the matrix resin. This paper explains the structure and configuration of solid rocket nozzle and deals with the desirable properties of the components. The process of ablation in a nozzle and how it protects the metallic backup structure from the high heat flux, pressure and high velocity of hot exhaust gases is explained. The experimental details of synthesis, processing and characterisation are explained. The different techniques of inspection, Non-destructive testing and property evaluation are discussed. Finally, the system for qualification of the ablative nozzle for use in a solid rocket motor nozzle is discussed.**

***Keywords*— carbon, silica, phenolics, ablatives, composites, char, erosion.**

## I. INTRODUCTION

Solid rocket motors are used in many satellite launch vehicles as boosters and lower stage motors. A solid rocket motor invariably consists of a motor case filled with solid propellant, an igniter for igniting the propellant and a convergent-divergent nozzle. The igniter fires the propellant which burns at a predetermined burn rate generating large quantities of exhaust hot gases which flow through the nozzle. The chemical energy of the propellant is converted into heat energy which in turn gets converted into kinetic energy while expanding through the convergent-divergent nozzle. The exhaust gases are of very high temperature and hence the nozzles should have adequate thermal protection on their inside surfaces to prevent their degradation during operation. The design of the nozzle involves designing the aerodynamic inside contour, thermal design for the thickness of the nozzle lining material and structural design to take care of the mechanical loads during the firing of the motor. The internal contour and the dimensions have to remain stable or should erode at a known rate to ensure predictable and acceptable motor behaviour. To ensure these pre-requisites, high performance ablative composite materials are to be processed and used in solid rocket motors.

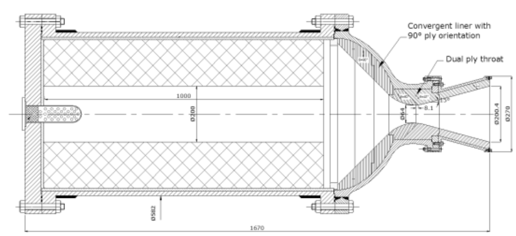


Fig. 1 A typical solid motor showing the igniter, motor case and nozzle

Figure 1 shows the cross-section of a typical solid rocket motor. The outer body of the motor case and the nozzle is made of metal. The motor case is lined with rubber insulation and the propellant is cast inside the case. The convergent-divergent nozzle is lined with high performance ablative composites which protect the metallic backup structure from the high temperature, high velocity exhaust gases expanding through the nozzle. A nozzle increases the kinetic energy of the propellant exhaust, thereby providing the necessary thrust augmentation.

This paper explains the process of ablation, salient features of ablative composites, development, processing, characterisation, testing and qualification of these high performance materials.

## II. Ablation and Ablative composites

### A. Ablation

Ablation is an orderly heat and mass transfer process in which a large quantity of heat energy is dissipated in a very short period of time by sacrificial loss of material at a rate which can be estimated. It is a very complex process including many physical and chemical transformations including phase changes like melting, vapourisation, sublimation and pyrolysis. Many endothermic reactions occur during the process.

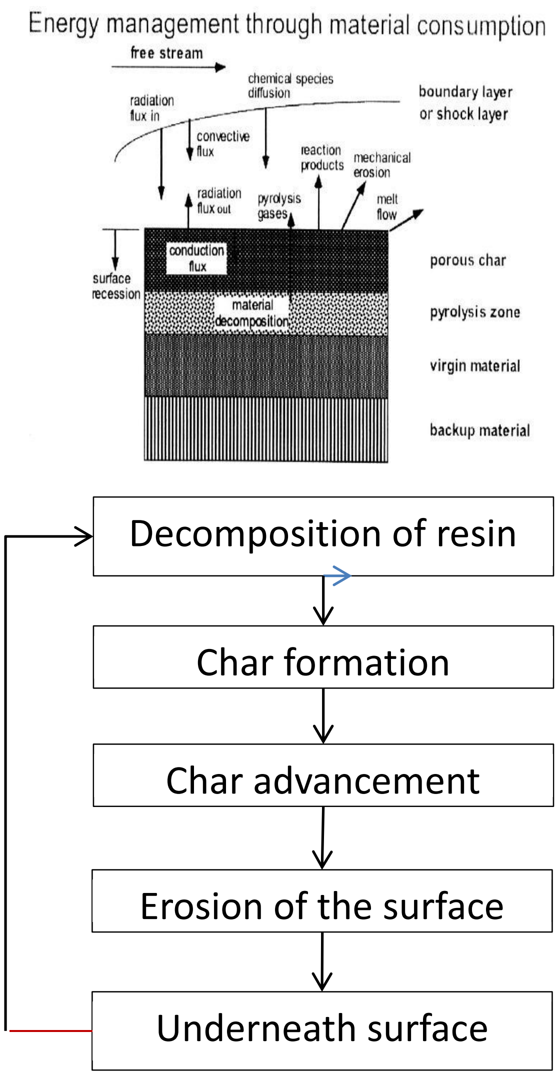


Fig. 2: The process of Ablation

When the ablative is subjected to a very high heat flux as the hot exhaust gases pass through the nozzle, the surface temperature increases rapidly. Due to the low thermal conductivity of the material, the temperature builds up on the surface rather than the heat getting conducted to the backup structure. As the temperature near the surface reaches the pyrolysis temperature of the resin in the composite, decomposition of resin takes place. This leads to the formation of char on the surface of the ablative. As time progresses, the extent of char increases or the char front advances into the thickness of the material. Then the surface material starts eroding; erosion of the material can be due to two reasons- one is because of the thermal degradation of the material and the other is mechanical erosion caused by metallic particle impingement due to the Aluminium particles of the solid propellant flowing along with the hot exhaust gases. As the layer on the surface erodes, the next layer gets exposed and the process continues.

During pyrolysis, the volatile gases evolving at the reaction zone finds its way through the charred zone taking away significant amount of heat. Similarly, melting of the resin as well as the fibres also consume some heat. With all these processes, a large quantity of heat is expended with sacrificial loss of material, thereby, protecting the metallic substrate from thermal degradation.

### B. Ablative Composites

By definition, Composite is a materials system composed of two or more physically distinct phases whose combination produces aggregate properties that are different from those of its constituents. Composites are heterogeneous at a microscopic scale but statistically homogeneous at a macroscopic scale. There is no chemical reaction between the constituents and their properties can be tailored to specific requirements.

Ablative composites are an elite class of composites which are made of high melting point fibers and polymeric resins with very high char yield. Commonly used reinforcements include carbon, graphite, silica, glass, asbestos etc and resins like phenolics, furfuryl alcohol etc.

An ideal ablative composite should possess high heat of ablation, high enthalpy of phase change, sufficient strength, high specific heat, high thermal shock resistance etc. At the same time, it should have low thermal conductivity, medium density, low molecular weight for the volatiles evolved during pyrolysis and as low an erosion rate as possible.

## III. Experimental

### A. Raw materials

Ablative composites were synthesised from phenolic resin as matrix and carbon fibres. Phenolic resin is synthesised from phenol and formaldehyde. The typical properties of the resin matrix are given in Table I.

Carbon fibers were used as the reinforcement. Rayon based Carbon fiber is preferred for Ablative applications as it provides lower thermal conductivity and higher Inter laminar Shear strength because of crenulated cross-section. Carbon fabric is made by weaving Carbon fibers with carbon content greater than 94%. This is made by successive carbonization of rayon. Polyacrylonitrile (PAN) and Pitch based carbon fabrics can also be used. 8 Harness Satin weave was chosen as the weave pattern considering the ability for ease of processing.

TABLE I
PHENOLIC RESIN PROPERTIES

| Sl. No | Important properties | |
|---|---|---|
| | **Parameters** | **Typical values** |
| 1 | Specific gravity at 30°C | 1.2 |
| 2 | Solid content, % | 63.5 |
| 3 | Viscosity at 30°C, cps | 250-300 |
| 4 | Degree of advancement, ml | 13.5 |
| 5 | Free phenol content, % | 5 |
| 6 | Free formalin content, % | 2 |

SEM images of Carbon fibers at 4000X are given below:

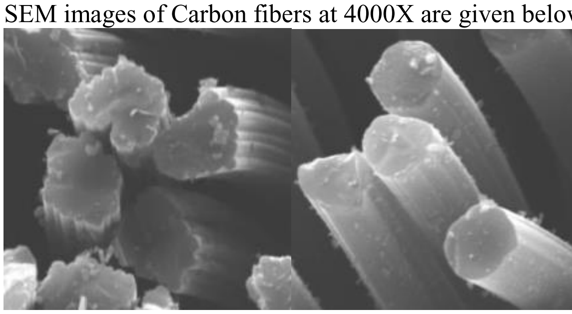

Fig. 3: SEM images of Carbon fibres showing crenulated cross-section

Typical parameter values of the carbon fabric used is listed below:

TABLE II
IMPORTANT PARAMETERS OF CARBON FIBERS

| Sl.No | Important properties | |
|---|---|---|
| | **Parameters** | **Typical values** |
| 1 | Carbon content, % | 94-96 |
| 2 | Sodium content, ppm | 600 |
| 3 | Ash content, % | 0.20 |
| 4 | pH | 8 |
| 5 | Breaking strength, kg/inch width | 80-100 |
| 6 | Areal density, gm/sq.m | 250-300 |
| 7 | Thickness, mm | 0.3-0.4 |
| 8 | Specific gravity | 1.75 |
| 9 | Thread count, ends/inch | 45-55 |

*B. Impregnation*

The carbon fabric was impregnated with phenolic resin. Initially, the fabric is dehydrated above 100°C to drive out the moisture. Then it is passed through a resin tank to absorb the resin. It is them passed through heating zones to advance the resin. The resultant material is called Carbon phenolic (CP) prepreg. The important parameters of the prepreg are,

TABLE III
IMPORTANT PARAMETERS OF CARBON PHENOLIC PREPREG

| Sl. No | Important properties | |
|---|---|---|
| | **Parameters** | **Achieved values** |
| 1 | Volatile content, (%) | 5.6 |
| 2 | Dry Resin content, (%) | 41.1 |
| 3 | Wet Resin content, (%) | 46.7 |
| 4 | Degree of advancement, Chang's index, (ml of water) | 25.6 |

*C. Processing of the liners*

The prepreg is cut into the form of plies using a template and are either stacked together or wound on a metallic mandrel. The prepreg layup is compacted either giving vacuum or in a hydraulic press to get good as-wrapped density.

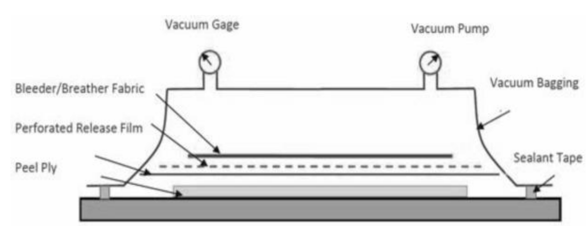


Fig. 4: Schematic of layup of prepreg

Fig.4 shows a schematic of the layup with bleeder/breather film, perforated release film and the vacuum bag in position. Perforated release film serves dual purpose; perforations allow the excess resin and volatiles to freely flow out of the liner and the release film prevents the unwanted adhesion of the liner to the mould. The bleeder material shall absorb the excess resin squeezed out of the liner. The vacuum bag is made from special grade polymer films capable of withstanding the curing temperature and pressure. For curing in Hydroclaves, impermeable high temperature resistant rubber bags with about 600% elongation are used.

*D. Curing or Polymerisation*

After layup is put in vacuum bag it was cured at 150$^{o}$C under pressure. Cross-linking of molecules of the polymer or polymerisation is achieved by curing under high temperature and pressure. Curing is done either in an oven, autoclave or hydroclave. In an oven, only heating is possible, whereas in an Autoclave/Hydroclave pressurisation is also done. The pressurising medium is air in an Autoclave which can go up to 10 bar pressure, while in a Hydroclave, pressure up to 70 bar can be applied since water is the pressurisation medium.

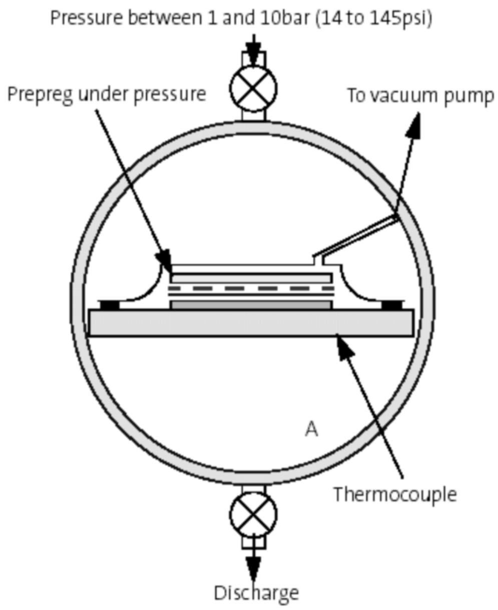


Fig. 5: Schematic of layup of prepreg placed in an Autoclave

## E. *Post Curing operations*

After curing, the ablative composite is machined to the required configuration using special tools. Polycrystalline diamond (PCD) or Tungsten Carbide tools were used due to the abrasive nature of the material.

## IV. RESULTS AND DISCUSSION

Dimensions of the required part were measured and Non-destructive testing was done to confirm that no defects were present in the liner. Common defects likely in ablative composites include delaminations, cracks, voids, porosity, resin lean lines, resin rich lines, resin starvation, resin patches, non-uniform resin distribution, waviness, wrinkles etc. Visual inspection, tap test and alcohol wipe test was done initially. This was followed by Ultrasonic inspection by Pulse echo and through transmission methods. Wherever the signal strength was less or suspected delaminations were reported, tangential radiography was done to rule out the presence of delaminations.

Co-cured specimens were tested for mechanical and thermal properties. Specimens were fabricated from the end rings of the liners as per ASTM standards and tested.

The test results are summarized in Table 4 and Table 5. Most critical thermal properties affecting the functional performance of the ablative composite are Heat of ablation and erosion rate at the service conditions. Heat of ablation and erosion rate were measured after subjecting the specimen to a heat flux of 750 Watts per unit area for 15 seconds. Specific heat and thermal conductivity were also evaluated. The achieved values are given below:

TABLE IV
THERMAL PROPERTIES OF THE ABLATIVE COMPOSITE

| | **Parameter** | **Achieved values** |
|---|---|---|
| 1 | Heat of ablation @ 750 W/sq.cm (cal/g) | 7250 - 8750 |
| 2 | Thermal conductivity (W/mK)- along ply | 0.45-0.51 |
| 3 | Thermal conductivity (W/mK)-across ply | 0.54-0.71 |
| 4 | Specific heat (J/kgK) | 849.5 |
| 5 | Erosion rate –along ply(mm/s) | 0.037 |
| 6 | Erosion rate –across ply(mm/s) | 0.033 |

Mechanical properties of the ablative composite are equally important as it has to withstand the pressure loads as well as the shear loads of the high velocity flow. Compressive strength, Inter laminar shear strength and Compressive modulus were evaluated. Since tensile loads are not experienced by the nozzle liners, tensile properties were not evaluated. The achieved values are given below:

TABLE V
MECHANICAL PROPERTIES OF THE ABLATIVE COMPOSITE

| | **Parameter** | **Achieved value** |
|---|---|---|
| 1 | Density (g/cc) | 1.440-1.456 |
| 2 | Compressive strength –along ply (MPa) | 246.94 |
| 3 | Compressive strength –across ply (MPa) | 390.02 |
| 4 | Compressive modulus –along ply (MPa) | 16.08 |
| 5 | Compressive modulus –across ply (MPa) | 11.87 |
| 6 | Inter laminar shear strength (MPa) | 27.07 |

## V. QUALIFICATION OF THE ABLATIVE COMPOSITE

After completion of the synthesis and characterization, the ablative composite is put into the actual operating environment. For this a subscale motor is designed and tested. New concepts are first qualified by conducting sub-scale hot tests. Test Simulation Motors (TSM) provide ideal platform for sub-scale tests. Pressure, temperature, strains, vibration and acoustic levels are measured in the hot test. Design margins on the nozzle are validated by post-test evaluation.

Dimensions and mass of the ablative liners are measured before and after the test to assess the mass loss, erosion rate etc. Elaborate instrumentation was carried out to collect data regarding the back wall temperature, pressure and strain during the operation. During the test, the ablative performed satisfactorily and all the back wall temperature measurements had read ambient values indicating that the ablative is capable of withstanding the operating conditions satisfactorily and thus can protect the metallic structure.

Detailed post-test evaluation was completed. Figure 6 shows a photograph of the subscale test in progress and Figure 7 gives the pressure-time trace for the static test indicating a satisfactory test. Figure 8 is a picture of the tested ablative surface. The eroded surface is clearly seen in this photograph.

Fig. 6: Subscale test for Qualification

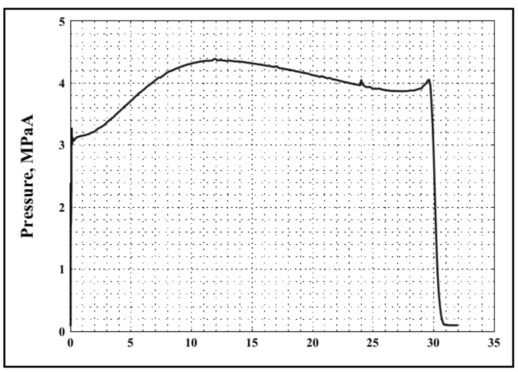


Fig. 7: Pressure-Time trace measured during the qualification test

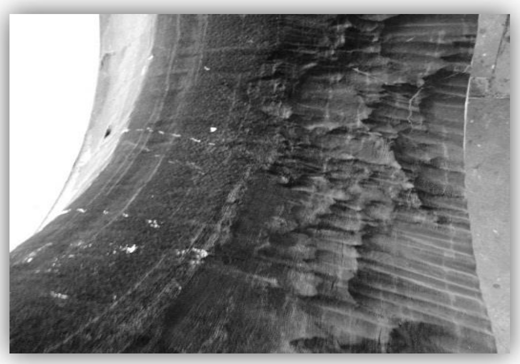

Fig. 8: Photograph of the ablative composite after the test

## VI. Conclusions

The development of high performance thermal protection ablative composites has been discussed in detail. The experimental details of synthesis and processing of carbon phenolic ablative composites are explained. The processed ablatives were characterized and all the critical properties have been evaluated. All the properties are meeting the required specifications. Inspection and Non-destructive testing of the components have been carried out to ensure the quality and reliability. Thus the material has been qualified for aerospace use in solid rocket motors.

## Acknowledgement

The authors gratefully acknowledge the permission, support, guidance and advice of Dy. Director and Director, VSSC for this developmental activity. We wish to thank the support rendered by the Non-Destructive testing division, Characterisation and testing division of VSSC for the timely testing and characterisation activities. Our sincere thanks to all the staff members of the processing section of Ablatives Division for their whole-hearted support in the synthesis and processing of the ablative composites during the experimental phase.

## References

[1] Sutton, K., *An Experimental study of a Carbon-phenolic ablation material*, NASA Technical Note NASA-TN-D 5930. (1970)

[2] Dr. M. Balasubramaniam, *Composite Materials and Processing,* CRC Press, USA, 2013.

[3] N. Winya, S. Chankapoe, C. Kiriratnikom., *Ablation, mechanical and thermal properties of fiber/phenolic matrix composites,* World Academy of Science, Engineering and Technology 69 2012

[4] Standard Test Method for Obtaining Char Density Profile of Ablative Materials by Machining and Weighing: ASTM E471 - 96(2011)

[5] T.L.Elegange and R.R. Bowman, *Nozzle fabrication for space shuttle solid rocket motor,* AIAA/SAE 14th Joint Propulsion Conference, July 1978.

[6] H.R. Clements and G.T. Ward, *Development of fabrication techniques for large solid booster nozzles*, AIAA 6th Solid Propellant Rocket Conference, Washington DC., February 1965.

[7] Mohan Kumar. L, Nikhil K Mawari, et al, *Development of Bias wrapping technology for Ablative liners in S139 Solid rocket motor,* INCCOM13 Proceedings, November 2014.

[8] Gutowski Timothy G, *Advanced Composite Manufacturing*, Wiley, 1997.

[9] Tomoko Sano (Editor), T. S. Srivatsan (Editor), Michael W. Peretti (Editor), *Advanced Composites for Aerospace, Marine, and Land Applications,* Wiley, 2014.

# Structural Design and Mass Optimisation of Grid Fin for Launch Vehicles

Ajayakumar A G [#1], Vipin G P [*2], Sarathchandradas [#3]

[#]*Department of Mechanical Engineering, SCT College of Engineering, Trivandrum, Kerala, India*

[1]ajayakumarriet92@gmail.com

[3]sarat_chandradas@rediffmail.com

* *ASMG, MVIT, Indian Space Research Organisation, Trivandrum, Kerala, India*

[2]vipin_gopalan@vssc.gov.in

***Abstract*— Grid fins (or lattice fins) are a type of flight control surface used on rockets and bombs, which consist of lattice shaped structure attached together to form a fin. The major advantage of such fins are, they can easily assembled to the launch vehicle and can be operated for stipulated time duration whenever required. The deployment mechanism imparts more dynamic loads on to the fin and so the structural dynamics play a vital role in its design. To get maximum stability, the fin mass should be minimum as possible by the functional point of view. But the structure should withstand all the static and dynamic loads for the operation period. The lattice structure makes the structure more complex as per the realization aspects. A metallic version of the grid fin structure is attempted to evolve a design methodology. The aero loads and its moments are taken as the design inputs and the structural design is carried out in this work. Modal analysis of structure is also carried out or the design. The finite element tool (ANSYS Workbench) is used for design optimization.**

***Keywords*— Grid fin, rockets, deployment mechanism, structural dynamics, modal analysis,**

## I. Introduction

The grid fin, also known as a lattice control surface or a wing with internal framework, can provide a missile with stability and control as well as a planar fin. Advantages of the grid fin over the conventional planar fins are higher strength to-weight ratio and lower hinge moment. Therefore it can contribute to mitigate the requirements for a control actuator of the fin. On the other hand, its higher drag is a significant disadvantage. The most common grid fin has a square grid pattern. Grid fins are widely used in Crew Escape Systems (CES) of manned space missions of many countries.

The Indian human spaceflight programme is a proposal by the Indian Space Research Organization (ISRO) to develop and launch the ISRO Orbital Vehicle, which is to carry a two-member crew to Low Earth Orbit. HSP requires a Crew Escape System (CES) which is employed for a rapid recovery of the crew in case of exigency at launch pad or during initial phase of the mission.To provide the required static aerodyna micstability at the time when Crew Escape System (CES) is activated, 4 numbers of Grid fins are used.

During the normal launch phase functioning of these grid fins as aero stabilizers are not required. Then they are stowed against the cylindrical body which helps to reduce overall dimension of the vehicle and minimize aerodynamic disturbance. In case of launch abort situation the four grid fins deploys to its desirable value for effective functioning.

In the current investigation, a metallic version (Aluminium alloy 2014-T6) of the grid fin structure is attempted to evolve in order to develop a design methodology. The aero loads and moments are taken as the design inputs and the structural design is carried out. The dynamic loads due to deployment are also checked with the design.

Initial grid fin configuration is taken from results of initial aerodynamic studies is shown in figure 1.1. Which consist of an outer rectangular fin box of 1500*1500*150 and an inner grid of intersecting small chord planar surfaces through which the air passes.

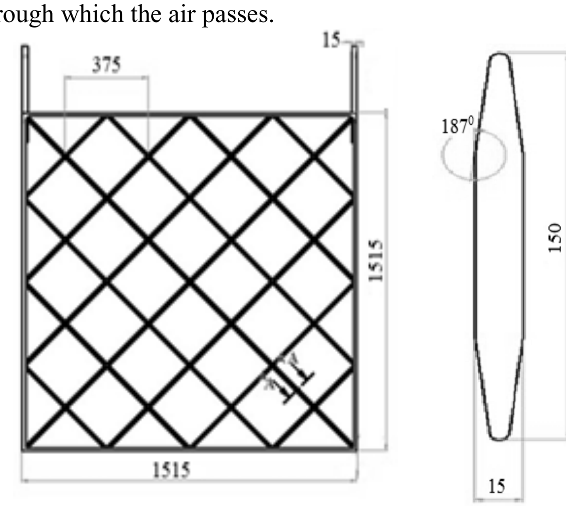


Figure 1.1. Grid fin geometry

## II. LOADS ON GRID FIN

The aerodynamic loads produced due to its structure are considered as static loads (Table 2.1).

TABLE 2.1
Loads on grid fin

| Rolling moment $M_R$ | Yawing moment $M_Y$ | Pitching moment $M_P$ |
|---|---|---|
| -62.59 kN-m | 28.73 kN-m | 2.57 kN-m |

In deployed condition of grid fin, its tendency to rotate about bottom hinge point is controlled by telescopic attachments. When the telescopic attachment makes the stoppage to deployment that will exert an impact load on to the fin. This effect is also studied in the present work and is considered as dynamic load. Figure 2.1 shows the conceptual arrangements of grid fin system.

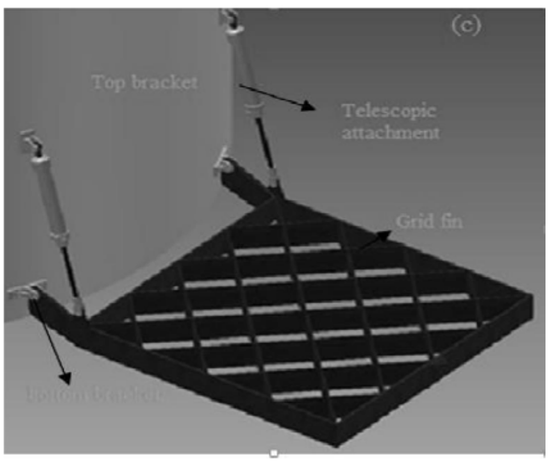


Figure 2.2. Grid fin configuration

## III. FINITE ELEMENT ANALYSIS

Finite element analyses were carried out for structural design of grid fin. Highest moment is taken as the first design load then checked for other loads too.

### *A. Rolling moment*

*1) Boundary conditions*

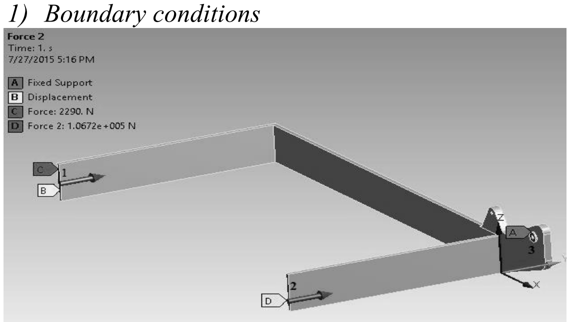


Figure 3.1. Rolling moment- boundary conditions

The figure 3.1 shows the boundary conditions for rolling moment. Where region 3 is fixed to bottom bracket. The moment load is converted in to two forces on regions 1 and 2.

*2) Results and discussions*

From the Ansys workbench static structural analysis for rolling moment load shown above. It is found that the maximum Von mises stress induced in structure is 3183.7 MPa. Aluminium alloy 2014-T6 is incapable of taking this high stress. Its ultimate tensile stress value is about 483 MPa. So it is needed to modify the structure to reduce this high stress range. Figure 3.2 shows the step wise reduction of this high stress value and optimization of mass.

From analysis of aero model it is clear that the stress is higher at regions around frame- shroud bracket end. For share this high load an additional rib structure is introduced with a size of 760 mm*150 mm*15mm in model A. In model B to reduce mass to desire level, materials are removed from frame except junctions (junctions are those regions where grids are jointed to frame). The modified model B is weighted 10.385 kg. The model's maximum Von mises stress under rolling moment is 1139.5 MPa. Higher stress regions are represented in fig itself. In model C two set of diagonal ribs are introduced for further reducing of stress value. In this model the two cross diagonal ribs helps to decrease the stress value to 621.4 MPa. The additional material added increases the model mass to 13.911.

In model D cross rib structures multiplied in the high stress regions. Fillets are used to reduce stress concentration at corners of ribs, the thickness at the hinge point increased to 35mm from 25mm. From the FEA results it is found that the maximum stress value is reduced to 368.85 MPa is shown in figure 5.26. The factor of safety increased to 0.24 for the final model.

*Yawing moment*

Yawing moment is the moment which tends to bend the frame downwards. Its magnitude is 28.73 kN-m. The yawing moment can converted in to a force acting at the centroid of the grid fin. For the load application in FEM this load is converted in to equivalent pressure profile. The resultant pressure is evaluated as 0.086 MPa. The boundary conditions and analysis results for yawing moment are shown in figure 3.3. Final model of rolling moment analysis is considered as the model for yawing moment analysis. The yawing moment model have mass of 29.001 and the maximum vonmises stress under yawing moment analysis is 234.85 MPa and have a margin of safety 0.51. So the same model selected in rolling moment is good for yawing moment also.

Pitching moment is the lowest moment acting on the grid fin and its value is 2.57 kN-m. The selected in rolling and yawing is checked for pitching moment analysis. Pitching moment analysis.

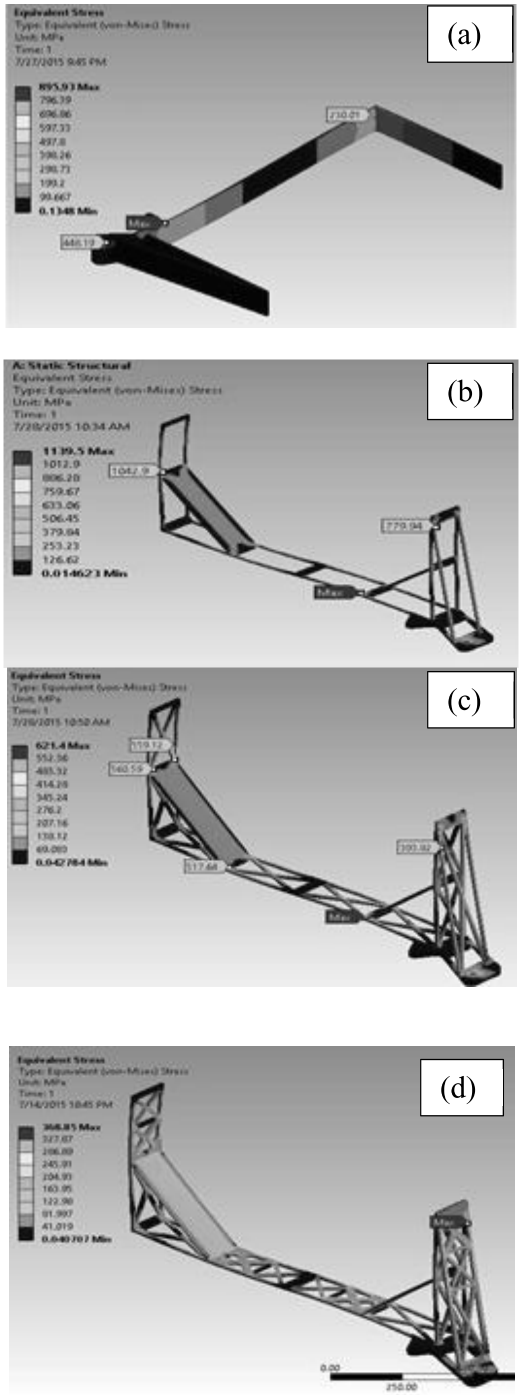


Figure 3.3. FEA results of Rolling moment

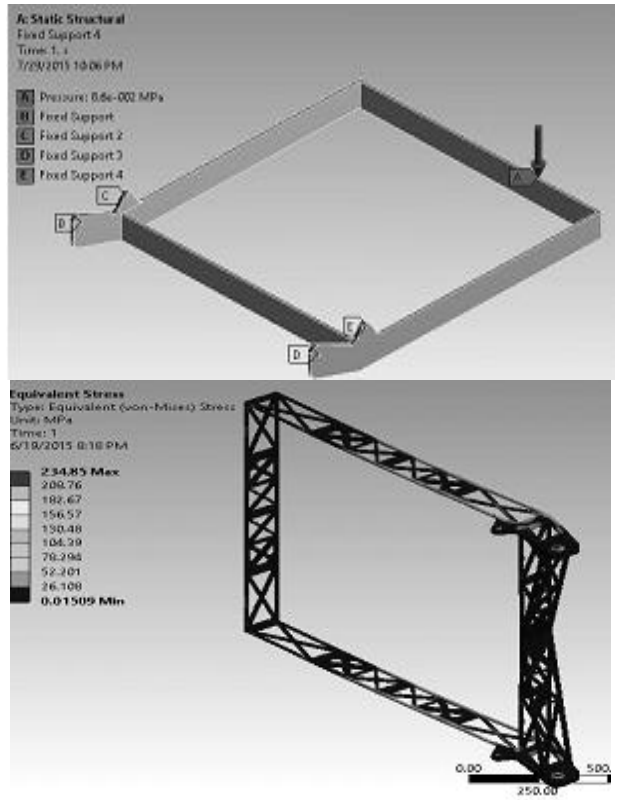

Figure 3.3. Yawing moment- boundary conditions,FEA results

*B. Pitching moment*

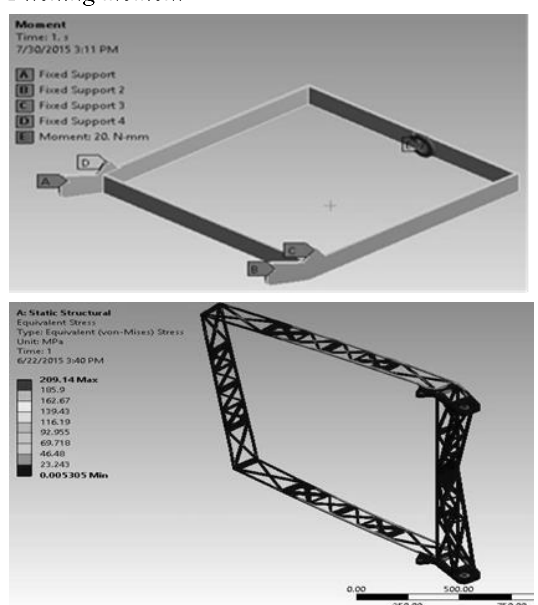

Figure 3.4. Pitching moment- boundary conditions,FEA results

As shown in figure 3.4 regions A, B, C and D are fixed in all directions. The regions A and B are connected to shroud through frame-shroud brackets. The regions C and D are connected to telescopic attachment. In deployed condition these four regions are restricted to move in any directions and are assumed to be fixed regions.

The maximum Von mises stress induced in grid fin due to pitching moment is 209.14 MPa. So the model is in safer region for material aluminium alloy 2014-T6 with a margin of safety 0.57. The FEA results of pitching moment is shown in figure 3.4.

*C. Pressure load on grid*

In deployed condition air flow should happen through the rectangular grid pattern. The air passes through the grid pattern exert a pressure force on the grid. The highest value of this pressure is considered as the static pressure on the grid fin and its value is 35 kPa. The solid model of grid has a total weight of 81.909 kg and it must have maximum stiffness to withstand this pressure. The design of grid as solid is an over design and increase the total weight of grid fin. To avoid over weight and it is better to design grid as a shell structure. The shell need a minimum thickness in order to avoid shell buckling. The design requirement is to find a suitable shell thickness with a buckling factor range of 8 to 10. To avoid more computation difficulty before proceeding with the full model the smallest unit of grid fin is analysed to optimize grid thickness.

*1) Boundary conditions*

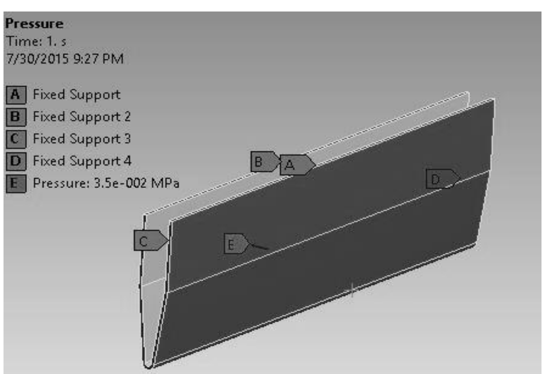


Figure 3.5: Pressure load – Boundary conditions

Figure 3.5 shows the half model and boundary conditions used in the FEA analysis. The regions A, B, C and D are assumed to be fixed. Where regions A and B are the faces at the symmetrical plane. The regions C and D are considered as fixed regions for analysis because these regions may be part of junction of similar four units of grid or in contact with grid fin frame. The outer surfaces are subjected to a pressure of 35 kPa. The thickness of grid shell is designated by ‘t’.

*2) Results and discussions*

The model is analyzed using linear buckling analysis in ansys workbench the results obtained for various shell thickness is shown in table 3.1.

TABLE 3.1
Grid size optimization

| Model | Thickness of shell (t) | Buckling load factor | Mass of full grid structure |
|---|---|---|---|
| a | 1 | 1.5719 | 13.882 |
| b | 1.5 | 6.5985 | 20.956 |
| c | 1.6 | 8.5294 | 22.012 |
| d | 1.7 | 10.811 | 23.267 |
| e | 1.8 | 13.577 | 24.606 |

The result has been found that for a shell thickness of 1 mm the buckling load factor is only 1.57. The required BLF of 10 is obtained for a shell thickness of 1.7mm. The approximate weight of grid fin’s grid structure for shell thickness 1.7 is 23.267 kg. Grid fin’s frame configuration of static analysis have a weight of 29.001 kg. Then from all the four analysis of static loads the final configuration weight is 52.268 kg.

## IV. MODAL ANALYSIS

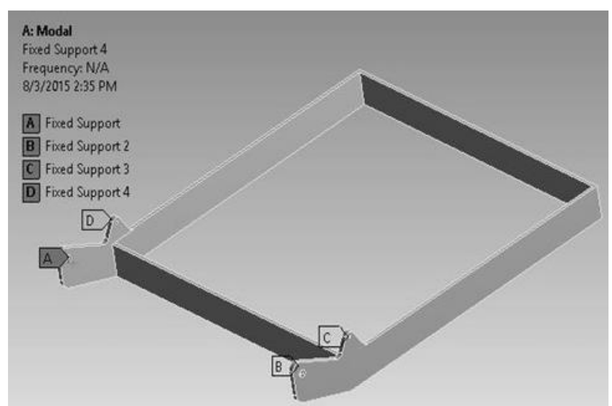


Figure 4.1. Modal analysis boundary conditions

Modal analysis is the study of the dynamic properties of structures under vibrational excitation. The analysis gives direct insight into the root cause of the vibration problems. Most often the desired modes are the lowest frequencies because they can be the most prominent modes at which the object will vibrate, dominating all the higher frequency modes. Modes are inherent properties of a structure, and determined by the material properties (mass, damping, and stiffness), and boundary conditions of the structure. If the material properties, structural design or the boundary

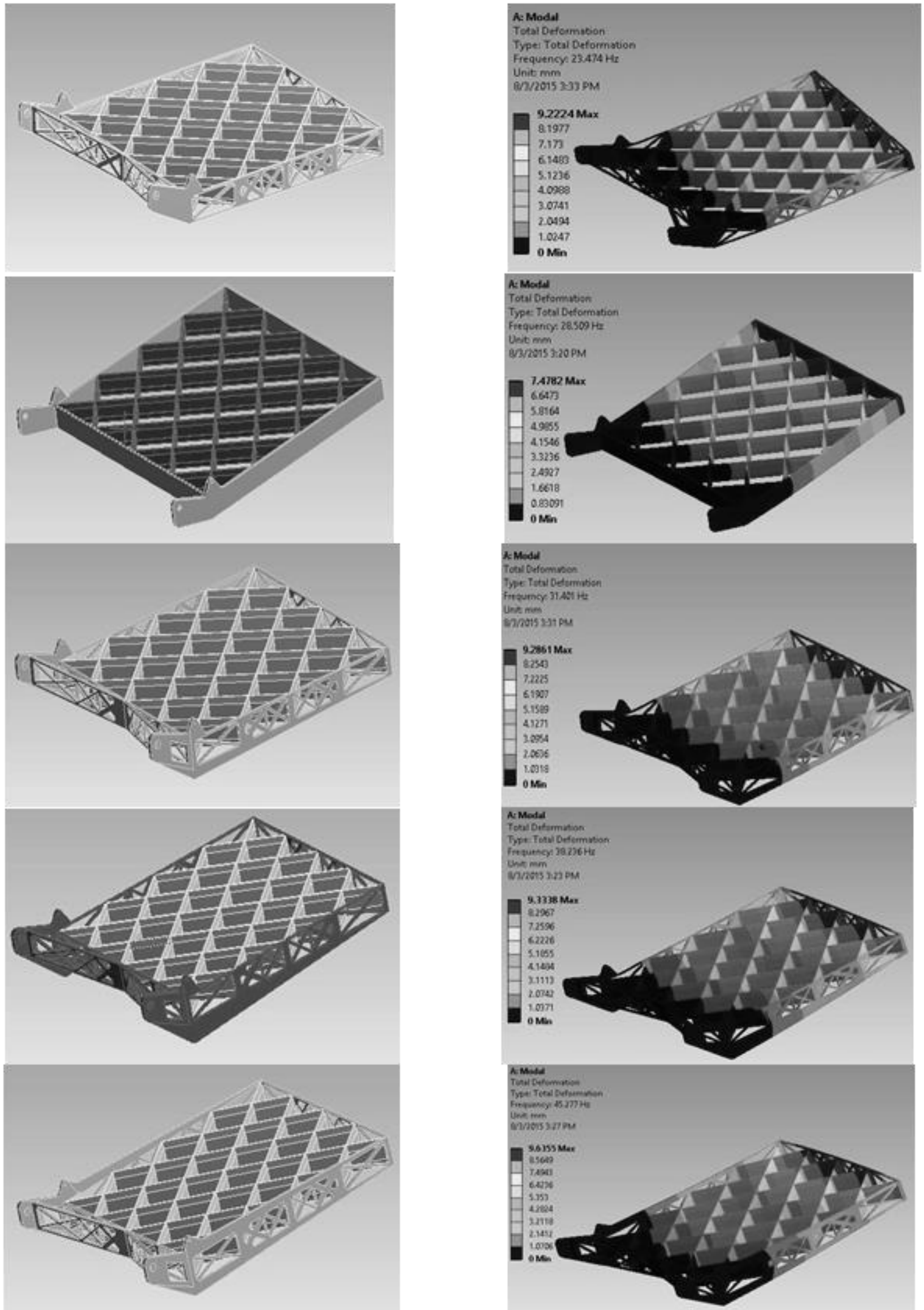


Fig. 4.2 Modal analysis

conditions of a structure change, its modes will change. In modal analysis, damping and external force are neglected.

In case of grid fin it is needed to fade away all local vibrations. Since the air is flowing from top of grid fins horizontal plane to downwards the expecting first mode of vibration is similar to the vibration of a cantilever beam fixed at one end (transverse vibration). And from design requirement the first mode of vibration should be greater than 40 Hz.

*A. Boundary conditions*

In model analysis, damping and external forces are neglected. So the boundary conditions include only the fixed regions. The figure 4.1 shows the model analysis boundary conditions. The regions A and B are connected to shroud through grid fin-shroud bracket and regions C and D are connected to telescopic attachments. In deployed condition all the four regions are considered to be fixed in nature.

*B. Results and discussions*

In modal analysis five configurations of grid fins are subjected to modal analysis using Ansys workbench modal analysis. First model is the output model from static analysis, second model is the aero configured model of grid fin and other three models were modified models of model A. The three new configurations are based only on the depth of grid fin frame arm at frame-telescopic attachment region as shown in figures. It is noted that there were no local vibrations in all the five models even the grid changed to shell of thickness 1.7 mm from 15 mm. From model analysis it is found that both model A and B cannot reach the requirement of 40 Hz natural

frequency. The final model have a first mode natural frequency of 45.277 Hz. And the model have a weight of 58.563 kg. The figure 4.2 shows the variation of natural frequencies first modes of vibration of five models.

## V. CONCLUSION

Through this work a noble method to evolve a design methodology and to structurally configure an aerodynamic structure (grid fin) is attempted.

The initial aerodynamic configuration of grid fin obtained from previous work is modified to produce an optimum structure which have better strength to with stand all load regimes. The maximum aerodynamic loads are taken as static loads. Principle of superposition method is used in static analysis. The resultant aerodynamic moments are considered as the sum of rolling, yawing and pitching moments. The final configuration obtained from static analysis have margin of safety of 0.24.

In the final stage of grid fin design, the modified model is subjected to modal analysis. A modified design with mass of 58 kg is obtained with first mode natural frequency of 45 Hz.

## REFERENCES


[1] Marco Debiasi, "Development of New Grid-Fin Design for Aerodynamic Control" , Temasek Laboratories, National University of Singapore, Singapore,

[2] DENG You-qi1. MA Ming-sheng, ZHENG Ming, ZHOU Nai-chun "Navier-Stokes Computation of Grid Fin Missile Using Hybrid Structured-Unstructured Grids", chinese journal of aeronautics, Vol. 19, No. 4, November 2006

[3] WU Lei, LU Chuan-jing, HUANG Tao, LI Jie "Research on the hydrodynamic characteristics of cavitating grid fins" Journal of Hydrodynamics Ser.B, 2006,18(5): 537-541

[4] Parul aghi, roschelle r. Martis, ajay misra "Numerical study of subsonic flow over a cascade of three plates" International Journal of Mechanical And Production Engineering, ISSN: 2320-2092, Volume- 2, Issue- 4, April-2014

[5] Salman Munawar, "Analysis of grid fins as efficient control surface in comparison to conventional planar fins" 27th international congress of the aeronautical sciences

[6] Rakesh Kumar, Ajay Misra, and A.K. Ghosh "Modelling of Cascade Fin Aerodynamics Near Stall using Kirchhoff's Steady-state Stall Model" Defence Science Journal, Vol. 61, No. 2, March 2011, pp. 157-164

[7] Marco Debiasi "Development of New Grid-Fin Design for Aerodynamic Control"

[8] Daniel A. Pruzan and Michael R. Mendenhall "Grid Fin Stabilization of the Orion Launch Abort Vehicle" American Institute of Aeronautics and Astronautics

[9] K. Sridhar, T. Vijayalakshmi, I. Balaguru, S. Senthilkumar "Comput ational fluid dynamic analysis of missile with grid fins " ACTA TECHNICA corviniensis- bulletin of engineering ISSN2067-3809, year 2012.

[10] Yan Zeng, Jinsheng Cai , Marco Debiasi, and Tat Loon Chng "Numerical Study on Drag Reduction for Grid-Fin Configurations "47th AIAA Aerospace Sciences Meeting Including The New Horizons Forum and Aerospace Exposition, Orlando, Florida, 5 - 8 January 2009.

[11] Marco Debiasi1, Zeng Yan, and Chng Tat Loon "Swept-back Grid Fins for Transonic Drag Reduction" 28th AIAA Applied Aerodynamics Conference, Chicago, Illinois, 28 June - 1 July 2010.

[12] E. Y. Fournier1 "Wind tunnel investigation of a high l/d projectile with grid fin and conventional planar control surfaces" 19th International Symposium of Ballistics, Interlaken, Switzerland, 7–11 May 2001.

[13] J Sreenivasulu , Dr. Patil M M and A E Sivaramakrishnan "Aerodynamic Analysis of a Rocket Configuration with Grid Fin" Proceedings of the 37th National & 4th International Conference on Fluid.

# Integrated Structural and Frequency Analysis of S200 Wire Tunnel Cowling Assembly Used in ISRO's LVM3-X Vehicle


J Paul Murugan [#1], Thomas kurian [*2], J Jayaprakash [$3], T. Jayachandran [**4]

[#] *Hardware Design and Realisation Division, Solid Motors Design Group, PRSO*

[*] *Hardware Design and Realisation Division, Solid Motors Design Group*

[$] *Solid Motors Design Group, PRSO*

[**] *PRSO Entity*

*Vikram Sarabhai Space Centre*
*Indian Space Research Organisation, Trivandrum, India*

1paulmurugan1iitm@gmail.com
[2]thomas_kurian@vssc.gov.in
[3]j_jayaprakash@vssc.gov.in
[4]t_jayachandran @vssc.gov.in



***Abstract*— S200 Pitch plus (PP) and Pitch Minus (PM) Motor have wire tunnel weld pads that are welded at an interval of 500 mm distance on the cylindrical shell. Each Motor is having three segments viz, Head end segment (HES), Middle segment (MS) and Nozzle end segment (NES). One of the wire tunnel weld pads in the Middle segment of PM Motor was knocked off at work centre (L&T) during handling of the hardware. Hence the distance between weld pads became to 1000 mm which is not accepted with current cowling scheme. This broken location is near the tongue ring side of the middle segment. Initially it was proposed to use Aluminium bond pads at this location with the length of the cowling maintained as 1973 mm. There was no split provided in the cowlings to take care of the differential radial dilation effects at segment joint locations. Based on the analysis with this scheme, it was found that the bonds were not capable of taking the loads due to internal pressure and aerodynamic loads. Also, the load on the M5 screw attached cowling to detachable pad was high. Hence, a new scheme was recommended without bond pads at broken location. Two types of detailed integrated analyses without considering the bond pads with 1) 1973 mm cowling length and 2) with split at segment joint location for the internal pressure and aerodynamic loads were carried out. Based on this analysis results, the proposed cowling integration scheme was cleared for LVM3 vehicle. This paper briefly outlines the details of the analyses carried out for the proposed cowling scheme without bond pads.**



***Keywords* -Weld pad, wire tunnel, cowling, FEM, screw, Integration, aero load**


## I. INTRODUCTION

LVM3-X vehicle is having two strap-on S200 Solid Rocket Motors. S200 Solid Rocket Motor have wire tunnel weld pads that are welded at an interval of 500 mm distance on the cylindrical shell (Fig.1). Weld pads on motor case (Refer Fig.2) are primarily used for mounting the cowling and wire tunnel using fasteners. Though the external load acting on these pads (i.e. due to aerodynamic forces and inertia) are benign, the stress developed on the Motor case due to internal proof pressure in the presence of such local discontinuity is significant. Also the load on the fastener and weld is significantly affected by the aero dynamic load. Weld pad located on the cylindrical shell, where uniform dilation occurs, will not be critical when cowling assembled over

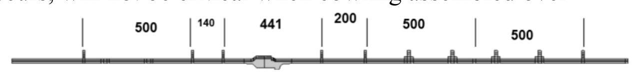


Figure 1: Arrangement of weld pads in the cylindrical shell (distance in mm)

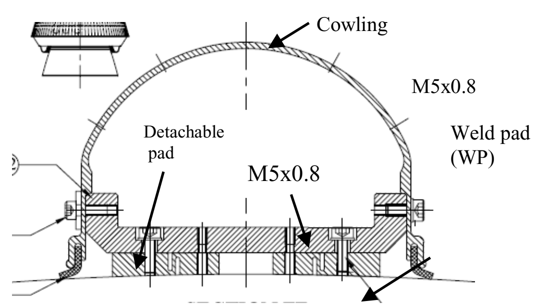


Figure 2: configuration of the weld pad with detachable pad, cowling and M5 fastener

that. But differential dilation is more between the case and segment joint. Hence the split in the cowling at this location will be critical with respect to bolt load is concerned. One of the wire tunnel weld pads in the Middle segment of Motor at pitch minus (PM) was knocked off at work centre during handling of the hardware. This broken location is near the tongue ring side of the middle segment. The integrity of this broken weld pad was studied and a cowling scheme without bond pad was proposed. This paper briefly outlines the details of the analyses carried out for the proposed cowling scheme without bond pad.

## II. WIRE TUNNEL COWLING ARRANGEMENT SCHEMES FOR PM MOTOR

Two cowling option were proposed at broken location (Refer Fig.3) of the weld pad.

Option-1: The length of the existing cowling was 1500 mm. Due to breakage of the weld pad at MS side; the length of this cowling is increased to 1973 mm. This cowling has to run over the HES+MS segment joint. It is the first option considered without bond pads. WP-1-GR means weld pad-1 on Groove ring side.

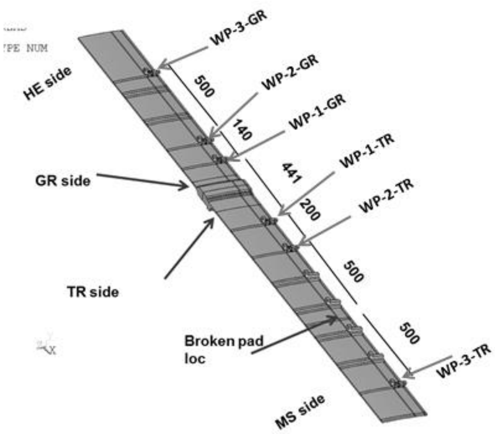


Figure 3: cowling arrangement (Option-1)

Option-2: In the modified scheme based on the analysis, the split was provided at either ends of the segment joint. The details of the cowlings in this scheme are given in Fig.4.

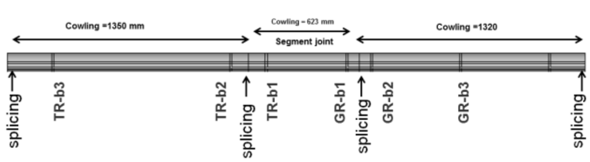


Figure 4: cowling arrangement (Option-2)

Cowling 1: (for HES/MS segment joint location) length between weld pads in mm = 441+76+108= 625mm (approx.). i.e. cowling length is 625 mm. Here one pairs each of the weld pads at ends are connected to the cowling.

Cowling 2 (Location at knocked out weld pad side on MS): Length between weld pads on TR side = 100+1000+250 =1350 mm (approx.). i.e. cowling length is 1350 mm. Here also two sets of weld pads are connected with cowling. i.e.1st support on MS: weld pad 463 mm after segment joint with 100 mm overhang 2nd support on NES: weld pad 1463mm after segment joint with 250mm overhang

Cowling 3: Length between weld pads on GR side of HES =70+500+500+250 =1320mm (approx.). i.e. cowling length is 1320 mm. Here three sets of weld pads are connected with cowling.

## III. FINITE ELEMENT MODEL AND LOADS

Cyclic symmetric Geometry (20°) model considered in the analysis. i.e. one side weld pad in the circumferential direction is considered (Refer Fig.5). Second order 3-D solid elements are used for modelling the Motor case, weld, weld pads, bond pads and cowling. Solid bolt are used in the interface of weld pad to detachable attachment. Beam elements are used for modelling the bolts at the interface between cowling and weld pad. 3-D surface contact elements (12 pairs) are considered at all interfaces. At weld location between weld pad and Motor case nodes are merged. Segment joint is modelled to take care of the differential radial dilation. Loads and boundary condition: Two types of load steps are considered. In the load step-1 (LS-1), preload and pressure is considered.

- Preload is applied at all fasteners.
- In Flight condition, Thrust load relieved condition was considered for the MEOP = 6 MPa

Load step-2 (LS-2):

- Aero dynamic Load of 44 kPa (35kPa x1.25) is considered as internal pressure over the cowling.

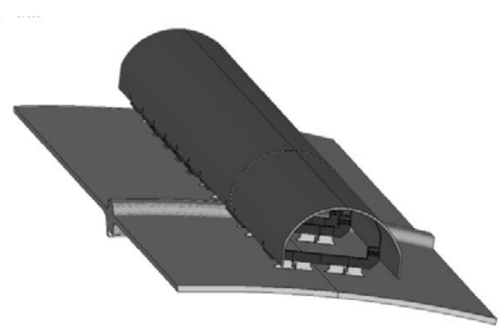

Figure 5: Integrated 3-D Finite element model of motor case with interfaces

## IV. RESULTS AND DISCUSSION

Structural analysis was carried out considering the above mentioned loads for both options.

<u>Results for option-1:</u> Material linear properties are only considered whereas geometric non linearity is taken into account. Table-1 shows the load in the weld pads adjacent to the broken weld pad location. Max. load of 8671.2 N (884 kg) was found to be at the weld pad (WP-3 of TR side) which is located at 1000 mm location. Min. MS over allowable shear strength of the weld is 0.94. Radial dilation in the Motor case and cowling for pressure load only is shown in Fig.6. Radial dilation in the Motor case and cowling for pressure and aero load is shown in Fig.7. The

max. radial dilation is found to be at the broken weld pad location. The differential radial dilation in between the weld pads (WP-1 and WP-3) is 1.1 mm due to pressure only. The differential radial dilation between the cowling and motor case at this location is 4.65mm. This cause the higher bending moment on the M5 bolts connecting the cowling to weld pad for the (pressure + aero load). Table-2 shows the stress (MPa) in the M5 screw near to TR-1 (weld pad to detachable pad) for the pressure and Aero load for option-1. Due to this higher stress in the bolt, option-2 involving splitting of cowling at segment joint location was suggested.

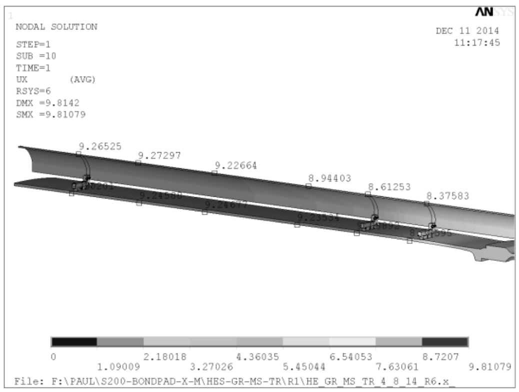


Figure 6: Radial dilation (mm) due to pressure only for option-1

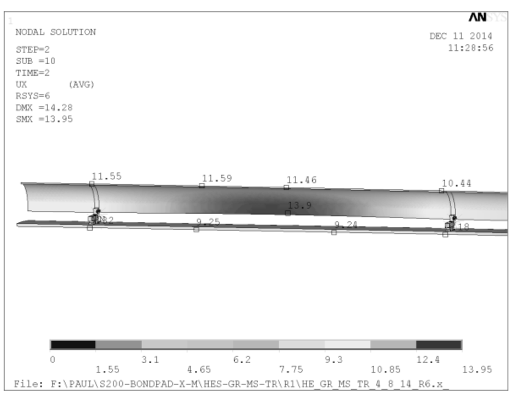


Figure 7: Radial dilation (mm) due to pressure + aero load for option-1

Results for option-2:

Table-3 shows the load in the weld pads on the broken location for option-2. The max. load of 8715 N (888 kg) was found to be at the weld pad (WP-3 of TR side) which is located at 1000 mm location for the pressure and aero load. Min. MS over allowable shear strength of the weld is 0.93. Radial dilation in the Motor case and cowling for pressure aero load is shown in Fig.8. The max. radial dilation is found to be at the broken weld pad location. The differential radial dilation in between the weld pads (WP-1 and WP-3) is 0.98 mm due to pressure only condition. The differential radial dilation between the cowling and motor case at this location is 3.32 mm.

Total stress in the M5 screw is 997.2 MPa for the pressure and aero load. MS over 0.2% PS is 0.03. Table-4 shows stress (MPa) in the M5 screw of cowling to weld pad attachment due to pressure + aero load for option-2. Total stress in the M5 screw is 954.9 MPa for the pressure and aero load. MS over 0.2% PS is 0.07. However this margin will increase while considering the material nonlinearity and the achieved properties of the 1250 MPa class bolt. The analysis was carried out considering the varying load (Refer Fig.9) around circumference of the cowling. The max stress in the bolt is 989.25 MPa at broken location for the varying load (Refer Table-5). MS over 0.2% PS is 0.04.

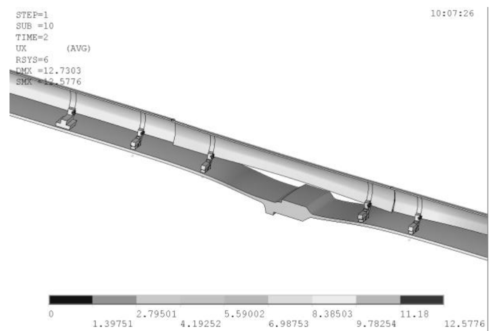


Figure 8: Radial dilation (mm) due to pressure + aero load for option-2

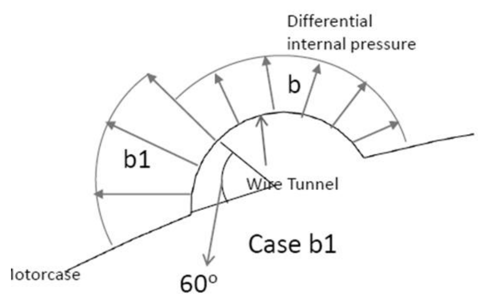


Figure 9: Variation of aero load around circumference

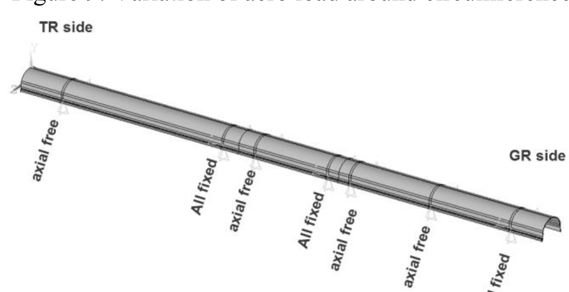


Figure 10: Boundary condition for frequency analysis for option-2

## V. FREQUENCY ANALYSIS

The cowling is assembled from the HE side of Groove ring to towards Middle segment of tongue ring. The end of the cowling where splicer plate exists is free to move in the axial direction. Fig. 10 shows the FE model and boundary

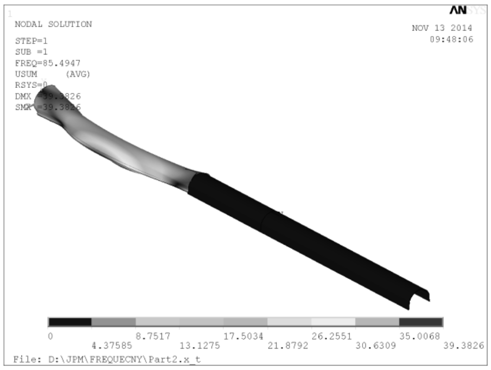

Figure 11: First mode natural frequency (Hz)

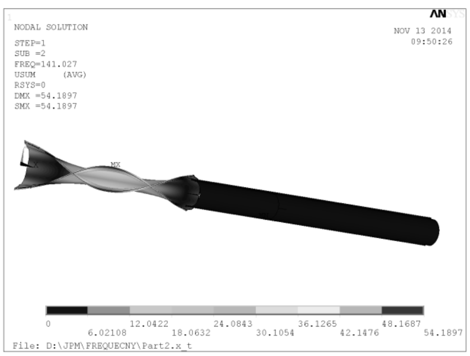

Figure 12: Second mode natural frequency (Hz)

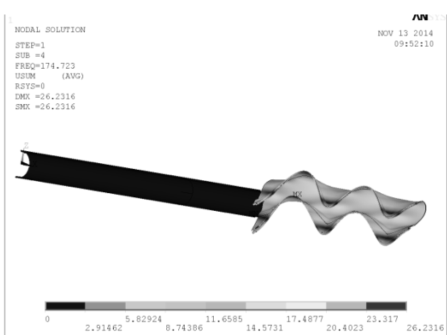

Figure 13: Third mode natural frequency (Hz)

conditions used for the frequency analysis for option-2. The mass of 2.7 kg/m length for the wire tunnel cowling is considered in this analysis. Density of the Al. alloy cowling is 2700 kg/m$^3$. The first mode (unsymmetrical bending) frequency of 85.5 Hz occurs (Fig11) at the broken weld pad location. It was meeting the minimum requirement of 60 Hz. The second mode is symmetric bending with a frequency of 141Hz that occurs at the same location (Fig.12). The natural frequency in the normal weld pad location (i.e. 500 mm distance) is 174.7 Hz (Refer Fig.13).

## V. SUMMARY AND CONCLUSION

Integrated structural and frequency analysis of S200 cowling scheme at broken weld pad location was carried for the two options. The max stress in the bolt (1000 mm pad location) is 989.25 MPa adjacent to the broken pad location. MS over 0.2% PS is 0.04. Two weld pads are only connected in the two cowlings. Hence, single point failure condition for the cowling connection exists in this scheme at these locations. However Margin of safety is high at these interfaces. The first mode natural frequency is 85.7 Hz which is higher than the requirement of 60 Hz during the fight regime. Based on the above results, the modified cowling scheme (option-2) was implemented in the successful mission of LVM3-X vehicle.

## ACKNOWLEDGMENT

We sincerely acknowledge Shri. S. Somanath, Director, LSPC for his suggestion. Also thank Shri. R. Suresh, MISD and Shri. S Sivakumar, LVM3 project for their inputs. Wish to thank Dr. S.Unnikrishnan Nair PD, HSP for reviewing this paper.

## REFERENCES

[1] Aero loads on S200 wire tunnel cowling by VE, LVM3 project (Ref: LVM3: VE:21:2014, dtd, 24th April, 2014)

[2] Salvage scheme for missing weld pads at wire tunnel location for S200 PM Motor - reg. by MISD (Ref: Letter MISD: 313-13 dtd. February 18, 2013- Analysis of S200 Wire tunnel and destruct cover).

[3] Ansys User manual

[4] Splitting of S200 wire tunnel at segment joints- reg (circulation by Email only) (Ref: 1. Letter from LVM3 Project: LVM3-VE-50-2014, dtd 26/11/14; 2. Review by PD, LVM3 with LMIG & HDRD on 03/12/2014), dtd 6th Dec, 2014.

TABLE 1: LOADS (IN N) IN THE WELD PADS FOR THE PRESSURE AND AERO LOAD FOR OPTION-1

| | | LS-1: Pressure only (6MPa) | | | | | | | | LS-2: P+Aero load | | | | | |
|---|---|---|---|---|---|---|---|---|---|---|---|---|---|---|---|
| | Allowable shear strength (MPa) | Fx (Radial) | Fy (Hoop) | Fz (Axial) | Fr | area | Avg. shear stress | MS | | Fx (Radial) | Fy (Hoop) | Fz (Axial) | Fr | Avg. shear stress | MS |
| WP-1 (near TR) (both side weld) | 396 | -7104.1 | 356.28 | -1840.1 | 7347.19 | 84.84 | 86.60 | 3.57 | | -7986.7 | 233.91 | -1463.4 | 8123.0 | 95.75 | 3.14 |
| WP-1 (near TR) (one side weld) | 396 | -4392.4 | 5969.3 | -1732.6 | 7611.02 | 42.42 | 179.42 | 1.21 | | -5262.9 | 5930.4 | -1317.8 | 8037.7 | 189.48 | 1.09 |
| WP-2 (near TR) (both side weld) | 396 | -5306.5 | 419.76 | -1255.7 | 5469.18 | 84.84 | 64.46 | 5.14 | | -8016.7 | 155.61 | -1197.2 | 8107.1 | 95.56 | 3.14 |
| WP-2 (near TR) (one side weld) | 396 | -2391.6 | 6747.3 | -1200 | 7258.50 | 42.42 | 171.11 | 1.31 | | -5038 | 6655.3 | -1103 | 8419.7 | 198.48 | 1.00 |
| WP-3 (near TR) (both side weld) | 396 | -6732.3 | 802.96 | -246 | 7347.19 | 84.84 | 86.60 | 3.57 | | -8636.1 | -170.75 | 33.6 | 8637.9 | 101.81 | 2.89 |
| WP-3 (near TR) (one side weld) | 396 | -3426 | 7574.2 | -226.62 | 7611.02 | 42.42 | 179.42 | 1.21 | | -5594.2 | 6623.9 | 136.05 | 8671.2 | 204.41 | 0.94 |

TABLE-2: STRESSES (MPA) IN THE M5 SCREW NEAR TO TR-1 (WELD PAD TO DETACHABLE PAD) FOR THE PRESSURE AND AERO LOAD FOR OPTION-1

| | LS-1 (pre stress+ pressure) | LS-2 (Pre stress+ Pressure + Aero) |
|---|---|---|
| Pre stress (MPa) | 372 | 372 |
| Axial stress (MPa) | 372.5 | 468.4 |
| Bending (MPa) | 733.2 | 1071.6 |
| Total stress (MPa) | 1105.8 | 1540 |

TABLE-3: LOADS (IN N) IN THE WELD PADS FOR THE PRESSURE AND AERO LOAD FOR OPTION-2

| | LS-1: Pressure only (6MPa) | | | | | | | | | LS-2: P+Aero load | | | | | |
|---|---|---|---|---|---|---|---|---|---|---|---|---|---|---|---|
| | Allowable shear strength (MPa) | Fx (Radial) | Fy (Hoop) | Fz (Axial) | Fr | area | Avg. shear stress | MS | | Fx (Radial) | Fy (Hoop) | Fz (Axial) | Fr | Avg. shear stress | MS |
| WP-1 (near TR) (both side weld) | 396 | -5873.8 | 273.4 | -1881.1 | 6173.72 | 84.84 | 72.77 | 4.44 | | -7236.4 | 511 | -1573 | 7423.0 | 87.49 | 3.53 |
| WP-1 (near TR) (one side weld) | 396 | -3150 | 5803.4 | -1779.5 | 6838.76 | 42.42 | 161.22 | 1.46 | | -4559 | 6150.4 | -1479.5 | 7797.5 | 183.82 | 1.15 |
| WP-2 (near TR) (both side weld) | 396 | -6785.7 | 669 | -1062 | 6900.81 | 84.84 | 81.34 | 3.87 | | -7921.3 | 428.9 | -1284.4 | 8036.2 | 94.72 | 3.18 |
| WP-2 (near TR) (one side weld) | 396 | -3752 | 7216.3 | -1005.8 | 8195.37 | 42.42 | 193.20 | 1.05 | | -5244.4 | 6842.9 | -1223 | 8707.7 | 205.27 | 0.93 |
| WP-3 (near TR) (both side weld) | 396 | -6572.6 | 805.6 | -267.5 | 6627.19 | 84.84 | 78.11 | 4.07 | | -7943.3 | 458.8 | -74.7 | 7956.9 | 93.79 | 3.22 |
| WP-3 (near TR) (one side weld) | 396 | -3277.6 | 7551.6 | -247.6 | 8235.94 | 42.42 | 194.15 | 1.04 | | -5470.5 | 6784.7 | -39.6 | 8715.5 | 205.46 | 0.93 |
| WP-4 (near GR) (both side weld) | 396 | -6861.7 | 848.3 | -873.7 | 6968.92 | 84.84 | 82.14 | 3.82 | | -7174.2 | 673.7 | -1012.9 | 7276.6 | 85.77 | 3.62 |
| WP-4 (near GR) (one side weld) | 396 | -2703.6 | -5472 | -92.3 | 6104.16 | 42.42 | 143.90 | 1.75 | | -4669.7 | 6029.7 | -907.1 | 7680.2 | 181.05 | 1.19 |
| WP-5 (near GR) (both side weld) | 396 | -5560 | -153.5 | -1580.9 | 5782.42 | 84.84 | 68.16 | 4.81 | | -7118.1 | 159.9 | -1258.5 | 7230.3 | 85.22 | 3.65 |
| WP-5 (near GR) (one side weld) | 396 | -2567 | 6127.4 | -1485.9 | 6807.53 | 42.42 | 160.48 | 1.47 | | 4017 | 6694 | -1170 | 7894.0 | 186.09 | 1.13 |
| WP-6 (near GR) (both side weld) | 396 | -6899.5 | -534.2 | -2121 | 7237.89 | 84.84 | 85.31 | 3.64 | | -7590.8 | -476.7 | -1716.9 | 7797.1 | 91.90 | 3.31 |
| WP-6 (near GR) (one side weld) | 396 | -3768 | 6086 | -1998 | 7431.64 | 42.42 | 175.19 | 1.26 | | -4882 | 5953.4 | -1597.3 | 7863.1 | 185.36 | 1.14 |

TABLE-4: STRESSES (MPA) IN THE M5 SCREW NEAR TO TR-1 (WELD PAD TO DETACHABLE PAD) FOR THE PRESSURE AND AERO LOAD FOR OPTION-2

| Stress (MPa) | LS-1 (pre stress+ pressure) | LS-2 (pressure+ aero) |
|---|---|---|
| Pre stress | 372 | 372 |
| Axial | 372.5 | 375.2 |
| Bending | 567.6 | 581.9 |
| Total stress | 940.1 | 954.9 |

TABLE-5: STRESS (MPA) IN THE M5 SCREWS CONNECTING COWLING TO WELD PAD DUE TO PRESSURE & THE CIRCUMFERENTIALLY VARYING AND UNIFORM AERO LOADS FOR OPTION-2

| Bolt location | Max. Total stress (MPa) for pressure + Aero load | |
|---|---|---|
| | uniform aero load | Varying aero load |
| | | |
| TR-b1 | 931.7 | 962 |
| | | |
| TR-b2 | 954.9 | 961.5 |
| | | |
| TR-b3 | 997.14 | **989.25** |
| | | |
| GR-b1 | 936.37 | 930.2 |
| | | |
| GR-b2 | 917.2 | 945.6 |
| | | |
| GR-b3 | 994.1 | 969.9 |

# Design and Analysis of Spiral Flexure Configuration in Satellite Valves


Ayisha Rubna P*[1], Shankar Krishnapillai[4]**, D Venkittaraman*[2], A Manimaran*[3]

** Liquid Propulsion System Centre (LPSC), ISRO, Thiruvananthapuram, Kerala, India*

*[1]arubnap@gmail.com

*[2]venkitt@hotmail.com

*[3]maranavanamuthu@gmail.com

*** Machine Design Section, Department of Mechanical Engineering, IIT Madras, India*

**[4]skris@iitm.ac.in



***Abstract*— This paper presents the design and analysis of a novel spiral flexure spring element which effectively replaces the conventional helical spring to achieve higher stroke in satellite valves. This design can find application in the actuator of satellite fluid flow control components .While designing an actuator for satellite component applications, higher cyclic life is one of the prime factors considered to ensure operational life of the satellite; say around 15 years. This demands millions of cyclic life capability for a fluid component. At present where higher stroke is demanded, helical spring is used at the cost of cyclic life. In order to gain the advantage of higher cyclic life, together with higher stroke, it is essential to study the feasibility of using flexure configurations. A fluid component design with a spiral flexure valving element is chosen for analysis. This paper deals with design and analysis of spiral flexure with 17-7 PH steel as the material.**



***Keywords:* Flexure, valving element, vonMises stress, ANSYS, EDM**


## I. INTRODUCTION

Flexure springs are thin metallic sheets in which patterned slots are cut to get the required stiffness and deflection, keeping the stress within the endurance limit of the material. These can be used instead of the helical springs to increase the cyclic life of the moving parts. Since flexures are thin sheets, we can even reduce the size/weight of the component made out of the flexure compared to conventional springs. Flexures are clamped tightly with spacers to the housing at the outer diameter and to the plunger at inner diameter so that it guides plunger movement when the component actuates. Due to this flexure, there will not be any sliding contact between the parts.

Various flexure spring configurations are already available in the applications like cryo-coolers used in space application, linear compressors and electro-dynamic shakers. But the feasibility of these configurations for higher strokes has to be studied. It is seen from the literature, the spiral flexure configuration can give higher stroke in less envelop as compared to other flexures. Hence spiral flexure configured actuator is attractive for high thrust applications with larger cyclic life. This paper deals with design of flexure springs and valving element for higher stokes and longer cyclic life without any sliding contacts.

## II. HELICAL SPRING LOADED AND FLEXURE SPRING LOADED VALVING ELEMENTS

Helical spring loaded assembly is generally used in satellite actuator components wherever cyclic life is not a concern. In the helical spring mounted assembly, helical spring supports the poppet at one end with an initial preload (refer Fig.1.a). Other end of the plunger carries the soft seal, which is tightly held on the outlet port so as to provide sufficient leak tightness. Movement of the plunger is guided by the sliding clearance between, the plunger surface and housing. Due to this sliding there are possibilities of contamination generation, which can cause the propellant leakage through the control valve and also there is a possibility of plunger jamming. Hence this design is not suitable wherever large number of the cycle life is required.

In the flexure mounted assembly as shown in fig.1.b, poppet is suspended by flexures with an initial preload. Outer periphery of flexure clamped tightly to the housing with spacers and inner periphery with plunger. When the plunger is stationary, soft seal in the plunger is tightly held against the outlet port with initial preload to provide sufficient leak tightness. As the valve actuates, it allows propellant flow though outlet by guiding plunger movement with flexures. This configuration promises high cyclic life, leakage-free and compact design.

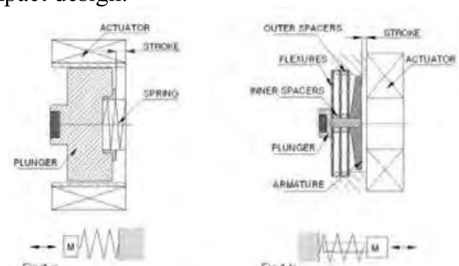


Fig.1 Schematic of the helical spring mounted and flexure mounted valving element

## III. DESIGN PROCEDURE FOR FLEXURE

The design of flexure is quite challenging, and the main focus is to limit the axial von-Mises stress and should be less than the endurance limit of the material. Hence the material selected for flexure should have very high cyclic fatigue life, and it should be compatible with propellant used during valve operation. Typical materials used for flexure today are beryllium copper and spring steel. 17-7 PH steel at condition C is having higher endurance limit and is compatible with the satellite operating fluids. Hence this material is selected for our design. Flexures are assembled in a valving element assembly typically as shown in the fig.2.The design of this assembly is carried out in such a way that natural frequency of the valving element should be high enough to avoid resonance. The valving element should be kept at the centre of the flexure pack to reduce lateral movement of the armature.

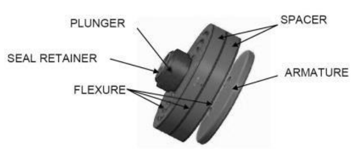


Fig.2 Valving element assembly in satellite valves

*STUDY ON TYPES OF FLEXURE*

A study is carried out on various configurations of the flexures like spiral, spider, s-curve and semi-circular configurations for higher stroke application.

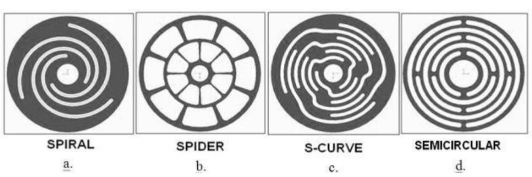


Fig. 3 various configurations of the flexures.

Figure.3 shows the various configurations of the flexure studied. Fig. 3a shows the spiral configuration; which can provide higher stoke in smaller envelop, keeping the stress less. Among these flexures, spider and s-curve flexures have higher stiffness and stress for the same envelop than spiral and semi-circular flexures.

Structural analysis of 1 to 4 configurations is carried out using ANSYS software. The analysis results are produced in Table 6.1 Endurance limit of the material used for flexure (17-7PH steel at condition C) is 770MPa. The above comparative study is done by clamping the outer periphery of the flexure and applying load at the inner periphery. Analysis results are presented in table 4.1.

The above analysis is carried out to obtain a flexure configuration, which can provide an axial deflection of more than 1.8 mm, keeping the stress within the endurance limit of the material. Analysis of the test result shows that spiral flexure satisfied the above mentioned criteria for less envelop; hence for further studies, spiral configuration is selected.

TABLE-4.1 COMPARATIVE STUDY OF THE FLEXURE CONFIGURATIONS

| SL No. | Configuration | Flexure OD (mm) | Thickness (mm) | vonMises stress (MPa) | Deflection (mm) | Stiffness (N/mm) |
|---|---|---|---|---|---|---|
| 1. | Spiral | 23.7 | 0.32 | 700 | 2 | 2.5 |
| 2. | Spider | 30 | 0.2 | 700 | 1 | 5.1 |
| 3. | S-curve | 27.5 | 0.32 | 700 | 1 | 5.1 |
| 4. | Semicircular | 28.5 | 0.32 | 700 | 1.63 | 3.13 |

## IV. SPIRAL FLEXURE DESIGN

Among the different types of the available spirals, spiral profile in the logarithmic spiral is smooth and gradual as compared to other types. For the given application, outer diameter of the spiral is limited to be less than 21mm for reducing the size of the valving element. Fig. 3.a shows typical spiral flexure configuration.

Parametric coordinates of the spiral profile used for modeling the flexure is given below.

$$X = ae^{(bt)}\cos(\theta t)$$

$$Y = ae^{(bt)}\sin(\theta t)$$

$$Z = 0$$

Where 'a' is the distance of starting point of spiral from the centre, 'b' is the shrinking factor of the spiral and θ is the subscribed angle of the spiral.

*A. Effect of spiral profile variables on stress and displacement:*

Tetrahedral solid element is used for modeling the flexure in ANSYS and three elements are modeled across the thickness. After referring the literature [1], the variables 'a', 'b' and 'θ' are taken as the spiral variables for analytical study.

*1) Effect of 'a':*

**TABLE 5.1 Effect of 'a' on deflection and stress**

| a(mm) | deflection(mm) | vonMises Stress(MPa) |
|---|---|---|
| 2.5 | 0.86618 | 878.24 |
| 2.8 | 0.87035 | 678.18 |
| 3.1 | 0.93221 | 567.76 |
| 3.4 | 1.0112 | 520.85 |
| 3.7 | 1.1018 | 470.87 |
| 4 | 1.1953 | 472.64 |
| 4.1 | 1.2269 | 472.77 |

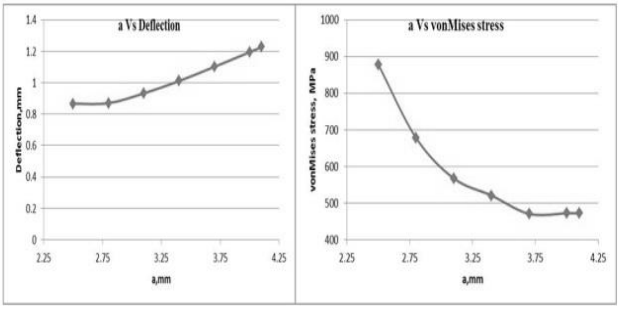


Fig.4 Effect of ‘a’ on deflection and vonMises stress

From the equations given in the section 7, we see that as ‘*a*’ increases, distance of the spiral from the centre pole increases and also the solid gap between the spiral slots and size of spiral increases. So as ‘a’ increases, maximum von-Mises stress decreases and deflection increases. See table 5.1 and fig 4.

*2) Effect of ‘b’:*

Now, ‘b’ is changed keeping other variables constant.

**TABLE 5.2 Effect of ‘b’ on deflection and vonMises stress**

| b(no unit) | deflection(mm) | vonMisesStress(MPa) |
|---|---|---|
| 0.6 | 4.2459 | 3258.5 |
| 0.7 | 2.0081 | 13885 |
| 0.8 | 1.4468 | 837.49 |
| 0.9 | 1.2209 | 597.17 |
| 1 | 1.1018 | 470.87 |
| 1.1 | 1.0265 | 418.94 |
| 1.125 | 1.0097 | 406.93 |

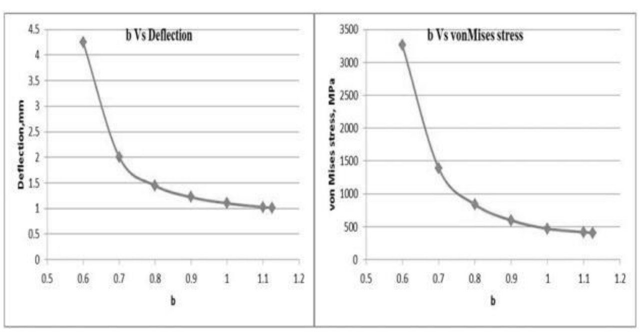


Fig.5 Effect of ‘b’ on deflection and vonMises stress

As ‘b’ increases, spiral widens, ie solid gap between slots increases. Hence von-Mises stress and deflection decreases. See table 5.2 and fig.5.

*3) Effect of ‘θ’:*

**TABLE 5.3 Effect of ‘θ’ on deflection and vonMises stress**

| θ(°) | deflection(mm) | vonMises Stress(Mpa) |
|---|---|---|
| 90 | 0.019116 | 54.574 |
| 180 | 0.075868 | 195.11 |
| 270 | 0.39631 | 360.45 |
| 360 | 1.1018 | 470.87 |
| 450 | 2.2911 | 697.83 |
| 540 | 4.3443 | 1281 |
| 630 | 10.528 | 4621.5 |

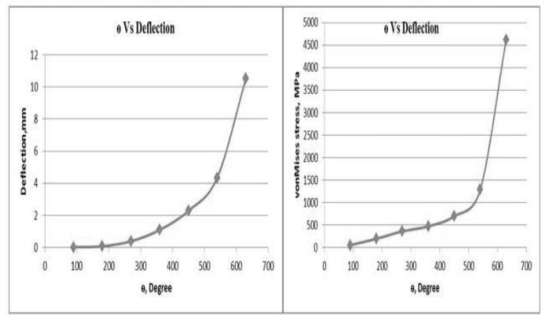


Fig. 6 Effect of ‘θ’ on deflection and vonMises stress.

As ‘θ’ increases, length of spiral increases, more material will be scooped out from the flexure; at the same time solid gap between the spirals decreases. Hence deflection and von-Mises stress increases as ‘θ’increases [1]. See table 5.3 and fig.6.

*B. Effect of spiral flexure thickness on stress and displacement:*

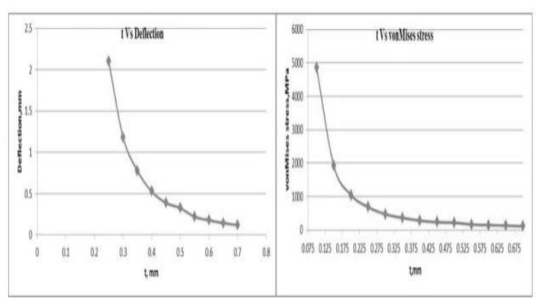


Fig.7 Effect of‘t’ on deflection and vonMises stress.

As the thickness increases, stiffness increases and deflection decreases [2]; therefore vonMises stress decreases [2]. Fig. 7 &8 and table 5.4 details how these parameters vary w.r.t thickness change.

TABLE 5.4 Effect of 't' on deflection and vonMises stress

| Thickness (mm) | Deflection (mm) | stress(MPa) |
|---|---|---|
| 0.2 | 4.0171 | 1047.9 |
| 0.25 | 2.1 | 682.47 |
| 0.3 | 1.184 | 473.37 |
| 0.35 | 0.77775 | 360.11 |
| 0.4 | 0.52677 | 280.7 |
| 0.45 | 0.38808 | 230.34 |
| 0.5 | 0.32542 | 217.57 |
| 0.55 | 0.2192 | 162.95 |
| 0.6 | 0.17848 | 146.49 |
| 0.65 | 0.14439 | 128.81 |
| 0.7 | 0.11921 | 110.92 |

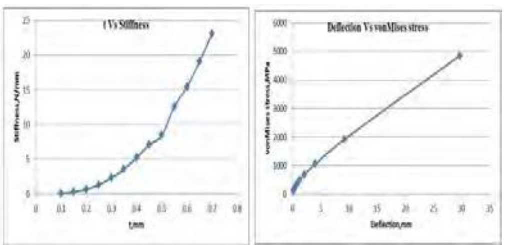

Fig.8 Effect of 't' on stiffness and Deflection on vonMises stress.

*C. Effect of number of spirals of the spiral flexure spring:*

TABLE 5.5 Effect of 'Number of spirals' on deflection and vonMises stress

| Number of spirals | Deflection (mm) | Stress (MPa) |
|---|---|---|
| 1 | 0.46984 | 466.53 |
| 2 | 0.68592 | 460.63 |
| 3 | 1.1018 | 470.87 |
| 4 | 1.6491 | 778.82 |
| 5 | 3.0203 | 1840.3 |

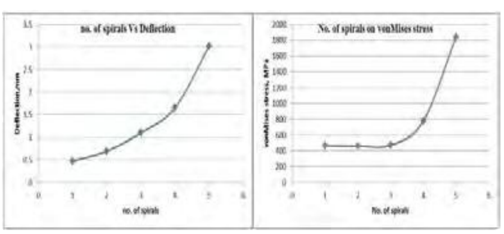

Fig.9 Effect of No. of spirals on deflection and von-Mises stress.

Table 5.5 and fig. 9 gives the effect of number of spirals on deflection and stress for a load of 3.5N applied at the inner end of the flexure, keeping the outer periphery of the flexure fixed. As the number of spirals increases, solid gap between spirals reduces. Therefore deflection increases gradually [2] and stress remains same. When the number of spirals is such that the solid gap between the spirals is too small, stress increases abruptly.

Analysis shown that that effect of stress on 'OD' and ID of the flexure sheet is in- significant; there for not mentioned in this paper

Based on the above study, the final design values of spiral flexure is arrived given below:

**Table 5.6 SELECTED DESIGN PARAMETERS FOR SPIRAL FLEXURE**

| Parameter | Value |
|---|---|
| Geometry | Spiral |
| a (mm) | 3.7 |
| b | 1 |
| θ(°) | 360 |
| t (mm) | 0.32 |
| Spiral ID (mm) | 7.2 |
| Spiral OD (mm) | 20.7 |
| Sheet ID (mm) | 4.2 |
| Sheet OD (mm) | 23.7 |
| Number of spirals | 3 |
| Material | 17-7PH steel at condition C (Endurance limit: 770MPa) |

## V. CONCLUSION

For higher stroke application of flexure, spiral profile is found to be suitable compared to helical spring. Stiffness of the spiral flexure is found to be constant over the operating range of the stroke. Analysis results of the flexure stiffness matches with the experimental results in the operating range of stroke. Valving element of the flexure is suitably designed to avoid resonance. Spiral flexure can be easily fabricated with CNC EDM machine.

## REFERENCES

[1] Siddarm Biradar et al. International Journal of Emergingtrends in Engineering and Development, Issue 4, Volume 5 (Aug-Sep 2014), ISSN 2249-6149.

[2] Wang wenrui et al.Numeric Simulation on Spiral Flexure Spring Stiffness Influence Factors of Stirling Cryocooler, Issue 15, Volume 12 (2013).

## APPENDIX

*A. ANSYS analysis:*

*1) Fatigue Analysis:*

Fatigue analysis was done using ANSYS Work bench. Fatigue analysis in the flexure level is done by giving an initial deflection of 0.7mm and then applying a repeated load of 2.64N at the centre of the flexure. Since the stiffness of the flexure is 2.4N/mm; a static deflection of 0.7mm can provide an initial seat load of 6.7N by arranging 4 numbers of the flexures in parallel; which is sufficient for obtaining the sufficient leak tightness by proper design of the valve seat. Repeated load of 2.64N can provide a stroke of 1.1mm, which is sufficient for a 4mm diameter outlet port.

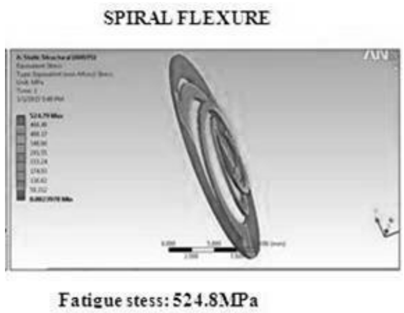


Fig. 10 Fatigue analysis on spiral flexure

In the first case, fatigue analysis is carried out in the single flexure mode. Fatigue stress of the spiral flexure found to be 525MPa. ie within the Endurance limit. Refer fig 10.

Now, the valving element was designed with four flexures arranged in parallel. Using Goodman theory, valving element was designed keeping the C.G of the valving element in the middle of the flexure pack. Maximum von-Mises stress found to be 603N/mm$^2$ with FOS (Factor of safety) of 1.17 and it is found to be at the flexure spiral slot starting end. See fig 11.

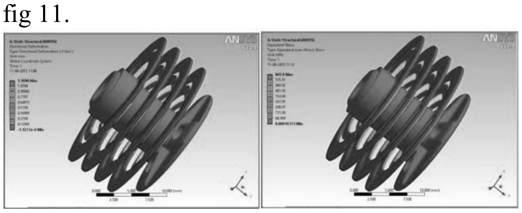

Fig. 11 Fatigue analysis results of spiral flexure-valving element.

Fig 12 gives the graphical representation of the load applied during fatigue test and theory used in the analysis. Since the parallel arrangement of four flexures can provide an initial load of 6.75N and a dynamic load of 10.56N; during the cyclic loading plot, initial static load is kept as zero and the dynamic load of 10.56N is kept repeated. Goodman theory is used for fatigue analysis.

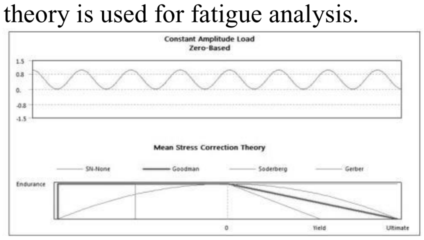


Fig. 12 Fatigue analysis plots for repeated loading and failure theory visualization of spiral flexure.

The reason behind using Goodman theory during fatigue analysis is that design by soderberg therory is of very conservative and that by using Gerber theory is with more margines.

*2) Nonlinear study of spiral flexure:*

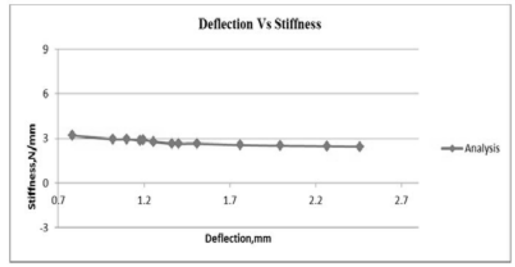


Fig 13Analysis result of stiffness Vs Deflection of spiral flexure

In the nonlinearity study of stiffness Vs deflection on spiral flexure, material non linearity and geometrical non linearity can come in to picture. For considering material nonlinearity, stress Vs strain characteristics of material are the input.

Analysis result of deflection Vs stiffness is constant for a stroke more than 2.5mm(refer fig. 13), But stress is more than endurance limit for a stroke greater than 2.2mm. Hence the spiral spring can be operable up to a stroke of 2.2mm.

*3) Random vibration:*

Since the gap requirement between the valving element and housing is critical inorder to avoid rubbing/hitting, displacement of the valving element due to vibration is to be obtained. For this, random vibration analysis is carried out in the axial and lateral directions of the valving element.

**Table 8.1 Input spectrum for random vibration**

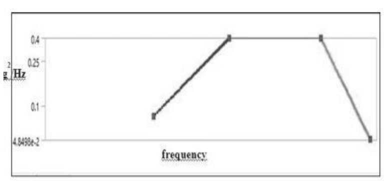


| VIBRATION SPECTRUM | |
|---|---|
| Frequency (Hz) | Input |
| 20-100 | +3db/Octave |
| 100-700 | 0.4 g$^2$/Hz |
| 700-2000 | -6db/Octave |
| Over all rms | 20.9g |
| Duration | 120sec |

The input spectrum used for the random vibration analysis is given in the table 8.1. Plot on the input spectrum is created by converting input amplitude corresponding to each frequency range in terms of mm$^2$ per Hertz.

During random vibration, maximum lateral movement of armature in the Y and Z directions are 58µm and 118µm respectively. Housing of the valve thus designed keeping a minimum radial gap of 120µm exists between housing and armature.

Fig 14 shows the valving element assembly. Fabrication of the spiral spring is done with Electro Discharge

Machining (EDM); in which CNC codings are used to control the required spiral profile. See fig 15.

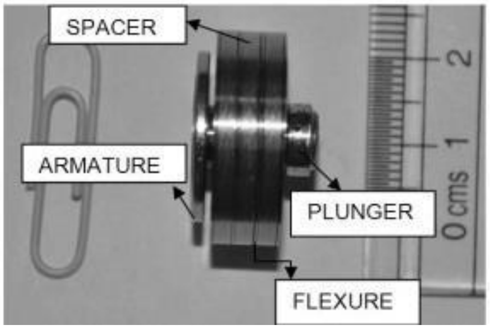


Fig 14. Valving element assembly

*B. Stiffness calibration of the spiral flexure:*

The machine used for the calibration is SimpleTech machine with 0-20kg load capacity and 0.001kg Least count. The flexure pack assembly is deflected in steps of 0.1mm and the force is measured from which one can estimate the stiffness of the flexure. Fig 16 shows the flexure calibration test setup.


Fig. 15 Spiral flexure geometry

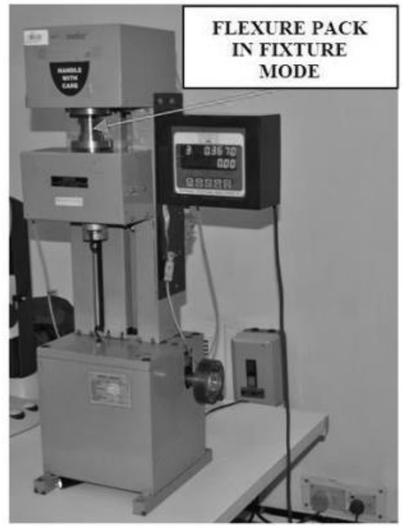


Fig.16 Flexure calibration test set-up

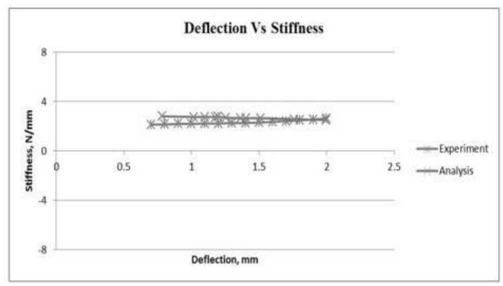


Fig.17 Comparison of Stiffness Vs Deflection in analysis and experiment

During the stiffness evaluation using ANSYS, axial stiffness of the individual flexure is found to be 2.4N/mm. When flexure calibration was done with a pack of four flexures, axial stiffness was found to be 9-10N/mm(≈2.5N/mm per flexure) ie +4% deviation with respect to analytical result. Fig.17 shows the comparison of deflection Vs axial stiffness obtained from analysis and experiment for spiral flexure.

# Aerodynamic Analysis of Wing with Store Configuration Using Open-Source Computational Fluid Dynamics Tool: $SU^2$


Bharatesha Kumar B M[#1], Keshav S Malagi *[2], P.S. Shivakumar Gouda [#2]

[#1]*Department of Mechanical Engineering, SDMCET, Dharwad, Karnataka, India*
[1]bharatesh0644@gmail.com

[*2]*Council of Scientific and Industrial Research National Aerospace Laboratories*
*Computational and Theoretical Fluid Dynamics Division, P B No. 1779, HAL Airport Road, Bengaluru, India*
[2]sp12969@my.bristol.ac.uk



***Abstract* — The Combat aircrafts are required to carry stores. The presence of stores will have a bearing on the aerodynamics control structural aspects of the aircraft. The aerodynamics will form a critical factor in this as the air-loads form an input to both control and structure of aircraft; the control deals with handling quality of the aircraft and the structure deals with structural integrity. Hence induction of any store on an aircraft has to go through the aerodynamics control and structural studies; aerodynamics being critical. In this study, the focus is on computational aerodynamic study. CFD simulations of aircraft with store configuration are carried out using open source tool-SU2. Effect of grid refinement on aerodynamic loading is studied. Further viscous and Inviscid solutions are compared to assess the sufficiency of Inviscid solutions. Finally aircraft without store is also computed. Comparisons are carried out for with and without store configuration. Such studies are required for assessing the design of aircraft to carry stores.**



***Keywords*: Aerodynamics, Air-loads, CFD, Store configuration, Grid Refinement, Viscous, Inviscid, $SU^2$**


## I. Introduction

We all know the importance of the military aircrafts; they are used by the armed forces to keep the nation safe from the expected and unexpected situations that may result in harming the lives and property. Some of the Indian used military aircrafts are Sukhoi Su-30MKI, HAL Tejas, Mikoyan MiG-29, Mig 21 and Dassault Mirage 2000. Generally, the initial design of the combat aircrafts does not involve store issue. In many cases a new store is required to be added to an existing aircraft; hence the behaviour of the aircraft becomes an important area of study. Further, these stores have to be released while in flight; the safe separation of the store from aircraft becomes critical factor in allowing a particular aircraft to carry a particular store. This process will involve aerodynamics, control and structural aspects of aircraft in the presence of store and in the event of release of stores. The presence and release of store causes changes in aerodynamic loadings and this change will have direct impact on control and structural aspects of aircraft

Tholudin Mat Lazim, Shabudin Mat, Huong Yu Saint explain about the interference effect store on a Malaysian fighter aircraft used by Royal Malaysian Air Force. The CFD simulation was done for the aircraft model whose size was reduced to 20% of its original size in subsonic speed range and compared with the experimental results. The experimental results included only the mid-span of the wing where the store was located and were validated with the CFD results. And it was found that; introduction of store to the parent body reduced lift ($C_L$ reduction from 0.25 to 0.17) and also increased the drag ($C_D$ increased from 0.01 to 0.13) of the aircraft. [1]

Yunus Emre Sunay, Emrah Gulay & Ali Akgul have made a detailed study to validate the trajectory motion of the generic wing-pylon-store model called EGLIN test case. Both Euler and Navier-Stokes computations were made on this test case. The grid used for Euler calculation includes 2.1 million cells (approx.), and the grid used for N-S calculations includes 3.4 million cells (approx.). The tools used for simulations were Gambit (v2.4.6), TGRID (v5.0.6); and Fluent commercial program (v12.0.16) for solving the grids. The CFD simulations were compared with the experimental results and both were found to be matching very well with respect to experimental results. [2] The EGLIN test case is a standard test case and is used universally for validation purpose in research fields, academic projects etc.

John H. Fox conducted an experiment for the generic wing-pylon and finned store in AEDC (Arnold Engineering Development Centre) 4T wind tunnel at Air Force Research Laboratory. The experiment fetches the surface pressure values on model considered, also the trajectory motion of the store configuration is captured at Mach=0.95 (transonic speed) & M=1.2 (supersonic speed). Various studies have been done on this paper in academic projects, researches and even in industrial applications. [3].

The current study involves CFD analysis of AEDC mode/wing-pylon-store and then validating with the wind tunnel test results of AEDC model that was scaled down to 5% of the full-scale model.

## II. METHODOLOGY

As explained earlier in the introduction that, many studies have already been made on the wing with store configuration model [1][2][3][4], A different approach is followed in the study of wing with store configuration; the justification of which can be explained in several ways, the current study includes the grid refinement of the model for Euler calculations, once the accuracy is reached, further the study was extended to viscous computations. **Table 1** shows the grid sizes of various grids used for Euler as well as viscous simulations.

Table **1** Grid sizes used for Euler and Viscous calculations

| Calculations | Type of Grid | Grid size |
|---|---|---|
| Euler Calculations | Coarse grid with store configuration | 3,862,950 cells |
| | Medium grid with store configuration | 8,927,636 cells |
| | Fine grid with store configuration | 12,836,848 cells |
| | Fine grid without store configuration | 3,429,219 cells |
| RANS-SA calculations | Fine grid with store configuration | 16,844,171 cells |
| | Fine grid without store configuration | 5,535,406 cells |

### *A. Grid Generation and Refinement for Euler calculations*

In the current study, Pointwise is used to generate computational grids, an open-source CFD solver 'Stanford University Unstructured' (SU2) [5] is used and Tecplot 360-post processor software [6] is used.

Further, grid refinement for Euler calculations was done in two cases; in first case: volume cells are made denser from coarser to medium grid; in second case: the connector points are increased on store configuration by keeping the same dense volume cells as shown in the Fig. 1**.**

The Fig. 1 details about the grid refinement done in case of Euler calculations; it can be noted that there is no inner domain in coarse grid, further in the medium and fine grids an exclusive inner domain is made in order make the volume cells denser so that the flow can be resolved accurately.

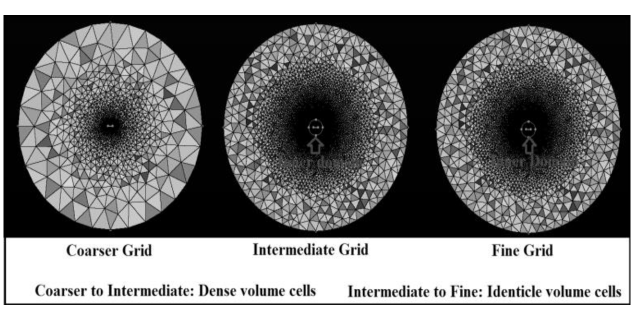


**Fig. 1** Grid refinement of volume cells for Euler calculations

As explained in second case, the grid refinement on the store configuration is shown clearly in **Fig 2.** From coarse to medium grid, there is no change in the connector points for the entire model including store configuration; however, the transformation from medium to fine grid, there are closely packed cells.

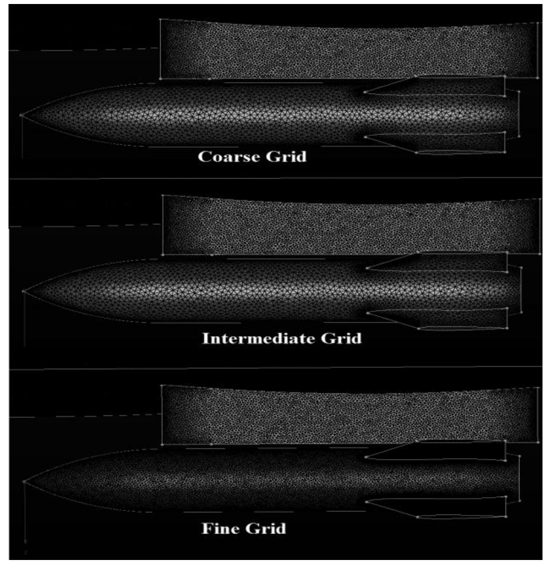


Fig. 2: Grid refinement for store configuration

### *B. Grid generation for viscous calculations*

By using same dimensions as that of the fine grid used for Euler calculations, a fine grid was generated for viscous computations [7]. Each connector points on store configuration were reduced to 60% of that of the fine grid used for Euler calculations. A rectangular block encapsulating the store configuration was generated with denser volume cells compared to other volume cells. This enables us to capture accurate flow over the store configuration. Initial wall spacing taken is 5.6422E-5 and the growth rate is 1.2. **Fig. 3 & 4 (below**) shows the grid generated for viscous calculations. Ten layers of Prism (anisotropic) cells are generated over the wall surface of the wing-pylon-store model to capture the viscous flow. A special feature from Pointwise i.e. T-Rex was used to generate the prism layers. Further, wake baffles were constructed for all the fins in order to resolve the wake (as shown in **Fig. 3 (e)**). The boundary conditions used are: *wing-pylon*, *finned-store* as 'Wall' and *outerboundary* as 'pressure far-field' and *symmetry* as 'Symmetry'. These boundary conditions are same for all the grids used for Euler calculations.

An open-source CFD solver Stanford University Unstructured ($SU^2$) is used in this study to solve the above mentioned grids. The input files for $SU^2$ are 'configuration file' with extension '.cfg', grid file in '.su2' format while solving in the parallel mode in Linux operating system [5]. The .cfg files are configured with necessary and important commands like convergence parameters such as *Slope*

*Limiter=Venkatakrishnan* [9], total number of iterations, reference values etc. The Euler solutions are run for up-to 5000 iterations and the viscous solutions are run up-to 20,000 iterations.

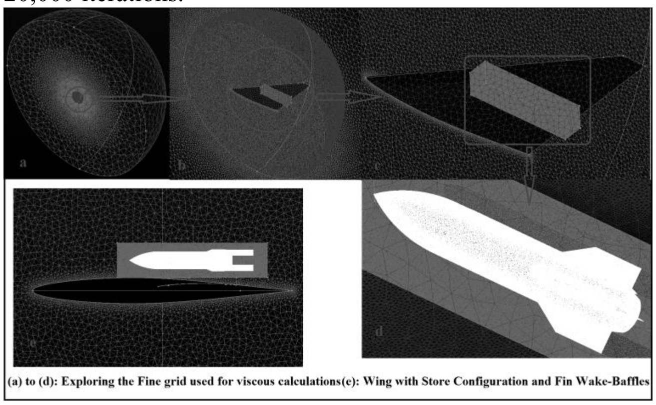


**Fig. 3:** (a) to (d) shows fine grid; (e) shows the wing with-store configuration, used for viscous computations

The below mentioned **Fig. 4** shows the T-Rex layers generated over the wall surfaces of the fin and the store nose of the store configuration

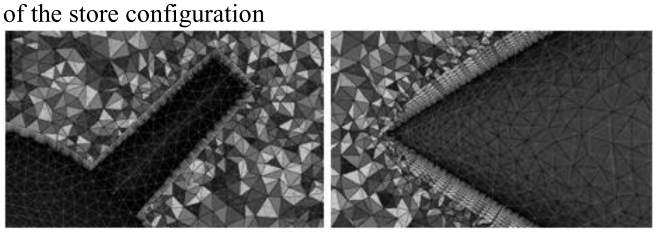

Fig. 4: T-Rex layers on Fin-1 (left); T-Rex layers on store nose (right)

After solving the grid files, among the solved output files, 'surface_flow.dat' [5] is used to extract surface pressure values on the wall of the wing-pylon and finned store model. Features like 'Blanking', 'Slicing', 'Record and Play Macros' are used in Tecplot 360 post processor to obtain $C_P$ curves on the model.

*C. Data Extraction*

The grids once after being solved in $SU^2$ solver, the extraction of the surface pressure values ($C_P$) at many sections on the wing-pylon, store & fins is achieved with the help of *slice* & *Extract* options in Tecplot 360 [8]; a post-processing software. The illustration of data extraction on wing-pylon, store & fin are as shown below in **Fig. 5.**

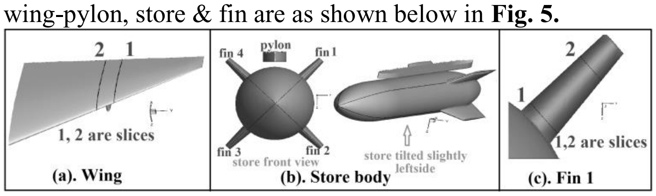


**Fig. 5:** An illustration of slices taken on (a) wing-pylon, (b) store-body and (c) store-fin 1 for data extraction

## III. Results And Discussion

This section contains the computational results obtained for the AEDC configuration at various sections as showed in **Fig. 5.** The computations have been carried out using $SU^2$ tool. Both Euler and RANS with SA [7] computations have been carried out. The Euler computations have been carried out using three sets of grids to ensure grid refinement and the viscous computations have been carried out with RANS-SA model on sufficiently fine grid as mentioned in the **Table 1.** The fine grid for viscous computations has been chosen based on experience and no grid refinement has been made. Results of Euler computations have been compared with viscous computations. Further, both the Euler and viscous computations have been carried out by considering the AEDC configuration without the store. This has been done to assess the effect of store on main body. The comparison of results with store and without store has been carried out for both the cases.

*A. Comparison of Euler solutions for coarser, medium & fine grids having store configuration with experimental results*

The below section shows the comparison of the $C_P$ values obtained for 'wing-pylon', 'store body' & 'store-fins' respectively.

*(1) $C_P$ values on wing surface:* The figures 6(a) and 6(b) show negative $C_P$ versus position of the slice taken on the wing (X/C). The $C_P$ values obtained on both the upper and lower sides of the wing are displayed. The slices are taken from tip to the wing at and nearer to the store configuration

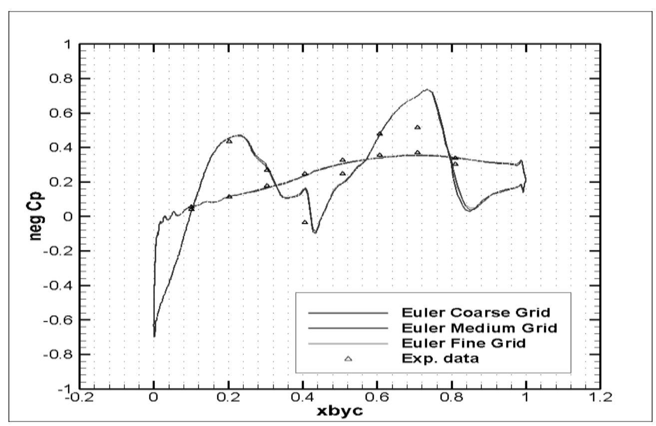


**Fig. 6(a):** At 54.2% of wing span

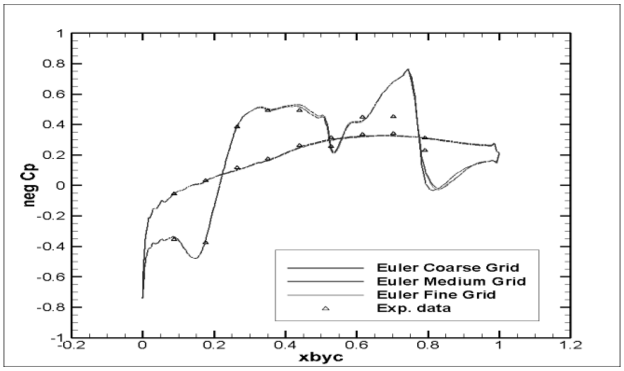


**Fig. 6(b):** At 45.2% of wing span

It is clear from the above Fig. 6(a) & 6(b) that the computed values of surface pressure values are in good agreement with respect to the experimental results. As a matter of fact, all the coarse, medium & fine grids are in good agreement with the experimental results. In order to avoid the effect of grid, we have taken the coarser grid to be sufficiently fine; which is why there is not much variation in the coarse, medium and fine grids.

*(2) $C_P$ values on store body*: The figures 7(a) and 7(b) show negative CP versus the position of slice taken on store body (X/C) for comparison of Euler & viscous computations. Here 4 slices are taken. The slices are cut radially around the store body (Refer Fig. 5(b)), the first slice being inclined 45 degree from the pylon which is taken as roll reference body i.e. zero degree line. Later slices are taken at 90 degree intervals. The slices are taken at 45, 135, 225 & 315 degrees in positive clockwise direction from the pylon. Here, the slices are taken in such a way that, the cutting plane (slice) passes through chord length of the fins and parallel to span of fins.

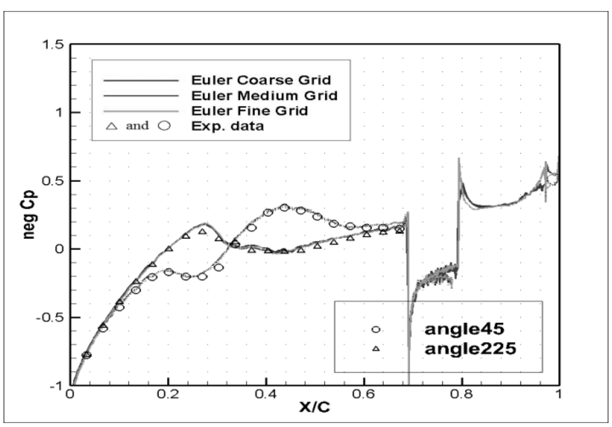


Fig. 7(a): $C_P$ values on store body taken at 45 & 225 degrees

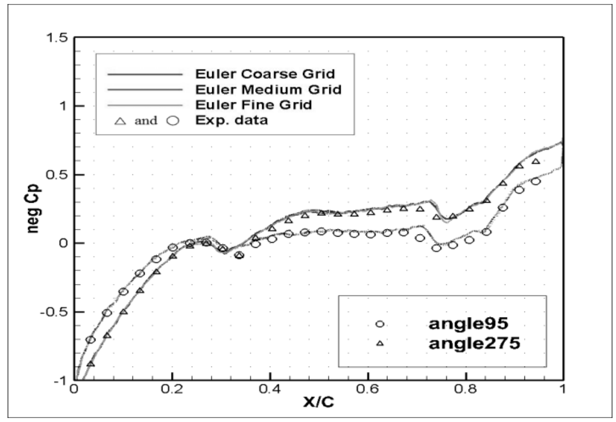


**Fig. 7(b):** $C_P$ values on store body taken at 95 & 275 degrees

From Figures 7 (a) and (b), it is clear that the computed values and the experimental values are in good agreement with each other. The coarse grid is made sufficiently fine in order to avoid grid effects. Hence not much variation is seen between coarse, medium and fine grids results.

*(3) $C_P$ values on Fin 1*: In the AEDC model, there are four fins (Refer Fig. 5), CFD analysis of each fin is done by extracting the surface pressure data. Two slices are taken on Fin 1 as shown in fig. 5(c), the graphs are plotted at each slice. The figures 8(a) and 8(b) shows the $C_P$ curves for Fin 1. Let φ be the Radial distance from Centre of Gravity (CG) of the store body, the slices are taken at certain radial distances with cutting plane being normal to the fin. Precisely, φ = {0.0357, 0.0496} which is a non-dimensional value.

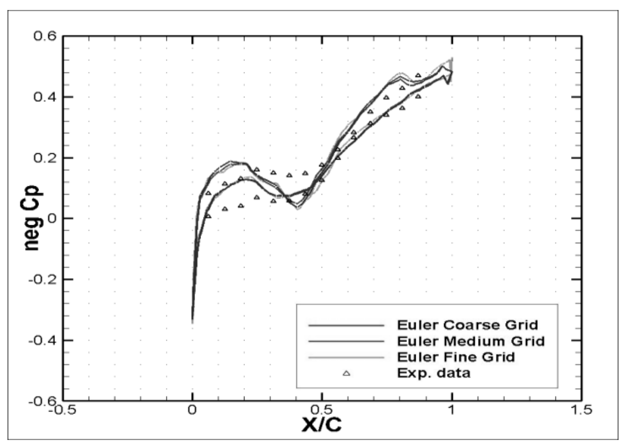


Fig. 8(a): Cp values at φ=0.3937C

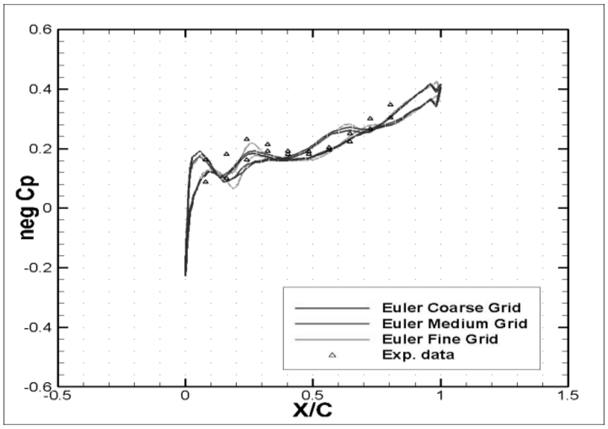


**Fig. 8(b):** Cp values at φ=0.0496C

4) *$C_P$ values on Fin 2*: The below fig. 9(a) & 9(b) shows $C_P$ vs. X/C plots for Fin 2. The slices are taken at radial distance φ;

φ = {0.0357, 0.0496} which is a non-dimensional value.

5) 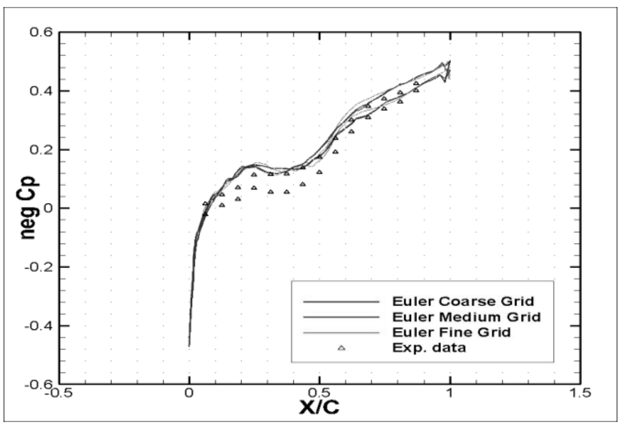


Fig. 9(a): Cp values at φ=0.3937C

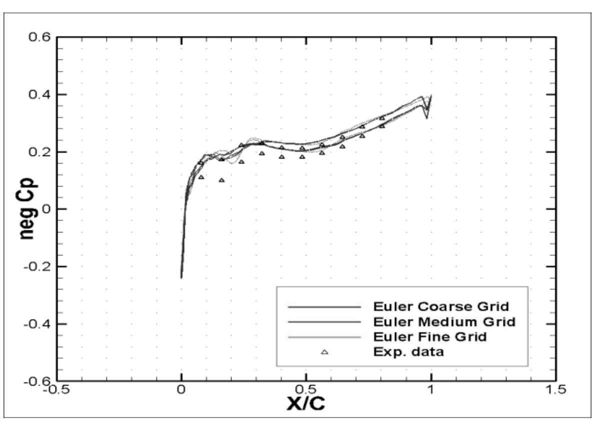


Fig. 9(b): Cp values at φ=0.0496C

6) *$C_P$ values on Fin 3*: The below figures 10(a) & 10(b) shows $C_P$ vs. X/C plots for Fin 3. The slices are taken at radial distance φ;

*7)* φ = {0.0357, 0.0496} which is a non-dimensional value.

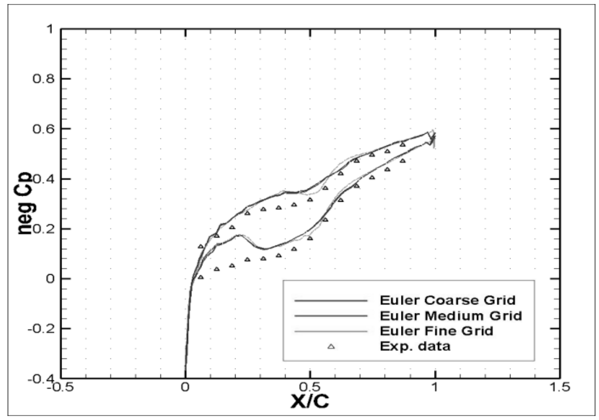


Fig. 10(a): Cp values at φ=0.3937C

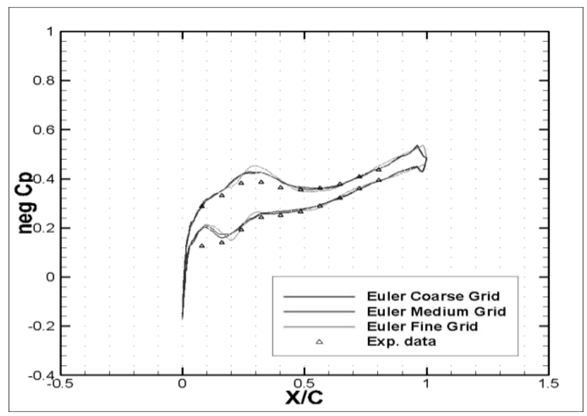


Fig. 10(b): Cp values at φ=0.0496C

8) *$C_P$ values on Fin 4*: The figures 11(a) and 11(b) shows $C_P$ versus X/C plots for Fin 4. The slices are taken at radial distance φ;

*9)* φ = {0.0357, 0.0496} which is a non-dimensional value.

*10)* 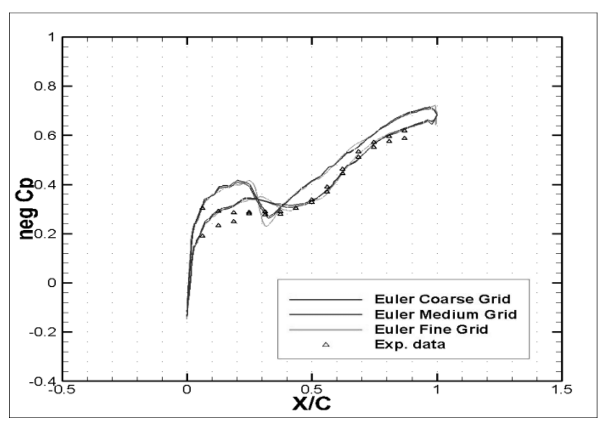


Fig. 11(a): Cp values at φ=0.3937C

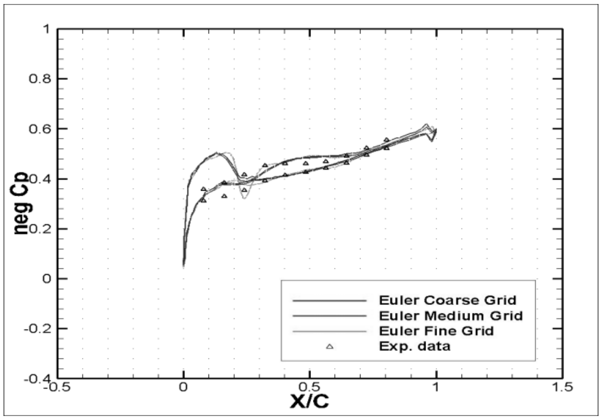


Fig. 11(b): Cp values at φ=0.0496C

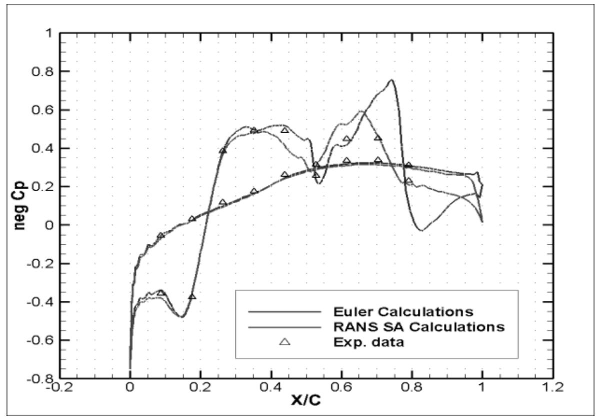


Fig. 12(b): $C_P$ values at 45.2% of wing span

It is clear from the Figures 8 to Figures 11 that, the computed results are not matching very well as that of wing-pylon and store body. Although, the trends are captured very well except for the magnitude. The scale of Y-axis representing $C_P$ makes this clear.

B. *Comparison of Euler and viscous solutions exclusively for fine grid having store configuration with experimental results*

The main idea in solving the fine grid used for viscous computations is to compute the accurate results over the fin region; as we observed some mismatch between the Euler computations & experimental results at fin regions. By experience, a fine grid was generated for viscous calculations by generating 10 T-Rex layers on the wall surface of the model. More details about the grid used for viscous computation is given in Table V**.**

*11) (1) $C_P$ values on wing surface**:** The Figures 12(a) and 12(b) show negative $C_P$ versus X/C values. The $C_P$ values are obtained both on upper and lower sides of the wing.*

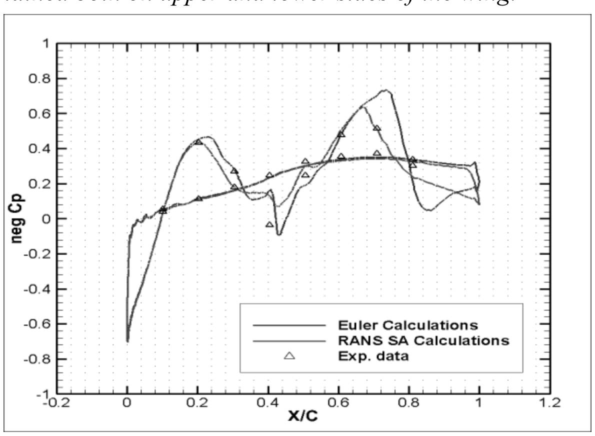


Fig. 12(a): $C_P$ values at 54.2% of wing span

It is clear from figures 12(a) and (b) that, the viscous computations with RANS-SA match well with the experimental results. The difference in RANS-SA and Euler is not very high.

*(2) $C_P$ values on Store body**:*** The figures 13(a) and (b) show $C_P$ versus X/C values drawn for comparison of Euler & viscous computations.

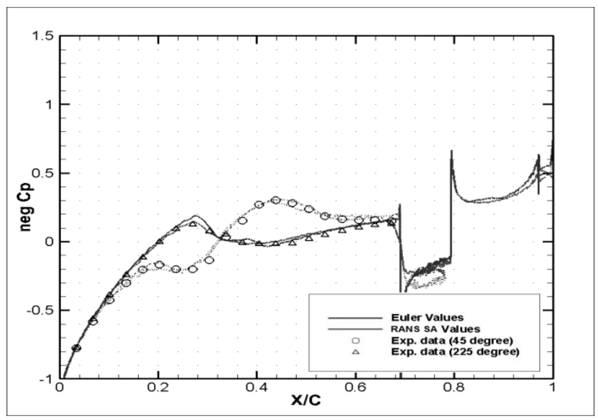


Fig. 13(a): $C_P$ values on store body taken at 45 & 225 degrees

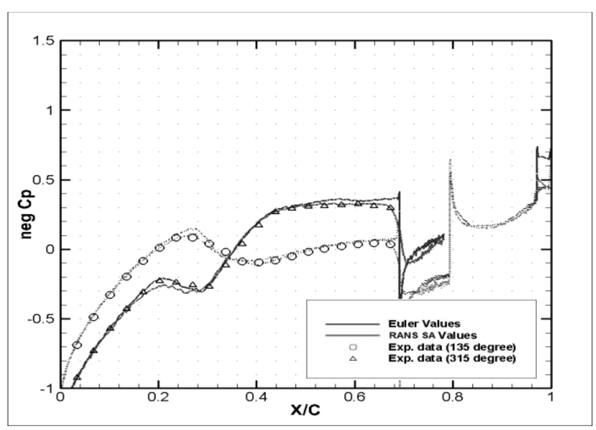


Fig. 13(b): $C_P$ values on store body taken at 45 & 225 degrees

12) *(3) $C_P$ values on Fin 1*: The Figures 14(a) and (b) shows $C_P$ versus X/C plots for Fin 1. The slices are taken at radial distance φ;

13) φ = {0.0357, 0.0496} which is a non-dimensional value.

14) 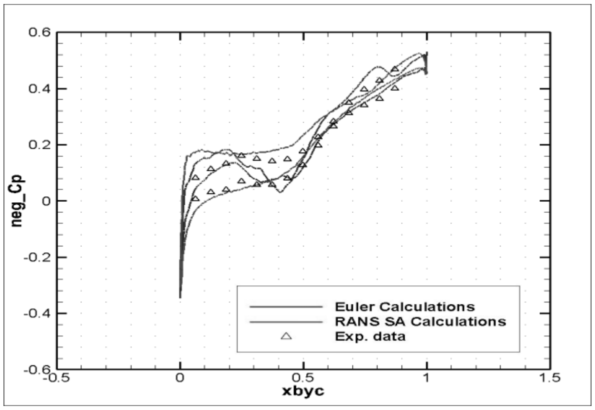


**Fig. 14(a):** Cp values at φ=0.3937C

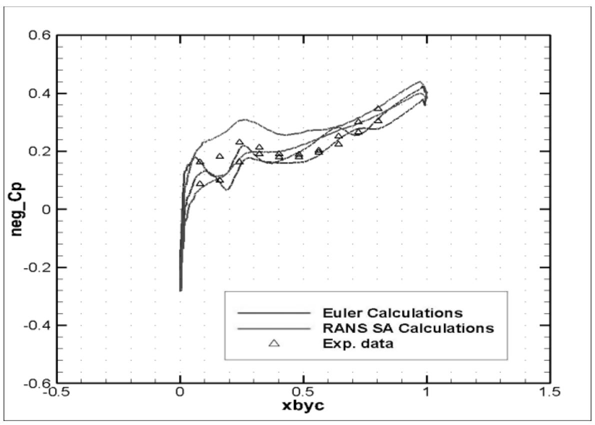


Fig. 14(b): Cp values at φ=0.0496C

The mismatch of Euler computations with the experimental data have been overcome in this section, it is clear from the Figures 12 to 14, that the viscous computations are closer to the experimental data than the Euler computations. Thus, it can be said that the viscous results are more accurate than the Euler computations.

The $C_P$ plots for other slices and remaining three fins drawn for fine grid (viscous computed) match more accurately than Euler solutions. We will discuss this further by taking the integral quantities of lift and drag.

15) *(1) Integrated quantities of drag & lift for Euler and RANS-SA Computations*:

16) The computed values for variable such as Coefficient of Drag ($C_D$), Coefficient of Lift ($C_L$) and Coefficient of Moment ($C_{M(X,Y,Z)}$) i.e. pitching along X, rolling along Y and yawing along Z direction; and Coefficient of Force ($C_{X,Y,Z}$) are shown in Table 2 and 3.

The values are shown for coarse, medium and fine grids used for Euler computations and fine grid used for viscous computations. The computations are done for the AEDC test model with-Store-configuration at its carriage position.

17) *(2) Integrated quantities of drag & lift for Wing-Pylon*: Below table shows $C_L$, $C_D$, $C_{M(X,Y,Z)}$ i.e. Roll, Pitch & Yaw and $C_F$ values exclusively for Wing-Pylon.

**Table 2:** $C_L$, $C_D$, $C_{M(X,Y,Z)}$ & $C_{F(X,Y,Z)}$ values for Wing-Pylon

| | **Coarse Grid** (Euler computations) | **Medium Grid** (Euler computations) | **Fine Grid** (Euler computations) | **Fine Grid** (Viscous computations) |
|---|---|---|---|---|
| **$C_L$** | 0.0029 | 0.0032 | 0.0032 | 0.0009 |
| **$C_D$** | 0.0241 | 0.0243 | 0.0243 | 0.0249 |
| **Roll** | 0.0010 | 0.0012 | 0.0012 | 0.0003 |
| **Pitch** | -0.0040 | -0.0041 | -0.0042 | -0.0031 |
| **Yaw** | -0.0070 | -0.0070 | -0.0070 | -0.0071 |
| **Cx** | 0.0241 | 0.0243 | 0.0243 | 0.0249 |
| **Cy** | -0.0081 | -0.0082 | -0.0083 | -0.0084 |
| **Cz** | 0.0029 | 0.0032 | 0.0032 | 0.0009 |

18) *(2) Integrated quantities of drag & lift for Finned-Store*: Below table shows $C_L$, $C_D$, $C_{M(X,Y,Z)}$ and $C_F$ values exclusively for Finned-Store.

Table 3: $C_L$, $C_D$, $C_M$ & $C_{F(X,Y,Z)}$ values for Finned-Store

| | **Coarse Grid** (Euler computations) | **Medium Grid** (Euler computations) | **Fine Grid** (Euler computations) | **Fine Grid** (Viscous computations) |
|---|---|---|---|---|
| **$C_L$** | -0.0018 | -0.0018 | -0.0018 | -0.0016 |
| **$C_D$** | 0.0035 | 0.0035 | 0.0035 | 0.0034 |
| **Roll** | -0.0005 | -0.0005 | -0.0005 | -0.0005 |
| **Pitch** | 0.0013 | 0.0013 | 0.0013 | 0.0013 |
| **Yaw** | -0.0024 | -0.0023 | -0.0023 | -0.0023 |
| **Cx** | 0.0035 | 0.0035 | 0.0035 | 0.0034 |
| **Cy** | -0.0019 | -0.0018 | -0.0018 | -0.0017 |
| **Cz** | -0.0018 | -0.0018 | -0.0018 | -0.0016 |

From Table 2**,** it can be seen that the difference in fine and medium grids Euler calculations is not much. It reconfirms out grid refinement study. Further, we can see that Drag is slightly higher on viscous computations compared to Inviscid as expected. In general, the difference on integrated quantities of $C_L$ and $C_D$ are not very high for viscous and inviscid solutions. Particularly for the store, the difference between Inviscid and viscid is negligible.

The comparison of the wing-without-store-configuration and wing-with-store-configuration (both Euler and viscous computations) with respect to experimental results is made; wing-with-store-configuration matched well with the experimental results as the experimental data obtained is in the presence of store configuration.

## IV. Conclusions

Aerodynamic analysis of wing-pylon-store is carried (AoA=0 degrees & Mach No.=1.2) out using $SU^2$- tool and validated with AEDC experimental test data. Three sets of computations for coarser, medium and fine grids have been carried out for inviscid simulations. The grid independent solution is established. The solutions match well with the available experimental results. Further to analyse viscous effects RANS-SA computations were carried out and compared with inviscid computations. The comparison showed that on wing-pylon and store body, the difference in $C_p$ agreement is not very much. But on the fins, the viscous results match better compared to inviscid with experimental results. However, it is interesting to note that the overall integrated quantities of $C_L$ and $C_D$ are of importance on store trajectory prediction; $C_L$ and $C_D$ are the inputs to trajectory prediction equations. Considering this aspect, it seems inviscid approximation may be good enough. Further studies are required to actually compute trajectory with both approximations to fully establish this conclusion.

## ACKNOWLEDGMENT

The authors would like to thank the Computational and Theoretical Fluid Dynamics Division, National Aerospace Laboratories, Bengaluru for allowing us to carry out the project work. The authors would also like to acknowledge Department of Mechanical Engineering, SDMCET, Dharwad for their continuous support throughout the project work.

## REFERENCES

[1] Tholudin Mat Lazim, Shabudin Mat, Huong Yu Saint, "Computational Fluid Dynamic Simulation (CFD) and Experimental Study on Wing-external Store Aerodynamic Interference of a Subsonic Fighter Aircraft", *Acta Polytechnica* Vol. 43 No. 5/2003

[2] Yunus Emre Sunay, Emrah Gulay, Ali Akgul, "Numerical Simulations of Store Separation Trajectories using the EGLIN Test", *Scientific Technical Review*, 2013, Vol 63, N0.1, pp 10-16

[3] John H. Fox, "Generic Wing, Pylon and moving Finned Store", *Sverdrup Technology, Inc./AEDC Group, Arnold Engineering and Development Center (AEDC), Arnold AFB, USA*, June 1996

[4] Robert F. Tomaro, Frank C. Witzeman and William Z. Strang, "A Solution on the F-18C For Store Separation Simulation using *Cobalt*$_{60}$", AIAA 99-0122

[5] https://github.com/su2code/SU2/wiki/

[6] https://en.wikipedia.org/wiki/Tecplot

[7] Francisco Palacious, Thomas D. Economon, Aniket C. Aranake, Sean R. Copeland, Amrita K. Lonkar, Trent W. Lukaczyk, David C. Monosalvas, Kedar R. Naik, A. Santiago Padron, Brendan Tracey, Anil Variyar and Juan J. Alanso, "Stanford University Unstructured (SU2): Open Source Analysis and Design Technology for Turbulent Flows", *AIAA 2014-0243, National Harbor, Maryland, 52nd Aerospace Sciences Meeting*

[8] Tecplot 360 EX 2014 R1 Help Viewer (6/7/14) build

[9] V. Venkatakrishnan, "Convergence to steady state Solutions of the Euler Equations on Unstructured Grids with Limiters", *Journal of Computational Physics 118, 120-130 (1995)*

# Numerical Investigation on Effect of Turbulence Modelling in a Supersonic flow Across an Intake Geometry Using OpenFOAM

Naveen Yesudian[1], Sankar Raju.N[2], Arul T.S[3] Soma Sundaram.S[4]

*Department of Mechanical Engineering, SSN College of Engineering, Anna University, Chennai, India*

[1]yesudiannaveen@gmail.com

[2]sankarraju94@gmail.com

[3]arul.ts10@gmail.com

[4]somasundarams@ssn.edu.in

***Abstract*— Numerical analysis of supersonic flows using Open FOAM, an open source CFD tool, is performed for double ramp model. Two-dimensional, unsteady, compressible, turbulent flow equations have been solved. Initially a grid independent study is performed for the model and deviations are studied and henceforth a suitable mesh with minimum deviations is considered for further studies. Then a comparative study of simulations of k-epsilon and k-omega turbulence models is performed. It is found that the deviation of k-omega turbulence model is comparatively lower than k-epsilon model with respect to the experimental results. Therefore implementation of the k-omega turbulence model would be efficient for solving supersonic flows using OpenFOAM.**

***Keywords* - Compressible flow, Numerical Simulation, Shock Interaction, RANS model.**

## I. INTRODUCTION

The design of intake geometries has been of great interest to engineers in the design of scramjet engines. The engine comprises of three main parts such as inlet, combustion chamber and nozzle. The inlet is basically a duct before the combustion chamber and its function is to provide the required amount of air at the specified pressure to the engine for combustion. The inlet increases the pressure of the atmospheric air which has to be sent to the combustion chamber. In the case of turbofan engines the high pressure rise is obtained by means of a compressor. However, in the case of a ramjet engine this is done by means of a series of oblique shocks that are generated from the inlet surfaces. Thus the design has to be such that the shocks strike the surfaces at correct angles to provide the necessary reflections for the shocks to propagate through the engine.

The approach consists of splitting the shock wave into a series of oblique shocks, each resulting in a similar pressure increase. The efficiency of the intake compression process strongly depends upon the boundary layer over the intake surface which also has an effect on the combustor performance [1]. Haberle and Gulhan[2] carried out experimental investigation of 2D hypersonic scramjet inlet and compared it with numerical simulations. They used a double ramp model as intake geometry and oblique shocks were generated from the surfaces.

OpenFOAM is an open source CFD software which is finding its use in various CFD problems. The advantages of using this software is that the necessity to purchase licenses is obviated and hence parallel processing can be carried out simultaneously using different computers. Also user defined codes can be generated to solve complex problems for which predefined codes do not exist. Numerical simulation of supersonic flows was performed by Malsur Dharavath *et al.* [3] using a commercial package. They showed that the RANS model is better than the high fidelity LES calculations in capturing the mixing of two supersonic dissimilar gases. Experimental investigation of shock wave interaction and the effect of curved edges on shock wave diffraction were performed by Gnani *et al.* [4]. It was shown that the ramp and symmetrical wedges showed difference in behaviour for curved edges.

The numerical simulations of the formation of multiple reflected shocks in convergent portion for supersonic flow were carried out by Manish Kumar Jain and Sanjay Mittal [5]. The governing equations were solved using stabilized finite element formulation. The streamline-upwind/Petrov-Galerkin (SUPG) stabilization method was employed to stabilize the computations against numerical oscillations. The effect of intake geometry on start-up problems was presented. Three dimensional experimental study of air compression for supersonic inlets was performed by A.V.Lokotko and A.M.Kharitonov [6]. Simulation using FLUENT for a supersonic intake was carried out by Sivakumar and Babu [7] using k-$\epsilon$ turbulence model. The numerical results were validated with the experimental data. The mas flow rate and shock locations were predicted exactly at the correct locations, but the static pressure losses were over-predicted. The intake geometry considered for the present study is taken from the experiments carried out by Schneider and Koschel [8].The objective of this paper is to determine the best suited turbulence model for high speed compressible flow. The k-$\epsilon$ and k-$\omega$ models are compared using OpenFOAM for solving the governing equations involved in the problem.

## II. SIMULATION DETAILS

The intake geometry is based on the double ramp model. This type of model is widely used in supersonic aircraft engines. It consists of a double inclined ramp and cowl-lip geometry as shown in Fig.1. The numerical domain is explained as follows: A distance of 150 mm is provided before the start of the ramp to allow free stream and a distance of 150 mm is provided as height to prevent the shock reflection.

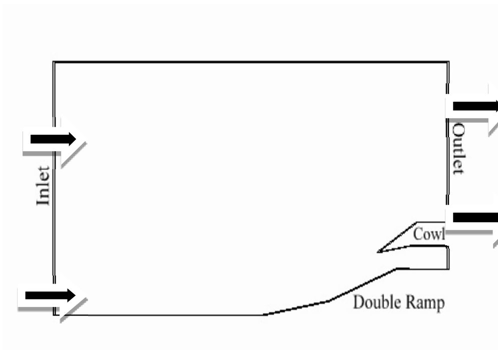


Figure 1: CAD model of geometry

The experimental data for wall pressures at the ramp and cowl is available in literature [8]. Since the cross flow pressure variation data are not available in the literature, two dimensional calculations are carried out to reduce computational time and power. The air is assumed to behave as an ideal gas following the equation of state with a constant specific heat of 1.005 kJ/kgK and $\gamma$ = 1.4. The flow is considered compressible and assumed to have a constant turbulent viscosity of $1.8\times10^{-5}$Pa.s and Prandtl number is given to be 0.7. The boundary conditions are given for a Mach number of 2.99. The inlet boundary has been provided with a velocity of 696.36 m/s, a static pressure of 15 kPa and a static temperature of 135 K. The turbulence has been calculated considering the length scale to be the height of the inlet and turbulence intensity to be 5%.The values of k, $\varepsilon$ and $\omega$ are calculated to be 1818.512 $m^2/s^2$, 1274262.8 $m^2/s^3$ and 7785.696 $s^{-1}$ respectively from standard formulae. The walls are assumed to be stationary and adiabatic.

The methodologies followed are basically second order schemes. Temporal discretization has been carried out using second order implicit schemes, while the gradient and divergence are discretised using Gauss linear schemes. Iterations were spaced at a time-step size of $5\times10^{-7}$s.

## III. GRID INDEPENDENCE STUDY

Three different meshes are used to determine the optimal mesh size and to ensure grid independence. The pressure data at the ramp and cowl walls are compared. Initially a mesh of base size 1mm was generated with a cell count of 36000 (shown as Mesh1). Few more cells were added in the regions of gradients and the cell count has been increased to 37000 cells (Mesh 2). This mesh has been further refined to 38000 cells (Mesh 3).There is a deviation of 29.63% in P/Po between Mesh 1 and Mesh 2,while the deviation between Mesh 2 and Mesh 3 is less than 0.5%. And hence forth Mesh 2 has been considered for further analysis.

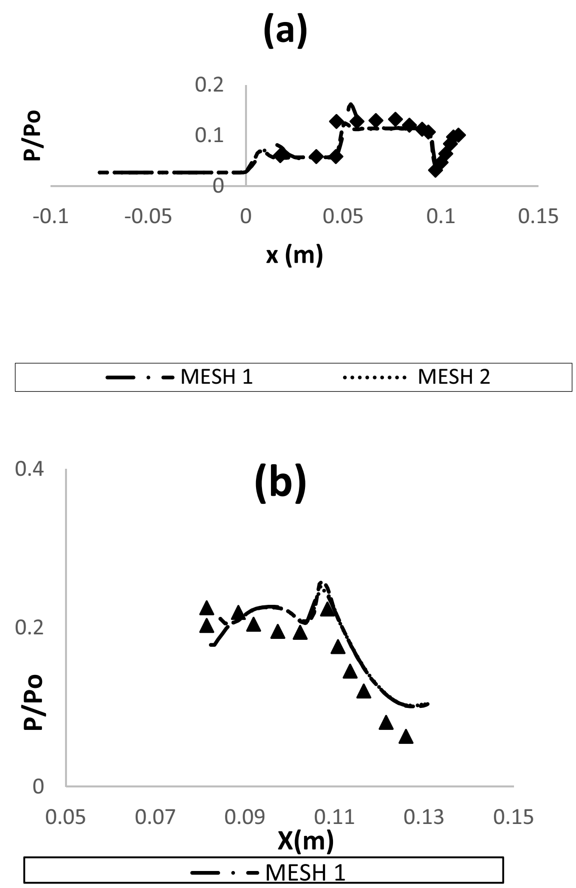


Figure 2: Plot showing variation of P/P0 with respect to axial distance at (a) ramp (b) cowl. X= 0 indicates the leading edge of the ramp.

## IV. RESULTS AND DISCUSSION

The validation was carried out for the k-$\epsilon$ and k-$\omega$ models with the experimental data from Schneider and Koschel [8]. The values of static pressure determined along the walls of the ramp and cowl are converted to a non-dimensional quantity by dividing it with the inlet free stream stagnation pressure. These values are plotted against the axial distance X in Fig.3. The initial oblique shock created by the leading edge of the ramp at X=0. The location of the second oblique shock and the peak pressure obtained, triggered by the second segment of the ramp are also captured well. However, there is a slight deviation in the predicted values against experimentally measured values. At the end of the ramp there is a sudden drop in the pressure, indicating the presence of an expansion fan.

In the case of the cowl, it has been found that though the trends are captured well there is a deviation with the measured values. It can be seen that there is a steep drop in the pressure indicating an expansion fan at the end of the cowl. There is a deviation of 38.2% between experimental and k-epsilon turbulence model while the deviation in the case of k-omega is 18.4%. And henceforth k-omega model of turbulence is found to be better k-epsilon turbulence model.

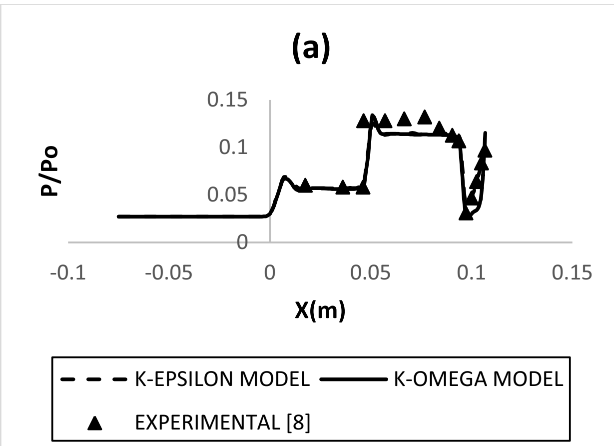


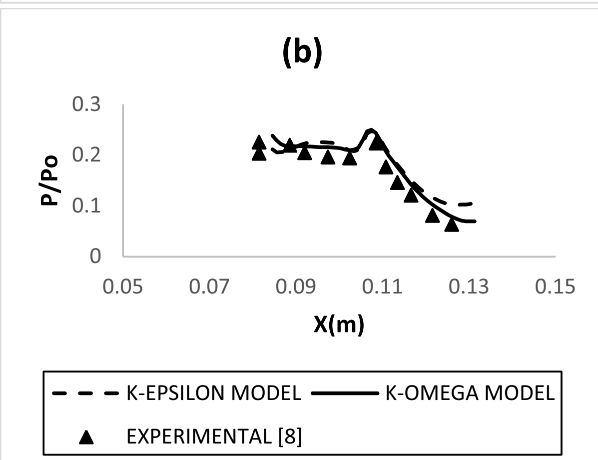


Figure 3: Plot showing variation of P/P0 with respect to axial distance at (a) ramp (b) cowl.

Contours of pressure variation in the numerical domain are shown in Fig. 4. The air under pressure enters from the left and leaves at the right of the domain. There is no pressure change from x= -0.075 to x=0 as it is free stream. The shocks generated from the first and second ramps are clearly captured and have different intensities of pressure. The peak pressure and drop in pressure is also captured clearly as seen in the contour. It is seen from the contour plot that the shock deflects downwards from the tip of the cowl and hits back at ramp at x=0.05 and hence forth a shock train is formed between the cowl and ramp. It is seen that an expansion fan is formed at x=0.11 and correspondingly a pressure drop occurs.

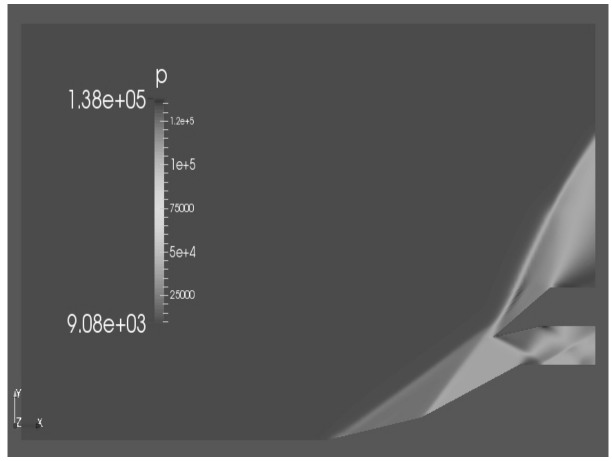


Figure 4: Contour plot of pressure data in the numerical domain. The flow direction is from left to right.

Contours of the variation of Mach number in the numerical domain are shown in Fig. 5. It is seen that the Mach number remains constant from x= -0.075 to x=0 due to the absence of pressure variation as explained above. There is a decrease in Mach number at the start of both the ramps for corresponding pressure peaks. Further downstream, a slight increase in Mach number is observed due to the expansion fan at x=0.11 as a result of the reflected shocks. The least Mach number is seen at the upper surface of the cowl. However, due to the unavailability of experimental data at the upper surface, the parameters at the lower surface are plotted and validated.

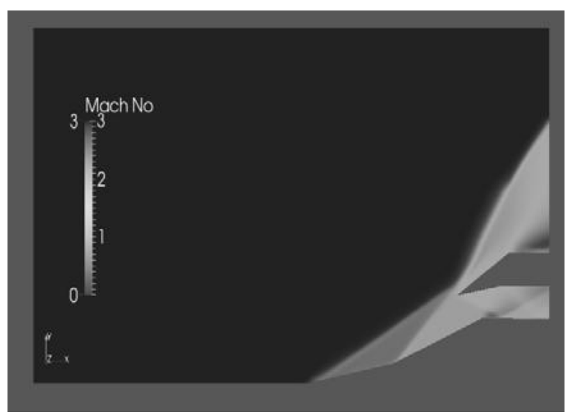


Figure 4: Contour plot of Mach number in the numerical domain. The flow direction is from left to right.

## V. CONCLUSIONS

Numerical analysis of the supersonic flow for the intake geometry available in literature has been carried out. A detailed study of various meshes for the analysis has been performed and a suitable mesh is taken for further analysis. Then a numerical simulation of k-epsilon turbulence model and k-omega turbulence model is performed and it is found that the deviation of k-omega turbulence model is comparatively low. And henceforth k-omega turbulence model is more appropriate for supersonic flow simulations for the open source CFD software tool OpenFOAM.

## ACKNOWLEDGEMENT

The authors would like to thank the Department of Mechanical Engineering, SSN College of Engineering, Chennai, for providing a platform to perform this research. The authors would also like to thank the OpenFOAM community for providing their software tool for this analysis.

## REFERENCES

[1] Krishnan, L., N. D. Sandham, and Johan Steelant. "Shock-wave/boundary-layer interactions in a model scramjet intake." AIAA journal 47.7 (2009): 1680-1691.

[2] Häberle, Jürgen, and Ali Gülhan. "Investigation of two-dimensional scramjet inlet flowfield at Mach 7." Journal of Propulsion and Power 24.3 (2008): 446-459.

[3] Malsur Dharavath, P. Manna, Debasis Chakraborty. "Numerical exploration of dissimilar supersonic coaxial jets mixing". IAA journal (2015):0094-5765.

[4] F.Gnani, K.H.Lo, H. Zare-Behtash, K.Kontis. "Experimental investigation on shock wave diffraction over sharp and curved splitters". IAA journal(2014):0094-5765

[5] Manish Kumar Jain and Sanjay Mittal. "Euler flow in a supersonic mixed-compression inlet". International Journal for numerical methods in fluids (2006): 1405-1423.

[6] A.V.Lokotko and A.M. Kharitonov. "On the possible formation of a vortex flow in a supersonic inlet with three-dimensional compression". Fluid Dynamics journal, Vol.41, No.4 (2006):649-660.

[7] Sivakumar, R., and V. Babu. "Numerical simulations of flow in a 3-D supersonic intake at high Mach numbers." Defense Science Journal 56.4 (2006): 465-476..

[8] Schneider, A. & Koschel, W.W. Detailed Analysis of a mixed compression hypersonic intake. International Society of Air Breathing Engines (ISABE), 1999, ISABE 99-7036.

# Performance Characteristics of Slanted Entry and Exit Nozzles

I Dakshina Murthy[1], P.Lovaraju[2]

*Department of Aerospace Engineering,*

*Lakireddy Balireddy College of Engineering, Mylavaram, Andhra Pradesh, india*

[1]murthy.lbce@gmail.com
[2]lovaraju@gmail.com

***Abstract*— In the present study, flow characteristics of two slanted nozzles have been investigated. One is slanted entry nozzle, designed for M 2.0 exposed to NPR's (Nozzle Pressure Ratios) 1.136, 1.263, 1.395, 1.526, 1.658, 1.79, 1.921 and 2.05 with inlet plane cutting angles of $20^0$ and $40^0$ . The other one is, slanted exit nozzle designed for M 3.0 exposed to the NPR's 2, 2.5, 3, 3.5, 4, 4.5, 5, 6 and 7 with exit plane cutting angles of $30^0$ and $70^0$. The main interest in this study is to check whether such a nozzle, can choke and deliver supersonic flow at the exit. The present study also explores the wall pressure distribution inside the nozzle and flow separation inside a slanted nozzle. The studies reveal that the nozzle can choke and deliver supersonic flow.**

## I. INTRODUCTION

Flows through the supersonic nozzles are of interest in basic research. This investigation was initiated to gain the better understanding of the flow through the convergent divergent nozzle with slanted entry and exit. The objective is to check whether such nozzles attached to a stagnation chamber and driven by different pressure ratios, choke and deliver supersonic flow at the exit. C. Senthil Kumar et. al.,[1] studies reveals that a slanted entry CD nozzle placed in supersonic stream chokes and delivers supersonic stream at its exit. Nazar Muneam Mahmood et.al., [2] reported that, characteristics of fluid change with axial location in a variable area nozzle when the fluid is an ideal gas and the flow through it is steady and isentropic. Kunal Pansari, et. al., [3] investigated that shock strength increases significantly by increasing ($M_1$), whereas shock location does not vary much with ($M_1$). Mohan Kumar G et. al., [4] reported that optimum expansion of gas at exit is critical for efficient operation of nozzle. Dimitri Papamoschou et. al., [5] reported that for large NPR and $A_e$=$A_t$, the shock is unsteady and the range of its axial motion is approximately one half of the local test section height. SETUP

## II. EXPERIMENTAL SETUP

The experiments for slanted entry nozzles and slanted exit nozzles were conducted in the open jet facility at Aerodynamics laboratory, Lakireddy Balireddy College of Engineering.The layout of open jet facility is shown in Fig. 1. High pressure air enters the settling chamber through a tunnel section with a gate valve followed by a pressure regulating valve and a mixing length. The settling chamber is connected to the mixing length by a wide angle diffuser. The flow is further conditioned inside the settling chamber by closely meshed grids meant for minimizing turbulence. A nozzle was fitted at the end of the settling chamber with “O” ring sealing to avoid leakage. The settling chamber temperature was same as the ambient temperature and the back pressure was the ambient pressure.

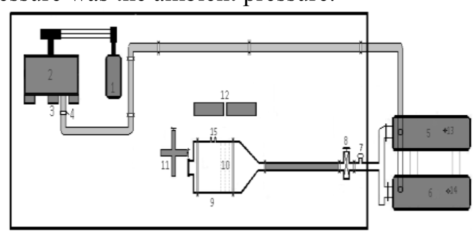

Fig. 1. Layout of the Open Jet Facility

1. 20 hp induction motor
2. Reciprocating compressor
3. Activated charcoal filters
4. Non-return valve
5. Storage tank 1
6. Storage tank 2
7. Pressure gauge
8. Pressure regulating valve
9. Stagnation chamber
10.Screens
11.Traversing system
12.U-tube manometers
13.safety valve 1
14. Safety valve 2
15.Two pressure ports

## III. EXPERIMENTAL MODELS

### *A. Design on Nozzles for Slanted Entry Configuration:*

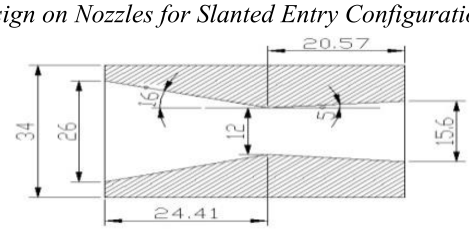


(a) Straight Cut

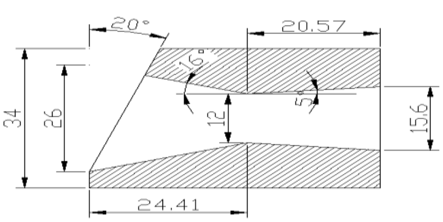


(b) Slanted Entry ($20^0$ Deg)

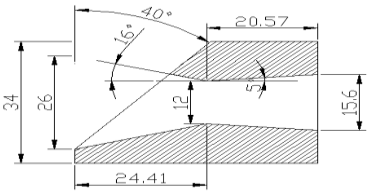


(c) Slanted Entry ($40^0$ Deg)

Fig 2. Schematic Diagram of C-D Nozzles Designed for M = 2

*B. Design on Nozzles for Slanted Exit Configuration:*

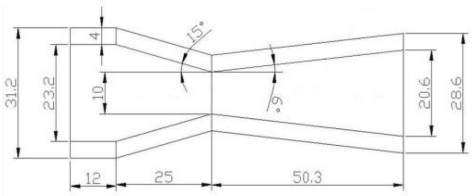


(a) Straight Cut

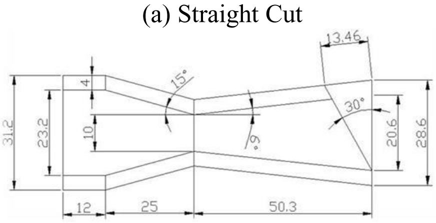


(b) Slanted Exit ($30^0$ Deg)

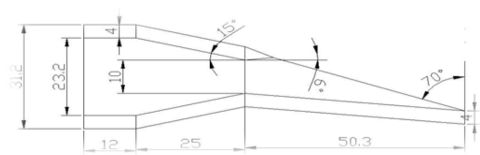


(c) Slanted Exit ($70^0$ Deg)

Fig 3. Schematic Diagram of Nozzles Designed for M = 3

## IV. Results and Discussion

In the present study two types of slanted nozzle configurations were studied. Slanted entry nozzle, designed for M 2.0 exposed to NPR's 1.136, 1.263, 1.395, 1.526, 1.658, 1.79, 1.921 and 2.05 with slanted cutting angles of $20^0$ and $40^0$. Based on the one-dimensional isentropic theory the slanted entry nozzle is able to choke at NPR 1.012 and the normal shock will be present at the exit up to NPR 1.738. The second one is, slanted exit nozzle designed for M 3.0 exposed to the NPR's 2, 2.5, 3, 3.5, 4, 4.5, 5, 6 and 7 with exit plane cutting angles of $30^0$ and $70^0$. Based on the one-dimensional isentropic theory the slanted entry nozzle is able to choke at NPR 1.013 and the normal shock will be present at the exit up to NPR 3.55.

### *A. Flow Characteristics of Slanted Entry Nozzles*

Figures 4(a), (b) and (c) represent the wall pressure distribution for straight entry, slanted entry ($20^0$) and slanted entry ($40^0$) respectively. The tests were conducted at different Nozzle Pressure Ratios (NPR) like 1.136, 1.263, 1.395, 1.526, 1.658, 1.79, 1.921 and 2.05. The wall pressure ($P_w$) measured is non-dimensionalised with stagnation chamber pressure ($P_0$), and the nozzle axial distance (X) is non-dimensionalised with length (L) of the nozzle.

As seen in the Fig. 4 (a) the flow phenomenon is distinctly different from the isentropic theory. It can also be seen that for NPR's 1.136, 1.263, 1.395 and 1.526 the flow accelerates till the throat and followed by deceleration in the divergent portion. For the NPR 1.658 there observed a sudden rise in the wall static pressure just after the throat followed by reduction in wall pressure. This effect may be due to the presence of normal shock in the divergent portion. The further increment in the pressure ratio, i.e., for NPR's 1.79, 1.921 and 2.05 there observed a pressure loss after throat which represents the supersonic flow. Further there observed a rise in the pressure, this may be because of the separation occurred in the divergent portion. Figures 4 (b) and 4 (c) represent the flow characteristics of slanted entry nozzles. From the figures it is seen that the wall pressure distribution is distinctly different from straight entry nozzle. There observed a rise in the wall pressure in the convergent portion as the NPR increases. It is also observed that the wall pressure rise in the convergent portion. It is superior as the cutting angle increases. The wall pressure distribution in the divergent portion is almost similar for the slanted entry nozzles when compared with nozzle without cut. Form the observations, it can be inferred that the nozzle with slanted entry can also be chocked and is able to deliver supersonic flow.

Figures 5 (a) to (h) represent the comparison of the nozzles with and without Slanted Cut for different NPRs. From the graphs it is observed that at lower NPRs like 1.136, 1.263 and 1.395, the wall pressure distribution for nozzle with straight cut and $20^0$ cut is all most similar and distinctly different from the nozzle with $40^0$ cut. At higher NPRs, the wall pressure distribution in convergent and divergent portion for all the entry nozzle configurations were similar.

### *B. Flow Characteristics of Slanted Exit Nozzles*

Figures 6 (a), (b) and (c) represent the wall pressure distribution for straight entry, slanted exit ($30^0$) and slanted exit ($70^0$), respectively. The tests were conducted at different Nozzle Pressure Ratios (NPR) like 2, 2.5, 3, 3.5, 4, 4.5, 5, 6 and 7. Here also the wall pressure ($P_w$) measured is non-dimensionalised with stagnation chamber pressure ($P_0$), and the nozzle axial distance (X) is non-dimensionalised with length (L) of the nozzle.

Figure 6 (a) shows the wall static pressure distribution for the nozzle without cut. In the convergent section the wall static pressure for the all NPRs is same. The pressure at the throat is changing with respect to the change of NPR. In the divergent section wall static pressure continuous to decrease for NPR 3 onwards as the normal shock is present, as this is NPR is less than 2.45. The static pressure increases and velocity decreases. Figure 6 (b) shows the wall static pressure distribution for the nozzle with $30^o$ cut at exit plane.

The cut is mainly is to check weather this nozzle will deliver supersonic flow as that of nozzle without cut. The main argument comes because the exit plane divergent portion is spoiled. Even otherwise it has to deliver supersonic flow. In this nozzle also in the convergent section all wall static pressure distribution for all the NPR's is almost same. At the throat the minimum pressure is assumed for all the NPR's. As the nozzle pressure ratio increases the wall static pressure at throat decreases. The wall static pressure continuously decreases for NPRs 2 to 4. This is because of the presence of normal shock inside the divergent section.

Figure 6 (c) shows the Wall static pressure distribution for the nozzle with $70^o$ cut at exit plane. In the convergent section the wall static pressure distribution is same at all NPR's. The pressure at the throat is the function of NPR. In the divergent section the wall static pressure distribution continuously decreases at the throat for NPR 6 and 7. For NPR 2 the wall static pressure rises just beyond the throat. For NPR 2.5, 3, 3.5, 4 and 4.5, the rise in the static pressure is downstream of throat. This downstream location moves with NPR. Since this cut is $70^o$ to the exit plane this is almost removing major portion of nozzle on one side. As NPR increases the flow encounters a free boundary and solid boundary from the throat. This causes the shocks to get like reflection on the solid boundary side and unlike reflection on the free boundary side.

Figure 7 (a) shows the wall static pressure distribution for the straight and slanted nozzles for NPR 2.0. In this we can observe that wall static pressure distribution is same in the convergent section for all nozzles. After convergent portion for slanted nozzle with $70^0$ cut the static pressure rises just beyond the throat. Figure 7 (b) shows the static wall pressure distribution for the straight and slanted nozzles for NPR 2.5. In this also static pressure is same in convergent portion and static pressure rises from $8^{th}$ pressure tap for the slanted nozzle with $70^0$ cut. Figure 7 (c) shows the static wall pressure distribution for the straight and slanted nozzles for NPR 3.0. In this also static pressure is same in convergent portion and static pressure rises from $9^{th}$ pressure tap for the slanted nozzle with $70^0$ cut.

For the slanted nozzle with $30^0$ cut, as nozzle pressure ratio increases the wall static pressure at throat decreases. The wall pressure continuously decreases for NPRs 2 to 4. The wall static pressure gradually increases. This is because of the presence of normal shock inside the divergent section.

For the slanted nozzle with $70^0$ cut, For NPR 2.5, 3, 3.5, 4, 4.5, the rise in the static pressure is downstream of throat. This downstream location moves with NPR. Since this cut is $70^o$ to the exit plane, this is almost removing major portion of nozzle on one side. As NPR increases the flow encounters a free boundary and solid boundary from the throat. This is shown in the Figs. 7 (d) to 7 (i).

*C. Shadowgraph*

Shadowgraphs are usually considered mainly useful for revealing strong density gradients of the flow. The flow pattern was photographed using a shadowgraph system with a helium spark arc light source in conjunction with 150 mm concave mirror. The surface finish of the mirror is $\lambda/6$ and the focal length is 1.6 m. The concave mirror is mounted on a stand. The shadowgraph image for flow through the slanted nozzles is shown in Figs. 8 (a) to (c). Figure 8 (a) shows the shadowgraph view of the CD-nozzle without cut at the exit plane. In this we can observe the formation of shock waves in the flow field. Figure 4.5(b) shows the shadowgraph view of the CD-nozzle with $30^o$ cut at the exit plane. In this we can observe the formation of shock waves in the flow field. In this we can observe the jet direction will be slightly different from the previous one. Figure 8 (c) shows the shadowgraph view of the CD-nozzle with $70^o$ cut at the exit plane. In this we can observe that the formation of the jet is not along the axis. This is called thrust vectoring.

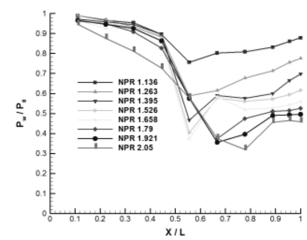


Fig .4(a) Wall Pressure Distribution For Straight Entry at Different NPR's

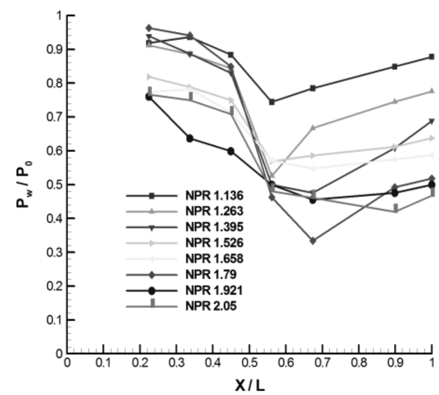


Fig. 4(b) Wall Pressure Distribution For Slanted Entry ($20^0$ Cut) at Different NPR's

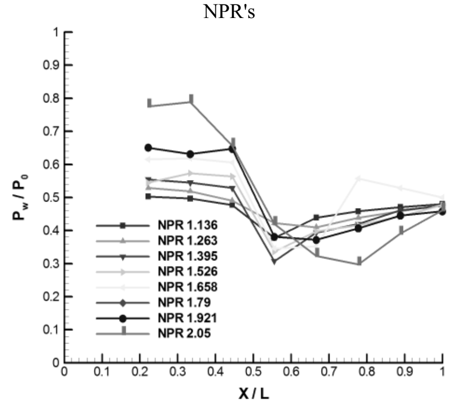


Fig.4(c) Wall Pressure Distribution For Slanted Entry ($40^0$ Cut) at Different NPR's

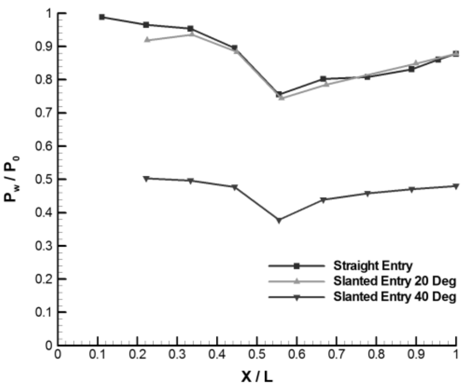


Fig. 5(a) NPR 1.136

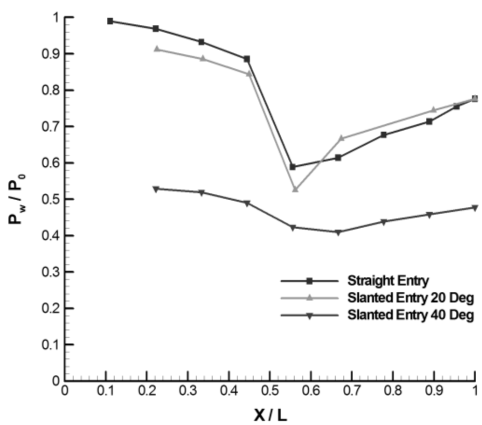


Fig.5(b) NPR 1.263

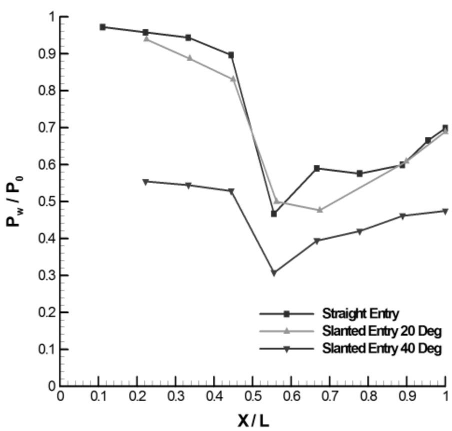


Fig.5(c) NPR 1.395

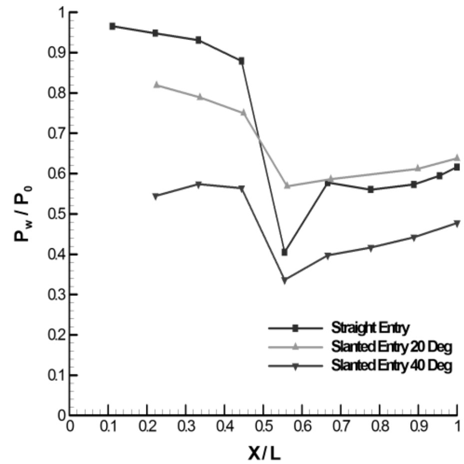


Fig. 5(d) NPR 1.526

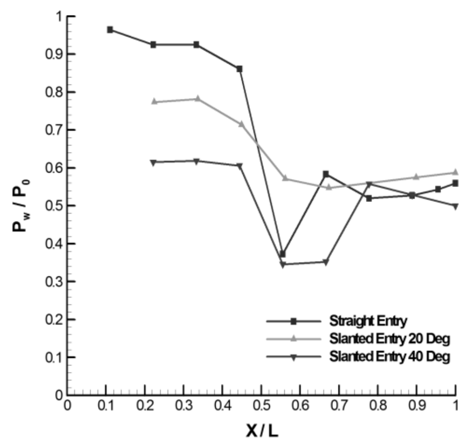


Fig.5(e) NPR 1.658

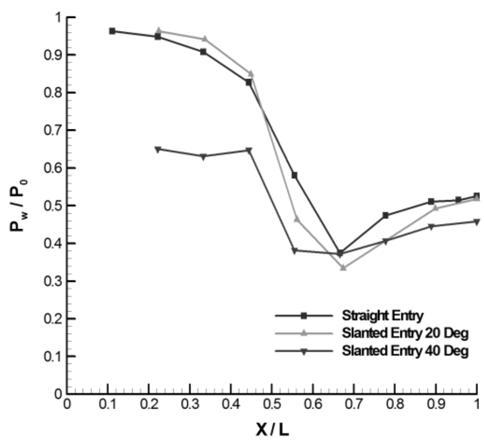


Fig.5(f) NPR 1.79

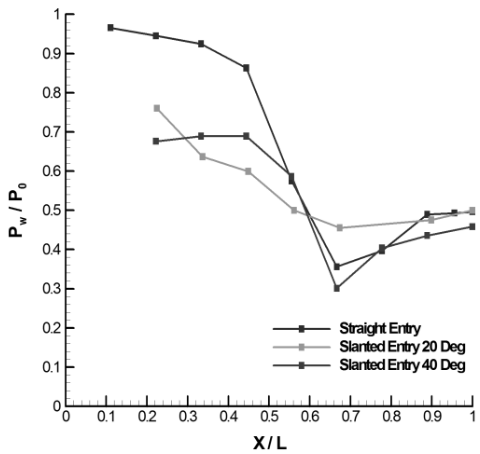


Fig.5(g) NPR 1.921

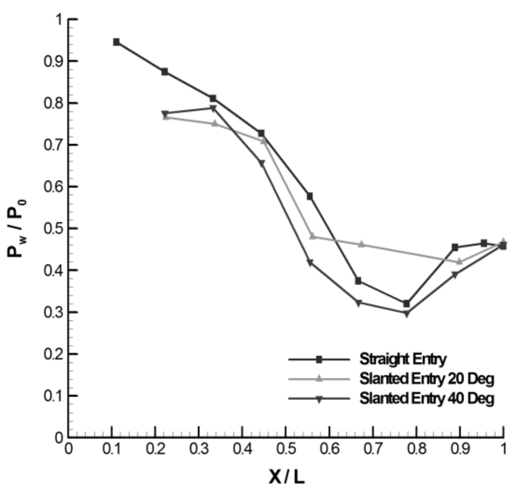


Fig.5(h) NPR 2.05

Fig 5 Wall Pressure Distribution For straight and Slanted Entry Nozzles for different NPR's

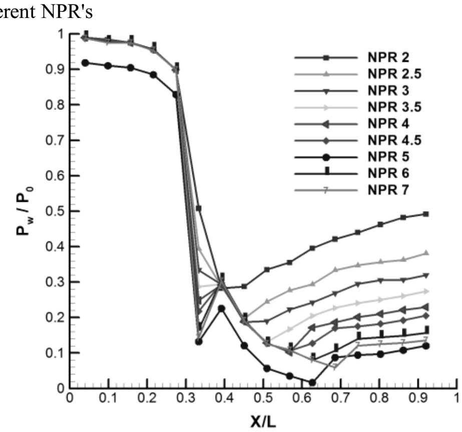


Fig. 6(a) Wall Pressure Distribution for Straight Exit Nozzle for Different NPR's

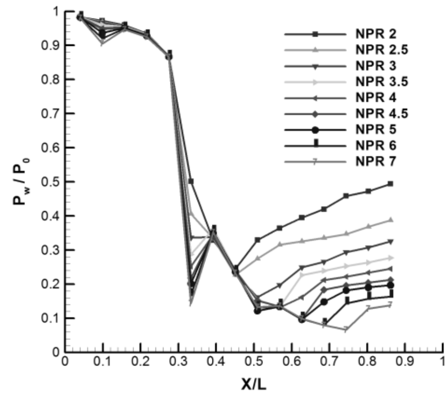


Fig.6(b) Wall Pressure Distribution for Slanted Exit ($30^0$ cut) Nozzle For Different NPR's

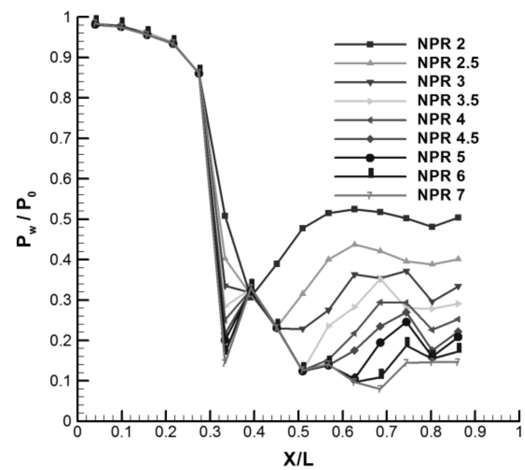


Fig.6(c) Wall Pressure Distribution for Slanted Exit ($70^0$ cut) Nozzle for Different NPR's

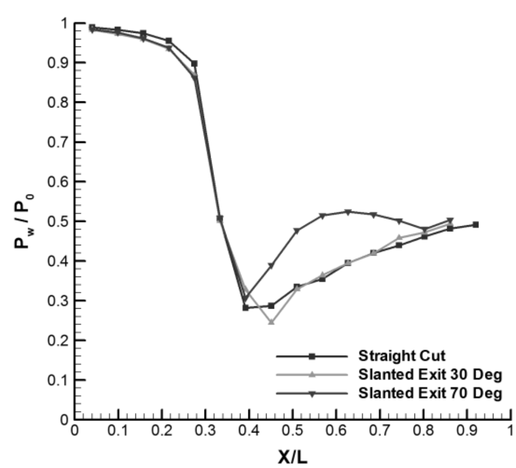


Fig.7(a) NPR 2

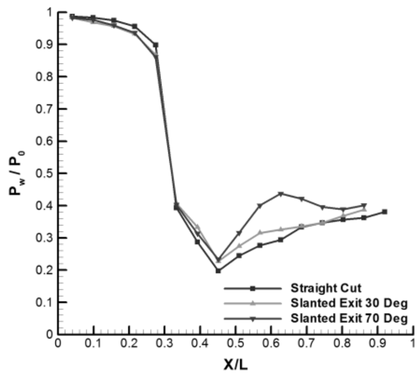


Fig.7(b) NPR 2.5

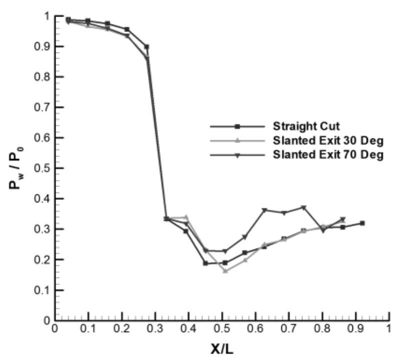


Fig.7(c) NPR 3

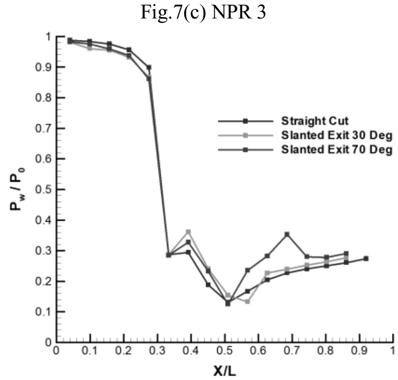


Fig.7(d) NPR 3.5

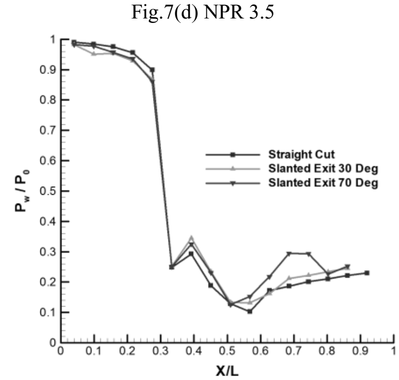


Fig.7(e) NPR 4

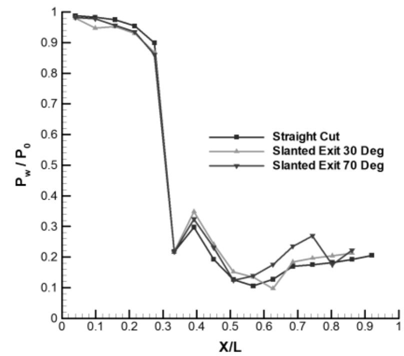


Fig.7(f) NPR 4.5

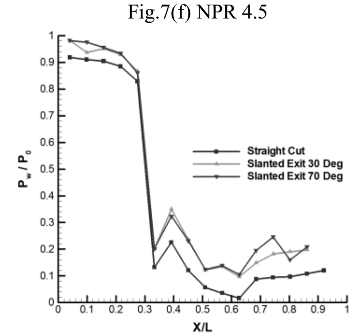


Fig.7(g) NPR 5

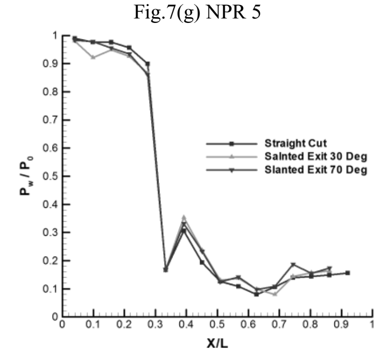


Fig.7(h) NPR 6

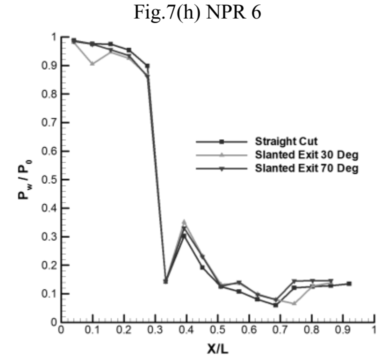


Fig.7(i) NPR 7

Fig 7. Wall Pressure Distribution For M = 3 Nozzle With and Without Cut

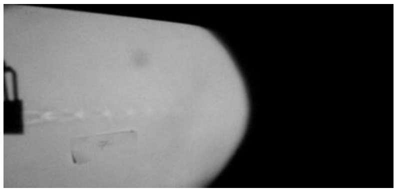

Fig.8 (a) Straight Exit

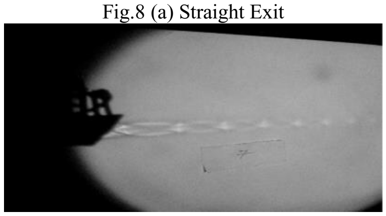

Fig.8 (b) Slanted Exit with $30^0$ cut

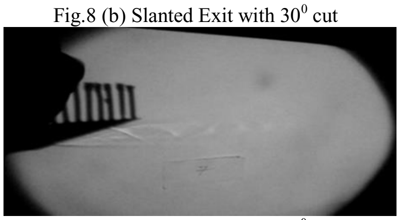

Fig.8 (c) Slanted Exit with $70^0$ cut

Fig 8. Shadowgraph for M = 3 nozzle with and without cut

## V CONCLUSION

An experimental investigation has been conducted to study the flow characteristics of slanted nozzles (both at the entry and exit) run by different NPR's. The slanted nozzles placed across a pressure gradient chokes and deliver supersonic stream at the exit for different operating conditions studied. In spite of slanted entry, the flow could able to choke at the throat and expands further to generate supersonic flow in the divergent portion of the nozzle up to the separation point. The cutting in the divergent portion it is beneficial in the weight reduction as the weight of the vehicle is reduced. It is beneficial in the fuel economy point of view. Hence, slanted entry and exit nozzles may be thought of as a model of weight reduction and thrust vectoring in aerospace applications.

## REFERENCES

[1] Senthil Kumar et. al., "Performance of Slanted Entry Nozzle Run by a Supersonic Stream" 42nd AIAA/ASME/SAE/ASEE Joint propulsion conference &Exhibit, 9-12 July 2006.

[2] Nazar Muneam Mahmood "Simulation of Back Pressure Effect on Behavior of Convergent Divergent Nozzle" University of Diyala, Journal of Engineering Sciences. ISSN 1999-8716.

[3] Kunal Pansari and S.A.K Jilani "Numerical Investigation of Performance of Convergent Divergent Nozzle" International Journal of Modern Engineering Research (IJMER) Vol. 3,issue.5,sep-oct. 2013 pp-2662-2666.

[4] Mohan Kumar Get.Al.,Design And Optimization of De Lavel Nozzle to Prevent Shock Indused Flow Separation Advances in Aerospace Science and Applications. ISSN 2277-3223 Volume 3, Number 2 (2013), Pp.119-124 Research India Publications

[5] Dimitri Papamoschou and Andreas Zill Fundamental Investigation of Supersonic Nozzle Flow Separation AIAA-2004-1111.

[6] S.A. Khan And E.Radhakrishnan, "Active Control of Suddenly Expanded Flows From over Expanded Nozzles", International Journal of Turbo And jet Engines(IJT),Vol.19,No.1-2,Pp.119-126 2002.

[7] K.Rajagaru Nathan, K.Vijayaraja, S.Elangovan, E.Rathakrishnan,"Effect of Annular Rib Position In Suddenly Expanded Supesonic Flow", Proceedings of The International Conference on Aerospace Science And Technology, Bangalore, India,2008.

# Effect of Various Winglets on Aerodynamic Characteristics of Wing

G.K. Chandra Mouli[1], Syed Shiraz Ahmed[2], P. Lovaraju[3]

*Department of Aerospace Engineering, Lakireddy Bali Reddy College of Engineering*

*L.B. Nagar, Mylavaram, Andhra Pradesh, India*

[1]gkchandramouli@gmail.com
[2]syedshiraz_october@yahoo.co.in
[3]lovaraju@gmail.com

***Abstract* - This paper presents the results of the pressure distribution and the drag analysis over a wing attached with different kinds of winglets. Four kinds of winglets are considered and compared in this work. Winglets used are single sided fence, double sided fence, blended winglet and split blended winglet. This study is carried out at flow velocities of 20 m/s and 30 m/s. The angles of attack chosen are $0^o$, $5^o$, $10^o$ and $15^o$. From the analysis it is clear that flow field is disturbed by the attachment of winglets in comparison with the wing without any attachment. The winglets attached to the wing help in modifying the flow field over the wing, which in turn influences the downstream trailing vortices and drag acting on the wing.**

***Keywords* – Induced Drag, Winglets, Drag Reduction, Blended Winglet, Split-Blended Winglet, Single Sided Fence, Double Sided Fence**

## I. INTRODUCTION

As the emerging field, aircraft industry is concentrating on the reduction of fuel usage and towards the efficient working of the aircraft with fewer loads in structure. So, introduction of winglets has brought a revolution in the field of aircraft. Winglet is an additional structure that is provided to reduce the induced drag on a flying aircraft and is attached at the tip of wing. These are basically considered by observing the bird while flying and the way it uses its feathers to reduce the drag acting on its wings.

Drag is a force which plays an ascendant role in restricting the forward motion of an aircraft. A decently dominant component of the drag force, about 30- 40%, is Induced Drag (drag due to lift). When air flow takes place over a finite wing there is a pressure imbalance created which is due to the design of the wing. As a by-product of this pressure imbalance, the flow near the wing tips tends to curl around the tips, being forced from the high pressure region just underneath the tips to the low-pressure region on top thereby creating vortices. The vortices that are created at the tip of the wing are called as trailing vortices. The formation of these tip vortices has an influence over the flow field around the aircraft (especially behind the wings).

The basic concept of circulation or vortex is observed from the inception of the aerofoil theories by Kutta-Zhukowski in 1902, Kelvins circulation theorem for starting vortices over aerofoils, and, over finite wing is proposed by Prandtl during 1911-1918 which stated that Induced Drag is the additional drag component that is created by the trailing vortices at the wing-tips of a finite wing [1, 7].

Addition of winglets reducing the strength of the trailing vortices which further leads to the stabilization of flow over the wing. Richard Whitcomb of NASA first looked at the modern applications of winglets to transport aircraft [2]. Whitcomb showed that winglets could increase an aircraft's range by as much as 7%, and also stated that these winglets will make the twin vortices formed at the trailing edge of the wing to move away from the body of aircraft. It has been found that wingtip devices can improve drag due to lift efficiency by 10 to 15% if they are designed as an integral part of the wing. Different types of winglets exist but they have the same purpose reducing induced drag. A combination of optimal dihedral and geometrically twisted winglets should provide enhanced L/D (lift to drag ratio) for subsonic wings over a range of Mach numbers [3]. In particular, it has been found that winglets improve the flow in the tip region and thereby improve the effectiveness of the ailerons [4]. The forward spiroid winglet displaces the wake upwards, i.e., above the primary tip vortex while the aft spiroid case moves the wake below the primary tip vortex [1].

Winglets are being incorporated into most new transport aircraft, including business jets, the Boeing airlines and military transport as addition of winglets might lead to aircraft's increased operating range, improved take-off performance, higher operating altitudes, improved roll rate, shorter time-to-climb rates, less take-off noise, etc.

The measurement of pressure and drag analysis are done on the model of the wing to which different winglets are attached. Four models of winglets were considered for the study. The models used for comparison are wing without winglet, wing with single sided fence, wing with double sided fence, wing with blended winglet and wing with split blended winglet.

## II. EXPERIMENTATION

### A. *Experimental Setup*

Experiments are carried out in a suction type low-speed wind tunnel in the department of Aerospace Engineering, Lakireddy Bali Reddy College of Engineering, Mylavaram. The maximum velocity possible in this tunnel is around 35 m/s. The cross-section of the test section is 300 X 300 mm with a length of 600 mm. The contraction ratio of the wind tunnel is 9:1.

A three component strain gauge balance is used with the wind tunnel so as to digitally read the lift, drag and pitching moment acting on the model.

*B. Experimental Procedure*

The wing selected for the experimentation is made using the NACA $63_1$-015A aerofoils. The wing is spanned around 120 mm with the mid chord of 100 mm. The taper ratio of the wing made is 4:3. Hence, the chord of the aerofoil at the tip of the wing is 75 mm. Different types of winglets are attached to the tips of the same wing for the experimentation purposes. The winglets are designed as per the considerations given in references [5, 6]. The different types of winglets are shown in Fig. 1.


Fig. 1(a) Blended Winglet


Fig. 1(b) Split Blended Winglet


Fig. 1(c) Single sided fence


Fig. 1(d) Double sided fence

Fig. 1 Photographic views of different winglet models

Two kinds of measurements were made on the model of the wing using different types of winglets at $0^o$, $5^o$, $10^o$ and $15^o$ angles of attack at test–section velocities of 20 and 30 m/s.

*Drag Measurement:* The drag force acting on the wing with different configurations of winglets attached to it is measured using the three component strain gauge balance. The drag force is converted into the Co-efficient of Drag by dividing it with the dynamic pressure times the span of the wing.

*Pressure Measurement:* The static pressures at different locations on the upper surface of the wing are measured with the help of the multi-tube manometer. Pressure ports are made in the span-wise and chord-wise direction of the wing along its centreline. The pressure at desired location along the mid-chord and mid-span over the upper surface of the wing are measured. All the pressure readings are converted in coefficients of pressures and plotted.

## III. RESULTS AND DISCUSSIONS

In this investigation, four types of winglets are chosen. It is to be noted that the static pressures are calculated only on the upper surface of the wing. Plots are made for comparison of different winglets with the change of angles of attack along span-wise and chord-wise direction. A comparison is also made for drag values for different winglets attached to the wing.

*A. Pressure distribution along the span-wise direction*

Figures 2(a) to 2(d) contains the plots of variation of the co-efficient of pressure with x/b in the span-wise direction (from tip to root) at a flow velocity of 20 m/s for different angles of attack. It is observed from the plots that flow is unstable on the wing with single sided fence and wing with split blended winglet at the tip at $0^o$ angle of attack. The presence of winglet causes the pressure co-efficient near the tip of the wing to increase. This happens due to the circulation of the flow at that location in the span-wise direction.

It can also be observed that at an angle of attack of $10^o$, the flow of all the models get closer to achieve stability. The split blended winglet model is observed to have the highest stability at an angle of attack of $10^o$.

At an angle of attack of $15^o$ and a velocity of 20 m/s, the flow over the upper surface of the wing without winglet is unstable and the same can be observed in the Fig. 2(d). This instability of the flow over the wing is controlled due to the presence of winglets. By observing the plots from Figs. 2(a) to 2(d), it is clear that the wing with blended winglet has more stability along the span-wise direction of the wing.

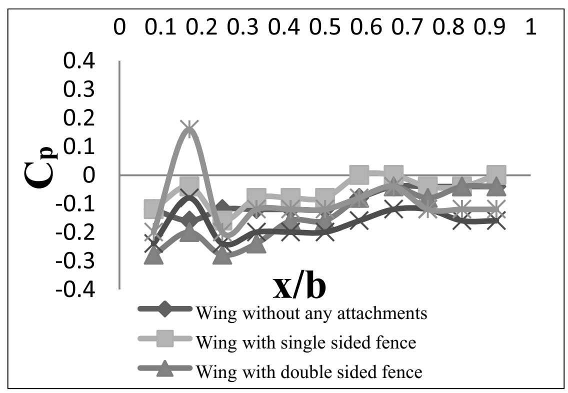

Fig. 2(a) At V∞ = 20m/s, α = $0^o$

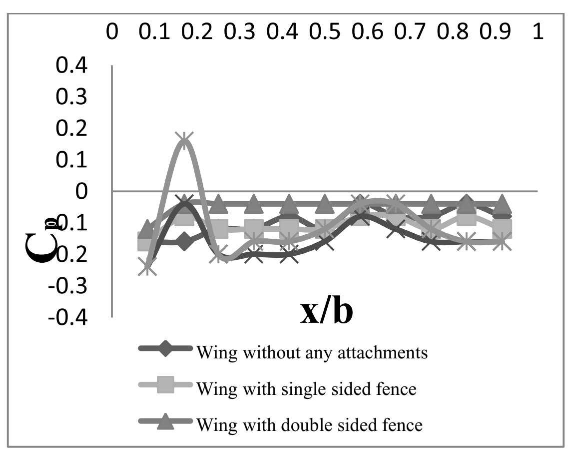

Fig. 2(b) At V∞ = 20m/s, α = $5^o$

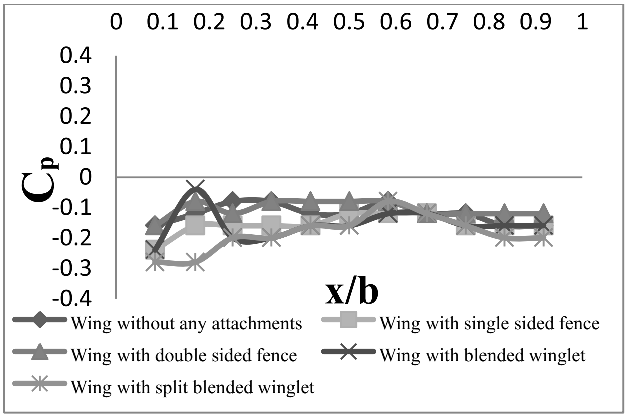


Fig. 2(c) At V∞ = 20m/s, α = 10°

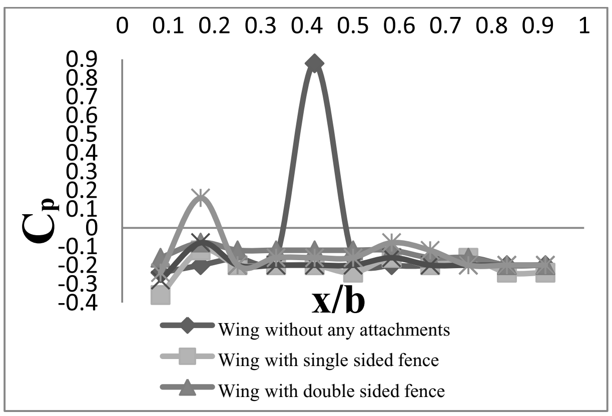


Fig. 2(d) At V∞ = 20m/s, α = 15°

Fig. 2 Pressure distribution along span-wise direction with different angles of attack at 20 m/s

The plots in the Figs. 3(a) to 3(d) represent the variation of co-efficient of pressure of different winglets at flow velocity of 30m/s along span-wise direction. It can be observed that the flow is getting stabilized at higher velocities and the flow is following similar pattern to that of pressure plots at flow velocity of 20m/s.

At different angles of attack, wing with single sided fence and wing without winglets have major flow disturbances over the surface of the wing and as the angle of attack is increasing the instability of flow is altering. Due to the presence of winglets the flow over wing is stabilized and this stability alters with change of angle of attack. In Fig. 3(d) we can see the sudden variation at nearly mid-chord location of the wing which is due to stalling angle of attack.

From Fig. 2 and Fig. 3 it can be noted that as the velocity of the flow increases, the flow over wing is getting stabilized and at both the velocities the stability of flow is higher for the model of wing with blended winglet.

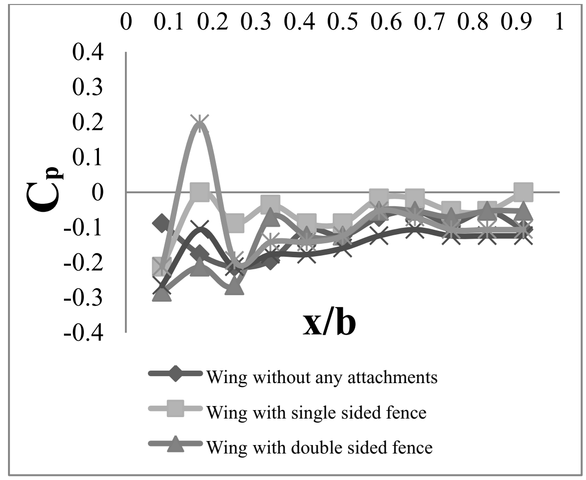


Fig. 3(a) At V∞ = 30m/s, α = 0°

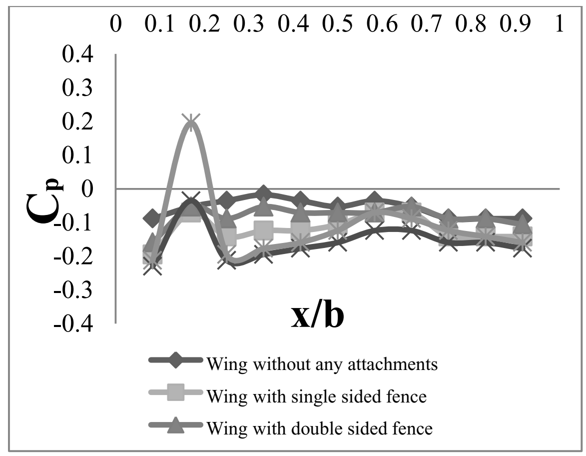


Fig. 3(b) At V∞ = 30m/s, α = 5°

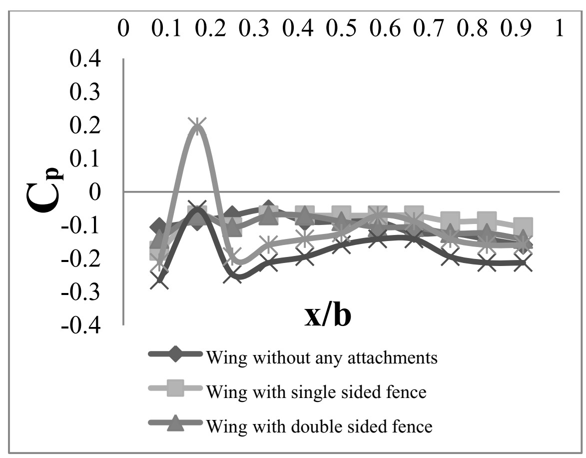


Fig. 3(c) At V∞ = 30m/s, α = 10°

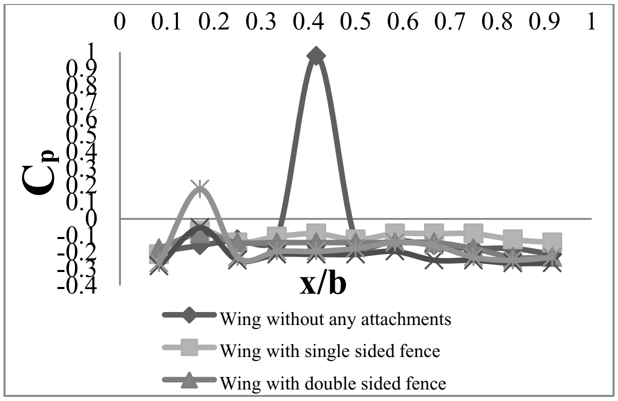


Fig. 3(d) At V∞ = 30m/s, α = 15°

Fig. 3 Pressure distribution along span-wise direction with different angles of attack at 30 m/s

*B. Pressure distribution along the chord-wise direction*

Figures 4(a) to 4(d) represent the variation of coefficient of pressure along the mid-chord of the wing from the leading edge to the trailing edge of the wing at a flow velocity of 20 m/s. From these plots, it can be inferred that as the angle of attack increases, a low pressure zone is formed near the leading edge of the wing. The low pressure zone continues to increase as the angle of attack is increased. After the x/c value of 0.6, the flow over the surface of the wing tends to stabilize itself. As the x/c value reaches 0.8, the flow over the wing gets disturbed due to the influence of the trailing vortices at the tip.

The model of the wing with blended winglet attached to it reacts the most to the change of angle of attack near the leading edge of the wing.

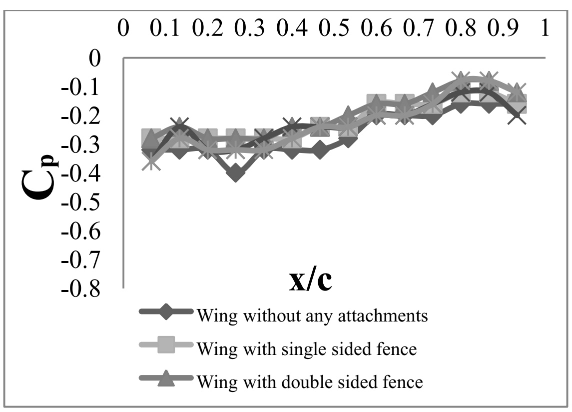


Fig. 4(a) At V∞ = 20m/s, α = 0°

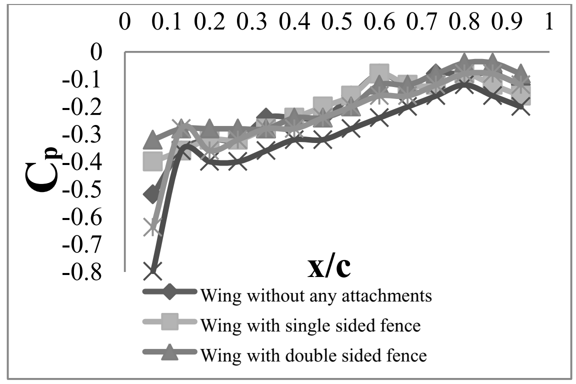


Fig. 4(b) At V∞ = 20m/s, α = 5°

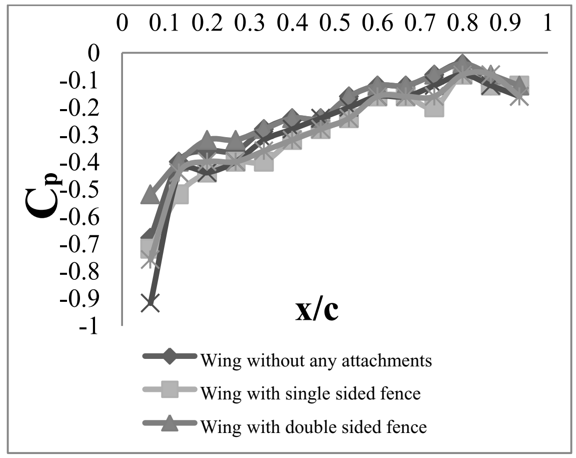


Fig. 4(c) At V∞ = 20m/s, α = 10°

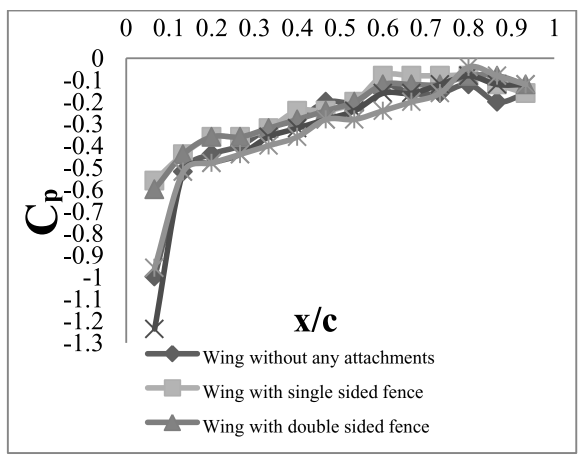


Fig. 4(d) At V∞ = 20m/s, α = 15°

Fig. 4 Pressure distribution along chord-wise direction with different angles of attack at 20 m/s

Figures 5(a) to 5(d) represent the variation of co-efficient of pressure along the mid-chord from the leading edge to trailing edge of the wing at a velocity of 30 m/s. When these plots are compared to the plots in Figs. 4(a) to 4(d), it is observed that all the models tend to stabilize the flow at a higher velocity (30 m/s). It can again be seen that the co-efficient of pressure decreases near the leading edge as the angle of attack increases at a velocity of 30 m/s. This decrease is however less when compared to the plots at a flow velocity of 20 m/s. The model of wing with blended winglet again tends to achieve the lowest co-efficient of pressure near the leading edge at a velocity of 30 m/s.

Amongst all the plots represented in Figs. 5(a) to 5(d), the model with split blended winglet always has the highest co-efficient of pressure, but the pressures are fluctuating when compared to all the other winglet models at a flow velocity of 30 m/s.

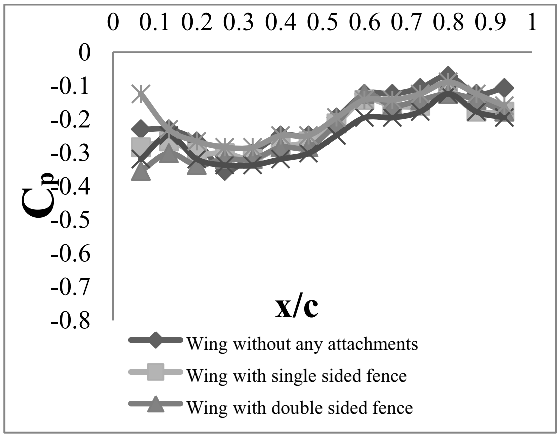


Fig. 5(a) At V∞ = 30m/s, α = 0º

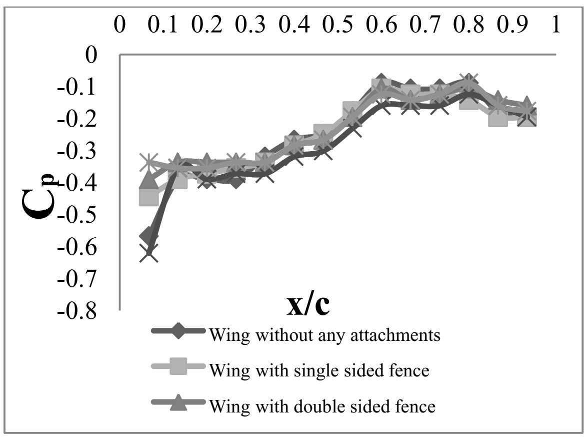


Fig. 5(b) At V∞ = 30m/s, α = 5º

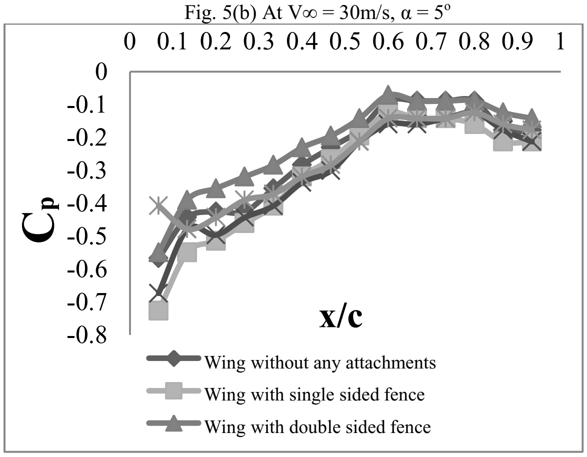


Fig. 5(c) At V∞ = 30m/s, α = 10º

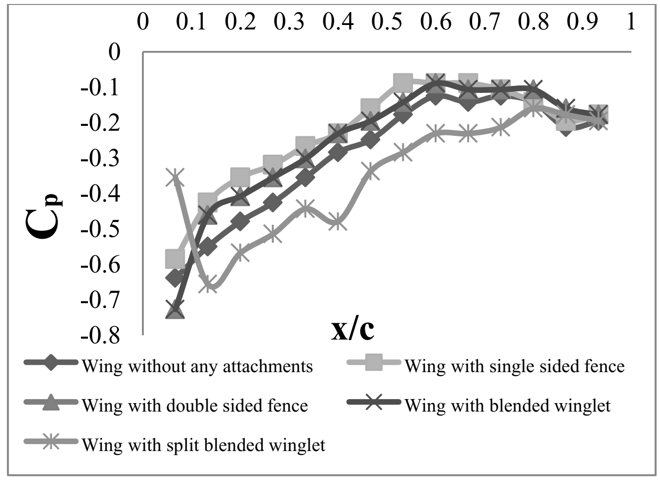


Fig. 5(d) At V∞ = 30m/s, α = 15º

Fig. 5 Pressure distribution along chord-wise direction with different angles of attack at 30 m/s

*C. Drag variation for different winglets*

The plots in Figs. 6(a) and 6(b) represent the variation of coefficient of drag with angles of attack at flow velocities of 20m/s and 30m/s respectively. These plots contain an additional set of readings of drag of wing model without the induced drag so as to find out the effects of various winglets used for reducing the induced drag. The drag force is measured by restricting the third dimensional (span-wise) flow over the wing by confining the walls of the wind tunnel's test-section. In this measurement induced drag force will not be present.

From these plots, it can be inferred that the presence of winglets does not eliminate the induced drag completely. It is already known that wing without any winglet attached to it has the highest induced drag.

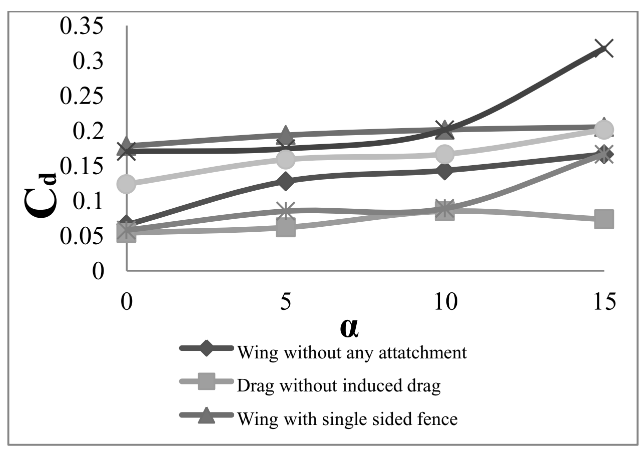


Fig. 6(a) At V∞ = 20m/s

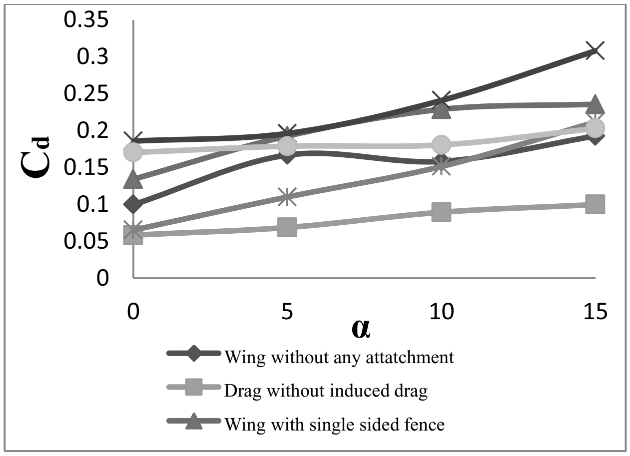


Fig. 6(b) At V∞ = 30m/s

Fig. 6 Variation of Coefficient of drag with angle of attack for different winglets

From the plots in Figs. 6(a) & 6(b), it is seen that when single sided fence, double sided fence and split blended winglets are attached to the wing, the drag increases. This might not be due to the increase of induced drag, but because of the increase in surface interference due to the presence of the winglets.

It can also be observed from the drag plots that the drag increases with an increase of angle of attack. Also, the wing with split blended winglet has higher values of drag when compared to the wing without any winglets. This increase in drag is small even though the surface area of the whole wing is increased due to the presence of split blended winglet. It can hence be inferred that the reduction of induced drag due to the presence of split blended winglet recovers the increase in drag due to the increase in surface area.

## IV. CONCLUSION

From the pressure distributions along span-wise and chord-wise directions, it is observed that the flow over the wing tries to stabilize itself with the increase in velocity. It is noted that major flow disturbances occur near the tip of the wing. When compared to all the winglets, the lowest pressure zone at the tip is formed only for the split blended winglet due to the flow disturbance created at the wing tip by the presence of the winglet. It is also inferred that as the angle of attack of the wing increases, the static pressure on the upper surface of the wing near its leading edge decreases. From the co-efficient of drag plots, it can be observed that the split blended winglet, even though having a greater surface area, has co-efficient of drag approximately equal to that of a wing without any winglet. It can hence be inferred that the split blended winglets has a higher decrease in the induced drag as compared to all the winglets except the blended winglet.

From all the observations made, it is very much clear that the wing with blended winglet has the drag values closer to that of the wing without induced drag. It can hence be stated that a wing with blended winglet gives the highest reduction in induced drag.

## REFERENCES

[1] M. Nazarinia, M. R. Soltani and K. Ghorbanian, “Experimental Study of Vortex Shapes behind a Wing Equipped with Different Winglets,” JAST, Vol. 03, No.1, pp 1-15, March 2006.

[2] Whitcomb R. T., “Methods for Reducing Aerodynamic Drag,” (NASA Conference Publication 2211, Proceedings of Dryden Symposium, Edwards, California, 16 September 1981.

[3] Gianluca Minnella, Yuniesky Rodriguez and Jose Ugas, “Aerodynamic Shape Design Optimization of Winglets”, Florida International University, Florida, US, EML 4905, October 2010.

[4] Lambert Dimitri, “Numerical Investigation of Blended Winglet Effects on Wing Performances”, Aalborg (DK) - Liège (BE), FACE 10 - 3iem Epreuve Ing. Civil. Electroméc. Aéro, June 2008.

[5] Louis B Gratzer, “Split blended winglet”, U.S Patent US 2012/0312928 A1, Dec. 13, 2012.

[6] Zdenek Johan, Garches, “Wing/Winglet configuration and aircraft including it”, U.S. Patent US 2007/0131821 A1, June. 14, 2007.

[7] John D. Anderson, J.R, “Introduction to Flight”, Third Edition, Mc Graw--Hill International editions, Aerospace Science Series.

[8] Mohammad Ilias Inam, Mohammad Mashud, Abdullah-Al-Nahian and S. M. S. Selim, “Induced Drag Reduction for Modern Aircraft without Increasing the Span of the Wing by Using Winglet,” IJMME-IJENS Vol: 10, No: 03, June 2010.

# Finite Element Modelling of Vibratory Weld Conditioning

Joy Varghese V M[#1], Aparna P Mohan[*2]

[#]*Department of Mechanical Engineering, Rajiv Gandhi Institute of Technology, Kottayam, Kerala, India*

[1]joyvarghesevm@gmail.com

[*] *Department of Mechanical Engineering, Sree Chitra Thirunal College of Engineering, Trivandrum, Kerala, India*

[2]aparna886@yahoo.com

***Abstract*— Welding plays a major role in industries like automobile, aerospace and ship building. The welding process itself demands for very high heat density. Due to localized heat input there are heating and cooling cycles during welding. This thermal cycle in turn creates thermal stresses; it may sometimes exceed the limit of elasticity. In such cases, the plastic deformation can occur resulting in residual stress which ultimately will reduce the strength of welded structure or it may even lead to failure of the structure. Hence methods to reduce residual stress have become necessary. Vibratory weld conditioning (VWC) is an important alternative for conventional post weld heat treatment for the reduction of residual stress in welded joints. In VWC a vibrating load is applied on the work piece during welding process. This paper presents finite element analysis of VWC and an experimental analysis carried to prove effect of vibration on welding residual stress.**

Keywords— **Vibratory Weld Conditionin (VWC), residaul stress, Tungsten Inert Gas welding (TIG), arc welding modeling.**

## I. Introduction

Welding is an efficient metal joining process which is widely used in various industries. The alternate heating and cooling cycles during welding lead to development of residual stresses in the material. The residual stress developed in the material can be either tensile or compressive. Stresses can be within the elastic limit of the material or sometimes it may exceed the yield strength of the material. In latter cases plastic deformations can occur which may lead to the failure of material. Post weld stress relieving methods like heat treatment, shot peening, and normalizing can reduce residual stress to a certain amount but it consumes extra time and resources. Vibratory weld conditioning (VWC) is the process of giving a high frequency low amplitude force on the material during the process of welding. The stress induced due to vibrations will be superimposed on the existing stress pattern (compressive or tensile) which finally results in a reduction of peak tensile residual stress.

The reduction of residual stress is due to micro structural as well as macro structural changes. The micro structural change that occurs during the process is very small whereas macroscopical changes are inevitable. When a vibratory force is applied on the weld pool, nucleation occurs hence grain size gets reduced and the grains are arranged perfectly without any voids or inclusions. Also when vibration is applied the dissolved gases present in the weld pool will be released. This may result in reduced porosity in the welded part. The vibration of liquid metal also results in the increased rate of heat transfer. The above mentioned effects create only negligible reduction in residual stress. This paper mainly discusses about the reduction of residual stresses macroscopically. The vibratory stress relief (VSR) is another important method for reducing residual stress. In VSR the inducing of a forceful vibration to the weldment will be done after the completion of welding process.

Shingeru Aoki [1] revealed the effects of imposing a vibrational load during welding by using two kinds of random vibration loads, white noise (containing all frequency components) and filtered white noise (fundamental natural frequency of specimen). He proved that tensile stress gets reduced when the specimen is welded during vibration. Jijin Xu [2] explained effect of vibratory weld conditioning in pipes. VWC reduces residual hoop stress at outer surface of pipe as well as maximum residual stresses.

In present study, analysis were carried out using Finite element analysis software ANSYS to determine the residual stress developed during VWC. The VWC process is simulated by applying a vibratory load close to the natural frequency of the plate during welding. An experimental work for comparing hardness of material, in the cases of TIG welded plates and VWC plated using Brinell hardness testing machine, was also carried out.

## II. Specification of Material Used

Mild steel plates of dimensions 100 mm × 50 mm × 8 mm were considered for both experimental and numerical analysis. The temperature dependent thermo physical properties of mild steel as suggested by previous researchers [3] are used for the analysis. The latent heat of fusion due melting of based during welding is accommodated by enthalpy method.

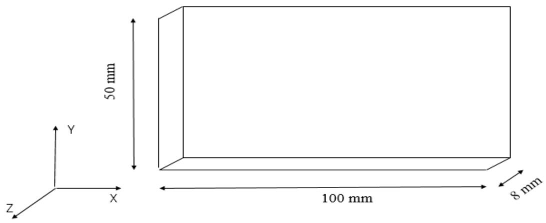


Fig. 1 Physical dimensions of the analysis domain

## III. WELDING PROCEDURE

These mild steel specimens are butt welded using Tungsten Inert Gas welding (TIG). The welding parameters are as described in Table 1. The welding was carried out without using any filler materials and gases flow rate was 40 l/min.

TABLE 1 Welding parameters

| Weld Length [mm] | Weld speed [mm/s] | Weld current [A] | Weld voltage [V] |
|---|---|---|---|
| 100 | 3 | 180 | 20 |

## IV. FINITE ELEMENT ANALYSIS

Finite element simulation of welding procedure is carried out for determining residual stresses. An uncoupled thermo-mechanical structural dynamic analysis is carried out for getting temperature as well as residual stress distributions. Three dimensional numerical model of the plate was created in ANSYS software and mesh convergence study was done for different element edge sizes. Finally a model that contains 5112 elements with maximum element edge length of 4 mm is selected for analysis. Symmetry boundary conditions are also assumed along the weld line. Hence only one half of the plate was need to be simulated. Fine elements were used at the weld center-line compared to the free end. Thermal analysis was first completed for solving thermal profiles and then mechanical analysis was executed which reads thermal profiles as input.

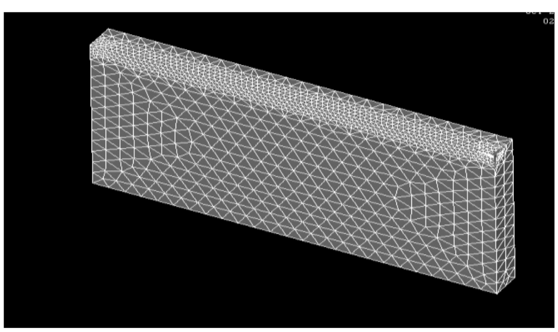

Fig. 2 Meshed plate modelled in ANSYS

## V. THERMAL ANALYSIS

The thermal profiles are first obtained by conducting thermal analysis and mechanical analysis is carried out by incorporating the thermal results. Conduction and convection heat transfer is employed as boundary conditions. Convection is applied over all the faces of the plate by assuming suitable empirical relation as suggested by [4]. The welding procedure was simulated using a modified double ellipsoidal heat distribution model as suggested by Sabapathy [5].

$$Q(x, y, z) = \frac{\eta U I 6\sqrt{3}}{\pi abc\sqrt{\pi}} \exp\left\{-3\left(\frac{z}{a}\right)^2 -3\left(\frac{y}{b}\right)^2 -3\left(\frac{x+v(\tau-t)}{c}\right)^2\right\} \quad (1)$$

Where x,y,z are local space coordinates, U-welding voltage I –welding current, t –time, $v$- welding speed, $\tau$-reference time and a,b,c are the heat distribution parameters as in figure 3.

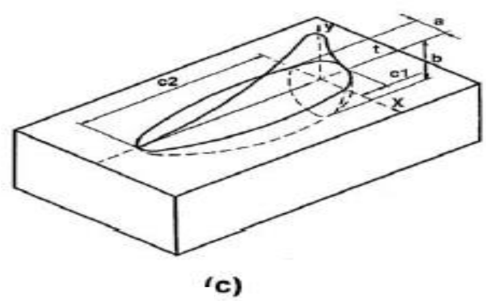


Fig.3 Modified double ellipsoid heat distribution model

For thermal analysis the modified Newton-Raphson method is used for heat balance iteration. The heat load is assumed to be applied over the plate during welding and after welding simulation was continued up to time corresponding to 2 hours of cooling in order to ensure complete cooling of base plate after welding. Three dimensional conduction euquation was solved using above boundary conditions during thermal analysis.

## VI. STRUCTURAL ANALYSIS

The structural analysis is the second stage of analysis which involves the use of thermal histories predicted from thermal analysis. Due to thermal expansion and contraction the strain increases in the material. The addictive decomposition of strain in the element collectively comprises the total strain in the material. The total strain in the material comprises of elastic strain, plastic strain and thermal strain. The elastic strain increment is calculated using the isotropic Hook's law with temperature-dependent Young's modulus and Poisson's ratio. The thermal strain increment is computed using the coefficient of thermal expansion. The plastic strain increment, a rate-independent elastic–plastic constitutive equation is considered with the Von Mises yield criterion, temperature-dependent mechanical properties and linear isotropic hardening rule.

In this study the reduction of residual stress is dealt with the introduction of a vibratory force function. The forcing function used is $F=F_0 \sin(\omega t)$ where $F_0$ is the amplitude of vibration, $\omega=2\pi f$ angular frequency, t is the time point. The natural frequency of the plate is found to be 283.12 Hz. The analysis was done in frequencies close to the natural frequency of the material. During welding 3000N force was assumed to be applied. The load is given at the weld line and the other end of the plate which is opposite to weld line is constrained to zero degrees of freedom. After the completion of welding the constraints as well as forcing function is removed and the plate is allowed to damp freely so that the plate slowly stops vibrating. Damping coefficient of 0.001 is considered in the analysis.

## VII. RESULTS AND DISCUSSION

Experimental data for vibration stress relief is not available in literature. Hence hardness test was conducted in order to validate the numerical results by showing the effects of vibration on hardness of weld zones. Hardness test was performed using Brinell hardness testing machine for plates welded without vibration and with vibration. In the case of VWC the work pieces were fixed in a bench wise and random vibrations were applied during welding plates using wooden hammer. Hardness is measured at the weld pool, heat affected zone (HAZ), and at a distance 3.5mm from weld center-line. The hardness is found to be decreased in the plate with vibratory weld conditioning than that with non-vibratory welded plate.

TABLE.2 Brinell hardness number of plates welded with and without vibration

| Measuring points | BHN (With Vibration) | BHN (Without vibration) |
|---|---|---|
| Weld pool | 285.3 | 363.3 |
| HAZ | 155.7 | 187.33 |
| 3.5mm from weld pool | 187.3 | 228.8 |

From above analysis it can be concluded that vibration during welding reduces hardness of material, hence it is assumed that stiffness of material is reduced due to vibrations which shows reduction of residual stresses.

### A. *Thermal Analysis*

Figure 4 shows the thermal profile when the welding torch is at the middle of the plate. Peak temperature is found to be 1769$^{o}$C at the middle of the weld pool.

### B. *Residual stress Analysis*

Figure 5 shows the residual stress distribution along the length of the plate at a depth of 4mm from the weld centre in the case of VWC plate and TIG welded plate plotted by simulating both cases as explained in pervious sections.

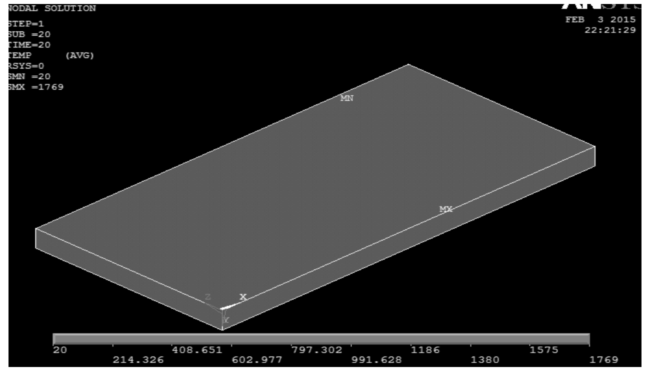


Fig. 4 Temperature distribution during welding

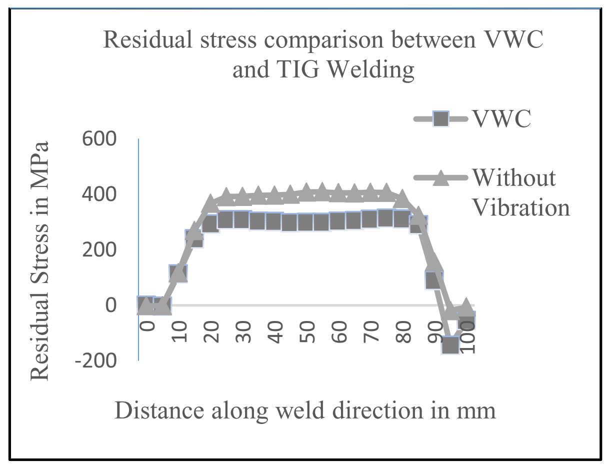


Fig. 5 Comparision of logitudinal residual stress distribution in VWC and normal TIG welded plates

From above graph it can be observed that the high tensile stresses are there at the middle of the plate and stress value are comparatively less at the edges of plate due to the edge effect. The peak tensile stress is around 400MPa in the case of TIG welding and 300MPa in the case of VWC. There is a reduction of around 100MPa due to VWC. Meanwhile at the edges the compressive stresses are found to be increased due to the vibration.

## VIII. CONCLUSION

Numerical simulations and experimental results show significant effects of vibration on residual stresses and hardness of material. Hence it can be concluded that VWC reduces the peak residual stress values.

## REFERENCES


[1] Aoki, Tadashi Nishimura, Tetsumaro Hiroi, Seiji Hirai, Reduction method for residual stress of welded joints using harmonic vibrational load, Nuclear Engineering and Design, vol 237,pp 206-212, 2007.

[2] Jijin Xu*, Ligong Chen, Chunzhen Ni; Effect of vibratory weld conditioning on the residual stresses and distortion in multipass girth-

butt welded pipes. International Journal of Pressure Vessels and Piping vol 84, pp 298–30, 2007.

[3] Joy Varghese V M , Sumanth M R, Suresh M R, Numerical Simulation of Residual Stress in A Spot Welded Low Carbon Steel Plate, Procedia Engineering , vol 38 , pp 2913 – 2921, 2012.

[4] Kim I S, Basu A, A mathematical model of heat transfer and fluid flow in the gas metal arc welding process, Journal of materials processing technology, vol 77, pp 17-24, 1998.

[5] Sabapathy P N, Wahab M A, Painter M J, Numerical models of in service welding of gas pipe lines, Journal of materials processing technology, vol 118, pp 14-21, 2001.

# Effect of Temperature on Intermetallic Layer Formation During Annealing of Friction Clad Al on Steel

Sudeendran K[1], Rajan T

*Department of Mechanical Engineering, Government Engineering College, Sreekrishnapuram, Palakkad, Kerala, India*

[1]sudeendran14@gmail.com

***Abstract*** — **Friction cladding is a solid state process, where a material is allowed to deposit on a substrate using friction energy. Friction cladding can be used to deposit aluminium on steel. Steel offers the benefits of high strength and economy, whereas the aluminium offers the benefits of high oxidation and corrosion resistance. Though, literature has many investigations on the possibility of deposition of aluminium on steel, there are limited literatures available on the effect of subsequent annealing treatment on the changes in the clad material. This paper reports the effect of annealing treatment on the friction clad Al-Steel couple. In this investigation friction cladding was done to deposit aluminium on the low carbon steel surface. Clad layer thickness was in the range of 48-54 µm. The clad layer had small amount of Fe particles embedded in it. The sample was annealed for 2 hours at 700  C and 730  C, respectively. During annealing there was inter diffusion across aluminium-steel interface and it lead to the formation of intermetallic layers. Total intermetallic layer thickness was about 100-110 µm, when annealed at 700  C. The intermetallic layer was mainly made up of Fe2Al5 layer. When annealing temperature was raised to 730  C, the total intermetallic layer thickness was about 30-40 µm. Considerably larger fractions of FeAl2, Fe3Al and FeAl were observed in the total intermetallic layer. The reduction in the total intermetallic layer, when annealed at 730  C is attributed to gravity driven flow of liquid aluminium and consequent drop in available aluminium content at a position.**

***Keywords*** — **Friction surfacing, Intermetallic layers, Heat treatment, Annealing, Thickness reduction**

## I. INTRODUCTION

Steel is one of the important engineering materials used for construction, transportation, naval, agricultural, power generation and transport applications. In many of the engineering applications, life is limited by the degradation at the surface or the subsurface regions. A few of the degradation modes faced by the steel components during their applications are corrosion, oxidation, wear and abrasion. To minimize the component damage and extend the life of the components, different types of coatings and manufacturing processes are being developed. From performance point of view, aluminium clad steel is a highly promising material. Aluminium clad steel is a layered material, in which the beneficial properties of both steel and aluminium are exploited. For a user, steel offers the benefits of high strength and lower cost. Al offers the benefit of oxidation resistance and corrosion resistance. Al enriched surfaces (aluminides) also offer the benefits of high hardness, abrasion and wear resistance.

There are many methods available for cladding of steel with aluminium. Explosive welding, roll bonding, dip coating, foil aluminizing, friction surfacing are a few to name [1]. Friction surfacing is a solid state processing method using frictional energy to coat a steel surface with a layer of aluminium, made available using a consumable Al rod. In friction surfacing, the consumable tool is made to rotate with respect to the substrate steel. At the steel-aluminium interface, a part of the mechanical energy used for rotating the tool is converted into frictional heat [2]. By selecting appropriate parameters, only consumable tool could be made to plasticize and get deposited on the surface of the substrate. When the tool is made to travel with respect to the substrate, the plasticized tool would be deposited as a clad layer. With optimized processing conditions, a continuous, smooth and uniformly deposited Al layer would be possible on the steel surface. Production of Al clad steel through friction surfacing route is relatively less explored and there are hardly any investigations reported on the changes in the Al clad layer during post heat treatment. This paper reports the effect of temperature on the intermetallic layer formation during annealing of friction clad aluminium on steel.

## II. EXPERIMENTAL DETAILS

### A. *Friction Surfacing*

Mild steel plates were used as substrates in this investigation. They were cut into dimensions of 150 mm (width) x 210 mm (length) x 6 mm (thickness). Using a milling machine a surface roughness of the order of 5-7 µm was obtained. Commercial pure Al was used for cladding steel. Al was in the form of a rod of 25 mm diameter and 100 mm length. Al was deposited under different processing conditions. The tool plunge depth and tool transverse speed were kept constant as 40 mm and 35 mm/min respectively. Contact force was varied as 3, 4 and 5 kN and the rotation speed was varied as 400, 600 and 800 rpm. During rotation, Al gets heated up rapidly, undergoes plastic deformation and during transverse travel, plasticized Al gets deposited on the steel surface. A schematic of the process is presented in Figure 01. Large area in the steel substrate was covered with repeated passes using an overlap of about 25%. Experiments were done under normal atmosphere conditions. Deposits were classified on the basis of nature of deposit, continuity, uniformity and tool bulge.

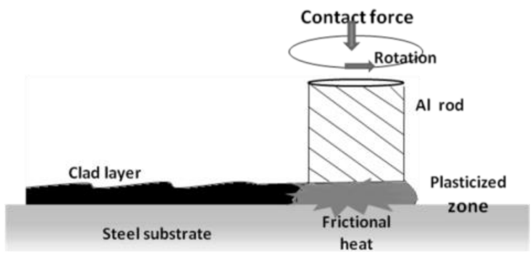


Fig. 1 Schematic of the friction surfacing process

*B. Heat Treatment and Characterization*

Good deposits were observed under a certain combination of processing parameters. The sample processed using contact force: 5 kN, tool rotation speed: 400 rpm gave a continuous deposit with uniform width. This sample was used for characterization and further heat treatment. Heat treatment was done to explore the possibility of intermetallic formation. Heat treatment temperature was the variable and it was varied as 700 and 730 °C. Heat treatment time was 2 hours and under atmospheric conditions. The sample was kept horizontally with friction surfaced layer on the top. After heat treatment, the samples were characterized by using x-ray diffractometry (XRD, CuKα radiation), scanning electron microscopy (SEM, Make JEOL, model 6580LA), and energy dispersive spectroscopy (EDS, Make Oxford) to study the formation of intermetallic phase constituents. Hardness of the inter metallics was estimated using microhardness tester (Make Shimadzu, model HMV G20ST).

## III. RESULTS

*A. Characterization of the Al Clad Sample (Without Heat Treatment)*

Figure 2 a shows a macro view of the Al clad steel sample. A total of area of 120 mm x 50 mm was covered with 4 passes. A small portion in the sample was magnified and morphological investigation was done and it is shown in Figure 2 b.

The surface shows features indicating flow of the plastic flow due to shear flow. Chemical analysis using EDS was done on this full region and it showed that the area is about 98.5 at% Al and 1.5 at% Fe. Figure 02 c shows corresponding EDS spectrum. Al clad sample was sectioned perpendicular to its length, metallographically polished and observed in SEM for microstructural features.

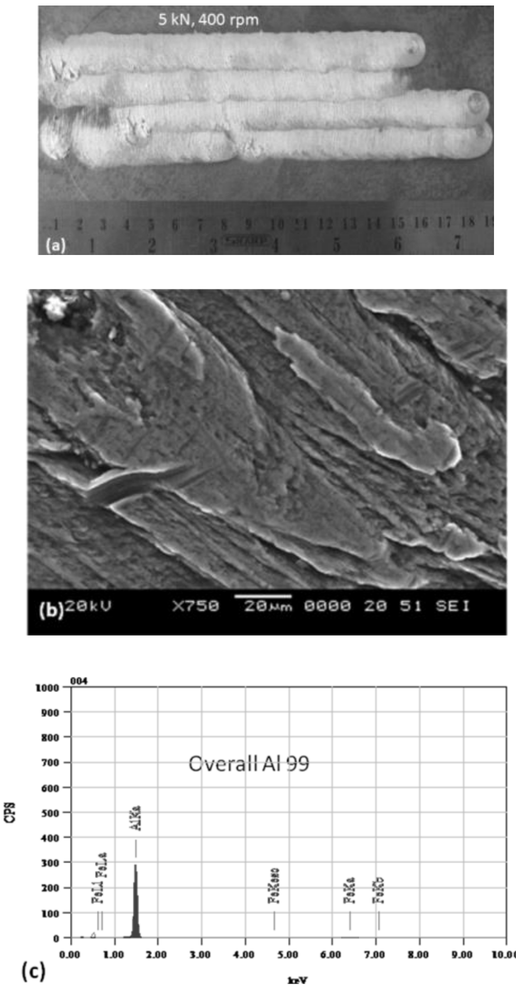


Fig. 2 (a) Macro view of the sample processed, (b) SEM micrograph showing morphological features in the clad surface, (c) EDS spectrum on the sample surface shown in Figure 2(b)

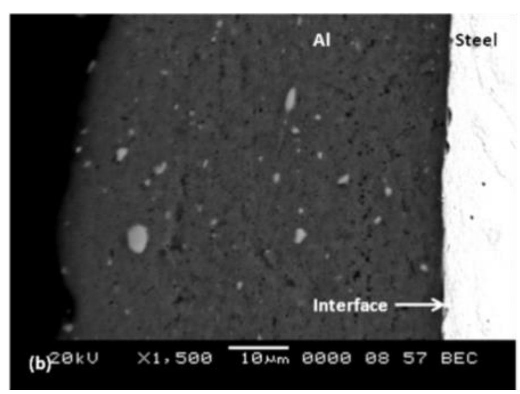


Fig. 3 (a) Cross sectional micrograph of the Al clad region. Arrow indicates fragmented steel particles, (b) Micrograph magnified from region shown in Figure 3 (a)

Figure 3 (a) shows a cross sectional micrograph of the sample. Micrograph shows an Al rich clad layer on the steel surface. Thickness of the clad layer was in the range of 48-54 µm. Al clad layer is embedded with a large number of Fe particles (shown with an arrow). Particles are fine and many of them are in the submicron scale (Figure 03 b). Interface between clad layer and steel substrate is good without any voids. Figure 04 show the XRD profile of the Al clad sample (Identified as S1, NHT). It shows clear peaks corresponding to Al. There is no distinct iron peaks, indicating fraction of iron is very low. Also, there is a peak corresponding to $FeAl_{3.2}$ ($Fe_4Al_{13}$). At this point we were not able to detect this phase in SEM micrographs.

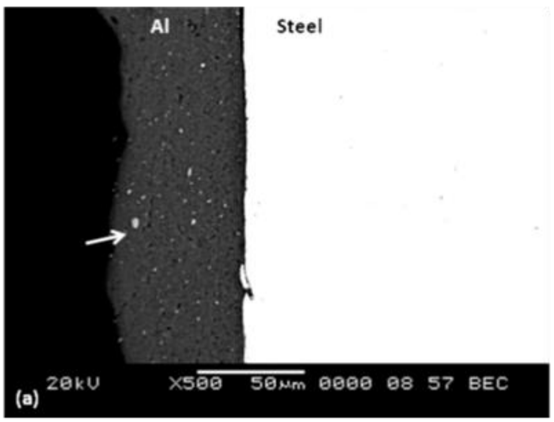


Fig. 4 XRD profiles of as-clad and after heat treatments at 700 °C and 730 °C for 2 hour duration

A. *Characterization of the heat treated Samples*

Figure 4 shows XRD profiles of samples heat treated at temperatures of 700 °C and 730 °C for 2 hours. For comparison, XRD profile of non-heat treated sample is also shown. In the heat treated samples, peaks corresponding to Al are absent and they are replaced by peaks corresponding to $Fe_2Al_5$ and $FeAl_{3.2}$. It indicates that Al clad layer is replaced by intermetallics during heat treatment. Small intensity for oxide peaks is also observed.

Figure 6 shows morphological features on the sample heat treated at 730 °C for 2 hours. The surface shows acicular morphology, most probably of $FeAl_{3.2}$. EDS analysis (Figure 06 b) indicates Al:77 and Fe:23. We notice a clear change in the morphology during heat treatment at 730 °C compared to heat treatment at 700 °C.

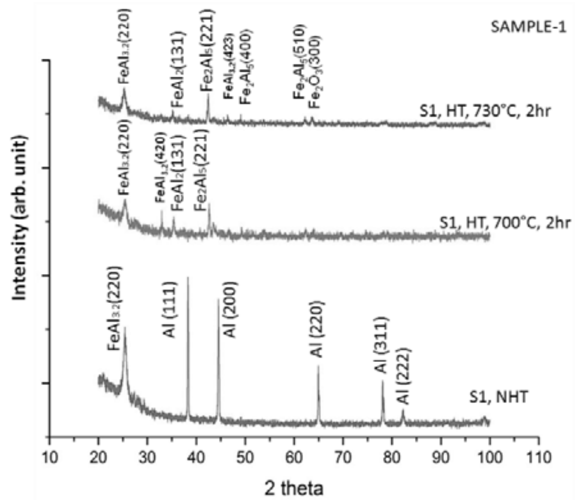


Figure 5 (a) shows SEM micrograph on the surface of heat treated sample (at 700 °C for 2 hours). There is no visible indication of complete melting and resolidification. EDS analysis (in at%) (Figure 5 b) indicated that Fe:24, Al:76.

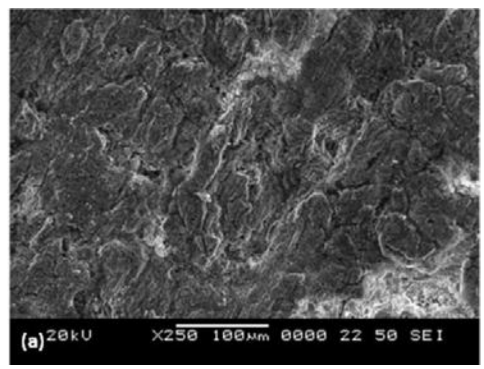


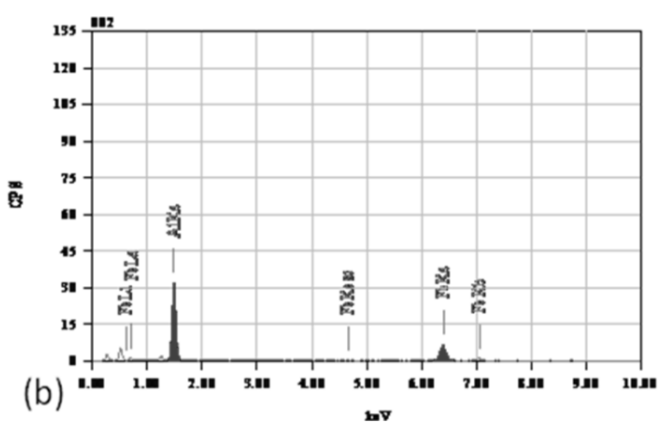


Fig. 5 (a) Morphology of Al clad sample after heat treatment at 700 °C for 2 hours, (b) EDS on the region shown in Fig 5 (a)

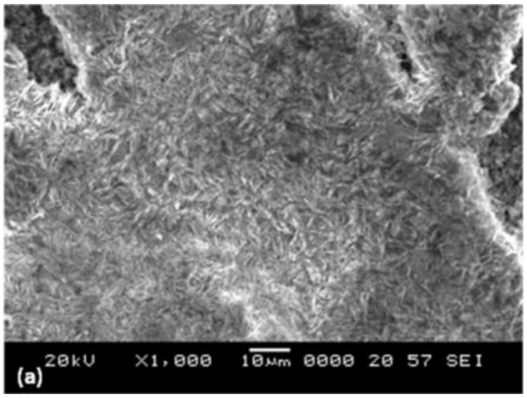


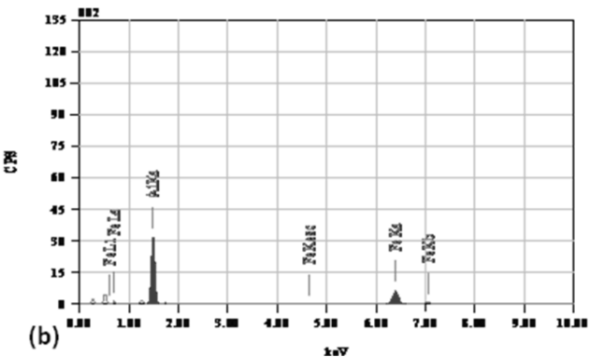


Fig. 6 (a) Morphology of Al clad sample after heat treatment at 730 °C for 2 hours, (b) EDS on the region shown in Fig 5 (a)

Figure 7 (a) shows cross sectional micrograph of the Al clad sample processed at 700 °C for 2hours. About 100-110 µm of the top is converted into intermetallic (IM) layer. The interface between IM layer and the substrate steel is showing tongue like morphology which is commonly observed in Al dip coated steels [3]. On the steel side a layer of coarse grains is observed, indicating grain growth during heat treatment. Figure 7 (b) shows a micrograph which is magnified from the region shown in Figure 7 (a). EDS analysis was done at various regions and based on EDS values possible intermetallic layers are identified and shown in Figure 7 (b). On the top of the coating, a thin region corresponding to $Fe_4Al_{13}$ is observed. Below that a thick region, corresponding to $Fe_2Al_5$ is observed. Thickness of the $Fe_2Al_5$ layer is not uniform. Maximum thickness is about twice of minimum thickness. After that a discontinuous layer of $FeAl_2$ is observed. Next, a continuous, uniformly thick layer corresponding to FeAl is noted. Followed to this, a thin layer with chemical composition corresponding to $Fe_3Al$ is observed. Inside $Fe_2Al_5$ layer a large number of bright colored particles were observed. Composition of coarse white particles is matching with that of FeAl. Also, a large number of porosities are observed.

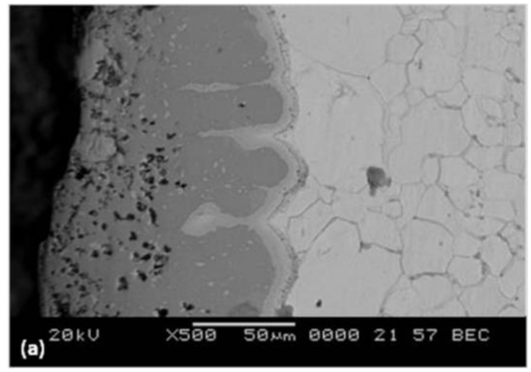


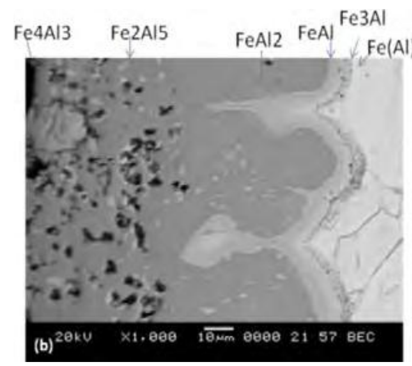


Fig. 7 (a) Micrograph showing IM layer formation during heat treatment at 700 °C for 2 hours, (b) Identification of different layers using EDS data

Figure 8 (a) shows cross-sectional micrograph of the sample heat treated at 730 °C for 2 hours. An IM layer of thickness varying in the range 28-34 um is observed. Compared to sample processed at 700 °C, this sample show less amount tongue like morphology. The IM layer at higher magnification is shown in Figure 08 b. In this sample also, following phase sequences are observed from top towards steel side. At the top, a thin layer of $Fe_4Al_{13}$ followed by a thick layer of $Fe_2Al_5$ is observed. In $Fe_2Al_5$, $FeAl_2$ is embedded and it makes almost a continuous layer. Volume fraction of $FeAl_2$ is much higher compared to that at 700 °C and thickness is not uniform.

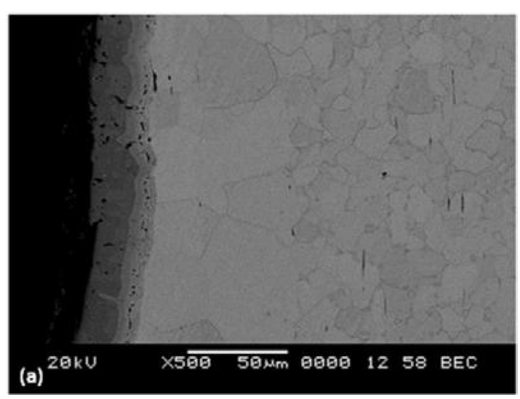

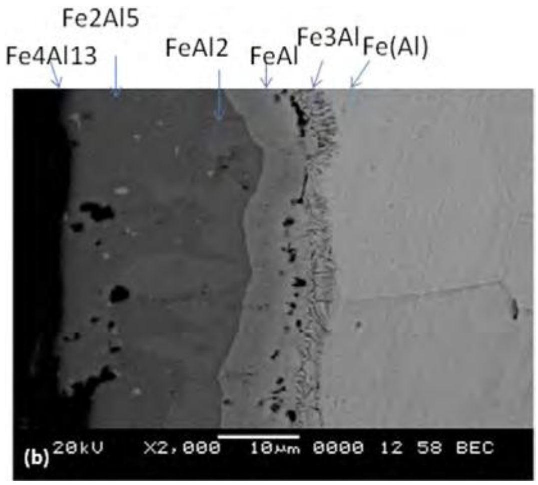


Fig. 8 (a) Micrograph showing IM layer formation during heat treatment at 730 °C for 2 hours, (b) Identification of different layers using EDS data

Below that a continuous and almost uniform thickness of $Fe_3Al$ is observed. Finally a distinct region of solid solution of Al in Fe is observed.

## IV. DISCUSSION

### A. *Intermetallic (IM) Layer Formation*

XRD plots and scanning electron micrographs shown in Figure 1, Figure 4, Figure 7 and Figure 8 shows that during heat treatment, clad Al and substrate steel undergoes reaction to produce a number of intermetallic layers. The chemical composition changes gradually across Al clad layer and the substrate steel, after heat treatment. It may be noted that the equilibrium phase diagram of Al and Fe (Figure 9) show a number of intermetallic phases [4].

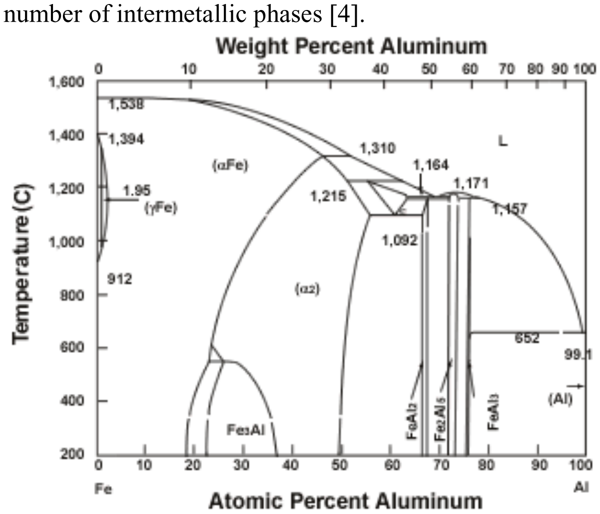


Fig. 9 Equilibrium phase diagram between Al and Fe [4]

All these phases have a range of solute solubility under equilibrium conditions. Phases like $Fe_3Al$ and FeAl have a wide range of solubility, whereas, others have a narrow range of solute solubility. Formation of intermetallic phases takes place due to reactive diffusion, wherein diffusion brings two species together which undergoes a reaction to produce an intermetallic phases [5]..

Another interesting aspect is the thickness of the IM layer. As displayed in Figure 7 and Figure 8, the IM layer after annealing at 700 °C is higher than as clad sample. This can be explained as following. Diffusion rate of Fe into liquid Al is higher compared to Al in solid Fe. This results in the migration of interface away from the initial surface. Also, the intermetallic phases like $FeAl_3$, $Fe_2Al_5$ and $Fe_3Al$ are non-cubic phases and their atomic packing factor will be less compared to that of pure Fe or pure Al. All these factors contribute to an increase in the volume after heat treatment.
Also, Figures 7 and 8 show that the total IM layer after heat treatment at 730 °C is less compared to that at 700 °C. This is attributed to lateral spreading of Al layer, when it is heated to higher temperature.

### B. *Lateral Spreading of As-Clad Al Layer*

Liquid Al-steel combination can be thought as a system of reactive wetting [4]. The formation of an interfacial layer of a compound affects the spreading of liquid layer. Formation of an intermetallic layer at the interface depends on the reaction kinetics at the interface and the rate of diffusion of Fe across the interface or through the product which has already formed. Interfacial reactions at the interface lead to the formation of a continuous layer of new compound [6]. In general, spreading rate of the liquid standing above a solid surface can be explained using reaction product control model [7]. According to this model, when a reactive liquid metal layer is dropped on the substrate, a thin layer of reaction product forms at the interface. Liquid will exist above the reaction product (schematically shown in Figure 11). When angle of contact $\theta>\theta_N$, direct contact between the liquid and substrate takes place [8]. Now local chemical reaction affects spreading kinetics. At the heat treatment temperature, the clad Al rich layer becomes liquid. The liquid is expected to be like a pancake of uniform thickness and with curves at the rims. At the contact line the liquid tends to spread due to gravity. The drop in energy due to spreading is in tune with the dissipation of energy due to surface tension. Dissipation of energy near the contact line is given by equilibrium spreading coefficient $S_{eq}$.

$$S_{eq}=\gamma_{sv}-(\gamma_{SL}+\gamma_{Lv}) \qquad \dots (2)$$

In equation 2, $\gamma$ is the surface tension of the film, suffixes s,v and L indicates solid, gas and liquid phases. When $S_{eq}$ is negative, tendency for spreading is favoured. $S_{eq}$ also measures energy available for spreading

From equation (2), surface tension plays an important role in spreading of Al. The surface tension of the film is a function of composition and temperature. At 730 °C, surface tension of the liquid is lower compared to that at 700 °C and spreading tendency is higher. Also, if dissolved Fe is greater than 0.9 at%, the liquidus temperature raises rapidly (Figure 9). At 700 °C, it is possible that some of the Fe particles are not dissolved fully. Also, the rate of diffusion increases as temperature increases, which again promotes dissolution of more Fe particles. The microstructure at 700 °C shows large amount of Fe rich phases (FeAl) embedded in $Fe_2Al_5$. At 730 °C, more of these particles are dissolved as observed in cross sectional micrographs (Figures 7 and 8).

## V. Conclusion

Friction surfacing was used to clad commercial pure Al on mild steel plates. As clad sample had a layer of Al of thickness in the range of 48-54 µm. The sample had small particles of Fe embedded in it. The clad region was converted in to aluminides by heat treatment. The samples heat treated at 700 °C for 2 hours had a relatively thick, IM layer compared to samples heat treated at 730 °C for 2 hours. This difference is attributed to rapid spreading of molten clad layer when heat treated at 730 °C compared to spreading at 700 °C. This has lead to a change in the intermetallic layer thickness. Intermetallic layer was predominantly made up of $Fe_2Al_5$ layer followed by FeAl layer. A zone of coarsened grain was observed in the substrate steel region.

## Acknowledgment

The authors gratefully acknowledge the support extended by the Department of Metallurgical and Materials Engineering, National Institute of Technology Karnataka, Surathkal, India to carry out this research.

## References

[1] H.D Manesh, A.K Taheri,. The effect of annealing treatment on mechanical properties of aluminum clad steel sheet. Materials and Design, 24 (2003), pp. 617-622.

[2] G.M Bedord*, Friction surfacing for wear applications.* Metals and Materials, 11 (1990), pp. 702-705.

[3] Springer, H., Kostka, A., Payton, E.J., D. Raabe, D., Kaysser-Pyzalla, A., Eggeler, G. *On the formation and growth of intermetallic phases during interdiffusion between low-carbon steel and aluminum alloys.* Acta Materialia, 59 (2011) 4, pp. 1586–1600.

[4] Tang, N.Y. *Determination of liquid phase boundaries in Zn-Fe-Mx systems.* Journal of Phase Equilibria, 21 (2000) 1, pp. 167–176.

[5] Jindal, V., Srivastava, V.C., Das, A., Ghosh, R.N. *Reactive diffusion in the roll bonded iron-Aluminum system.* Materials letters, 60 (2006), pp. 1758-1761.

[6] Landry, K., EustathopouloS, N. *Dynamics of wetting in reactive metal/ceramic systems: Linear spreading.* Acta Materialia, 44 (1996) 10, pp. 3923-3932.

[7] Dezellus, O., Eustathopoules, N. *Fundamental issues of reactive wetting by liquid metals.* Journal of materials Science, 45 (2010)16, pp. 4256-4264.

[8] Lin, L., Murray, B.T., SU, S., Sun, Y., Efraim, Y., Baum, H.T., Singler, T.J. *Reactive wetting in metal-metal systems.* Journal of Physics-Condensed Matter, 21(2009), Article 464130.

# Chilldown Study of Cryogenic Turbopump Bearing Coolant Cavity

Jeswin Joseph[1], Gagan Agrawal[2], Deepak K. Agarwal[3], JC Pisharady[4], S. Sunil Kumar[5]

*Liquid Propulsion Systems Centre, ISRO, Valiamala, Trivandrum, Kerala, India*

[1]j_jeswin@lpsc.gov.in

[2]agl.gagan@gmail.com

[3]d_agarwal@lpsc.gov.in

[4]jc_pisharady@lpsc.gov.in

[5]sunil_plamood@yahoo.com

***Abstract*— A computational model is developed using SINDA/FLUENT code to investigate chilling performance of cryogenic turbo pump bearing coolant cavity. The chilldown study is carried out with coolant gas flow followed by two-phase cryogenic propellant flow. The model includes the mathematical formulation for the complex two-phase flow process and predicts transient behaviour of pump cavity surface temperature during chilldown. The model is validated with the turbo-pump chilldown experimental test data. Subsequently, analyses are carried out to study the effect of different chill gas flow rate on cavity chilldown performance. The analytical model is used to determine the required flow rate to chill the cavity below the limiting temperature.**

***Keywords*— Cryogenic, LOX, GHe, Pump cavity, Chilldown**

## I. INTRODUCTION

Turbo-pumps used in cryogenic propellant-based launch vehicles are chilled to cryo-temperatures prior to engine operation. This is to ensure that only liquid phase flow of propellant is fed into the thrust chamber during engine ignition, which otherwise could lead to improper combustion. Since the pump possesses huge thermal mass, it is essential to chill it in before flight start, followed by cryogenic propellant chilldown during flight. Pre-launch chilling of pump and propellant feedline is carried out using gaseous helium (GHe), which has the advantage of high specific heat, resulting in better chilling performance.

Major source of heat in-leak into the pump is through turbine which is exposed to ambient prior to and during engine ignition. To minimize the conductive heat flux from turbine, a cavity is provided adjacent to the bearings of the pump as can be seen in Fig.1. During chilling phase, fluid flows from pump inlet through the cavity and cools the bearing. Since flight duration is limited, it will not be sufficient to chill the cavity at required temperature at the start of engine ignition. This leads to the admission of cryogenic propellant into the hot cavity during engine operation resulting in sudden two-phase transients and improper combustion. It is therefore essential to determine cryogenic turbopump chilldown performance during propellant phase chilling and to investigate the need for gaseous phase chilling of pump bearing cavity for smooth operation of cryogenic engine.

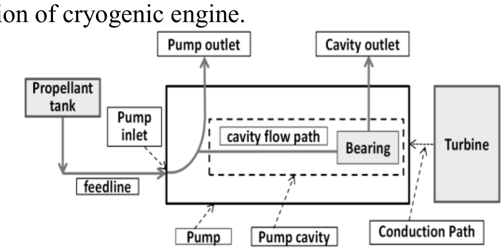


Fig.1. Schematic of turbo-pump flow path

Several analytical investigations were reported in literature for chilldown of cryogenic lines. A mathematical model was developed by Chi [1] for aluminum pipe chilldown, which is based on the assumption of constant flow rate, constant heat transfer coefficient and constant fluid properties. Lockart and Martinelli [2] conducted an experimental chilldown study and developed a semi empirical correlation for pressure drop in two-phase flow in horizontal line. Subsequently Rogers [3] developed a two-phase flow friction factor using Martinelli model for estimating pressure drop in two-phase flowing system. Bronson and Edeskuty [4] studied flow regimes in a horizontal pipe during chilling with liquid nitrogen and concluded that stratified flow is predominant during cryogenic chilldown. Bruke et al. [5] developed a control volume formulation to predict chilldown time of a long stainless steel tube by flowing liquid nitrogen.

Van Dresar et al. [6] conducted chill down experiments for both $LN_2$ and $LH_2$ for a wide range of fixed volumetric flow rates and concluded that an optimum flow rate exists at which the amount of consumed liquid for chilldown is minimized. Steward et al. [7] presented a theoretical study of line chilldown, based on transient numerical modelling, using a one-dimensional finite difference formulation. Heat transfer coefficients were determined using superposition of single-phase forced convection correlations with pool boiling correlations for both nucleate and film boiling. The study concluded that peak pressure surge increases with increasing inlet pressure and the peak surge pressures are small when the inlet liquid is saturated at the driving pressure. A detailed finite volume based numerical model was developed by Cross et al. [8] for chilldown of a cryogenic transfer line based on transient heat transfer effects. Subsequently, Alok Majumdar [9] developed a numerical algorithm considering fluid transient effect and incorporated it into the generalized Fluid System Simulation Program (GFSSP), a finite volume based network flow analysis code. Recently, Gagan et al [10] developed mathematical model for determining the effects of two-phase chill down in a cryogenic feedline. Significant pressure surge was observed during initial chilldown transients.

This paper presents a numerical model of cryogenic feedline including turbo-pump cavity flow path. The model considers transient two-phase chilldown transients and is validated with in-house experimental data from turbo-pump chilldown tests. The model uses finite difference discretization for fluid network to predict thermo-fluid transients during chill down of cryogenic lines.

## II. Formulations and Model Description

A mathematical model is developed using SINDA/FLUINT code to study the chilldown performance of a typical cryogenic pump cavity. Flow in a pipe is modelled as a series of discrete fluid nodes connected via flow lines. Figure 1 shows the schematic of flow path modelled for pump cavity chilldown analysis. It consists of a propellant feed system connected to liquid oxygen (LOX) tank with flow controlled by orifice after the LOX storage tank. Flow inside the pump is bifurcated to the cavity line and vent through cavity outlet port as shown in Fig2.

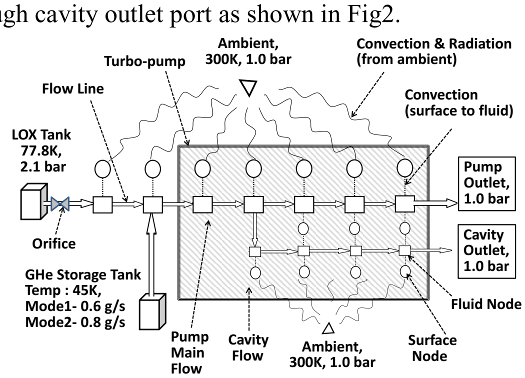


Fig. 2 Computational model for flow path through turbopump

Fluid nodes in flow path are connected with line surface node by convective heat transfer and surface nodes are connected with ambient by convective as well as radiative heat transfer. Mass and energy conservation equations are solved at the fluid nodes in conjunction with the thermodynamic equation of real fluid while momentum conservation equations are solved at the fluid to fluid node connectors.

### A. *Mass Conservation*

Fluid nodes have a definite volume and therefore mass and energy storage capability. The net mass flow from the fluid node must equate to the rate of change of mass in the control volume as shown in equation 1.

$$\dot{m}_u - \dot{m}_d = dm/dt \tag{1}$$

In the steady state formulation, the right side of the equation is zero. This implies that the total mass flow rate into a node is equal to the total mass flow rate out of the node.

### B. *Energy Conservation*

The energy conservation equation is expressed on the basis of the first law of thermodynamics. The energy conservation equation based on enthalpy can be written as below.

$$dU/dt = (h_u.\dot{m}_u - h_d.\dot{m}_d) + Q \tag{2}$$

Where

$$Q = h_c.A_S.(T_s - T_f) \tag{3}$$

The rate of increase of internal energy in the control volume is equal to the rate of energy transport into the control volume minus the rate of energy transport from the control volume.

### C. *Momentum Conservation*

The governing equation for flow connectors is simply a complex form of Newton's second law. The momentum conservation equation for a fluid connector can be written as below.

$$\frac{d\dot{m}}{dt} = \frac{A}{L}.[(P_u - P_d) + f_r.\dot{m}^2 - K_f.\dot{m}^2] \tag{4}$$

A recoverable loss is essentially a pressure drop that becomes a pressure gain if the flow is reversed. This is most often caused by area and density changes between the inlet and the outlet of the flow line. Recoverable loss coefficient is calculated as shown in Eq. (5).

$$f_r = \frac{2.(\rho_d A_d - \rho_u A_u)}{\rho_u.A_u.\rho_d.A_d.(A_u + A_d)} \tag{5}$$

Single-phase frictional pressure drop is calculated using a Darcy friction factor showing in Eq. 6.

$$f = 8.\left[\left(\frac{8}{Re}\right)^{12} + \frac{1}{(a+b)^{3/2}}\right]^{1/12} \tag{6}$$

Where

$$a = \left[-2.457.\ln\left(\left(\frac{7}{Re}\right)^{0.9} + \frac{0.27\varepsilon}{D}\right)\right]^{16} \tag{7}$$

$$b = \left(\frac{37530}{Re}\right)^{16} \tag{8}$$

At low Reynolds numbers, roughness has no effect and the formula reduces to the familiar f= 64/Re. Two-phase pressure drop is calculated using Lockhart-Martinelli correlations [2].

D. *Resident Mass*

The resident mass in fluid node volume can be expressed from the equation of state for a real fluid as below.

$$m = \frac{P.V}{R.T.z} \tag{9}$$

For a given pressure and enthalpy, the temperature and compressibility factor in Eq. (9) is determined from the thermodynamic property program developed by Hendricks et al. [11].

E. *Two-Phase Properties*

The vapor quality of a saturated liquid-vapor mixture is calculated based on enthalpy ratio as shown in Eq.10.

$$x = \frac{(h - h_l)}{(h_v - h_l)} \tag{10}$$

For homogeneous mixture of liquid and vapor, the density, specific heat, and viscosity are computed from the following relations:

$$\phi = (1- x)\, \phi_l + x\, \phi_v \tag{11}$$

where $\phi$ represents specific volume, specific heat or viscosity.

F. *Heat transfer*

Each fluid node is connected with a surface node and surface node is connected with boundary node for energy transfer as shown in Fig 2. The energy conservation equation for the solid node is solved on the basis of thermal mass of surface node and convective heat transfer between solid to inside fluid and ambient. The energy conservation equation for the solid can be expressed as shown in Eq.12.

$$Q_{a-s} - Q_{s-f} = m.C_p \frac{dT}{dt} \tag{12}$$

$Q_{a-s}$ represents heat transfer from ambient to wall by convection and radiation. $Q_{s-l}$ is heat transfer from the wall surfaces to the fluid inside by convection as shown in Eq.13.

$$Q_{s-f} = h_c.As.(T_s - T_f) \tag{13}$$

Convective heat transfer coefficient ($h_c$) is calculated by different correlations according to the fluid state inside the flow line. Dittus-Boelter formulation is used to calculate $Q_{s-f}$ for single phase fluid in turbulent flow as shown in Eq.14 and 15.

$$h_c = Nu\ .\ k\ /\ D \tag{14}$$

$$Nu = 0.023.(Re)^{0.8}.(Pr)^{0.4} \tag{15}$$

Miropolskii's correlations [12] are used to calculate heat transfer coefficient for two-phase homogeneous mixture as shown below.

$$h_c = Nu\ .\ k_v\ /\ D \tag{16}$$

Where

$$Nu = 0.023(Re_{mix})^{0.8}.(Pr_v)^{0.4}.(Y) \tag{17}$$

$$Re_{mix} = \left(\frac{\rho.u.D}{\mu_v}\right).\left[x + (1 - x).\frac{\rho_v}{\rho_l}\right] \tag{18}$$

$$Pr_v = \frac{C_p \mu_v}{k_v} \tag{19}$$

$$Y = 1 - 0.1\left[\frac{\rho_v}{\rho_l} - 1\right]^{0.4} (1 - x)^{0.4} \tag{20}$$

Chen's correlation [13] is used to calculate heat transfer coefficient for nucleate boiling regime. In film boiling condition, heat transfer from solid to liquid is convection as well as radiation also. Bromley's correlation [13] is used for convective heat transfer coefficient in film boiling regime as shown in Eq. 21.

$$h_c = 0.62\left[\frac{k_v^3 \rho_v g(\rho_l - \rho_v)\left(h_{fg} + 0.4 c_p \Delta T\right)}{L_h \mu_v \Delta T}\right]^{0.25} \tag{21}$$

Critical thickness $L_h$ is based on recommendation of Leonard [16] as in Eq.22.

$$L_h = 8.646\left[\frac{\sigma^4 h_{fg}^3 \mu_v^5}{\rho_v(\rho_l - \rho_v)^5 g k_v^3 \mu_v \Delta T^3}\right]^{\frac{1}{11}} \tag{22}$$

A combination of the Newton-Raphson method and the successive substitution method are used to solve the set of equations as mass conservation (Eq. (1)), momentum conservation (Eq. (4)), and resident mass (Eq.(9)) equations.

## III. RESULTS AND DISCUSSION

The mathematical model is developed based on finite difference formulations, taking into account the flow and thermal transient during chilldown. The study is carried out for gas phase chilling as well as 2-phase propellant chilling. Gas phase chilling is carried in ground prior to launch. Pre-launch phase chilling is carried out using cold GHe for 4000s, with flow rate of 40g/s. GHe passes through the feedline but not through cavity flow path, resulting in conductive cooling of the cavity. Launch phase chilling using 85K LOX, commences 95s after lift-off for the duration of 200s. During this time, the pump cavity chilling is controlled by cavity outlet passage of 4mm diameter. The model is validated using turbopump chilldown test data. Subsequently, results of the analysis carried out with validated model are discussed as follows.

A. *Model Validation*

Model validation using test data is shown in Fig.3. The validation plot depicts the comparison between fluid temperature measured and simulated at pump cavity outlet during propellant phase chilling of in-house chilldown experiment.

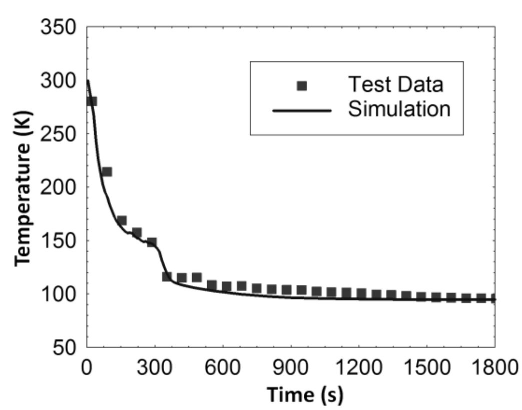


Fig. 3 Model validation using fluid temperature at pump cavity outlet

It can be seen from the figure that the fluid is in gaseous phase up to 300s as its temperature is more than the saturation temperature (102K) corresponding to inlet pressure of 3.0bar. The figure shows comparison of experimental data with simulation.

B. *Chilldown of pump cavity*

Cryogenic system including feedline and pump should be at required temperature at the start of engine flow through the propellant feed system. To achieve an adequate chilled condition, a sufficient duration is required to chill the propellant feed system. Since the chilling time during flight phase is not sufficient to chill the pump and feedline, it becomes important to chill the system before the launch itself. Here study is carried out to determine the effect of pre-chilling of pump cavity on chilling performance. Figure 4 shows the cavity surface temperature when cavity is not pre-chilled but pump and feedline are pre-chilled using GHe. Since GHe passes through pump inlet and outlet but not through the cavity, cavity surface cools down only by solid conduction.

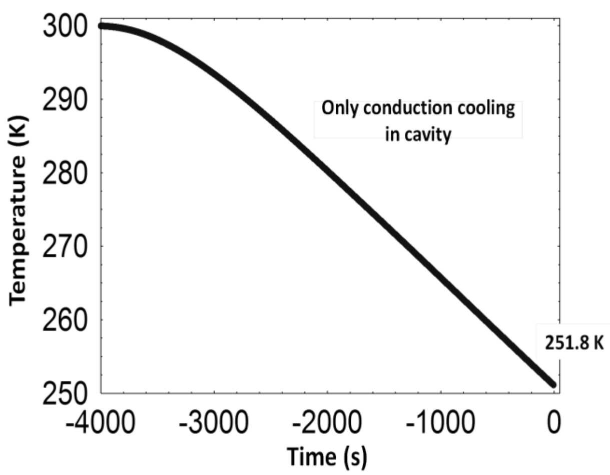


Fig. 4 Cavity surface temperature during pre-launch chilling operation without cavity flow

It can be seen from Fig.4 that cavity surface temperature falls from 300K to 251.8K due to the conduction from the pump material towards the cavity during GHe chilling. The propellant chilldown starts at 95s and LOX is admitted into the cavity. During propellant chilling cavity surface is chilled through conduction as well as convection. At 295s inlet pressure is increased to 2.1bar which results in the increase in flow rate and faster cooling of pump cavity.

Figure 5 shows the cavity surface temperature during propellant phase chilling. It can be seen from the figure that cavity surface temperature falls to 244K at the end of propellant phase chilling. Time t=0s corresponds to lift-off and t=295s corresponds to engine start-up. It is to be noted that required cavity temperature is the saturation temperature (97.7K) corresponding to inlet pressure of 2.1 bar. There is large difference between cavity surface temperature and required temperature which leads to undesirable two-phase transients and improper combustion of propellant.

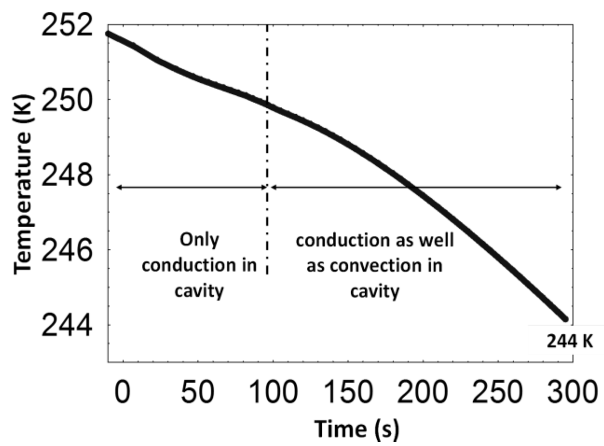


Fig. 5 Cavity surface temperature during propellant chilldown phase without cavity flow during pre-launch

The chilling performance can be improved by increasing the amount of coolant fluid through the cavity during pre-chilling phase as well as flight chilling phase. Since, use of increased amount of propellant for flight chilling will reduce the pay load capacity of the launch vehicle, increasing the coolant flow during pre-chilling is the only desirable option.

C. *Parametric study on pre-chilling of pump cavity*

Pre-launch chilldown analysis of turbopump bearing cavity is carried out with flow rate of 1g/s. The simulated cavity surface temperature is shown in Fig. 6.

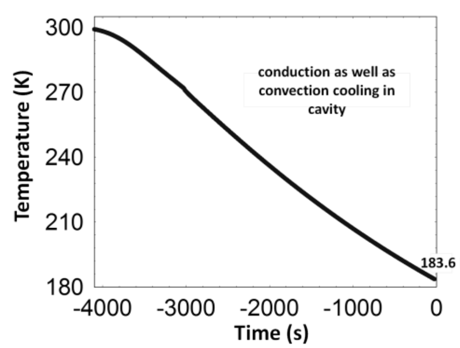


Fig. 6 Cavity surface temperature during pre-launch chilling operation with cavity flow

It can be seen from the Fig.6 that the cavity surface temperature has dropped to 183.6K during pre-chilled compared to 251.8K at cavity surface when cavity is not pre-chilled as shown in Fig 4.

The cavity surface temperature during flight phase is shown in Fig. 7. It can be noted from the Figure 7 that the cavity temperature plot is in increasing trend after Pre-chilling. It is because GHe passes through the cavity during pre-chilling which results in surface cooling of the cavity but bulk material of pump near cavity is at higher temperature then the surface temperature. As the flow through the cavity is stopped at the end of pre-chilling the surface starts taking conductive heat from the pump material near to the cavity. At the start of propellant chilling (95s), the cavity temperature again starts falling and reaches 172K at the end of propellant chilling.

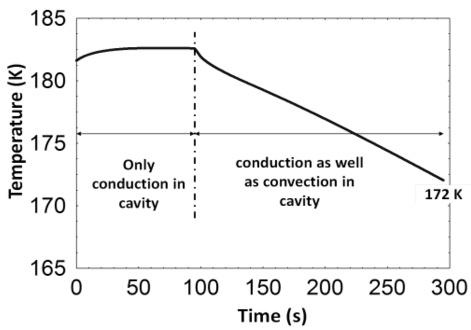


Fig. 7 Cavity surface temperature during propellant chilldown phase with cavity flow during pre-launch

It can be seen from the Fig.7 that the cavity surface temperature at the end of propellant phase chilldown (295s) is still much higher than the required saturation temperature of 97.7K corresponding to pump inlet pressure of 2.1 bar. Hence, a parametric study is carried out with increasing the GHe flow rate through the cavity during pre-chilling phase.

Figure 8 shows the cavity surface temperature in the case of increased GHe flow rates by 2 times and 3 times during pre-chilling. At the end of pre-chilling, the cavity temperature reaches 120K and 90.2K in case of twice flow rate and thrice flow rate through the cavity respectively.

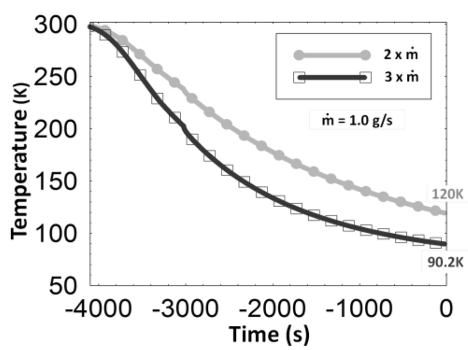


Fig. 8 Cavity surface temperature during pre-launch chilling operation with different cavity flows

The cavity temperatures during flight phase for these two cases are shown in Fig.9. At the end of propellant chilling the cavity temperatures are 114K and 90K for the cases of 2 times and 3 times flow rate respectively. In the case of 3 times increased flow rate, the cavity temperature at the end of chilling process reaches below the required temperature of 97.7K which will be resulting the smooth and steady propellant flow during engine operation.

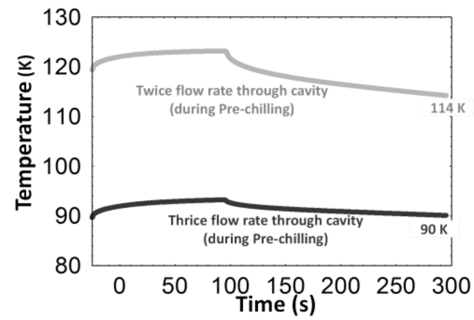


Fig. 9 Cavity surface temperature during propellant chilldown phase with different cavity flows during pre-launch

## IV. CONCLUSION

Analytical transient chilldown model of a cryogenic feed system including turbopump flow path is developed considering gas as well as liquid flow through the propellant feedline and pump. The numerical model is validated with data from chilldown tests on turbopump. Subsequently, analyses are carried out to determine the cavity surface temperature during pre-chilling and propellant chilling phases of turbo-pump. The study shows that the cavity surface temperature is significantly high at the start of engine ignition if cavity is not chilled during pre-launch chilldown operation. Successive analysis with pre-chilled cavity showed major reduction in cavity surface temperature at engine ignition. Parametric studies on pre-chilling flow rates of GHe through cavity shows that the increase in cold GHe flow rate by 3 times of existing flow rate is sufficient to reduce the cavity surface temperature below saturation temperature of LOX (97K) at the start of engine operation, thereby significantly minimizing the risk of improper engine start.

## ACKNOWLEDGMENT

The contributions of Mr. Rijish Kumar P, Mr. Harikumar K and Turbo-pump team of Liquid Propulsion Systems Centre (LPSC) towards the experimental data for validation of the model are greatly acknowledged.

## REFERENCES

[1] Chi, J.W.H., 1965. Cooldown Temperatures and Cooldown Time during Mist Flow, Advances in Cryogenic Engineering, Vol. 10, pp. 330–340.

[2] Lochkhart, R.W., Martinelli, R.C., 1949. “Correlations for two phase flow in pipes", Chemical Engg. Prog.45 : pp. 39-48.

[3] Rogers, J.D., 1968. “Two phase friction factor”. AICHE, j.14 (6), pp. 895–902.

[4] Bronson, J.C., Edeskuty, F.J., 1962. Cooldown of cryogenic systems, Advances in cryogenic engineering, vol 7, pp. 198-205.

[5] Burke, J.C., Byrnes, W.R., Post, A.H., and Ruccia, F.E., 1960. Pressurized Cooldown of Cryogenic Transfer Lines, Advances in Cryogenic Engineering, Vol. 4, pp. 378-394.

[6] Van Dresar, N.T., Siegwarth, J.D., and Hasan, M.M., 2002. Convective Heat Transfer Coefficient for Near-Horizontal Two-Phase Flow of Nitrogen and Hydrogen at Low Mass and Heat Flux, Cryogenics Vol. 41, pp. 805-81.

[7] Steward, W.G., Smith, R.V., and Brennan, J.A., 1970. Cooldown Transients in Cryogenic Transfer Lines, Advances in Cryogenic Engineering, Vol. 15, pp. 354–363.

[8] Cross, M. F., Majumdar, A. K., Bennett,Jr. J. C., and Malla, R. B., 2002. "Modeling of Chill Down in Cryogenic Transfer Lines". Journal of Spacecraft and Rockets, Vol. 39, No.2, pp. 284–289.

[9] Alok Majumdar, 2004. "Numerical Modeling of Conjugate Heat Transfer in Fluid Network". Thermal Fluid Analysis Workshop, Jet Propulsion Laboratory, Pasadena, California.

[10] Agrawal, Gagan, S.Sunil Kumar and Deepak Agarwal, "Pressure Surge During Cryogenic Ffeedline Chilldown Process", Journal of Thermal Science and Engineering Applications, 2015, DOI : 10.1115/1.4030840.

[11] Hendricks, R.C., Baron, A.K., and Peller, I.C., 1975. "GASP: A Computer Code for Calculating the Thermodynamic and Transport Properties for Ten Fluids: Parahydrogen, Helium, Neon, Methane, Nitrogen, Carbon Monoxide, Oxygen, Fluorine, Argon, and Carbon Dioxide", NASA TN D–7808. F

[12] Miropolskii, Z.L.,1963. Heat Transfer in Film Boiling of a Steam-Water Mixture in Steam Generating Tubes, Teploenergetika, Vol. 10, pp. 49–52.

[13] Ghiaasiaan S.M., 2007. Two-Phase Flow, Boiling and Condensation: In Conventional and Miniature Systems. UK: Cambridge University Press, Chap. 4, 5, 11and 12, pp. 121- 365.

[14] Leonard J.E., 1977. "Low-Flow Film Boiling Heat Transfer on Vertical Surfaces", Part 2, "Empirical Formulations and Application to BWR-LOCAD Analysis", Solar and Nuclear Heat Transfer, AICHE Symposium Series, No 164, Vol. 73.

# Theoretical Studies on Fibre Bragg Grating based Flowmeter

Sankar Ram Thekkethil[#*1], K. E. Reby Roy[*3], Rijo Jacob Thomas[*4], R. Ramalingam[#2]

[#]*Institute for Technical Physics*

*Karlsruhe Institute of Technology - Campus North, 76344 Eggenstein-Leopoldshafen, Germany*

[1]sankarram90@gmail.com

[2]rajini-kumar.ramalingam@kit.edu

[*]*T. K. M. College of Engineering, Kollam, Kerala, India*

[3]rebyroy@tkmce.ac.in

[4]rijojthomas@tkmce.ac.in

***Abstract*— The paper summarises the theoretical calculations and simulations performed for the development of a fibre Bragg grating (FBG) sensor based mass flow meter, that can be used at cryogenic temperatures also. The concept of using the drag force induced by a flowing fluid on a bluff body placed in the flow, to measure the rate of flow is used in this work. An optical fibre with a FBG sensor embedded in it will be placed perpendicular to the flow. The fibre will act as the bluff body, while the FBG sensor will pick up the bending strain induced in the fibre due to the drag force. The amount of bending strain which can be measured as a shift in Bragg wavelength can be calibrated for to provide the mass flow rate.**

***Keywords*— Fibre Bragg grating, FBG Sensor, Cryogenic, Flow meter, Mass flow measurement**

## I. Introduction

Accurate measurement of fluid flow characteristics is a prominent part in any machinery that comprises fluid flow or convection heat transfer. In most scientific apparatuses it is required that the flow meter doesn't have a prominent effect on the flow. The mounted meter, ideally should not induce a pressure drop or change the temperature of the flow. Due to recent developments in the area of cryogenics such as those in areas of space technology or super conductivity, the flow measurement of cryogens has introduced new challenges in the area of instrumentation. The brittle behaviour of materials at low temperatures and the thermal stresses due to large changes in temperature restrict the use of many existing designs and materials for these applications. The pressure drops due to the introduction of the measurement device also pose a serious concern in cryogenic flows. The chances of cavitation are quite high in case of cryogens, since the temperature of flow is very near to its saturation temperature. This makes mass flow meters based on differential pressure such as laminar flow meters or orifice meters a bad solution for such applications.

There are other intrinsic difficulties associated with the use of traditional sensor technologies in superconductors and space applications. The absence of gravity restricts use of many flow measuring methods such as rotameters. The high electromagnetic fields present in superconductors will introduce errors in the commonly used electronic flow meters. Other requirements for such applications include small size, remote sensing capabilities, replicability, long life etc.

### A. Fibre Bragg Grating Sensors

A fibre Bragg grating (FBG) is an optical filter embedded in an optical fibre, by means of placing a set of gratings at specified distances. A grating is an area of altered refractive index, placed in a homogeneous domain.

A FBG sensor is introduced in an optical fibre by using high power UV laser. Two UV laser beams are allowed to intersect at a specific angle on an optical fibre. The constructive and destructive interference of the UV will alter the bonding of doping elements in the fibre creating areas of varying refractive indices. The distance between the gratings can be fixed by fixing the wavelength of the UV laser and the angle of incidence (θ) (Fig. 1).

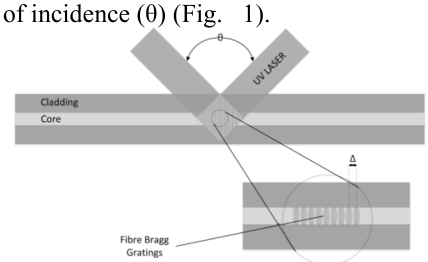


Fig. 1 Schematic of fabrication of FBG sensor

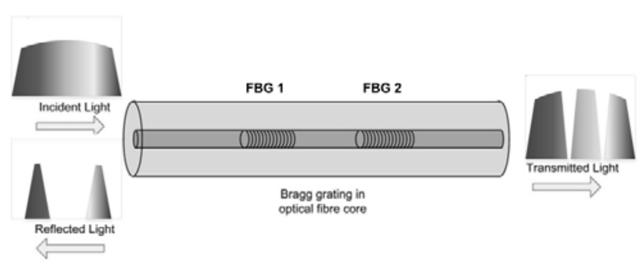


Fig. 2 Operation of a FBG sensor

The operation of a FBG sensor can be explained as a filter. When a beam of white light, i.e. light with full spectrum, is passed into a FBG sensor, the sensor reflects light of a specific wavelength while allowing all other wavelengths to pass through without distortion (Fig. 2). In case of multiple sensors placed in a single fibre (multiplexing), the reflected wavelength can be selected so that each FBG sensor has a distinct operational range.

The single wavelength that is reflected by an FBG sensor is called the Bragg wavelength and is a dependent on the grating period ($\Delta$). The Bragg wavelength is correlated as [1]

$$\lambda_b=2\Delta\eta_{eff} \tag{1}$$

where $\eta_{eff}$ is the effective refractive index of the optical fibre (fibre core).

When strain is applied on a FBG sensor, the distance between the gratings or the grating period changes. This will attribute as a change in the reflected wavelength as defined by Eqn. 1. This change in the reflected wavelength is called Bragg shift ($\Delta\lambda_b$).

This property of an FBG sensor to measure very large strains (up to 5000 µm/m) with good accuracy has enabled its use in measurement of various physical parameters such as displacement, temperature, pressure, strain, vibration, acceleration, velocity, torsion, fluid flow etc. The inherent properties of a FBG sensor and use of optical fibre also deliver various advantages such as remote sensing, passive operation, corrosion resistance, multiplexing capabilities of up to 10 FBG sensors in a single optical fibre by using wavelength division multiplexing (WDM), small size (150 µm dia), measurement of multiple parameters using a single fibre, imperviousness to electrical & magnetic interference, long distance signal transfer without repeaters etc.

### B. *FBG as a flow sensor*

Numerous independent researches have been conducted worldwide on the use of FBG sensors as a flow meter. A large numbers of studies were concentrated on the use of FBG sensors in flow measurement by suing the principle of anemometry. A laser beam was used to heat the FBG sensor to a stable temperature. The flowing fluid will carry away a part of heat reducing the temperature. The change in temperature which can be sensed by the FBG sensor itself will give an indication of the flow rate [2]. Another approach used was to use FBG to measure the temperature of fluid downstream to a heating coil[3]. The temperature of downstream fluid will be according to the flow rate. These approaches showed minimum pressure drop but were not applicable in many cases due to the heat addition to the flow. These devices were predominantly fluids at atmospheric conditions and were not pertinent for cryogenic liquids.

A different conception explored by various researchers was the use of FBG sensors in target type flow meters [4]. In this concept, a target body is placed in the fluid. The impact of fluid on the target will create a stress on the support structure. This stress can be measured using FBG sensors. Though this concept was theoretically applicable for cryogenic fluids, the pressure drop across the sensor was usually high.

An innovative concept was presented in [5] where instead of the impact force, the drag force due to the fluid flow was used to movement of a target. Here the target was designed to be a cylinder placed close to the pipe walls. Thus this design eliminated the problem of pressure drop. Few studies were conducted in this direction showing promising results.

## II. Single fibre flowmeter

In this design, the concept of using a discrete target body is eliminated. Instead the FBG fibre is placed directly in the path of flow, such that the fibre is perpendicular to the direction of flow. The viscous drag created due to the flow will cause a bending force on the on the fibre.

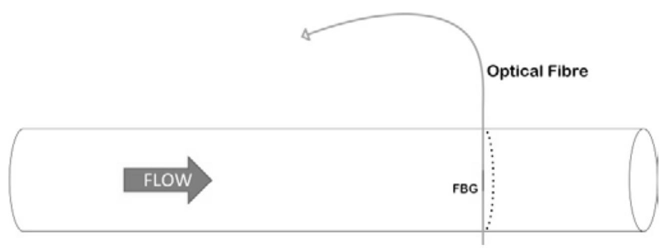


Fig. 3 Operation of FBG based flow meter

### C. *Operation Principle*

The operating principle of this design is the viscous drag created by a fluid when flowing past a bluff body is proportional to its velocity or mass flow rate. The mass flow rate ($\dot{m}$) can be related to the flow velocity (v) as

$$\dot{m}=v*\rho*A \tag{2}$$

where $\rho$ is the density of fluid and A is the cross sectional area. Then the drag force ($F_d$) due to the flow can be calculated by substituting the mass flow rate in the drag equation as

$$F_d = 0.5\ C_d*A_p*\dot{m}^2/(\rho*A^2) \tag{3}$$

where $C_d$ is the drag coefficient, which can be estimated as 1.1 for a cylinder placed perpendicular to flow. $A_p$ is the projected area of the fibre which can be expressed in terms of the diameter of fibre ($d_f$) and length of fibre (L) as

$$A_p = d_f*L \tag{4}$$

The bending strain experienced by fibre can be the calculated by applying beam theory. The FBG fibre may be assumed to be a beam, of which both ends are fixed. The drag force can be assumed to be an Uniformly Distributed Load (UDL) acting on it. With that assumption, the total strain on the FBG sensor may be given by the equation,

$$\varepsilon = F_d*L/(3*0.78*d_f^3*E_{eff}) \tag{5}$$

where $E_{eff}$ is the effective Young's modulus.

For the given value of mechanical strain (ε) the response of a FBG sensor in terms of Bragg wavelength shift ($\Delta\lambda_{b1}$) can be evaluated as [6]

$$\Delta\lambda_{b1} = (1-P_e) * \varepsilon * \lambda_b \qquad (6)$$

in which $P_e$ is the effective strain-optic coefficient of the fibre, which is given as follows

$$P_e = 0.5 * n^2 * [P_{12} - \nu(P_{11}+P_{12})] \qquad (7)$$

where $P_{11}$ and $P_{12}$ are the components of strain-optic tensor, n is the fibre core refractive index and ν is the Poisson's ratio. For a typical FBG sensor there values can be estimated as $P_{11} = 0.113$, $P_{12} = 0.252$, $\nu = 0.16$ and $n = 1.482$.For a FBG sensor with Bragg wavelength 1550 nm, the expected strain sensitivity can be found out as 1.2 pm for an applied strain of 1 μm/m.

The FBG sensor is further sensitive to temperature changes in its surroundings. This is due to the thermal strain created in the optical fibre. The Bragg wavelength shift due to change in temperature ($\Delta\lambda_{b2}$) is expressed as a function of change in temperature, ΔT as [7]

$$\Delta\lambda_{b2} = (\alpha + \xi)\, \Delta T \qquad (8)$$

where α is the thermal expansion coefficient and ξ is the thermo-optic coefficient which for a germanium doped silica fibre are $0.55\text{x}10^{-6}$ and $8.6\text{x}10^{-6}$ respectively. The expected sensitivity for a fibre Bragg grating at 1550 nm is approximately 13.7 pm/K.

Since these two factors affecting the wavelength shift are independent, the total Bragg shift ($\Delta\lambda_b$) can be expressed as the sum of individual shifts.

$$\Delta\lambda_b = \Delta\lambda_{b1} + \Delta\lambda_{b2} \qquad (9)$$

This property is quite significant in the use of FBG sensors, since the sensor used for strain measurement will automatically measure the temperature changes also. So during measurement, a second FBG sensor must be used so that it only measures the temperature changes and thus can be used as a thermal compensator.

*D. Sensor Design*

In this work, the flow sensor was designed for a pipe of Ø18 mm. An operational range of 0-5 g/s was decided for the testing of gases. From Eqn. 3 it is evident that for a given mass flow rate, the drag force experienced by a bluff body placed in a fluid flow is inversely proportional to the density of fluid. Since cryogenic fluids exhibit an density nearly 200 times that of their gases, for testing of cryogens, a mass flow rate of up to 30 g/s was taken so that considerable velocity is gained by the fluid. Based on these parameters, the maximum Reynold's number was calculated for different fluids [7].

TABLE I

MAXIMUM EXPECTED REYNOLD'S NUMBERS FOR VARIOUS FLUIDS

| **Fluid** | **Temperature K** | **Reynold's Number** |
|---|---|---|
| Air | 293 | 13960 |
| Nitrogen Gas | 293 | 21800 |
| Nitrogen Gas | 77 | 72340 |
| Liquid Nitrogen | 77 | 14355 |
| Helium Gas | 293 | 17160 |
| Helium Gas | 4 | 306070 |
| Liquid Helium | 4 | 682090 |

When testing nitrgen gas or air, which are having a low viscosities, error due to vortex induced vibrations are expected in the measurements. Helium Gas and liquid cryogens being more viscous are will dampen the vibrations giving a better output signal. Also at high Reynold's numbers, the frequencies of vortex induced vibrations are high, leading to less vibration of fibre.

It was also verified that for the given range of operation, compressible flow does not occur, which can lead to pressure waves in the fluid domain.

The drag force was calculated for the gases and cryogenic fluids under consideration, for their respective range of mas flow rates using the Eqn. 3. The results are shown in Fig. 3 and Fig. 4.

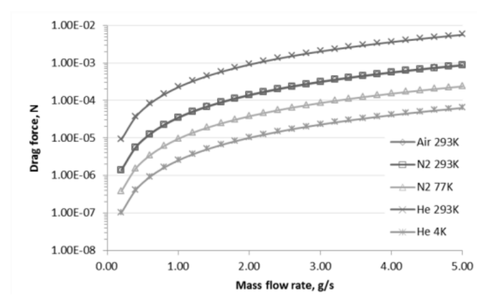


Fig. 4 Drag force ($F_d$) vs mass flow rate (ṁ) for gases

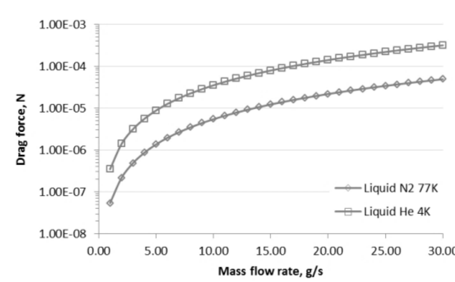


Fig. 5 Drag force ($F_d$) vs mass flow rate (ṁ) for liquids

TABLE II

DESIGN PARAMETRS OF CORE AND CLADDING

| | **Diameter (m)** | **Young's modulus (Pa)** |
|---|---|---|
| **Core** | $9 \times 10^{-6}$ | $7.33 \times 10^{10}$ |
| **Cladding** | $2 \times 10^{-4}$ | $2.50 \times 10^{9}$ |

Based on these values of drag force, the strain on fibre was calculated considering the FBG fibre as a fixed beam, on which the drag force is acting as a Uniformly Distributed Load (UDL). Equation 5 can be used to determine the strain in the fibre.

The effective Young's modulus ($E_{eff}$) required for the calculation is estimated using the equation

$$d_f^2 * E_{eff} = (d_f^2 - d_c^2)\ E_f + d_c^2 * E_c^2 \quad (10)$$

where subscripts 'f' and 'c' denotes the cladding and core respectively. Taking the values from Table II, the Young's modulus ($E_{eff}$) can be calculated to be 2.65 x $10^9$ Pa.

Proportional to on the values of stain developed in the fibre, the FBG sensor will exhibit a shift in wavelength ($\Delta\lambda_b$), which is governed by Eqn. 6. The wavelength shifts for different fluids were plotted and the response of the sensor was studied based on these values. It was seen that the output of the FBG sensor shows large variations for different fluids at the same mass flow rate. This is due to the large variations in density and viscosity of the fluids with respect to temperature.

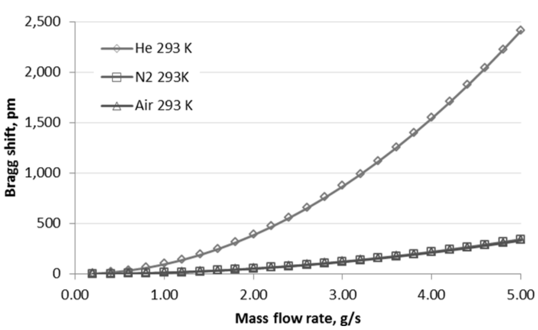


Fig. 6 Bragg shift ($\Delta\lambda_b$) vs mass flow rate ($\dot{m}$) for gases at atmospheric temperature (293 K)

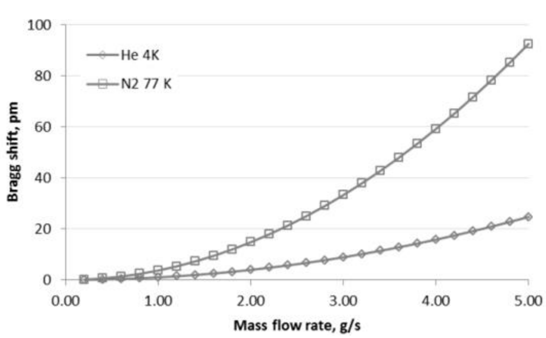


Fig. 7 Bragg shift ($\Delta\lambda_b$) vs mass flow rate ($\dot{m}$) for gases at respective saturation temperatures

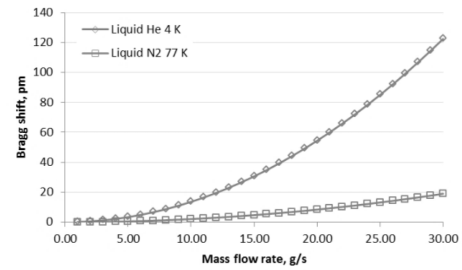


Fig. 8 Bragg shift ($\Delta\lambda_b$) vs mass flow rate ($\dot{m}$) for liquids at respective saturation temperatures

## III. Performance Study

Based on the theoretical studies conducted, the response and the performance parameters of the FBG sensor was predicted.

### *E. Gases at Atmospheric Temperature*

Helium, nitrogen and air at atmospheric temperature (293 K) were considered for this study. Among these, both air and nitrogen showed very similar response which is as expected. Helium showed a maximum shift of 2409.3 pm for a flow rate of 5 g/s, while nitrogen and air showed a Bragg shift of 344 pm and 332.5 pm respectively. Nitrogen showed an sensitivity of 30.2 pm/(g/s) at low flow rates (0-2 g/s) and a sensitivity of 112.7 pm/(g/s) at high flow rates (3-5 g/s). The respective values for air were 29.2 pm/(g/s) and 109.07 pm/(g/s). Helium on the other hand showed a much higher sensitivity with 212.02 pm/(g/s) at low flow rates and 790.25 pm/(g/s) at higher flowrates.

The average sensitivities over the whole range was ~70 pm/(g/s) for air and nitrogen while ~500 pm/(g/s) for helium. Assuming the error during measurement to be ±2 pm, the resolution of the sensor may be calculated as ~0.5 g/s for nitrogen or air and ~0.2 g/s for helium.

### *F. Gases at Saturation Temperatures*

At their saturation temperatures due to the low viscosities of the gases the flow velocities will be lower than that of the same gas at room temperature and same mass flow rate. This in turn can reduce the drag force and lead to low sensitivities.

At their saturation temperatures, Helium showed a maximum Bragg shift of 24.6 pm at 5 g/s whereas nitrogen showed a 92.4 pm. At low velocities, the sensor sensitivity was calculated to be 8.1 pm/(g/s) for nitrogen and 2.1 pm/(g/s) for helium. At higher velocities, the sensitivities increased to 30.3 and 8.09 pm/(g/s) for nitrogen and helium respectively.

The overall sensitivity of nitrogen and helium over the whole range was 19.2 and 5.1 pm/(g/s). Further studies and experimental verification is required before understanding the feasibility of the sensor at this range. Further changes in the sensor design such as the pipe diameter etc. can aid in attaining a higher sensitivity. Due to the lower sensitivity, the senor resolution was ~2 g/s for nitrogen and ~4 g/s for helium.

### *G. Cryogenic Liquids*

Cryogenic liquid due to very high densities, need only a very small velocity to provide a good mass flow rate. So the range of mass flow rates to be tested was increased for cryogenic liquids, so that a good velocity can be obtained. The performance of the sensor while using cryogenic liquids were tested in a range of 0-30g/s. Here the low range sensitivities were taken between 0-10 g/s and high range sensitivities were taken between 20-30 g/s.

For liquid nitrogen at 30 g/s the fluid velocity was 0.18 m/s creating only a small shift of 18.9 pm in the Bragg wavelength. The low and high range sensitivities were calculated to be 0.23 and 1.07 pm/(g/s) for liquid nitrogen while 1.5 and 7 pm/(g/s) for liquid helium. Overall sensitivities of 0.65 and 4.2 pm/(g/s) were obtained for liquid nitrogen and liquid helium. The resolution of the instrument was calculated to be 15 g/s and 5 g/s for nitrogen and helium respectively.

## IV. CONCLUSIONS

An innovative notion to use the FBG sensor to measure the mass flow rate for fluids was conceptualised through this work. The proposed design can be used at atmospheric and cryogenic temperatures. It will be impervious to electromagnetic fields and will only induce a negligible pressure drop.

The performance characteristics of the sensor were studied and sensitivity and resolution of the sensor were calculated. Further validation of this theoretical model will be done by experimental studies.

## ACKNOWLEDGMENT

This work was supported by the German Federal Ministry of Economics and Technology (03ET1008A).

## REFERENCES

[1] Byoungho Lee, "*Review of the present status of optical fiber sensors*", Optical Fiber Technology, Volume 9, Issue 2, April 2003, Pages 57-79, ISSN 1068-5200, http://dx.doi.org/10.1016/S1068-5200(02)00527-8.

[2] Xinhuai Wang, Xinyong Dong and Yan Zhou, "*Optical Fiber Flowmeter Using Silver-coated FBG Cascaded by Waist-enlarged Bitaper*" Progress In Electromagnetics Research Symposium Proceedings, China, 835-838

[3] Shim, J. H., Cho, S. J., Yu, Y. H., Sohn, K. R., "*Gas-flow sensor using optical fibre Bragg grating (FBG)*," Journal of Navigation and Port Research International Edition, 32(9), 717-722, ISSN-1598-5725 (2008).

[4] Xueguang Qiao, Qian Zhang, Haiwei Fu, Dakuan Yu. "*Design of the target type flowmeter based on fiber Bragg grating and experiment*" J. Chin. Opt. Lett., 2008, 6(11): pp.815-817

[5] Ramalingam, R., Neumann, H., Süsser, M., "*Mass flow sensor and method for determining the mass flow in a pipe*" Patent Application Publication, US 20130014594 A1 (2013).

[6] Othonos, A., "*Fiber Bragg gratings*," Review of Scientific Instruments, 68, 4309-4341, (1997)

[7] Venkataraman Narayanan Venkatesan; K-P. Weiss; R. Ramalingam; "*Strain Calibration of Substrate-Free FBG Sensors at Cryogenic Temperature*" International Conference on Sensor Systems and Software, Oct 26–27, 2015

[8] Haefer, R. A., : *Kryo-Vakuumtechnik: Grundlagen and Anwendungen*, Springer-Verlag, Berlin 1981, https://www.itep.kit.edu/english/192.php, dt. 15/09/2015.

# Numerical Investigation on the Supercritical Heat Transfer of Cryogenic Methane in Regenerative Coolant Channels

Muhammed Naseef V. [1], Arun M. [2], Jose Prakash M. [3]

*Department of Mechanical Engineering, TKM College of Engineering, Kollam, India*

[1]vnaseef@gmail.com

[2]arun.m@tkmce.ac.in

[3]jpmmech@yahoo.co.in

*Abstract*— **Supercritical flow and heat transfer have important application in the regenerative cooling of rocket engines. Strong thermophysical property variations exhibited by methane near the pseudocritical point influences the heat transfer process. Three dimensional conjugate heat transfer of cryogenic methane inside a subscale rocket engine coolant channel at supercritical pressures with asymmetric heating imposed on the bottom surface is numerically investigated. This study mainly focuses on the effect of aspect ratio, heat flux and operating pressure on the supercritical heat transfer of cryogenic methane with copper as the regenerative coolant channel wall material. The result indicates that the above parameters have significant effect on the heat transfer. Significant efforts are done to identify the optimum aspect ratio and it is found that for the present study the optimum value of aspect ratio is 4. The results revels that significant heat transfer deterioration is observed at the bottom wall of the coolant channel at high heat flux. It is observed that the heat transfer deterioration decreases as the operating pressure is increased.**

*Keywords*— **supercritical heat transfer, cryogenic methane, aspect ratio, psuedocritical temperature, volumetric heat capacity**

## I. Introduction

The heat generated in a rocket thrust chamber mostly expels through exhaust gases. But a fair amount of heat is transferred to the chamber walls. The challenge to the designer is to safeguard the chamber wall material exposed to high temperatures (2500K to 3600K) and high heat fluxes (up to 160MW/$m^2$). Several cooling methods are successfully adopted to meet this challenge. Regenerative cooling is one of the widely used cooling techniques. In regenerative cooling technique a high velocity coolant, usually fuel itself, is passed through coolant channels which is circulated on outer surface of the thrust chamber wall and absorbs heat energy. The heated coolant (fuel) then passes to the injector and injected to the combustion chamber at a pressure higher than chamber pressure.

In recent years, cryogenic methane is used as an alternative to the traditional liquid propellants. This is mainly due to the unique advantages of cryogenic methane over traditionalpropellants, e.g. higher density, lesser challenging storage requirement and higher vaporization temperature. Also it has got higher specific impulse, superior cooling capacity and higher coking limit compared to another commonly used fuel, Kerosene.

Engine performance increases by operating at high chamber pressures, which results in proportionally higher heat fluxes to the chamber walls. The coolant has to be supplied at a higher pressure than chamber pressure. Heat transfer, fluid flow, and combustion of cryogenic propellants at supercritical pressures draw major attention in recent years. In the supercritical region fluctuations in pressure and temperature of fluid even in a small scale will lead to significant thermophysical property variations. Thus heat transfer characteristics of the fluid exhibits unique features due to this sharp variations of thermophysical properties. As the coolant flows along the regenerative passage its temperature increases and its state may cross the pseudocritical range.

Because of importance in industrial field like nuclear reactors, boilers etc., major investigations of supercritical heat transfer phenomena have been carried out in water and CO2 [1-6]. In these days cryogenic methane is considered as an alternate rocket propellant because of its unique characteristics over other liquid propellants. Only very few studies of supercritical heat transfer with the cryogenic-propellant methane are available in the open literature [7-10]. Thorough investigation is needed to understand various aspects of heat transfer and fluid flow of cryogenic methane at supercritical condition.

Pizarelli [7] conducted 3D numerical studies on supercritical methane flowing in a rectangular cooling channel. Results indicated that property variations could significantly affect the heat transfer characteristics. Ruan and Meng [8] studied influence of channel geometric ratios on fluid flow and heat transfer. They conducted a three dimensional numerical analyses for turbulent supercritical heat transfer of the cryogenic propellant methane flowing inside a rectangular engine cooling channel with asymmetric heating on the top surface of the channel. They didn't consider the wall thickness of the cooling channel. Their results illustrated that heat transfer deterioration phenomena could occur during a supercritical heat transfer process owing to strong thermophysical property variations near the pseudocritical temperature at the near wall zone. The applicability of Bishop heat transfer coefficient was also tested for its suitability for supercritical heat transfer predictions of the cryogenic methane flowing inside a rectangular channel. Wang et al.[10] considered wall thickness of cooling channel and thermal conductivity of wall material, so that effect of conjugate heat transfer due to heat flux distribution can be illustrated.

In the present numerical study the effect of operating pressure, wall heat fluxes and aspect ratio on conjugate heat transfer of cryogenic methane in a subscale rocket engine cooling channel with copper as the channel wall material is considered. The bottom surface of the coolant channel is asymmetrically heated with a constant wall heat flux. Geometry has created in close similarity in shape of the coolant channel with actual rocket engine coolant channels; so the results obtained herein could be used for optimization of rocket engine cooling systems. The variation in thermal conductivity of the cooling channel wall material with temperature is also considered. Studies have been conducted to see the effect of Aspect Ratio (AR), operating pressures and wall heat fluxes on the heat transfer and wall temperature distribution.

## II. NUMERICAL APPROACH

In this study a three dimensional cooling channel which closely matches with that of a real rocket engine cooling channel is considered. The geometry and their boundary conditions are illustrated in figure. 1.

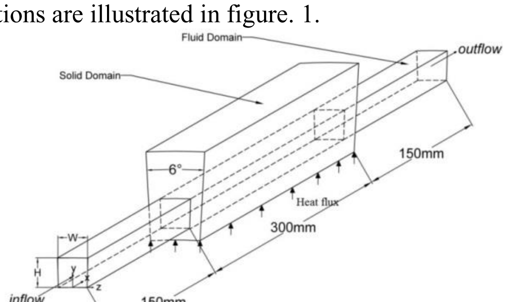


Fig.1. Geometry of the cooling channel

The major issue in solving fluid flow and heat transfer analysis is defining the accurate values of their thermophysical properties. The thermophysical properties at supercritical condition strongly depend upon both temperature and pressure. The relevant properties of methane are listed in the table 1. The values of thermophysical properties of methane for a pressure of 6, 8, 10 and 12 MPa from NIST data base [13] and are incorporated in the numerical simulation through user defined functions.

The thermophysical property variations of methane at a supercritical pressure of 6, 8, 10 and 12 MPa from NIST data base are illustrated in figure 2.

TABLE 1
THERMODYNAMIC PARAMETERS OF METHANE

| Parameters | Values |
|---|---|
| Mol. Wt. g/mol | 16.04 |
| Critical Temperature, K | 190.4 |
| Critical Pressure, MPa | 4.6 |
| Critical Volume, $cm^3$/mol | 99.2 |

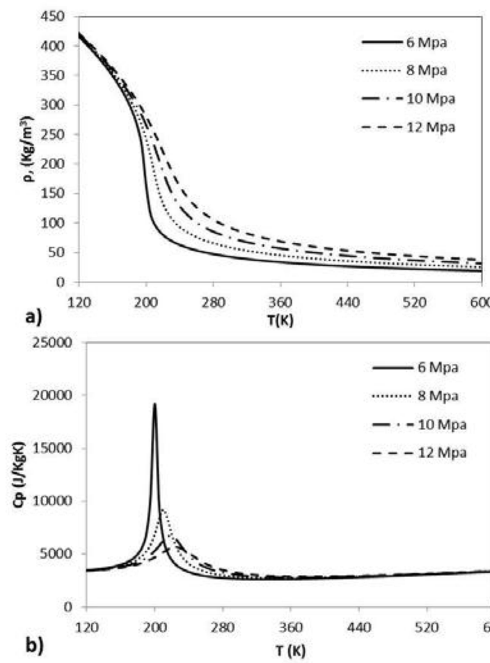


Fig. 2. Thermophysical property variations of methane with temperature: a) Density (ρ), b) Specific heat (Cp).

The pressure based numerical algorithm in ANSYS Fluent [11] has been applied along with the user defined property functions to incorporate drastic property variations. Standard inlet, outlet, wall and symmetry boundary conditions are applied to the computational domain. At the inlet boundary the fluid velocity and temperature were specified and operating pressures are changed to 6, 8, 10 and 12 MPa. Heat flux boundary conditions are applied at the heated wall and the outer surface of the top wall is assumed to adiabatic. Symmetry boundary conditions are applied at the outer surfaces of the side walls.

## III. MODELLING AND SIMULATION

For the present study geometric configurations of a typical subscale rocket engine with a constant combustion chamber with wall thickness of 9mm is selected. The inside and outside radius of the combustion chamber are fixed as 47.8mm 56.8mm respectively. The number of cooling channels is fixed as 60. Due to the geometrical symmetry of the combustion chamber a sectorial portion of $6^0$ is chosen for the preparation of the computational domain. The thickness of the bottom wall of the coolant channel is fixed as 1.2 mm. The details of the geometry considered are illustrated in figure. 3.

In order to study the effect of Aspect Ratio (AR) on the heat transfer characteristics five cases have been considered. The details are shown in table 2. In all the cases the combustion chamber wall thickness is fixed as 9mm, the wall thickness at the bottom of the coolant channel as 1.2mm and

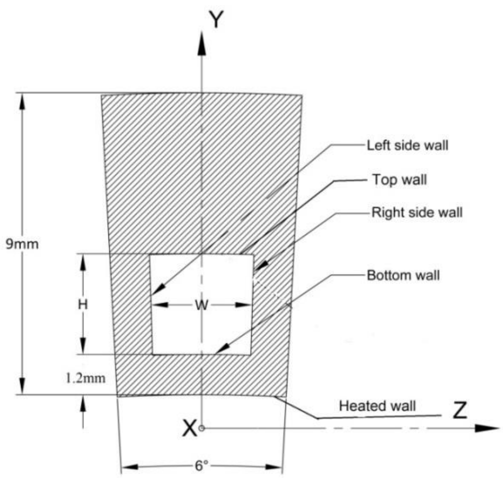


Fig.3 Dimensions of Channel Cross-Section

channel cross-sectional area (A) as 9mm$^2$.The five different aspect ratios are obtained by varying channel height (H) and width (W). An entry length of 150mm is provided to obtain a fully developed flow inside the coolant channel. The test section of 300mm in length is asymmetrically heated with a constant wall heat flux enforced on the bottom of the solid channel surface, referred as heated wall. The exit section is provided with 150mm length to avoid the outlet boundary condition effect on the accuracy of the heat transfer calculations. In all the cases the inlet velocity is fixed at 15m/s and inlet temperature as 120K.

Careful grid independence studies have been conducted before the commencement of the numerical computations. Grid system having an element size of $4\times10^{-04}$ m is found sufficient to produce reliable numerical results. The boundary layer resolution near the walls is optimised by using the inflation option available with ANSYS Meshing [12]. Since k-ε turbulent model with an enhanced wall treatment has been applied, care is taken to keep the $y^+$ values for all the fluid and solid interfaces satisfying a value of $y^+ \leq 1$. This is done to accurately capture the sharp temperature gradient in the near wall region at supercritical pressures

## IV. RESULTS AND DISCUSSION

### A. *Effect of aspect ratio on wall temperature*

The combustion chamber walls are exposed to very high heat fluxes during the rocket engine operations and this high heat energy transferred during the combustion must be absorbed by the coolant in order to provide better temperature distribution along the chamber walls. If the fluid layers adjacent to the wall are either at the critical region or nearer to it, there will be heat transfer deterioration due to the sudden property variation particularly in specific heat capacity and density.

.

TABLE 2

ASPECT RATIO VALUES

| Aspect Ratio (AR) | H | W |
|---|---|---|
| 1 | 3 | 3 |
| 2 | 3√2 | 3/√2 |
| 3 | 3√3 | √3 |
| 4 | 6 | 3/2 |
| 5 | 3√5 | 3/√5 |

The variations in temperatures(T) of heated wall (hw), bottom wall (bw), side wall (sw) and top wall (tw) along the axial direction for aspect ratios for 8 MPa pressure are shown in figure.4. It is observed that heated wall temperature increases along the flow direction. At 8 MPa the maximum value of heated wall temperature is 474K and it decreases as the aspect ratio is increased from 1 to 5. However the difference in wall temperatures for AR4 and AR5 is marginal. For AR=1, average heat flux through bottom wall is 49.7% of imposed heat flux and this quantity reduces as the aspect ratio increases. This is due to the better heat flux redistribution through the side walls. For example with aspect ratio 5 the amount of average heat flux reaching the fluid through the bottom wall is only 30% of the imposed heat flux. From Aspect ratio 3 onwards the more heat is transferred to the fluid through the side walls. As the aspect ratio is increased from 1 to 5, average wall temperature at the bottom, side and top walls decreases by 33%, 43%, and 45% respectively.

It is clear from the above results that optimum value of aspect ratio for 8 MPa pressure is AR= 4. The effect of aspect ratio studies are extended for 10 and 12 MPa and similar trends in wall temperature is observed. It is also observed that for 10 and 12 MPa the optimum value of aspect ratio remains same as that for the 8Mpa.

### B. *Effect of Pressure on Wall Temperature*

The variation of heated, bottom, side and top wall temperatures along the flow direction for AR=4 at different pressures are illustrated in the figure.5. It is found that increasing operating pressure would decrease heated wall temperature, which indicates reduction in heat transfer deterioration. But at higher pressures this reduction is marginal due to lesser property variations of methane. Volumetric heat capacity, a product of density and specific heat, plays an important role in the reduction of heated wall temperature at higher pressures. A detailed explanation will be given in next section.

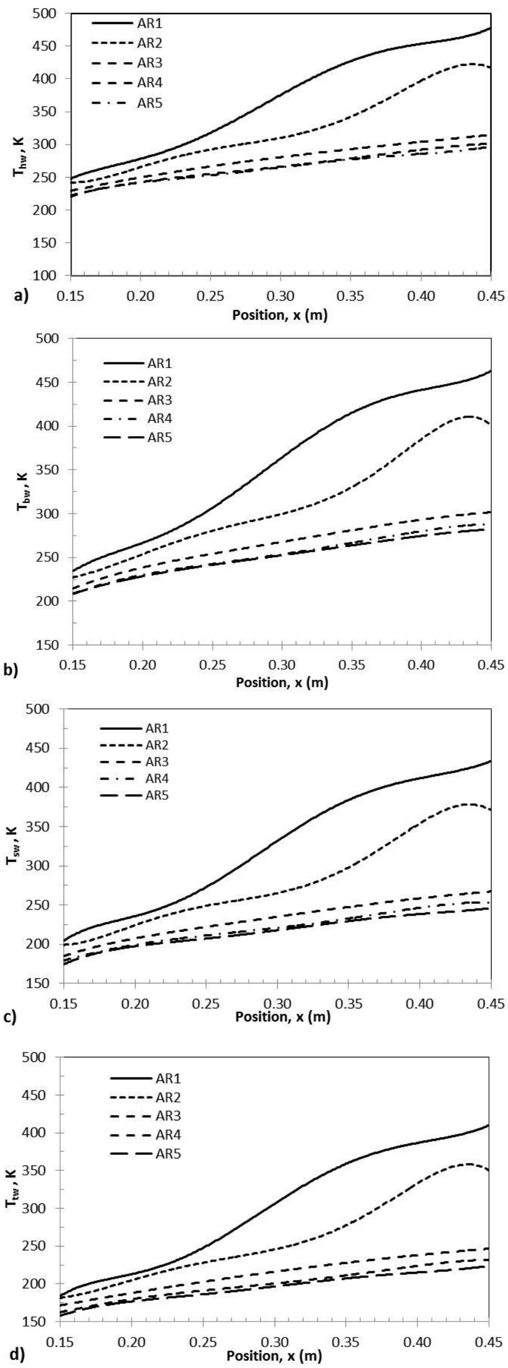


Fig. 4. Variation in temperature on a) heated wall, b) bottom wall, c) side wall and d) top wall along the flow direction at 8 MPa pressure

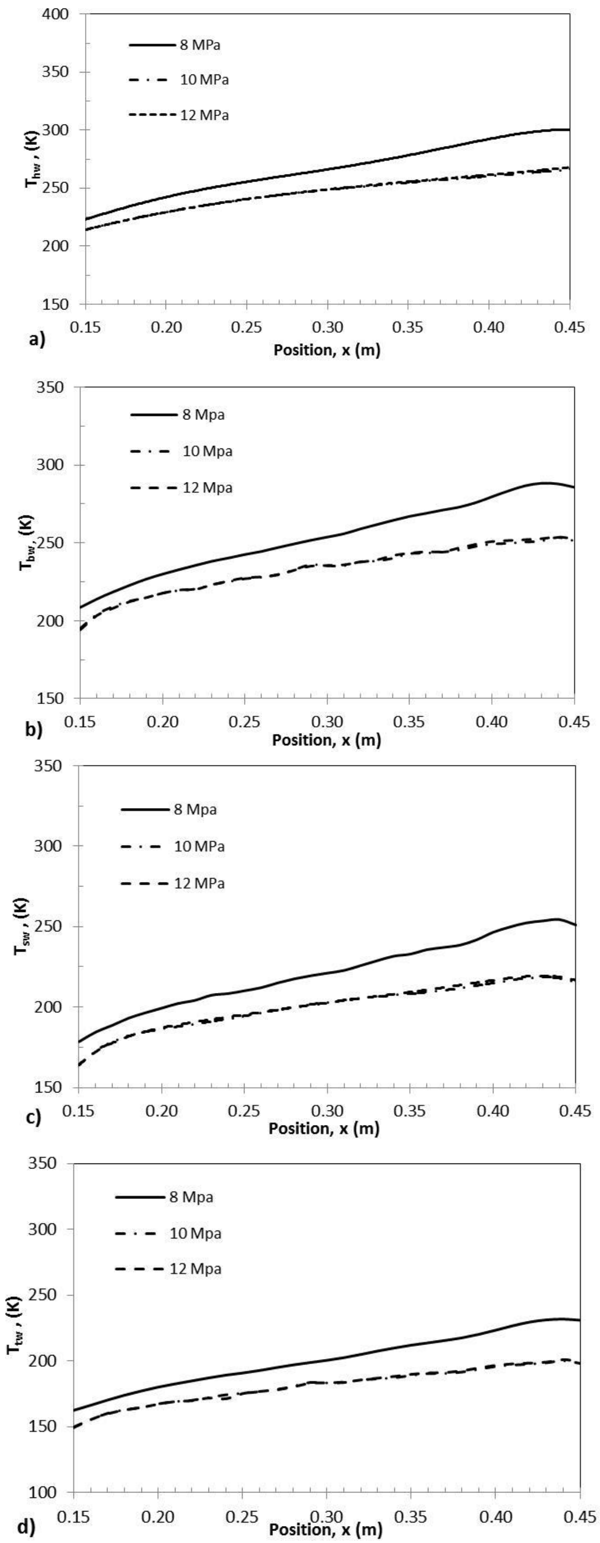


Fig 5. Variation in temperature on a) heated wall b) bottom wall c) side wall d) top wall along flow direction for AR4 at different pressures

*C. Variation of Volumetric Heat Capacity with Pressure*

Volumetric heat capacity, a product of density and specific heat can be treated as a measure of heat carrying capacity of the coolant. Volumetric heat capacity increases with increase in operating pressure. The variations of volumetric heat capacity at 8, 10 and 12 MPa with temperature are shown in the figure 6. At all pressures, below the pseudocritical temperature the volumetric heat capacity is higher and the coolant will be able to absorb large amount of heat in this regime. But once the fluid temperature crosses the pseudocritical temperature, there is a sudden reduction in volumetric heat capacity which indicates heat transfer deterioration. From the design point of view, attempts must be made to keep the fluid temperature below the critical temperature to attain the maximum possible heat transfer.

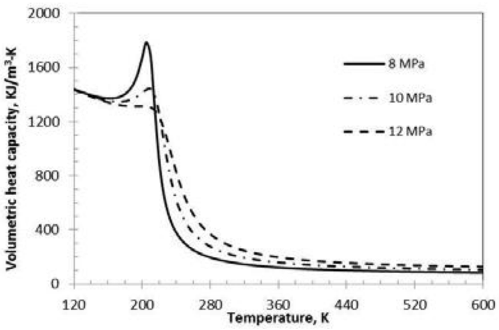


Fig.6. Variation in Volumetric heat capacity with temperature at different pressures.

In order to illustrate the heat transfer deterioration in the present problem, the variation in volumetric heat capacity of the fluid layer at the bottom wall at different pressures for optimum aspect ratio is shown in figure. 7.

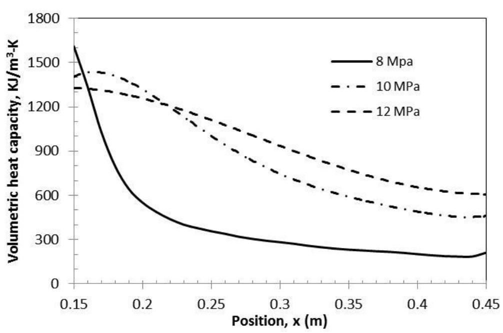


Fig.7. Variation in volumetric heat capacity of bottom wall for AR4 at different pressures

It is observed that volumetric heat capacity for 8 MPa is very less compared to that at 10 and 12MPa. However the difference in volumetric heat capacity at 10 and 12MPa is small.

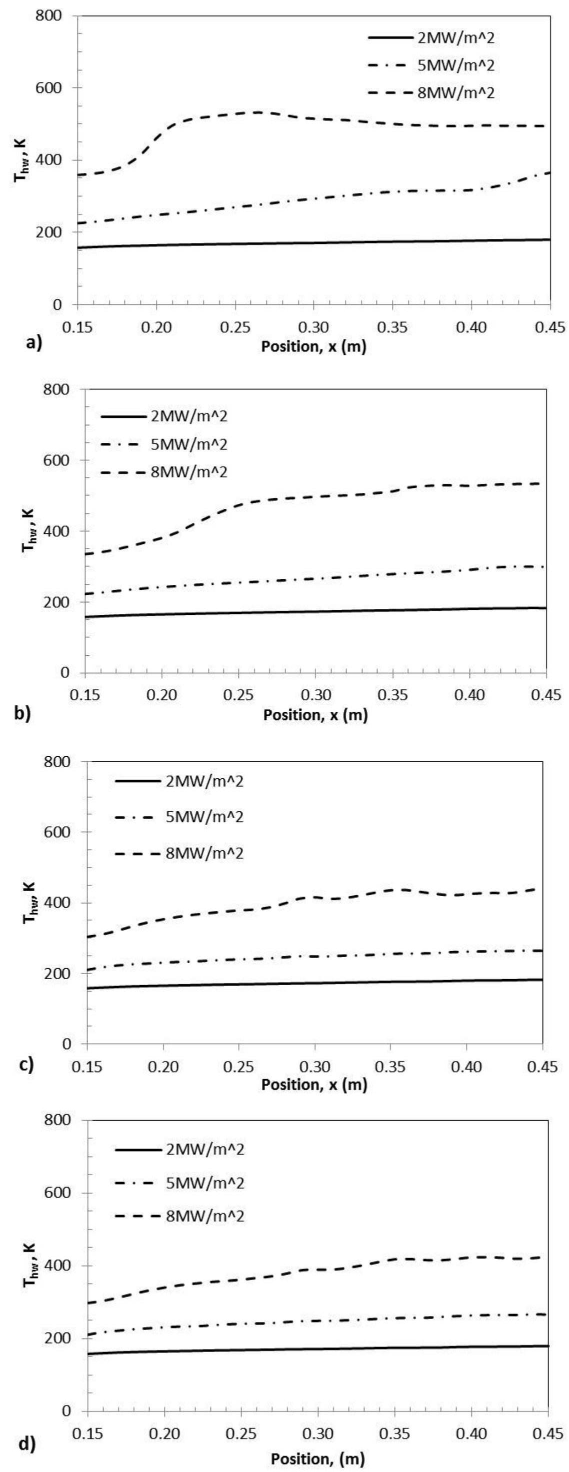


Fig.8. Variation in heated wall temperature along flow direction for copper wall material at a) 6 MPa b) 8MPa c) 10 MPa and d) 12 MPa pressure.

*D. Effect of Wall Heat Flux*

In practical sense, the wall heat flux could vary along coolant channel and may exhibits higher local values in some certain locations. To study the effect of imposed wall heat fluxes on coolant flow the simulations are carried out on optimum aspect ratios. Operating pressures selected are 6, 8, 10, 12 MPa, while the various heat fluxes selected are 2, 5 and 8 $MW/m^2$. Figure.8 shows the variation of wall temperature in the axial direction at the heated wall of the coolant channel for different operating pressures with copper as wall material.

The result indicates that heated wall temperature increases with increase of wall heat flux. In the figure 8. a, at a higher heat flux of 8 $MW/m^2$, a sudden increase of wall temperature observed, indicating heat transfer deterioration. This phenomenon is explained by drastic thermophysical property variations near supercritical region at near wall fluid layers. As fluid is heated up downstream, volumetric heat capacity further reduces and a sudden hike in heated wall temperature would occur. As wall temperature further increases property variations weakens, thus lifting heat transfer deterioration phenomenon. As operating pressure increases the hike in wall temperature diminishes which is an indication of heat transfer enhancement. From this, we can infer that higher operating pressures in the coolant channel could be used to enhance heat transfer characteristics where they experience higher wall heat fluxes.

## V. CONCLUSIONS

Numerical studies have been carried out to investigate the turbulent supercritical heat transfer of the cryogenic propellant methane flowing in the rocket engine cooling channel with asymmetric heating at the bottom surface. Effects of geometric aspect ratio, operational pressure and wall heat fluxes have been investigated. The following conclusions have been derived out of this study.

1. Heat transfer characteristics of the coolant is strongly influenced by the variation in thermophysical properties near the critical region
2. Geometrical Aspect Ratio (AR) would produce significant effect on the heat transfer in the cooling channels.
3. The optimum aspect ratio is 4, and at a pressure of 8 MPa average heated wall temperature decreases by 29% as aspect ratio is increased from 1 to 4.
4. Above 10 MPa, the coolant pressure has little influence on the wall temperatures.
5. The difference in bulk fluid temperature is marginal with aspect ratio and operating pressures.
6. Significant heat transfer deterioration is observed at the inlet region of the bottom wall at high heat flux. This deterioration decreases as the operating pressure is increased.

## ACKNOWLEDGMENT

The authors would like to acknowledge TEQIP II, Ministry of Human Resources Development (MHRD), Govt. of India and to the Management and Principal TKMCE Kollam for providing excellent computing facility at the Institution.

## REFERENCES

[1] K.Yamagata, K. Nishikawa, S. Hasegawa, T. Fujii and S. Yoshida, "*Forced Convective Heat Transfer to Supercritical Water Flowing in Tubes*", International Journal of Heat and Mass Transfer, Vol.15, 1972, pp.2575-2593.

[2] Koshizuka S., Takano N. and Oka Y., "*Numerical Analysis of Deterioration Phenomena in Heat Transfer to Supercritical Water*", International Journal of Heat and Mass Transfer, Vol.38, No.3, 1995, pp.3077-3084.doi:10.1016/0017-9310(95)00008-W

[3] Lee S.H. and John R. Howell, " *Laminar Forced Convection at Zero Gravity to Water near the Critical Region*", Vol.10, No.3, 1996, 504-510.doi:10.2514/3.817

[4] Liao, S. M., and Zhao, T. S., "*An Experimental Investigation of Convection Heat Transfer to Supercritical Carbon Dioxide in Miniature Tubes*," International Journal of Heat and Mass Transfer, Vol. 45, No. 25, 2002, pp. 5025–5034. doi:10.1016/S0017-9310(02) 00206-5

[5] P.X. Jiang, Y.J. Xu, J. Lv, R.F. Shi, S. He, J.D. Jackson, "*Experimental Investigation of Convection Heat Transfer of CO2 at Supercritical Pressures in Vertical mini tubes and in Porous media,*" Appl. Thermal Engineering. Vol.24, 2004, pp. 1255–1270.

[6] He, S., Jiang, P. X., and Xu, Y. J., Shi, R.-F., Kim,W. S., and Jackson, J. D., *"A Computational Study of Convection Heat Transfer to CO2 at Supercritical Pressures in a Vertical Mini Tube*," International Journal of Thermal Sciences, Vol. 44,No.6, 2005, pp.521-530 doi:10.1016/j.ijthermalsci.2004.11.003

[7] Pizzarelli, M., Nasuti, F., and Onofri, M., "*Flow Analysis of Transcritical Methane in Rectangular Cooling Channels*," AIAA Paper 2008-4556, July 2008.

[8] Ruan B., Meng H., "*Supercritical heat transfer of cryogenic-propellant methane in rectangular engine cooling channels*", Journal of Thermophysics and Heat Transfer, Vol. 26, No. 2, 2012, pp.313-321.

[9] Wang, Y.-Z., Hua, Y.-X., and Meng, H., "*Numerical Study of Supercritical Turbulent Convective Heat Transfer of Cryogenic Propellant Methane*," Journal of Thermophysics and Heat Transfer, Vol. 24, No. 3, 2010, pp. 490–500.

[10] Wang L., Chen Z and Meng H., "*Numerical Study of Conjugate Heat Transfer of Cryogenic Methane in Rectangular Engine Cooling Channels at Supercritical Pressures*", Applied Thermal Engineering, Vol. 54, 2013, 237-246.

[11] "Ansys Fluent 14.5 User's Guide", Ansys, Inc., Canonsburg USA, 2012.

[12] "Ansys Meshing 14.5 User's Guide", Ansys, Inc., Canonsburg USA, 2012.

[13] NIST Standard Reference Data base.

# Numerical Studies on the Effect of Chamber Diameter on the Flow Field and Heat Transfer in a Uni-Element Cryogenic Rocket Thrust Chamber

Dheeraj Raghunathan[#1], Arun M.[*2], Jose Prakash M.[*3]

[#] *Dept. of Mechanical Engineering, School of Engineering, Cochin University of Science and Technology (CUSAT), Ernakulam, Kerala, India*

[1]dheeraj.raghunathan@gmail.com

[*]*Dept. of Mechanical Engineering, TKM College of Engineering, Kollam, Kerala, India*

[2]helloarunm@gmail.com

[3]jpmmech@yahoo.co.in

***Abstract-*** **This paper describes the Computational Fluid Dynamics (CFD) simulation of combustion, heat transfer and fluid flow in a uni-element subscale cryogenic thrust chamber. The flow field in the thrust chamber and the wall temperature distribution are obtained using a conjugate heat transfer algorithm. Numerical studies have been carried out to see effect of the distance between outer injector circle and chamber wall (back step height) on the heat transfer characteristics of the rocket thrust chamber. Validation of the calculation scheme is done by comparing the results obtained with those reported in literature. The concentration of propellant near the wall depends on the back step height and it increases with decrease in back step height. It is also found that the average temperature and average heat flux at the inner surface of the thrust chamber wall decrease with decrease in back step height.**

***Keywords*****— Computational fluid dynamics, Numerical methods Back step height, combustion, uni-element, conjugate heat transfer, chamber diameter, wall heat flux.**

## I. INTRODUCTION

Combustion process in a liquid propulsion rocket engine is highly complex phenomena in which a sequence of exothermic chemical reactions between a fuel and an oxidizer take place. Understanding of the combustion phenomena at elevated pressure is necessary to promote continual performance enhancements for existing and future propulsion applications. The combustion gas temperature is much higher than the melting points of most of the chamber wall materials. Therefore it is either necessary to cool these walls or prevent transfer of high amount of heat reaching the walls.

Currently, there are significant efforts underway to develop robust numerical models that can be used to simulate combustion and film cooling in a rocket chamber, thereby allowing for a reliable engine design before the overall system is assembled and tested. Numerical simulation helps to save considerable amount of time and money in designing new rocket engines. The effect of combustor gas velocity on the performance of a pair of impinging heptane jets reacting in a highly atomized oxygen atmosphere was evaluated by Marcus F. Heidmann [1]. Characteristic velocity as a function of chamber length was obtained for different chamber diameters with corresponding contraction ratios. In shorter combustors, highest performance was obtained with the large-contraction-ratio combustors. In longer chambers, the reverse trend of performance with contraction ratio was observed. The effect of reversing propellants in coaxial injection on combustor performance was determined by Martin Hersch [2] by burning gaseous hydrogen with liquid oxygen in a rocket combustor. With annularly injected liquid oxygen the combustion noise level was lower and the injector face was less subject to high heat-transfer rates. Square chambers such as those used in early experiments by Moser et al. [3], Foust et al. [4], and De Groot et al. [5], are most convenient for optical diagnostics but potentially introduce geometry-specific corner flows that are not present in engines and are difficult to present in CFD analyses. Oefelein and Yang [6] used LES techniques in conjunction with detailed treatments of the thermodynamic and transport properties at supercritical conditions to provide quantitative simulations characterizing the flame structure and diffusion processes in the flame zone of a single shear-coaxial injector element.

Timothy D.Smith et al. [7] conducted an experimental test program to evaluate the performance of a rocket engine injector designed for use with gaseous hydrogen and gaseous oxygen propellants in a 7-element coaxial injector. A comparison was made with the best available design correlation and injector performance was based upon the calculated values for characteristic exhaust velocity (C*) efficiency. Streamtube analysis indicates that there was significant mixing between the streams. However, a qualitative analysis of the results lead to the conclusion that a coaxial gas-gas injector design can provide a high level of performance despite the significant presence of excess hydrogen. Zong et al. [8] also used LES methods to investigate cryogenic fluid injection and supercritical mixing in the absence of combustion as well as the combustion dynamics of liquid oxygen and methane based upon a general fluid equation-of-state procedure. Marshall et al. [9] conducted experiments for measuring wall heat flux in a rocket chamber consisting uni-element shear coaxial injector element operating on gaseous oxygen and gaseous hydrogen propellants. Wall heat flux measurements were made for two cases, with and without preburner. Benchmark quality wall heat flux data sets for CFD code validation and verification were obtained for different chamber pressures and different mixture ratios. Lin et al. [10] compared RANS calculations from the finite-difference Navier-Stokes and loci-CHEM codes to assess the capability for predicting combustor wall heat flux in a GO2/GH2 shear-coaxial uni-element injector. Their calculations also compared and evaluated different types of turbulent wall treatments. Pal et al. [12] conducted experimental studies on a uni-element cryogenic thrust chamber which is regeneratively cooled and measured the heat flux. Justin M. Locke et al. [13] conducted wall heat flux measurements in a circular cross-section rocket chamber for three uni-element injector elements (two versions of a shear coaxial element and a swirl coaxial element) operating on liquid oxygen (LOX) / gaseous methane (GCH4) propellants. Experiments were conducted at the design pressure and three other reduced pressures for each injector at three different mixture ratios. They found out that the local wall heat flux measurements show higher heat flux levels for the swirl coaxial injector than the two versions of the shear coaxial injector at near injector face locations. The shear coaxial injector with the higher fuel-to-oxidizer momentum flux ratio showed higher heat flux levels in the near injector face region. The configuration with the LOX post recessed showed higher heat flux levels in the near injector face region than its LOX post flush counterpart, indicating that the mixing cup provided by recessing the LOX post has a positive effect on the mixing and combustion characteristics of the injector.

Fico et al. [14] conducted a comparative study of different wall-functions models developed in order to improve wall heat flux prediction capabilities. These models have been embedded in a Reynolds averaged Navier-Stokes pressure-based solver employing a high Reynolds number k−ε turbulence model. UMIST Wall Functions, despite their rigorous approach and their accurate evaluation of wall quantities in the near-wall cell, provide the lowest wall heat flux profile along the nozzle, with a 40% error in the throat section. Gas-gas analyses of uni-element combustors were studied in Sozer et al. [15] with a view toward refining the turbulence-chemistry interactions and near wall treatment to get better computational validations. Two different experimental GO2/GH2 single element shear coaxial were modelled and tested with a CFD framework based on RANS turbulence closure and finite rate chemistry. Impacts of grid refinement, different choices of chemistry mechanisms and near wall treatments were assessed. In both test cases, grid refinement resulted in a reduced mixing rate and hence a downstream shift of the flame. Effect of the refinement on wall heat flux profiles were less pronounced. Lee et al. [16] developed a LES combustion model for the prediction of wall-heat transfer in rocket engines and confined combustors eloped. Their model employs a flamelet-formulation including a source term to account for convective heat-loss effects. The thermochemical composition of the non-adiabatic flamelet structure is obtained from the solution of the unsteady flamelet equations, and is parameterized in terms of mixture fraction, temperature, and scalar dissipation rate. Comparisons with adiabatic modelling results show that the consideration of wall heat losses results in a significant reduction in the temperature in the recirculation zone and a 25% reduction in the OH mass fraction at the combustor exit. Chenzhou Lian et al. [17] conducted unsteady analysis on the flow field of a uni-element rocket combustor for two different diameters. The simulations were done on 2D model of uni-element rocket combustors and were limited to flow analysis. The conclusions were mostly based on how the recirculation regions affect the propellant flow and combustion. The problems associated with heat transfer to the walls were not discussed.

Overall, many CFD simulations have been attempted in an effort to develop useful computational tools for understanding injector flows in a broad range of combustion environments. A key challenge associated with validation has been identifying pertinent experimental measures that can effectively discriminate between computational models.

A full-scale rocket engine typically incorporates hundreds of individual fuel-oxidizer element pairs with a large combustion chamber and a nozzle. The injectors of such rocket engines are arranged radially along concentric circles. The distance between the outer injector circle and the chamber wall, called as the back step height influence the heat transfer to the chamber wall. Uni-element rocket combustor studies based on varying the combustion chamber diameter provides the fundamental information about heat transfer and flow interactions on thrust chamber wall. This paper focuses on the effect of back step height on the heat transfer and fluid flow characteristics in a uni-element rocket thrust chamber.

## II. MODELING AND ANALYSIS

The schematic diagram of the thrust chamber considered for the present study is shown in figure 1 [12]. The injector used is coaxial type and it is 53 mm long, which provides appropriate entry lengths required for development of the turbulent boundary layers in the fuel and oxidizer streams.

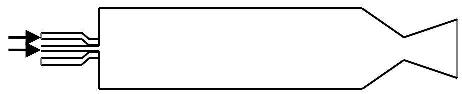

Fig. 1 Schematic diagram of the thrust chamber with injector

The total length of the thrust chamber is 337 mm and that of the combustion chamber is 286 mm. The inlet diameter of the central oxidizer jet is 7.92 mm, the exit diameter is 5.26 mm, and the oxidizer post is recessed 0.43 mm behind the chamber face. The inner and outer diameters at the inlet of the annular fuel jet are 12.7 and 25.4 mm, respectively. The corresponding exit diameters are 6.30 and 7.49 mm respectively. The throat diameter is 8.17 mm and the area ratio is 2.16. To study the effect of back step height on the heat transfer characteristics of the thrust chamber, three cases have been considered (i) chamber diameter 25.4 mm (ii) chamber diameter 38.1 mm (iii) chamber diameter 50.8 mm. In the above cases the dimensions of the injector, throat and exit of the nozzle are kept the same. Even though the geometry is symmetrical about the axis, a three dimensional model is considered to get a better insight in to the interaction of the oxidizer and fuel streams. The model of the thrust chamber is shown in figure 2.

Fig. 2 Three dimensional model of the geometry

The computational domain consists of fluid and solid domains and it is descretized using tetrahedral mesh. The package used for the analysis is a finite volume based commercial software ANSYS Fluent 14.5[23].The turbulence models used is standard k-ε model with wall function strategies. Combustion is simulated using non-premixed model, and in this instead of solving individual species equations, the transport equations are reduced to two parameters known as mean mixture fraction and mixture variance. Single mixture fraction is used here and it uses β distribution for the predications of assumed Probability Density Function (PDF). Radiation model chosen is P-1 model with absorption coefficient as 0.01.

## III. BOUNDARY CONDITIONS

The oxidizer stream consists 0.906 moles of oxygen, 0.0940 moles of water, and is injected into the chamber at a temperature of 711 K. The fuel stream consists of 0.857 moles of hydrogen, 0.143 moles of water, and is injected at 800 K. The flow rate of oxidiser is 0.0904 kg/s and that of fuel is 0.0331 kg/s. Supersonic boundary conditions are applied at the exit of the nozzle. Adiabatic boundary condition is applied at the walls of the injector and the temperature of the face plate is taken as 755 K. Two cases have been considered concerning the boundary conditions at the outer surface of the walls of the combustion chamber and nozzle. In the first case, it is assumed that the chamber wall is regeneratively cooled to an average temperature of 700K and in the second the wall is adiabatic.The properties and species dominating the equilibrium chemistry is obtained from CEC-71, a computer program used for predicting the thermodynamic properties of combustion products. The species dominating the equilibrium combustion are $H_2$, $O_2$, $H_2O$, OH, H, O and $H_2O_2$. The emissivity of the inner surface of the combustion chamber is taken as 1 and the scattering coefficient is taken as 0.001 with isotropic behaviour. The selection of P-1 radiation will enable one or more transport equation.

## IV. RESULTS AND DISCUSSION

Numerical analyses have been carried out to study the effect of back step height on the flow field and heat transfer characteristics of a uni-element cryogenic thrust chamber. The simulation is carried out for various chamber diameters and also for different wall boundary conditions. Table 1 shows the details of the various cases.

TABLE 1

DETAILS OF VARIOUS CASES

| Case | Chamber Diameter(mm) | Wall Temperature(K) |
|---|---|---|
| 1 | 50.8 | 700 |
| 2 | 50.8 | Adiabatic |
| 3 | 38.1 | 700 |
| 4 | 38.1 | Adiabatic |
| 5 | 25.4 | 700 |
| 6 | 25.4 | Adiabatic |

### A. *Validation of the Calculation Scheme*

Validation of the calculation scheme is done by comparing the results obtained from the numerical studies with those obtained from experimental studies [21]. The temperature distribution at the outer surface of the chamber wall which is obtained from experiments was incorporated as a User Defined Function (UDF).

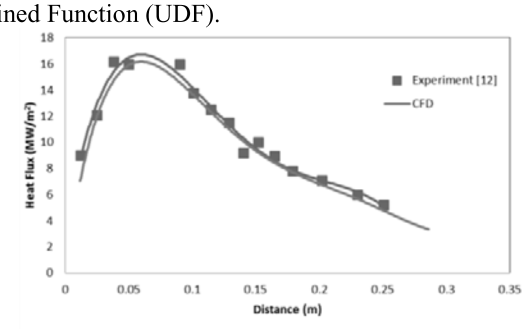


Fig 3 Variation of heat flux at the inner surface of the chamber wall in the axial direction (Chamber diameter 38.1 mm)

Figure 3 shows the variation of heat flux at the inner surface of the chamber wall obtained from numerical studies. The values obtained from experimental studies is also shown for comparison. There is fair agreement between the values of heat flux obtained from both studies.

*B. Effect of chamber diameter on temperature of combustion products*

The contours of temperature at the mid-plane of the thrust chamber are shown in figure 4. The flame is seen to develop at the interface between the incoming fuel and oxidizer streams and it gradually spreads.

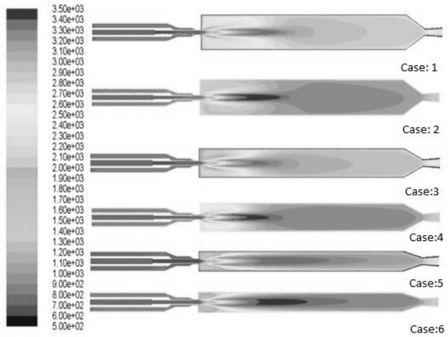


Fig. 4 Contours of Temperature

The length of the flame increases with decrease in back step height. The temperature of the combustion products is more in the case of adiabatic wall boundary condition. It can be seen that the temperature of the gas near the face plate is lower for 25.4 mm diameter chamber compared to other cases. This may be due to the entrainment of unburned propellants caused by recirculation.

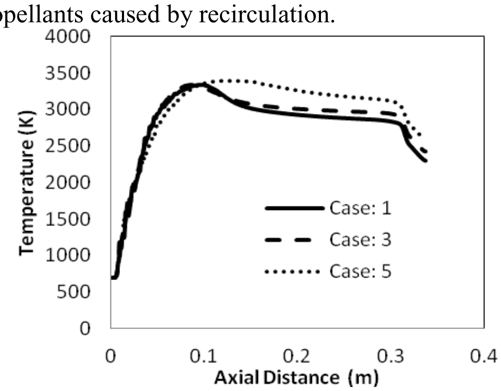


Fig. 5 Variation of temperature along the axis with thermal boundary condition

The variation of temperature of the combustion products along the axis of the thrust chamber is shown in figures 5 and 6. The temperature of the gases is low near the face plate and it increases rapidly to a maximum value, and then slowly decreases. There is sudden drop in the gas temperature in the nozzle due to thermodynamic expansion. The peak is observed where the most efficient combustion takes place and the position of this peak is an indicator of flame length.

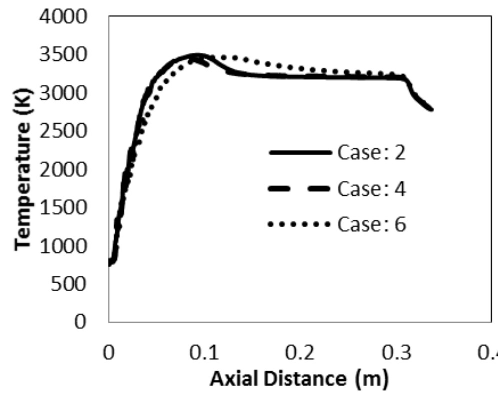


Fig. 6 Variation of temperature along the axis with adiabatic boundary condition

*C. Effect of chamber diameter on propellant concentration*

Figure 7 shows the contours of hydrogen at the mid plane of the thrust chamber. In all cases the mole fraction of $H_2$ is more near the face plate compared to other parts of combustion chamber and this .may be due the recirculation of the propellants. It can also be observed that the hydrogen concentration near the face plate decreases with increase in chamber diameter.

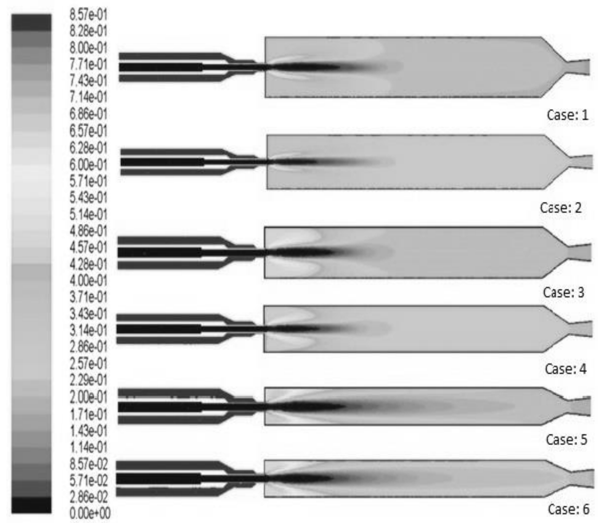


Fig. 7 Contours of mole fraction of $H_2$

Figure 8 shows the variation of mass fraction of $H_2$ at the inner surface of the wall with thermal boundary conditions. The concentration of hydrogen throughout the inner surface is more in the case of 25.1 mm diameter chamber compared to the other cases. Similar trends are obtained with adiabatic wall boundary condition.

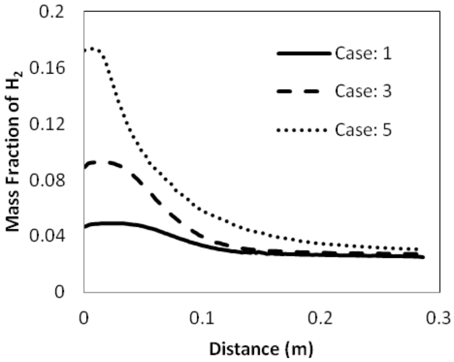


Fig. 8 Variation of Mass fraction of $H_2$ near the inner surface of the wall along the axial direction.

*D. Effect of chamber diameter on streamline pattern*

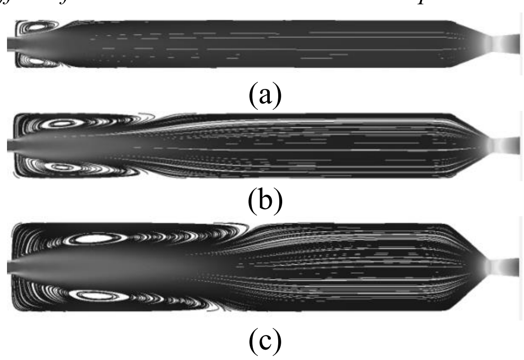


Fig. 9 Streamline pattern for chamber diameters of (a) 25.4mm (b) 38.1 mm (c) 50.8 mm

The streamline patterns of the flow are shown in figure 9 and indicate the presence of recirculation regions adjacent to the injector face. As the reactants enter the chamber they experience a sudden increase in area that results in creation of recirculation region adjacent to the injector face. This recirculation region pulls hot gas from the main combustion region toward the wall which results in high localized temperature gradient. The recirculation region extends to around 0.032m, 0.085 m and 0.15m respectively for chamber diameters of 25.4 mm 38.1mm and 50.8 mm. The recirculation regions strongly affect the mixing and heat transfer characteristics.

*E. Effect of chamber diameter on turbulence intensity*

The contours of turbulence intensity at the mid plane are shown in figure 10. The maximum value of turbulence intensity is more in the case of 25.4 mm diameter case and it decreases with increase in back step height and the region at which the maximum turbulence intensity occurs shifts towards right as the chamber diameter increases.

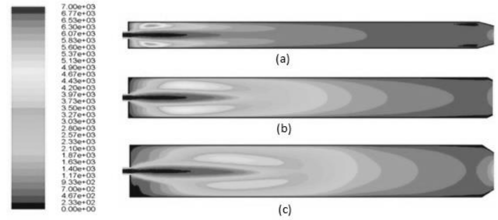


Fig. 10 Contours of Turbulence intensity (a) 25.4mm (b) 38.1mm c) 50.8 mm

## *F. Effect of chamber diameter on wall heat flux*

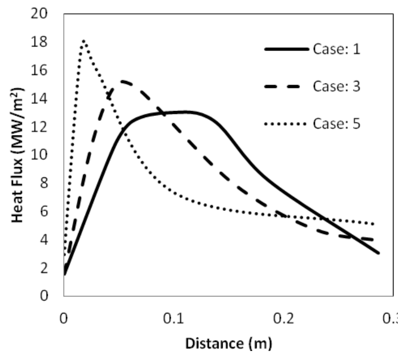


Fig. 11 Variation of heat flux at the inner surface of the chamber wall in the axial direction

The wall heat flux for thermal boundary condition is shown in the figure 11. The maximum value of heat flux in 25.4 mm diameter chamber is about 18 $MW/m^2$ and occurs in a region close to the face plate. As the chamber diameter increases the value of maximum heat flux reduces and the region at which maximum heat flux occurs shifts towards right. In the regions away from the injector face plate, heat flux increases with increase in back step height.

*F. Effect of chamber diameter on wall temperature*

The variation of the temperature at the inner surface of the wall in the axial direction for thermal boundary condition and adiabatic boundary condition are shown in figures 12 and 13. The wall temperature for thermal boundary condition is a mere reflection of the wall heat flux. With adiabatic boundary condition the temperature at the inner surface of the wall decreases with decrease in chamber diameter.

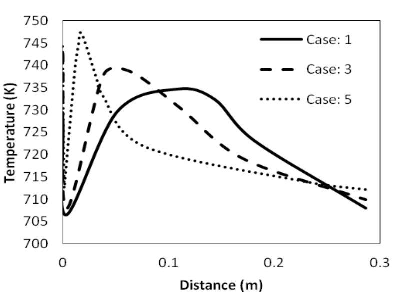


Fig. 12 Variation of inner surface temperature of wall in the axial direction with thermal boundary condition

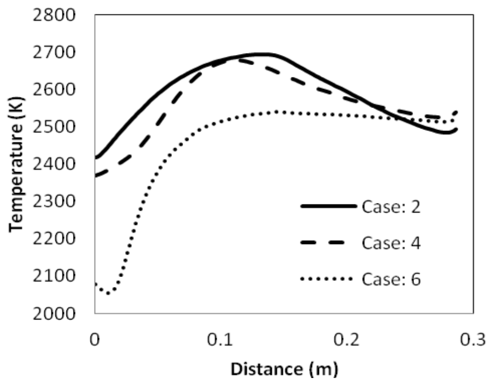


Fig. 13 Variation of inner surface temperature of wall in the axial direction with adiabatic boundary condition

## V. CONCLUSIONS

Numerical simulations have been carried out to study the effect of back step height on the combustion and heat transfer characteristics of a uni-element rocket thrust chamber. The following conclusions are derived out of the present study. (i) The heat flux and temperature at the wall are governed strongly by the propellant mixing and combustion processes in the chamber. (ii) Concentration of H2 near the wall depends on the back step height and it increases with decrease in back step height. (iii) The extent of the recirculation region depends on the back step height and the recirculation zone is longer for larger diameter chamber. (iv) The value of maximum heat flux increases with decrease in back step height, however the average heat flux decreases with decrease in back step height. (v) With adiabatic wall boundary conditions the average temperature at the inner surface of the wall decreases with decrease in back step height.

## ACKNOWLEDGMENT

The authors would like to acknowledge TEQIP- II, Ministry of Human Resource Development (MHRD), Government of India for providing support and the Management and Principal, TKM College of Engineering, Kollam, for providing excellent computing facilities at the college.

## REFERENCES


[1] Heidmann, M., "Experimental Effect of Chamber Diameter on Liquid Oxygen - Heptane Performance" NASA TN D-65, 1959.

[2] Hersch, M., "Effect of Interchanging Propellants on Rocket Combustor Performance with Coaxial Injection," NASA TN D-2169, 1964.

[3] Moser,M. D, Pal, S., and Santoro, R.J., "Laser Light Scattering Measurements in GO2/GH2Uni-Element Rocket Chamber", 33rd Aerospace Sciences Meeting and Exhibit, Jan.1995, Reno, NV,AIAA Paper 1995-0137,1995.

[4] Foust, M. J., Deshpande, M., Pal, S., Ni, T., Merkle, C. L., and Santoro, R. J., "Experimental and analytical Characterization of a Shear Coaxial Combusting GO2/GH2 Flowfield," 34th AIAA Aerospace Sciences Meeting and Exhibit, AIAA Paper 1996-0646, Reno, NV, 15-18 Jan.1996

[5] De Groot, W., A., McGuire, T., J., and Schneider, S., J., "Qualitative Flow Visualization of an 110N Hydrogen/Oxygen Laboratory Model Thruster", AIAA Paper 1997-2847, 1997.

[6] Oefelein, J. C., and Yang, V., "Modeling High-Pressure Mixing and Combustion Process in Liquid Rocket Engines," Journal of Propulsion and Power, Vol. 14, No. 5, 1998, pp. 843-857.

[7] Smith, T. D., Klem, M. D., Breisacher, K. J., Farhangi. S and Sutton, R., "Experimental Evaluation of a Subscale Gaseous Hydrogen/Gaseous Oxygen Coaxial Rocket Injector," Technical Report, NASA/TM-2002-211982

[8] Zong, N., Meng, H., Hseih, S. Y., and Yang, V., "A numerical Study of Cryogenic Fluid Injection and Mixing Under Supercritical Conditions," Physics of Fluids, Vol. 16, No. 12, 2004, pp. 4248-4261..

[9] Marshall W. M., Pal S., and Santoro R. J., "Benchmark Wall Heat Flux Data for a GO2/GH2 Single Element Combustor," AIAA Paper No. 2005-3572, July 2005.

[10] Lin, J., West, J., Williams, R., and Tucker, P., "CFD Code Validation of Wall Heat Fluxes for a GO2/GH2 Single Element Combustor",41st AIAA/ASME/SAE/ASEE Joint Propulsion Conference and Exhibit, AIAA Paper 2005-4524, Tucson, AZ, 10-13 July 2005.

[11] Oefelein, J. C., "Mixing and Combustion of Cryogenic Oxygen-Hydrogen Shear-Coaxial Jet Flames at Supercritical Pressures," Combustion Science and Technology, Vol. 178, 2006, pp. 229-252.

[12] Pal, S., Marshal, W., Woodward, R and Santoro, R., "Heat Flux Measurements in a GO2/GH2 Shear Coaxial Injector", Third International Workshop on Rocket Combustion Modeling, IWRCM, Paris, France, Mar. 2006

[13] Locke, J., Pal, S and Woodward, R "Chamber Wall Heat Flux Measurements for a LOX/CH4 Uni-element Rocket," 43rd AIAA/ASME/SAE/ASEE Joint Propulsion Conference & Exhibit, July 2007, Cincinnati, OH

[14] Fico, V., Cutrone, L., Battista, F., "Assessment of Wall-functions k-ε Turbulence Models for the Prediction of the Wall Heat Flux in Rocket Combustion Chambers," 44th AIAA/ASME/SAE/ASEE Joint Propulsion Conference & Exhibit, AIAA Paper 2008-455821, Hartford, CT, July 2008.

[15] Sozer, E., Vaidyanathan, A., Segal, C., and Shyy, W. " Computational Assessment of Gaseous reacting Flows in Single Element Injector", 47th AIAA Aerospace Sciences Meeting and Exhibit, AIAA Paper 2009-449, Orlando, FL, 5-8 Jan.2009.

[16] Lee, D. J., Thakur, S., Wright, J., Ihme, M., and Shyy, W., "Characterization of Flow Field Structure and Species Composition in a Shear Coaxial Rocket GH2/GO2 Injector: Modeling of Wall Heat Losses,"47th AIAA/ASME/SAE/ASEE Joint Propulsion Conference & Exhibit, AIAA Paper 2011-6125, San Diego, California, July-August 2011.

[17] Chenzhou Lian., Charles L. Merkle and Guoping Xia., "Effects of Chamber Diameter on the Flow field in Unielement Rocket Combustors", Journal of propulsion and power, Vol. 28, no.3, May-June 2012.

[18] "ANSYS Fluent 14.5 User's Guide" Fluent Inc. Southpointe USA, 2012

# Experimental Investigation on the Effects of Cryogenic Cooling on Chip Breakability and Tool Wear in Turning of 316L Stainless Steel

Rahul Sivam M[1], Jesna Mohammed[2], Reby Roy. K.E[3]

*Department of Mechanical Engineering, TKM College of Engineering, Kollam, Kerala, India*

[1]mrahulsivam@gmail.com

[2]rebyroy@tkmce.ac.in

3jesnamohammed@tkmce.ac.in

***Abstract*— The zest for high productivity necessitate higher material removal rate. Such machining ends in higher cutting temperature. This high temperature affects the tool life and product quality. The inability of conventional coolants for efficient cooling, give birth to sustainable manufacturing methods like cryogenic cooling, which is environment friendly and recycling free. The current study investigates the influence of liquid nitrogen while turning AISI 316 L Stainless steel. Comparative results between the dry and cryogenic machining on the basis of tool wear, chip thickness and shear angle are in favourable to cryogenic machining. Reduced tool wear and improved chip breakability is obtained along with 14%-45% reduction in chip thickness.**

***Keywords*— cryogenic cooling, sustainable manufacturing, liquid nitrogen, turning, stainless steel**

## I. Introduction

Attaining maximum material removal rate at the expense of minimum tool wear rate is the aim of every industry [1]. This performance index greatly depends on the higher cutting temperature that produced in high speed machining. Due to the failure of cutting tools at higher temperatures, it is difficult to obtain accurate dimensions and surface finish. This problem can be remedied by reducing cutting zone temperature by providing efficient cooling system. Conventional coolants are having certain drawbacks like low heat transfer rate at high speed machining and being hazardous to the environment [2].

Cryogenic coolants like liquid nitrogen, cryogenic carbon dioxide [3, 4] etc. are suitable alternative for conventional coolants. Liquid nitrogen is utilised as a coolant in this study. Experimental studies done formerly using liquid nitrogen [5-8] show better surface finish and tool life. Liquid nitrogen is preferred as it is inert, available in abundance and comparatively cheaper. Also it is advantageous because it is colourless and odourless.

The present study is an experimental investigation on the influence of cryogenic liquid Nitrogen in turning of 316 L Stainless steel. AISI 316L stainless steel is an excellent corrosion resistant and biocompatible material [9] which is having wide applications in chemical as well as biomedical industries. SS 316L has been used for orthopaedic applications like bone fixation, artificial joints etc.

## II. EXPERIMENTAL SETUP AND PROCEDURE

Experiment consists of dry and cryogenic machining environments. Both are carried out in a power full lathe, with 4 different feed rate and 3 speeds. Cutting speeds and feed rates were selected based upon the machinery's hand book and tool manufacturer's recommendation [10]. Depth of cut is taken as constant 1mm. For every speed, feed combinations separate multi coated carbide insert were used. Tool holder of PCLNR 2020 K 12 is used to hold cutting insert. In the cryogenic condition, $LN_2$ is supplied from the cryocan through a nozzle having 2 mm exit diameter at a flow rate of 3g/s. The nozzle is fixed to the tool post in such a way that the jet of nitrogen should reach the tool chip interface. For that, the supply line is provided with a flexible hose. The nozzle is fixed at a distance of 50mm from the cutting zone. The continuous flow of liquid nitrogen is achieved by providing a compressed air supply to the cryocan. Thus the flow rate is controlled by controlling air pressure at the top of cryocan. This pressure control is by means of a pressure regulator placed at the compressed air supply line. A flow meter is connected at the outlet line to measure the flow rate. For each environment (dry and cryogenic) separate work pieces of AISI 316L stainless steel were used. To avoid the deviation in result, both the work pieces are taken from same parent material. The details of machining parameters and tool specifications are given in Table I.

In the present study, to compare the tool wear occurred during dry and cryogenic machining, a separate machining test is conducted about 5 min and inserts were analysed by the help of SEM (Scanning Electron Microscope) images. The chip is thickness is measured by using precision micro meter. Fig.1 shows schematic diagram of the experimental setup.

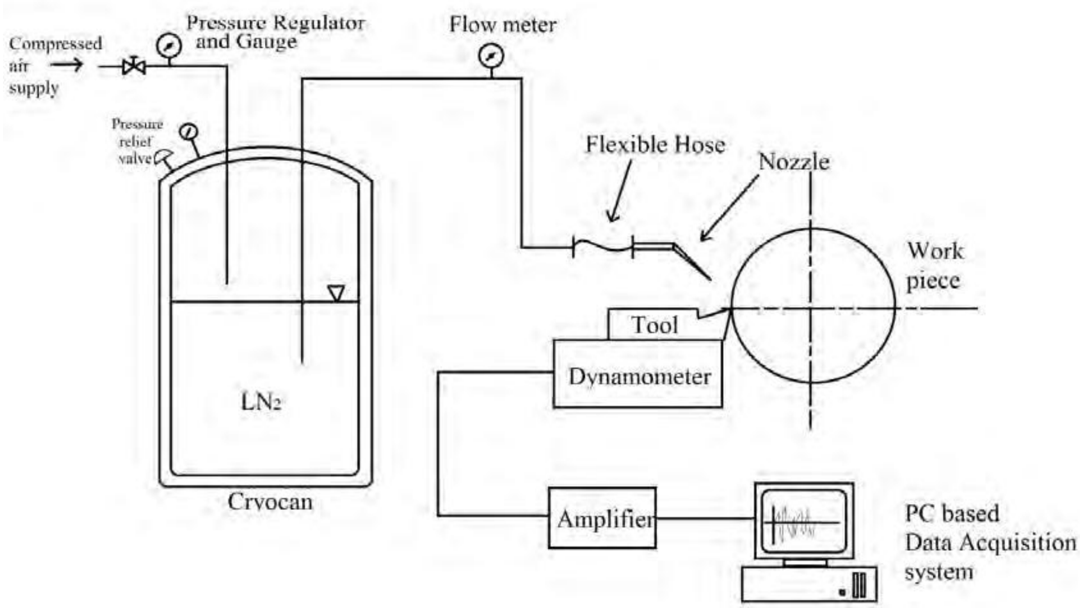


Fig.1 Experimental setup for cryogenic machining

TABLE I
EXPERIMENTAL CONDITIONS

| | |
|---|---|
| Work material | AISI 316L stainless steel |
| Dimension | Ø 60 mm X 300 mm |
| Machining operation | turning |
| Machine tool | Nagmati 175 Lathe |
| Cutting tool | CNMG 12 04 08 RP KCP25 (Multi coated carbide insert) Rake angle: -5$^o$, Nose radius: 0.8 mm |
| Tool holder | PCLNR 2020 K 12 |
| Machining parameters: | |
| Cutting velocity (m/min) | 61.5, 94.2 and 145.1 |
| Depth of cut | 1mm |
| Feed rate (mm/rev) | 0.048, 0.096, 0.143, 0.20 |

## III. RESULTS AND DISCUSSION

### A. *Chip thickness*

Thickness of chip and its shape is an important factor when considering chip breakability. Chip thickness is measured by using a precision micrometer. Along with the feed rate, cryogenic as well as dry machining shows a proportional increase in chip thickness. It is also observed that at higher cutting velocities, thickness attains smaller values. The variation in chip thickness is shown in Fig. 2.

A considerable amount of cutting temperature is reduced by the application of cryogenic liquid nitrogen. It acts as an efficient lubrication system between tool-work piece and tool chip interface.

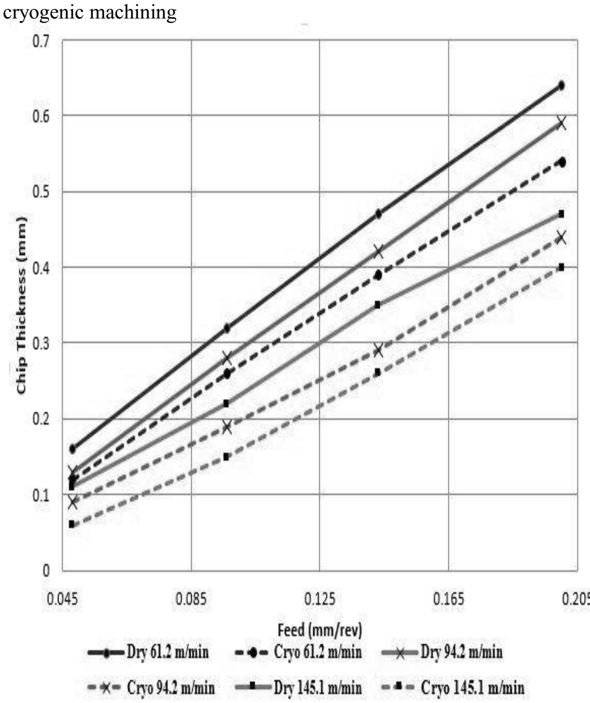


Fig. 2 Variation in chip thickness with feed rate

As a result the contact friction is reduced resulting in reduction of chip thickness. The thickness is reduced to 14% to 45 % by cryogenic cooling when compared to dry machining. 45 % of reduction is obtained at a cutting speed of 145.1 m/min. The measured thickness is tabulated in Table II

TABLE II
CHIP THICKNESS

| Sl No | Cutting Speed (m/min) | Feed (mm/rev) | Chip Thickness (mm) | | % Reduction |
|---|---|---|---|---|---|
| | | | Dry | Cryo | |
| 1 | 61.2 | 0.048 | 0.16 | 0.12 | 25 |
| 2 | | 0.096 | 0.32 | 0.26 | 18.75 |
| 3 | | 0.143 | 0.47 | 0.39 | 20 |
| 4 | | 0.2 | 0.64 | 0.54 | 15.6 |
| 5 | 94.2 | 0.048 | 0.13 | 0.09 | 30 |
| 6 | | 0.096 | 0.28 | 0.19 | 32 |
| 7 | | 0.143 | 0.42 | 0.29 | 30 |
| 8 | | 0.2 | 0.59 | 0.44 | 25.4 |
| 9 | 145.1 | 0.048 | 0.11 | 0.06 | 45 |
| 10 | | 0.096 | 0.22 | 0.15 | 31.8 |
| 11 | | 0.143 | 0.35 | 0.26 | 25.7 |
| 12 | | 0.2 | 0.47 | 0.4 | 14.8 |

*G. Shear angle*

Shear angle is an important parameter when chip breakability and tool wear is concerned. If the shear angle is larger the plane of shear will be short and thus cutting force will be less. The angle of shear is calculated using the formula [11].

$$\tan \Phi = (r \cos \gamma) / (1 - r \sin \gamma)$$

Were $\Phi$ = Shear angle

$\gamma$ = Rake angle

r = chip thickness ratio

(The ratio between thickness of the chip produced to uncut chip thickness)

The graph showing the variations in shear angle is plotted in Fig. 3. In comparison of the shear angle under dry and cryogenic machining an increase in shear angle is observed under cryogenic machining as there is a reduction in the cutting zone temperature. Reduction in chip thickness that observed is due to the reduction of shear plane. 14%-62% increase in shear angle is identified in cryogenic machining. This will aid the chip breakability. While cryogenic machining, with the increase in feed rate the shear angle found reducing. Indeed, the temperature produced during the high cutting speed is what reduces this shear angle by shifting the fracture mechanism from brittle fracture to ductile fracture. In addition, the friction between chip-tool rake face and crater wear is also reduced by cryogenic cooling.

*H. Chip morphology*

The Images of the chip formed is shown in Table III. In conventional machining operation continuous chips create interference to the operator. In slow speed machining, (61.2 m/min) with the increase in feed rates the curls formed also got increased. The thickness of the chip obtained is more for dry machining than cryogenic machining. It is easy to break the thin chip produced at higher speeds with a chip breaker. This is very helpful in automated machining were chip disposal is a major issue. Chip of cryogenic turning at 61.2 m/min are discontinuous. This is due to the brittle fracture that happens at lower speeds as a result of cryogenic cooling. By the application of liquid nitrogen at cryogenic temperature increase the hardness and reduce the ductility of the work piece. It is also noted that the chips produced at intermediate cutting speed (94.2 m/min) are lengthier and shapeless which causes disturbances to smooth machining in dry environment. In cryogenic machining the chips curls are less in high speeds that low speed machining. In addition, the edges of the chips in cryogenic machining are burr free. Such chips are capable of producing better surface finish. The reduction of chip thickness is clear from the comparison of images.

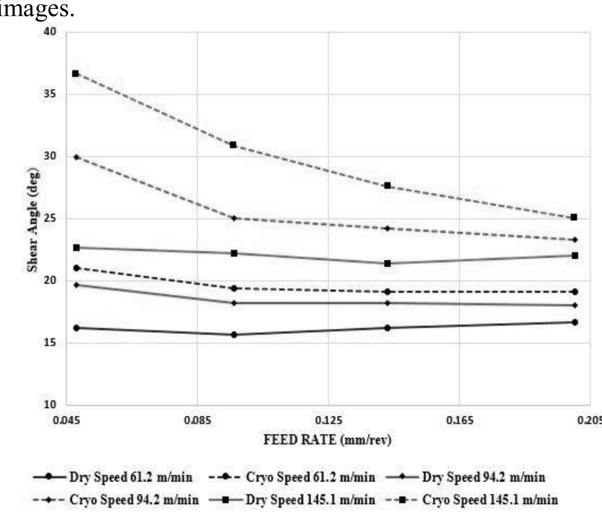


Fig.3 Comparison of shear angle

*I. Tool Wear*

The tool life depends upon factors like cutting velocity, time of machining, hardness of the work and tool material etc. In present experimental study multi coated carbide inserts were used.

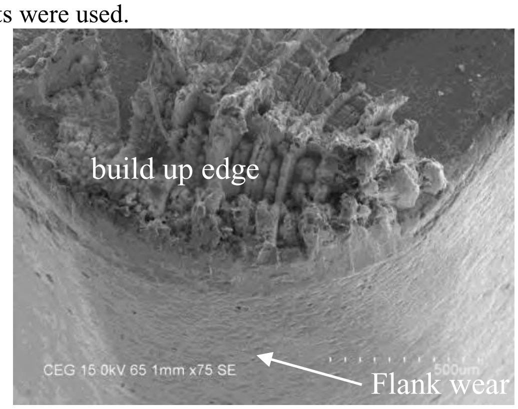


Fig. 5 SEM images of tool insert after 5 min of dry Machining

TABLE III
Chip Images

| Speed (m/min) | Feed (mm/rev) | Dry | Cryogenic $LN_2$ |
|---|---|---|---|
| 61.2 | 0.048 |  | 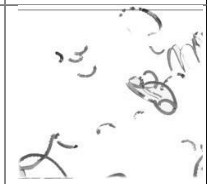 |
| | 0.096 | 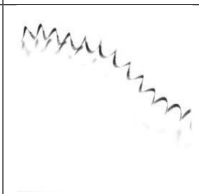 |  |
| | 0.143 | 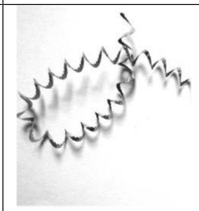 | 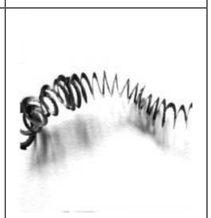 |
| | 0.20 | 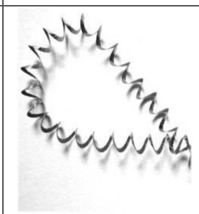 | 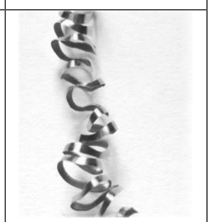 |
| 94.2 | 0.048 | 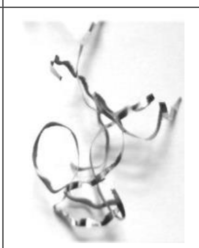 | 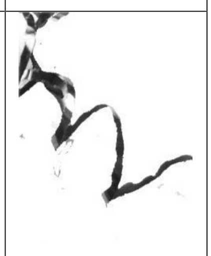 |
| | 0.096 | 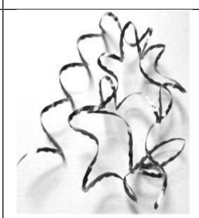 | 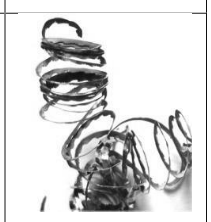 |
| | 0.143 | 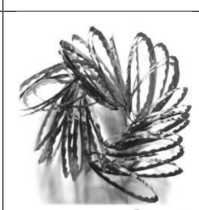 | 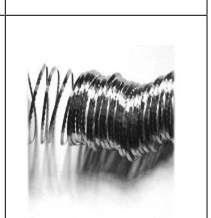 |
| 145.1 | 0.048 |  | 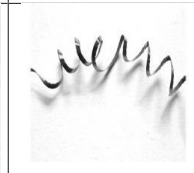 |
| | 0.096 | 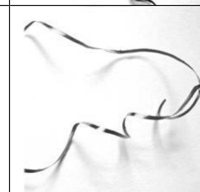 | 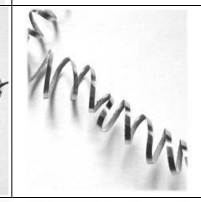 |
| | 0.143 | 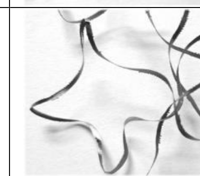 |  |
| | 0.20 | 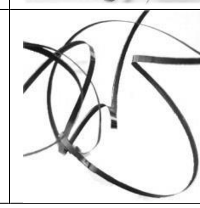 | 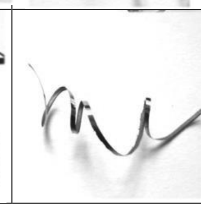 |

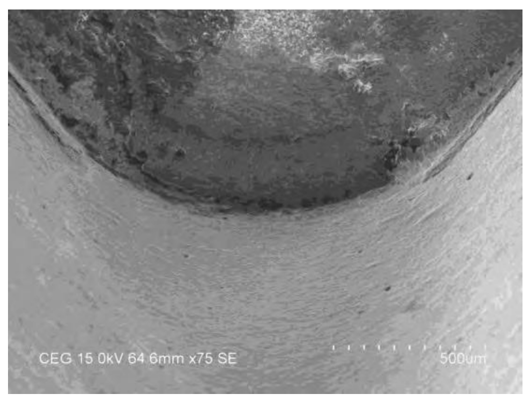


Fig. 6 SEM images of tool insert after 5 min of cryogenic Machining

It poses excellent wear resistance. In industry formation of build-up edge (BUE) is the major problem encountered when machining stainless steels. Especially at higher cutting speeds. In this study, SEM is used for analysing the tool wear.

The tool tip at a cutting speed of 145.1 m/min and a feed rate of 0.20 mm/rev is shown in Fig. 5 and 6 after 5 minutes of continuous machining at dry and cryogenic environment.

Analysing the SEM Images of insert that used for dry machining, it is clearly understood that build-up edge (BUE) is formed on the rake face. This BUE act as another cutting edge at the time of machining. This results in reduced surface finish. The intensive temperature that produced on high speed machining at the cutting zone is the reason for the formation of BUE. The presents of flank wear can also be identified on the clearance edges. In cryogenic machining, less flaking was observed in high speed machining. The flaking that occurred in dry machining, due to a adhesion between the chip and the tool rake as a result of high temperature during dry machining.

## IV. CONCLUSIONS

Based on the comparison of the results of dry and cryogenic machining, it can conclude that:

- Better chip breakability is obtained by the application of cryogenic coolant while the chip thickness is reduced to 14% - 45%. This is advantageous in CNC turning operations were chip breakability is major concern.
- The reduction in temperature causes the reduction of shear plane which results in an increase of the shear angle by 14% - 62%. This leads to reduction in chip thickness and tool wear. The crater wear due to friction between chip and tool rake face is reduced by this increased shear angle.
- Tool wear rate is reduced by the intensive cooling at the cutting zone. Formation of build-up edge was the major drawback of machining of low carbon stainless steels, which is completely avoided by reducing cutting zone temperature. The rate of flank wear also reduced considerably.

Cryogenic cooling is advantageous at high cutting speed and feed rates. It can be a suitable and sustainable alternative when environmental aspects are taken care.

## ACKNOWLEDGMENT

The authors acknowledge the technical and infrastructural support given by faculty and staff of Department of Mechanical Engineering, Anna University, Chennai.

## REFERENCES

[1] Vishal S. Sharma, Manu Dogra and N.M. Suri "Cooling techniques for improved productivity in turning" *International Journal of Machine Tools & Manufacture,* vol. 49, pp 435–453, Jan. 2009

[2] Z.Y. Wang and K.P. Rajurkar "Cryogenic machining of hard-to-cut materials", *Wear*, vol. 239, pp 168–175, Dec 2009.

[3] Yakup Yildiz and Muammer Nalbant "A review of cryogenic cooling in machining processes", *International Journal of Machine Tools & Manufacture,* vol. 48, pp 947–964, Feb 2008.

[4] B. Dilip Jerold and M. Pradeep Kumar, "Experimental investigation of turning of AISI 1045 steel using cryogenic carbon dioxide as the cutting fluid", *Journal of Manufacturing Processes,* vol. 13, pp. 113–119, Apl. 2011.

[5] Paul S, Dhar NR, Chattopadhyay AB. "Beneficial effects of cryogenic cooling over dry and wet machining on tool wear and surface finish in turning AISI 1060 steel". *Journal of Materials Processing Technology* vol. 116, pp. 44–8, Oct. 2001.

[6] Shane Y. Hong, Irel Markus and Woo-cheol Jeong, "New cooling approach and tool life improvement in cryogenic machining of titanium alloy Ti-6Al-4V", *International Journal of Machine Tools & Manufacture*, vol. 41, pp. 2245–2260, Mar. 2001.

[7] B. Dilip Jerold and M. Pradeep Kumar, "Experimental comparison of carbon-dioxide and liquid nitrogen cryogenic coolants in turning of AISI 1045 steel", *Cryogenics,* vol. 52, pp. 569–574, 2012.

[8] M. Dhananchezian and M. Pradeep Kumar, "Cryogenic turning of the Ti–6Al–4V alloy with modified cutting tool inserts", *cryogenics,* vol. 51, pp. 34–40, Oct. 2011.

[9] J.R Davis. "Handbook of Materials for Medical Devices", ASM international, USA, 2003.

[10] Cutting Feeds and Speeds for Turning Stainless Steels 1021-1031 data sheet, *Machinery's Handbook* 29th Edition, New York, USA.

[11] Shaw MC. "Metal cutting principles". Oxford, Clarendon Press, UK, 1991.

# Beneficial Effects of Cryogenic Cooling on Chip Breakability, Shear angle and Tool Wear in Turning AISI 1050 Steel

Arun S[1], Jesna Mohammed[2], Reby Roy. K.E[3]

*Department of Mechanical Engineering, TKM College of Engineering, Kollam, Kerala, India*

[1]arunsreekumar92@gmail.com

[2]jesnamohammed@tkmce.ac.in

[3]rebyroy@tkmce.ac.in

***Abstract***— **Chip form and cutting tool wear are two important aspects commonly considered in evaluating the performance of a machining process. Machining industries essentially aim for a high metal removal rate and better product quality. Major problems in achieving high productivity and quality are caused by the high cutting temperature developed during machining. The high cutting temperature in machining causes dimensional deviation and premature failure of the cutting tools. The conventional cutting fluid is an environmental contaminant and the government has imposed strict regulations limiting the dumping of cutting fluid waste. Recently, cryogenic cooling, an environment friendly clean technology is used for the desirable control of cutting temperature and enhancement of the tool life. The present study deals with the experimental investigation on the role of cryogenic cooling by liquid nitrogen on chip breakability, shear angle and tool wear in turning AISI 1050 medium carbon steel at different industrial speed-feed combinations. The results have been compared with dry machining. The results of the present work indicate substantial benefit of cryogenic cooling on chip breakability, shear angle and tool wear.**

***Keywords***— **cryogenic cooling, liquid Nitrogen, turning**

## I. Introduction

High production machining of steel inherently generates high cutting zone temperature. Such high temperature adversely affects the quality of the product (dimensional accuracy, surface finish and integrity) and the tool life [1].

As a solution for this, it is essential to reduce the temperature in the cutting zone by the optimum selection of the machining parameters, coated tools and proper cutting fluids. In the conventional process, the cutting fluid, when applied in the cutting zone, fails to enter the chip-tool interface and hence fails to reduce the cutting temperature [2]. The application of conventional cutting fluids causes several health and environmental problems. Environmental pollution occurs due the chemical dissociation or breakdown of the cutting fluids at high temperature during machining. It also corrodes the parts of machine tool and work piece. Also the setup for the conventional coolant system requires extra floor space and additional systems for pumping, storage, filtration, recycling, chilling etc. which imposes high cost. These factors lead to the requirement of an environmentally acceptable and economically feasible coolant. Liquid nitrogen has been explored for this purpose as a cryogenic coolant since 1950s in the metal cutting industry. When compared to conventional wet machining solutions which negatively impact our environment in their production, use and disposal when liquid nitrogen touches the air, it evaporates, leaving only nitrogen, an inert, non-greenhouse gas which makes up 78% of the air we breathe.

The present study deals with the experimental investigation on the role of cryogenic cooling by liquid nitrogen on chip breakability, shear angle and tool wear in turning AISI 1050 medium carbon steel which is a highly industrial relevant material having wide applications.

## II. Experimental Setup

For the present experimental work, medium carbon steel AISI 1050 of diameter 60 mm and length 300mm was plain turned in a rigid and powerful lathe (NAGMATI-175) using multi-coated carbide insert (CNMG 120408-XF GC30).The turning process is carried out at industrial speed-feed combinations ( 3 different speeds and 4 feed rates) under dry and cryogenic machining. For each environment (dry and cryogenic conditions) separate work piece is used and they are taken from same parent material in order to avoid deviation in results. A tool holder PCLNR 2020 K12 is used to hold the cutting insert. The ranges of the cutting velocity and feed rate were selected based on the tool manufacture’s recommendation. Chip thickness for the chips obtained in machining the work piece in different cutting conditions is measured using a precision micrometre. Cryogenic machining is carried out by supplying $LN_2$ from the cryocan

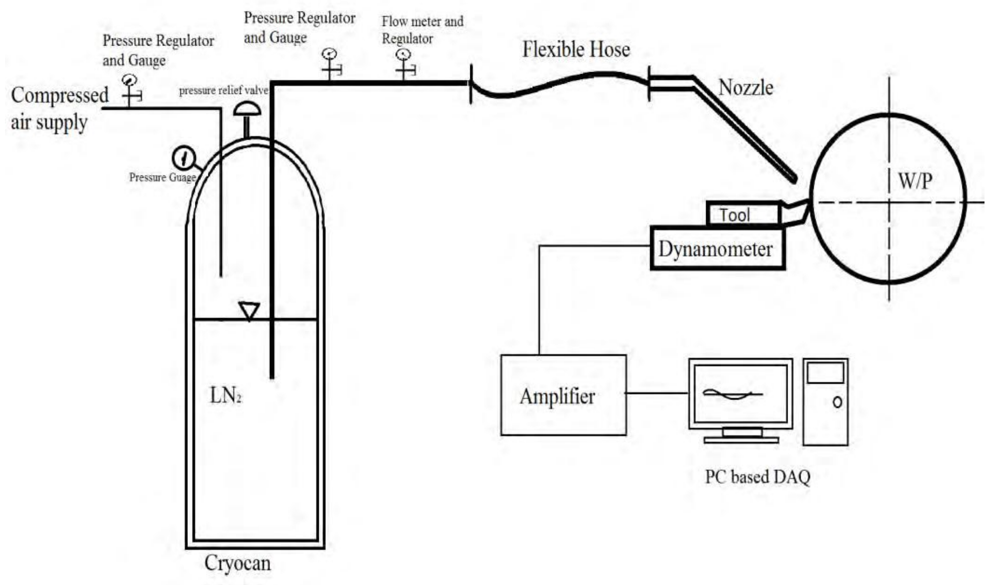


Fig.1 Experimental setup for cryogenic machining

through a nozzle whose outlet tip having Ø 2 mm. The distance between the nozzle and the cutting zone is fixed as 50mm A Pressure regulator is attached to the cryocan for maintaining the pressure in the flow of $LN_2$. A flow meter is also attached for maintaining the flow rate of the $LN_2$. A flexible hose is provided to fix the nozzle in such a way that the $LN_2$ should impinge directly on the chip-tool interface. Fig.1 shows the experimental setup for cryogenic machining.

TABLE I
EXPERIMENTAL CONDITIONS

| | |
|---|---|
| Machine tool | NAGMATI-175 Lathe, India |
| Work specimen | |
| Material | AISI 1050 STEEL |
| Size | Ø 60 mm X 300 mm |
| Applications | Ships, Automobiles, Aircrafts & Weapons |
| Cutting insert | Multi-coated carbide, CNMG120408-XFGC30, Kennametal |
| Tool holder | PCLNR 2020 K 12 |
| Process parameters | |
| Cutting speed | 40.51, 94.2, 145.1 m/min |
| Feed rate | 0.051, 0.096, 0.143 and 0.191 mm/rev |
| Depth of cut | 1 mm |
| Nozzle diameter 2 mm | |
| $LN_2$ flow rate | 3 g/s |

## II RESULTS AND DISCUSSION

### A. *Chip thickness*

Chip shape and size plays an important role in chip breakability. The chip thickness for the chips obtained in different cutting conditions is measured by using a precision micrometer. It is evident from the table that the chip thickness increases with increase in feed rate. Also, as the cutting speed obtains high values, chip thickness decreases. The maximum value of chip thickness obtained at low cutting speeds. The values of chip thickness obtained in cryogenic condition is very much less than that in dry cutting. The values of chip thickness obtained in machining the work piece in different cutting conditions is shown in Table II.

Cutting temperature at the cutting zone is reduced by cutting fluid through heat convection. As the temperature of the $LN_2$ is very much less than the cutting temperature, it can reduce the contact friction between tool and chip with high efficiency lubricating action and cooling effect. The cutting temperature is reduced on the application of $LN_2$ better than dry cutting. This is due to the fact that $LN_2$ penetrates better in the cutting zone than any other conventional coolants. The reduction in chip thickness is obtained in cryogenic machining due to the reduction in adhesion and friction between the tool and the chip.

The chip breakability is good in cryogenic machining when compared with dry machining. Higher percentage reduction in chip thickness is obtained in low cutting speeds. Reduction in chip thickness is about 18%-34% on cryogenic machining when compared to dry machining.

TABLE II
CHIP THICKNESS

| Sl No | Cutting Speed (m/min) | Feed (mm/rev) | Chip Thickness (mm) | | % Reduction |
|---|---|---|---|---|---|
| | | | Dry | Cryo | |
| 1 | 40.51 | 0.051 | 0.09 | 0.065 | 27.7 |
| 2 | | 0.096 | 0.19 | 0.125 | 34.2 |
| 3 | | 0.143 | 0.30 | 0.2 | 33.3 |
| 4 | | 0.191 | 0.41 | 0.29 | 29.2 |
| 5 | 94.2 | 0.056 | 0.08 | 0.06 | 25 |
| 6 | | 0.096 | 0.16 | 0.115 | 28.1 |
| 7 | | 0.143 | 0.25 | 0.19 | 24 |
| 8 | | 0.191 | 0.362 | 0.27 | 25.4 |
| 9 | 145.1 | 0.056 | 0.07 | 0.052 | 25.7 |
| 10 | | 0.096 | 0.135 | 0.11 | 18.5 |
| 11 | | 0.143 | 0.22 | 0.18 | 18.1 |
| 12 | | 0.191 | 0.345 | 0.26 | 24.6 |

The variation of the chip thickness with cutting speed and feed is shown in Fig.2

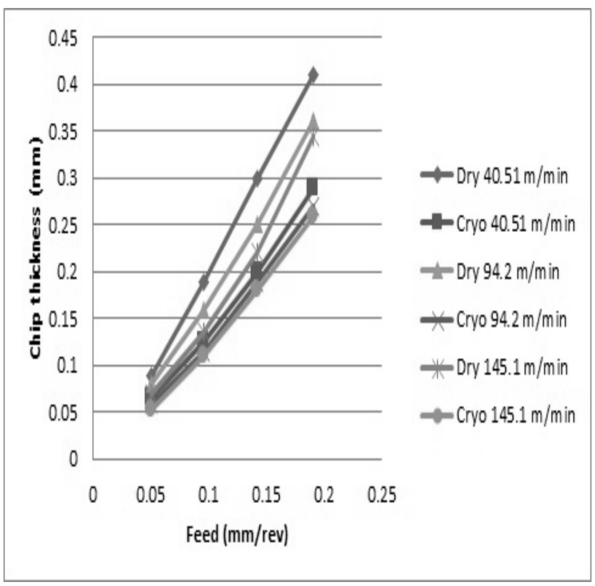


Fig. 2 Variation in chip thickness with feed rate

*J. Chip morphology*

Regardless of the tool being used or the metal being cut, the chip forming process occurs by a mechanism called plastic deformation. This deformation can be visualized as shearing. That is when a metal is subjected to a load exceeding its elastic limit. The crystals of the metal elongate through an action of slipping or shearing, which takes place within the crystals and between adjacent crystals. The form of chips produced in metal cutting is an important aspect to be considered for economical and precise machining. Long and unbroken chips usually create hindrance to the manual operator. In general any coolant or lubricant used for machining should help in proper chip control [3]. The images of the chips obtained during machining process are shown in Table II.

During the dry machining process, it was found that most of the chips formed were accumulated on the cutting insert causing damage to both tool and finished surface of the work part. Chip breakability was found to be good in cryogenic machining. Due to the pressurized jet of cryogenic coolant, effective chip control can be achieved in cryogenic machining when compared to dry cutting.

At cutting velocity 40.51 m/min, dry machining produced long snarled chips. The chips formed were very long in length creating hindrance to the manual operator. With increase in feed rate, closely curled thick chips were formed which got stuck into the cutting insert and adversely affected the surface finish of the work part. When $LN_2$ is applied to the chip-tool interface, short tubular chips with less thickness were obtained.

This is due to the fact that cryogenic coolant reduces the cutting zone temperature effectively thereby reducing the contact friction between tool and the chip. In cryogenic machining, the chips are well broken at the cutting velocity of 40.51 m/min with the feed rates of 0.051 mm/rev, and for the same feed rates, the chips are adequately broken at the cutting velocities of 94.2 and 145.1 m/min respectively. The chips are well broken for the feed rates 0.143 and 0.191 mm/rev with cutting velocities 94.2 and 145.1 in cryogenic machining. The chips are adequately broken in cryogenic machining at the cutting velocities 40.51, 94.2 and 145.1 m/min with feed rate of 0.051 mm/rev .At higher cutting velocity 145.1 m/min, Chip breakability was even found to be better in the case of cryogenic machining as the $LN_2$ penetrates better in the chip-tool interface thereby reducing the stickiness of the chip with the tool rake and also reducing the contact friction.

*K. Shear angle*

Shear angle plays an important role in chip breakability. When cutting tool is introduced into the work material, plastic deformation takes place in a narrow region in the vicinity of the cutting edge. This region is called shear zone. At high speeds, this zone can be assumed to be restricted to a plane called shear plane inclined at an angle $\Phi$ called shear angle. The value of shear angle depends upon work piece materials, cutting conditions, material of tool, geometry of tool etc. When the shear angle is small, the plane of the shear will be larger, chip is thicker and therefore high force is required to remove the chip. When the shear angle is large, the plane of shear will be shorter, the chip is thinner and hence less force is required to remove the chip.

Using the measured chip thickness, shear angle for all cutting conditions in different cutting speeds and feed rates is calculated. It is calculated using the formula [3]

Tan Φ = (r cos γ) / (1-r sin γ)

Were Φ = Shear angle

γ = Rake angle

r = chip thickness ratio = Uncut chip thickness/deformed chip thickness

Fig. 3 shows the variation of shear angle with different feed rates at different cutting speeds.

When analysing the shear angle, it is noted that the shear angle increases with increase in cutting speeds. Also with increase in feed rates, shear angle decreases.

TABLE II
CHIP IMAGES

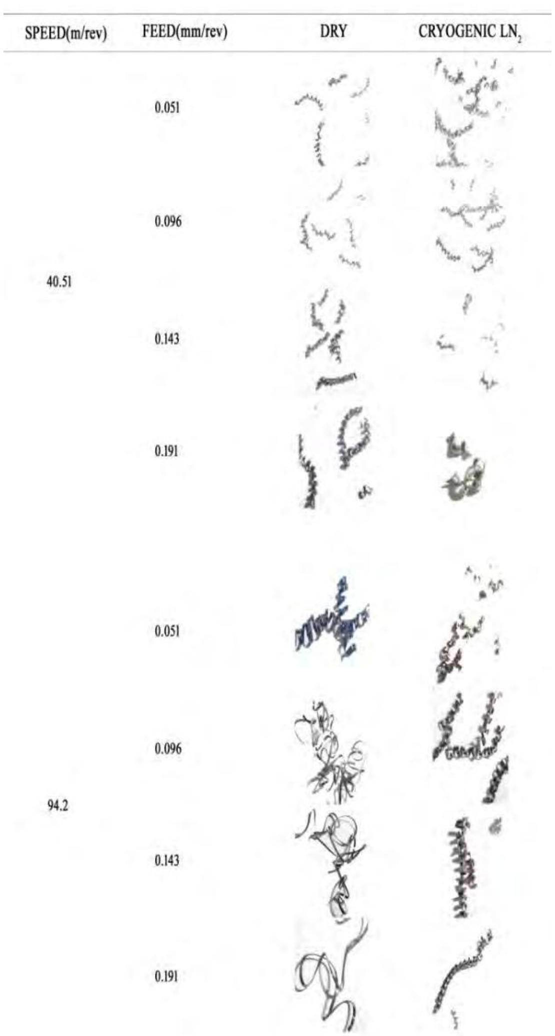


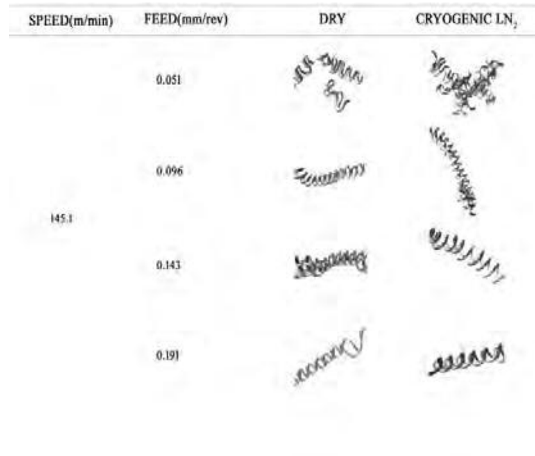


Comparing the shear angle under dry and cryogenic machining, it is observed that there is an increase in shear angle in cryogenic machining. It is due to the fact that there is a reduction in the temperature at the cutting zone by the application of cryogenic coolant. The reduction in chip thickness is thus obtained under cryogenic condition as the plane of shear is reduced due to the increase in shear angle. It is found that the increase in shear angle is about 15%-39% in cryogenic machining when compared to dry cutting. It is also noted that the application of $LN_2$ in the chip-tool interface increased the shear angle in all cutting parameters. The increase in shear angle produces lower cutting forces in cryogenic machining when compared to dry cutting.

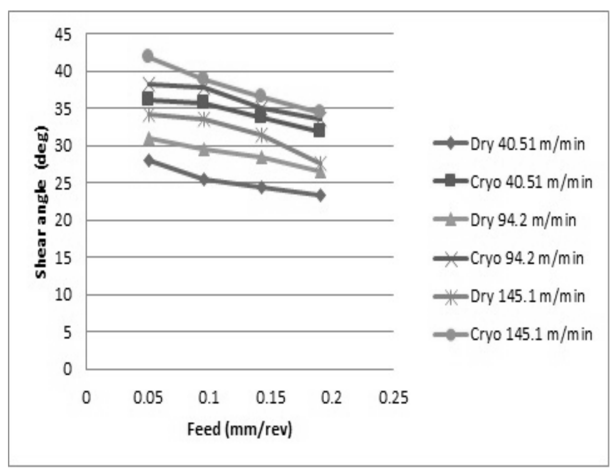


Fig. 3 Variation in shear angle with feed rate

*L. Tool wear*

Cutting tool life is one of the most important economic considerations in metal cutting. The cutting tools in conventional machining, particularly in continuous chip formation processes like turning, generally fails by gradual wear by abrasion, adhesion, diffusion, chemical erosion, galvanic action etc. depending upon the tool–work materials and machining condition. Tool wear initially starts with a relatively faster rate due to what is called a break-in wear caused by attrition and micro chipping at the sharp cutting edges. Cutting tools may also often fail prematurely, randomly and catastrophically by mechanical breakage and plastic deformation under adverse machining conditions caused by intensive pressure and temperature and/or dynamic loading at the tool tips particularly if the tool material lacks strength, hot-hardness and fracture toughness. [4].

SEM images of worn tools after 5 minutes of machining in dry and cryogenic machining at maximum cutting speed and feed rate were taken. Tool wear is maximum at the highest speed-feed combination. i.e., when the cutting speed is 145.1 m/min and feed rate is 0.191 mm/rev. The SEM images of tools are shown in Figure 4 & Figure5.It is observed that tool wear is more under dry machining when compared with cryogenic machining. The wear on the tool flank is mainly due to the abrasion and attrition. In cryogenic machining, less abrasion and attrition wear was observed at the flank surface and also less crater wear was observed due to a reduction in the cutting temperature. Crater wear appears as a shallow trough in localized areas. Crater wear will increase until it reaches the cutting edge causing chipping or fracture. Crater wear patterns indicate that the tool material is diffusing into the using into the chip. It is related to very high temperatures on the tool face. Flaking appears to be a large chip in tool. There will be one or two large areas missing the tool face. The flaking that occurred in dry machining was higher than that in cryogenic cooling, due to a strong adhesion between the chip and tool rake face as a result of high cutting zone temperature.

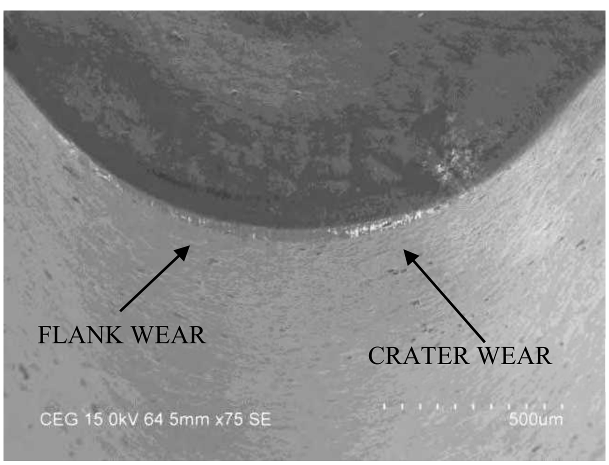


Fig.4 SEM images of tool insert after 5 min of dry Machining

## III. CONCLUSIONS

The cryogenic Nitrogen is used as the cutting fluid for turning AISI 1050 steel and the major conclusions and the results of the experimental work conducted can be summarized as follows:

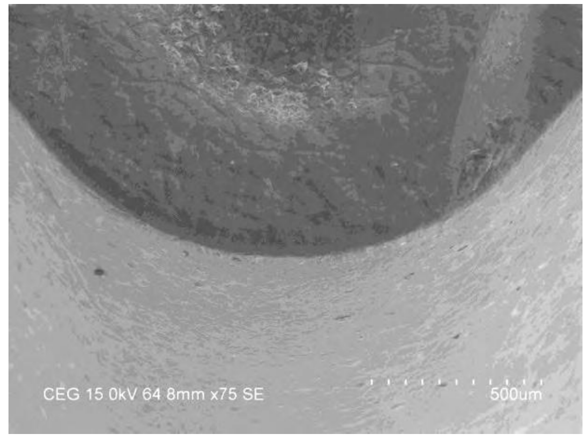


Fig.5 SEM images of tool insert after 5 min of cryogenic Machining

- Chip breakability is found to be good in cryogenic machining when compared to dry machining. The chip thickness is reduced by 18%-34% due to the application of $LN_{2.}$
- Shear angle is increased by 15%-39% in cryogenic machining due to the reduction in cutting temperature by the application of $LN_2$.
- Tool wear is reduced in cryogenic machining when compared to dry machining. Less crater wear and flank wear is observed in cryogenic machining due the effective reduction in cutting temperature.

Cryogenic cooling is found to be more advantageous as far as the high speeds and feed rates are concerned. Liquid Nitrogen is a potential alternative for other coolants which is more eco-friendly and effective.

## ACKNOWLEDGEMENT

The authors are grateful to the Head of the Department, Department of Mechanical Engineering, Anna University Chennai for providing the infrastructural facility to carry out the experimental work. The authors are also thankful for the technical supporting staff for extending their kind help during the machining process.

## REFERENCES

[1] S. Paul, N.R. Dhar, A.B. Chattopadhyay, "Beneficial effects of cryogenic cooling over dry and wet machining on tool wear and surface finish in turning AISI 1060 steel", *Journal of Materials Processing Technology*, vol. 116, 44-48, 2001.

[2] B. Dilip Jerold, M. Pradeep Kumar, "Experimental comparison of carbon-dioxide and liquid nitrogen cryogenic coolants in turning of AISI 1045 steel", *Cryogenics,* vol. 13, 113-119, 2011.

[3] B. Dilip Jerold, M. Pradeep Kumar, "Experimental investigation of turning AISI 1045 steel using cryogenic carbon dioxide as the cutting fluid", *Journal of Manufacturing Processes ,* vol. 52, 569–574, 2012

[4] N.R Dhar, M. Kamruzzaman, "Cutting temperature, tool wear, surface roughness and dimensional deviation in turning AISI-4037 steel under cryogenic condition", *International Journal of Machine Tools & Manufacture,* vol. 47, 754-759, 2007.

# Numerical Prediction of Oxygen Expulsion from a Typical Cryogenic Storage Tank

Rahul B.R. [1], K.E. Reby Roy [2], Jesna Mohammed [3]

*Department of Mechanical Engineering, TKM College of Engineering, Kollam, Kerala, India*

[1]rbr431@gmail.com

[2]rebyroy@yahoo.com

[3]jesnamohammed@tkmce.ac.in

*Abstract*—**The Cryogen Expulsion with the aid of Self-pressurization, as a result of vaporization can occur in many scientific and technical applications like Cryogenic storage tanks in space applications, pressurized water reactors in nuclear reactors etc. For space applications we can release the cryogen from the storage tank by heat input from a known source to the system rather than using a mechanical pumping system. As the cryogen is heated, the system gets pressurized by warm gas, transfer's heat to the cryogen cause evaporation of cryogen. This work aims to investigate the mass expulsion and phase change happening in a cryogenic tank filled with Oxygen at an initial temperature of 90 K subjected to various heating conditions to the system. During the heat transfer from outside to the cryogen it get boiled off and pressurized inside the chamber and forced the cryogen to pump through the small diameter outlet of the venting line fitted on the top side of the cryogen tank. The recent improvements of the multiphase flow modelling in the ANSYS FLUENT code make it now possible to simulate these mechanisms. Here we used Volume of Fluid Model as the multiphase model in conjunction with evaporation–condensation mass transfer model. In this paper we are proving the capability of VOF model for predicting mass expulsion due to phase change with the aid of Self-pressurization in storage vessels.**

***Keywords*— CFD, Two-phase flow, Self-Pressurization, Volume of Fluid (VOF), Level Set Method**

## I. INTRODUCTION

Space missions - including rocket launchers, interplanetary space flights, and the space stations require an understanding and managing of the cryogenic liquid propellants under varying acceleration conditions.This understanding is essential because cryogenic liquid dynamics have a significant impact on the engine operation, vehicle dynamics, spacecraft design, and even the overall mission. Moreover, the thermal effect in a cryogenic propellant has huge influence on the spacecraft safety as well as fuel dynamics [4].Whenever heat inleak from incident solar radiation, aerodynamics heating or from some other heating source to the cryogenic storage tank, the stored cryogen causes thermal stratification and fuel vaporization since the boiling temperature of cryogenic propellant is extremely low. The heat transfer associated with phase-change is a complex phenomenon encountered in engineering applications, such as Cryogen storage vessels in Rocket engines, pressurized water reactors in Nuclear power plants etc.

The Cryogenic storage vessel is partially filled with vapor at a temperature higher than the liquid cryogen. This vapor space, called the ullage, is also stratified due to gravitational effects. In addition to heat conduction through metal and insulation, the thermodynamics and fluid mechanics of the propellant also play a role in determining boiloff rate. Therefore, it is essential to use a code that has the capability to model all of the processes that influence boiloff[2]. Accurate numerical prediction of the associated heat and mass transfer is a challenging research area. However it is a difficult task to predict the heat transfer and the simultaneous mass transfer across the interface since the physical properties and the associated parameters differ on either sides of the interface. The development of a computational analysis capability of the dominant thermal and fluid-dynamic processes can play a significant role in predicting pressurization and accompanying temperature and velocity distributions in the tanks [3]. Computational modelling can provide accurate prediction of the highly transient interface occurrence due to mass transfer coupled with the phase change due to evaporation. Many researchers have conducted studies on the cryogenic storage tank under normal and micro-gravity conditions.

Aydelott *et al.* investigated tank self-pressurization in a small-scale partially filled liquid hydrogen container under normal gravity. He concluded that size and geometry of the vessel, liquid fill fraction, rate and distribution of heat transfer and gravity level affects the rate of pressure rise in a closed cryogenic container [1]. Ohta *et al.* numerically simulated the first interphase mass transfer problem using VOF method. They investigated mass transfer from a rising drop in a solvent extraction process [6]. M.M. Hasan *et al.* did experiment on investigation of self-pressurization and thermal stratification of a 4.89m$^3$ $LH_2$ storage tank subjected to low heat flux (0.35, 2.0, and 3.5 W/m$^2$) under normal gravity conditions at fill levels of 83 to 84 percent (by volume).Their Results show that the pressure rise rate and thermal stratification increase with increasing heat flux [7]. Li Chen *et al.* predicted a numerical model for two-phase flows with a varying density in which a modified volume of fluid method is combined with a semi-implicit algorithm (SIMPLE) [8].

H. Gary Grayson *et al.* developed computational fluid dynamics modeling capability for cryogenic tanks which is used to simulate both self-pressurization from external heating and also depressurization from thermodynamic vent operation. They investigate axisymmetric models using a modified version of the commercially available FLOW-3D software [9]. Xiao-Yong Luo *et al.* developed a formula for second-order projection method combined with the level set method to simulate unsteady, incompressible multifluid flow with phase change. A subcell conception is introduced in a modified mass transfer model to accurately calculate the mass transfer across the interface[10]. Jan.B. Haelssig *et al.* presented a VOF methodology for direct numerical simulation of interface dynamics and simultaneous interphase heat and mass transfer in systems with multiple chemical species[11].

Jaeheon Sim and Chih-Kuang Kuan investigated a 3-D adaptive Eulerian-Lagrangian method for multiphase flow computation with phase change model for the simulation of spacecraft fuel tank self-pressurization. They observed that the transport phenomena play an important role in the Self-pressurization of a liquid fuel tank, and conduction-only solution underestimates the pressure rise, the heat transfer in the vapor region has a large influence on the pressurization, especially in the beginning and the full Navier-Stokes and energy equation solution is required to respect the heat transfer via both convection and conduction in both vapor and liquid phases [4]. Harikrishna Raj and K.E. Reby Roy developed a CFD model to predict the pressure rise in a closed cylinder with water as working fluid and the multiphase model used is VOF[5].

Previous works reported in literature dealt with comparatively low and high pressurization rates. High self pressurization rates can occur in critical engineering areas like pressurized water reactors of nuclear power plants in case of plant failure or in cryogenic storage vessels when suddenly exposed to high temperatures, Cryogenic storage tanks in rocket engines etc.

The Self-pressurization occurrence can be explained with the help of a tank moderately filled with liquid as shown in Fig. 1. We can characterize two control volumes bounding the liquid and vapor phases. The saturated liquid vapor interface is a thin layer which allows for surface evaporation and heat transfer between the ullage gas and the liquid. Self-pressurization and the succeeding phase interaction is a coupled phenomenon of heat and mass transfer between the phases.

Heat inflowing from the tank walls will be carried to the liquid vapor boundary by natural convection created by density gradients in the liquid. As the warm fluid reaches the interface, evaporation will occur resulting in ullage compression and a subsequent increase in tank pressure

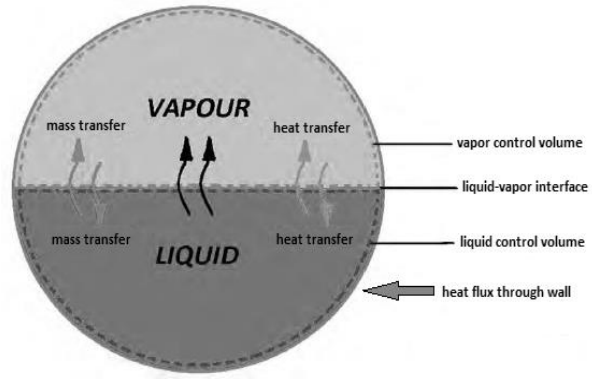


Fig. 2 Moderately filled Vessel- Two control volumes bounding each phase (Courtesy of Harikrishna Raj *et al.*)

.

The present work focussed on the constant mass expulsion for a specific time from the cryogenic storage vessel using heat input supply with the aid of self-pressurization inside the tank. Another complexity of the work is, during the mass expulsion from the system, it will be liable for the reduction of pressure build-up inside the chamber to provide a constant mass flow rate to outside. For numerical assessment a typical storage vessel configuration is chosen with a venting line is immersed into the system for a certain depth, multiphase VOF coupled level-set model accompanying evaporation-condensation mass transfer with varying heat flux input conditions. Through solution of the continuity, momentum, energy and species equations, Computational Fluid Dynamics (CFD) enables the prediction of velocity, pressure, temperature and concentration profiles in very complex systems[11]. Commercially available CFD software package ANSYS FLUENT 14.5 is used for doing this simulation.

## II. MODELLING AND ANALYSIS

### *A. CFD MODELLING*

The complete set of fluid dynamic and multiphase flow equations could be solved numerically with the development and advancement of CFD codes. The present study used commercially available ANSYS FLUENT 14.5 software package, to solve the balance equation set via domain discretisation using control volume approach [5]. These equations are solved by converting the complex partial differential equations into simple algebraic equations. An implicit method for solving the mass, momentum, and energy equations is used in this study. The $k$-ε turbulence model with standard wall functions are used due to their proven accuracies in solving multiphase problems. Effect of normal acceleration due to gravity of is included.

### *B. GEOMETRY AND BOUNDARY CONDITIONS*

The cylindrical vessel of diameter 100mm and height 100 mm filled 70% with liquid oxygen, 30% with gaseous oxygen and a venting line is immersed to the cylinder to a depth of 80mm as shown in Figure 2. The diameter of the immersed venting tube is 5mm. The 3-Dimensional figure is included for better understanding of the current problem. The ullage volume must be given for all practical conditions because even with high insulations to the tank there is some heat in leak to the storage tank thereby the pressure of the tank increasing to unacceptable level and prone to bursting. The ullage volume is filled with gaseous oxygen at 90.2 K and the remaining fluid oxygen at bottom side having a temperature of 90K. The current problem is done with 2-Dimensional axisymmetric model. A three dimensional model will give more accurate results but it requires heavy computation time for getting results with current scenario. So other than three dimensional, the domain is simplified to a two dimensional axisymmetric model. The analysis with axisymmetric model will give results with acceptable accuracy close to three dimensional models.

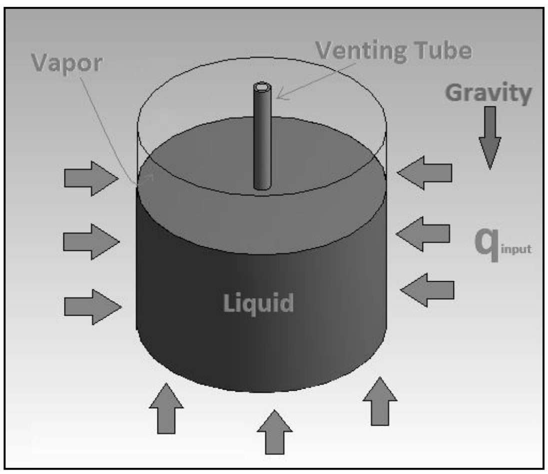


Fig. 2 Three Dimensional model of the computational domain for better understanding of the complete domain

The effect of sensible heating before vaporization can also be incorporated with this boundary conditions. Geometry is modelled using ANSYS Design Modeller. Structured quad mesh gives the best results in multi-phase calculations and hence the same is used for meshing. Fig.3 shows the combined picture of 2-D axisymmetric model and meshed model of the computational domain. A mesh sensitivity analysis is performed that enabled the optimization of the mesh size. A total of 12200 elements are present in the meshed domain.

The boundary conditions given for each simulation is the heat flux supply to the computational domain. For each simulation different heat flux input are given i.e. 2000, 4000, 6000 and 8000W/m$^2$ .Operating conditions like pressure and gravity has great importance on the simulation. An initial operating pressure of 1 bar under normal gravity is applied. It is assumed that the analysis is done after chill down process and once the steady state is attained. The initial conditions to the domain are patched with corresponding temperature and volume fraction. Here the domain is divided into three regions i.e. lower region of tank (0 to 70mm) is patched as liquid, upper portion (70 to100mm) is patched as vapor and the area above the tank including the protrusion of venting tube (100 to120mm) is patched as air at standard atmospheric conditions.

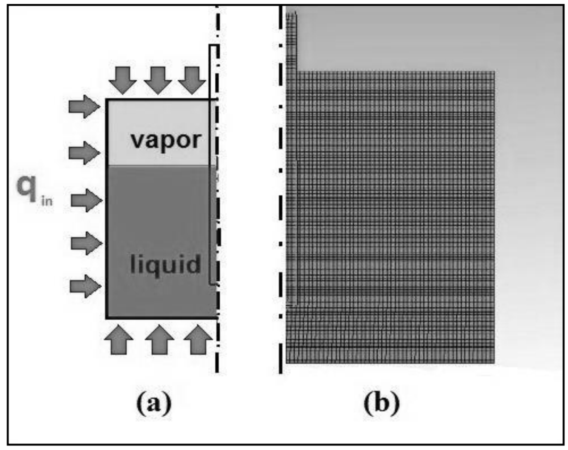


Fig. 3 Two Dimensional axisymmetric model of the computational domain. (a) 2D model incorporating the boundary conditions, (b) Meshed domain of 2D axisymmetric model

### C. MODELLING OF MULTI-PHASE

The numerical simulations presented in this work are based on the ANSYS FLUENT VOF model coupled with Level set method. The VOF model is designed for two or more immiscible fluids in which the position of the interface between the fluids is of interest. The level-set method is a popular interface-tracking method for computing two-phase flows with topologically complex interfaces. This is similar to the interface tracking method of the VOF model. In the level-set method, the interface is captured and tracked by the level-set function, defined as a signed distance from the interface. Because the level-set function is smooth and continuous, its spatial gradients can be accurately calculated. This in turn will produce accurate estimates of interface curvature and surface tension force caused by the curvature. However, the level-set method is found to have a deficiency in preserving volume conservation. On the other hand, the VOF method is naturally volume-conserved, as it computes and tracks the volume fraction of a particular phase in each cell rather than the interface itself. The weakness of the VOF method lies in the calculation of its spatial derivatives, since the VOF function (the volume fraction of a particular phase) is discontinuous across the interface. To overcome the deficiencies of the level-set method and the VOF method, a coupled level-set and VOF approach is provided in ANSYS FLUENT.

### D. MODELLING ASSUMPTIONS

The flow is assumed to be transient, and the pressure based solver is used. Standard wall functions have been selected and the effect of drag, lift and slip interaction has not been investigated. Initially it is assumed that ullage volume is completely filled with oxygen vapor and the liquid zone is completely filled with liquid oxygen.

### *E. SOLUTION STRATEGY AND CONVERGENCE*

Self-pressurization due to evaporation is inherently transient. Transient analysis is carried out with a time step of 0.0001 seconds. A first order upwind discretisation scheme is used for the momentum equation, volume fraction, energy, turbulence kinetic energy and specific dissipation rate. First order implicit transient formulation is used. In pressure-velocity coupling, coupled pressure velocity coupling scheme is used. The coupled algorithm solves the momentum and pressure-based continuity equations together. Other solution strategies used are the reduction of under relaxation factors of momentum, the volume fraction, the turbulence kinetic energy and the turbulence dissipation rate. However, simulations were usually done for 2 seconds of real flow time.

## III. RESULTS AND DISCUSSION

### A. *VALIDATION*

Pressurization in liquid hydrogen tank investigated by Jaeheon Sim *et al.* [4] is used for validation. A 50% filled liquid hydrogen vessel is heated uniformly on all its sides. Self-pressurization due to evaporation occurs as a result of the heat flux. As reported in the paper, the saturation pressure after 1000 seconds and 2000 seconds is 101750 and 102350 Pascal respectively. A closed cylinder model without mass expulsion is simulated for validation purpose and the obtained saturation pressure after the corresponding time interval using the present methodology is 101820 and 102374 Pascal respectively. Results obtained from the present methodology are in good agreement with the published results.

### B. *MASS EXPULSION FROM TANK*

*1) Oxygen tank at different heat flux condition*

The self-pressurisation phenomena commonly seen on cryogenic storage tank due to the heat in leak from the surrounding to the tank thereby boil off taking place. As the cryogen is getting heated the tank gets pressurized and vaporised gas transfers heat to the cryogen. The combined heat and mass transfer processes greatly influence the tank pressure, thereby mass transfer from immersed venting tube in the cryogenic storage vessel. Numerical simulations have been conducted on a simplified 2D geometry of cryogenic storage tank with an immersed venting tube. The simulation is carried out with various heat flux input and initial patching of temperature at the computational domain

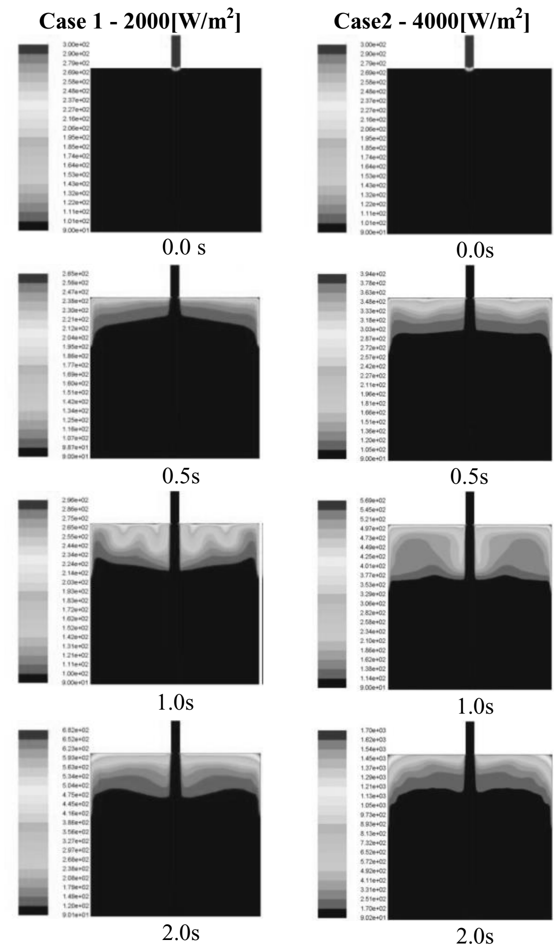


Fig. 4 Comparison of Temperature contours of Cryogenic tank subjected to a heat flux of 2000W/m$^2$ and 4000W/m$^2$

.

The above figures 4 and 5 shows the contours of temperature of liquid Oxygen at various heating condition in a typical storage tank with an immersed venting tube. The liquid Oxygen at 90 K is filled by seventy percentage of the total volume of the tank and the remaining 30 percentages is filled by vapour oxygen at 90.2 K. Fig 6 and 7 showing the volume fraction contours of oxygen at various heating condition.

From the Fig. 8 the volume fraction trend of oxygen for 8000 and 6000 heat flux condition is of almost similar fashion. The increment of heat flux obviously cause sudden and vigorous boiling inside the chamber and due to increase in pressure and the liquid expulsion is quickly done. The vaporisation rate is so large in 6000 and 8000 heat flux than with the 2000 and 4000 heat flux condition

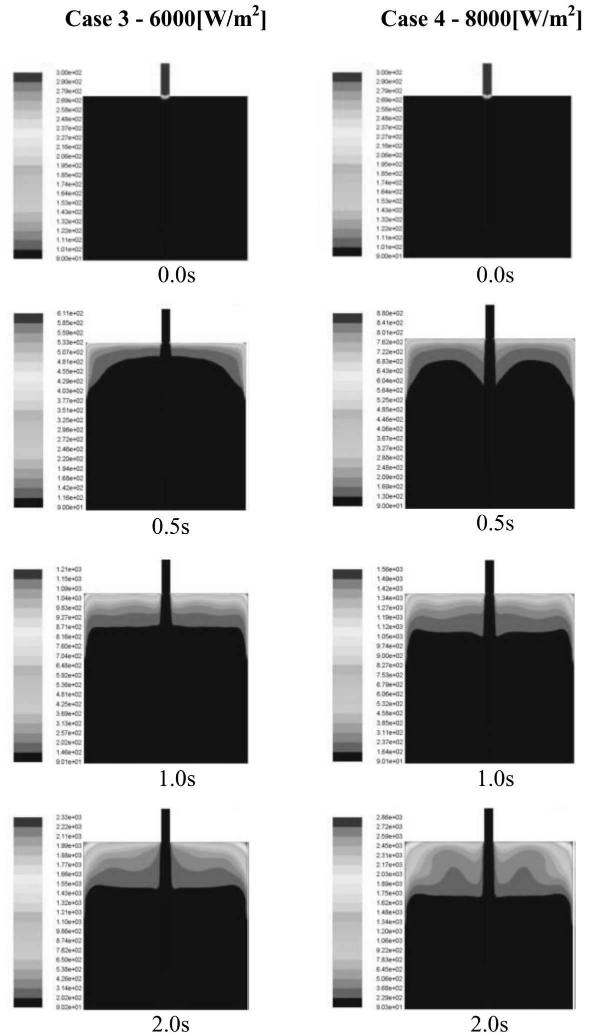


Fig. 5 Comparison of Temperature contours of Cryogenic tank subjected to a heat flux of 6000W/$m^2$ and 8000W/$m^2$

From this volume fraction plot against flow time it is observed that the liquid volume fraction suddenly decreasing subjected to the heat flux condition from 6000 to 8000.

So the vapour is obtained within a definite time if large heating conditions are given. For a time of 1 sec, the liquid volume fraction of oxygen with minimum heat flux condition i.e. 2000 W/$m^2$ having less variation. If our area of concern is getting liquid oxygen from venting tube from the effect of pressurisation, the heat flux condition must be lies between 2000 W/$m^2$ to 4000 W/$m^2$

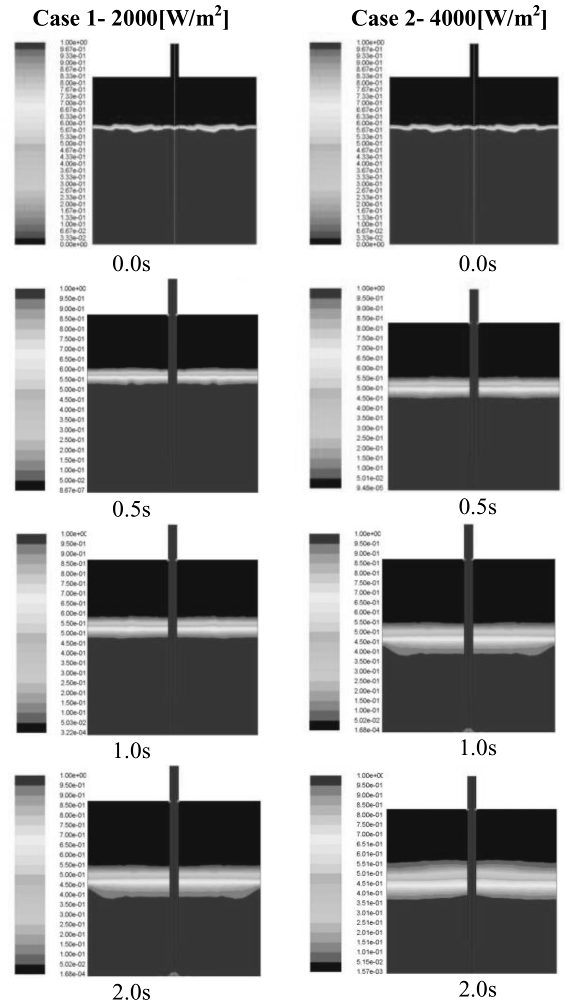


Fig. 6 Comparison of Liquid volume fraction contours of Cryogenic tank subjected to a heat flux of 2000W/$m^2$ and 4000W/$m^2$

.

From the above tables we can see that the volume fraction of the oxygen changing for different heat flux conditions. It changes rapidly when the heat flux increased .At the time of 0 second (starting condition), red coloured region in the volume fraction contour is where the liquid having the volume fraction 1, and the colour variation shows the volume fraction gradient. At the time of 2 seconds the red colour on the volume fraction contour is not perfectly liquid but it is a mixture of liquid and vapor. The blue colour in the volume fraction contour showing the vapor region in the tank. Initially the liquid is stand still at the tank but due to the heat flux inflow to the tank, the liquid getting vaporised due to large amount of energy that is sufficient for the phase change process.

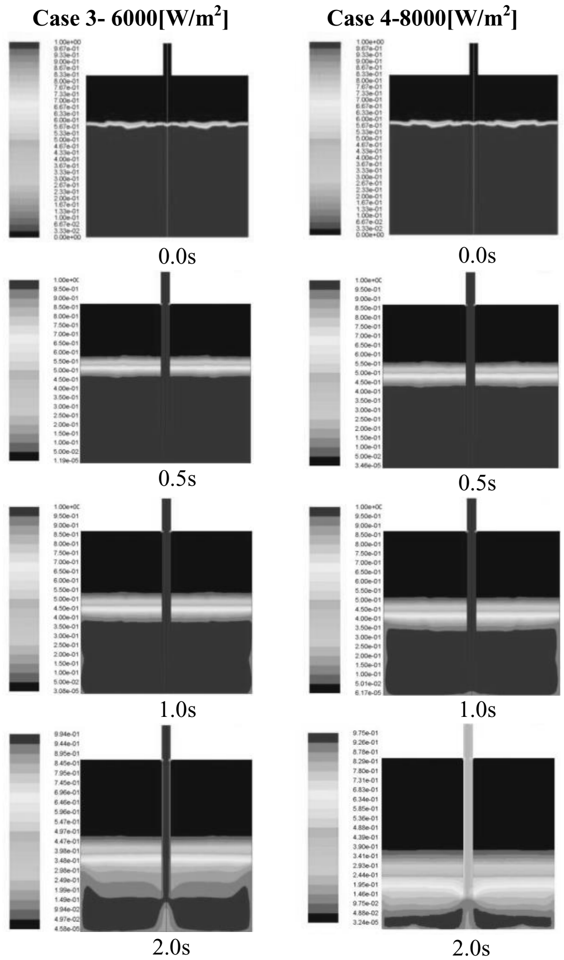


Fig. 7 Comparison of Liquid volume fraction contours of Cryogenic tank subjected to a heat flux of 6000W/m$^2$ and 8000W/m$^2$

The vaporisation process cause the pressure build-up inside the chamber thereby the vapor phase pushed the liquid. Suddenly the liquid oxygen pushed out through the moderately immersed venting line in the tank.

Fig. 8 shows the liquid volume fraction of oxygen at various heat flux condition against flowtime. For the heat flux condition of 2000W/m$^2$ the liquid volume fraction slighlty changes from 0.5 to 2 seconds and the change is very little . But at heat flux of 4000 W/m$^2$ more boil off happens thereby volume fraction patterns goes downward than the first one.The volume fraction curves of 6000 and 8000 W/m$^2$ gives a similar trend but variation is faster with less time for the large heat flux condition. From 1 to 2 seconds,heat flux condition of 8000 W/m$^2$ gives a sudden dip of volume fraction from 0.98 to 0.88 . In Fig. 9 the mass flow rate curves of cryogen for various heat flux conditions against flowtime is plotted.

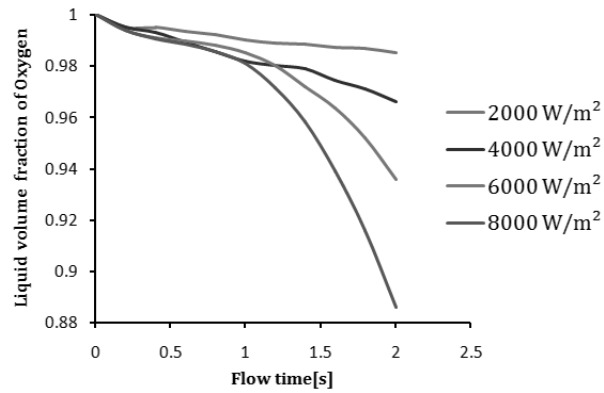


Fig. 8 Liquid volume fraction plot of Oxygen against flow time for various heat influx conditions

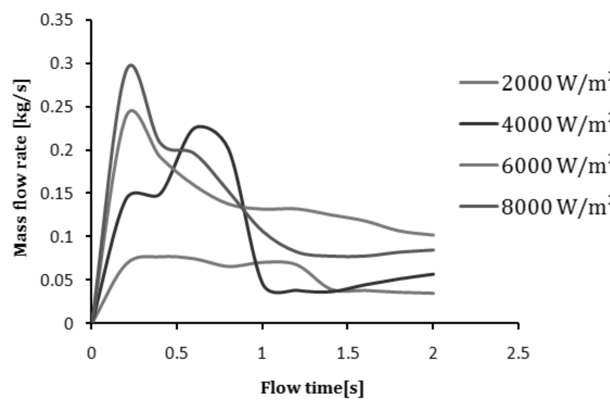


Fig. 9 Mass flow rate of Cryogen against flow time for various heat flux input

The heat flux condition of 2000 W/m$^2$ gives constant mass flow rate with less fluctuation from 0.3 to 1.26sec. At 4000W/m$^2$ mass flow rate is fluctuating due to vigorous boiling of cryogen. For heat flux condition of 6000 and 8000 W/m$^2$, the oxygen give a sudden hike in mass flow rate (0.23 and 0.3kg/sec at 0.2 sec) and then gradually decreased. At the 6000 W/m$^2$ heat flux condition, a constant mass flow rate of 0.1kg/s from 1 to 2sec. The higher heating condition shows higher pressure rise in the beginning thereby sudden mass expulsion due to the fast heat transport to the cryogen.

## IV. Conclusions

Numerical simulations have been conducted for mass expulsion of oxygen from cryogenic storage vessel with the pressurization by various heat flux supply. The simulations give an insight into the boiling flow pattern, volume fraction variations, velocity variations, temperature variations inside the cryogen by varying the heat flux to the computational domain. For getting constant mass flow rate for a specific time, the 2000W/m$^2$ heat flux condition is suitable. By heating with 6000W/m$^2$ heat flux condition, a constant mass flow rate is obtained from 1 to 2 sec but volume fraction of liquid is dipped steeply.

ACKNOWLEDGMENT

The authors gratefully acknowledge the Department of Mechanical Engineering, TKM College of Engineering, Kerala, for making available the facilities at CFD Centre, which helped to complete the work successfully.

REFERENCES

[1] Aydelott J.C, "Effect of Gravity on Self-pressurization of Spherical Liquid- Hydrogen Tankage", NASA-TN-D-4286, 1967.

[2] Majumdar, Alok, Steadman Todd & Maroney, Johnny, "Numerical Modelling of Propellant Boil-off in Cryogenic Storage Tank", National Aeronautics and Space Administration, Washington, DC 20546-0001, NASA/TM, 2007-215131, November 2007.

[3] Stephen J. Mattick et al., "Progress in Modelling Pressurization in Propellant Tanks", 46th AIAA/ASME/SAE/ASEE Joint Propulsion Conference & Exhibit July 2010, Nashville, TNM.

[4] Jaeheon Sim and Chih-Kuang Kuan and Wei Shyy, "Simulation of Spacecraft Fuel Tank Self-pressurization Using Eulerian-Lagrangian Method", 49th AIAA Aerospace Sciences Meeting including the New Horizons Forum and Aerospace Exposition 4 -7 January 2011, Orlando, Florida

[5] Hari Krishna Raj & K.E. Reby Roy, "Numerical prediction of higher self-pressurization rates in a typical storage vessel"/ International Journal of Engineering Science and Technology , ISSN : 0975-5462 Vol. 4 No.07 July 2012

[6] M. Ohta,M. Suzuki, "Numerical analysis of mass transfer from a free motion drop in a solvent extraction process" , Solvent Extraction Research and Development, Volume 4 (1996) 138–149.

[7] M.M.Hasan, C.S Lin and N.T. Van Dresar,"Self-Pressurization of a Flightweight Liquid Hydrogen Storage Tank Subjected to Low Heat Flux",1991 ASME/AIChE National Heat Transfer Conference Minneapolis, Minnesota, July 28-31, 1991

[8] Li Chen and Yuguo Li, "A numerical method for two-phase flows with an interface, Environmental Modelling & Software 13 (1998) 247-255

[9] H.Gary Grayson et. al, "CFD Modeling of Helium Pressurant Effects on Cryogenic Tank Pressure Rise Rates in Normal Gravity", 43rd A1AAMSME SAE/ASEE Joint Propulsion Conference and Exhibit 8 -11 July 2007, Cincinnati, Ohio, pi -10

[10] Xiao-Yong Luo, Ming-Jiu Ni, Alice Ying, and M. A. Abdou, "Numerical Modelling for Multiphase Incompressible Flow with Phase Change", Numerical Heat Transfer, Part B, 48: 425 - 444, 2005, p 425-445

[11] J.B. Haelssig, A.Y. Tremblay, J. Thibault, S.G. Etemad, "Direct numerical simulation of interphase heat and mass transfer in multi component vapour–liquid flows" , International Journal of Heat and Mass Transfer 53 (19–20) (2010) 3947–3960.

[12] Liebenberg, D. H. and Edeskuty, F. J, "Pressurization Analysis of a Large- Scale Liquid Hydrogen Dewar", Int. Advances in Cryogenic Engineering. Plenum Press, 1965, pp. 284

[13] Vineeth Ahuja , Ashvin Hosangadi and Chin P Lee, "Computational Analysis of Pressurization in Cryogenic Tanks",44rd AIAA/ASME'SAE/ASEE Joint Propulsion Conference & Exhibit 1-23 July 2008, Hanford. CT

[14] Samuel W. J. Welch and John Wilson, "A Volume of Fluid Based Method for Fluid Flows with Phase Change" ,Journal of Computational Physics160, 662–682 (2000)

[15] Neil T. Van Dresar and Robert J. Stochl ,"Pressurization and Expulsion of Cryogenic Liquids: Generic Requirements for a Low-Gravity Experiment", NASA Technical Report NASA TM-104417,June, 1991

[16] Stephen Barsi, Mohammad Kassemi, Charles H. Panzarella, J and Iwan D. Alexander,"A Tank Self-Pressurization Experiment Using a Model Fluid in Normal Gravity",American Institute of Aeronautics and Astronautics(AIAA) Paper 2005-1143

[17] Y.A.Cengel,M.A.Boles –Thermodynamics:An Engineering Approach, 4th edition, McGraw-Hill,New York,2002

[18] Randal F Barron - Cryogenic Heat Transfer, Taylor and Francis,1999

# Effect of Slenderness Ratio on the Performance of a Compact Cryogenic Regenerative Heat Exchanger

Abhiroop V.M #1, K.E. Reby Roy *2

#Department of Mechanical Engineering, St. Thomas Insititute for Science and Technology,Trivandrum, Kerala, India
1Abhiroop.v.m@gmail.com

*Department of Mechanical Engineering, TKM College of Engineering, Kollam, Kerala, India
2rebyroy@yahoo.com

***Abstract*— A numerical model is developed for predicting the heat transfer phenomenon and chill down process along a compact cryogenic regenerator. The cryogenic fluid used for analysis is nitrogen and the regenerator material used for the present study is aluminum. As the liquid nitrogen at initial temperature of 74K passes along the regenerator at room temperature transient boiling phenomenon occurs. The present study aims to provide a better understanding of the transient boiling process in the regenerator element of elliptical cross section with staggered overlapping arrangement and also to predict the chill down time of the given material configuration. A 2D analysis is done using CFD code ANSYS 14.5.Parametric studies have been done with different slenderness ratios and flow Reynolds numbers.**

***Keywords*— CFD, Two-phase flow, Compact Regenerator, Slenderness Ratio, Mixture-Method**

## I. INTRODUCTION

Chill down of transfer lines occurs in most of the cryogenic fluid flow problems. Cryogenic fluid transfer cases occurs in many areas like cryogenic treatment of metals,superconductivity, space applications, cryo-preservation, MRI's, cryo-surgery and many other applications. Better understanding of cryogenic heat transfer is very much essential to reduce chill down time which saves the requirement of cryogenic fluids. In most of the cryogenic fluid flow problems the liquid cryogen at a very low temperature enters the transfer line or heat exchanger which will be at room temperature initially. As the liquid passes through the hot transfer lines vaporization of liquid occurs which may cause pressure and flow surges in the fluid. As flow time increases a steady state will be achieved when the transfer line is completely chilled to the fluid temperature. Proper understanding of the chilldown phenomenon is very much desirable for designing the transfer lines.

Many studies have been reported on cryogenic chilldown analysis.A semi empirical correlation for pressure drop and in two phase flow along a horizontal transfer line was developed by Lockart and Martinelli[1].Bruke et al[2] formulated suggested a control volume method for predicting chill down time along a long stainless steel tube using nitrogen as working fluid. Studies conducted by Bronson and Edeskuty[3] reported that stratified flow is predominant during chilldown . Chilldown along an aluminum pipe was studied by Chi[4] and an analytical model was developed based on certain assumptions. A two phase flow friction factor was suggested by Rogers [5] using Martinelli model. A one dimensional finite difference formulation was used for understanding chill down based on transient numerical modeling by Steward et.al [6].Hear transfer coefficients were determined, and concluded that that peak pressure surge increases with increasing inlet pressure . Van Dresar et al. [7] conducted studies on chilldown with nitrogen and hydrogen as working fluids concluding that an optimum flow rate exits when liquid consumption is minimum. Cross et al. [8] developed a finite volume based numerical model for chilldown of a cryogenic transfer line based on transient heat transfer effects. Sunil Kumar and Ajaylal [9] have done an experimental study on cryogenic feed line and concluded that there is an increase in feed line pressure surge with increase in inlet source pressure.

This paper presents a numerical model considering the chill down process and heat transfer rate along a regenerative heat exchanger. The present analysis is done to compare the heat transfer rate and chill down time along regenerators with difference in arrangement of matrix elements. The geometry used for the study is staggered matrix elements with elliptical cross section. Comparative studies are done using mesh elements of two different slenderness ratios. The influence of flow Reynolds number is also compared.

## II. PROBLEM FORMULATION AND SOLUTION PROCEDURE

The A 2D mathematical model is developed using CFD code ANSYS 14.5.The numerical model is capable of calculating the phase change and heat transfer phenomenon. The present problem is analyzed at unsteady state with multiphase conditions. The unsteady state analysis deals with the effect of parameters like Reynolds number, slenderness ratio of regenerative matrix, free flow area, geometry and arrangement of regenerative material. For simplicity of the current problem a transient analysis with two dimensional geometry is considered.

The flow is assumed to be unsteady incompressible, so pressure based solver is used for the numerical analysis. The model used here is multiphase VOF (volume of Fluid) model, Energy equation is used as it involves heat transfer, and the viscous model used is Realizable k-ε Model with standard wall functions. The SIMPLE (Semi-Implicit Method for Pressure-Linked Equations) algorithm is used as the solution method. This algorithm is essentially a guess-and-correct procedure for the calculation of pressure on the staggered grid arrangement.

To initiate the SIMPLE calculation process a pressure field is guessed and the discretized momentum equations are solved using the guessed pressure field to yield the velocity components. The correct pressure is obtained by adding a pressure correction to the guessed pressure field.

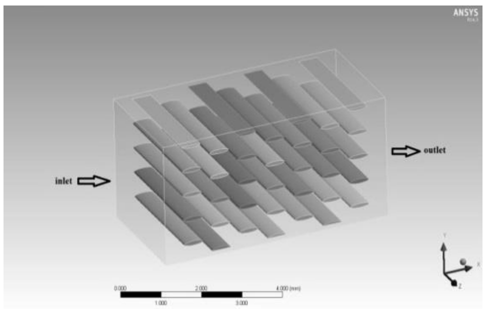


Fig. 1 3 Dimensional geometry of the regenerator

The figure 1 shows the actual 3D geometric configuration of the regenerator used for the present study. The inlet and outlet flow directions are also indicated. But for CFD analysis a 2D symmetric model is considered for simplicity.

The boundary conditions defined are:

i. Velocity inlet
ii. Pressure outlet
iii. Adiabatic wall
iv. Symmetric wall

The regenerative matrix used for analysis is elliptical cross section with staggered arrangement.

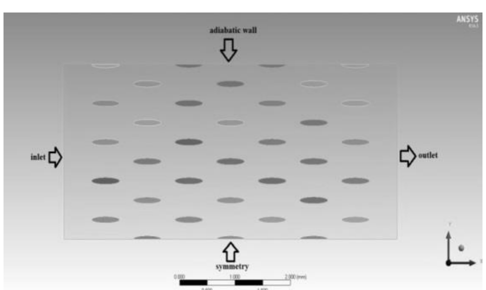


Fig. 2 Two Dimensional geometry of regenerative matrix elements with slenderness ratio 5

Case studies are performed with slenderness ratio of matrix elements 5 and 10.Parametric studies are also made for different flow Reynolds numbers ranging from 800 to 3000.

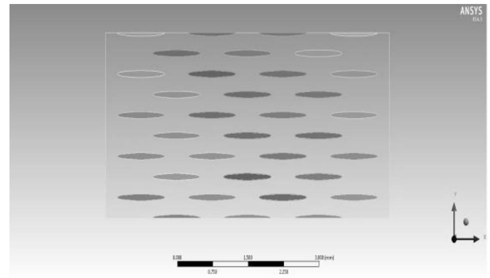

Fig. 3 2D geometry of regenerative matrix elements with slenderness ratio 10

Two different geometries with slenderness ratios 5 and 10 are investigated. The Figure 2 and Figure 3 show the 2D geometrical arrangement of elements with slenderness ratios 5 and 10. As slenderness ratio increases the porosity of the regenerator decreases which will increase the heat transfer area. For analysis the mesh was created using meshing module of the ANSYS 14.5 WORKBENCH. Careful grid independent studies have been conducted. The meshed model is analyzed in module FLUENT of ANSYS 14.5. The initial temperature of the domain is set to 300K and initial volume fraction of air is set to unity. The temperature of liquid nitrogen entering the regenerator is 74K.The inlet velocities are defined such that Reynolds number varies from 800 to 3000. The material of the regenerator is aluminum.

## III. RESULTS AND DISCUSSION

In the present numerical analysis, cryogenic regenerative heat exchangers with slenderness ratios 5 and 10 are studies. Parametric studies were also performed with four different Reynolds numbers. The slenderness ratio of the matrix elements is varied by changing the dimension of major axis keeping length of minor axis constant. Since the flow areas remained almost constant so the pressure drop is also constant for both geometries. Even though there will be a small variation due the viscous effect as there is an increased surface area for higher slenderness ratio.

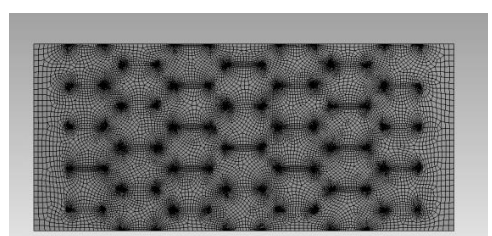

Fig. 4 Meshed Domain of Symmetric Model

Figure 3. shows the meshed domain of the 2D symmetric model used for analysis.It consists of 32588 elements and 28777nodes.

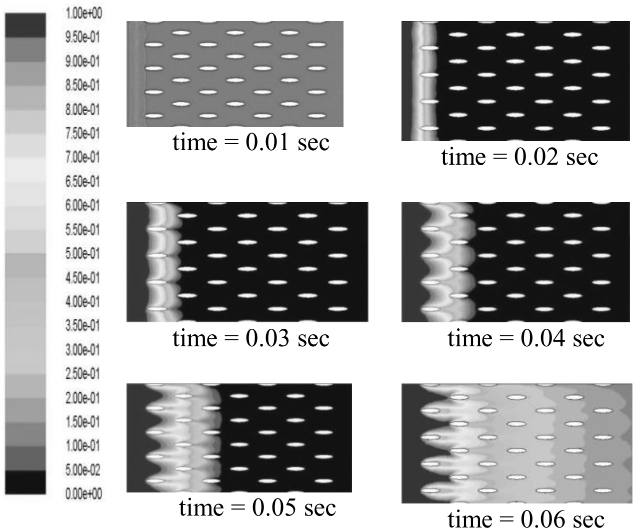


Fig. 5 Volume fraction contours of nitrogen for slenderness ratio 5

Figure.5 and 6. shows the contours of volume fraction of nitrogen along the regenerator for a flow Reynolds number 800.

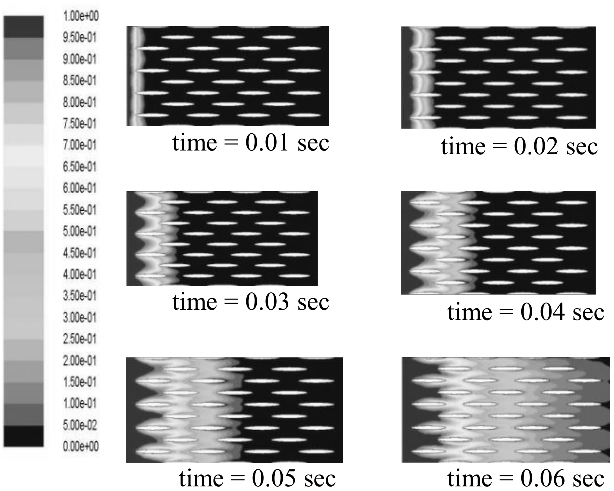


Fig. 6 Volume fraction contours of nitrogen for slenderness ratio 10

The figures clearly indicates that as flow time proceeds the regenerator is filled by nitrogen Comparing the contours corresponding to a flow time of 0.1seconds, we can clearly see that nitrogen proceeds more along the length for the regenerator with slenderness ratio 5.And this is because of the increased porosity for regenerator with slenderness ratio 5where frictional drop is less than that of regenerator with slenderness ratio 10.

The temperature variations along the regenerator for both cases are indicated by figure 7 and figure 8. It can be seen that the chill down time is less for the second case with slenderness ratio 10. The improved heat transfer rate due to increase in surface area of contact between liquid nitrogen and regenerator surface has contributed to the decrease in chill down time for higher slenderness ratio.

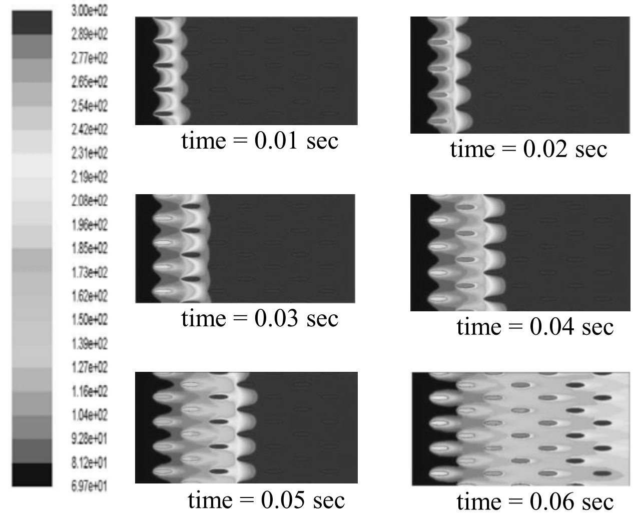


Fig. 7 Temperature contours of nitrogen for slenderness ratio 5

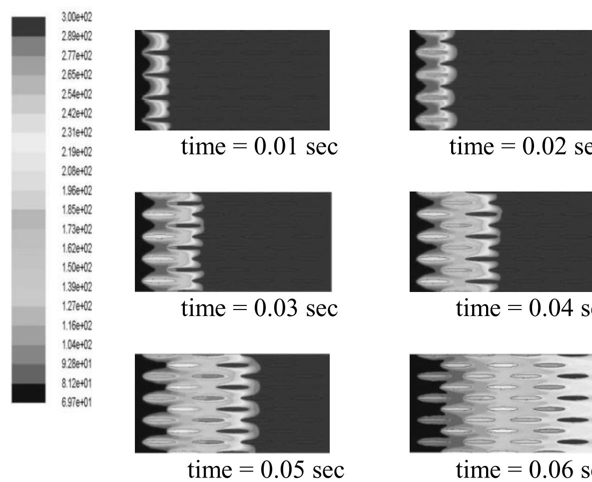


Fig. 8 Temperature contours of nitrogen for slenderness ratio 10

Figure 9 shows the comparison of heat transfer coefficient for slenderness ratio 5 at various Reynolds numbers ranging from 800 to 3000. From the graph it is clear that when Reynolds number decreases heat transfer rate increases. For Reynolds number ranging from 800 to 3000 the maximum heat transfer rate varies from 14,500W/m$^2$K to 4000W/m$^2$K. For lower velocities of low heat transfer rate is more. The variation each curve for varying flow times is due to the two phase flow of the liquid through the regenerator.

Figure. 10 shows the comparison of heat transfer coefficient for slenderness ratio 10 at various Reynolds numbers ranging from Here heat transfer rate varies from 18,000W/m$^2$K to 4500W/m$^2$K.Heat transfer rates in both cases are high for lower Reynolds number (Re= 800).

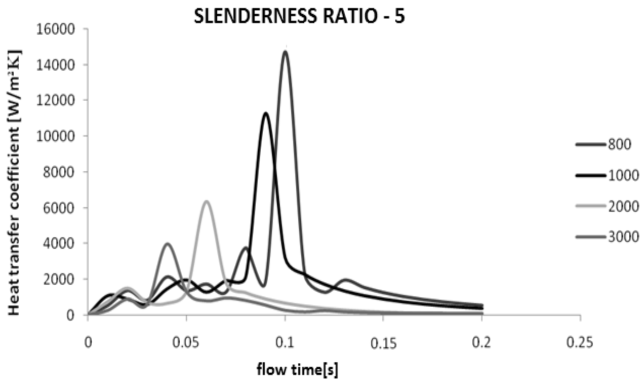


Fig. 9 Comparison of heat transfer coefficient at different Reynolds numbers for slenderness ratio 5

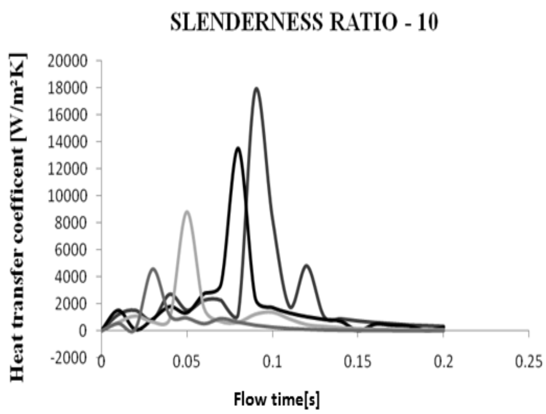


Fig. 10 Comparison of heat transfer coefficient at different Reynolds numbers for slenderness ratio 10

As flow velocity increases the heat transfer rate decreases. Comparing the geometries, the heat transfer coefficient is more when slenderness ratio is higher .For the same Reynolds number of 800, heat transfer coefficients are 14500W/m $^2$ K and 18,000W/,m$^2$K corresponding to slenderness ratios 5 and 10. The improved heat transfer rate is due to the increase in heat transfer area.

## IV. Conclusions

The CFD results presented in the work are useful in understanding the flow and heat transfer phenomenon in a regenerative heat exchanger with two phase flow. The influence on slenderness ratio is mainly discussed. The increase in slenderness ratio will increase the heat transfer rate along the regenerator. Regenerator matrix element discussed in the present papers is elliptical cross section. Slenderness ratio is varied by increasing the length of the major axis keeping minor axis constant. So by increasing the slenderness ratio the flow area is not reduced. As the slenderness ratio increases the porosity of the regenerator decreases. On increasing the slenderness ratio from 5 to 10, the heat transfer rate has improved by 3500W/m $^2$ K.

In summary, regenerator's mesh elements with of higher slenderness ratio will improve the heat transfer characteristics. But as increase in slenderness ratio decreases porosity, which may increase the frictional drop. In the present study the increase frictional pressure drop is negligible due to smaller velocity of flow. So for lower flow rates regenerators with higher slenderness ratios may be recommended.

## Acknowledgment

The authors gratefully acknowledge the Department of Mechanical Engineering, TKM College of Engineering, Kerala, for making available the facilities at CFD centre, which helped to complete the work successfully.

## References

[1] Lochkhart, R.W., Martinelli, R.C., 1949."Correlations for two phase flow in pipes", Chemical Engg. Prog.45 : pp. 39-48.

[2] Burke, J.C., Byrnes, W.R., Post, A.H., and Ruccia,F.E., 1960. Pressurized Cooldown of Cryogenic Transfer Lines, Advances in Cryogenic Engineering,Vol. 4, pp. 378-394.

[3] Bronson, J.C., Edeskuty, F.J., 1962. Cooldown of cryogenic systems, Advances in cryogenic engineering, vol 7, pp. 198-205.

[4] Chi, J.W.H., 1965. Cooldown Temperatures and Cooldown Time During Mist Flow, Advances in Cryogenic Engineering, Vol. 10, pp. 330–340.

[5] Rogers, J.D., 1968. "Two phase friction factor".*AICHE*, j.14 (6), pp. 895–902.

[6] Steward, W.G., Smith, R.V., and Brennan, J.A., 1970.Cooldown Transients in Cryogenic Transfer Lines, Advances in Cryogenic Engineering, Vol. 15, pp.354–363.

[7] Van Dresar, N.T., Siegwarth, J.D., and Hasan, M.M.,2002. Convective Heat Transfer Coefficient for Near- Horizontal Two-Phase Flow of Nitrogen and Hydrogen at Low Mass and Heat Flux, *Cryogenics* Vol. 41, pp. 805-81.

[8] Cross, M. F., Majumdar, A. K., Bennett,Jr. J. C., and Malla, R. B., 2002. "Modeling of Chill Down in Cryogenic Transfer Lines". *Journal of Spacecraft and Rockets*, Vol. 39, No.2, pp. 284–289.

[9] S Sunil Kumar, Ajaylal P.R., 2011. "Pressure surges during cryogenic fluid entry into warm feed line". Proceedings of the 21th national and 10th ISHMTASME Heat and mass transfer conference, IIT Madras India.

[10] Y.A.Cengel,M.A.Boles -Thermodynamics:An Engineering Approach, 4th edition, McGraw-Hill,New York,2002

[11] Randal F Barron - Cryogenic Heat Transfer, Taylor and Francis,1999

# Coupled Heat and Mass Transfer Analysis of an Adiabatic Regenerator – Unique Approach

B. Kiran Naik[1], Amit Kumar[2], Ankit Soni[3], P. Muthukumar[4], C. Somayaji[5]

*Mechanical Engineering Department, IIT Guwahati, Assam, India*

[1]k.bukke@iitg.ernert.in

[2]amit2012@iitg.ernet.in

[3]ankit2012@iitg.ernet.in

[4]pmkumar@iitg.ernet.in

[5]cmsomayaji@iitg.ernet.in

***Abstract*— Regenerator is one of the key components in the solar driven liquid desiccant dehumidification system, whose efficiency influences the performance of the total system. This paper describes a unique mathematical model for the preliminary design of the regeneration process in a counter flow adiabatic regenerator. The model includes the solution to air flow rate ratio, thermal effectiveness, moisture effectiveness and tower height, and these parameters are correlated with the heat and mass transfer process for predicting the desired operating parameters. The predicted parameters for the desorption process have very good agreement with the experimental data reported in the literature. The mathematical model developed in this study can be used as a tool for predicting the regenerator performance characteristics. The influence of operating parameters (relative humidity and solution to mass flow rate ratio) on the performance of the regenerator are studied in detail by varying the tower height and the results are presented in this paper.**

***Keywords*— Desiccant, dehumidification, heat and mass transfer, moisture effectiveness, thermal effectiveness, evaporation rate**

## I. INTRODUCTION

Solar driven liquid desiccant air conditioning system is one of the promising alternative to vapour compression or vapour absorption type air conditioning system [1]. In that, regenerator is one of the important part which converts weak solution to a concentrated solution by a process known as desorption. The schematic of heat and mass transfer process that occur across the regenerator is shown in Fig. 1. Initially, the hot liquid desiccant which is coming out of the solar collector sprayed into the regenerator comes in contact with the ambient air flowing in a counter flow direction. Due to the vapour pressure difference between the weak liquid desiccant and ambient air, evaporation of water vapour take place. During this process of regeneration, two types of heat is released, One latent heat of vaporization due to evaporation process and two chemical heat of mixing due to exothermic reaction. In an adiabatic regenerator no heat is released to the surroundings and therefore, increase in temperature of the ambient air and simultaneously decrease in temperature of desiccant solution occur. At the end of the process, desiccant solution is concentrated and ambient air is humidified.

During desorption (regeneration) process, heat and mass interactions occur between the air and the liquid desiccant solution. The driving force for heat transfer is due to temperature difference whereas for mass transfer is their vapour pressure difference [2]. The complicity of heat and mass transfer dealt way back from 1969, Treybal [3] was the first person who described the heat and mass transfer process for an absorption by proposing a mathematical model. From then many researchers developed various mathematical models for coupled heat and mass transfer analysis using finite difference model [4-6], ε-NTU model [7-8] and simplified models [9-11].

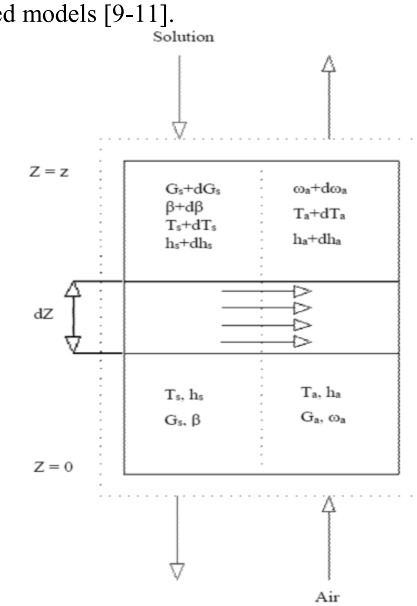


Fig. 1 Energy and mass balance across the regenerator

Fumo and Goswami [4], Babakhani et al. [5] and Liu et al. [6] compared their analytical solution with the experimental data and concluded that their models were valid with some reasonable assumptions. Stevens [7], presented an effectiveness model using lithium bromide as a liquid desiccant solution and validated with experimental data showed a discrepancy of 23% and found disagreement for outlet specific humidity and air temperature. Chengqin et al. [8] developed a model for heat and mass transfer interactions in the packed bed liquid desiccant dehumidifier/regenerator. Gandhidasan [9] introduced the dimensionless parameters such as moisture and thermal effectiveness and formulated the evaporation rate in terms of heat exchanger effectiveness, mass flow rate of air and thermal effectiveness. The proposed model has been compared with the experimental findings and found that the prediction matched within 13% with the experimental data. Martin and Goswami [10] and Ren et al. [11] studied, how to increase the contact time between the liquid desiccant and the ambient air in order to improve the heat and mass transfer interactions by proposing a simplified model.

It is observed from the literature that many researchers developed mathematical models for predicating the performance of a regenerator [3-11]. The novelty of the proposed model is introducing the correlation between the mass transfer coefficient and moisture effectiveness as well as heat transfer coefficient and thermal effectiveness for finding the evaporation rate. No one has correlated the moisture and thermal effectiveness with the tower height of the regenerator which describes the desired design conditions as well as performance of the regenerator. Furthermore, the model developed for coupled heat and mass transfer processes, can be used for estimating all the exit parameters of a regenerator with the known inlet parameters.

## II. HEAT AND MASS TRANSFER ANALYSIS OF LIQUID DESICCANT REGENERATOR

The coupled heat and mass transfer analysis of a liquid desiccant regenerator/dehumidifier was first developed by Treybal in 1969. A schematic of a counter flow heat and mass transfer processes between air and desiccant solution is represented in Fig.1.

The following assumptions are made in order to simplify the analysis

- Adiabatic regeneration process
- Change in mass flow rate of air is negligible
- Properties of desiccant solution and ambient air is assumed to be constant with respect to the temperature
- The desiccant vaporization rate is negligible compared to flow rates of fluid
- Heat and mass transfer processes at the interface area are equal to the specific area of packing

### 2.1 Air side

The enthalpy on air side is given by

$$h_a = C_{p,a}T_a + \omega(C_{p,v}T_a + \delta) \tag{1}$$

On differentiation Eq. 1 can be obtained as

$$dh_a = (C_{p,a} + \omega C_{p,v})dT_a + d\omega(C_{p,v}T_a + \delta) \tag{2}$$

Energy balance across the air side flow is written as

$$\begin{aligned} G_a(h_a + dh_a) - G_a h_a &= \\ \alpha_h a_t (T_s - T_a)dZ &+ G_a d\omega\left(C_{p,v}T_a + \delta\right) \end{aligned} \tag{3}$$

Combining Eq. (2) & (3), the air temperature gradient is obtained as

$$\frac{dT_a}{dZ} = \frac{\alpha_h a_t (T_s - T_a)}{G_a(C_{pa} + \omega C_{pv})} \tag{4}$$

Eq. 4 can be integrated as

$$\int_{T_{a,i}}^{T_{a,o}} \frac{dT_a}{(T_a - T_s)} = \int_0^z \frac{-\alpha_h a_t}{G_a(C_{pa} + \omega C_{pv})} dZ \tag{5}$$

After integrating Eq. 5, final equation can be obtained as

$$\frac{(T_{a,o} - T_{a,i})}{(T_{s,i} - T_{a,i})} = 1 - \exp\left(\frac{-\alpha_h a_t z}{G_a(C_{pa} + \omega C_{pv})}\right) \tag{6}$$

The most common performance measures for evaluating the regenerator potential to regenerate the desiccant solution are thermal and moisture effectiveness.

#### *2.1.1 Thermal effectiveness*

A dimensionless parameter given by Gandhidasan [4] in terms of outlet air temperature and inlet temperatures of ambient air and solution is

$$\xi_T = \frac{(T_{a,o} - T_{a,i})}{(T_{s,i} - T_{a,i})} \tag{7}$$

From Eqs.6 & 7, the thermal effectiveness ($\xi_T$) in terms of heat transfer coefficient ($\alpha_h$), height (h) and flow rate of air is formulated as

$$\xi_T = 1 - \exp\left(\frac{-\alpha_h a_t z}{G_a(C_{pa} + \omega C_{pv})}\right) \tag{8}$$

*2.1.2 Heat transfer coefficient*

From Eq.8, heat transfer coefficient in terms of thermal effectiveness and height is introduced as

$$\alpha_h = \frac{G_a(c_{p,a} + \omega C_{p,v})}{a_t z} \ln\left(\frac{1}{1-\xi_T}\right) \tag{9}$$

*2.1.3 Mass balance for air side*

The mass transfer rate across the interface is equal to the change in humidity ratio and the equation is written as

$$G_a d\omega = \alpha_m a_t(\omega_e - \omega)dZ \tag{10}$$

Eq. 10 is integrated as

$$\int_{\omega_{a,i}}^{\omega_{a,o}} \frac{d\omega}{(\omega_e - \omega)} = \int_0^z \frac{\alpha_m a_t}{G_a} dZ \tag{11}$$

After integrating Eq.11, final equation can be obtained as

$$\frac{(\omega_o - \omega_i)}{(\omega_e - \omega_i)} = 1 - \exp\left(\frac{-\alpha_m a_t z}{G_a}\right) \tag{12}$$

*2.1.4 Moisture effectiveness*

The regenerator moisture effectiveness based on humidity difference across the regenerator is given as follows

$$\xi_m = \frac{(\omega_o - \omega_i)}{(\omega_e - \omega_i)} \text{ [4]} \tag{13}$$

From Eqs. 12 & 13 the moisture effectiveness (humidity effectiveness, $\xi_m$) in terms of mass transfer coefficient ($\alpha_m$), height (h), specific surface area of packing ($a_t$) and flow rate of air ($G_a$) is formulated as

$$\xi_m = 1 - \exp\left(\frac{-\alpha_m a_t z}{G_a}\right) \tag{14}$$

*2.1.5 Mass transfer coefficient*

From Eq.14, mass transfer coefficient in terms of humidity effectiveness and height is introduced as

$$\alpha_m = \frac{G_a}{a_t z} \ln\left(\frac{1}{1-\xi_m}\right) \tag{15}$$

*2.2 Solution side*

Energy balance across the solution side flow is written as

$$\begin{aligned}&(G_s + dG_s)(h_s + dh_s) - G_s h_s \\ &= \alpha_h a_t (T_a - T_s)dZ - G_a d\omega(C_{p,v} T_a + \delta)\end{aligned} \tag{16}$$

The enthalpy on the solution side is given by

$$dh_s = C_{p,s} dT_s \tag{17}$$

*2.2.1 Evaporation rate*

The rate of water vapour evaporated from the solution to the air side is referred as evaporation rate (λ) and is given by

$$d\lambda = G_a d\omega \tag{18}$$

The change in the solution side flow rate is equal to the rate of water vapour evaporated from the desiccant solution, it is given by

$$dG_s = -d\lambda \tag{19}$$

By combining Eqs (16), (17) & (19), the solution side temperature gradient is obtained as

$$\frac{dT_s}{dZ} = -\frac{1}{\gamma C_{p,s}} \left( \begin{aligned} &(C_{p,a} + \omega C_{p,v}) \frac{dT_a}{dz} \\ &- \frac{d\omega}{dZ}\left(C_{p,s} T_s - (C_{p,v} T_a + \delta)\right) \end{aligned} \right) \tag{20}$$

Where $\gamma = \frac{G_s}{G_a}$

*2.2.2 Mass balance for solution side*

Since, the mass of the desiccant is constant during the desorption process, the mass balance across the solution side is written as

$$G_{s,i} \beta_i = G_{s,o} \beta_o \tag{21}$$

The rate of water vapour evaporated from the desiccant solution is transferred to the ambient air by a process known as desorption. Simply, the evaporation rate represents the amount by which the desiccant solution concentrated. So, Eq. 21 can be formulated as

$$G_{s,i} \beta_i = (G_{s,i} - G_a\ (\omega_o - \omega_i))\beta_o \tag{22}$$

From Eq.22, the solution concentration at the outlet in terms of inlet flow rate, solution concentration and evaporation rate is given by

$$\beta_o = \left( \frac{1}{1 - \left( G_a(\omega_o - \omega_i) \middle/ G_{s,i} \right)} \right) \beta_i \tag{23}$$

TABLE 1
COMPARISON OF PRESENT DATA WITH THE EXPERIMENTAL DATA OF FUMO AND GOSWAMI [4]

| | $T_{a,o}$ | $\omega_o$ | $T_{s,o}$ | $X_o$ | $\lambda$ |
|---|---|---|---|---|---|
| Case 1: $G_{a,i} = 0.833$ kg/m$^2$s, $T_{a,i} = 30.40$℃, $\omega_i = 0.0183$ kg$_{wv}$/kg$_{da}$, $G_{s,i} = 6.463$ kg/m$^2$s, $T_{s,i} = 65.0$℃, $X_i = 34.0$ % by mass | | | | | |
| Experimental results | 58.9 | 0.0579 | 58.6 | 34.5 | 1.55 |
| Present study with $\xi_m = 0.505$, $\xi_T = 0.824$ | 58.73 | 0.0581 | 59.16 | 33.83 | 1.56 |
| Percentage difference | 0.29 | -0.35 | -0.96 | 1.94 | -0.65 |
| Case 2: $G_{a,i} = 1.098$ kg/m$^2$s, $T_{a,i} = 30.10$℃, $\omega_i = 0.0180$ kg$_{wv}$/kg$_{da}$, $G_{s,i} = 6.206$ kg/m$^2$s, $T_{s,i} = 65.1$℃, $X_i = 34.1$ % by mass | | | | | |
| Experimental results | 59.3 | 0.0532 | 57.8 | 34.8 | 1.81 |
| Present study with $\xi_m = 0.443$, $\xi_T = 0.834$ | 59.18 | 0.0534 | 58.51 | 33.89 | 1.82 |
| Percentage difference | 0.20 | -0.38 | -1.23 | 2.62 | -0.55 |
| Case 3: $G_{a,i} = 1.438$ kg/m$^2$s, $T_{a,i} = 29.8$℃, $\omega_i = 0.0177$ kg$_{wv}$/kg$_{da}$, $G_{s,i} = 6.479$ kg/m$^2$s, $T_{s,i} = 65.1$℃, $X_i = 34.5$ % by mass | | | | | |
| Experimental results | 57.5 | 0.0488 | 56.6 | 35.2 | 2.10 |
| Present study with $\xi_m = 0.379$, $\xi_T = 0.785$ | 57.40 | 0.0490 | 57.55 | 34.26 | 2.12 |
| Percentage difference | 0.17 | -0.41 | -1.68 | -0.17 | -0.95 |
| Case 4: $G_{a,i} = 1.097$ kg/m$^2$s, $T_{a,i} = 35.10$℃, $\omega_i = 0.0180$ kg$_{wv}$/kg$_{da}$, $G_{s,i} = 6.349$ kg/m$^2$s, $T_{s,i} = 65.1$℃, $X_i = 33.4$ % by mass | | | | | |
| Experimental results | 58.5 | 0.0551 | 57.4 | 34.1 | 1.91 |
| Present study with $\xi_m = 0.472$, $\xi_T = 0.780$ | 58.38 | 0.0554 | 58.31 | 33.18 | 1.92 |
| Percentage difference | 0.20 | -0.54 | -1.59 | 2.69 | -0.52 |
| Case 5: $G_{a,i} = 1.102$ kg/m$^2$s, $T_{a,i} = 40.0$℃, $\omega_i = 0.0178$ kg$_{wv}$/kg$_{da}$, $G_{s,i} = 6.354$ kg/m$^2$s, $T_{s,i} = 65.0$℃, $X_i = 33.6$ % by mass | | | | | |
| Experimental results | 58.9 | 0.0548 | 57.6 | 34.2 | 1.91 |
| Present study with $\xi_m = 0.468$, $\xi_T = 0.756$ | 58.80 | 0.0550 | 58.59 | 33.38 | 1.92 |
| Percentage difference | 0.17 | -0.36 | -1.72 | 2.40 | -0.52 |
| Case 6: $G_{a,i} = 1.132$ kg/m$^2$s, $T_{a,i} = 30.20$℃, $\omega_i = 0.0143$ kg$_{wv}$/kg$_{da}$, $G_{s,i} = 6.370$ kg/m$^2$s, $T_{s,i} = 65.2$℃, $X_i = 34.0$ % by mass | | | | | |
| Experimental results | 57.6 | 0.0513 | 57.2 | 34.7 | 1.97 |
| Present study with $\xi_m = 0.438$, $\xi_T = 0.783$ | 57.49 | 0.0515 | 58.05 | 33.77 | 1.98 |
| Percentage difference | 0.19 | -0.39 | -1.48 | 2.68 | -0.51 |
| Case 7: $G_{a,i} = 1.097$ kg/m$^2$s, $T_{a,i} = 29.40$℃, $\omega_i = 0.0210$ kg$_{wv}$/kg$_{da}$, $G_{s,i} = 6.440$ kg/m$^2$s, $T_{s,i} = 65.5$℃, $X_i = 33.6$ % by mass | | | | | |
| Experimental results | 58.5 | 0.0541 | 58.3 | 34.2 | 1.70 |
| Present study with $\xi_m = 0.426$, $\xi_T = 0.806$ | 58.34 | 0.0543 | 58.97 | 33.41 | 1.71 |
| Percentage difference | 0.27 | -0.37 | -1.15 | 2.31 | -0.59 |
| Case 8: $G_{a,i} = 1.116$ kg/m$^2$s, $T_{a,i} = 30.30$℃, $\omega_i = 0.0182$ kg$_{wv}$/kg$_{da}$, $G_{s,i} = 5.185$ kg/m$^2$s, $T_{s,i} = 65.4$℃, $X_i = 34.4$ % by mass | | | | | |
| Experimental results | 57.6 | 0.0507 | 57.0 | 34.9 | 1.71 |
| Present study with $\xi_m = 0.650$, $\xi_T = 0.778$ | 57.46 | 0.0509 | 57.93 | 34.16 | 1.72 |
| Percentage difference | 0.24 | -0.39 | -1.63 | 2.12 | -0.58 |
| Case 9: $G_{a,i} = 1.101$ kg/m$^2$s, $T_{a,i} = 29.90$℃, $\omega_i = 0.0180$ kg$_{wv}$/kg$_{da}$, $G_{s,i} = 7.541$ kg/m$^2$s, $T_{s,i} = 65.2$℃, $X_i = 34.3$ % by mass | | | | | |
| Experimental results | 59.0 | 0.0556 | 57.9 | 34.9 | 1.95 |
| Present study with $\xi_m = 0.461$, $\xi_T = 0.824$ | 58.87 | 0.0558 | 58.61 | 34.11 | 1.96 |
| Percentage difference | 0.22 | -0.36 | -1.23 | 2.26 | -0.51 |
| Case 10: $G_{a,i} = 1.111$ kg/m$^2$s, $T_{a,i} = 30.0$℃, $\omega_i = 0.0187$ kg$_{wv}$/kg$_{da}$, $G_{s,i} = 6.245$ kg/m$^2$s, $T_{s,i} = 60.3$℃, $X_i = 34.4$ % by mass | | | | | |
| Experimental results | 55.8 | 0.0447 | 54.2 | 34.8 | 1.36 |
| Present study with $\xi_m = 0.400$, $\xi_T = 0.851$ | 55.70 | 0.0449 | 54.77 | 34.24 | 1.37 |
| Percentage difference | 0.18 | -0.45 | -1.05 | 1.61 | -0.74 |
| Case 11: $G_{a,i} = 1.084$ kg/m$^2$s, $T_{a,i} = 29.70$℃, $\omega_i = 0.0184$ kg$_{wv}$/kg$_{da}$, $G_{s,i} = 6.315$ kg/m$^2$s, $T_{s,i} = 70.0$℃, $X_i = 34.5$ % by mass | | | | | |
| Experimental results | 62.6 | 0.0666 | 60.0 | 35.3 | 2.45 |
| Present study with $\xi_m = 0.592$, $\xi_T = 0.816$ | 62.45 | 0.0668 | 61.14 | 34.22 | 2.46 |
| Percentage difference | 0.24 | -0.30 | -1.90 | 3.06 | -0.41 |

| | | | | | |
|---|---|---|---|---|---|
| Case 12: $G_{a,i}$ = 1.099 kg/m$^2$s, $T_{a,i}$ = 29.7℃, $\omega_i$ = 0.0177 kg$_{wv}$/kg$_{da}$, $G_{s,i}$ = 6.400 kg/m$^2$s, $T_{s,i}$ = 64.8℃, $X_i$ = 32.8 % by mass | | | | | |
| Experimental results | 57.6 | 0.0542 | 56.8 | 33.4 | 1.89 |
| Present study with $\xi_m$ = 0.474, $\xi_T$ = 0.795 | 57.47 | 0.0546 | 57.65 | 32.59 | 1.91 |
| Percentage difference | 0.23 | -0.74 | -1.5 | 2.42 | -1.06 |
| Case 13: $G_{a,i}$ = 1.116 kg/m$^2$s, $T_{a,i}$ = 30.30℃, $\omega_i$ = 0.0182 kg$_{wv}$/kg$_{da}$, $G_{s,i}$ = 6.428 kg/m$^2$s, $T_{s,i}$ = 65.0℃, $X_i$ = 34.9 % by mass | | | | | |
| Experimental results | 57.9 | 0.0501 | 57.5 | 35.4 | 1.67 |
| Present study with $\xi_m$ = 0.396, $\xi_T$ = 0.795 | 57.77 | 0.0503 | 58.25 | 34.71 | 1.68 |
| Percentage difference | 0.22 | -0.40 | -1.30 | 1.95 | -0.6 |

Comparison is made between the predicted values calculated by the developed mathematical model and experimental values presented by the Fumo and Goswami. During the experimental studies, the packed column of height 0.6 m with a specific area of 210 m$^2$/m$^3$ was maintained. A comparison of typical experimental data for 13 cases [4] with the results obtained from the present study is presented in Table 1. According to the results presented in Table 1, there is a very good agreement between the predicted results obtained from the present model and the experimental data of Fumo and Goswami for the desiccant solution outlet temperature and concentration, the ambient air outlet temperature and humidity ratio and the water evaporation rate. In all the cases, the present mathematical model yields the air outlet temperature and the desiccant concentration slightly greater than the experimental values and the difference is less than 3.1%, whereas for solution outlet temperature, outlet specific humidity of the ambient air and the evaporation loss, the theoretical results are slightly less than the experimental results and the maximum variation is about -1.9%. Fumo and Goswami [4], Gandhidasan [9] and Babakhani [5] studied the effects of various design parameters such as the inlet air temperature and humidity ratio, the inlet desiccant temperature and concentration, the air and the desiccant flow rate on the evaporation rate and the moisture effectiveness in detail. But the influence of thermal effectiveness on the performance of the regenerator is not specified. Therefore, in this paper, the effect of the air flow rate and the inlet temperature on the thermal effectiveness during the regeneration process is presented in Figs. 2(a) & 2(b). A comparison between the experimental results presented by Fumo and Goswami [4] and the present model is shown in same Fig. 2(a) & 2(b). Further the effects of moisture effectiveness, thermal effectiveness, relative humidity and solution to air flow rate ratio on the evaporation rate are investigated using the present model. The operating parameters that have been kept constant are listed in Table 2. Slope of thermal effectiveness curve (% change in the variable /% change in thermal effectiveness) in these figures provides an estimation of the influence of these variables on the thermal effectiveness. The thermal effectiveness decreases with the increase of air flow rate with a slope of -0.16 (Fig. 2 (a)). It may be noted that at low air flow rate, the air will be in contact with the liquid desiccant solution for a longer period of time, giving a higher change in temperature difference ratio (Fig. 2 (a)). The thermal effectiveness enhances with the decrease of air inlet temperature with a slope of -0.84 (Fig. 2 (b)) and there is a linear decrement of air inlet temperature for higher temperature difference ratio. Since the vapour pressure of the air is highly dependent on the temperature, at higher air inlet temperatures, vapour pressure is high therefore lower tendency of heat transfer from the solution side to the ambient air.

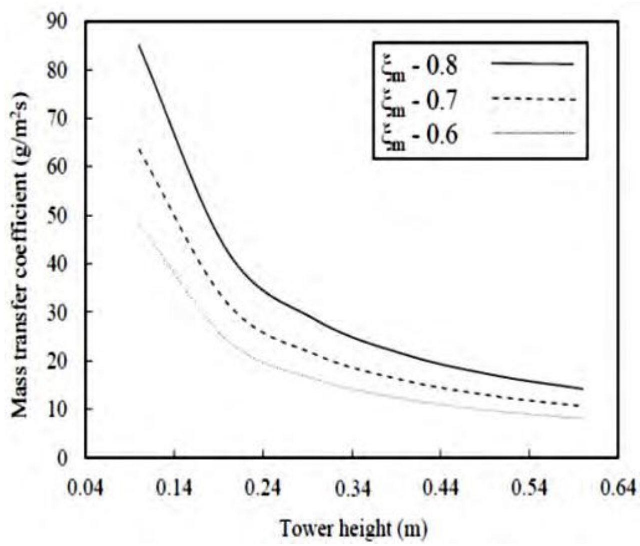


Fig. 3 The effect of mass transfer coefficient on moisture effectiveness

Fig. 3 illustrates the results obtained for the mass transfer coefficient for different moisture effectiveness by varying the height from 0.1 m to 0.6 m. In Fig.3, the variation of mass transfer coefficient is determined in using a new correlation developed in terms of moisture effectiveness, height, air mass flow rate and specific area (Eq. 14). For the given operating conditions, as the moisture effectiveness increases, the mass transfer coefficient also increases. The higher the moisture effectiveness yields the greater rate of mass transfer from the solution side to the ambient air. This is due to the fact that as the moisture effectiveness increases the change in solution concentration increases and hence there is an increase in the mass transfer coefficient. From Fig.3, it is also observed that the mass transfer coefficient decreases

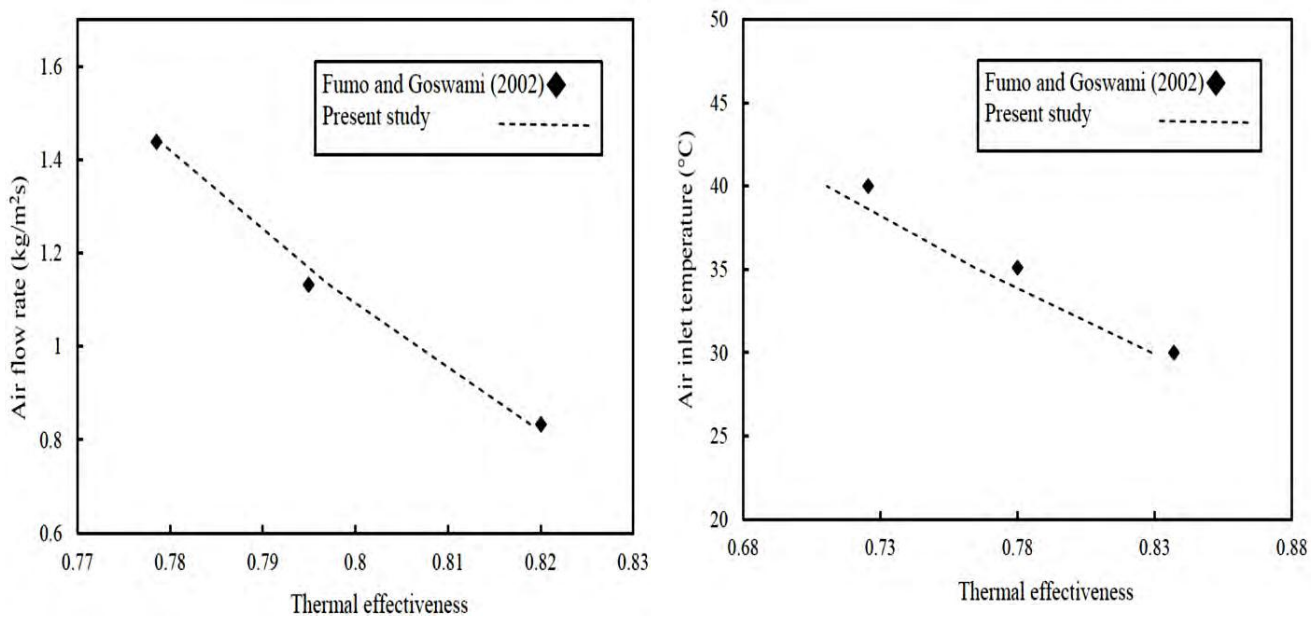


Fig. 2 Comparison of present model with the experimental data of Fumo and Goswami [4]: a) Influence of thermal effectiveness on air flow rate and b) Influence of thermal effectiveness on air inlet temperature

TABLE 2
REGENERATOR PARAMETERS USED IN THE ANALYSIS

| **Operating parameters** | **Unit** | **Operating range** |
|---|---|---|
| Air inlet temperature | °C | 31 |
| Specific humidity | $kg_v/kg_{da}$ | 0.02 |
| Air flow rate | $Kg/m^2s$ | 1.110 |
| Desiccant inlet temperature | °C | 65 |
| Desiccant flow rate at the inlet | $kg/m^2s$ | 6.367 |
| Desiccant concentration | % by mass | 34 |
| Mass transfer coefficient | $Kg/m^2s$ | $5.55 \times 10^{-3}$ |
| Heat transfer coefficient | $W/\ m^2K$ | 14.317 |
| Specific area | $m^2/m^3$ | 210 |
| Tower height | m | 0.1-0.6 |
| Moisture effectiveness | - | 0.5 |
| Thermal effectiveness | - | 0.8 |

logarithmically as a function of moisture effectiveness with the increase in height. This may be explained that as the tower height increases, decrease in vapour pressure of the solution take place. For a given $\xi_m$ of 0.8, increasing the tower height from 0.1 m to 0.6 m, decreases the mass transfer coefficient by 83 %.

The effect of thermal effectiveness on the heat transfer coefficient is illustrated in Fig. 4, by varying the tower height (0.1 m to 0.6 m) for different temperature difference ratios (0.6 to 0.8). A new correlation which has been developed for the heat transfer coefficient (Eq. 8) in terms of thermal effectiveness, air mass flow rate, specific area and tower height is used for determining the variation of heat transfer rate across the height of the regenerator. Two defined tendencies has been observed from Fig. 4. One tendency is the apparent logarithmic decrement of the thermal effectiveness for an increase in the tower height. This is due to fact that, as the tower height increases, the desiccant solution temperature (function of vapour pressure) decreases, giving a lower change in heat transfer rate. For a given $\xi_T$ of 0.8, increasing the tower height from 0.1 m to 0.6 m, decreases the heat transfer coefficient by 80 %. The second defined tendency is the apparent increase in heat transfer coefficient as the thermal effectiveness increases. This can be explained from Fig. 4 that higher the thermal effectiveness, higher the change in desiccant solution temperature and hence there is an apparent increase in heat transfer coefficient.

The influence of relative humidity (R.H.) on the evaporation rate ($\lambda$) is shown in Fig. 5. To investigate this effect, the relative humidity is varied from 70 % to 90 % that can be obtained during the peak summer seasons in a humid climate. As illustrated, when the relative humidity is increased, evaporation rate is decreased. It happens because lower the relative humidity implies a lower air vapour pressure and consequently higher potential for mass transfer. From Fig. 5, it is also observed that for a length beyond 0.58 m, the evaporation rate is constant in case of a relative humidity 90 % or 80 % or 70 %. This is due to the fact that as the height increases, the relative humidity approaches to saturation point (R.H. – 100 %) as well as the heat and the mass interactions between the desiccant solution and the ambient air decreases and hence there is a constant evaporation rate beyond a particular tower height for different relative humidity's. Therefore, it is advisable that the height of the tower should be optimized depending upon the operating conditions

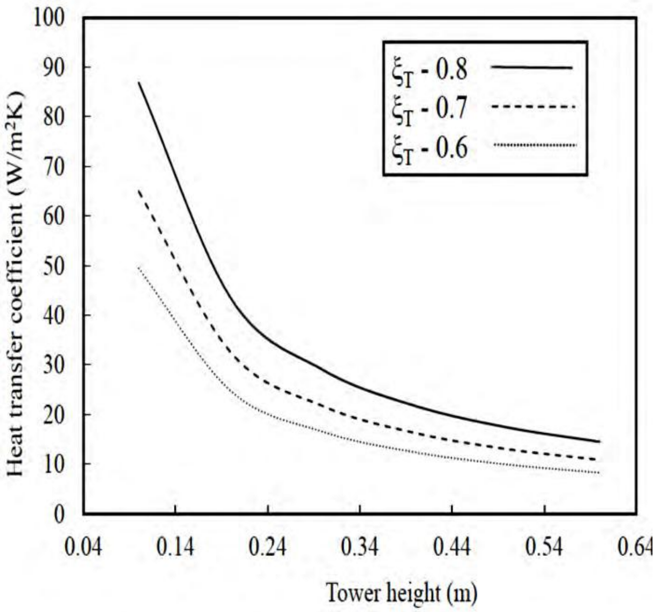


Fig. 4 The effect of heat transfer coefficient on thermal effectiveness

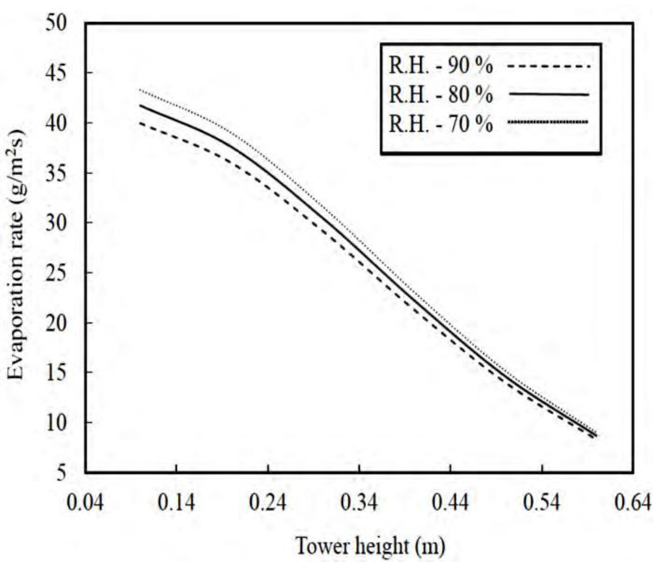


Fig.5 The influence of relative humidity on evaporation rate

Figure 6 shows the results obtained for the concentration at different solution to air flow rate ratios (L/G ratios), by varying tower height from 0.1 m to 0.6 m. For any given flow rate ratio, as the height increases, the solution concentration increases. Since the concentration is highly dependent on vapour pressure, the lower the solution vapour pressure, the higher the evaporation rate and consequently gives the lower potential for mass transfer interactions.

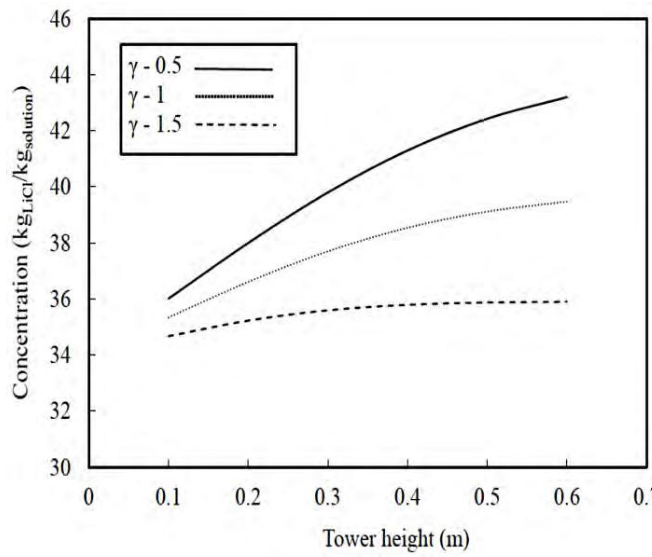


Fig.6, The effect of concentration on solution to air flow ratio

From Fig. 6, it is also observed that as the flow rate ratio increases desiccant solution concentration decreases. This happens because as the flow rate ratio decreases, the solution to the air contact will be for longer period of time, giving a higher change in concentration. For a given $\gamma = 0.5$, increasing the tower height from 0.1 m to 0.6 m, increases the solution concentration by 19 %.

## III. CONCLUSIONS

Weak desiccant solution (LiCl-$H_2O$) regeneration process using the ambient air as an absorber is studied by proposing a unique mathematical model using dimensionless parameters such as thermal effectiveness in terms of heat transfer coefficient and moisture effectiveness. The developed mathematical model shows very good agreement with the available experimental data [4]. It is observed that operating variables such as solution to flow rate ratio, air inlet temperature, relative humidity, moisture effectiveness and thermal effectiveness are having greater impact on regenerator performance. It is also found that for a constant area beyond a certain height the evaporation rate for any relative humidity is merely equal and approaches to saturation point. For a detailed study of desorption process across an adiabatic regenerator, this model gives an accurate performance prediction with some reasonable assumptions.

## REFERENCES

[1] F.N. Ani, E.M. Badawi and K.S. Kannan, The effect of absorber packing height on the performance of a hybrid liquid desiccant system, *Renewable Energy*, vol. 30, pp. 2247–2256, 2005.

[2] J. D. Killion and S. Garimella, A critical review of models of coupled heat and mass transfer in falling-film absorption, *International Journal of Refrigeration*, vol. 24, pp.755–797, 2001.

[3] R.E. Treybal, *Mass transfer operations*, 3rd ed., New York: McGraw-Hill, pp.186–211, 1969

[4] N. Fumo and D.Y. Goswami, Study of an aqueous lithium chloride desiccant system: Air dehumidification and desiccant regeneration, *Solar Energy*, Vol. 72, pp.351–361, 2002.

[5] D. Babakhani and M. Soleymani, Simplified analysis of heat and mass transfer model in liquid desiccant regeneration process, *Journal of the Taiwan Institute of Chemical Engineers*, vol. 41, pp.259–267, 2010.

[6] X Liu, Y Jiang, J Xia and X Chang, Analytical solutions of coupled heat and mass transfer processes in liquid desiccant air dehumidifier/regenerator, *Energy Conversion and Management*, vol. 48, pp.2221–2232, 2010

[7] D.I. Stevens, J.E. Braun and S.A. Klein, An effectiveness model of liquid-desiccant system heat/mass exchangers, *Solar Energy*, vol. 42, pp.449–455, 1989

[8] R. Chengqin, J. Yi, and Z. Yianpin, Simplified Analysis of Coupled Heat and Mass Transfer Processes in Packed Bed Liquid Desiccant-Air Contact System, *Sol. Energy*, vol. 80, pp. 121-129 2006.

[9] P. Gandhidasan, Quick performance prediction of liquid desiccant regeneration in a packed bed, *Solar Energy*, vol. 76, pp.409–416, 2005.

[10] V. Martin and D.Y. Goswami, Heat and mass transfer in packed bed liquid desiccant regenerators – An experimental investigation, *Transactions of ASME*, vol. 121, pp.162–170, 1999.

[11] C. Ren, Y. Jiang, and Y. Zhang, Simplified analysis of coupled heat and mass transfer processes in packed bed liquid desiccant-air contact system, *Solar Energy*, vol. 80, pp.121–131, 2006.

# Design and Fabrication of Parabolic Trough Collector

Ramesh Krishnan S.

*Mechanical Engineering Department, Rajiv Gandhi Institute of Technology, Kottayam, Kerala, India*

rameshs.krishnan@gmail.com

***Abstract***— **Solar thermal power plants are the most interesting options for renewable electricity production. Solar collectors are the heart of most solar systems. This paper explains the effective utilization of solar energy using parabolic trough collectors. It gives an information on the steps taken from the initial design stages and choice of a parabolic trough solar concentrator, through the fabrication process, and finally through the test stages of the project. This particular collector is designed to utilize the energy provided by the sun to heat water. Due to restrictions of cost and space, a miniature version of typical parabolic troughs used today was made. Because of the small scale of the project, actual use of the parabolic trough to heat water may not be feasible. An analysis of the collector efficiency is also performed which is the ratio of the energy absorbed by the working fluid (water) to the energy incident on the collector.**

***Keywords***— **solar energy, parabolic trough collector, tracking system, collector efficiency, analysis.**

## I. INTRODUCTION

Among the wide range of renewable energy technologies for electricity production, solar thermal power plants are among the interesting options as solar energy is abundant and free. Different types of solar collectors can be used which may be broadly classified into non concentrating collectors and concentrating collectors. Flat plate collectors and evacuated tube collectors are examples of non-concentrating collectors. But compared to this type, concentrating collectors can achieve high temperatures and high efficiency. Among the solar collectors, parabolic trough solar collector (PTSC) is one of the lowest cost solar electric power options which is a type of concentrating collector. It tracks the sun during the day and concentrates the solar radiation on a receiver tube located at the focus of the parabolic shaped mirror. The thermal efficiency of the PTSC depends on the accuracy with which the collector follows the sun.

## II. PARABOLIC TROUGH COLLECTOR

It is the most characteristic one axis tracking collector, concentrating solar energy to generate temperature up to 400ºC for solar thermal power production. In trough collector the mathematical properties of parabola are exploited. The rays of light parallel to y axis of the mirrored parabola will be reflected and focused at the focal point at a distance f from vertex.

A PTSC consists mainly of (i) a focusing device (ii) an absorber/receiver and (iii) a tracking device for continuously following the sun. Reflectors concentrate direct solar radiation onto the receptor located on the focal line of the parabola. The fluid to be heated is circulated through the absorber piping. PTSC has a very low thermal loss coefficient and is so suited for application at high temperatures.

Fig. 1 A parabolic trough collector

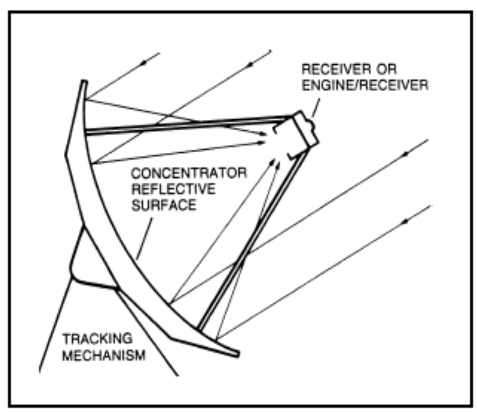


Fig. 2 Elements of a Parabolic Trough Collector

### *F. Materials for reflecting surfaces*

For reflecting system, mirrors of high quality and good reflectance properties are required. Glass and polished aluminium surfaces are commonly used. Optical and mechanical properties, durability, resistance to hail, rain, dust, other environmental influences, thermal expansion and contraction etc. are to be considered.

*A. Materials for absorber*

The factors on which the choice of absorber materials depends on modulus of elasticity, melting point, yield strength, cost, ease of fabrication, corrosion resistance and resistance to stagnation temperature. Commonly copper, steel and aluminium are used.

*B. Absorber surface coating materials*

Higher absorbability for solar radiation, durability when exposed to weathering, sunlight and high stagnation temperature, cost effectiveness and protection to the base material are the desirable characteristics of an acceptable coating for absorber. Black automotive manifold paints and instrument blacks are good choices for absorber coatings.

*C. Heat transfer fluids*

The fluids used should have high stability at high temperatures, low material maintenance and transportation cost, low pressure and must be non-corrosive.

## III. DESIGN AND FABRICATION OF PARABOLIC TROUGH COLLECTOR

A working model of PTSC is designed and fabricated. The parabolic profile is obtained using graphical method.

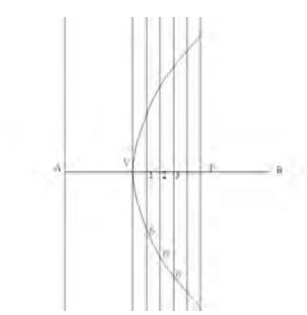

Fig. 3 Generation of parabolic profile

Then by iterative process, an acrylic sheet is made into the shape of a parabola with an absorber pipe through the focal point of the parabola. An aluminium foil is adhered to the surface of the acrylic sheet to increase the reflectivity of the sheet and to avid its brittleness due to continuous exposure to sunlight. The parabolic truss is fabricated using metal strips and fabricated by arc welding.

TABLE I
MATERIALS USED FOR MAKING PTC

| Sl. No. | Component of fabricated part | Material used |
|---|---|---|
| 1 | Reflecting surface | Mirror finished acrylic sheet |
| 2 | Absorber | GI pipe coated with black paint |
| 3 | Truss | Mild steel |
| 4 | Packing sheet | Plastic sheet for supporting acrylic sheet |

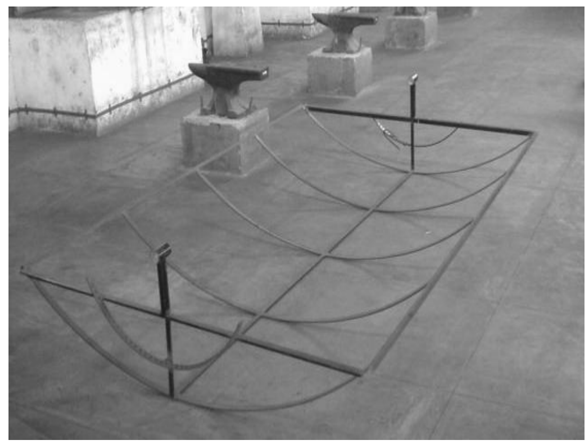

Fig. 4 Fabricated truss of the PTC

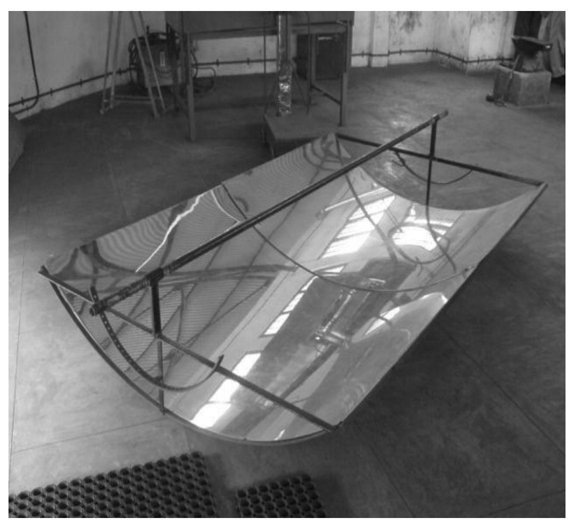

Fig. 5 Truss- reflecting surface assembly

Fig. 6 Final stage of fabricated PTC

## IV. IMPLEMENTATION OF TRACKING SYSTEM

The solar to thermal energy conversion efficiency of PTSC is determined by measuring temperature rise of water as it flows through the receiver when it is properly focused. The thermal efficiency of PTSC is a function of intercept factor which in turn depends on the accuracy with which the collector follows the sun. The optical efficiency of the collector is a function of mirror surface reflectance, glass envelope transmittance, heat collection element absorption and intercept factor i.e., optical efficiency $\eta_o = f\ (\rho, \tau, \alpha, \gamma)$. So the tracking error is to be reduced as much as possible.

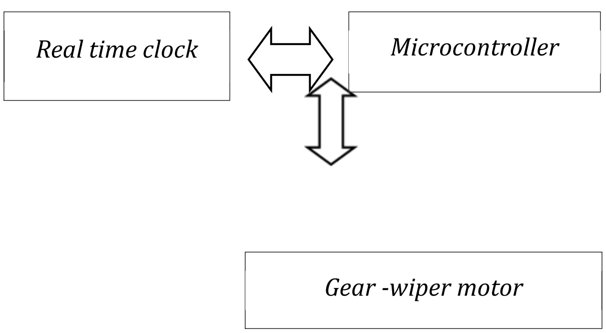


Fig. 7 Block diagram of electronic circuit

Given that the sun's apparent speed of rotation across sky is 0.25º/minute, a fixed rate control mode is used for tracking purpose. The tracking system consists of a microcontroller based timer circuit. The programmed microcontroller will trace the motion of sun and drives the parabolic trough system by a gear and wiper motor mechanism.

A. Driving source for tracking

A wiper motor is used as driving motor as it has the advantage of having range of torque. The standard input voltage requirement for the wiper motor is 12V DC. Other specifications include current 7.5A, speed 43rpm, power 90 W.

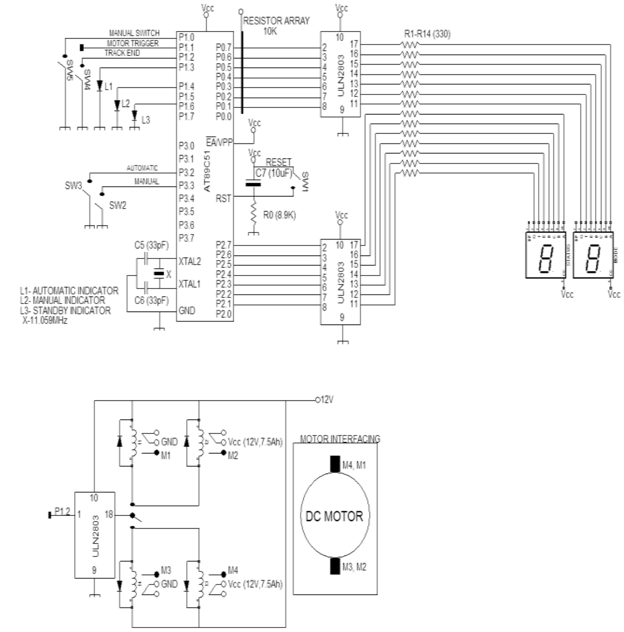


Fig. 8 Circuit diagram of micro controller unit

### *D. Reduction of speed and multiplication of torque*

It takes a lot of force to move the whole truss back and forth across the tracking path. In order to generate a large force, a worm gear is used on the output of the motor. The worm gear reduction can multiply the torque of the motor by about 50 times while slowing the output speed of the motor by 50 times. A reduction gear set which reduces the speed in the ratio 12:1.

Fig. 9 Gear drive for the tracking system

## V. EXPERIMENTAL SET UP

The experimental set up for the solar collector mainly consists of stand, parabolic collector, receiver pipe, tracking mechanism, supply tank and measuring jar.

### *A. Stand*

The entire experimental set up is supported on tripod stands at both ends which are made of GI pipe at a height of 1m from the ground level.

*B. Parabolic collector*

The parabolic collector is fabricated to the following dimensions: length – 2500mm, width- 1500mm.

*C. Supply tank and measuring jar*

The tank for supply of water to the inlet of receiver pipe is made of concrete. A valve is fitted at the outlet of the tank to adjust the flow rate. A flexible pipe is connected from this valve to the inlet of receiver pipe. A measuring jar is placed at the outlet for collecting the hot water and for measuring the mass flow rate.

*D. Tracking system*

The tracking system consists of a wiper motor for driving the system, gear system, electronic circuit for continuously tracking the sun and a 12V battery.

## VI. PERFORMANCE OF EXPERIMENT

The parabolic collector is placed under the sun so that the rays fall on the focal line of the parabola. The water is allowed to flow through the receiver tube. The measuring jar is kept at the outlet of the receiver tube. A stop watch is used to measure the mass flow rate of water. Time taken for collecting 250ml if water is noted using the stopwatch. The ambient temperature and inlet temperature of inlet water are also noted. The readings are noted down every 30 minutes and temperature of outlet water is also noted using thermometer. The experiment is repeated for different mass flow rates.

*A. Observation and tabulation*

The observations made were tabulated as shown below.

TABLE II
OBSERVATIONS OF DAY 1

| Sl.No. | Time | mass flow rate (kg/s) | Outlet temp ºC | Efficiency% |
|---|---|---|---|---|
| 1 | 1100 | 0.00771 | 43.5 | 9.13 |
| 2 | 1130 | 0.00771 | 44 | 9.45 |
| 3 | 1200 | 0.00771 | 43 | 8.81 |
| 4 | 1230 | 0.00771 | 41 | 7.56 |
| 5 | 1300 | 0.00771 | 44 | 9.45 |
| 6 | 1330 | 0.00771 | 46 | 10.71 |
| 7 | 1400 | 0.00771 | 38 | 5.67 |
| 8 | 1430 | 0.00771 | 33 | 2.51 |

Atm. temp = 30.5 ºC; inlet water temp = 29 ºC

TABLE III
OBSERVATIONS OF DAY 2

| Sl. No. | Time | mass flow rate (kg/s) | Outlet temp ºC | Efficiency% |
|---|---|---|---|---|
| 1 | 1000 | 0.01395 | 41 | 13.67 |
| 2 | 1030 | 0.01395 | 40.5 | 13.10 |
| 3 | 1100 | 0.01395 | 41.5 | 14.24 |
| 4 | 1130 | 0.01395 | 41.5 | 14.24 |
| 5 | 1200 | 0.01395 | 42 | 14.81 |
| 6 | 1230 | 0.01395 | 43 | 15.95 |
| 7 | 1300 | 0.01395 | 41.5 | 14.25 |
| 8 | 1330 | 0.01395 | 44 | 17.09 |
| 9 | 1400 | 0.01395 | 46 | 19.37 |
| 10 | 1430 | 0.01395 | 48 | 21.64 |
| 11 | 1500 | 0.01395 | 51 | 25.07 |
| 12 | 1530 | 0.01395 | 46 | 19.37 |

Atm. temp = 31ºC; inlet water temp = 29 ºC

From the observed values, it is clear that the temperature of outlet water vary according to the intensity of sun rays which is not constant throughout the day.

*B. Calculations*

The concentration ratio and collector efficiency which affect the performance of parabolic collector are calculated.

*1) Concentration ratio:* It is the ratio of the aperture area of the system to the area of the receiver. i.e.,
CR = (area of the aperture/area of the receiver)
Area of the aperture = length * breadth
= 2500 x 1500 = $3.75 \times 10^6$ $mm^2$
Area of the receiver = circumference of the receiver pipe x its length = $2 \times \pi \times r \times l$
= $2 \times \pi \times 15.7 \times 2500 = 2.47 \times 10^5$ $mm^2$
CR = $(3.75 \times 10^6) / (2.47 \times 10^6) = 15.21$

*2) Collector efficiency:* It is the ratio of energy absorbed by the water to the energy incident on the collector. i.e.,
$\eta = (Q / AS) \times 100$
Where Q = useful heat gain
A = aperture area
S = solar constant (amount of incoming solar radiation per unit are measured on the outer surface of the Earth's atmosphere whose value is $1367 W/m^2$.
Q = mCp dT where m is the mass flow rate, Cp is the specific heat of water (4.187 kJ/kg K) and dT is the difference between inlet and outlet temperatures of water.
Considering the data obtained on the first day the maximum efficiency can be calculated as follows:
Useful heat gain Q = 0.00771 x 4.187 x (46 - 29) = 0.5488kW.
Input AS = 2.5 x 1.5 x 1367/ 1000 = 5.126kW.
Efficiency $\eta$ = (0.5488 / 5.126) x 100 = 10.71%.

Similarly the maximum efficiency obtained in the second day can be arrived at as given below:

Q = 0.01395 x 4.187 x (51 – 29) = 1.285 kW

AS = 2.5 x 1.5 x 1367/ 1000 = 5.126kW.

Efficiency η = (1.285 / 5.126) x 100 = 25.07%

## VII. CONCLUSION

Compared to the theoretical range of efficiency value, the obtained efficiency is low. Thermal losses can occur through heat transfer by conduction through the surface of the parabolic trough and into the frame. Heat loss due to convection can also be a major issue on the receiver pipe surface. Heat loss due to convection can also be a major issue on the receiver pipe surface. Fluctuation in wind speed throughout testing likely caused more heat loss than expected. This could be combated by insulating the top surface of the receiver tube, or enclosing the trough using glass or Plexiglas with high transmittance. Better insulation of the back of the reflecting surface would also help with the heat lost due to conduction. The shape of the parabola may also not have been perfect due to issues during construction. These could all affect the amount of incident radiation on the copper receiver tube and thus the amount of heat transferred to the concentrator fluid. Poor thermal characteristics of the receiver tube and coating also have an impact on the efficiency. These thermal losses likely reduced the amount of useful solar gain for the concentrator. The cracks present in the reflecting surface also might have affected the reflexivity.

The advantages in using parabolic trough collector are that it is pollution free and hence considered being ecofriendly, it has no fuel requirement and that skilful labour is not required. However heating of water is not much efficient during winter and cloudy days. So it is highly climate dependant. Also intensity of radiation from sun is not constant throughout the day. Again PTC cannot be used during night time.

Although the technology of a PTC is less expensive among the available solar power options, its initial cost of installation is high. A possible reduction in the cost of parabolic solar power is possible through the methods like plant scale up i.e., increasing the size of plant and by development of advanced technologies like improved thermal storage, concentrator and receiver designs, use of a more proper receiver fluid etc.

It can be concluded that the parabolic trough technology has the potential to begin compete directly with conventional power technologies in the near future.

## REFERENCES


[1] Gard H.P. and Prakash J, *Solar Energy Fundamentals and Applications*, 1st revised ed.,2002 pp 166-140

[2] Cohen G., *Operation and Efficiency of large scale solar thermal power plants*, Optical Materials Technology for energy efficiency and solar energy conversion, SPIE V 2017, 332-337.

[3] Martin M. and Berdahl P., , "Characteristics of Infrared sky radiations, Solar energy V33, 321-336, 1984

[4] Integrated Solar combined cycle systems using parabolic trough technology, Technical and Financial Review, Spencer Management Associates, Diablo March 1996.

[5] Odeh S.D., Morrison G.L.and Behnia M., Thermal Analysis of Parabolic trough collectors for electric power generation.

[6] MarionW. And Wilcox. S., Solar radiation Data Manual for flat plate concentrating collectors, National Renewable Energy Laboratory, Golden Colarado, April 1994, Report NREL/TP 463-5607.

# Numerical Investigations on Flow Channel of Bipolar Plate in Proton Exchange Membrane Fuel Cell

Jobin Sebastian [#1], P. Karthikeyan [*2], Rajesh Baby [#3]

[#] *Department of Mechanical Engineering*
*St. Joseph's College of Engineering and Technology, Palai, Kerala, India*
1jobinseb93@gmail.com
[3]rbaby55@gmail.com

[*] *Department of Automobile Engineering,*
*PSG college of Technology Coimbatore, Tamil Nadu, India*
[2] apk@aut.psgtech.ac.in

***Abstract*— This paper reports the results of a numerical investigation on Proton Exchange Membrane (PEM) fuel cell. The three-dimensional model of bipolar plate in a PEM fuel cell with serpentine flow field design has been used for study. The numerical model is three dimensional steady, incompressible, single phase and isothermal includes the governing of mass, momentum, energy and species equations. All of these equations are simultaneously solved in order to get current flux density in the 1:1,1:2,2:1,2:2(Landing : Channel) flow channel of bipolar plate is the main analysis of this paper. Among different flow field designs serpentine flow field can give better performance of PEMFC. In this serpentine flow field, 1:1 flow channel gives greater power density. This paper also discusses about the variation in the active area of flow field in the bipolar plate of PEM fuel cell.**

***Keywords*— Proton Exchange Membrane fuel cell, Membrane Electrode Assembly, Bipolar plate, Power density, Active area**

## I. INTRODUCTION

Due to the rapid depletion of fossil fuel energy resources and climate change, fuel cell technologies have received much attention in recent years owing to their high efficiencies and low emissions. A new power source is needed which should be energy efficient, low pollutant emissions and has an unlimited supply of fuel. Fuel cell is an electrochemical device which directly converts chemical energy stored in fuels such as hydrogen to electrical energy without combustion. The most important feature of this fuel cell is that it can be used in portable electronic applications such as mobile phones, laptops and so on. Fuel cells are different from batteries in that they require a continuous source of fuel and oxygen or air to sustain the chemical reaction whereas in a battery the chemicals present in the battery react with each other to generate an electromotive force. Fuel cells can produce electricity continuously for very long time, when these inputs are supplied [11]. Fuel cells are now closer to commercialization than ever, and they have the ability to fulfill all of the global power needs while meeting the environmental expectations. There are many types of fuel cells being currently researched today, such as Proton Exchange Membrane Fuel Cell (PEMFC), Direct Methanol Fuel Cell (DMFC), Phosphoric Acid Fuel Cell (PAFC), Solid Oxide Fuel Cell (SOFC) and Molten Carbonate Fuel Cell (MCFC) [1-9]. Fuel Cells are electrochemical electricity generators of high efficiency which can produce heat at temperatures which range from 50 to 100$^{o}$C. With fuels such as oil, coal or natural gas, the pollutant emission levels are 10–1000 times lower than in conventional energy conversion systems depending on the type of applications [3]. When a carbon-containing fuel is used, the $CO_2$ emissions are significantly lower than in conventional systems, due to the higher efficiency. With hydrogen as a fuel the pollutant emission is zero at the point of use. This paper mainly focuses on:

1. Numerical studies on variation in current density of various landing to channel ratios (1:1,1:2,2:1,2:2) of the flow channel in the bipolar plate of a PEM fuel cell considering the serpentine flow field.

2. Effect of variation in the active area in the bipolar plate in a PEM fuel cell.

## II. WORKING OF PEM FUEL CELL

A fuel cell consists of an anode, cathode and an electrolyte which allows charges to move between the two sides of the fuel cell. Electrons are drawn from the anode to the cathode through an external circuit, producing electricity. At the anode, the electrochemical oxidation of the fuel produces electrons that flow through the bipolar plate to the external circuit, while the ions generated migrate through the electrolyte to complete the circuit. The electrons in the external circuit drive the load and return to the cathode catalyst where they recombine with the oxidizer in the cathodic oxidizer reduction reaction [14]. The output products of the fuel cell are: chemical products, heat and electric power.

On the anode side, hydrogen diffuses to the anode catalyst where it later dissociates into protons and electrons. These protons often react with oxidants causing them to become what are commonly referred to as multi-facilitated proton membranes. The protons are conducted through the membrane to the cathode, but the electrons are forced to travel in an external circuit because the membrane is electrically insulating [4].On the cathode catalyst, oxygen molecules react with the electrons and protons to form water. The electrons in the external circuit drive the load and return to the cathode catalyst where they recombine with the oxidizer in the cathodic oxidizer reduction reaction. PEM fuel cells use a solid polymer as an electrolyte and porous carbon electrodes containing a platinum catalyst [15]. Equations (1), (2) and (3) shows the chemical reactions in a fuel cell.

Anode reaction: $2H_2 \rightarrow 4H^+ + 4e^-$ ………..… (1)

Cathode reaction: $O_2 + 4H^+ + 4e^- \rightarrow 2H_2O$ …….(2)

Overall cell reaction: $2H_2 + O_2 \rightarrow 2H_2O$ ………..…..(3)

Like any electrochemical device, the reaction occurs at a specific voltage, and the current density is a function of the active surface area of the electrode. Thus series/parallel electrical configurations are necessary to achieve the voltage and current necessary to do work, such as stationary backup power for a bank, hospital and so on [6]. Series combinations are achieved by placing multiple single cells into a stack to get the desired voltage, and parallel combinations are achieved by placing multiple stacks together to achieve the desired current. These configurations can also be used to feed reactant and coolant flow within a stack.

## III. FUEL CELL MODELLING

The process for modelling and simulating fuel cell performance involves three basic steps. Preprocessing, solver and post processing. The components of serpentine fuel cell are modelled using ANSYS Workbench. Figure 1 shows a 3 Dimensional view of a meshed assembly of a PEM fuel cell. Structured meshing is used for this complex geometry. Fine mesh is used at the interface and at the flow channel [10].

### *A. Significance of bipolar plate in PEM fuel cell*

Bipolar plates (BPs) are a key component of PEM fuel cells with multifunctional character. They uniformly distribute fuel gas and air, conduct electrical current from cell to cell, remove heat from the active area, and prevent leakage of gases and coolant. BPs also significantly contributes to the volume, weight and cost of PEM fuel cell stacks [12]. Hence, there are vigorous efforts worldwide to find suitable materials for BPs. The materials include non-porous graphite, coated metallic sheets, polymer composites, etc. Bipolar plates account for the bulk of the stack; hence it is desirable to produce plates with the smallest possible dimensions permissible. Bipolar plates constitute more than 60% of the weight and over 30% of the overall cost in a fuel cell stack. For this reason the weight, volume and cost of the fuel cell stack can be significantly reduced by improving layout configuration of the flow field and by using of lightweight materials.

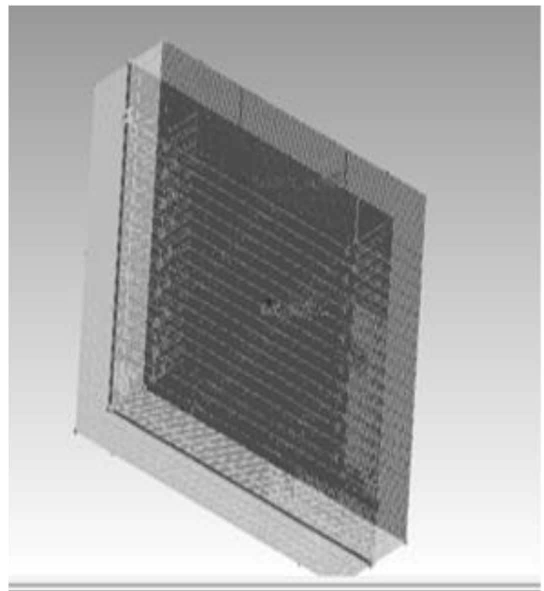

Fig. 1 Meshed assembly of PEM fuel cell

TABLE I
DIMENSIONS OF THE FUEL CELL COMPONENTS USED FOR THE NUMERICAL STUDY

| Sl. No | Component Name | Width (mm) | Height (mm) | Thickness (mm) |
|---|---|---|---|---|
| 1 | Bipolar plate | 100 | 150 | 10 |
| 2 | Gas Diffusion Layer | 100 | 150 | 0.02 |
| 3 | Catalyst Membrane | 100 | 150 | 0.12 |
| 4 | Membrane | 100 | 150 | 0.3 |

### *B. Numerical modelling of bipolar plates*

Bipolar plate used in the present study is shown in figure 2. The components of serpentine fuel cell which is modelled using ANSYS Workbench. The components are modelled as per the dimensions mentioned in the table 1. All the components are modelled individually and then assembled into single component. The assembly consists of central membrane sandwiched between anode and cathode layers. The gas diffusion layer is very delicate and thin compared to other parts [5].


Fig. 2 Bipolar plate used in the present study

The solid flow channel is initially modelled and cross section is cut along the serpentine pattern. The assembly is a separate module wherein all parts to be assembled is placed. The various channels with different landing to channel ratios (L:C=1:1, 1:2, 2:1, 2:2) are designed and analysed for an active area of 70cm$^2$. The mesh type used is cartesian since, for the same cell the accuracy of the solution in cartesian meshes is the highest.

*C. Governing Equations*

Fuel cell behaviour is governed by a set of coupled, non-linear differential equations [3]. These equations must be solved using a finite volume numerical approximation technique. Physical phenomena occurring in a fuel cell can be represented by solution of conservation equations like mass, momentum, energy, species and current transport. In addition, equations those deal specifically with a phenomenon in a fuel cell may be used where applicable.

*2) Conservation of Mass*: $\partial\rho/\partial t + \nabla.(\rho v) = 0$

Where:

$\rho$ = *density, Kg m$^{-3}$*

$v$ = *velocity, m s$^{-1}$*

*3) Conservation of momentum:* The equation is:

$(\partial(pv))/\partial t + \nabla.(\rho vv) = -\nabla p + (\mu^{eff}\ \nabla v) + S_m$

Where:

p = fluid pressure, Pa

$\mu^{eff}$ = mixture average viscosity, Kg m$^{-1}$s$^{-1}$

$S_m$ = momentum source term

4) *Conservation of energy:* The energy conservation equation is: $(\rho c_p)_{eff}\ \partial T/\partial t + (\rho c_p)_{eff}\ (v.\ \nabla T) = \nabla.(k_{eff}\ \nabla T) + S_e$

Where:

*P =fluid pressure*

*$C_p$=mixture average specific heat capacityJKg$^{-1}$ K$^{-1}$*

*T = temperature, K*

$S_e$ = energy source term

*5) Conservation of species:* The species equation is

$$\frac{\partial(\varepsilon\rho X_i)}{\partial t} + \nabla.(v\varepsilon\rho X_i) = \nabla.(\rho D_i^{eff}\nabla X_i) + S_{s,i}$$

Where:

$X_i$ = mass fraction of gas species, i=1, 2,3…n

*$S_{s,i}$ = source or sink terms for the species.*

*6) Conservation Of Charge:* $\nabla.(K^{eff}_s\ \Delta\varphi s) = S_{\varphi s}$

Where:

$K^{eff}$ = Electrical conductivity in solid phase, S cm$^{-1}$

$\varphi_s$ = Solid phase potential

*$S\varphi$*=Source term representing volumetric heat transfer

## IV. RESULTS AND DISCUSSION

*A. Validation of the numerical analysis*

The numerical results are validated with experimental results for 2:2 flow channel pattern at PSG college of Technology.

*B. Effect of L: C of flow channel of the bipolar plate on power density.*

Among the various configurations analysed, it is found that the bipolar plate with landing to channel ratio 1:1 has got the maximum power density .51W/cm$^2$ and hence it can be concluded that the bipolar plate having 1:1 landing to channel ratio is the best among these.

Table 2 gives the variation in current density and power density for different landing to channel ratios such as (1:1, 1:2, 2:1, 2:2). Power density is calculated from the corresponding voltage and power density values. Performance curves and polarization curves of different flow channels are plotted from these values. From figure 3 the 1:1 flow channel will give the peak power density.

TABLE 2
VARIATION OF CURRENT DENSITY AND POWER DENSITY FOR DIFFERENT LANDING TO CHANNEL RATIOS SUCH AS (1:1, 1:2, 2:1, AND 2:2)

| Voltage (V) | 1:1 | | 1:2 | | 2:1 | | 2:2 | |
|---|---|---|---|---|---|---|---|---|
| | I (A/ $cm^2$) | P (W/ $cm^2$) | I (A/ $cm^2$) | P (W/ $cm^2$) | I (A/ $cm^2$) | P (W/ $cm^2$) | I (A/ $cm^2$) | P (W/ $cm^2$) |
| 0.05 | 1.62 | 0.08 | 1.60 | 0.08 | 1.54 | 0.07 | 0.81 | 0.07 |
| 0.3 | 1.59 | 0.47 | 1.35 | 0.40 | 1.34 | 0.40 | 1.13 | 0.33 |
| 0.4 | **1.29** | **0.51** | 1.23 | 0.49 | 1.22 | 0.49 | **1.02** | **0.40** |
| 0.5 | 1.00 | 0.50 | **1.01** | **0.50** | **1.00** | **0.50** | 0.61 | 0.30 |
| 0.85 | 0.08 | 0.07 | 0.01 | 0.01 | 0.09 | 0.07 | 0.03 | 0.02 |
| .95 | 0 | 0 | 0 | 0 | 0 | 0 | 0 | 0 |

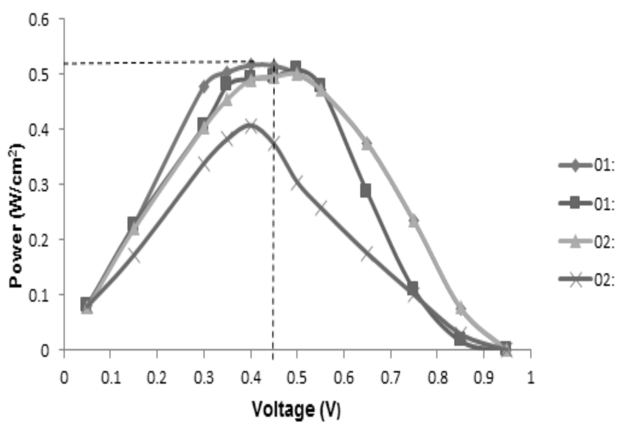


Fig 3 Power Density vs Voltage

*C. Effect of active area on power density*

As the active area of a bipolar plate in a PEM fuel cell the power density also increases. The active area can be changed depending upon the type of application for which the fuel cell is to be used. As the area increases the current density also increases. But the active area can be changed depending upon the type of application for which the fuel cell is to be used.

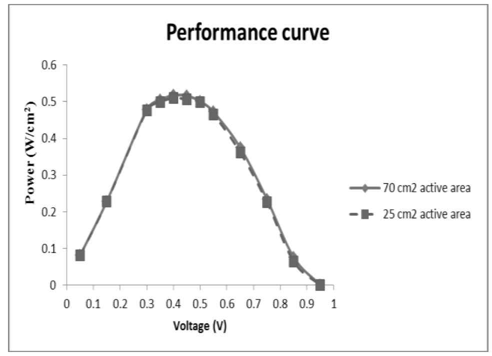


Fig 4 Performance curve for different active areas

Figure 4 shows the performance curves of fuel cells having bipolar plates with landing to channel ratios 1: 1 and active areas 70cm2 and 25$cm^2$. Both the curves follow the same path and only a minute difference exists in between them. The maximum power output is at 0.4 V for both active areas and is 0.51 W/$cm^2$. This indicates that the active area for a fuel cell does not have much influence on the power output. But care has to be taken to select the active area wisely depending upon the particular applications.

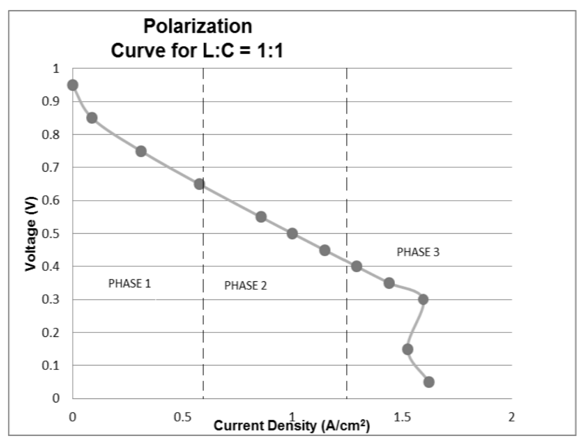


Fig 5 Polarization Curve of Graphite bipolar plates

In the figure 5, the decrease in voltage as the current density increases is due to over potential loss, concentration loss, and ohmic loss. At phase 1, the loss in cell potential is due to over potential loss or activation loss. Over potential is the potential difference between a half-reaction's thermodynamically obtained reduction potential and the potential at which redox event is experimentally observed. It is directly related to a cell's voltage efficiency. Overpotential is specific to each cell design and will vary between cells, and operational conditions.

In the phase 2, the voltage loss is due to ohmic resistance in the flow channel of bipolar plates. These losses simply occur due to the resistance to flow in the bipolar plates. They are of the standard Ohmic form, but usually written in terms of area resistance and current density.

At the phase 3, there will be maximum loss due to the concentration loss. Due to this the flow of gaseous reactants is difficult to reach the reaction site. The slow transport of reactants to the electrochemical reaction sites will slow down the removal of output products from the reaction site.

At the cell level, reactant gas distribution is ensured by flow fields. Thus the design of flow fields is essential to have uniform distribution of reactant gases over the active surface area of the electrodes [13]. Uniform distribution of reactant gases is desired because it translates into uniform current density. Flow field design must take into account: thermal management, water management, reactant flow rate and pressure drop.

## V. CONCLUSION

The influence of various flow channel designs on PEM fuel cell with serpentine flow field has been carried out by using ANSYS Fluent by varying the landing to channel ratios. These values are used to calculate the total power produced by comparing them, the configuration with highest power output capability are selected.

Among the various configurations analysed the maximum power output is 0.517 W/cm$^2$ at 0.40 V for bipolar plate with landing to channel ratio 1: 1. The maximum power densities for fuel cells having bipolar plates with landing to channel ratios 1: 2, 2: 1 and 2: 2 are 0.509, 0.501 and 0.408 W/cm$^2$ respectively. Hence it can be concluded that the bipolar plate having landing to channel ratio 1: 1 is the best among these configurations.

The maximum variation in power densities between fuel cells with bipolar plates having active areas of 75 and 25 cm$^2$ is 0.013 W/cm$^2$ only. This shows that the active area of a bipolar plate in a PEM fuel cell has no significant impact on the power density. But the active area is to be chosen depending upon the type of application for which the fuel cell is to be used.

The active area can be changed depending upon the type of application for which the fuel cell is to be used The main challenges faced during the development of a fuel cell from research to product stage is the reliability of performance while scaling up and stacking up of fuel cells to match the requirements of a power source. However, in real world applications, when the power requirement is more, the active area will be much more than 70cm$^2$ which requires scaling up or increasing the active area of the Membrane Electrode Assembly (MEA).

## REFERENCES


[1] H. Wang, J. J. Martin, D. Yang, and Jianxin M, “A review on water balance in the membrane electrode assembly of proton exchange membrane fuel cells”, Vol. 34, 2009, pp. 9461–9478.

[2] Dong-hao Ye, and Z. Zhan, “A review on the sealing structures of membrane electrode assembly of proton exchange membrane fuel cells”, Vol. 231, 2013, pp. 285-292.

[3] S. M. R. Niya, and M. Hoorfar, “Study of proton exchange membrane fuel cells using electrochemical impedance spectroscopy technique”, Vol. 240, 2013, pp. 281-293.

[4] T. Ous, and C. Arcoumanis, “Degradation aspects of water formation and transport inProton Exchange Membrane Fuel Cell”, Vol. 240, 2013, pp. 558-582.

[5] L. Cindrella a,b, A.M. Kannana, J.F. Lina, K. Saminathana, Y. Hoc, C.W. Lind, and J. Wertze, “Gas diffusion layer for proton exchange membrane fuel cells—A review”, Vol. 194, 2009, pp. 146-160

[6] B. G. Pollet, I. Staffell, and J. L. Shangc, “Current status of hybrid, battery `and fuel cell electric vehicles: From electrochemistry to market prospects”, Vol. 84, 2012, pp. 235-249

[7] K. Jiao, and Xianguo Li, “Water transport in polymer electrolyte membrane fuel cells”, Vol. 37, 2011, pp. 221-291

[8] R. Taherian, M. J. Hadianfard, and A. N. Golikand, “Manufacture of a polymer-based carbon nanocomposite as bipolar plate of proton exchange membrane fuel cells”, Vol. 49, 2013, pp. 2420-251

[9] K. Hemmes, G. Barbieria, Y. M. Lee, and E. Drioli, “Process intensification and fuel cells using a Multi-Source Multi-Product approach”, Vol. 51, 2012, pp. 88-108

[10] F. Arbabi, R. Roshandel, and G. Karimi Moghaddam, “Numerical Modeling of an Innovative Bipolar Plate Design Based on the Leaf Venation Patterns for PEM Fuel Cells”, Vol. 25, 2012, pp. 177-186

[11] A. Boudghene Stambouli, “Fuel cells: The expectations for an environmental-friendly and sustainable source of energy”, Vol. 15, 2011, pp. 4507-4520

[12] S. Bhatt, B. Gupta, V. K. Sethi, and M. Pandey, “Polymer Exchange Membrane (PEM) Fuel Cell: A Review”, Vol. 22, 2012, pp. 226-237

[13] Y. Hung, H. Tawfik, and D. Mahajan, “Effect of Terminal Design and Bipolar Plate Material on PEM Fuel Cell Performance”, Vol. 4, 2013, pp. 43-47

[14] S. Litster1, and G. McLean, “PEM fuel cell electrodes”, Vol. 130, 2004, pp. 61-76

[15] A. Arvay a, P. Koski c, L. Cindrella d, P. Kauranen c, and A.M. Kannan,“Characterization techniques for gas diffusion layers for proton exchange membrane fuel cells”, Vol. 213, 2012, pp. 317-337.

# An Efficient Hybrid PSO-ABC Multiobjective Optimization Algorithm and its Application to Engineering Design Problems

Siva kumar G[#1], K Shankar[*2], Thomas kurian[#3], J Jayaprakash[#4]

[#] *Hardware Design and Realisation Division, Solid Motors Design Group, PRSO*

*Vikram Sarabhai Space Centre,Indian Space Research Organisation, Trivandrum,India*

[1]sivacool86@gmail.com

[3]thomas_kurian@vssc.gov.in

[4]j_jayaprakash@vssc.gov.in

[*] *Department of Mechanical Engineering, IIT Madras, Chennai, India*

[2]skris@iitm.ac.in

*Abstract*— **Aiming at improving the exploration ability in multi-objective particle swarm optimization algorithm and enhancing the slow convergence rate in multi-objective artificial bee colony algorithm, a hybrid strategy is proposed. Based on the constrained Pareto dominance criteria one population evolves with the basic PSO operators whereas another population evolves with the basic ABC operators. With elitism strategy, the external archive captures the diverse elite candidates from the swarm and bee population. A diverse elite candidate residing in the least crowded region in the criteria space is dynamically selected, by a novel strategy, as leader for the internal swarm. The size of the external archive is truncated based on parameter less crowding distance. Effectiveness of the algorithm is validated and compared with NSGA-II by using a set of eleven difficult test functions selected from literature. Further, the performance, efficiency and applicability of the algorithm, in solving two practical machine design problems, were compared with well-known NSGA-II. From the available results it was found that the hybrid algorithm outperformed NSGA-II and DSMOPSO in convergence and diversity characteristics of Pareto set.**

*Keywords*— **PSO, ABC, NSGA-II, elitism, diversity, constrained Pareto dominance criteria**

## I. INTRODUCTION

The main aim in a multi-objective optimization problem is to find the Pareto optimal set in the decision space by performing significant computations in the design spaces. Every point in a Pareto optimal front represents a unique combination of maximum/minimum objective values. The contradicting goals in a multi-objective optimization problem are: to find a set of solutions as close as possible to the Pareto-optimal front (Convergence) and to find a set of solutions as diverse as possible (Diversity/Spread) [1]. In this field, NSGA-II, using a Fast Elitist Non dominated sorting and parameter less crowding distance approach, is considered to be the best [2]. Particle swarm optimization (PSO) is a population based heuristic optimization method inspired by the choreography of a bird flock. PSO is superior because it is stochastic population based random process with a sense of direction and memory. The strength of PSO lies in simplicity and fast convergence rate [3]. All the existing multi-objective based PSO suffer from the following serious setbacks like having weak global search ability and using complex global and personal update strategies. Artificial Bee Colony algorithm (ABC) is based on the intelligent behavior of the honey bee swarms [4]. The strength of ABC lies in simplicity and good global search ability (Global exploration and exploitation).But, the existing multi-objective based ABC have a slow rate of convergence and fail to maintain proper diversity/spread of the Pareto set. In view of the above of contradicting features and defects in multi-objective based PSO and ABC, the motivation for this work is to develop a hybrid algorithm which inherits the strengths of both these algorithms at same time overcomes all the above said defects.

The hybrid algorithm basically combines the main operators of DSMOPSO [5] and MOABC [6]. An external archive is used to collect diverse elite candidates. Size of the external archive is truncated to user defined limit based on the least crowding distance removal strategy [5]. A novel leader selection scheme for PSO operator is proposed here. It dynamically selects a diverse elite candidate residing in the least crowded region as the leader based on a counter.

The rest of paper is organized as follows: Section II and III gives a brief description of multi-objective ABC and PSO procedures respectively. In section IV proposed hybrid algorithm is described. Stimulation results using standard benchmark functions are shown in Section V. Section VI discusses the comparison of performance of algorithm with NSGA-II for selected engineering design problems. Finally, Section VII gives a brief conclusion to the paper.

## II. Multi-objective Artificial Bee Colony (MOABC)

There are three phases in the MOABC: (1). Employed bee phase. (2). Onlooker bee phase. (3). Scout bee phase. In the employed bee phase, for each bee an elite bee is randomly selected. A neighbor is generated for each bee based on the basic ABC equation given in (1).The design limits for neighbor are checked. The neighbor replaces the bee if it constrain dominates it otherwise the trail of the bee is incremented by one.

$$V_{id} = x_{id} + \varphi_{id}(x_{id} - x_{kd}) \quad (1)$$

Where i represents the food source, d represents the design parameter and k represents the randomly selected elite individual. $V_{id}$ Represents the new neighbor and $\varphi_{id}$ is a random value between -1 and 1. In the onlooker bee phase, a roulette wheel scheme randomly selects a bee from population based on the probability $p_k$ given in (2).Again an elite bee is randomly picked for each selected bee. A neighbor is generated using (1). The design limits for neighbor are checked. The neighbor replaces the selected bee if it constrain dominates it otherwise the trail of the bee is incremented by one.

$$fit(\overrightarrow{x_m}) = \frac{dom(m)}{Food\ no} \quad (2)$$

Here $fit(\overrightarrow{x_m})$ is the normalized fitness for food source m *.dom(m)* is the number of food sources dominated by food source *m.*

$$p_k = \frac{fit(\overrightarrow{x_k})}{\sum_{m=1}^{Food\ no} fit(\overrightarrow{x_m})} \quad (3)$$

In scout bee phase, stagnant members in bee i.e for which the trail had exceeded the predefined limit, are identified. The identified members are randomly positioned in the feasible region design space based on the equation (4) and their trail counter is set to 0. [6]

$$x_{ij} = xmin_{ij} + rand * \left(xmax_{ij} - xmin_{ij}\right) \quad (4)$$

Newly found diverse elite candidates are added to the external archive and its size is truncated by least crowding distance removal strategy.

## III. Multi-objective PSO (MOPSO)

The MOPSO first initializes a random swarm in the feasible region. During the evolutionary cycle, particles in the swarm are allowed to fly based on the velocity and displacement update equations of basic PSO given in (5) & (6).

$$v(t+1) = \Psi v(t) + C_1 r_1\left(P_{best}(t) - x(t)\right) + C_2 r_2\left(G_{best}(t) - x(t)\right) \quad (5)$$

$$x(t+1) = x(t) + v(t+1) \quad (6)$$

$x$ is the current position of the particle; $v$ is the velocity of particle; $\Psi$ is the inertia weight coefficient (0.4-0.9);$C_1$ is the Cognitive Acceleration component =2; $C_2$ is the Social acceleration component=2 [7]; $P_{best}(t)$ is the historically best candidate that particular particle has found so far: $G_{best}(t)$ is the historically best candidate that the swarm has found so far; $r_1$ & $r_2$are random numbers between 0 and 1;

Velocities of the particles are clamped to prevent oscillations [8].

$$v \in [-v_{max}, v_{max}] \quad (7)$$

If $< -v_{max}$ , then $v = -v_{max}$; else if $v > v_{max}$ , then $v = v_{max}$;

$$v_{max} = 0.25 \times (x_{max} - x_{min}) \quad (8)$$

In the flying process, each particle updates its personal best based on constrained Pareto dominance criteria. New diverse Elite candidates from swarm are added to the external archive. Size of the external archive is truncated based on least crowding distance removal strategy. A diverse elite candidate receding in the least crowded region is selected as leader to promote diversity. A random mutation mechanism with small probability is introduced to enhance the global search capability [5].

## IV. Hybrid PSO-ABC Multi -objective algorithm(HMOOP)

The algorithm combines the procedure for MOABC and DSMOPSO. The outline of the algorithm is shown in the figure 1. They are two key operators for the algorithm:

Hybrid PSO-ABC (Population, trail, leader selection counter)
Initialization
  Initialize the swarm and bee population
  Perform Non Dominated sort of the combined population
  Add the diverse elite candidates to external archive
Repeat
  Perform displacement and velocity update of the swarm
  Update the personal best of the swarm
  Perform Employed bee phase, Onlooker bee phase and scout bee phase of the bee
  Perform a Non Dominated sort of the combined population of bee and swarm
  Add diverse elite candidates to the external archive
  Truncate the size of external archive
  Select the leader from the external archive
Until
Return External archive

Fig. 3 Pseudo code of Hybrid PSO-ABC Multi-Objective Algorithm

### *A. Evolutionary update of external archive*

Algorithm uses an external archive to preserve the non-dominated individuals (elite candidates) found during the flight process [5]. As the evolution process proceeds a lot of elite candidates are found and most of them happen to reside in crowded regions in the objective space. In order to pull the algorithm out of these crowded regions and to increase its search capacity, the size of the external archive is limited to a user-defined value. To maintain the external swarm size to the user defined value, algorithm uses a crowding distance based truncation strategy.

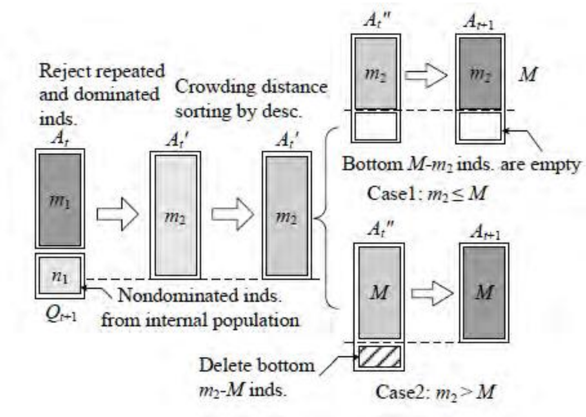


Fig. 2 Evolutionary update of external archive [5]

### *B. Novel Leader selection operator*

The operator first sorts the external archive based on crowding distance in a descending order. All boundary candidates are selected repeatedly, till there leader counter exceeds 5 (user defined limit.). Then, it selects the next diverse candidate receding in less crowded region based on the crowding distance parameter and selects it repeatedly till the leader counter exceeds 5(user defined limit).The operator is dynamic in nature such that it does not allow same elite candidate to be selected for more than 5 times. At the same time any new diverse elite candidate, found at any time during the evolution, will be selected. All the diverse candidates are selected with equal weightage for optimum number of times. This ensures that the Pareto front is uniformly distributed and improves the global search ability of algorithm

## V. STIMULATION RESULTS

The performance of HMOOP was compared with NSGA-II, DSMOPSO and by conducting a trail of experiments for a set of standard benchmark functions.

### *A. Test problems*

Three sets of test problems are selected from literature. First set of test problems includes unconstrained bi-objective problems: KUR [9], POL [10], ZDT1 [11], ZDT2 [11], ZDT3 [11] and ZDT6 [11].KUR and POL have a disconnected and non-convex Pareto optimal front. All ZDT problems, except ZDT6, have 30 design variables. Second set of test problems of test problems includes constrained bi-objective problems: TNK [12], SRN [2] and CONSTR [2].All has two design variables and two constraints. Third set of test problems includes unconstrained tri-objective problems: Sphere [2] and DLTZ2 [1]. Sphere has two design variables whereas DLTZ2 has 12 design variables. The ideal Pareto set for first and second problem set were taken from [13].

### *B. Performance metrics*

1) *Computational Time (t)*: The time taken by the algorithm in finding a Pareto set is measured. Actually it is not performance metric but since the no of iterations taken by each algorithm are not of the same order. This quantity gives an indication of no of function evaluations performed.

2) *Generational distance (GD):* This performance metric gives a measure of convergence rate of the algorithm. It indicates how far the obtained Pareto set is from the ideal Pareto set. The ideal value of generational distance (GD) is 0. A smaller value of GD demonstrates a better convergence to the Pareto set [14].

$$GD = \frac{\left(\sum_{i=1}^{|Q|} d_i^{\,p}\right)^{1/p}}{|Q|} \tag{9}$$

Here, Q is the ideal Pareto set whereas P represents the obtained Pareto set. $d_i$ is the Euclidean distance between the $i^{th}$ element in the Q and nearest neighbor of $i^{th}$ element in P.

$$d_i = min_{k=1}^{|p|}\left(\sqrt{\sum_{m=1}^{M}(f_m^i - F_m^k)^2}\right) \tag{10}$$

Here, $F_m^k$ is the m $^{th}$ objective value of the k $^{th}$ member of P. $f_m^i$ is the m $^{th}$ objective value of the i $^{th}$ member of Q.

3) *Spread (Δ):* This performance metric gives a measure of diversity or distribution of the Pareto set. It is also take care of extend of spread. A smaller value of spread indicates a uniformly distributed Pareto set [15].

$$\Delta = \frac{\sum_{m=1}^{M} d_m^e + \sum_{i=1}^{|Q|}|d_i - d|}{\sum_{m=1}^{M}(d_m^e + |Q|d)} \tag{11}$$

$d_i$ is the Euclidean distance measure between neighboring solutions and d is the mean value of these distances. The parameter $d_m^e$ is the Euclidean distance between the extreme solutions of P and Q corresponding to the m-th objective function.

### *C. Experiment*

The following are the common parameters for experiment: 1).No of Trails of Experiment: 10; 2).Population size for a code: 100; 3).Size of the Pareto front: 100

TABLE VI
INPUT PARAMETERS FOR ALGORITHMS

| Code | Input parameters |
|---|---|
| NSGA-II | Distribution index for SBX crossover = 20<br>Distribution index for Mutation =100.<br>Mutation probability: 0.1 |
| DSMOPSO | $C_1$=2, $C_2$=2,Ψ=0.4-0.9,Constriction factor=1<br>Mutation Probability:0.1 |
| HMOOP | $C_1$=2, $C_2$=2,Ψ=0.4-0.9,Constriction factor=1<br>Mutation Probability:0.1<br>Maximum Leader counter index=5<br>Maximum Trail limit=60 |

### D. *Discussion of results*

All the codes were run from a same PC under identical conditions.

TABLE II
RESULTS FOR FIRST PROBLEM SET

| Problem | Code | N | Mean Performance metric | | |
|---|---|---|---|---|---|
| | | | **t(in s)** | **GD** | **Δ** |
| ZDT1 | NSGA-II | 1500 | 37.95 | 0.00193 | 0.4917 |
| | DSMOPSO | 500 | 9.07 | 0.00020 | 0.3837 |
| | HMOOP | 100 | 4.92 | 0.00019 | 0.4569 |
| ZDT2 | NSGA-II | 1500 | 37.37 | 0.00109 | 0.3058 |
| | DSMOPSO | 500 | 15.55 | 0.000138 | 0.0481 |
| | HMOOP | 30 | 4.36 | 0.000134 | 0.0635 |
| ZDT3 | NSGA-II | 2000 | 37.37 | 0.003294 | 0.4919 |
| | DSMOPSO | 1200 | 14.56 | 0.00002 | 0.3680 |
| | HMOOP | 100 | 4.32 | 0.00046 | 0.5004 |
| ZDT6 | NSGA-II | 2000 | 49.45 | 0.00991 | 0.5506 |
| | DSMOPSO | 1000 | 34.19 | 0.0012 | 0.3821 |
| | HMOOP | 30 | 4.92 | 0.01363 | 0.5829 |
| POL | NSGA-II | 500 | 7.8 | 0.2540 | 0.9869 |
| | DSMOPSO | 300 | 7.44 | 0.0612 | 0.5017 |
| | HMOOP | 100 | 1.69 | 0.0605 | 0.9855 |
| KUR | NSGA-II | 500 | 9.82 | 0.0363 | 0.469 |
| | DSMOPSO | 2500 | 22.4 | 0.0034 | 0.249 |
| | HMOOP | 100 | 3.38 | 0.0031 | 0.986 |

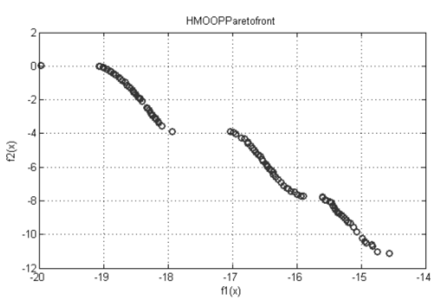


Fig. 3 HMOOP Pareto front for KUR problem

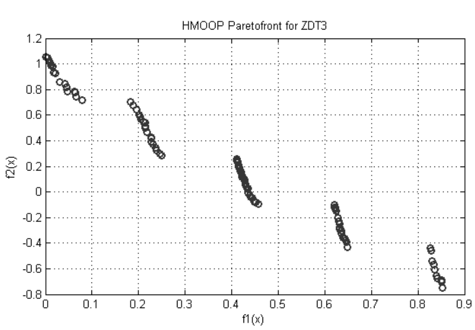


Fig. 4 HMOOP Pareto front for ZDT3 problem

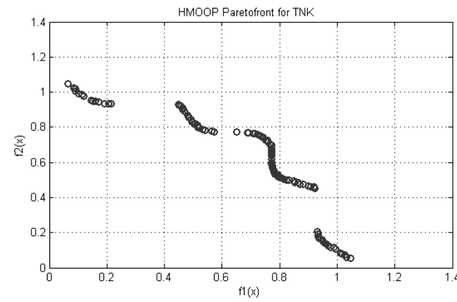


Fig. 5 HMOOP Pareto front for TNK problem

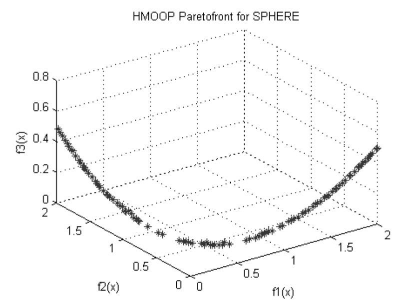


Fig. 6 HMOOP Pareto front for SPHERE problem

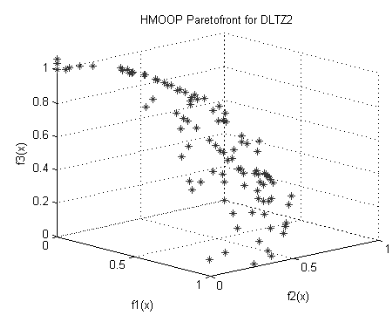


Fig. 7 HMOOP Pareto front for DLTZ2 problem

TABLE III
RESULTS FOR SECOND PROBLEM SET

| Problem | Code | N | Mean Performance metric | | |
|---|---|---|---|---|---|
| | | | **t(s)** | **GD** | **Δ** |
| TNK | NSGA-II | 500 | 17.63 | 0.00087 | 0.4263 |
| | DSMOPSO | 500 | 6.62 | 0.00078 | 0.3079 |
| | HMOOP | 100 | 3.37 | 0.00077 | 0.3850 |
| SRN | NSGA-II | 500 | 5.97 | 0.9982 | 0.9946 |
| | DSMOPSO | 500 | 4.93 | 0.9970 | 0.9915 |
| | HMOOP | 30 | 2.29 | 0.9892 | 0.9969 |
| CONSTR | NSGA-II | 500 | 11.54 | 0.000718 | 0.6717 |
| | DSMOPSO | 500 | 11.25 | 0.000713 | 0.5491 |
| | HMOOP | 30 | 1.77 | 0.000781 | 0.7928 |

TABLEIV
RESULTS FOR THIRD PROBLEM SET

| Problem | Code | N | t(s) |
|---|---|---|---|
| SPHERE | NSGA-II | 300 | 4.94 |
| | DSMOPSO | 200 | 4.08 |
| | HMOOP | 50 | 2.53 |
| DLTZ2 | NSGA-II | 4000 | 77.15 |
| | DSMOPSO | 3000 | 83.86 |
| | HMOOP | 100 | 4.73 |

For first problem set, time taken by HMOOP is significantly less than that for NSGA-II and DSMOPSO. HMOOP had better GD than NSGA-II for all the test problems in this set and better GD than DSMOPSO for ZDT1, POL and KUR problems. HMOOP had better spread than NSGA-II for all the test problems except for KUR problem. In the problems, DSMOPSO had the better spread than HMOOP.

For second problem set, time taken by HMOOP is significantly less than that for NSGA-II and DSMOPSO. HMOOP had better GD than NSGA-II and DSMOPSO for all the test problems in this set except CONSTR problem. HMOOP had better spread than NSGA-II for all the test problems except for CONSTR problem. In the problems, DSMOPSO had the better spread than HMOOP.

For third problem set, only computational times were reported. For third problem set, time taken by HMOOP is significantly less than that for NSGA-II and DSMOPSO.

It can be concluded that for majority of cases, HMOOP had better convergence and diversity in comparison to NSGA-II.

## VI. ENGINEERING DESIGN PROBLEMS

Two engineering design problems are selected to test the efficiency and applicability of the algorithm for multi-objective design optimization. The performance of HMOOP is compared with NSGA-II. The parameters used for NSGA-II and HMOOP are similar to one used for stimulation.

### A. Welded Beam Design

Problem is to design a welded beam for minimum cost and minimum deflection subject to constrains on shear stress on the weld(τ), bending stress on the beam (σ), buckling load on the bar ($P_c$), end deflection of the beam (δ) and side constraints. It is multi-objective optimization problem with four design variables and six constrains. [16].

$$Min.\begin{cases} Cost\ of\ welding = f_1(\bar{x}) = (1+c_1)h^2 l + c_2 bt(l+L) \\ Deflection\ of\ the\ beam(\delta) = f_2(\bar{x}) = \dfrac{4Pl^3}{Ebt^3} \end{cases} \quad (12)$$

Subjected to:

$$\begin{cases} g_1(x) = h - b \le 0 \\ g_2(x) = \delta - 0.25 \le 0 \\ g_3(x) = \tau - \tau_{max} \le 0 \\ g_4(x) = \sigma - \sigma_{max} \le 0 \end{cases}$$

Where,

$$\begin{cases} \tau = \sqrt{(\tau')^2 + 2\tau'\tau''\left(\dfrac{l}{2R}\right) + (\tau'')^2}\ ;\ \tau' = \dfrac{P}{\sqrt{2}hl}\ \ and\ \ \tau'' = \dfrac{MR}{J}\ ; \\ M = P\left(L + \dfrac{l}{2}\right); R = \sqrt{\dfrac{l^2}{4} + \dfrac{(h+t)^2}{4}}; J = 2\left\{\dfrac{hl}{\sqrt{2}}\left[\dfrac{l^2}{12} + \left(\dfrac{h+t}{2}\right)^2\right]\right\} \\ \sigma = \dfrac{6PL}{bt^2}; P_c = \dfrac{4.013\sqrt{EG\left(\dfrac{l^2 b^6}{36}\right)}}{L^2}\left(1 - \dfrac{t}{2L}\sqrt{\dfrac{E}{4G}}\right) \end{cases}$$

Here,
$h \in [0.125,2]; l \in [0.1,10]; t \in [0.1,10]; b \in [0.125,2];$
$c_1 = 0.10471\dfrac{\$}{inch^3}; c_2 = 0.04811\dfrac{\$}{inch^3};$
$L = 14\ inch; P = 6000\ lb; E = 30 \times 10^6 Psi;$
$\tau_{max} = 13{,}600 Psi;\ \sigma_{max} = 30{,}000 Psi;\ G = 12\ \times 10^6 Psi$

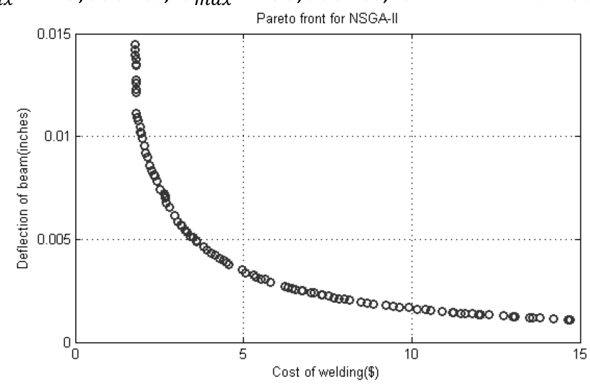


Fig. 8 NSGA-II Pareto front for welded beam design

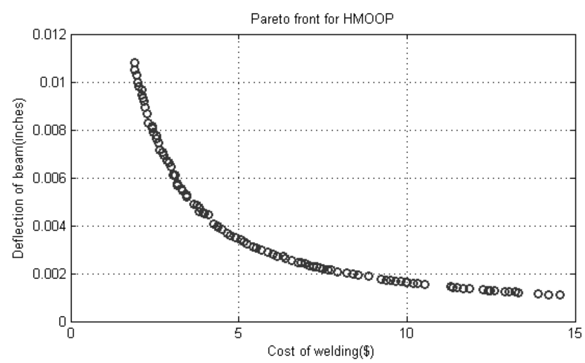


Fig. 9 HMOOP Pareto front for welded beam design

HMOOP took 10.13s whereas NSGA-II took 12.05s to capture the Pareto front. It can be seen that HMOOP is also capable of maintaining a uniform distribution of solutions. It found the minimal cost solution as 1.9022 $ with deflection 0.01082 inches, and the minimal deflection as 0.00109 inches with a cost of 14.5565 $. NSGA-II found the minimal cost solution as 1.773 $ with deflection 0.01447 inches, and the minimal deflection as 0.00109 inches with a cost of 14.694 $. Hence, HMOOP is efficient and is able to find a wide variety of Pareto-optimal solutions.

### *B. Disk brake design*

The objectives of the design are to minimize the mass of the brake and to minimize the stopping time. The variables are the inner radius of the discs, outer radius of the discs, the engaging force and the number of friction surfaces and are represented as $x_1$, $x_2$, $x_3$ and $x_4$ respectively. The constraints for the design include minimum distance between the radii, maximum length of the brake, pressure, temperature and torque limitations. The problem is a mixed, constrained, multi-objective problem [17].

$$Minimize \begin{cases} f_1(\bar{x}) = 4.9 \times 10^{-5}({x_2}^2 - {x_1}^2)(x_4 - 1) \\ f_2(\bar{x}) = \dfrac{9.82 \times 10^6({x_2}^2 - {x_1}^2)}{x_3 x_4({x_2}^3 - {x_1}^3)} \end{cases} \tag{13}$$

Subject to:

$$\begin{cases} g_1(x) = (x_2 - x_1) - 20 \geq 0 \\ g_2(x) = 30 - 2.5(x_4 + 1) \geq 0 \\ g_3(x) = 0.4 - \dfrac{x_3}{\left(3.14({x_2}^2 - {x_1}^2)\right)} \geq 0 \\ g_4(x) = 1 - \left(2.22 \times \dfrac{10^{-3} x_3({x_2}^3 - {x_1}^3)}{({x_2}^2 - {x_1}^2)^2}\right) \geq 0 \\ g_5(x) = \left[2.66 \times \dfrac{10^{-2} x_3 x_4({x_2}^3 - {x_1}^3)}{({x_2}^2 - {x_1}^2)}\right] - 900 \geq 0 \end{cases}$$

Where,$55 \leq x_1 \leq 80; 75 \leq x_2 \leq 110; 1000 \leq x_3 \leq 3000; 2 \leq x_4 \leq 20$

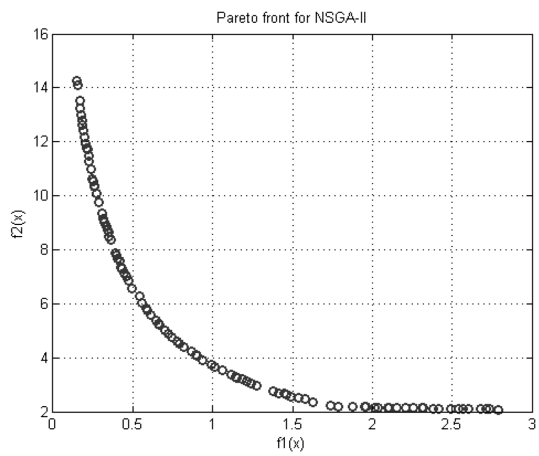


Fig. 10 NSGA-II Pareto front for Disk brake design

HMOOP took 5.8s whereas NSGA-II took 8.9s to capture the Pareto front. It can be seen that HMOOP is also capable of maintaining a uniform distribution of solutions. It found the minimal stopping time as 0.1274 units with maximum mass of 16.66 units, and the minimal mass as 2.07 units with a maximum stopping time of 2.79 units. NSGA-II found the minimal stopping time as 0.15 units with maximum mass of 14.26 units, and the minimal mass as 2.07 units with a maximum stopping time of 2.78 units. Clearly, here HMOOP is superior to NSGA-II as it captures a wide variety of Pareto-optimal solutions with less time.

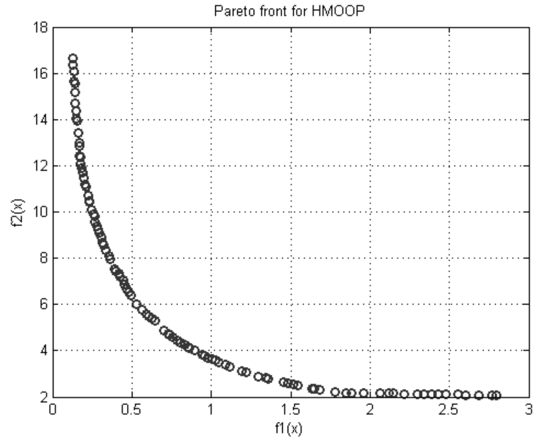


Fig. 11 HMOOP Pareto front for Disk brake design

## VII. CONCLUSIONS

The proposed hybrid algorithm inherits the fast convergence rate of PSO and retains the global exploration and exploitation capability of ABC algorithm with less computational complexity. The novel leader selection strategy captures diverse elite candidates receding in complex broken Pareto fronts. Stimulation results show that the algorithm can handle multi-dimensional design spaces and complex objective spaces with broken optimal Pareto fronts. It also demonstrated the ability of the algorithm to handle more than two objective functions. Welded beam design and disk brake design validated the efficiency and applicability of the algorithm for multi-objective design optimization. Further, results showed the algorithm outperformed NSGA-II in achieving convergence and diversity of the optimal Pareto set.

## ACKNOWLEDGMENT

The authors express their gratitude and sincere thanks to the academic community of IIT Madras, Chennai and scientific staff of ISRO. Authors are deeply indebted to their dependents for their constant moral support and encouragement.

## REFERENCES

[1] K.Deb,“Multi-Objective Optimization using Evolutionary Agorithms.”1st edition John Wiley & Sons,Ltd, 2001.

[2] K.Deb,A.Pratab,S.Agarwal,T.Meyarivan,"A fast and elitist multiobjective genetic algorithm: NSGA-II" IEEETrans.on Evolutionary Computation, vol. 6, pp. 182-197, June 2002.

[3] J. Kennedy and R. C. Eberhart, "Swarm Intelligence." San Mateo, CA:Morgan Kaufmann, 2001.

[4] Karaboga D, Basturk B,“ A powerful and efficient algorithm for numerical function optimization artificial bee colony (ABC) algorithm.”, J Global Optim ,39:459-71,2007.

[5] Li Zhongkai; Zhu Zhencai; Zhang huiqin, "DSMOPSO: A distance sorting based multiobjective particle swarm optimization algorithm," Natural Computation (ICNC), 2010 Sixth International Conference on , vol.5, no., pp.2749,2753, 10-12 Aug. 2010.

[6] R. Akbari, R. Hedayatzadeh, K. Ziarati, B. Hassanizadeh,“A multi-objective artificial bee colony algorithm” Swarm Evol. Comput., 2, pp. 39–52, 2012.

[7] S. sumathi and S. Paneerselvam, “Computational Intelligence Paradigms Theory and Applications Using MATLAB”, Taylor & Francis, Boca Raton, Fla, USA,pp 658-659, 2010.

[8] Kiranyaz, Serkan, Ince, Turker, Gabbouj, Moncef, “Multidimensional Particle Swarm Optimization for Machine Learning and Pattern Recognition”, Springer-Verlag Berlin Heidelberg, pp. 48-49, 2014.

[9] F. Kursawe, “A variant of evolution strategies for vector optimization,”in Parallel Problem Solving from Nature, H.-P. Schwefel and R. Männer,Eds. Berlin, Germany: Springer-Verlag, pp. 193–197, 1990.

[10] C. Poloni, “Hybrid GA for multiobjective aerodynamic shape optimization,”in Genetic Algorithms in Engineering and Computer Science, G.Winter, J. Periaux, M. Galan, and P. Cuesta, Eds. New York: Wiley, pp. 397–414, 1997.

[11] E. Zitzler, K. Deb, and L. Thiele, “Comparison of multiobjective evolutionary algorithms: Empirical results,” Evol. Comput., vol. 8, no. 2, pp.173–195, Summer 2000.

[12] M. Tanaka, “GA-based decision support system for multicriteria optimization,”in Proc. IEEE Int. Conf. Systems, Man and Cybernetics-2, pp. 1556–1561, 1995.

[13] Ideal Pareto set : http://jmetal.sourceforge.net/problems.html

[14] Veldhuizen, D.V,”Multiobjective Evolutionary Algorithms: Classifications,Anaylses, and New Innovations” Ph.D.Thesis,Dayton,OH: Airforce Institiute of Technology. Technical report No.AFIT/DS/ENG/99-01, 1999.

[15] Kalyanmoy Deb and Tushar Goel, “Controlled Elitist Non-dominated Sorting Genetic Algorithms for Better Convergence”, Evolutionary Multi-Criterion Optimization, Lecture Notes in Computer Science Volume 1993, pp 67-81, 2001.

[16] Ray T, Liew KM A swarm metaphor for multiobjectivedesign optimization. Eng Optim 34:141–153, 2002.

[17] Y. N. Wang, L. H. Wu, and X. F. Yuan, “Multi-objective self-adaptive differential evolution with elitist archive and crowding entropy-based diversity measure,” Soft Computing, vol. 14, no. 3, pp. 193–209, 2010.

# Computational Modeling, FEA & 3D Printing of Biomimetic PCL-HA Composite Scaffolds for Bone Tissue Engineering

Lezly Cross[1], Shamnadh. M[2]

*Department of Mechanical Engineering, TKM College of Engineering, Kollam, Kerala, India*

[1]lezlycross@gmail.com

[2]shamnadhm@gmail.com

***Abstract*— Tissue engineering (TE) is an inter-disciplinary area which aims to create, repair and/or replace tissues and organs by combining the use of cells, biomaterials, and/or biologically active molecules. The field highlights mainly on the use of porous 3D scaffolds for the regeneration of damaged or worn out tissues. The current bone tissue engineering strategy consisted of creating a Computer Aided Design (CAD) model of a 3D porous scaffold employing optimum design parameters and fabricate it from polycaprolactone (PCL)-hydroxyapatite (HA) bio composites using a 3D Printer (FDM technology). The scaffolds were developed from layers of directionally aligned microfilaments, using the computer-controlled extrusion and deposition process. In vitro characterization methods were carried out to predict the performance of the engineered constructs. Finite Element Analysis (FEA) was carried out to investigate and compare the results obtained with that of the mechanical compression testing of 3D scaffold models.**

***Keywords*— tissue engineering; scaffolds; polycaprolactone; hydroxyapatite; fused deposition modeling; finite element analysis**

## I. INTRODUCTION

Three-dimensional scaffolds play an important part in scaffold directed tissue engineering because they provide crucial functions as extra-cellular matrices onto which cells can be seeded on to, grow, and subsequently form fresh tissues. To design scaffolds for load bearing tissue replacement, researchers often requires to accommodate multiple biological, mechanical and geometrical design constraints. With definite control of the scaffold external and internal geometry, porosity, pore diameter and interconnectivity, the essential structural integrity, mechanical strength, and transport characteristics, can be furnished for an exemplary micro-environment for cell and tissue in-growth and healing [1].

Additive manufacturing is a significantly emerging field of research for the fabrication of bio resorbable scaffolds in tissue engineering of bone defects. Bio resorbable scaffolds are used in bone tissue engineering to act as a controlled ECM where the cells can attach, differentiate and regenerate tissue. Additive manufacturing methods helps to regulate the microarchitecture of the scaffold which in turn prescribes the geometry of the newly developed tissue [2].

Fused deposition modeling (FDM) is a paramount commercial process for fabricating three-dimensional objects by extrusion of semi-molten filament material from computer spawned solid or surface models (CAD) like in a typical rapid prototyping process. FDM uses a compact temperature controlled extruder to force out a thermoplastic filament material and deposit the semi-molten polymer onto a print bed in a layer by layer process [3].

## II. MATERIALS AND METHODS

### A. Materials

Poly (ε-caprolactone): PCL has a surprisingly low glass transition temperature of -60$^0$C, compared to other bio resorbable polymers used for biomedical applications. It occurs as a rubbery form at room temperature, and moreover has a low melting temperature of 60$^0$C. Another peculiar property of PCL is its high thermal stability. When compared to other tested aliphatic polyesters of decomposition temperatures ($T_d$) between 230$^0$C and 250$^0$C, PCL showed a $T_d$ of 350$^0$C. PCL with number average molecular weight ($M_n$) ca. 80,000 (catalog no. 440744) in the form of 3mm pellets was obtained from Sigma-Aldrich Inc. (St. Louis, U.S.A).

Hydroxyapatite: HA or HAp is a complex phosphate of calcium and is the primary structural constituent of vertebrate bone. It is a very important material for bio ceramics and its appearance is a white powder. HA micro powders with molecular formula $Ca_5(OH)(PO_4)_3$ and average particle size of ≤125µm was synthesized and obtained from the SCT Biomedical Research Institute (TVM, Kerala).

PCL pellets were desiccated at 45°C for 16 hours in a vacuum oven. The physical blend of PCL-HA (25% wt) was attained by adding the PCL pellets and HA powder into the blades of the compounding unit of a Brabender Twin Screw Extruder TSE 20/40 (IIST, Trivandrum) shown in Fig. 1. The compounding was sustained in small uniform lots to ascertain uniformity and constancy. The temperature inside the mixing unit chamber was held at 120°C for uniform blending. The composite lumps were then further dried in a vacuum oven.

*B. Extrusion of PCL-HA Composite Filaments*

The filament fabrication was carried out using a Brabender® Twin Screw Extruder TSE 20/40. Composite pellets were melted at 210°C in the heated chamber by the rotating twin screw rotors. After a hold-time of 10 min, the temperature was reduced to 200°C and the composite melt was extruded through a die exit diameter of 0.07" (1.82 mm). The blade rotor speed was set at 45 rpm. The extruded filaments were cooled in an ice water bath positioned 25 mm below the die exit and the filament was further stretched using a strand stretching unit. This optimum combination of temperature, blade speed and height to water quenching settings produced a filament diameter of 1.7±0.10 mm. The PCL-HA filaments were fabricated to have a constant diameter to pass through the inlet of the extruder of the custom 3D Printer. The filaments were then expelled off the moisture content and kept in a desiccator before the start of the fabrication phase.

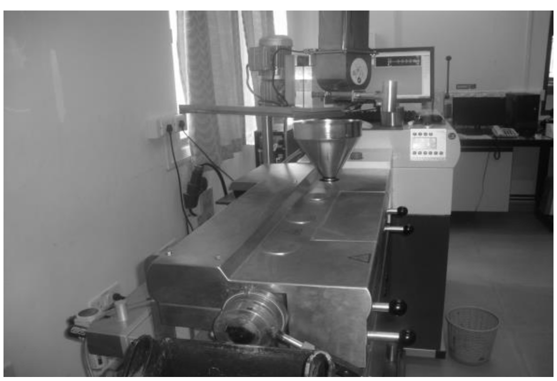

Fig. 1 Brabender® Twin Screw Extruder TSE 20/40

*C. Scaffold Design and Fabrication*

A 3D Printer (Life-Maker, FDM technology) device, developed at the Maker City (Kerala, India), was used to fabricate the 3D porous scaffold models (Fig. 2). Cylindrical models measuring 8mm (Diameter) and 6mm (Height) were initially designed in a CAD software (SolidWorks 2013, Dassault Systèmes S.A.) (Fig. 3a). The STL file format was then imported to the slicing software (Repetier-Host) where it was automatically sliced. This method consists of a slicing algorithm that allocates the STL model into a series of 2D layers of predefined thickness to prepare the contours of the model.

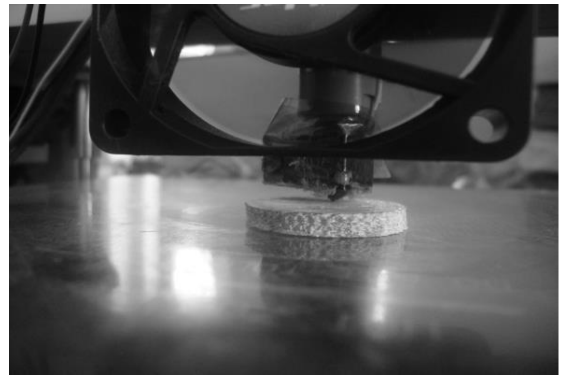

Fig. 2 Life-Maker performing scaffold fabrication

The amount and direction of the micro-filaments (called “raster” in FDM’s context) were determined by organizing several build parameters for the successive layers. The build parameters include the road width of rasters, fill gap between rasters, strut thickness and raster angle [4]. Specific combinations of these parameters and the liquefier temperature and head speed were needed to achieve smooth and constant material flow and raster deposition with adequate adhesion between the nearby layers. Two lay-down patterns $0/90^0$ and $0/60/120^0$ were used to form the honeycomb patterns of square (Fig. 3b) and triangular (Fig. 3c) pores, respectively. A fill gap of 0.6mm and 1.0mm and a road width of 0.6mm were selected. The strut thickness provided was 0.5mm. A cage framework was integrated into the scaffold models to yield better mechanical strength and stability.

Scaffolds were fabricated in two different aspects. Four scaffold prototypes were fabricated (designated A1, A2, B1 and B2). In stage 1, the strut direction for scaffold type A1 and A2 was alternated by 90° from layer to layer, while type A1 had a fill gap of 1.0mm, type A2 was given a fill gap of 0.6mm. In stage 2, for scaffold specimens of type B1 and B2, a 3-angled lay-down pattern of $0^0/60^0/120^0$ (honeycomb-like architecture of 3D triangular pores) was designed where the strut direction was alternated by $60^0$ from layer to layer, while type B1 had a fill gap of 1.0mm, type B2 was given 0.6mm. The models were then sliced using the FDM software.

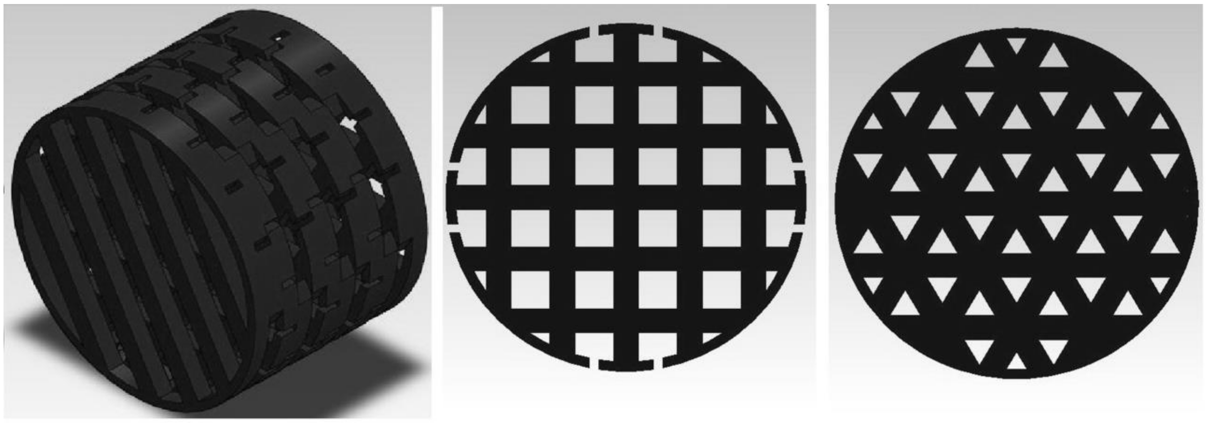

**a)** 3D Scaffold CAD Model **b)** Lay-down pattern of 0/90° forming square honeycomb pores **c)** Lay-down pattern of 0/60/120° forming triangular honeycomb pores

Fig. 3 Scaffold Design

The information was then interfaced to the FDM equipment where the 3D structures were printed in a layer by-layer fashion permitting the extrusion of the material through a T10 (0.254 mm) nozzle tip. The feed material used in the 3D printer to fabricate the scaffolds was PCL-HA bio composites with a melting point of 190$^{\circ}$C in the form of filaments of uniform diameter 1.75mm. Table 1 outlines the various scaffold designs along with their porosities and pore sizes. The liquefier temperature was set at 200±10$^{0}$C, and an optimum head speed (12 mm/s) was selected for consistent material deposition.

## III. CHARECTERIZATION OF SCAFFOLDS

### *A. Porosity*

The theoretical porosity P (%) of the CAD models was evaluated based on the total volume occupied by the struts and the volume of the cylindrical model. Each porosity value was generally calculated as:

$$P = V_a – V_t / V_a \text{ X } 100\% \tag{1}$$

Where, $V_a$ (mm$^3$) is the apparent volume calculated based on the geometry of the scaffold cylindrical block, and $V_t$ (mm$^3$) the scaffold true volume. The value of $V_t$ was calculated from the "Mass Properties" tool from SolidWorks.

### *B. Morphology*

Morphological analysis and surface topography of the 3D structures was carried out using a scanning electron microscope attached with energy dispersive X-Ray analysis (SEM-EDS) system (S-4700-II, Hitachi, USA) to visualize and evaluate the physical integrity of the material filaments and layers, as well to understand if the previously designed pore geometry and size were maintained constant during the fabrication.

### *C. Mechanical Testing*

Mechanical compression tests were conducted on the cylindrical PCL & PCL-HA scaffolds (n = 6 samples) (30mm × 10mm cylinders) using a Universal Testing Machine (INSTRON series 5984, USA) with a 1 kN load-cell adopting the guidelines for compression testing in ASTM standard D695-96. The specimens were compressed at a rate of 1mm/min up to a strain level of approximately 0.6 with the load F (kN) versus deformation d (mm) values recorded throughout. A stress–strain curve was automatically plotted by the BLUEHILL® software based on the stress σ (MPa) and strain ε (%) values of the test specimen. For the tested specimens, the effective modulus of elasticity (compressive stiffness) E (MPa) and the compression strength at yield σy (MPa) was calculated from the stress-strain curve.

### *D. Finite Element Analysis*

The compressive strength for the porous scaffolds were calculated in a macro scale finite element model by using ANSYS Workbench 15.0 (Pennsylvania, U.S.A) and it is to be compared with the results from the mechanical testing of scaffolds with designed porosity. The testing geometries were imported directly into the Structural Mechanics Module in ANSYS Workbench. The models were meshed using 67428 tetrahedral elements and 129235 nodes for B1 specimens with and without cage structures. The models were fixed on the bottom surface in the direction of the applied displacement. The elastic moduli evaluated from the mechanical testing of the PCL-HA (75:25) composite material systems were imported as the bulk elastic modulus for the scaffolds [5] and the Poisson's ratio was assumed to be 0.3 [6]. Material properties were assigned homogenous and isotropic based on optical microscopy and the structure also has been assumed completely elastic.

TABLE I

SCAFFOLD DESIGNS FOR MECHANICAL EVALUATION AND POROSITIES OF MODELS

| Design | Lay down pattern | Distance between struts (Fill Gap) | Pore size | Porosity of scaffolds |
|---|---|---|---|---|
| A1 | $0/90^0$ | 0.6 mm | 785μm | 58% |
| A2 | $0/90^0$ | 1.0 mm | 870μm | 69% |
| B1 | $0/60/120^0$ | 0.6 mm | 650μm | 52% |
| B2 | $0/60/120^0$ | 1.0 mm | 710μm | 60% |

## IV. RESULTS AND DISCUSSION

### A. *Scaffold Design and Fabrication*

Scaffold Gross Morphology: Scaffolds were designed and fabricated with cylindrical external geometry and fully interconnected square and triangular pores (Fig. 4). Process parameters were applied according to the material properties and scaffold geometry [7]. The gaps, struts and internal pore connectivity, as observed under SEM (Fig. 5), demonstrate the use of the Life-Maker 3D Printer to fabricate PCL-HA scaffolds at the micro-scale range. These SEM images clearly depict that the FDM-fabricated microarchitecture of the scaffolds via the $0^0/60^0/120^0$ layered structure can attain a favorable pore size of ~658 x 487µm. Adhesion between successive layers turned out to be good. In general, scaffolds of two groups of porosity values were produced. Using a T10 tip, scaffolds having optimum porosity were fabricated in the range of 52-69%.

Porosity: The mean porosity of the original PCL-HA scaffolds of dimension 30(d) x 10(h) $mm^3$ was about 62%. The observed porosity changes over the strut fill gap distance

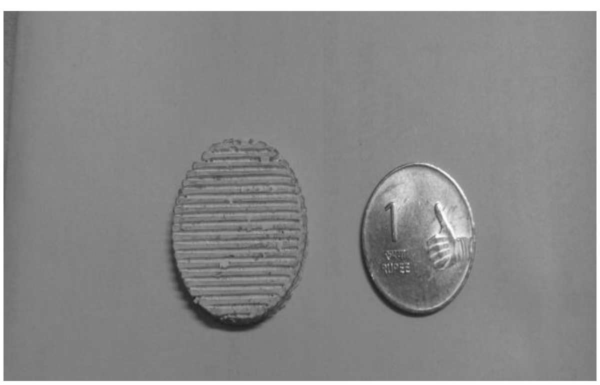

Fig. 4 Overview of the fabricated PCL-HA scaffold

was tabulated and presented in Table 1.

### B. *Mechanical Testing*

The mechanical compression tests were conducted up to about 60% strain. The stress-strain (σ – ε) curves of PCL & PCL-HA (25% wt) scaffolds are plotted in Fig. 6. It can be observed from the graph that the PCL-HA (25%wt) scaffold is stiffer and more resistant to the deformation force, by the steeper tangent. Also, its yield point occurs before the PCL scaffold indicating its less ductile property. Mechanical tests demonstrated that the composite PCL-HA (25% wt) scaffolds were about 1.8 times stiffer than the PCL scaffolds, due to the HA bioceramic reinforcement. The compressive stiffness of the PCL-HA (25% wt) scaffolds was found to be 54.11 MPa. The compressive yield strength of the scaffolds

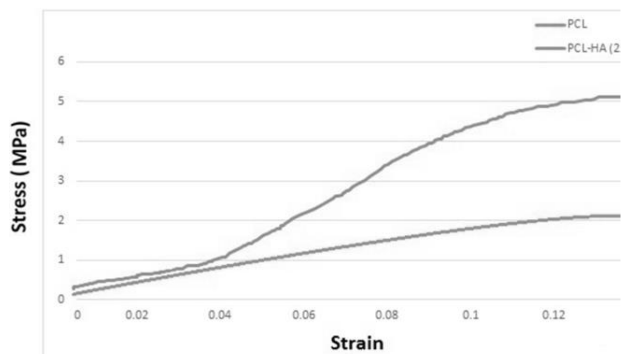


Fig .6 Stress-strain (σ – ε) curves of PCL & PCL-HA scaffolds

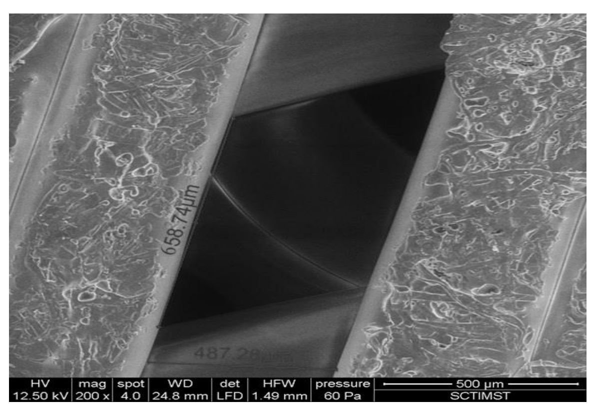


Fig. 5 SEM image showing the pore size of the scaffold

was measured to be 2.87 MPa.

Mechanical tests revealed that the composite PCL-HA (25% wt) scaffolds were about 1.8 times stiffer than the PCL scaffolds, due to the HA bioceramic reinforcement (Fig. 7). Although, the average yield strength was slightly higher, it was not significant. This was anticipated as the overall bulk material within the struts were stiffen by the inclusion of HA but majority of the matrix material was still

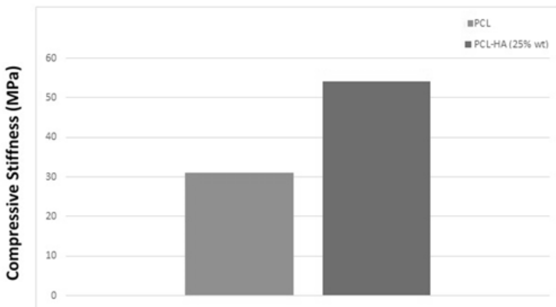


Fig.7 Compressive stiffness for the PCL-HA(25% wt) over PCL

setup was then integrated to the scaffold model B1 in order to evaluate the improvement in the mechanical properties of the structure. Type B1 scaffolds incorporating a cage structure had significant improvement in the compressive strength and was found to be approximately 3.38 MPa. These values were found to be in good accordance with the ultimate compressive strength of the trabecular bone which ranges from 0.22 to 10.44 MPa [8]. Plots of von-Mises stress distributions for the porous scaffolds (type B1 with and without the cage structures) are shown (Fig. 8a and Fig. 8b respectively). Although a large part of the stresses were evenly distributed in the scaffold models, there were minute stress concentrations at some contact points and these stresses did not transcend the yield stress for the bulk material. Compressive yield strength computed by FEA on the designed models were found to be in good agreement and correlated almost well with the measurements from the mechanical testing of specimens obtained experimentally with an average of 10.65% error.

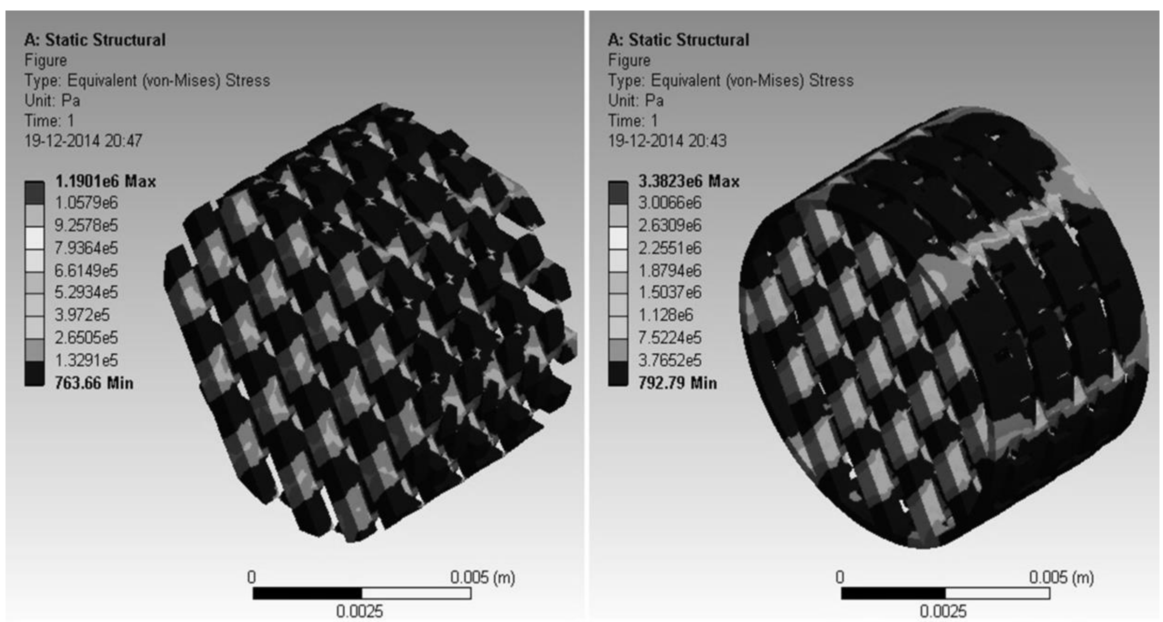


a) Scaffold without a cage structure

b) Scaffold incorporating a cage structure

Fig. 8 von-Mises stress distribution for scaffold models

the weaker PCL (75% wt).

### C. *Finite Element Analysis*

The effective compressive strength were computed for PCL-HA composite (75:25) using the CAD files which were previously designed. An effective compressive strength of approximately 1.19 MPa was evaluated for the scaffold model (type B1) initially without a cage structure. A cage

## V. CONCLUSIONS

Fused deposition modeling (FDM), a rapid prototyping technology, was investigated and successfully applied in this research to produce 3D porous scaffold models with fully interconnected channel networks, and highly controllable porosity and pore size. The composite blended material demonstrated good homogeneity and uniform blending of the HA micro particles. Characterization of the bio-composite structures demonstrated a regular geometry, optimum porosity and significant mechanical strength.

Through computational modeling and finite element analysis, we have demonstrated that the mechanical properties of these scaffolds can be predicted before fabricating with good accuracy. However, success in scaffold guided tissue engineering requires a patient specific anatomical modeling and fabrication of these models followed by the subsequent study and characterization of these biomimetic models in-vivo which is the proposed objective for future research.

## ACKNOWLEDGMENT

The authors acknowledge the technical support given by Maker City and most importantly the scientists at the SCT Biomedical Technology (BMT) Wing and the Chemistry Department of the Indian Institute of Space Science and Technology for their state-of-the-art resources and valuable assistance.

## REFERENCES

[1] D.W. Hutmacher., "*Scaffolds in tissue engineering bone and cartilage*," Biomaterials, 2000, 21: 2529-2543.

[2] Taboas JM, Maddox RD, Krebsbach PH, Hollister SJ., "*Indirect Solid Free Form Fabrication of Local and Global Porous, Biomimetic and Composite 3D Polymer-Ceramic Scaffolds*", Biomaterials, 24, pp.181-194. 2003.

[3] Iwan Zein, Dietmar W. Hutmacher, Kim Cheng Tan, Swee Hin Teoh., "*Fused deposition modeling of novel scaffold architectures for tissue engineering applications*", Biomaterials, Volume 23, Issue 4, 15 February 2002, Pages 1169-1185, ISSN 0142-9612.

[4] Yang S, Leong KF, Du Z, Chua CK., "*The design of scaffolds for use in tissue engineering. Part II. Rapid prototyping techniques*", Tissue Eng. 2002 Feb, 8(1), Pages: 1-11. PubMed PMID: 11886649.

[5] L. Shor, S. Güçeri, W. Sun., "*Solid Freeform Fabrication of Polycaprolactone/Hydroxyapatite Tissue Scaffolds*", Journal of Manufacturing Science & Engineering, 2008; 130:1–6.

[6] Eshraghi S, Das S., "*Micromechanical finite element modeling and experimental characterization of the compressive mechanical properties of polycaprolactone: hydroxyapatite composite scaffolds prepared by selective laser sintering for bone tissue engineering*", Acta Biomaterialia, 2012 August; 8(8): 3138–3143.

[7] Marco Domingos, Dinuccio Dinucci, Stefania Cometa, Michele Alderighi, Paulo Jorge Bártolo, and Federica Chiellini., "*Polycaprolactone Scaffolds Fabricated via Bioextrusion for Tissue Engineering Applications*," International Journal of Biomaterials, vol. 2009. Article ID 239643.

[8] Misch CE, Qu Z, Bidez MW., "*Mechanical properties of trabecular bone in the human mandible: implications for dental implant treatment planning and surgical placement* ", J Oral Maxillofacial Surg. 1999 June; 57(6):700-6

# Effect of Inflating Pressure on the Expansion Behaviour of Coronary Stent and Balloon: A Finite Element Analysis

Arjun R, Hashim V[1], Dileep P N

*Department of Mechanical Engineering, TKM College of Engineering, Kollam, Kerala, India*

[1]hashimtkmce@ gmail.com

***Abstract*—Stenting is one of the most important methods to treat atherosclerosis. Due to its simplicity and efficiency, the use of coronary stent has increased rapidly and more than hundred stent designs have been introduced in the market for angioplasty. The major problem found after stenting is restenosis (re narrowing of the treated artery).The study reveals that the design of the stent and implantation procedure are the two important factors influence the life and effectiveness of a stent. Mechanical behavior of the stent to be analyzed to develop an optimum design and finite element method is the most effective way of analyzing the stent. In this paper the finite element analysis of stent and stent with balloon is carried out to understand the expansion characteristics of the plain stent and stent with balloon with various inflating pressures. A bi linear elasto-plastic material model for stent and hyper elastic material model for balloon have been assumed. Expansion of the stent at various inflating pressures and stress concentration with respect to input pressure and time is plotted. The analysis will give the minimum inflation pressure for the given stent during implantation and hence a study can be used for the selection of stent and optimum inflating pressure for a specific design.**

***Keywords*—Atherosclerosis;Finite element analysis; Coronary stent; Hyperelastic; Restenosis; Inflating pressure**

## I. INTRODUCTION

Coronary heart disease is the leading cause of death worldwide. More than7 million people die each year by this disease. Even though the different clinical treatment methods are available the death rate still continues to be 1 in 4 men and 1 in 3 women in USA due to heart attack.

Coronary heart disease is one of the most common and serious effects of aging. Fatty deposits build up in blood vessel walls and it narrow down the blood flow passage. This phenomenon is known as atherosclerosis, potentially leads to blockage of the coronary arteries and a heart attack. It involves a generic thickening and loss of elasticity of arterial walls thus hardening of the arteries. Small lesions are present in the coronaries of large part of population. But only in a small rate of these cases such lesions evolve in a severe form. Currently atherosclerosis is supposed to be an inflammatory response to the injury caused by an endothelial dysfunction [1].

The most common problem that appears in stent implantation is restenosis. Restenosis is the re-narrowing of artery lumen even after angioplasty or stenting. Studies have shown that restenosis can be correlated with geometric properties of stents such as number of struts, strut width and thickness, and the geometry of cross section of each strut [2]. The geometric characteristics of stent determine the mechanical properties and the pressure loads that a stent can withstand when inserted into the lesion site or the affected coronary artery.

A large number of stents with different geometric and mechanical features are available in the market. Some of the issues in stent design and performance are the large deformations that a stent undergoes during balloon expansion, for which nonlinear elasticity and plasticity need to be considered [3]. One of the most effective methods to investigate the mechanical behaviour of the stent is finite element method. In comparison with expensive experiments carried out in hospitals and laboratories, numerical simulations accomplished using finite element method has advantages in both flexibility and cost [4].

In the present study, finite element analysis is carried out to assess the effect of inflating pressures on coronary stent and balloon. Stress strain characteristics of stent during inflation are found separately for only stent and stent with balloon. We have selected the design of most widely used Palmaz-Schatz stent for our study.

## II. MATERIALS AND METHODS

### *A. Materials*

The Palmaz-Schatz stent is a slotted tube of stainless steel 304 of outer diameter 3mm and inner diameter 2.9 mm with 10mm length. An elasto plastic material was assumed for the stent material. Material properties were chosen to approximately represent the behavior of stainless steel 304. Young's modulus = 193GPa; Density=7.86e-$^{6}$kg/m$^{3}$; Poisson ratio=0.27; Yield strength = 207MPa. [3]. The plastic strain data were also taken from literature to mimic the plastic deformation experienced by the stent during expansion (Table 1).

TABLE: 1 STRESS STRAIN VALUE OF SS 304

| No | Yield Stress | Plastic Strain |
|---|---|---|
| 1 | 138 | 0 |
| 2 | 168 | 0.01 |
| 3 | 172 | 0.02 |
| 4 | 207 | 0.05 |
| 5 | 241 | 0.14 |
| 6 | 267 | 0.28 |
| 7 | 276 | 0.37 |
| 8 | 310 | 1.41 |
| 9 | 345 | 2.94 |

A polyurethane rubber type material was used to represent the balloon. The balloon as a medium to expand the stent was modeled to be 12mm in length. The outer diameter of the balloon was 2.9mm and the thickness of the balloon is 0.1mm.The cylindrical rubber balloon is made of polyurethane which is described by a hyper elastic Mooney-Rivlin strain energy function given in equation 1.

$$W=C_{10}(I_1-3) + C_{01}(I_2-3) + 1/D_1(J-) \ldots\ldots\ldots\ldots(1)$$

Where $I_1$ and $I_2$ are the first and second stretch invariants, J is the volumetric stretch (third stretch invariant), $C_{10}$ (MPa), $C_{01}$ (MPa) and $D_1$are model parameters with values given in Table 2 (Chua et al.2003) [5, 6].

TABLE:2 HYPERELASTIC VALUES OF POLYURETHANE

| Material | ρ(kg/mm$^3$) | $C_{10}$ | $C_{01}$ | $D_1$ |
|---|---|---|---|---|
| Polyurethane | 1.07E-6 | 1.03 | 3.69 | 0 |

## III. MODELING AND ANALYSIS OF ONLY STENT

In the initial stage a model of Palmaz-schatz stent as shown in fig:1 is created in SOLID WORKS software having outer diameter 3mm and inner diameter of 2.9mm, length 10mm and thickness 0.05mm.An elasto-plastic material model was assumed for the stent material which is then analyzed in ABAQUS software to calculate stress distribution and deformation. [7]. Due to the symmetry of the stent by utilizing the correct boundary conditions, a one forth part as shown in figure 1was used to simulate the expansion process. Symmetric boundary conditions were imposed on the nodes of the stent in the plane of symmetry. Both ends of the stent were free from constraints. The stent was subjected to a surface load of uniform internal pressure ranging from 0.4 to1MPa at a constant rate for 1.635ms on the inner surface. The stent expand radially past its elastic limit to a maximum diameter before failure stress was reached. In order to reduce the computational time, it was necessary to set a short simulation time for the analysis. Although this is much shorter than the actual time required expanding the stent, the kinetic energy was checked throughout the entire analysis to ensure that it was negligible compared to the internal energy. Fully integrated elements were used in the model, because reduced integration elements are prone to hourglass deformation. Owing to the structure of model, which was thin and slotted, choosing reduced integration elements was not a good opinion, as a high level of hourglass deformation would be expected.

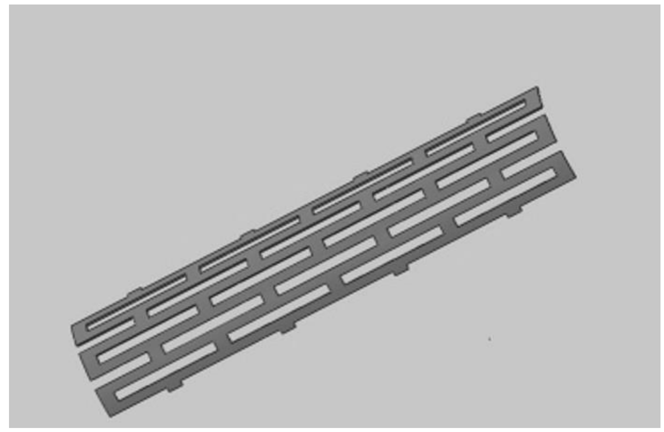

Fig.1 Model of Palmaz-Schatz stent

## IV. MODELING AND ANALYSIS OF STENT WITH BALLOON

By taking the advantage of symmetrical conditions, only a quarter of the stent and balloon was modeled. Symmetric boundary conditions were imposed on the nodes of the stent and balloon in the planes of symmetry where all the nodes perpendicular to y-axis were not allowed to move in y-direction and all the nodes perpendicular to x-axis were not allowed to move in x-direction. Both the ends of the stent were free from any constraints so that the expansion and shortening behavior of the stent would be observed. For modeling purpose, the balloon was assumed to be fully tethered at both ends and hence only the expansion in radial direction was permitted

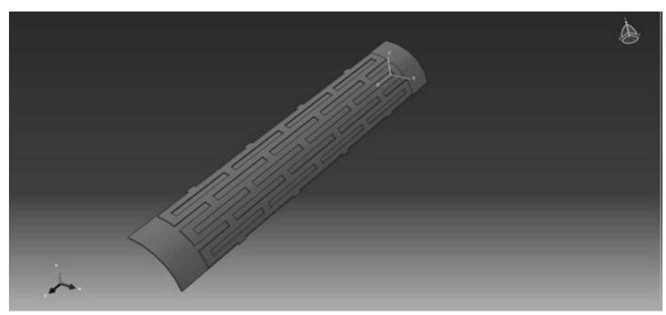

Fig. 2 Stent with balloon

An automatic surface to surface algorithm approach was selected in order to cope with the nonlinear contact problem between the two component surfaces. The pressure load was applied as a surface load on the inner surface of the balloon. Expanding the stent radially past its elastic limit to a maximum diameter before failure stress was reached. The balloon was subjected to a uniform internal pressure ranging from 0.4 to1MPa at a constant rate for 1.635ms

To analyze the expansion of stent along with balloon, the balloon was discretized by 60 elements along its modeled length and 40 elements in circumference with 1 element across the thickness. They were modeled with 8 nodded brick elements using ABAQUS finite element code. A surface to surface contact algorithm was used in order to cope up with the non linear contact problem between the two component surfaces. Material non linearity was accounted for the analysis. The outer surface of the balloon was taken as master surface and the inner surface of the stent as slave surface for the interaction. A penalty frictional formulation with a frictional coefficient of 0.3 was assumed as interaction property. A static general step with non linear geometry was used to analyze the expansion of stent along with balloon. Time period of 1.635ms was used with an initial increment size of 0.1 and maximum increment of 1.635.

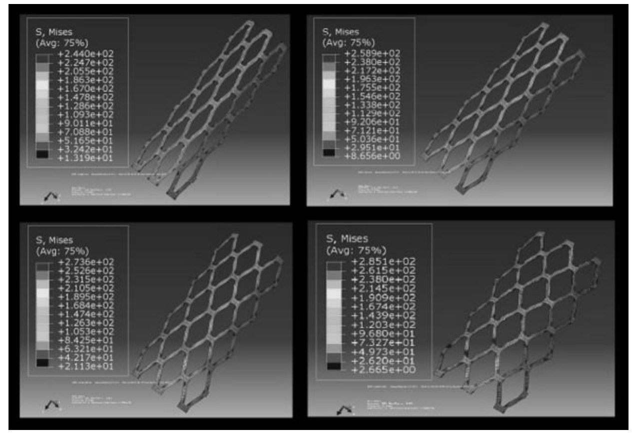


Fig. 3 Maximum and Minimum von Mises stress at varying inflating pressures (only stent)

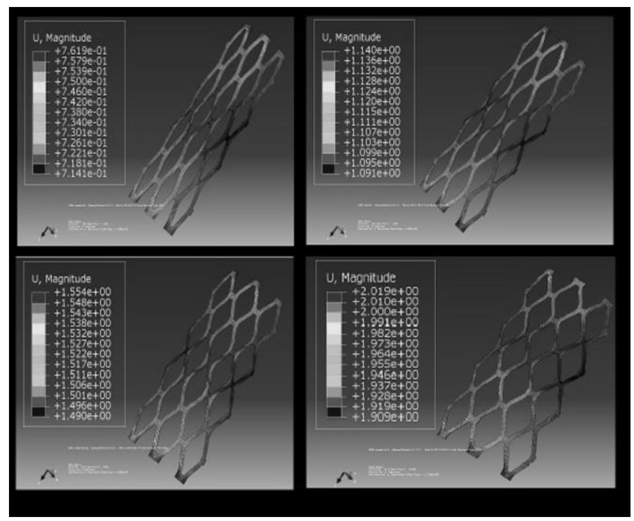


Fig. 4: Maximum and Minimum Deformations at varying inflating pressures (only stent)

## V. RESULTS AND DISCUSSION

### A. *Only stent*

As the stent expands, some parts of the structure in the stent are actually being loaded to their yield point. As a result, the stress in the stent is gradually increased. However, the stress in some areas of the stent is typically high. These areas are found to be located at the four corners of the cells and in the middle of the cells or in the bridging struts. This is because of the struts being pulled apart from each other to form a rhomboid shape of cells during the expansion. At this stage, some parts of the stent are actually going through the elastic deformation. When the stent structure is not able to store the applied forces anymore, first of all the weakest part of the structure collapses or these parts are plastically deformed. The neighboring parts follow through the deformation as the pressure increases. This deformation occurs in a chain reaction until the entire stent is plastically deformed into its new shape. The maximum von Mises stress obtained at an inflating pressure of .409MPa is 244MPa. In comparison with the similar analysis in [6] which shows the maximum von Mises stress of 249MPa, the obtained value in this work is quite acceptable. More over the stress distribution on the bridging strut are seen uniformly distributed and hence the methodology has been validated.

### B. *Stent with balloon*

The ends of the balloon are constrained to avoid dog boning effect of stent and may lead to irregular expansion and impact on artery wall. When the stent expands, because of different distribution of circumferential stress between the free ends and the central part, it bends on edges that causes the diameter at the end sides becomes larger than that of the middle of the stent, this phenomenon is called "Dog boning" By analyzing the stent with balloon model it is found that maximum stress will occur on the mid section of the balloon expandable stent model.

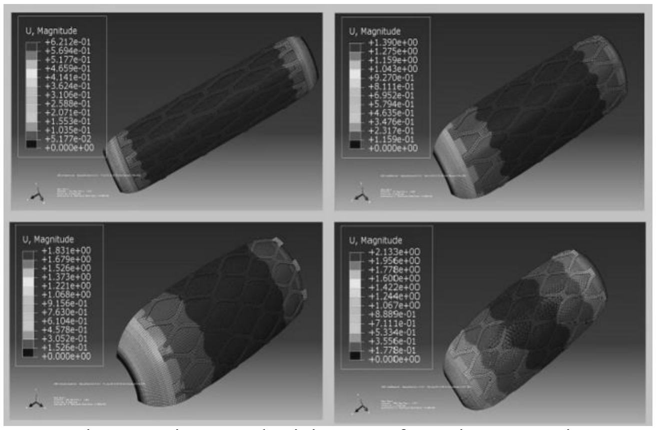

Fig. 5 Maximum and Minimum Deformations at varying inflating pressures on stent with balloon

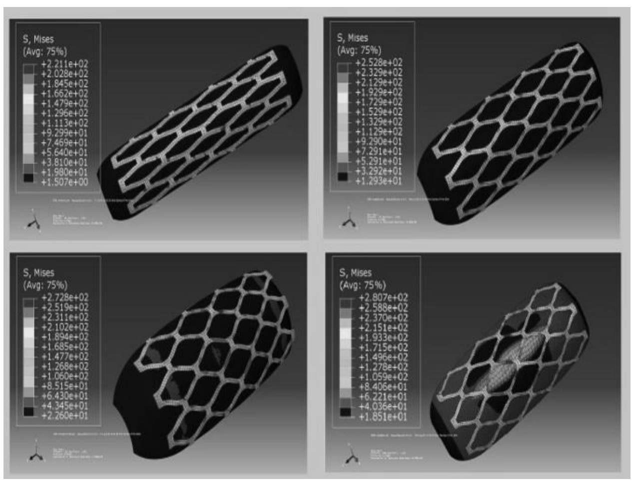

Fig. 6 Maximum and Minimum von Mises stress at varying inflating pressures (stent with balloon)

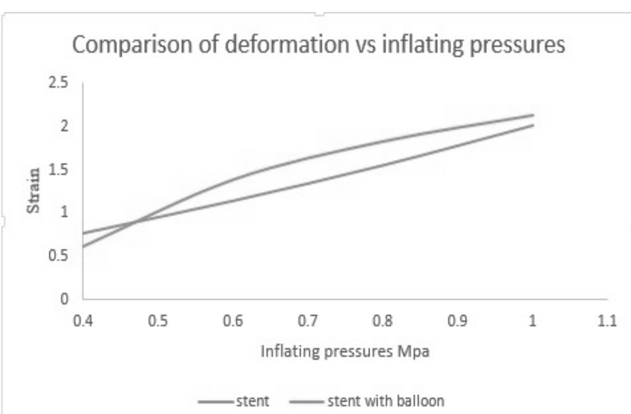


Fig. 7 Inflating pressure Vs Strain

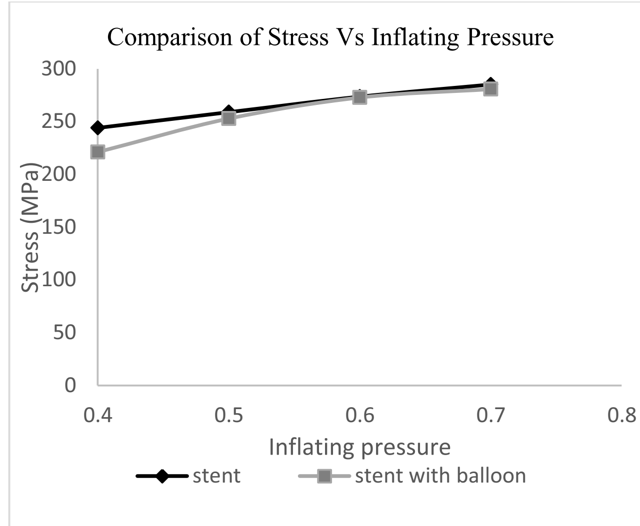


Fig.8 Inflating pressure Vs Stress

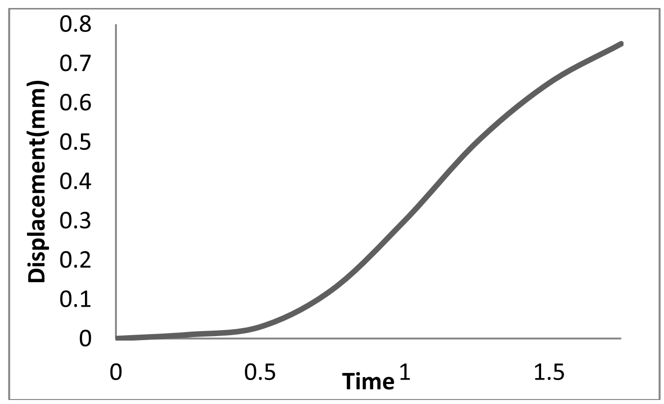


Fig.9 Displacement Vs Time graph for only stent

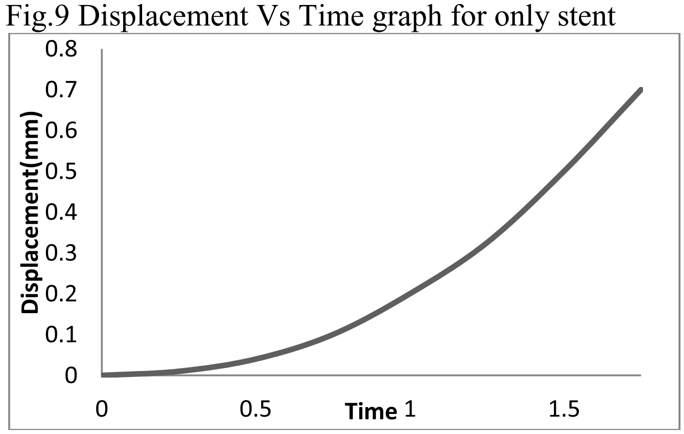


Fig.10 Displacement Vs Time graph for stent with balloon

## VI. CONCLUSIONS

The paper presents a methodology for modeling the expansion of coronary stents used in the treatment of blood vessel stenosis. In order to achieve a more realistic description of the stent implantation procedure, a commercially available palmaz-schatz stent is used. The model includes inflating pressure, stent and balloon .The stress and deformation on balloon and stent is analyzed with variable inflating pressure 0.4,0.6,0.8 and 1MPa . According to the analysis, the stress increases proportionally with inflating pressure. It is found that maximum stress at the four corners of the slots due to the struts being pulled apart from each other to form a ramboid shape with elastic and plastic deformation. The anlaysis of stent with balloon the stress is more on the mid section, since the two ends of the balloon are constrained to avoid dog boning effect. Graph of Displacement Vs Time is plotted for stent and stent with balloon separately. The result shows that the expansion is minimal up to 0.5ms and a sharp increase from 0.5 to 1ms for stent only. The expansion begins at 0.4ms and steady increment was seen for stent with balloon. In actual practice the stent will be expanded with balloon and the expansion is more uniform and steady with better result. The graph of Inflating pressure Vs Strain says only less pressure is required to expand stent with balloon compared to stent only. Both of these results prove that it is better to expand the stent with balloon to have uniform expansion and minimum stress concentration.

The result of the analysis shows the relationship between inflating pressure and deformation .The minimum pressure for getting a required deformation or expansion of stent can be found from this analysis. The lowest inflating pressure is always preferable since low stress concentration on strut and the chance of restenosis is minimum. Hence the study can be used in the selection of proper stent and optimum inflating pressure for a particular design.

## REFERENCES

[1] Schiavone and L G Zhao,"A study of balloon type, system constraint and artery constitutive model used in finite element simulation of stent deployment",Schiavone andZhao Mechanics of Advanced Materials and Modern Processes (2015) 1:1

[2] Julio C. Palmaz, "Intravascular stenting: from basic research to clinical application". Cardiovascular and Interventional Radiology (1992) 15 : 279-284

[3] S.N. David Chua, B.J. Mac Donald, M.S.J. Hashmi "Finite element simulation of stent and balloon interaction",Journal of Materials Processing Technology 143-144 (2003) 591-597

[4] F Migliavacca., L Petrini., V Montanari., I Quagliana., F Auricchio.,R. Pietrabissa "Mechanical behaviour of coronary stents investigated through the finite element method", J.of Biomechanics 35 (2002) 803-811

[5] S.N.David Chua, B.J.MacDonald, M.S.J.Hashmi "Effects of varying slotted tube(stent) geometry on its expansion behaviour using finite element method", J.of Material Processing Technology 155-156 (2004) 1764-71

[6] Rossella B., Francesca G., Francesco M., Gabriele D "Effects of different stent design on local hemodynamic in stented arteries", Journal of biomechanics 41 (2008) 1053-1055.

[7] [7] N Eshghi., M H Hojjati., M Imani., A.M. Goudarzi " Finite Element Analysis of Mechanical Behaviors of Coronary Stent", Procedia Engineering 10 (2011) 3056-3059

# Performance Evaluation of MR Damper by Finite Element Analysis

Riyas.I.P[1], A.Ashfak[2]

*Department Of Mechanical Engineering, T K M College of Engineering, Kollam, Kerala, India*

[1]riyasip7@gmail.com

[2]ashfaktkm@yahoo.com

***Abstract*— The research on magnetorheological (MR) damping technology is booming in recent years. In this paper, a finite element analysis of magnetorheological fluid (MR) damper is reviewed. A Finite Element model was built to analyze and examine a 2-D axisymmetric MR damper, RD-1005-3 Damper, fabricated by Lord Corporation. Six models were developed with MR Fluid 132-DGand their force-velocity characteristics were plotted at saturation current. Most efficient model at moderate cost was identified. The obtained results help designers to create more efficient and reliable MR dampers, and to predict the maximum damping force supplied by the damper.**

***Keywords*—Magnetorheological fluid (MRF),MR damper, finiteelement analysis.**

## I. INTRODUCTION

As a kind of smart material, a magneto rheologicalfluid (MRF) can change from the fluid state to the semi-solid one under an applied magnetic field, and yield the shear stress increment, which is the so-called magnetorheological (MR) effect. Many applications have been made utilizing this phenomenon in various industrial fields, such as MR dampers, clutches, brakes, mounting brackets for vehicles, and other machinery for vibration suppression.MR fluid dampers are semi-active control devices that are capable of generating the magnitude of force sufficient for large-scale applications. Magnetorheological fluids are of interest because of their ability to provide simple, quiet, and rapid-response interfaces between electronic controls and mechanical systems.

The promising MRF is comprised of magnetizable ferromagnetic particles with a diameter of 1–10 μm and the carrier fluid may be silicone oil or synthesized oil. The rheological behavior of an MRF changes with the applied magnetic field. The change is manifested by the development of yield stress that monotonically increases with the applied field. Fig.1 shows the particles will be formed into chain-like fibrous structures in the presence of a high magnetic field. The process of change is very quick, less than a few milliseconds, and can be easily controlled. The energy consumption is also very small, only several watts.

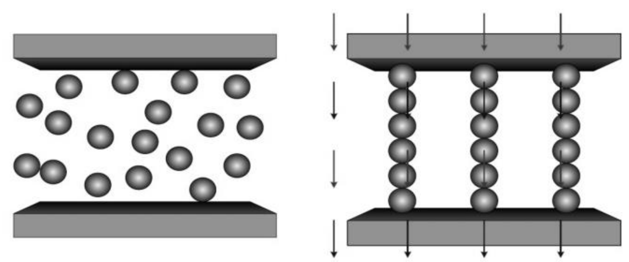


Fig.1 Response of MR fluid to the applied magnetic field

The first patent was issued to inventor JacobRabinow in the 1940s, magnetorheological (MR) fluids have remained mostly a laboratory curiosity with little practical use. In the late 1980s and 1990s, however, researchers began to get serious about developing the commercial viability of MR fluids.El-Aouar (2002)[1] modeled the MR damper with finite element (FE) analysis and discussed the regulations between the generated force and several other parameters. A. Ashfak (2011) [3] presents the design, fabrication and evaluation of magneto-rheological damper. The MR damper was tested and its results were obtained.

In this article, we focus on the magnetic design of an MR Damper and carried out the a finite element analysis of Magnetorheological fluid (MR) damper is reviewed. A Finite Element model was built to analyze and examine a 2-D axisymmetric MR damper, RD-1005-3 Damper, fabricated by Lord Corporation. Six models were developed with MR Fluid 132-DG and their force-velocity characteristics were plotted at saturation current. Most efficient model was identified.

## II. WORKING PRINCIPLE

Fig.2 shows the functional representation of an MR damper, with schematics of the components necessary for operation. The MR fluid is transferred from chamber above the piston to below (and vice versa) was pass through the MR valve.

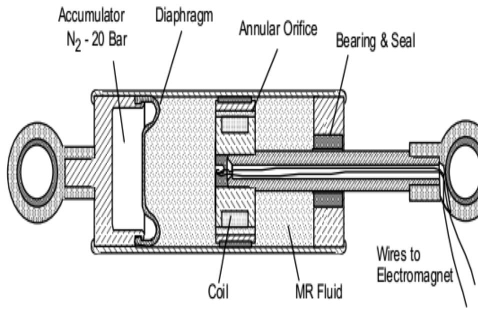


Fig.2 Schematic Representation of MR Damper

The MR valve is a fixed-size orifice with the ability to apply a magnetic field, using an electromagnet, to the orifice volume. This magnetic field results in a change in viscosity of the MR fluid, causing a pressure differential for the flow of fluid in the orifice volume. The pressure differential is directly proportional to the force required to move the damper rod. As such, the damping characteristic of the MR damper is a function of the electrical current flowing into the electromagnet. This relationship allows the damping of an MR damper to be easily controlled in real time.

Different configurations used for MR dampers are shear mode, flow mode, mixed mode and squeeze mode. Usually shear mode is used for low force applications. Hence MR dampers for vehicle suspensions are designed using the mixed mode or flow mode configurations.

## III. MR DAMPER MATHEMATICS

MR fluid behaves in two distinct modes: off state and activated state. While Newtonian like behavior is common in the off state, the fluid behaves as a Bingham plastic with variable yield strength when activated. Fluid flow is governed by Bingham's equations as shown below [1].

$$\tau = \tau_y(\mathrm{H}) + \eta\dot{\gamma} \qquad (1)$$

Fluid shear stress τ depends on magnetic field H and plastic viscosity η. τy represents the field dependent yield stress and ($\dot{\gamma}$) is the fluid shear rate.The pressure drop (ΔP) is assumed to be the sum of the viscous component ($\Delta P_\eta$) and a field dependent induced yield stress component ($\Delta P_\tau$) as shown below [1].

$$\Delta P = \Delta P_\eta + \Delta P_\tau = \frac{12\eta QL}{g^3 w} + \frac{c\tau_y L}{g} \qquad (2)$$

Q represents the pressure driven MR fluid flow and L, g and w represents the length, fluid gap and the width of the flow orifice that exists between the fixed magnetic poles as shown in the Fig.2.The constant c, varies from 2 to 3 depending on what $\frac{\Delta P_\tau}{\Delta P_\eta}$; i.e.c=2 when, $\frac{\Delta P_\tau}{\Delta P_\eta} \leq 1$; c=3 when, $\frac{\Delta P_\tau}{\Delta P_\eta} < 100$ [3]

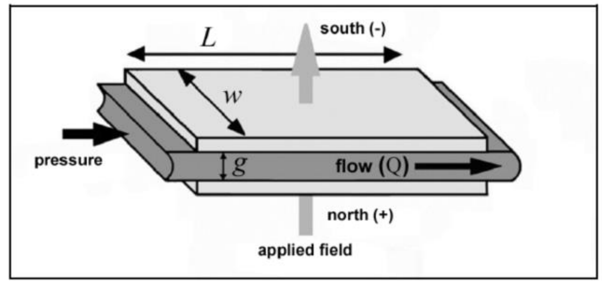


Fig.3 MR fluid in valve mode

The shear rate is a function of the fluid velocity[1]. Shear rate ($\dot{\gamma}$) is defined as

$$\dot{\gamma} = \frac{\mathrm{v}}{2\mathrm{g}} \qquad (3)$$

Where v = relative fluid velocity,
g = annular gap

The plastic viscosity (η) is a function of the shear rate ($\dot{\gamma}$) was characterized by an exponential equation of the form as below [1]

$$\eta = 6895 \text{ X } 0.006\dot{\gamma}^{-0.6091} \qquad (4)$$

The pressure differential is directly proportional to the force required to move the damper rod. To calculate the force that is developed along the MR fluid gap. We multiply the off-state pressure with the area of the piston ($A_\eta$) and the on-state pressure with the active fluid area ($A_\tau$). The total force developed is the sum of a viscous shearforce component and magnetic field dependent shear force component as below [3]:

$$F = \Delta P_\eta . A_\eta + \Delta P_\tau . A_\tau \qquad (5)$$

Since MR fluids behave as non- Newtonian fluids, the viscosity is not constant with varying fluid velocity (v). Therefore, it is important to define the shear rate as a function of the fluid velocity. Shear rate ($\dot{\gamma}$) is defined as shown below:

$$\dot{\gamma} = \frac{\mathrm{v}}{2\mathrm{g}} \qquad (6)$$

v = relative fluid velocity,
g = annular gap

The plastic viscosity (η) is a function of the Shear rate ($\dot{\gamma}$) was characterized by an exponential equation of the form as shown below [1]

$$\eta = 6895 \text{ x } 0.006\dot{\gamma}^{-0.6091} \qquad (7)$$

## IV. MODELLING AND THE FORCE-VELOCITY CHARACTERISTICS OF AN MR DAMPER

### *A. Design Configuration*

An axis-symmetric model in ANSYS is used in this study. The geometry, specifications and materials are the same as the RD-1005-3 MR damper [1] manufactured by the Lord Corporation as shown in Fig.4. The piston dimensions of MR damper according to Fig. 4 are given in Table I.

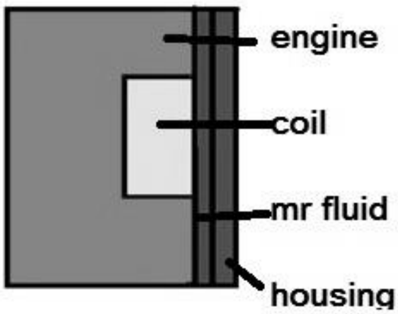


Fig 4. Modeled MR Damper

TABLE 1. RD-1005-3 DIMENSIONS

| Element | Dimension (mm) |
|---|---|
| Housing | 2.692 × 26.72 |
| MRF | 0.495 × 26.72 |
| Engine | 16.167 × 26.72 |
| Coil | 12.65 |

*B. Element Type and Input Parameters:*

PLANE13 in ANSYS is used as the element for the model. It is a 2-D quadrilateral Coupled-Field-Solid, which contains four nodes. PLANE13 has a 2-D magnetic, thermal, electrical and piezoelectric field capability with limited coupling between the fields. The element has nonlinear magnetic capability for modeling B−H curves.

For a static (DC) current, ANSYS requires the current to be input in the form of current density (current over the area of the coil) as shown below [1]:

$$J = \frac{NI}{A} \tag{8}$$

Where, J = current density, N = numbers of turns of wires (900),I= current (0 to 1.8 A, with an interval of 0.2A) &A = the electrical coil area. Flux parallel boundary condition was assumed. B-H curve for the MR Fluid were taken from reference [1]

*C. Calculating Magnetic Flux Densities and Fluid Shear Stress:*

After inputting the above parameters the problem was analyzed for various currents from 0 to 1.8 Amp. For a given current, we can determine the magnetic flux density at the Engine, MR Fluid, Coil and the Damper Housing for 0.2Amp current is as shown in Fig. 5. The higher flux density in the MR gap that was observed in Fig. 5 is also shown in this Fig. 6. The electrical current through the coil can be varied to change the magnetic flux density.

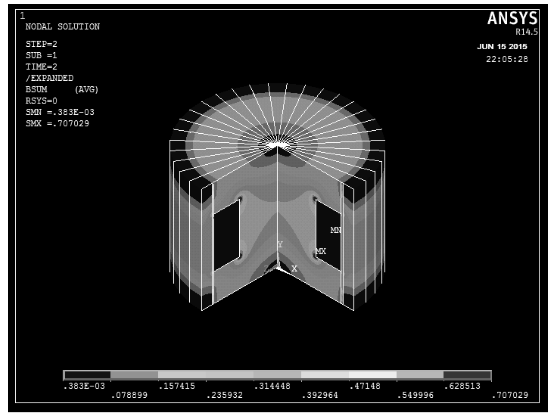


Fig 5. Magnetic Flux Densities Plot for 0.2A

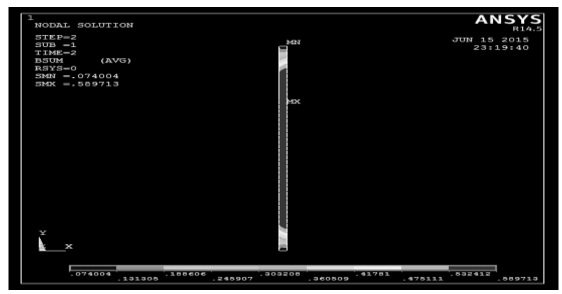


Fig 6. Magnetic Flux Densities along gap for 0.2A

From the numbers generated from nodal solution, we can find the average value of the magnetic flux density ($B_f$) by using the following [1]:

$$B_f = \frac{1}{2}(B_{Max} + B_{Min}) \tag{9}$$

The obtained magnetic flux density, through the fluid gap for various current after analysis were given in the table 2.

TABLE 2: $B_F$ FOR DIFFERENT CURRENTS

| Current (Amp) | Bf (T) |
|---|---|
| 0 | 0 |
| 0.2 | 0.322885 |
| 0.4 | 0.371 |
| 0.6 | 0.4514 |
| 0.8 | 0.57795 |
| 1.0 | 0.656331 |
| 1.2 | 0.7063 |
| 1.4 | 0.754816 |
| 1.6 | 0.804 |
| 1.8 | 0.855 |

The effect of magnetic induction on the shear stress ($\tau_y$) of some MR fluids can be characterized as shown below[1]:

$$\tau_y = 6.298{B_f}^4 - 25.824{B_f}^3 + 26.639{B_f}^2 - 0.438B_f \tag{9}$$

As the magnetic field's strength increases, the resistance to fluid flow at the activation regions increases until the saturation current has been reached.

*D. Plotting Force – Velocity Characteristics:*

The change in shear stress of the MR fluid causes a pressure differential for the flow of fluid in the orifice volume. Thus the "On-state" ($\Delta P_\tau$) and "Off –state" ($\Delta P_\eta$)pressure components can be calculated for each shear stress as discussed in section 3. Similarly the pressure differential is directly proportional to the force required to move the damper rod. Thus force can also be calculated as discussed in section 3. Using Matlab we provided the force – velocity plot of the model designed in ANSYS for a velocity input (0-0.635 m/sec), as shown in Fig. 7.

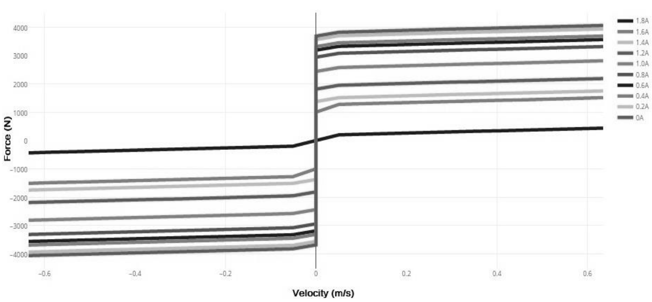


Fig. 7 Force vs. Velocity Characteristics for Different Current

Looking at the Fig. 7 and Table II, we can conclude that the fluid reached saturation at approximately 1.6 to1.8 Amps. The maximum force, results from 1.6 Amps, is nearly the same as the one at 1.8 Amps. Beyond 1.8 Amps, the damper would not provide a much higher force because it has reached its rheological saturation point.

## V. PROPOSED DAMPER MODELS

Six different models were developed by altering the MR damper piston. Here in this section the current considered is the saturation current (i.e.1.8Amp), under the consideration that beyond 1.8 Amps, the damper would not provide as much higher force because it has reached its rheological saturation point. For all the models discussed below the MR Fluid used was MRF 132-DG, developed by Lords Corporation. Fig. 8 to 13

*A. Model 1:*

It is the base model. Its dimension is same as that of the RD-1005-3 MR damper. Using MRF 132-DG and at 1.8Amp the analysis were done. Magnetic Flux densities were plotted. Figure 8 shows the model 1.

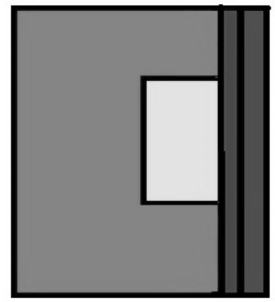

Fig 8. Model 1

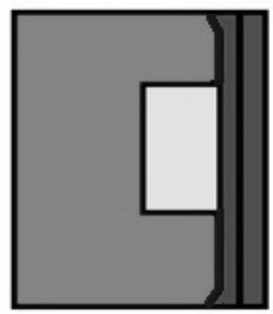

Fig 9. Model 3

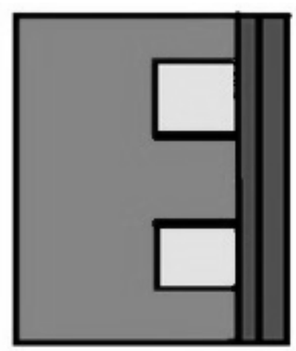

Fig 10. Model 3

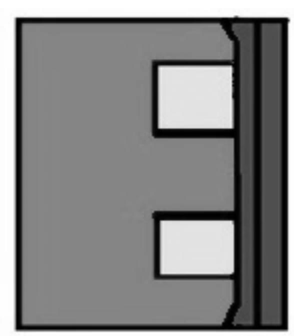

Fig 11. Model 4

*B. Model 2:*

Fig. 9 shows the model 3. This was developed by adding a 0.2mm fillet at both edges of the piston. This model shows a hike in magnetic flux densities.

*C. Model 3:*

Fig. 10 shows model 1. This model was the modification of model 1. Two coils were introduced instead of one. Dimensions of each coil were half of that of model one. 900 number of turns was divided 450 and applied to each coil. A considerable hike was noticed in magnetic flux density. Cost of manufacturing will be more than model 1.

*D. Model 4:*

Fig. 11 shows the model 3. This is the modification of model 3.Two coils were introduced instead of one. Dimensions of each coil were half of that of model one. 900 number of turns was divided 450 and applied to each coil and adding a 0.2mm fillet at both edges of the piston. A considerable hike was noticed in magnetic flux density. Cost of manufacturing and mass will be more than model 3.

## VI. SELECTION OF OPTIMUM DAMPER

*A. Obtaining Magnetic Flux densities and Plotting Force Velocity Characteristics.*

Analysis was done in ANSYS and average value of magnetic flux densities was plotted. The obtained magnetic flux density, through the fluid gap for 1.8 Amp after analysis for four models were given in the Table 3

TABLE 2: $B_F$ FOR DIFFERENT MODELS AT 1.8 AMP

| Model | Bf min | Bf max | B f (T) |
|---|---|---|---|
| Model 1 | 0.931872 | 1.75 | 1.34 |
| Model 2 | 1.127 | 1.79 | 1.45 |
| Model 3 | 1.286 | 1.94 | 1.613 |
| Model 4 | 1.28529 | 1.9532 | 1.62 |

we can generate the shear stress along the MR fluid gap using equation 9.Referring to section 3 we can generate the MR damper force responses.Using MATLAB we provided the force – velocity plot of all the four models designed in ANSYS for a velocity input (0-0.635 m/sec) and 1.8A current, as shown in Fig 12.

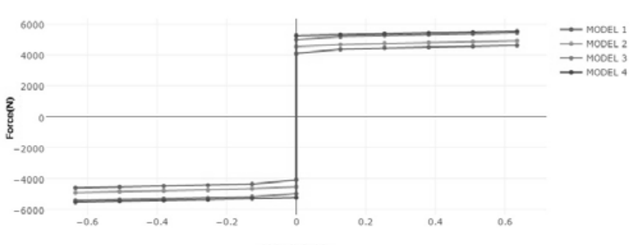


Fig 12. Damper Force characteristics for 4 Models at 1.8 Amp

*B. Selection of Optimum Damper:*

The maximum force reached at the saturation current is shown in Fig15. This data was obtained from Fig 14.

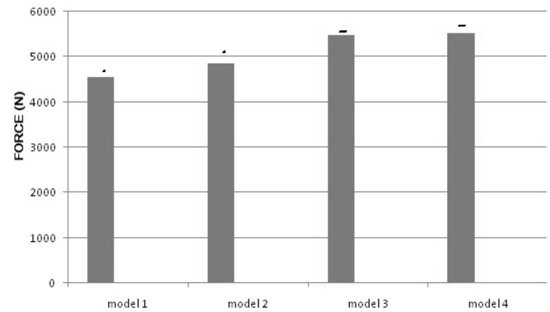


Fig 13. Maximum Forces Resulting for Four Different Piston Configurations

Studying Fig. 15, without increasing the size and number of turns among these four models, the Model 4 would be the most advantageous design, since it provides the largest force among the six models with same envelope area and less cost for manufacturing. Thus the "Optimum Designed Model" is Model 4.

## VII CONCLUSION

In the present paper, the performances of a MR fluid damper with four different configurations are studied. It can be concluded from the evaluation of the above models of MR damper that, the model with filleted ends gives optimum pressure drop with respect to magnetic flux density as well as flow rate. This implies that higher loads can be carried by the damper even with a small capacity.

## REFERENCES

[1] [1] W. H. El-Aouar, "Finite element analysis based modeling

[2] of magneto rheological dampers," Master of Science, Blacksburg, Virginia, September 2002.

[3] [2]G.Yang et al. "Large-scale MR fluid dampers: modeling and dynamic performance considerations", Science Direct J. Engineering Structures 24 (2002) pp 309–323.

[4] [3]A. Ashfak et al. "Design, Fabrication and Evaluation of MR Damper",International Journal of Aerospace and Mechanical Engineering5:1 2011pp 27-32.

[5] [4]AnsysInc, "Low Frequency Electromagnetic Analysis Guide", Guide Release 12.1 November 2009, pp 1-432.

[6] [5]David Simon & Mehdi Ahmadian, "Vehicle Evaluation of the Performance of Magneto Rheological Dampers for Heavy Truck Suspensions" ASME J. Vibration and Acoustics, July 2001, Vol. 123,pp 365-375

# Handle Interlock Mechanism Development: A Reliability Perspective

S. B. Rane[1], Ranjit A. Patil[2]

*Mechanical Engineering Department, Sardar Patel College of Engineering, Mumbai, India*

[1]s_rane@spce.ac.in

[2]ranjit6044@gmail.com

*Abstract*— **The paper illustrates reliability improvement of Handle Interlock mechanism of Industrial switchboards modules. Module is withdrawable part of switchboard, housing switchgear and control gear component for a feeder circuit. Reliability is calculated based on failure data before (stage I) and after improvement (stage II) by using life time distribution and reliability block diagram. In stage II reliability is improved by taking corrective actions on all possible failure modes. For obtaining more accurate result we need to test more components, so method is time consuming and expensive. The reliability of mechanism is improved from 37% to 99 % by redesigning the mechanism.**

*Keywords*— Reliability, Mechanism Development, FTA, Lifetime Distribution, Failure mode, Minitab

## I. INTRODUCTION

In most applications an interlock is used to prevent a machine from harming its operator or damaging itself by stopping the machine. Interlock shown below is used as SCPD [Short Circuit Protection Device] handle interlock.

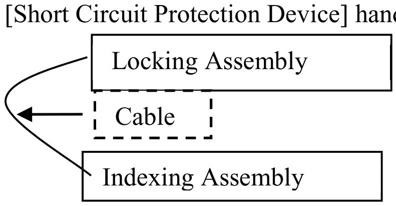


Fig. 1 Schematic of Handle Interlock Mechanism

In interlock mechanism indexing assembly interlocks the handle of SCPD by use of nylon cable. The major components of mechanism are as follows

Control fascia cover, Shaft shape component, Inner & Outer Cable, Cable support, Nylon cable, Base plate, Upper lever, Cam lock, Stopper lever with spring pin. Motion transfer in mechanism is shown in diagram given below.

### A. *Motion Transfer Diagram*

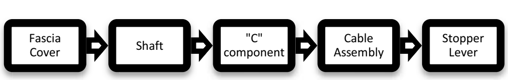


Fig. 2 Motion Transfer Diagram

The motion is transferred as follows:

1. The indexing subassembly houses the control fascia cover providing the access for mechanism handle, used to change the states of the module.
2. The motion of the control fascia cover is transferred by the 'C-Component' to the stopper lever mounted on the bracket through the cable assembly.
3. The stopper lever has a spring pin fixed on its surface and engages with the cam mounted on the SCPD handle shaft. The stopper lever movement is controlled by control fascia.
4. The cam on the SCPD extended shaft rotates when the knob is rotated. The cam is designed in such a way that, when the SCPD is ON, it restricts the movement of the stopper lever and control fascia cover.
5. When the SCPD is OFF and the control fascia cover opened, the spring pin on the stopper lever engages with the cam thus restricting it from switching ON.

### B. *IEC Standard*

International Electro-technical Commission gives following details about mechanical operation. IEC 61439 – Low Voltage switchgear and control gear assemblies.

This ensures that the components of the system are mounted in such a way that through normal use, they will not fail or change the capabilities of the switchboard. As per the standards the mechanism should withstand the 200 operations.

## II. LITERATURE SURVEY

Literature survey mainly consists of reliability, importance of reliability, reliability tools etc.

Different researchers define reliability as follows.

Reliability is the probability that an item will perform its assigned mission under specified conditions and for a given time t [1], [2], [5]. Reliability has become a key factor in the design and operation of today's large, complex, and expensive mechanical systems. The integrity of modern mechanical systems is strongly dependent upon the durability and reliability of the components. However, reliability theory depends heavily on an understanding of failure physics modelling and on the techniques of probability and statistics [6].

## III. Problem Definition

SCPD handle interlock links the mechanism handle (used to change different states of the module viz. Service, Test, Isolated) and SCPD (Short Circuit Protection Device) for Switchboard module. The main function of the interlock is to prevent the operator from an accident caused by arcing. So reliability of mechanism should be high.

The interlock is designed in order to serve the following purposes:

1. When SCPD is in ON condition, the access to main mechanism handle should be blocked
2. When the access to mechanism handle is opened, the operator is restricted to switch on SCPD.

## IV. Testing Details at Stage I and stage II

Reliability computation based on lifetime observation data plays an important role in almost all the aspects of mechanical manufacture industry, especially in design and production [7][8][9][10][11].Three mechanisms were manually tested for 300 operations.

TABLE I
TESTING DETAILS AT STAGE I AND STAGE II

| Sr. No | Number of operations | | Number of failures | |
|---|---|---|---|---|
| | Start | End | Stage I | Stage II |
| 1 | 0 | 50 | 1 | 0 |
| 2 | 51 | 100 | 5 | 0 |
| 3 | 101 | 150 | 6 | 0 |
| 4 | 151 | 200 | 8 | 0 |
| 5 | 201 | 250 | 6 | 0 |
| 6 | 251 | 300 | 5 | 6 |
| 7 | 300 | 315 | - | 3 |

Table I shows the test results.

For lifetime analysis, it is important to identify different types of failure in a component. A failure mode of a component is the consequence of the mechanism through which the component fails [12]. For reliability calculation Minitab 17 software is used in which first step is to find goodness of fit for selection of proper distribution.

## V. Result and discussion at Stage I

### A. *Goodness of Fit-*

Minitab displays up to two goodness−of−fit statistics to help us compare the fit of distributions. Anderson−Darling statistic is used for the maximum likelihood (MLE) and least squares estimation (LSE) methods. Pearson correlation coefficient is used for the least squares estimation method. The Anderson−Darling statistic is a measure of how far the plot points fall from the fitted line in a probability plot. The statistic is a weighted squared distance from the plot points to the fitted line with larger weights in the tails of the distribution. Minitab uses an adjusted Anderson−Darling statistic, because the statistic changes when a different plot point method is used. A smaller Anderson−Darling statistic indicates that the distribution fits the data better.The Pearson correlation measures the strength of the linear relationship between the X and Y variables on a probability plot. The correlation will range between 0 and 1, with higher values indicating a better fitting distribution.

For the analysis Maximum likelihood estimation is used due to following advantages like

1. Distribution parameters estimates are more precise than least squares (XY).
2. Allows you to perform an analysis when there are no failures when there is only one failure and some right censored observations.
3. The maximum likelihood estimation method has attractive mathematical qualities [13].

TABLE II

DETERMINING THE BEST-FIT DISTRIBUTION FOR THE OF FAILURE DATA OF STAGE 1 USING MAXIMUM LIKELIHOOD ESTIMATION IN MINITAB 17.

| Distribution | Anderson-Darling(adj) |
|---|---|
| Weibull | 1.423 |
| Lognormal | 1.563 |
| Exponential | 3.233 |
| Loglogistic | 1.412 |
| Normal | 1.424 |
| Logistic | 1.411 |
| 3 Parameter Weibull | 1.426 |
| 3 parameter Lognormal | 1.424 |
| 3-Parameter Loglogistic | 1.411 |
| Smallest Extreme Value | 1.428 |

Table II shows goodness of fit for failure data of stage 1. A smaller value of Anderson−Darling statistic indicates that the distribution fits the data better. From table Anderson darling statistic for 3-Parameter Loglogistic is closest to 0. So 3-Parameter Loglogistic distribution is selected [13].

All plots like probability, survival, and hazards shown in this work are obtained by using Minitab 17 software. Hence plots for different distributions are as follows

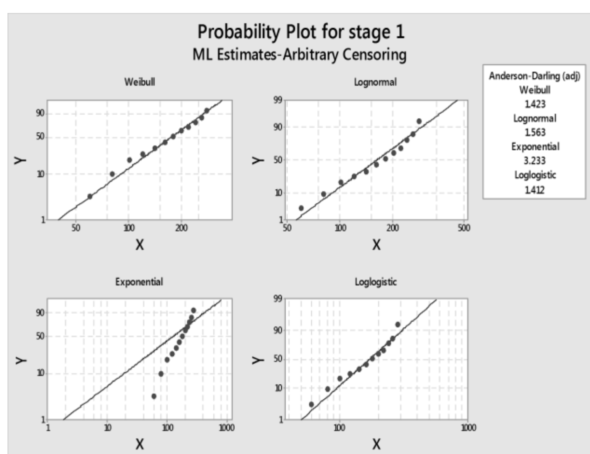


Fig 3(a)

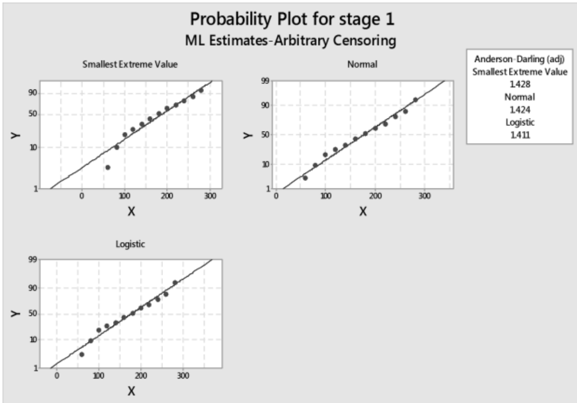


Fig 3(b)

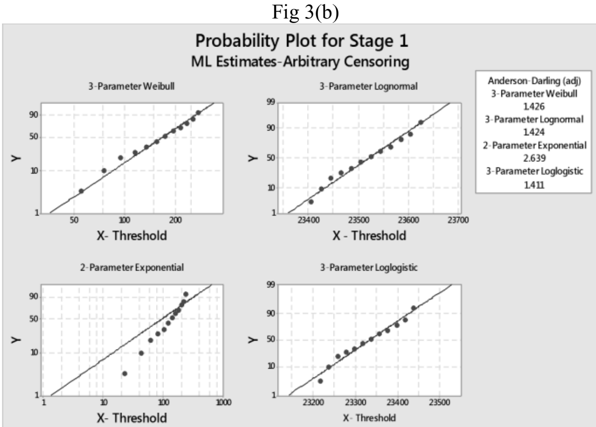


Fig. 3(C)

Fig. a, b &c Plots for various distribution showing goodness of fit of existing Interlock mechanism using MLE for data in table (stage 1)

Different plots show how various distributions have relationship with the failure data in table I. 3P Log logistic will give most appropriate results as its Anderson Darling Coefficient is close to zero.

## B. *Reliability Analysis*

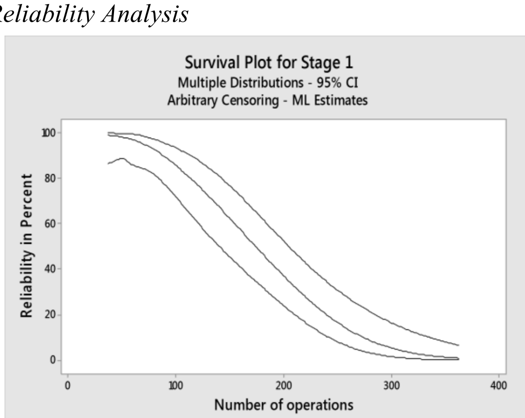


Fig. 4 Survival plot for stage 1

The survival plot shown in Fig.4 shows how drastically reliability reduces with increase in no. of operations.

TABLE III

RELIABILITY OF INTERLOCK MECHANISM

FOR NUMBER OF OPERATIONS FOR STAGE I

| Sr. No | Number of Operations | Reliability |
|---|---|---|
| 1 | 50 | 0.981825 |
| 2 | 100 | 0.8566 |
| 3 | 150 | 0.6233 |
| 4 | 200 | 0.37063 |
| 5 | 250 | 0.1663 |
| 6 | 300 | 0.05430 |

Table III shows that reliability decreases with increase in number of operations.

The Hazard plot shown in Fig.5 shows how drastically hazard rate increases with increase in no. of operations.

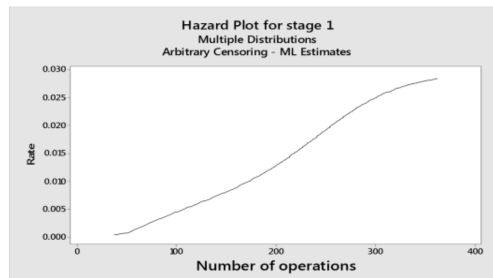


Fig.5 Hazard plot for stage I

## C. *Failure mode Reliability*

During testing it was found that there were 3 types of failure modes.

1. Slip between shaft and Control fascia
2. Slip between Shaft & C component
3. Improper Engagement between cam and spring pin

For these three failure modes different reliability graphs plotted in order to see separate effect of each failure mode.

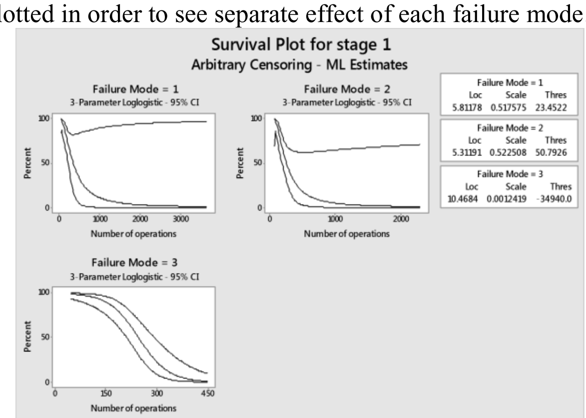


Fig. 6 Survival plots for different failure modes

The survival plot shown in Fig.6 shows how drastically reliability reduces with increase in no. of operations.

1. *Failure mode 1(R1) , Failure mode 2(R2)and Failure mode 3 (R3)*

TABLE IV

RELIABILITY OF FAILURE MODES OF INTERLOCK MECHANISM FOR NUMBER OF OPERATIONS FOR STAGE I

| Sr.no | Number of Operations | Reliability | | |
|---|---|---|---|---|
| | | Failure Mode 1 | Failure Mode 2 | Failure Mode 3 |
| 1 | 50 | 0.9925 | 1 | 0.9891 |
| 2 | 100 | 0.9451 | 0.9376 | 0.9666 |
| 3 | 150 | 0.8671 | 0.7970 | 0.9018 |
| 4 | 200 | 0.7743 | 0.6426 | 0.7448 |
| 5 | 250 | 0.6794 | 0.5084 | 0.4815 |
| 6 | 300 | 0.5904 | 0.4025 | 0.2284 |

Table IV shows reliability of failure mode1, 2 and 3 for different number of operations. From table IV reliability for 250 operation decreases to 0.6794, 0.5084 and 0.7448 which is low. But it was found that all failure modes were in series. Hence reliability of system is multiplication of all failure modes reliability at that number of operations. Total Reliability from RBD(R) =R1*R2*R3

TABLE V

RELIABILITY OF INTERLOCK MECHANISM FOR NUMBER OF OPERATIONS FOR STAGE I BY USING ALL FAILURE MODES.

| Sr. No | Number of Operations | Reliability |
|---|---|---|
| 1 | 50 | 0.9816 |
| 2 | 100 | 0.8565 |
| 3 | 150 | 0.6232 |
| 4 | 200 | 0.3705 |
| 5 | 250 | 0.1663 |
| 6 | 300 | 0.0542 |

Table V shows combined reliability of all failure modes for different number of operations.

TABLE VI

RELIABILITY OF INTERLOCK MECHANISM FOR NUMBER OF OPERATIONS FOR STAGE I BY USING ALL FAILURE MODES & LIFE TIME DISTRIBUTION

| Sr. No | Operations | Reliability | |
|---|---|---|---|
| | | RBD | LTD |
| 1 | 50 | 0.9816 | 0.981825 |
| 2 | 100 | 0.8565 | 0.8566 |
| 3 | 150 | 0.6232 | 0.6233 |
| 4 | 200 | 0.3705 | 0.37063 |
| 5 | 250 | 0.1663 | 0.1663 |
| 6 | 300 | 0.0542 | 0.05430 |

Table VI shows reliability of Interlock mechanism at stage 1 for different number of operations. From table VI reliability after 200 operation decreases to 0.3705. Reliability values of Lifetime distribution and Reliability block diagram methods are approximately equal. During testing we got different failure modes but for finding all possible failure modes Fault Tree Analysis is used.

## VI. ACTION TAKEN TO IMPROVE RELIABILITY

1. Find the failure modes during the testing & FTA
2. Find the Causes of failure.
3. Recommended Action on failures.
4. Testing after taking Recommended Action.

### A. *Fault Tree Analysis (FTA)*

Historically, the concept of fault tree was originated by Bell Telephone Laboratories in 1961 as a technique to perform a safety evaluation of the Minuteman Launch Control System [14]. Since then, there were significant improvements on mathematical and analytical techniques used in fault tree analysis. [15]

FTA procedure given by Yang in 2009 as follows

1. Select a top event for analysis.
2. Identify faults which could lead to the top event.
3. For each fault, list as many causes as possible in boxes below the related fault.
4. Draw the diagram of the fault tree.
5. Continue identifying causes for each fault until reach a root cause (reactive FTA), or one that can do something about (proactive FTA).
6. Consider counter measures. [16]

Fig. 7 shows the FTA of Handle Interlock Mechanism

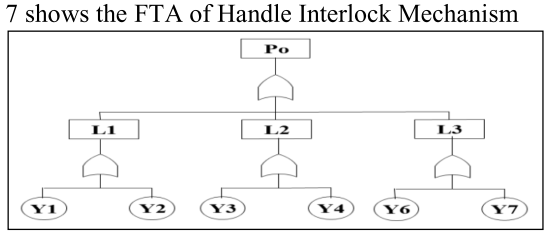


Fig. 7 FTA of Handle Interlock Mechanism

In figure Po is main event. L1, L2& L3 are intermediate events. And Y1, Y2, Y3, Y4, Y5.Y6& Y7 are basic events. Detailed of all events are as follows,

Po- Interlock fails to function, L1- control fascia assembly fails, L2-cable assembly fails, L3-Lever assembly fails, Y1-Slip between shaft and control fascia,Y2-Slip between shaft and C component.,Y3- Loosening of cable.,Y4- Improper length of cable.,Y5-Overtightntng of screw,Y6- Improper engagement of spring pin and cam.

### B. *Recommended Actions-*

By taking expert advice and team members' input we recommended action on every possible failure.

TABLE VII

IMPLEMENTED ACTIONS FOLLOWING FTA

| Sr. No | Causes of Failure | Action Taken |
|---|---|---|
| 1 | Over tightening of lever screw | Replaced lever mechanism by new mechanism |
| 2 | Improper cable length | Developed new formula for Calculating length of cable |
| 3 | Slip between shaft and hole | Integrated production of pin & cover by Insert moulding |
| 4 | Improper positioning of cable support | Location of cable support has been changed |
| 5 | Improper engagement of handle cam with spring pin | Cam profile has been changed |

Table VII shows major causes of failures and action taken on it. After a modification to the original version of a product and before mass production, the expected improvement in the product lifetime or reliability needs to be validated [17].

TABLE VIII
MODIFICATIONS IN MECHANISM FROM FTA

| Sr. No | Component | Modification |
|---|---|---|
| 1 | Lever Mechanism | Modified by new lever mechanism to reduce stress |
| 2 | Cable Support | Position adjusted in such way that both supports are in same plane. |
| 3 | Shaft and hole | Slipping reduced by integrated production of pin and cover by insert moulding |
| 4 | Cam | Cam is redesigned to lock spring pin easily. |

## VII. RESULT AND DISCUSSION AT STAGE II

### A. *Goodness of Fit:*

TABLE IX
GOODNESS OF FIT FOR STAGE II

| Distribution | Anderson-Darling(adj) |
|---|---|
| Weibull | 3.049 |
| Lognormal | 3.145 |
| Exponential | 4.104 |
| Loglogistic | 3.084 |
| Normal | 3.133 |
| Logistic | 3.080 |
| 3 Parameter Weibull | 3.029 |
| 3 parameter Lognormal | 3.133 |
| 3-Parameter Loglogistic | 3.080 |
| Smallest Extreme Value | 3.029 |

Table IX shows goodness of fit for failure data of stage II. From above data 3 Parameter Weibull distribution is selected as Anderson darling statistic for it is closest to zero.

To determine the best-fit distribution for the given data of Interlock mechanism in table I, MLE in Minitab 17 is used.

The plots in Fig.8 show how various distributions have relationship with the failure data in table IX. The distribution with Anderson-Darling coefficient close to 0 will give the most appropriate results. From the figure it can be concluded that 3P Weibull will give most appropriate results. Sample plots are shown in fig 8.

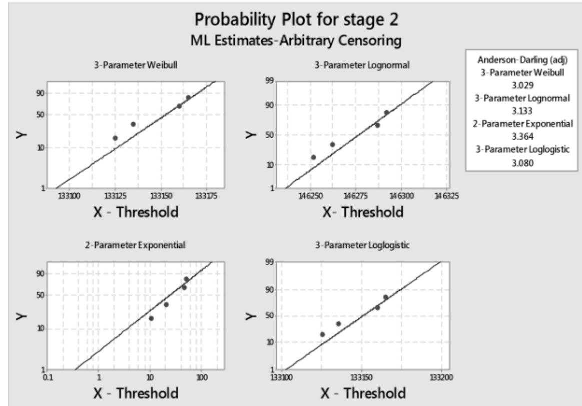


Fig. 8 Plots for various distribution showing goodness of fit of existing Interlock mechanism using ML for data in table.

The survival plot shown in Fig.9 shows how drastically reliability reduces after increase in 250 no. of operations

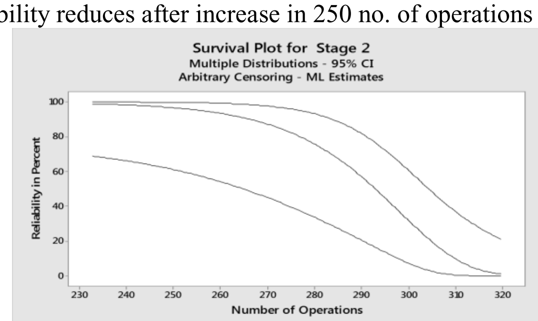


Fig.9 Survival plot for stage II

TABLE X
RELIABILITY FOR DIFFERENT NUMBER OF OPERATIONS AT STAGE II

| Sr.no | Operations | Reliability |
|---|---|---|
| 1 | 50 | 1 |
| 2 | 100 | 1 |
| 3 | 150 | 0.9999 |
| 4 | 200 | 0.9989 |
| 5 | 250 | 0.9676 |
| 6 | 300 | 0.31814 |

Table X shows that reliability of handle interlock mechanism is 0.99 for 250 numbers of operations.

The Hazard plot shown in Fig.10 shows how drastically hazard rate increases after increase in 250 no. of operations.

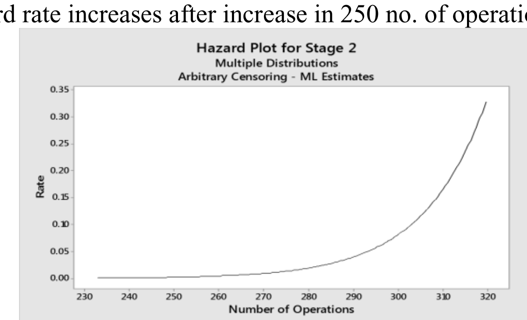


Fig.10 Hazard plot for stage 2

B. *Failure mode Reliability*

There were two failure modes observed during experimentation

1. Slip between shaft and Control fascia.
2. Slip between Shaft & C component.

For these two failure modes different reliability graphs plotted in order to see separate effect of each failure mode.

The survival plot in Fig.11 shows how drastically reliability reduces after increase in 250 no. of operations.

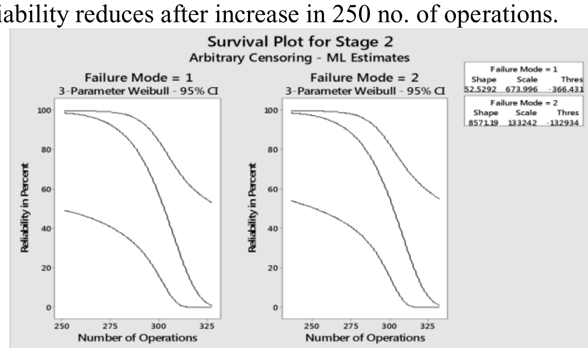


Fig.11 Survival plot for different failure mode

1. *Failure Mode 1& 2:*

TABLE XI
RELIABILITY FOR DIFFERENT NUMBER OF OPERATIONS OF FAILURE MODE1 AND MODE 2 AT STAGE II

| Sr. No | Operati-ons | Reliability Mode1(R1) | Reliability Mode2(R2) | Total Reliability(R) |
|---|---|---|---|---|
| 1 | 50 | 1 | 1 | 1 |
| 2 | 100 | 1 | 1 | 1 |
| 3 | 150 | 1 | 0.9996 | 0.9996 |
| 4 | 200 | 0.9989 | 0.99905 | 0.9979 |
| 5 | 250 | .99085 | 0.97654 | 0.967604 |
| 6 | 300 | 0.57539 | 0.5529 | 0.3181 |

Table XI shows that reliability of failure mode 1, and2 for 250 numbers of operations is 0.9989 and 0.9996. After that reliability decreases suddenly.

Total Reliability from RBD

$$R=R1*R2$$

Table XI shows that reliability of Interlock mechanism based on all failure modes for 250 numbers of operations is increased from 0.1663 to 0.9676. After that reliability decreases suddenly to 0.3181 for 300 numbers of operations.

TABLE XII
RELIABILITY OF RBD & LTD FOR DIFFERENT NUMBER OF OPERATIONS

| Sr. No | Operations | Reliability Stage 2 | |
|---|---|---|---|
| | | RBD | LTD |
| 1 | 50 | 1 | 1 |
| 2 | 100 | 1 | 1 |
| 3 | 150 | 0.9996 | 0.9999 |
| 4 | 200 | 0.9979 | 0.9989 |
| 5 | 250 | 0.967604 | 0.9676 |
| 6 | 300 | 0.3181 | 0.31814 |

Table XII shows reliability for different number of operations by using life time distribution and failure mode techniques. From table it is found that reliability values from both techniques are approximately equal. Reliability value for 250 operations is 0.9676, which is higher than Reliability obtained at stage 1.

## VIII. COMBINED RESULTS AND DISCUSSION

Below table XIII shows the total comparison of reliability at stage I and Stage II

TABLE XIII
COMPARISON OF RELIABILITY AT STAGE I & STAGE II

| Sr. No | Operations | Reliability Stage 1 | | Reliability Stage 2 | |
|---|---|---|---|---|---|
| | | RBD1 | LTD 1 | RBD 2 | LTD2 |
| 1 | 50 | 0.9816 | 0.981825 | 1 | 1 |
| 2 | 100 | 0.8565 | 0.8566 | 1 | 1 |
| 3 | 150 | 0.6232 | 0.6233 | 0.9996 | 0.9999 |
| 4 | 200 | 0.3705 | 0.37063 | 0.9979 | 0.9989 |
| 5 | 250 | 0.1663 | 0.1663 | 0.967604 | 0.9676 |
| 6 | 300 | 0.0542 | 0.05430 | 0.3181 | 0.31814 |

1. Reliability of handle interlock mechanism is improved 0.3706 from to 0.997 for 200 operations.
2. Reliability for 200 numbers of operations is almost 1 hence less chance of failure, this fulfill the requirement of IEC standard.
3. All failure modes were detected by using experimentation and Fault tree analysis. The recommended actions are also taken on them.

## IX. CONCLUSIONS

1. Reliability of handle interlock mechanism is improved by investigating the failures and taking recommended actions on them.
2. Values of reliability obtained by using LTD and RBD techniques are approximately same.
3. It shows that for 200 numbers of operations, mechanism have only 0.01% chance of failure and it is acceptable. Hence handle interlock mechanism is totally safe for 200 numbers of operations.
4. Interlock mechanism is operated maximum 6 times in a year for maintenance purpose, so life of mechanism is approximately 33 years.

## ACKNOWLEDGMENT

We thank Mr. S. P. Sharma and Mr. Akshay Jain for providing the opportunity to perform the research at Larsen and Toubro EAIC Powai. We thank Sardar Patel College of Engineering for supporting our efforts.

## REFERENCES

[1] Dhillon BS, Maintainability, maintenance, and reliability for engineers. CRC Press, Taylor & Francis Group, Boca Raton. (2006).

[2] Baecher GB, Christian JT Reliability and statistics in geotechnical engineering. Wiley, Chichester(2003).

[3] Nakagawa T (2005) Maintenance theory of reliability. *Springer series in reliability engineering. Springer, London.*

[4] Barlow RE, Proschan F, Mathematical theory of reliability, vol 17. Siam, Philadelphia (1996)

[5] Ayyub BM, McCuen RH Probability, statistics, and reliability for engineers and scientists. CRC press, *Taylor & Francis Group, Boca Raton. (2011)*

[6] J. Tang, “Mechanical system reliability analysis using a combination of graph theory and Boolean function,” *Reliability Engineering and System Safety* 72 (2001) 21±30

[7] D.Bocchetti, M.Giorgio, M.Guida, G.Pulcini, “A competing risk model for the reliability of cylinder liners in marine diesel engines,” *Reliab.Eng.Syst. Saf. 94* (8)(2009)1299–1307.

[8] H. Peng, D.W.Coit, Q.Feng, “Component reliability criticality or importance measures for systems with degrading components,” *IEEE Trans.Reliab.61(1)* (2012)4–12.

[9] L. Xing, A.Shrestha, Y.Dai, “Exact combinatorial reliability analysis of dynamic systems with sequence-dependent failures,” *Reliab. Eng. Syst. Saf.* 96 (10) (2011) 1375–1385

[10] G.D. Li, S.Masuda, D.Yamaguchi, etal., “A new reliability prediction modelling manufacturing systems,” *IEEE Trans. Reliab.59*(1) (2010) 170–177.

[11] M.J. Zuo, Lisnianski, W.Li, “A framework for reliability approximation of multi-state weighted k-out-of-n systems,” *IEEE Trans. Reliab*. 59(2)(2010) 297–308.

[12] Militaryhandbook:electronicreliabilitydesignhandbook/http://relex.com/ resources/mil/338b.pdfS; 1988.

[13] Reliability and Survival Analysis 2003–2005 Minitab Inc.

[14] D.F. Hasal, “Advanced concepts in fault tree analysis Aero-Space Division of the Boeing Company,” *Seattle, WA* (1965).

[15] Ericson CA. “Fault tree analysis—a history.” *In: Proceedings of the 17th international system safety conference*, Orlando, 1999.

[16] Yang Zong-Xiao, Zheng Yan-Yi, Xue Jin-Xue “Development of automatic fault tree synthesis system using decision matrix,”.*Int J Prod Econ* 121(1):49–56 (2009)

[17] S. HosseinMohammadian, Daoud Aıt-Kadi, “Design stage confirmation of lifetime improvement for newly modified products through accelerated life testing,” *Reliability Engineering and System Safety* 95 (2010) 897–905

# Structural Equation Model for Critical Success Factors of Healthcare Management Information Systems in India

Nizar Hussain M.

*TKM College of Engineering, Kollam, Kerala, India.*

nizarhussainm@yahoo.co.in

***Abstract-* It is claimed that successfully implemented Information and Communication Technology (ICT) can bring many benefits to the healthcare organisation. Many ICT applications remain underused by healthcare professionals and healthcare organisations. Human and organisational factors have frequently been identified as the main causes of ICT implementation underuse. Therefore, it is very important to identify the Critical Success Factors (CSF) necessary for the implementation of Healthcare Management Information Systems (HMIS). Existing models of CSF on information systems related to healthcare sector are practically less, globally, and almost nil with respect to India. Hence, the purpose of this research is to develop a conceptual model of CSF especially for HMIS adoption, use and redesign in India. Such identified factors for redesign will also have international bearing as redesign possibilities discussed are mainly based on emerging technologies. The rationale of the purpose is justified by the fact that India is a leader in developing information systems, especially medical applications. Further, India is emerging as an international destination for healthcare due to the advancement in medical technology and is offering high quality health services at reduced cost.**

**Keywords: Information and Communications Technology, Critical Success Factors, Healthcare Management Information Systems, structural Equation Model.**

## I. Introduction

Information and Communication Technology (ICT) has the potential to address many of the challenges that healthcare systems are currently confronting. ICT applications could improve information management, universal access to healthcare services, quality and safety of care, continuity of services, and costs containment [1]. It is reported that several ICT applications remain underused by healthcare professionals [2], [3]. Healthcare organisations, particularly physician practices, are often pointed out as noticeably lagging behind in the adoption of ICT [4]. Human and Organisational factors have frequently been identified as the main causes of ICT implementation failure [5]-[7]. The number of studies which stress upon the identification of critical success factors of healthcare Information Systems (IS) adoption are practically absent or are too less in number in the literature and the same is absent for the adoption of HMIS in India. Hence, the researcher has decided on the above theme for carrying out the research.

The following sections are organized as follows. Section 2 presents an extensive literature review on the topic. The conceptual model details and relationship between the variables involved along with their definition and corresponding constructs are discussed in Section 3. Managerial implications of this study are enumerated in section 4. Finally, the research is summarized in Section 5.

## II. Literature review

### *A. . Critical Success Factors*

Critical Success Factors (CSF) can be defined as key areas of performance that are essential for the organization to accomplish its mission. Critical success factors are those that must be accomplished by the individual or the organization which are considered successful by important stakeholders. Critical success factors are important to identify and understand as they focus the attention on vital few against trivial many that consume most of the manager's time [8].

A broad range of factors that can influence the success of HMIS have been mentioned in the literature. The purpose of this research is to identify the CSF that influences the adoption of Healthcare Information Systems used in India. The rationale is justified by the fact that India is a leader in developing information systems, especially, medical applications. Further, India is emerging in ‘Health Tourism’ due to the advancement in medical technology and offering high quality health services at reduced cost.

### *B. CSF for HMIS*

This section consists of the empirical studies done previously on success factors area which support the current research theoretically to derive the critical success factors for the HMIS. Perceived usefulness was the most frequent success factor encountered in the literature (29 studies). Ease of use was the second most commonly used success factor (17 studies) Attitude also has been considered highly relevant to HMIS success in many studies (9 studies). Scholars have established that self-efficacy and Training have a significant effect on HMIS success (7 studies each). Factors such as top management support (8 studies) and facilitating conditions (9 studies) are also having an impact on the success of HMIS. System Reliability, Information quality, Service care quality (5 studies each) and Social Influence (4 studies) are other identified factors affecting the behavioural intention of use of technologies as per literature. Summary of reviewed articles is shown in Table 1.

TABLE 1. SUMMARY OF REVIEWED ARTICLES

| Factors | Number of studies | References |
|---|---|---|
| Perceived usefulness | 29 | [7], [9-36] |
| Perceived ease of use | 17 | [7], [10], [13], [15], [21], [28], [29], [31], [32], [34--41] |
| Attitude | 9 | [13], [14], [16], [23], [27], [33], [38], [42], [43] |
| Self efficacy | 7 | [14], [44], [45], [46], [47-49] |
| Training | 7 | [18], [21], [24], [38], [44], [50], [51] |
| Management support | 8 | [17], [21], [22], [27], [29], [38], [52], [53] |
| Facilitating conditions | 9 | [9], [18], [19], [28], [32], [38], [40], [54], [55] |
| System reliability | 5 | [10], [15], [18], [22], [56], [57] |
| Information quality | 5 | [12], [40], [51], [57], [58] |
| Service care quality | 5 | [59-63], |
| Social influence | 4 | [22], [51], [64], [65] |

This research is aimed at conceptualizing a framework for the identification of variables that are critical to the success of Healthcare Management Information Systems (HMIS) adoption and use in India. Suitable scale is to be designed using constructs to study the variables and their relationships in the study. Scale developed is to be tested for its reliability and validity. Confirmatory Factor Analysis is planned to establish and confirm the fitness of the model using Structural Equation Modelling. Thus, the objectives of this research are:

- To identify the variables associated with HMIS adoption, use and other variables related to emerging technologies based on literature review;
- To develop a conceptual framework for the HMIS adoption study in India based on the variables identified;
- To develop a suitable scale using constructs to study the variables involved;
- To develop a structural equation model with the constructs identified.

## III. DEVELOPMENT OF CONCEPTUAL MODEL

### *A. The conceptual framework*

Based on the literature review and considering the emerging technologies that pave way for the redesign of HMIS, a conceptual model to describe HMIS success factors has been developed as discussed below. In this model, the critical success factors identified grouped in to five categories. They are individual characteristics, organizational characteristics, system characteristics, environmental characteristics, redesign characteristics and TAM elements.

The conceptual model is shown in Figure 1. The arrows indicated are either regression relationships or just the information flow. It consists of nine exogenous variables,

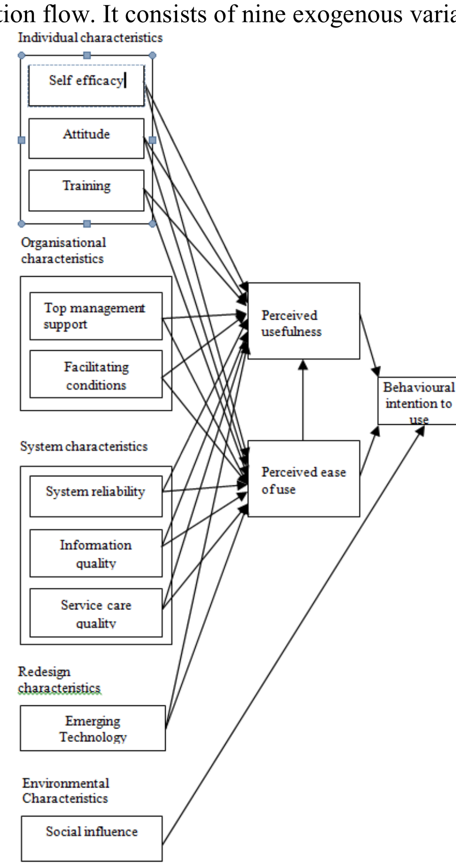


Figure 1. Conceptual model

namely, Self efficacy, Attitudes, Training, Top management support, Facilitating conditions, System reliability, Information Quality, Service care quality, Social influence and Emerging technologies, and, three endogenous variables, namely, Perceived usefulness, Perceived ease of use and Behavioural intention to use.

*B. Development of the instrument*

This section describes the development of the construct for the proposed model. All measures used in the survey instrument are either adapted from existing studies or based on expert opinion. In this study, all variables are measured using multiple items which are developed based upon the theoretical considerations suggestions in prior studies and author's contributions. With regard to the HMIS characteristics, the questionnaire is further adapted and modified.

Several scholars in the fields of healthcare information technology and Management Information System (MIS) reviewed the content of questionnaire. In addition, a group of public healthcare professionals also contributed for the revision of the questionnaire for ensuring the suitability and appropriateness of every measurement item. A five-point Likert scale from "strongly disagree (1)" to "strongly agree (5)" in a structured questionnaire is used to measure each variable in the model. The operational definition of variables used in the constructs, and the corresponding reference resources are presented in Table 2. The reliability and validity of the scale items are to be explored and relevant items related to each variable that make the scale more relevant are only planned to be included in the instrument.

TABLE 2. DESCRIPTION OF CONSTRUCTS AND SOURCE OF MEASUREMENT INSTRUMENT

| Variable | Definition | Number of items in the construct | Source |
|---|---|---|---|
| Self Efficacy | An individual's perception of his or her ability to use a computer system in accomplishing a job task. | 3 | [66] |
| Attitude | User's affection, or liking, for HMIS and for using them. | 3 | [67] |
| Training | Extent to which an individual has been trained about HMIS through courses, training, manuals, and so on | 2 | [68] |
| Top management support | Top-management support for, and favourable attitude towards HMIS, in general | 3 | [69] |
| Facilitating conditions | The adequacy of the deployment of IT infrastructure in an organisation to support job performance and to improve the quality of the users' job. | 3 | [70] |
| System reliability | The extent to which a system is dependable for the completion of a task without problems and breakdowns. | 3 | [71] |
| Information quality | Degree to which information produced has the attributes of accuracy, format, completeness, understandability, and report timeliness for the user. | 3 | [72] |
| Service care quality | Perception of how a HMIS provider delivers the service to user | 3 | [73] |
| Social Influence | Social influence is defined as the degree to which an individual perceives that it is important that he or she should use health IT. | 3 | [74] |
| Perceived usefulness | The degree to which a person believes that using a particular computer system would enhance his or her job performance. | 4 | [75] |
| Perceived ease of use | The degree to which a person believes that using a particular computer system would be free of effort. | 5 | [75] |
| Behavioural intention to use | The degree to which a healthcare professional's motivation intend to use the HMIS | 5 | [76], [77] |
| Emerging Technology | Novel information and communication technologies, namely, social media, biometric identification, business intelligence and the like which help improving HMIS | 8 | Author's own |

*C. Development of a Structural Equation Model*

Structural Equation Modelling (SEM) is defined as a collection of statistical techniques similar to factor analysis, path analysis, or multiple regression that takes into account the modelling of interactions, nonlinearities, correlated independent variables, measurement error, correlated error terms, multiple latent independent variables each measured by multiple indicators, and one or more latent dependent variables with multiple indicators. The advantages of SEM compared to multiple regression include the following: a) more flexible assumptions, such as the allowance for interpretation even in the presence of multi-collinearity; b) use of confirmatory factor analysis to reduce measurement error by having multiple indicators per latent variable; c) the appeal of testing overall models rather than individual coefficients; d) the capacity to test models with multiple dependent variables; e) the ability to model mediating variables; f) the capacity to model error terms; g) the usefulness to test coefficients across multiple between-subjects groups; and, h) the capability to handle non-normal data and incomplete data. Additionally, most SEMs consist of two parts, namely, the measurement model and the structural equation model. The measurement model specifies how the latent constructs are measured in relation to the observed variables, and further, it describes the measurement properties such as validities and reliabilities of the observed variables. Measurement models often suggest ways by which the observed measurements can be improved.

Several conventions are used in developing SEM path diagrams. Measured variables, also called observed variables, indicators, or manifest variables, are represented by squares or rectangles. Factors have two or more indicators and are also called latent variables, constructs, or unobserved variables. Factors are represented by circles or ovals in path diagrams. Relationships between variables are indicated by lines; lack of a line connecting variables implies that no direct relationship has been hypothesized. Lines have either one or two arrows. A line with one arrow represents a hypothesized direct relationship between two variables, and the variable with the arrow pointing to it is the Dependant Variable (DV). A line with a two-headed arrow indicates an unanalyzed relationship, simply a covariance between the two variables with no implied direction of effect. As in multiple regressions, nothing is predicted perfectly; there is always residual error termed as “e”. In SEM, the residual variance is the variance unexplained by the Independent variable (IV).

The SEM model for CFA on CSF related to HMIS adoption, use and redesign is shown in Figure 2. It consists of nine exogenous variables, namely, Self efficacy, Attitudes, Training, Top management support, Facilitating conditions, System reliability, Information Quality, Service care quality, Social influence, and Emerging Technology, and, three endogenous variables, namely, Perceived usefulness, perceived ease of use and Behavioural intention to use. There are forty eight indicators (q1 to q48) and 51 residual errors (e1 to e51).

## IV. Managerial implications

The practical implications of the study are enumerated below. This research is definitely useful for the HMIS developing firms as the study identifies and confirms redesigning possibilities. CSF studies on HMIS available in literature are less compared to other types of IS, globally, and as far India is considered studies in this direction are practically absent. The healthcare professionals will also get benefitted from this CSF study while planning and executing HMIS. Using the results from this study, the healthcare IS professionals will be able to identify the required capabilities

Competitive advantage by developing more useful and productive HMIS rather than chasing trivial factors. Technology driven HMIS enable hospitals to improve quality, service, speed at reduced costs, and facilitate coordination of care across multiple facilities / organisations.

and allocate necessary resources in order to gain and sustain

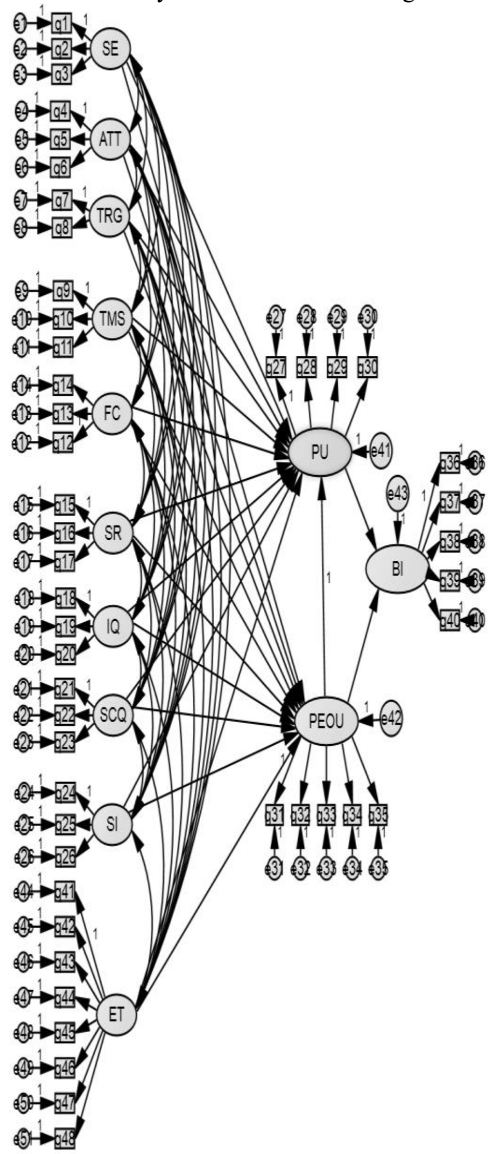


Figure 2. SEM model

## V. Conclusion

In order to make HMIS more beneficial for the healthcare sector, examination of a multitude of factors critical to use, acceptance and redesign of such systems have become a prime concern for professionals. The overall research goal is to provide new insight for predicting major variables as criterion measures of technology use, acceptance and redesign. Additionally, this research sought to introduce and evaluate critical variables that have not been explained by prior studies on TAM with respect to IS, especially, in connection with HMIS. The CSF identified through literature review are Perceived usefulness, Perceived ease of use, Self efficacy, Attitudes, Training, Top management support, Facilitating conditions, System reliability, Information Quality, Service care quality and Social influence. In addition to the above, Emerging Technologies that help redesign of HMIS have been incorporated in this study.

Previous research findings suggested that professional users and common users subtly differ in their usage behaviour and acceptance of technology. Thus, as there is great disparity and diversity in terms of technology users, there has been a push for researchers to look at real-time technology trends and practices in the work environment that may impact or influence professional users. As noted by other researchers, there is always a need for additional empirical support to validate proposed models and research frameworks across various geographical locations in India. Moreover, longitudinal studies might provide further empirical validity, reliability and generalization with this type of technology research.

## REFERENCES


[1] Health Canada, Towards a healthy future: Second report on the health of Canadians. Federal. Provincial and Territorial Advisory Committee on Population Health, Ottawa, 1999.

[2] Berner, E. S., Detmer, D. E., and Simborg, D., Will the wavefinally break? A brief view of the adoption of electronic medical records in the United States. J. Am. Med. Inform. Assoc. 12:3–7, 2005.

[3] Brooks, R. G., and Menachemi, N., Physicians' use of email with patients: factors influencing electronic communication and adherence to best practices. J. Med. Internet Res. 8:e2, 2006.

[4] Yarbrough, A. K., and Smith, T. B., Technology acceptance among physicians: a new take on TAM. Med. Care Res. Rev. 64:650–672, 2007.

[5] Aarts, J., Doorewaard, H., and Berg, M., Understanding implementation: the case of a computerized physician order entry system in a large Dutch university medical center. J. Am. Med. Inform. Assoc. 11:207–216, 2004.

[6] Lorenzi, N. M., Riley, R. T., Blyth, A. J., Southon, G., and Dixon, B. J., Antecedents of the people and organizational aspects of medical informatics: review of the literature. J. Am. Med. Inform. Assoc. 4:79–93, 1997.

[7] Pagliari, C., Clark, D., Hunter, K., Boyle, D., Cunningham, S., Morris, A., and Sullivan, F., DARTS 2000 online diabetes management system: formative evaluation in clinical practice. J. Eval. Clin. Pract. 9:391–400, 2003.

[8] Stahl, Michael J, Critical Success Factors, Encyclopedia of health care management, Sage Publications, 2001.

[9] Al Farsi, M., and West, D. J., Jr., Use of electronic medical records in Oman and physician satisfaction. J. Med. Syst. 30:17–22, 2006.

[10] Connelly, D. P., Werth, G. R., Dean, D. W., Hultman, B. K., and Thompson, T. R., Physician use of an NICU laboratory reporting system. Proc. Annu. Symp. Comput. Appl. Med. Care. 8–12, 1992.

[11] Crowe, B., and Sim, L., Implementation of a radiology information system/picture archiving and communication system and an image transfer system at a large public teaching hospital - Assessment of success of adoption by clinicians. J. Telemed. Telecare 10:25–27, 2004.

[12] D'Alessandro, D. M., Kreiter, C. D., and Peterson, M. W., An evaluation of information-seeking behaviors of general pediatricians. Pediatrics 113:64–69, 2004.

[13] Eley, D., Hegney, D., Wollaston, A., Fahey, P., Miller, P., McKay, M., and Wollaston, J., Triage nurse perceptions of the use, reliability and acceptability of the Toowoomba Adult Triage Trauma Tool (TATTT). Accident Emerg. Nurs. 13:54–60, 2005.

[14] Firby, P. A., Luker, K. A., and Caress, A. L., Nurses' opinions of the introduction of computer-assisted learning for use in patient education. J. Adv. Nurs. 16:987–995, 1991.

[15] Galligioni, E., Berloffa, F., Caffo, O., Tonazzolli, G., Ambrosini, G., Valduga, F., Eccher, C., Ferro, A., and Forti, S., Development and daily use of an electronic oncological patient record for the total management of cancer patients: 7 years' experience. Ann. Oncol. 20:349–352, 2009

[16] Hier, D. B., Rothschild, A., LeMaistre, A., and Keeler, J., Differing faculty and housestaff acceptance of an electronic health record one year after implementation. Medinfo 11:1300– 1303, 2004.

[17] Hou, I. C., Chang, P., and Wang, T. Y., Qualitative analysis of end user computing strategy and experiences in promoting nursing informatics in Taiwan. Stud. Health Technol. Inform. 122:613–615, 2006.

[18] Joos, D., Chen, Q., Jirjis, J., and Johnson, K. B., An electronic medical record in primary care: impact on satisfaction, work efficiency and clinic processes. AMIA Annu. Symp. Proc. 394–398, 2006.

[19] Jousimaa, J., Kunnamo, I., and Makela, M., An implementation study of the PDRD primary care computerized guidelines. Scand. J. Prim. Health Care 16:149–153, 1998.

[20] Kamadjeu, R. M., Tapang, E. M., and Moluh, R. N., Designing and implementing an electronic health record system in primary care practice in sub-Saharan Africa: a case study from Cameroon. Inform. Prim. Care. 13:179–186, 2005.

[21] Keshavjee, K., Troyan, S., Holbrook, A. M., and VanderMolen, D., Measuring the success of electronic medical record implementation using electronic and survey data. Proc. AMIA Symp. 309–313, 2001.

[22] Kouri, P., Turunen, H., and Palomaki, T., 'Maternity clinic on the net service' and its introduction into practice: experiences of maternity-care professionals. Midwifery 21:177–189, 2005.

[23] Larcher, B., Arisi, E., Berloffa, F., Demichelis, F., Eccher, C., Galligioni, E., Galvagni, M., Martini, G., Sboner, A., Tomio, L., Zumiani, G., Graiff, A., and Forti, S., Analysis of user satisfaction with the use of a teleconsultation system in oncology. Med. Inform. Internet Med. 28:73–84, 2003.

[24] Marcy, T. W., Kaplan, B., Connolly, S. W., Michel, G., Shiffman, R. N., and Flynn, B. S., Developing a decision support system for tobacco use counselling using primary care physicians. Inform. Prim. Care. 16:101–109, 2008.

[25] Magrabi, F., Westbrook, J. I., and Coiera, E. W., What factors are associated with the integration of evidence retrieval technology into routine general practice settings? Int. J. Med. Inform. 76:701–709, 2007.

[26] Martinez, M. A., Kind, T., Pezo, E., and Pomerantz, K. L., An Evaluation of community health center adoption of online health information. Health Promot. Pract. 2007.

[27] O'Connell, R. T., Cho, C., Shah, N., Brown, K., and Shiffman, R. N., Take note(s): differential EHR satisfaction with two implementations under one roof. J. Am. Med. Inform. Assoc. 11:43–49, 2004.

[28] Ovretveit, J., Scott, T., Rundall, T. G., Shortell, S. M., and Brommels, M., Improving quality through effective implementation of information technology in healthcare. Int. J. Qual. Health Care 19:259–266, 2007.

[29] Pare, G., Sicotte, C., and Jacques, H., The effects of creating psychological ownership on physicians' acceptance of clinical information systems. J. Am. Med. Inform. Assoc. 13:197–205, 2006.

[30] Popernack, M. L., A critical change in a day in the life of intensive care nurses: rising to the e-challenge of an integrated clinical information system. Crit. Care Nurs. Q. 29:362–375, 2006.

[31] Pourasghar, F., Malekafzali, H., Koch, S., and Fors, U., Factors influencing the quality of medical documentation when a paperbased medical records system is replaced with an electronic medical records system: an Iranian case study. Int. J. Technol. Assess. Health Care 24:445–451, 2008.

[32] Soar, J., Ayres, D., and Van der Weegen, L., Achieving change and altering behaviour through direct doctor use of a hospital information system for order communications. Aust. Health Rev. 16:371–382, 1993.

[33] Thoman, J., Struk, C., Spero, M. O., and Stricklin, M. L., Reflections from a point-of-care pilot nurse group experience. Home Healthc. Nurs. 19:779–784, 2001.

[34] Vanmeerbeek, M., Exploitation of electronic medical records data in primary health care. Resistances and solutions. Study in eight Walloon health care centres. Stud. Health Technol. Inform.110:42–48, 2004.

[35] Whittaker, A. A., Aufdenkamp, M., and Tinley, S., Barriers and facilitators to electronic documentation in a rural hospital. J. Nurs. Scholarsh. 41:293–300, 2009.

[36] Zheng, K., Padman, R., Johnson, M. P., and Diamond, H. S., Understanding technology adoption in clinical care: clinician adoption behavior of a point-of-care reminder system. Int. J. Med. Inform. 74:535–543, 2005.

[37] Di Pietro, T., Coburn, G., Dharamshi, N., Doran, D., Mylopoulos, J., Kushniruk, A., Nagle, L., Sidani, S., Tourangeau, A., Laurie- Shaw, B., Lefebre, N., Reid-Haughian, C., Carryer, J., and McArthur, G., What nurses want: diffusion of an innovation. J. Nurs. Care Qual. 23:140–146, 2008.

[38] Haynes, R. B., McKibbon, K. A., Walker, C. J., Ryan, N., Fitzgerald, D., and Ramsden, M. F., Online access to MEDLINE in clinical settings. A study of use and usefulness. Ann Intern Med. 112:78–84, 1990.

[39] Likourezos, A., Chalfin, D. B., Murphy, D. G., Sommer, B., Darcy, K., and Davidson, S. J., Physician and nurse satisfaction with an Electronic Medical Record system. J. Emerg. Med. 27:419–424, 2004.

[40] Pugh, G. E., and Tan, J. K., Computerized databases for emergency care: what impact on patient care? Methods Inf. Med. 33:507–513, 1994.

[41] Verhoeven, F., Steehouder, M. F., Hendrix, R. M., and van Gemert-Pijnen, J. E., Factors affecting health care workers' adoption of a website with infection control guidelines. Int. J. Med. Inform. 78:663–678, 2009.

[42] Lee, T. T., Mills, M. E., and Lu, M. H., The multimethod evaluation of a nursing information system in taiwan. Comput. Inform. Nurs. 27:245–253, 2009.

[43] Crosson, J. C., Isaacson, N., Lancaster, D., McDonald, E. A., Schueth, A. J., DiCicco-Bloom, B., Newman, J. L., Wang, C. J., and Bell, D. S., Variation in electronic prescribing implementation among twelve ambulatory practices. J. Gen. Intern. Med. 23:364– 371, 2008.

[44] Cheng, G. Y., Educational workshop improved information seeking skills, knowledge, attitudes and the search outcome of hospital clinicians: a randomised controlled trial. Health Info. Libr. J. 20(Suppl 1):22–33, 2003.

[45] Yeh, S. H., Jeng, B., Lin, L.W., Ho, T. H., Hsiao, C. Y., Lee, L. N., and Chen, S. L., Implementation and evaluation of a nursing process support system for long-term care: a Taiwanese study. J. Clin. Nurs. 18:3089–3097, 2009.

[46] Torkzadeh, G., T.P. Van Dyke, Effects of training on Internet self-efficacy and computer user attitudes, Comput. Hum. Behav. 18 (5) (2002) 479–494.

[47] Barbeite, F.G., E.M. Weiss, Computer self-efficacy and anxiety scales for an Internet sample: testing measurementequivalence of existing measures and development of newscales, Comput. Hum. Behav. 20 (1) (2004) 1–15.

[48] Bedard, J.C., C. Jackson, M.L. Ettredge, K.M. Johnstone, The effect of training on auditors' acceptance of an electronic work system, Int. J. Account. Inform. Syst. 4 (2003) 227–250.

[49] Hasan, B., The influence of specific computer experiences on computer self-efficacy beliefs, Comput. Hum. Behav. 19 (4) (2003) 443–450.

[50] Barsukiewicz, C. K., Computerized medical records: physician response to new technology. The Pennsylvania State University, Pennsylvania, 1998.

[51] Lai, F., Macmillan, J., Daudelin, D. H., and Kent, D. M., The potential of training to increase acceptance and use of computerized decision support systems for medical diagnosis. Hum. Fact. 48:95–108, 2006.

[52] Lapointe, L., and Rivard, S., Getting physicians to accept new information technology: insights from case studies. Can. Med. Assoc. J. 174:1573–1578, 2006.

[53] Travers, D., and Parham, T., Improving information access with an emergency department system. Proc. AMIA Annu. Fall Symp.121–125, 1997.

[54] Walji, M. F., Taylor, D., Langabeer, J. R., 2nd, and Valenza, J. A., Factors influencing implementation and outcomes of a dental electronic patient record system. J. Dent. Educ. 73:589–600, 2009.

[55] Cumbers, B. J., and Donald, A., Using biomedical databases in everyday clinical practice: the Front-Line Evidence-Based Medicine project in North Thames. Health Libr. Rev. 15:255– 265, 1998

[56] Rahimi, B., Timpka, T., Vimarlund, V., Uppugunduri, S., and Svensson, M., Organization-wide adoption of computerized provider order entry systems: a study based on diffusion of innovations theory. BMC Med. Inform. Decis. Mak. 9:52, 2009.

[57] Chisolm, D. J., McAlearney, A. S., Veneris, S., Fisher, D., Holtzlander, M., and McCoy, K. S., (2006), The role of computerized order sets in pediatric inpatient asthma treatment. Pediatr. Allergy Immunol. 17:199–206.

[58] Hains, I. M., Fuller, J. M., Ward, R. L., and Pearson, S. A., Standardizing care in medical oncology: are Web-based systems the answer? Cancer 115:5579–5588, 2009

[59] DeLone, W. H., E.R. McLean, The DeLone and McLean model of information systems success: a ten-year update, Journal ofManagement Information Systems 19 (4) (2003).

[60] Gillingham, W., A. Holt, J. Gillies, Hand-held computers in health care:what software programs are available? The New Zealand Medical Journal 115 (1162) (2002).

[61] Lu, Y, Y. Xiao, A. Sears, J. Jacko, Review and a framework of handheld computer adoption in healthcare, International Journal of Medical Informatics 74 (5) (2005).

[62] Sarker, S., J.S. Valacich, S. Sarker, Technology adoption by groups: a valence perspective, Journal of the Association for Information Systems 6 (2) (2005).

[63] Varshney, U., Pervasive healthcare, Computer 36 (2) (2003).

[64] Han YY, Carcillo JA, Venkataraman ST, Clark RSB, Watson RS, Nguyen TC, et al. Unexpected increased mortality after implementation of a commercially sold computerized physician order entry system. Pediatrics 2005;116:1506–12.

[65] Holden RJ, Scanlon MC, Brown RL, Karsh B. What is IT? New conceptualizations and measures of pediatric nurses' acceptance of carcoded medication administration information technology. Annu Meet Human Factors Ergon Soc 2008;52:768–72.

[66] Chau, P. (2001). Influence of computer attitude and self-efficacy on IT usage behavior. Journal of End User Computing, 13(1), 26-33.

[67] Venkatesh, V., Morris, M. G., Davis, G. B., & Da¬vis, F. D. (2003). User acceptance of information technology: Toward a unified view. Management Information Systems Quarterly, 27(3), 425–478.

[68] Goodhue, D. L., & Thompson, R. L. (1995). Task-technology fit and individual performance. Manage¬ment Information Systems Quarterly, 19(2), 213–236. doi:10.2307/249689.

[69] Igbaria, M., & Iivari, J. (1995). The effects of self-efficacy on computer usage. Omega International Journal of Management Science, 23(6), 587–605. doi:10.1016/0305-0483(95)00035-6.

[70] Bhattacherjee, A., & Hikmet, N. (2008). Reconceptualizing organizational support and its effect on information technology usage: evidence from the health care sector. The Journal of Computer Information Systems, 48(4), 69-75.

[71] Sutirtha Chatterjee, Suranjan Chakraborty , Saonee Sarker , Suprateek Sarker , Francis Y. Lau, xamining the success factors for mobile work in healthcare: A deductive study, Decision Support Systems 46 (2009) 620–633.

[72] Seddon, P. B., & Kiew, M. Y. (1996). A partial test and development of DeLone and McLean's model of IS success. Australian Journal of Information Systems, 4(1), 90–109.

[73] Brady, M. K., Cronin, J. J., & Brand, R. R. (2002). Performance-only measurement of service quality: A replication and extension. Journal of Business Research, 55(1), 17–31. doi:10.1016/S0148-2963(00)00171-5.

[74] Boonchai Kijsanayotina, Supasit Pannarunothaib, Stuart M. Speediec, Factors influencing health information technology adoption in Thailand's community health centers: Applying the UTAUT model, international journal of medical informatics 7 8 ( 2 0 0 9 ) 404–416.

[75] Venkatesh, V. F.D. Davis, A theoretical extension of the technology acceptance model: four longitudinal field studies, Manage. Sci. 46 (2) (2000) 186–204.

[76] Chau, P.Y.K. P.J.H. Hu, Investigating healthcare professionals' decisions to accept telemedicine technology: an empirical test of competing theories, Inform. Manag. 39 (4) (2002) 297–311.

[77] Gagnon, M.P. G. Godin, C. Gagne, J.P. Fortin, L. Lamothe, D. Reinharz, A. Cloutier, An adaptation of the theory of interpersonal behaviour to the study of telemedicine adoption by physicians, Int. J. Med. Inform. 71 (2003) 103–115.

# Machining Behaviour of Tantalum Nitride Coated Carbide k20 Insert on Titanium Alloy (Ti-8Al-1V)

Meenakshi Sundaram. C[1], Srinivasa Rao. S[2]

*Sri Venkateswara college of Engineering, Irrungattukottai , Pennalur,*

*Sriperumbudur, Tamil Nadu India.*

[1]cms.smw23@gmail.com

[2]ssrinivasarao3@gmail.com

***Abstract*— This paper presents the experimental investigation of plain turning on titanium alloy (Ti-8Al-1V) by tantalum nitride coated K20 carbide insert. Tantalum nitride thin film hard coated (by using sputtering technique) K20 carbide insert was studied. The main investigation is the turning performance of the insert by studying the machining parameters. All experiments were conducted on self-centring medium duty lathe of 2kW spindle speed under different turning conditions for 30 seconds duration. From the trials optimum parameters were selected and by using these parameters as constant cutting conditions, tool wear study is conducted on the coated inserts for the time duration of 60 minutes. Results are discussed with cutting speed on power consumption, tool wear and surface quality. Tantalum nitride coated insert performed good at higher cutting speeds with less feed rate and lower depth of cut.**

***Keywords*— Machining, Tantalum nitride thin film coated K20 insert, Tool wear, Surface roughness, Titanium alloy.**

## I. INTRODUCTION

Titanium alloys are now being utilized in modern aerospace, fan & compressor blades, discs, spacers, seals, rings, marine, automotive, and chemical industry due to their strength to weight ratio that can be maintained at elevated temperatures, excellent creep resistance, excellent corrosion and fracture resistance and low modulus of elasticity [1-3]. However, machining of titanium and its alloys can be considered very difficult due to its highly chemical reactivity and tendency to weld to the cutting tool, which resulted in edge chipping and rapid tool failure [3],[5],[6]. Grade 5 also known as Ti-8Al-1V is the most commonly used alloy. It has a chemical composition of 8 % aluminium, 1% vanadium. It is significantly stronger than commercially pure titanium while having the same stiffness and thermal properties excluding thermal conductivity. Among its many advantages, it is heat treatable. This grade is an excellent combination of strength, corrosion resistance, weld and fabricability. This alpha-beta alloy is the workhorse alloy of the titanium industry. The alloy is fully heat treatable in section sizes up to 15 mm and is used up to approximately $400^0$C. Since it is the most commonly used alloy –over 70% of all alloy grades melted are a sub-grade of Ti-8Al-4V, its uses span across many aerospace airframe and engine component and also major non aerospace applications in the marine, offshore and power generation industries in particular. Some of the applications are blades, discs, rings, vessels, cases, hubs, and biomedical implants [7]. The advancement in the development of the cutting tools for the past few decades showed little improvement in the mach inability of titanium alloys. Most of the cutting tool developed so far, including diamond ceramics and Cubic boron nitride, is highly reactive to titanium alloys, causing rapid wear especially at high cutting speeds [4],[9],[10].

In this direction, an investigation is made to optimize the feasibility of turning titanium alloy Ti-8Al-1V with tantalum nitride (having density 14.3g/mm3, melting point 3090 0 C) coated K20 carbide insert.

Table –1 shows the chemical composition of the work material. Table –2 gives the specification of the tool material. Table –3 gives the specification of the work material.

TABLE I

CHEMICAL COMPOSITION OF Ti-8Al-1V

| Element | Percentage |
|---|---|
| N | 0.05 |
| C | 0.08 |
| H | 0.0125 |
| Fe | 0.30 |
| O | 0.15 |
| Al | 8.10 |
| V | 0.99 |
| Mo | 1.1 |
| Ti | balance |

TABLE II

SPECIFICATION OF TOOL MATERIAL

| Insert (substrate) | K20 carbide |
|---|---|
| Type | CNMG 120408 |
| Coating process | Chemical vapour deposition (sputtering technique) |
| Coating material | Tantalum Nitride |
| Top rack angle | 0 degree |
| Tool holder | PCLNR 25*25 |

TABLE III

SPECIFICATION OF Ti-8Al-1V

| Parameters | Value |
|---|---|
| Density | 4.37 g/cc |
| Young's modules | 120 GPa |
| Tensile strength | 937 MPa |
| Yield strength | 910 MPa |
| Elongation | 10% |
| Brinell hardness | 10% |
| Melting point | Max. 1540 $^0$ C |

## II. EXPERIMENTAL PROCEDURE

Turning tests were carried out on a 60 mm dia bar of 175 mm length with dry machining condition (without coolant). All the tests were carried out on medium duty lathe of 2 kW spindle power. Cutting insert used was CNMG 120408 with top rake angle of 0 degree. Experimental parameters were of 3 different cutting speeds (50,75 and 100 m/min) with feed rate of 0.1, 0.2, and 0.3 mm/rev and depth of cut as 0.5,1.0 and 1.5 mm. Fig 1 shows the experimental set up. $L_{27}$ orthogonal array was used to conduct the experiments under dry machining conditions, analyse the machining parameters and graphs were drawn. Out of this, the best trial is investigated with the help of surface integrity and power consumed.

Using this parameter tool wear study was performed. Power was measured with the help of two watt meter method. (Model 96x96–dw 34 Sr.No:070521485 CTR 5A/415 V AC F.S 4 kW). Surface roughness was measured with the help of surface roughness tester. (Model: Mitutoyo surf test- 301). Tool wear was measured with the help of tool maker's microscope (Make: Mitutoyo).

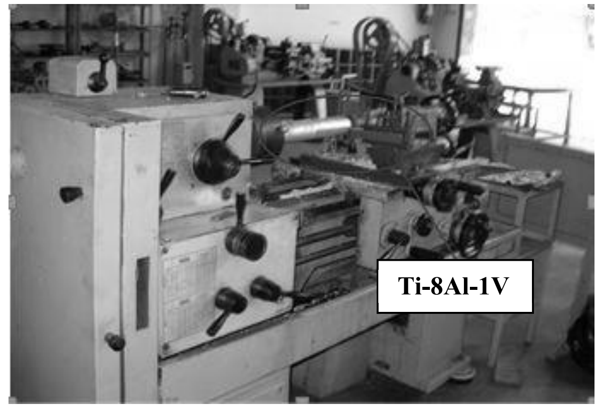


Fig. 1 Experimental Set-up

## III. RESULTS AND DISCUSSION

### A. *Effect of cutting speed on surface roughness*

It is observed that as cutting speed increases surface roughness decreases. Figs -2 and 3 show the cutting speed versus surface roughness when machined the work piece at 0.5 mm and 1.5 mm depth of cut respectively.

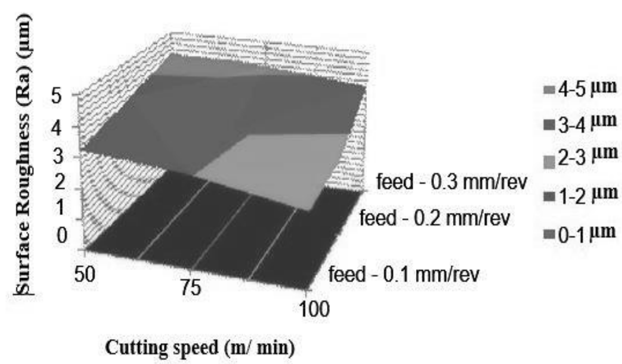


Fig. 2 Cutting speed versus surface roughness ( Depth of cut 0.5mm)

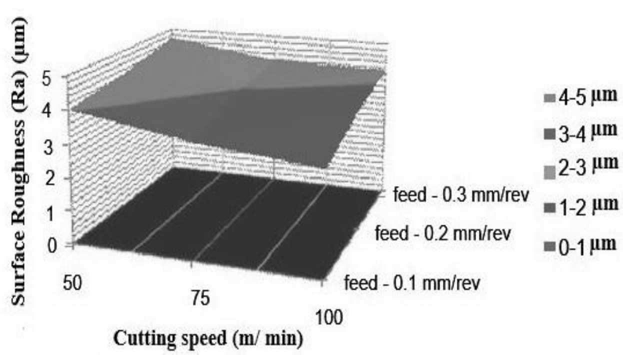


Fig. 3 Cutting speed versus surface roughness ( Depth of cut 1.5mm)

The same trend exists for the remaining combinations. It is believed that work piece tool interface friction is more at higher cutting speed. Coated carbide insert performed well in all chosen cutting speeds. The surface finish produced by the coated insert is superior. This is happened due to the wear resistance of the coated material tantalum nitride, which removes the material very easily. This coating protects the tip of the insert from wear for some extent. In all the combinations of the cutting parameters coated insert performs well. While cutting by coated insert surface roughness was less at lower speeds and slight increase in the higher speeds. It removed the material in the form of continuous chip of curling type. This happened till the coated material wore. After that, discontinuous chip was formed. It was observed that, when the coated insert was viewed under the optical microscope, the top surface of the insert was burnt. This is the fact, when machined with coated insert the coating material had reacted and burnt. Similar trend of curves showing in 1.5 mm depth of cut also.

### B Effect of cutting speed on power consumption

In figs 4 and 5 show that power consumed by main spindle is less at lower speeds. The power consumption is more at higher cutting speed. It is the fact that at higher cutting speed, power required to remove the material is more. Friction between the cutting tool and work piece is more. Similar trend is observed in all the other combinations. Fig 4 corresponds to depth of cut 0. 5 mm and fig 5 corresponds to depth of cut 1.5 mm. At higher cutting speeds formation of black colour on the machined surface, this is due to the fact titanium alloy is highly refractive material. It is observed that, when machining the titanium alloy with 1.5 mm depth of cut, power consumed by main spindle is near about 30 % more by comparing with depth of cut 0.5 mm. But in surface roughness there was not a much difference in surface finish by machining the material at depth of cut 0.5 and 1.5 mm. From this it is clearly understood that, depth of cut has less influence on surface finish

.

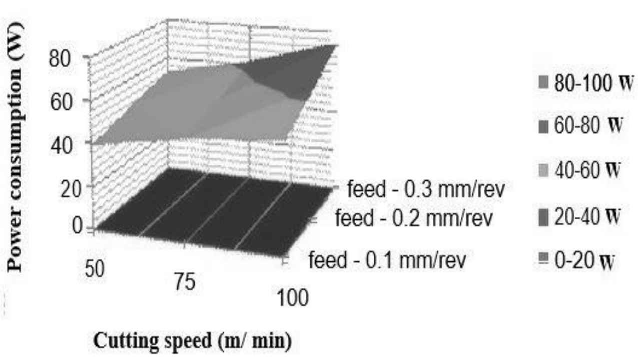


Fig.4 Cutting speed versus power consumed (Depth of cut 0.5mm)

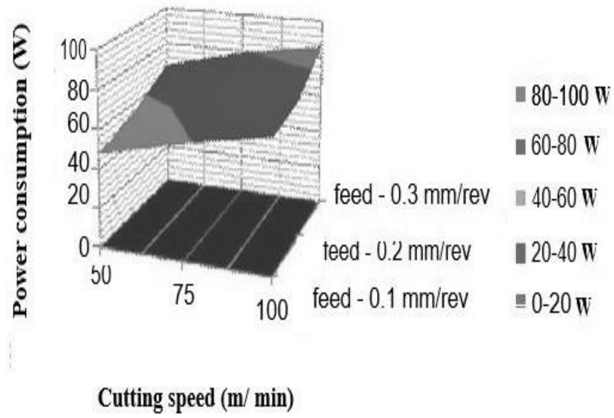


Fig.5 Cutting speed versus power consumed (Depth of cut 1.5 mm)

### C Tool wear

By setting the machining parameters as cutting speed 50 mm/min, feed rate of 0.1 mm/rev and depth of cut as 0.5 mm, tool wear study was performed for a time duration of 60 minutes. It is found that micro chipping of the cutting edge is observed due to hot hardening of the insert [8] and also the adhesive wear is noticed. Cutting edge of the insert is burnt fully after 60 minutes duration of machining. Fig – 6 shows the trend line of K20 coated carbide insert wear on the flank face. Fig – 7 & 8 shows optical image of the fresh K20 coated insert and insert after 60 minute duration of machining.

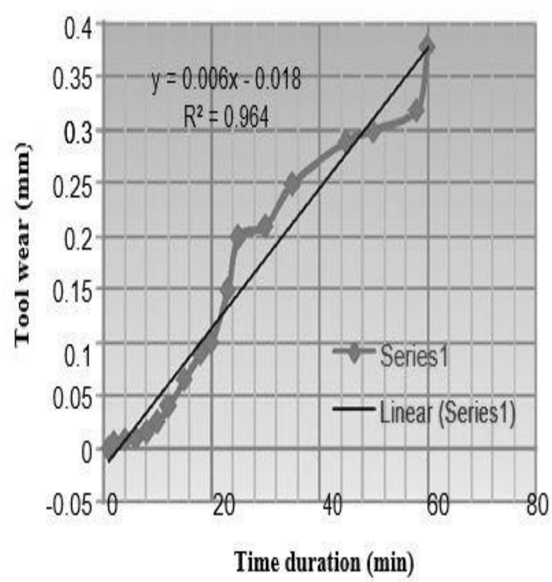


Fig.6 Time duration versus tool wear

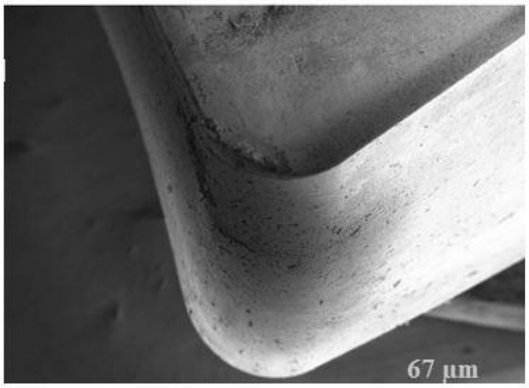


Fig.7 Fresh coated K20 insert.

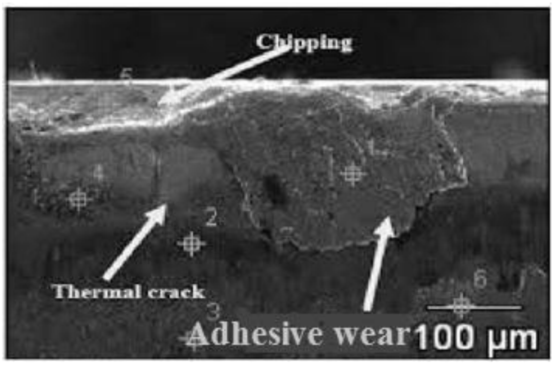


Fig.8 Worn out cutting edge after 60 minutes.

## IV. Conclusions

From the above investigation, the following observations were arrived:

The Tantalum nitride coated K20 cutting insert is quiet good for machining Ti-8Al-1V at lower cutting speed, with lower feed rate and low depth of cut.

Power consumed by main spindle is near about 30% more in 1.5 mm depth of cut by comparing with depth of cut 0.5 mm. It is observed that depth of cut has less influence on surface roughness.

Tantalum nitride coating improves the tool life by increasing the wear resistance.

Power consumption is low at lower cutting speeds, which supports that, this material possess good machinability. Continuous chip is formed while machining with tantalum nitride coated insert. Micro chipping and adhesive wear are noticed on the wear land. This is happened due to temperature. Burnt cutting edges are seen in optical microscopic image.

## References

[1] Koning,W, Applied research on the mach inability of titanium and its alloys, proc 47th meeting of AGARD structural and materials panel, sep-1978, Florence, cp256, pp 1-10, London 1979.

[2] Machado, A.R and Wallabank,J, "Machining of titanium and its alloys – a review" proc. Institution of Mechanical Engineers, vol. 204 pp 53-60, 1990.

[3] Augur, E.O and Wang Z.M., "Titanium alloys and their mach inability – a review" proc Journal of material processing technology, vol. 68, pp 262-274, 1997.

[4] Komanduri R and Von Turkovich B.F., "New observations on the mechanisms of chip formation when machining titanium alloys", Wear 69, pp 179-188, 1981.

[5] Polmer I.J, Light alloys, Metallurgy of the light metals, third edition, 1995, Arnold London, ISBN 0-340-063207.

[6] Lutjering G. Williams J.C, Titanium, 2003, Springer, ISBN 3-540-42990-5.

[7] Leyens. C, Peters. M, Titanium and titanium alloys, Fundamentals and applications, 2003, Wiley-vcy, Germany ISBN 3-27-30534-4.

[8] Hartung P.D, Kramer B.M, Tool wear in titanium machining, Annals of CIRP, 32(1) pp 75-80, 1982.

[9] Kahles J.F, Field. M, Eylon. D, Fores F.H, Machining of titanium alloys, Journal of Metals, pp 7-35, 1985.

[10] Yang. X, Liu R.C, Machining of titanium and its alloys, Machining science and technology, 3(1), pp 107-139, 1999.

# Studies on Structure and Properties of Zinc-Aluminium Alloys and Their Composites

O. Gurumurthy [#1], S.Venkateswaran [*2]

[#] *Department of Mechanical Engineering*

*BMS Institute of Technology & Management, Bengaluru, Karnataka, India.*

[1]ogmmech@bmsit.in

* *BMS Evening College of Engineering, Bengaluru , Karnataka, India.*

[2]lavenkin@yahoo.co.in

***Abstract*-- This paper discusses the findings of a detailed study of the mechanical properties of gravity die cast zinc-aluminium (ZA) alloys (ZA8, ZA12 and ZA27), without and with the addition of silicon carbide powder as particulate reinforcement.**

**Initial trials lead to the inference that amongst the Above 3 alloys, ZA27 exhibited the best mechanical properties and lowest density (or, highest strength to weight ratio).Continuing on the above inference, further work focused on the addition of ceramic reinforcement to this optimized alloy ZA27, and studying the properties of the composites thus produced. The ceramic material under consideration was silicon carbide. Green silicon carbide powder was added as reinforcement to the ZA27 alloy matrix in 2%, 4% and 6% by weight of the base alloy. As silicon carbide is a very hard material, it was expected to enhance the wear resistance substantially. Hence, the wear resistance of the ZA27+SiC composites was studied mainly to find out the beneficial effect of SiC addition.The results of the present work clearly indicate that on adding silicon carbide the wear resistance of the ZA alloy increases appreciably. The increase in wear resistance is higher corresponding to larger additions of silicon carbide. This inference is bound to lead to novel uses for ZA alloys.**

**Keywords: Zinc-Aluminium (ZA) alloy, Metal Matrix Composites (MMC), ZA8 (92%wt Zn & 8% wt Al).**

## I. Introduction

The high-aluminium containing zinc-based alloys comprise a new family of die-casting alloys that have proven themselves in a wide variety of demanding applications. These were designed to compete with bronzes and cast iron. Unique advantages are low melting temperature and energy-saving while melting, excellent castability, high as-cast strength and hardness, corrosion resistance and equivalent or even superior bearing and wear properties as compared to standard bronze and grey iron bearings.

Zinc-based alloys are the easiest to die cast. Ductility is high and impact strength is excellent, making these alloys suitable for a wide range of products. Zinc alloys can be cast with thin walls and excellent surface smoothness making preparation for plating and painting relatively easy.

The concept of application of Zn-Al bearings as substitution for the bronzes is not new. The first experiences are related to the period of the Second World War, when different Zn-Al alloys (with up to 30 % of Al) were used instead of bronze, primarily to conserve copper. Besides for bearings, the Zn-Al alloys were also applied for other applications such as machine elements, worm gears, and components of hydraulic installations.

## II. Objectives of the Present Work

*Following were the objectives of the present work:*

i) To study the structure and mechanical properties of Zinc-Aluminium alloys with varying aluminium contents.
ii) To produce composites using the optimized alloy as the base and silicon carbide as the reinforcement and to characterize the structure and mechanical properties.
iii) To assess the wear resistance of the composites in order to arrive at the optimum combination of properties and wear resistance. Wear properties of the material were studied with special interest in order to explore the possibility of using the composite material in wear resistant applications like bearings, bushings and other such applications.

## III. Experimental Details

Gravity die casting of the ZA alloys was accomplished by melting the metal in an electric resistance furnace (Fig.1). Commercially pure zinc (99.8%) and aluminium (99.90 %) were used to produce a series of ZA (ZA8, ZA12 and ZA27) test castings alloys in steel dies.

For dispersing the silicon carbide powder into the melts, molten metal was stirred using a custom made set-up (Fig. 2).

After solidification, the castings / MMCs were sectioned and tensile test specimens were machined as per ASTM specifications. These specimens were tested till fracture using a Hounsfield Tensometer and microstructural studies were carried out on usual conventional procedure.

Fig.1 Melting Process

Fig.2 Stirring for MMC production

## IV. Results And Discussion

### *A. Tensile strength and Elongation:*

The three alloys (ZA8, ZA12 & ZA27) differ radically from the standard zinc alloys in terms of composition, casting capability and engineering properties.

The load vs displacement curves for ZA8, ZA12, and ZA27 are shown in Fig. 3(a) to Fig.3(c).

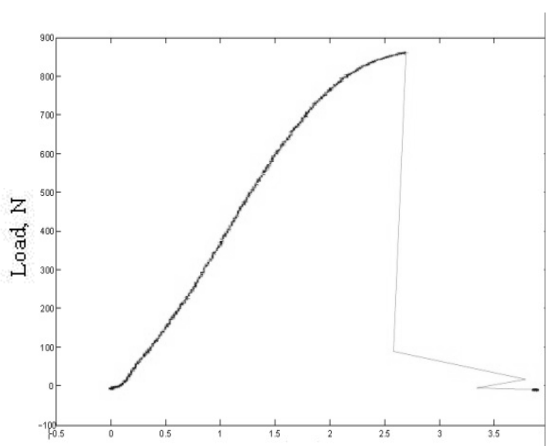


Displacement, mm

Fig. 3 (a). ZA8

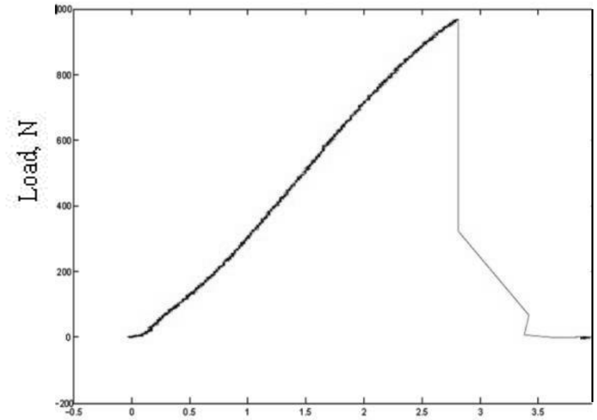


Displacement, mm

Fig. 3(b). ZA 12

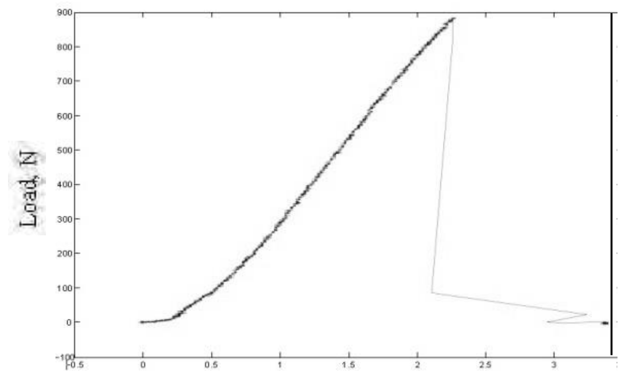


Displacement, mm

Fig. 3 (c). ZA27

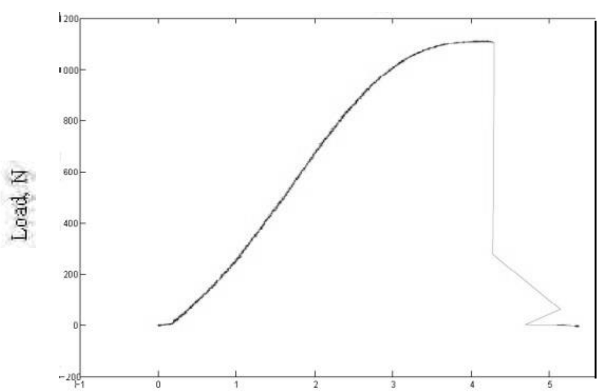


Displacement, mm

Fig. 3 (d). ZA27 + 2%SiC

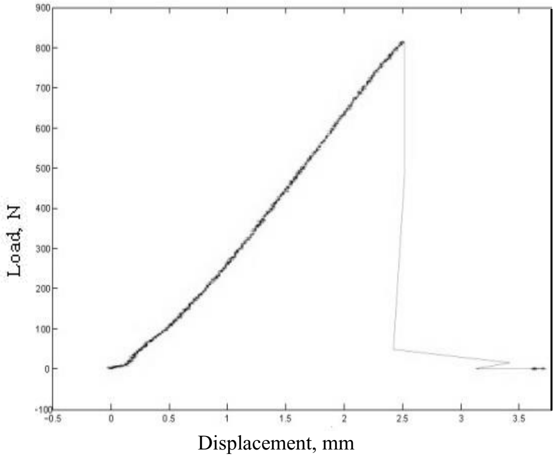


Fig. 3(e). ZA27 + 4%SiC

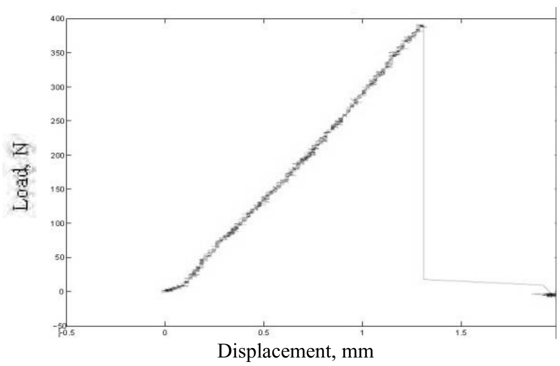


Fig.3(f). ZA27 + 6%SiC

Figure 3. Load vs. displacement graphs for ZA alloys, Fig.3 (a) to Fig.3(c) and ZA 27 alloy with Varying % of Silicon carbide, Fig.3 (d) to Fig.3 (f).

It is obvious from the above plots that of the 3 alloys studied, ZA27 exhibits the maximum UTS and elongation. Tensile strength increases in ZA alloys with increase in aluminium content from 8% to 27%. The values of UTS of the ZA27 alloy suggest that this alloy can substitute many other aluminium alloys for structural applications, with the inherent corrosion resistance. Based on these findings, further trials on MMCs were confined to ZA27 alloy as the base material. The Load Vs Displacement plots for the ZA27 based MMCs (containing respectively 2%, 4% and 6% silicon carbide reinforcement) are shown in Fig. 3(d) to Fig.3 (f).

It can be observed from the graphs that all the MMCs experience brittle fracture. Tensile strength of the composites is somewhat lower than that of the base alloy. Further, UTS reduced as the percentage of silicon carbide (SiC) increased from 2% to 6%.

*B. Wear resistance*

The pin-on-disc wear test equipment (Wear and friction monitor TR201C type) was employed for wear testing of ZA alloy specimens, corresponding to varying loads 2kg, 5kg and 8kg. The plots of wear rate for the base alloy ZA27 are shown in Fig.4. The corresponding plots for ZA27 alloy with silicon carbide reinforcements are shown in Fig. 5

It may be observed from Fig.5 that wear rate decreases with increase in aluminium content in the ZA alloy. Hence it may be concluded from the observations that the wear resistance of the ZA alloys increased with increase in the aluminium content.

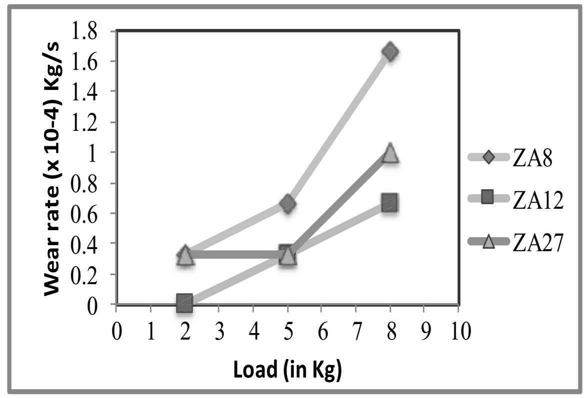


Fig 4. Load vs wear rate for ZA alloys (ZA8, ZA12 & ZA27)

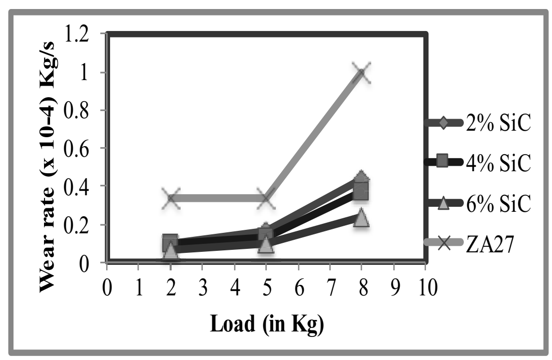


Fig. 5. Load vs wear rate for ZA27alloy based MMCs

From Fig.5, one may conclude that the wear rate of base alloy ZA27 is much higher than that of its composites. Further, wear rate decrease with increase in the SiC content. The positive effect of the reinforcement was clearly observed in increasing the wear resistance but at the cost of decreased tensile strength.

*C. Microstructures*

Metallographic specimens of die cast ZA 8, ZA12, ZA27 and ZA27+SiC were prepared by standard technique and examined using Metallovert microscope. The metallographic structures of the un-reinforced ZA8, ZA12 and ZA27 alloys are shown in Figs.7 to Fig.9 respectively.

It may be observed that the α-rich phase (shown in the images as darker regions) increases as the aluminium content goes up from 8% to 27%. In addition, the dendrite growth of α phase is observed in a η + α eutectic. Grain boundaries are also clearly observed in all the micro-structures.

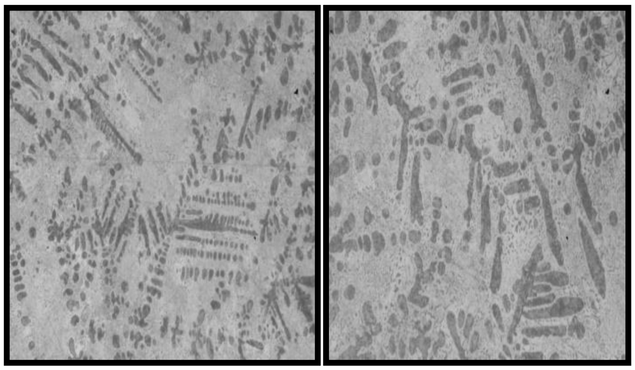

(a) 100 x (b) 200 x

Fig.6. Microstructure of ZA8 alloy

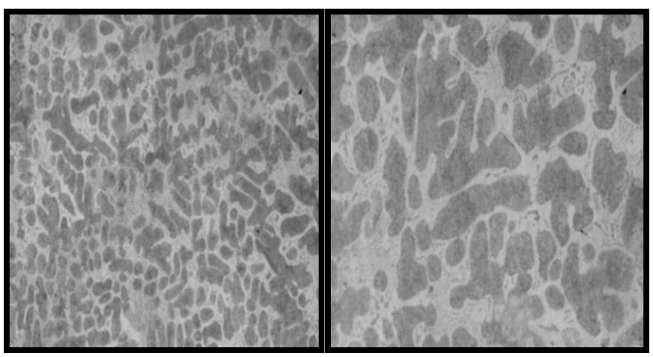

(a) 100 x (b) 200 x

Fig. 7. Microstructure of ZA12 alloy

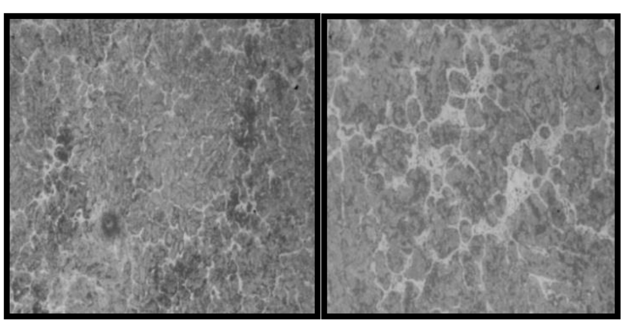

(a) 100 x (b) 200 x

Fig. 8. Microstructure of ZA27 alloy

The microstructures of ZA27 alloy based MMCs with 2%, 4% and 6% silicon carbide reinforcements are shown in Fig. 9, Fig. 10 & Fig. 11 respectively.

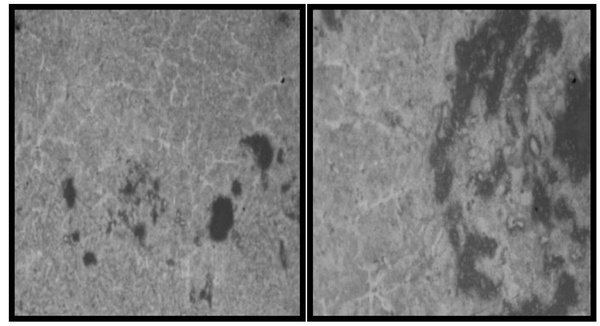

(a) 100 x (b) 200 x

Fig. 9. Microstructure of ZA27+2%SiC

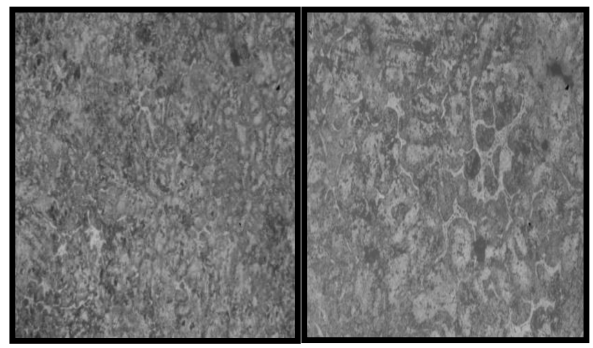

(a) 100 x (b) 200 x

Fig. 10. Microstructure of ZA27+ 4%SiC

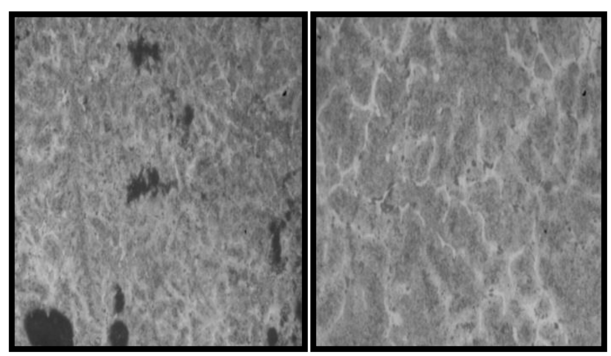

a)100 x (b) 200 x

Fig. 11 Microstructure of ZA27+ 6% SiC

The grain structure of all the MMCs appear to be similar to ZA27 alloy but with regions containing silicon carbide. The silicon carbide is evenly distributed in the solution except for the globular regions where the silicon carbide seems to have formed lumps during casting. Few regions of mild gas porosity too are seen.

## V. CONCLUSIONS

Based on the experimental investigation on ZA alloys (with varying aluminium contents) and subsequently on silicon carbide reinforced ZA27 alloy, the following salient conclusions can be drawn:

1. Aluminium content in ZA alloys plays an important role in determining the mechanical properties. As the aluminium content increases from 8.0% to 27%, mechanical properties exhibit a proportional increase.
2. The highest tensile strength is reached in the ZA 27 alloy (that contains 27% aluminium). The UTS of this alloy is far superior to that of all aluminium alloys and is comparable to that of plain carbon steels.
3. Wear resistance too seems to be influenced by the aluminium content. Higher the aluminium better is the wear resistance.
4. Further improvement is wear resistance appears to be a distinct possibility by incorporating ceramic reinforcements in ZA alloys.
5. When reinforced with silicon carbide particles (2.00% to 6.00% SiC), the war resistance of ZA27 increases appreciably.
6. Higher the SiC content better is the wear resistance. However, this improvement in wear resistance is accompanied by a drop in the tensile strength.
7. It may be stated that for novel applications that demand reasonably high tensile strength coupled with good wear resistance, ZA alloy based composites (in particular ZA27 with SiC reinforcement) could be the appropriate choice.

## ACKNOWLEDGEMENTS

The authors are highly indebted to Prof. S.Seshan, Emeritus Professor, Indian Institute of Science (IISc), Bangalore of his continuous support, words of advice and encouragement during this investigation.

## REFERENCES

[1] S.Muthukumarasamy and S. Seshan., “Structure and properties of fibre reinforced Zn-27% Al alloy based cast MMCs” Composites Vol. 26, 387 *June 1994.*

[2] Zhu, Y. H., “Phase transformations of eutectoid Zn-Al alloys”, J. Materials Science*,* Vol. 36, pp. 3973-3980, 2001.

[3] Shuqing Yan, Jingpei Xie, Zhongxia Liu, Wenyan Wang, Aiqin Wang and Jiwen Li.,“Influence on different Al contents on microstructure, tensile and wear properties of Zn based alloys” J. Mater. Sci. Technol., 2010, 26 (7), 648-652.

[4] William Mihaichuck.,“Advanced Technology Improves Zinc Castings, Eastern Alloys Inc.” Reprinted from Precision Metal June 1989.

[5] William Mihaichuck., “Zinc Alloy Bearings Challenge the Bronzes, Eastern Alloys Inc.” Reprinted from Machine Design December 10, 1981.

[6] Ž. Skoko*et al.*,“Microstructure of Al-Zn and Zn-Al Alloys”, Croatian. Chem. Acta82 (2009)

[7] Béla VARGA, *et al.,“*Phase Transformations in the Heat Treated nd Untreated Zn-Al Alloys”, Acta Universitatis Sapientiae, Electrical and Mechanical Engineering, 1 (2009) 207-213

[8] Zhu, Y. H J. *et al.,“*Structural Changes of α Phase in Furnace Cooled Eutectoid Zn-Al Based Alloy”, J Mater. Sci. Technol., Vol. 23 No.3, pp. 347-352, 2007.

# Static and Dynamic Analysis of Glass-Kevlar Hybrid Composite Plate

Dileep Kumar K[1], VV Subba Rao[2], Abinav M[3]

*Department of Mechanical Engineering, University College of Engineering*
*JNTUK, Kakinada, Andhra Pradesh, India.*

[1]davidkumar999@yahoo.com

[2]rao703@yahoo.com

3abinavmajety@gmai.com

***Abstract*** **- The growing technology in all field of engineering demands improved material properties i.e. Physical, mechanical, thermal, chemical, electrical and electronic properties of the materials. One of the alternative material found and performing progressive research from few years is the composite material, combining two or more than two materials on macroscopic scale results a material having superior properties which the neither of the constituent can have when acting independently. The main added advantage of composite material over conventional materials is the lightweight, highly corrosion resistance, stable mechanical properties over certain range of temperatures, high fatigue strength. The composite is the principal structure material in some applications like Missiles, Rockets, aircrafts wing panels, Submarine, Pedestrian Man hole covers and the defence under earth oil sump man hole covers composite structures are extensively used, because of its high strength to weight ratio, long life and better performance.**

**In the present paper an attempt is made on a rectangular glass-kevlar hybrid composite plate with simply supported on all edges to predict the static structural response for a pre-assumed load a concentrated load on the centre of the plate. It is also proposed to estimate dynamic behaviour. The design variables adopted is ply thickness. The work encompasses the analytical solution to static and dynamic analysis of composite plate (Deflection, Natural frequency and Specific damping capacity). Obtained results are compared for the best choice. In order to avoid repeated and rigorous hand calculations involved in the analytical procedure a suitable MATLAB code is developed.**

***Keywords*****—Deflection, Stress, Natural frequency, Specific damping capacity, Hybrid composite, MATLAB.**

## I. INTRODUCTION

Usage of strong, stiff, lightweight materials for application to diverse structures from aircraft, spacecraft, submarines, and surface ships to robot components, prosthetic devices, civil structures, pedestrian man hole area covers, automobiles, trucks, and rail vehicles-focus by using fiber-reinforced materials. Advanced composite materials, particularly continuous fibre-reinforced composites, are currently being used in a wide variety of structural applications.

Advanced composite materials, particularly continuous fibre-reinforced composites, are currently being used in a wide variety of structural applications. Hybrid composite materials of two or more reinforcements in a matrix material are being used for various applications.

Savithri and Vardhan[1] had studied the nonlinear behaviour of simply supported symmetrically laminated orthotropic plates subjected to uniform distributed loads using accurate displacement based higher order theory. Exact elastic solutions for some particular plate bending problems have been obtained by Pagno and Srinivasa [2]. Ghosh and Dey [3] had presented bending of laminated plates with four noded rectangular element with 7 degrees of freedom at each node. Kuppusamy and J.N.Reddy [4] had presented the three-dimensional nonlinear analysis of cross-ply rectangular plates using 8-noded iso parametric brick element. Brewer J. C. and P. A. Lagace [5] Studied delamination failures in the composite structures using Quadratic stress criterion. Brunelle, E. J. and S. R. Robertson, [6] had done research on dynamic behaviour of composite laminated thick plates. Fukuda, H., H. Tomatsu and J. Yasuda, [7] Studied the interaction between fiber and matrix in the three – dimensional domain.

## II. DEFLECTIONS AND STRESSES

Consider a Plate, with length a in the x direction, width b in the y direction. The lamina stiffnesses referred to principal co-ordinate system are given as:

$$Q = \begin{bmatrix} Q_{11} & Q_{12} & Q_{16} \\ Q_{16} & Q_{22} & Q_{26} \\ Q_{16} & Q_{26} & Q_{66} \end{bmatrix} \tag{1}$$

In plane stress assumption $\sigma_3$ , $\tau_{23}$, and $\tau_{13}$ are set to zero. Including the shear stress-shear strain relation, the relation between stresses and strains for the state of plane stress is written as

$$\begin{Bmatrix}\sigma_1\\ \sigma_2\\ \tau_{12}\end{Bmatrix}=\begin{bmatrix}Q_{11} & Q_{12} & 0\\ Q_{12} & Q_{22} & 0\\ 0 & 0 & Q_{66}\end{bmatrix}\begin{Bmatrix}\varepsilon_1\\ \varepsilon_2\\ \gamma_{12}\end{Bmatrix}$$

$$Q_{11}=\frac{E_1}{1-\upsilon_{12}\upsilon_{21}}$$

$$Q_{12}=\frac{E_1\upsilon_{21}}{1-\upsilon_{12}\upsilon_{21}}=\frac{E_2\upsilon_{12}}{1-\upsilon_{12}\upsilon_{21}} \tag{2}$$

$$Q_{22}=\frac{E_2}{1-\upsilon_{12}\upsilon_{21}}$$

$$Q_{66}=G_{12}$$

The transformed reduced stiffness or off-axis reduced stiffness [$Q_{ij}$] of each lamina referred to laminate co-ordinate system by using $\theta_k$ is given as.

$$\overline{Q_{ij}}=\begin{bmatrix}\overline{Q_{11}} & \overline{Q_{12}} & \overline{Q_{16}}\\ \overline{Q_{12}} & \overline{Q_{22}} & \overline{Q_{26}}\\ \overline{Q_{16}} & \overline{Q_{26}} & \overline{Q_{66}}\end{bmatrix} \tag{3}$$

$$\overline{Q_{11}}=Q_{11}Cos^4\theta+2(Q_{12}+2Q_{66})Sin^2\theta Cos^2\theta+Q_{22}Sin^4\theta$$
$$\overline{Q_{12}}=(Q_{11}+Q_{22}-4Q_{66})Sin^2\theta Cos^2\theta+Q_{12}(Sin^4\theta+Cos^4\theta)$$
$$\overline{Q_{22}}=Q_{11}Sin^4\theta+2(Q_{12}+2Q_{66})Sin^2\theta Cos^2\theta+Q_{22}Cos^4\theta$$
$$\overline{Q_{16}}=(Q_{11}-Q_{12}-2Q_{66})Sin\theta Cos^3\theta+(Q_{12}-Q_{22}+2Q_{66})Sin^3\theta Cos\theta$$
$$\overline{Q_{26}}=(Q_{11}-Q_{12}-2Q_{66})Sin^3\theta Cos\theta+(Q_{12}-Q_{22}+2Q_{66})Sin\theta Cos^3\theta$$
$$\overline{Q_{66}}=(Q_{11}+Q_{22}-2Q_{12}-2Q_{66})Sin^2\theta Cos^2\theta+Q_{66}(Sin^4\theta+Cos^4\theta)$$

The ABD laminate stiffness matrices using inter laminar locations (z) can be expressed as follows:

$$\mathrm{A_{ij}}=\sum_{k=1}^{n}\left(\overline{Q_{ij}}\right)(Z_k-Z_{k-1}) \tag{4}$$

$$\mathrm{B_{ij}}=\frac{1}{2}\sum_{k=1}^{n}\left(\overline{Q_{ij}}\right)(Z^2{}_k-Z^2{}_{k-1}) \tag{5}$$

$$D_{ij}=\frac{1}{3}\sum_{k=1}^{n}\left(\overline{Q_{ij}}\right)(Z^3{}_k-Z^3{}_{k-1}) \tag{6}$$

The deflection of the plate using stiffness matrix D can be calculated as:

$$\mathrm{w}^0(\mathrm{x},\mathrm{y})=\sum_{\mathrm{m}=1,3}^{\infty}\sum_{n=1,3}^{\infty}W_{mn}\sin\frac{m\pi x}{a}\sin\frac{n\pi x}{b} \tag{7}$$

$$Q_{mn}=\frac{16q_0}{mn\pi^2}\text{, for UDL}$$
$$Q_{mn}=\frac{4q_0}{mn\pi^2}\sin\frac{m\pi x_o}{a}\ \sin\frac{n\pi y_o}{b}\text{, for point load} \tag{8}$$

$$W_{mn}=\frac{Q_{mn}}{D_{11}\left(\frac{m\pi}{a}\right)^4+2(D_{12}+2D_{66})\left(\frac{m\pi}{a}\right)^2\left(\frac{n\pi}{b}\right)^2+D_{22}\left(\frac{n\pi}{b}\right)^4} \tag{9}$$

where $q_0$ is the magnitude of the load.

The theory which predicts the relations between strain and stress of a laminate is Classical Lamination Theory (CLT). The basic assumptions considered while deriving the relation between strain and stress of a laminate are - Each layer of the laminate is orthotropic. The laminate is thin with its lateral dimensions much larger than its thickness and it is loaded in its plane only i.e. the laminate and its layers are in the state of plane stress.

All displacements are small compared to the thickness of the laminate. Displacements are continuous throughout the laminate. In-plane displacements (u,v) vary linearly through the thickness of the laminate (z). Transverse shear strains are negligible.

The straight lines normal to the middle surface remain straight and normal to that surface after deformation. Strain-displacement and stress-strain relations are linear. Normal distances from the middle surface remain constant, i.e. the transverse normal strain is negligible compared with the in-plane strains.

The strains in the plate in each layer can be calculated as

$$\varepsilon_x=zk_x^0$$
$$\varepsilon_y=zk_y^0 \tag{10}$$
$$\gamma_{xy}=zk_{xy}^0$$

The locations of the layer interfaces are denoted by a subscripted z; the first layer is bounded by locations $z_0$ and $z_1$, the second layer by $z_1$ and $z_2$, the kth layer by $z_{k-1}$and $z_k$, and the nth layer $z_{n-1}$ and $z_n$.

The curvatures of the plate can be calculated as

$$k_x^0=-\frac{\partial^2\omega^0}{\partial \mathrm{x}^2}=\sum_{\mathrm{m}=1,3}^{\infty}\sum_{n=1,3}^{\infty}W_{mn}\left(\frac{m\pi}{a}\right)^2\sin\left(\frac{m\pi x}{a}\right)\sin\left(\frac{n\pi y}{b}\right)$$

$$k_y^0=-\frac{\partial^2\omega^0}{\partial \mathrm{y}^2}=\sum_{\mathrm{m}=1,3}^{\infty}\sum_{n=1,3}^{\infty}W_{mn}\left(\frac{n\pi}{b}\right)^2\sin\left(\frac{m\pi x}{a}\right)\sin\left(\frac{n\pi y}{b}\right) \tag{11}$$

$$k_{xy}^0=-2\frac{\partial^2\omega^0}{\partial \mathrm{y}^2}=-2\sum_{\mathrm{m}=1,3}^{\infty}\sum_{n=1,3}^{\infty}W_{mn}\left(\frac{m\pi}{a}\right)\left(\frac{n\pi}{b}\right)\cos\left(\frac{m\pi x}{a}\right)\cos\left(\frac{n\pi y}{b}\right)$$

The values of all the $B_{ij}$ will be zero for all symmetric laminates. Hence, the resultant moments can be calculated as:

$$M_x = D_{11}k_x^0 + D_{12}k_y^0$$
$$M_y = D_{12}k_x^0 + D_{22}k_y^0 \tag{12}$$
$$M_{xy} = D_{66}k_{xy}^0$$

The stresses in the plate in each layer can be calculated as

$$\begin{Bmatrix} \sigma_x \\ \sigma_y \\ \tau_{xy} \end{Bmatrix} = \begin{bmatrix} \overline{Q_{11}} & \overline{Q_{12}} & \overline{Q_{16}} \\ \overline{Q_{12}} & \overline{Q_{22}} & \overline{Q_{26}} \\ \overline{Q_{16}} & \overline{Q_{26}} & \overline{Q_{66}} \end{bmatrix} \begin{Bmatrix} \varepsilon_x \\ \varepsilon_y \\ \gamma_{xy} \end{Bmatrix} \tag{13}$$

The global co-ordinate system is related by principal co-ordinate system with transformation matrix. Using the stress transformation, the principal stresses can be calculated as

$$\begin{Bmatrix} \sigma_1 \\ \sigma_2 \\ \tau_{12} \end{Bmatrix} = [T] \begin{Bmatrix} \sigma_x \\ \sigma_y \\ \tau_{xy} \end{Bmatrix} \tag{14}$$

$$[T] = \begin{bmatrix} m^2 & n^2 & 2mn \\ n^2 & m^2 & -2mn \\ -mn & mn & m^2 - n^2 \end{bmatrix}$$

Where m= cosθ, n = sinθ.

The natural frequency of the composite plate can be calculated by using the relation

$$\omega_{mn} = \sqrt{\frac{\gamma_m^4 (D_{11})_p + \gamma_m^2 \gamma_n^2 2H_1 + \gamma_n^4 (D_{22})_p}{M}} \tag{15}$$

Where, $\gamma_m = \frac{m\pi}{a}$ and $\gamma_n = \frac{n\pi}{a}$

And M is area mass density of the composite plate. For different values of m and n, there corresponds a unique frequency and a corresponding mode shape.

## III. Parametric Study

Kevlar fibers have higher stiffness and lower density, but they are limited by very low compressive strength in the composite and high moisture absorption these fibers have high tensile strength. Aramid fibers are known for their large hardness and resistance to penetration. These fibers are less brittle than carbon or glass fibers. The mostly glass fibers are used after the Kevlar fibers. Aramid fibers are used where high impenetrability is required, e.g. bulletproof vests, bike tyres, airplanes wings, and sport equipment. These fibers are not as spread as glass or carbon fibers, mostly because of their cost, high water absorption. The material chosen is Kevlar/E-Glass hybrid composite with stacking orientation of [90/0/90/0/0/90/0/90] and stacking sequence of [K/E/K/E/E/K/E/K]. The thickness of the plate is $t_p$ = 10 mm.

The Kevlar/epoxy composite material has properties as longitudinal modulus $E_1$ = 87GPa, transverse modulus $E_2$ = 5.5GPa, shear modulus $G_{12}$ = 2.2GPa and Poisson's ratio $V_{21}$ = 0.34. The density is 1380Kg/m$^3$.

The E-Glass/epoxy composite material has properties as longitudinal modulus $E_1$ = 37.8GPa, transverse modulus $E_2$ = 10.9GPa, shear modulus $G_{12}$ = 4.91GPa and Poisson's ratio $V_{21}$ = 0.29. The density is 1920Kg/m$^3$.

While varying the aspect ratio, the width of the plate is kept constant as b=310mm.

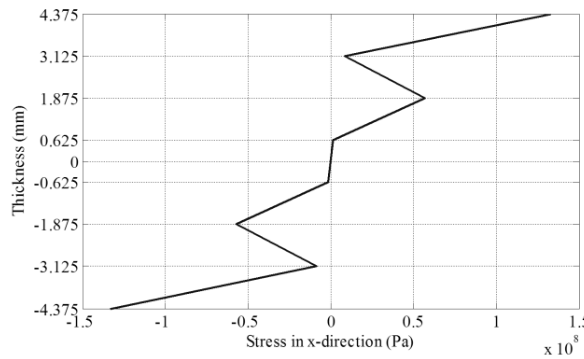


Fig. 1. Variation of stress ($\sigma_x$) through the thickness of square cross-ply laminate under concentrated load.

The maximum stress in x direction is observed in the top and bottom layers of the hybrid composite when subjected to concentrated load of 5000N as shown in the Fig. 1.

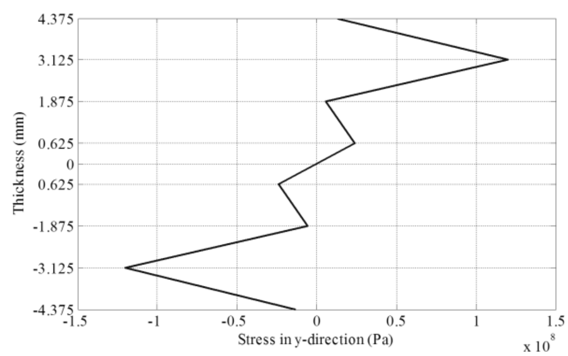


Fig. 2. Variation of stress ($\sigma_y$) through the thickness of square cross-ply laminate under concentrated load.

The variation of stresses $\sigma_x$ and $\sigma_y$ along the thickness of the cross-ply composite laminate under concentrated load of 5000N at the center of the plate are shown in the figure 1. and figure. 2 respectively. The maximum stress in y direction is observed in the second and seventh layers of the hybrid composite as shown in the Fig. 2.

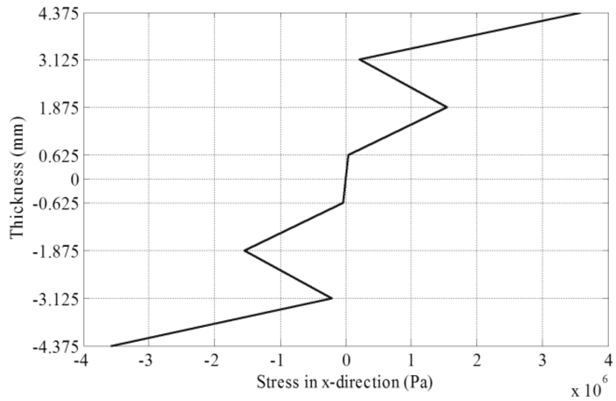


Fig. 3. Variation of stress ($\sigma_x$) through the thickness of square cross-ply laminate under uniformly distributed load.

The maximum stress in x direction is observed in the top and bottom layers of the hybrid composite when subjected to uniformly distributed load of 5000Pa as shown in the Fig. 3 .

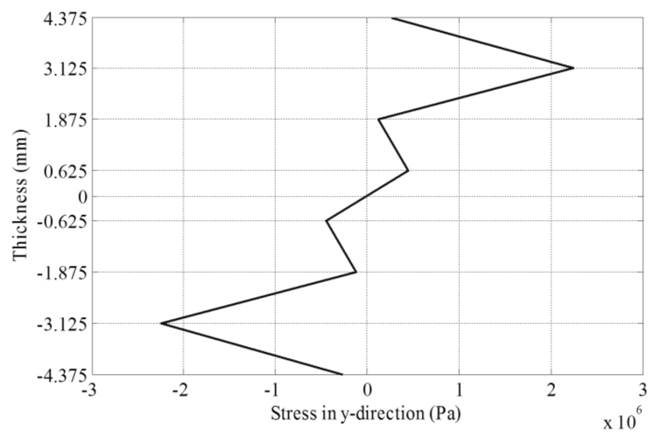


Fig. 4. Variation of stress ($\sigma_y$) through the thickness of square cross-ply laminate under uniformly distributed load.

The variation of stresses $\sigma_x$ and $\sigma_y$ along the thickness of the cross-ply composite laminate under uniformly distributed load of 5000Pa on the plate are shown in the figure. 3 and Figure 4 respectively. The maximum stress in y direction is observed in the second and seventh layers of the hybrid composite as shown in the Fig. 4.

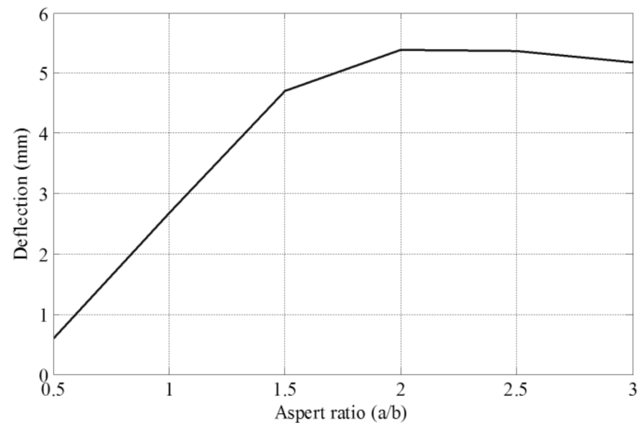


Fig. 5. Deflection (mm) under concentrated load versus aspert ratio (a/b) of the symmetric cross-ply composite laminate.

The maximum deflection is obtained at aspect ratio 2 in case of concentrated load of 5000N acting at the centre of the plate of a=b=310mm.

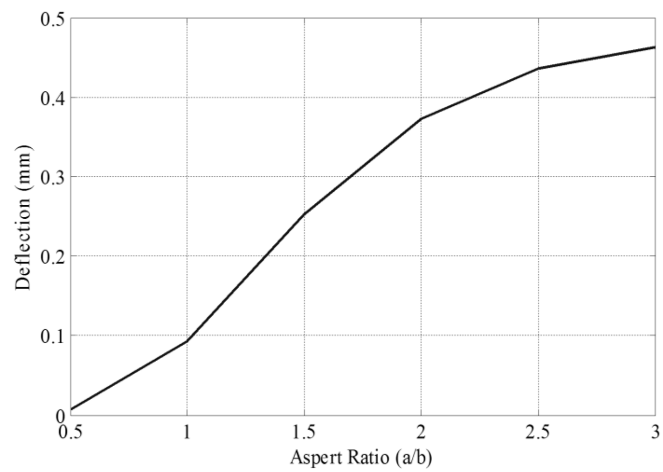


Fig. 6. Deflection (mm) under uniformly distributed load versus aspert ratio (a/b) of the symmetric cross-ply composite laminate.

The deflection in the cross-ply composite laminate for concentrated load and UDL for different aspect ratios are shown in the figure 5 and 6 respectively. These deflections are calculated by using the Eq. (7). The maximum deflection is increasing as the aspect ratio increases in case of concentrated load of 5000N acting at the centre of the plate of a=b=310mm.

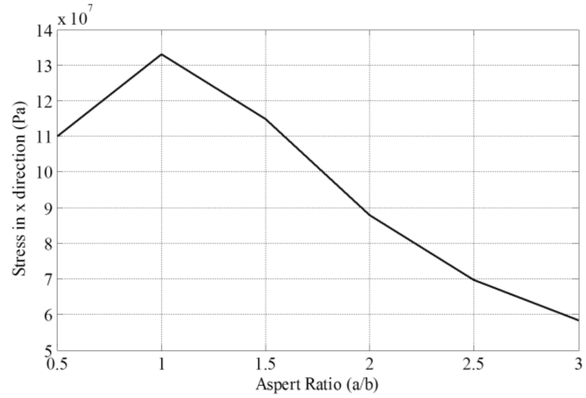


Fig. 7. Maximum stress (Pa) in x direction under point load versus aspert ratio (a/b) of the symmetric cross-ply composite laminate.

The maximum stress $\sigma_x$ can be observed at aspect ratio of 1 in case of concentrated load of 5000N.

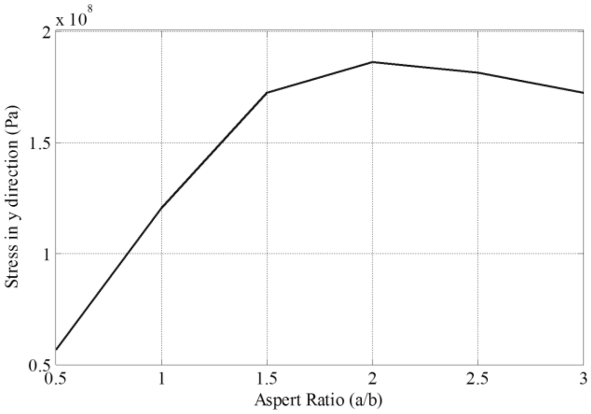


Fig. 8. Maximum stress (Pa) in y direction under point load versus aspert ratio (a/b) of the symmetric cross-ply composite laminate.

The effect of aspert ratio on the maximun stresses induced in the square composite laminate by concentrated load of 5000N are shown in the Fig. 7. and Fig. 8. In case of concentrated load, the maximum stress $\sigma_y$ can be observed at aspect ratio of 2.

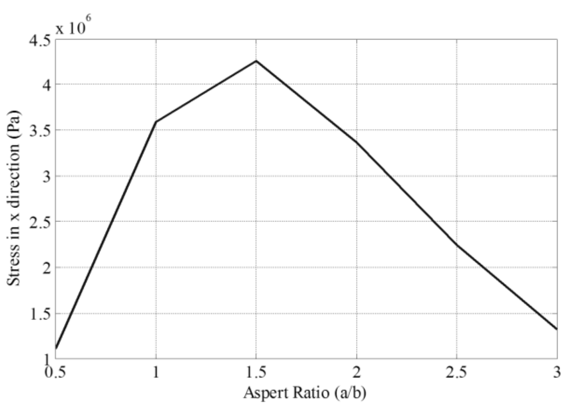


Fig. 9. Maximum stress (Pa) in x direction under uniformly distributed load versus aspect ratio (a/b) of the symmetric cross-ply composite laminate.

The maximum value of $\sigma_x$ is observed at aspect ratio 1.5 in case of uniformly distributed load of 5000Pa.

The effect of aspert ratio on the maximun stresses induced in the symmetric cross-ply composite laminate subjected to uniformly load of 5000Pa are shown in the Fig. 9. and Fig. 10. The maximum value of $\sigma_y$ is increasing as the aspect ratio is increasing in case of uniformly distributed load of 5000Pa

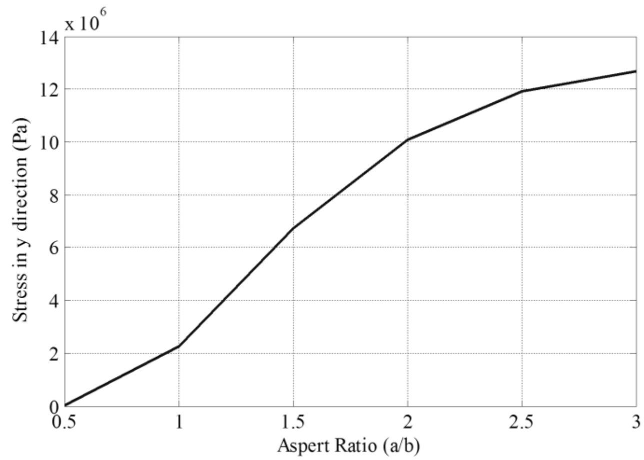


Fig. 10. Maximum stress (Pa) in y direction under uniformly distributed load versus aspect ratio (a/b) of the symmetric cross-ply composite laminate.

.

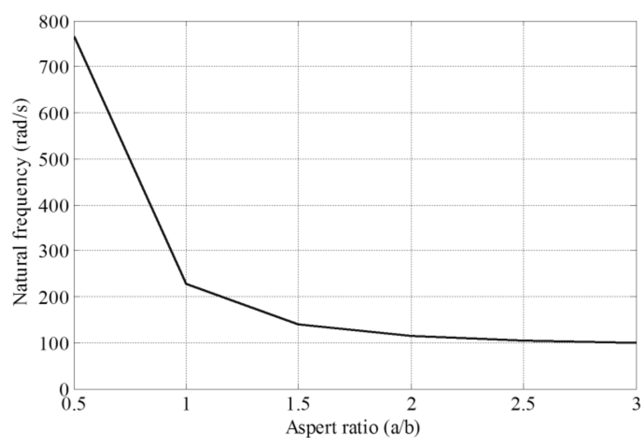


Fig. 11. Fundamental natural frequency (rad/s) versus aspect ratio (a/b).

The fundamental natural frequencies of the symmetric cross-ply laminate plate are tabulated in Table. I. These fundamental natural frequencies are calculated by using Eq. (15). The fundamental natural frequency is reduced as the aspect ratio increases.

TABLE VII
FUNDAMENTAL NATURAL FREQUENCIES (RADS/S) OF THE COMPOSITE LAMINATE FOR DIFFERENT ASPECT RATIOS

| Aspect ratio (a/b) | Frequency rad/s |
|---|---|
| 0.5 | 766.5427 |
| 1 | 226.6837 |
| 1.5 | 138.433 |
| 2 | 113.3053 |
| 2.5 | 103.8244 |
| 3 | 99.4578 |

## IV. CONCLUSIONS

In case of concentrated load, the maximum deflection is obtained at aspect ratio 2 and for UDL; the maximum deflection is increasing as the aspect ratio increases. In case of concentrated load, the maximum stress $\sigma_x$ can be observed at aspect ratio of 1 and for UDL; the maximum value of $\sigma_x$ is observed at aspect ratio 1.5. In case of concentrated load, the maximum stress $\sigma_y$ can be observed at aspect ratio of 2 and for UDL; the maximum value of $\sigma_y$ is increasing as the aspect ratio is increasing. The fundamental natural frequency reduces as the aspect ratio increases.

## REFERENCES

[1] Savithri and Vardan *Journal on non liner behavior of composite plates* 1995.

[2] Pipes and N. R. B J Pagano, ' *Inter laminar stresses in composite laminates under uniform axial extension*.' J. Composite Materials, 4 538-548 (1970).

[3] Ghosh, A. K. and S. S. Dey, *A Simple finite element for the analysis of laminated plates, Computers and Structures*, 44(3): 585-596, 1991.

[4] Kuppusamy, T. and J. N. Reddy, *A three dimensional nonlinear analysis of cross-ply rectangular composite plates*, *Computers and Structures*, 18(2): 263-272, 1984.

[5] Brewer, J. C. and P. A. Lagace, *Quadratic stress criterion of initiation of delamination, Journal of composite Materials*, 22: 1141-1155, 1988.

[6] Brunelle, E. J. and S. R. Robertson, *Vibrations of an initially stressed thick plate, Journal of Sound and Vibration,* 45: 406-416, 1976.

[7] Fukuda, H., H. Tomatsu and J. Yasuda, *Three-dimensional micromechanical approach to the strength of unidirectional composites*, Proceedings of 7th Japan-U.S. Conference on Composite Materials, 255-265, 1995.

[8] J. N. Reddy, *Mechanics of Laminated Composite plates and shells Theory and Analysis- second edition*.

# Experimental Studies on the Effect of $TiO_2$ Nanoparticles on the Mechanical Properties of Aluminium Matrix Nanocomposites

Adil Nazaruddin, T. S. Krishna Kumar[2], Ahammed Vazim K. A, Syed Muhammed Fahd

*Department of Mechanical Engineering, TKM College of Engineering*

*Kollam, Kerala, India*

[2]krishnakumarts@gmail.com

***Abstract*** **- Strength and hardness of aluminium can be increased through the addition of nanoparticles. Aluminium matrix nanocomposites (AMNC) are widely used in many engineering applications because of their low density, improved fracture toughness and high specific stiffness. In the present study, aluminium matrix nanocomposite (AMNC) samples were fabricated using $TiO_2$ nanoparticles as the reinforcement by using powered stir casting method. Mechanical properties such as tensile strength and hardness were evaluated and compared with that of pure aluminium. Microstructural evaluation and XRD studies were conducted on these prepared nanocomposite samples. The study reveals that the presence of $TiO_2$ nanoparticles in the aluminium matrix led to the improvement in the mechanical properties of the prepared nanocomposite samples. As the size of $TiO_2$ nanoparticles increases in the aluminium matrix, its hardness and tensile properties also increases. But when the size of $TiO_2$ nanoparticles changes from nanoscale to microscale, the tensile properties slightly reduced compared to that of nanocomposites. Microstructural evaluation and XRD studies showed a positive response to the addition of $TiO_2$ nanoparticles in the aluminium matrix indicating the better mechanical properties.**

***Keywords:*** **Aluminium matrix nanocomposites; $TiO_2$ nanoparticles; powered stir casting method; tensile strength; Microstructural evaluation.**

## I. Introduction

Metal matrix nanocomposites (MMNC) refers to the materials containing a ductile metal or alloy matrix in which some reinforcement nanoparticles are implanted. These nanocomposites combine the features of metals and ceramics. Adding nanoparticles to the metal matrix can improve its performance, often in large degrees, by simply capitalizing on the nature and properties of the reinforcement nanoparticle. Nanocomposite materials have become a suitable alternative to overcome the limitations of micro-composites.

Reduced weight, increased dimensional stability, higher electrical conductivity, higher chemical resistance, high thermal stability, high temperature creep resistance, improved specific strength and stiffness, high modulus of elasticity and wear resistance are some of the advantages of metal matrix nanocomposites when compared with other conventional materials.

A key challenge in the production of metal matrix nanocomposites is to homogeneously distribute the reinforcement particle in the metal matrix in order to achieve a defect-free microstructure. The vortex method is used to maintain a good distribution of the reinforcement particle in the metal matrix. A major problem concerned with the stir casting process is the isolation of reinforcement particles which is caused due to the settling of the reinforcement particles during melting and casting processes. Stir casting is the most economical method for producing aluminium based nanocomposites.

M. Ravichandran, S. Dineshkumar (2014), fabricated aluminium metal matrix composites through liquid powder metallurgy route. The aluminium matrix composite contains $TiO_2$ reinforcement particle was produced to study the mechanical properties such as tensile strength and hardness. The characterization studies also carried out to evident the phase presence in the composite and the results are discussed for the reinforcement addition with the mechanical properties. Results show that, the addition of 5 weight percentage of $TiO_2$ to the pure aluminium improves the mechanical properties. M. Karbalaei Akbari, O. Mirzaee, H.R. Baharvandi (2013), proposed a novel method focusing on nanoparticle distribution in aluminium matrix. Nano-$Al_2O_3$ particles were separately milled with aluminum and copper powders and incorporated into A356 alloy to manufacture A356/1.5 vol.% nano-$Al_2O_3$ reinforced composite via stir casting method. It was revealed that the presence of nano-$Al_2O_3$ particles in aluminum matrix led to a significant improvement in the mechanical properties of the composites compared with those of the aluminium alloy.

## II. EXPERIMENTAL PROCEDURE

In the present study, commercially pure aluminium was used as the base material. The reinforcement was chosen as titanium dioxide nanoparticles ($TiO_2$) with mean diameters of 15nm, 35nm, 50nm and 330nm in size. With the base metal as aluminium, the nanocomposite samples have been fabricated with 2.5 weight % of $TiO_2$ nanoparticles.

Pit furnace is used for the fabrication of aluminium as well as aluminium matrix nanocomposite samples. Pit furnaces can be either floor-mounted or pit-mounted. Fig.1 shows the schematic diagram of Pit furnace set up. Fabrication of aluminium samples is as follows. Initially, aluminium is cut into the required pieces as per the requirement. Then it is placed in a graphite crucible inside the Pit furnace. Charcoals are burned and packed around the crucible inside the pit furnace. One side of the pit furnace is connected with an electrically operated blower which sucks the air from the atmosphere and sends to the pit furnace for the continuous generation of heat. With the help of this blower, sufficient amount of air is supplied towards the charcoal. Thus aluminium starts to melt. After the aluminium is melted to about $700^0$C, the crucible is lifted using crucible lifting tongs. Then the crucible is placed in the pouring shank. Then the melt was poured into the mould using the pouring shank. After pouring the molten metal into the moulds, it is kept for some time to solidify. After the solidification process, the specimens were prepared for hardness test and tensile test.

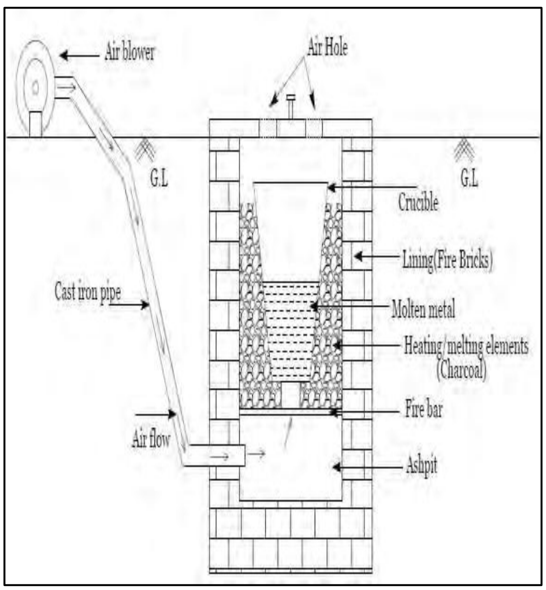


Fig. 1 Schematic diagram of Pit furnace set up

Powered stir casting method was used for the fabrication of aluminium matrix nanocomposite samples.

When aluminium starts to melt, powered stir casting equipment was used to stir at about 550rpm. With the help of steel tube, $TiO_2$ nanoparticles of size 15nm (2.5%) were added into the vortex of the aluminium matrix during stirring from the top of the crucible. The solution was stirred for about 5 minutes while keeping the pit furnace in working mode. Finally, it is casted into the required specimens for hardness test and tensile test. The same procedure was repeated with $TiO_2$ nanoparticles of sizes 35nm, 50nm and 330nm respectively. Schematic diagram of Powered stir casting set up is shown in fig. 2.

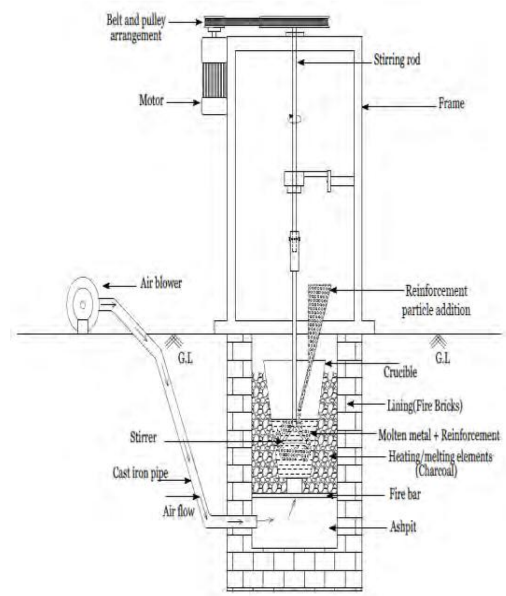


Fig. 2 Schematic diagram of Powered stir casting set up

## III. CHARACTERIZATION TECHNIQUES

Microstructural evaluation of all the nanocomposite samples were conducted using an optical microscope with the provision for image analysis. A section was cut out from the castings made. It was first belt grinded followed by polishing with different grade of emery papers. The final flat scratch-free surface was obtained by using a wet rotating wheel covered with a cloth. The abrasive used was diamond paste. Then they were washed, dried and etched with Keller's reagent and then examined under optical microscope.

X-PERT PRO diffractometer system was used for carrying out the X-ray diffraction studies for all the nanocomposite samples. The experimental results obtained were compared with that of the standard powder diffraction pattern using JCPDS ( Joint Committee on Powder Diffraction Standards) database. Hardness testing for all the nanocomposite samples were determined by using Rockwell hardness testing machine. Here, the Rockwell hardness test method consists of indenting the test material with a hardened steel ball indenter. The indenter was forced into the test material under a preliminary minor load of 10kgf. The tensile properties namely nominal breaking stress, actual breaking stress and ultimate stress were investigated in the Universal Testing Machine (UTM).

## IV. RESULTS AND DISCUSSION

The optical microscopic images of aluminium and aluminium matrix nanocomposite (AMNC) samples taken at 50X magnification are shown below from fig. 3 to fig. 7 respectively.

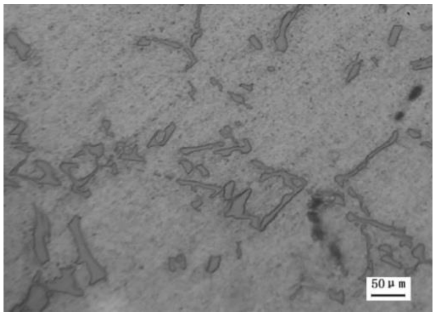

Fig. 3 Optical microscopic image of pure aluminium

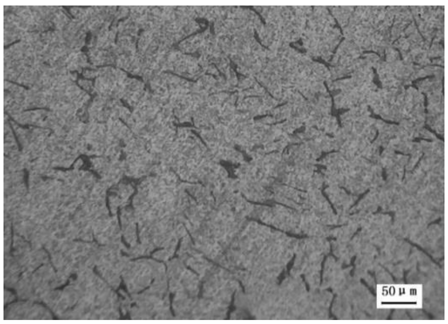

Fig. 4 Optical microscopic image of aluminium reinforced with 15nm sized $TiO_2$ particles

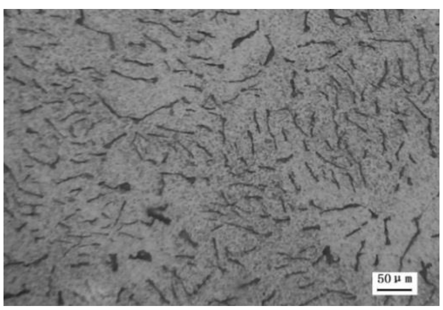

Fig. 5 Optical microscopic image of aluminium reinforced with 35nm sized $TiO_2$ particles

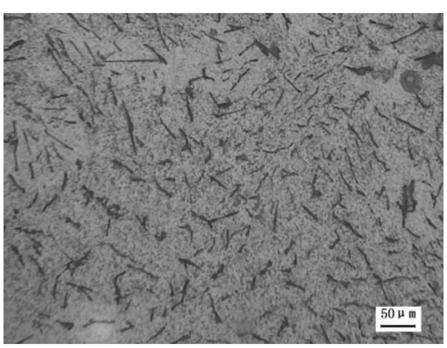

Fig. 6 Optical microscopic image of aluminium reinforced with 50nm sized $TiO_2$ particles

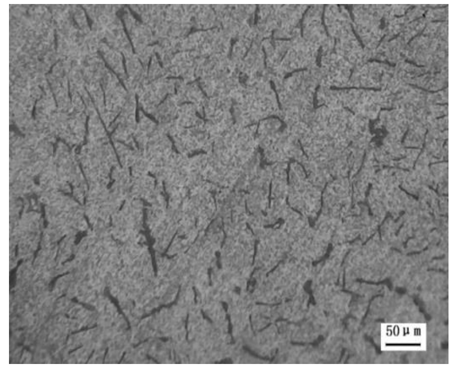

Fig. 7 Optical microscopic image of aluminium reinforced with 330nm sized $TiO_2$ particles

It is very clear from the above microscopic images that with the addition of different sized $TiO_2$ nanoparticles into the aluminium matrix, the grain size gets refined and thus shows the fine distribution of grains. Hence, the strength of the nanocomposites gets improved. Aluminium grain size refinement has a direct influence on mechanical properties of all the nanocomposite samples. The refinement of aluminium grain size with $TiO_2$ nanoparticle addition can be explained based on two different mechanisms: First one is the pinning of the previous grain boundary by the second phased nanoparticles and second one is the increase of nucleation sites for transformation [1].

Grain size variation is the reason for the variation in mechanical properties of all the nanocomposite samples. Grain size value for all the nanocomposites were obtained from the dewinter material plus software interfaced with the optical microscope. Comparison of grain size variation of aluminium with all the nanocomposite samples is shown in fig. 8.

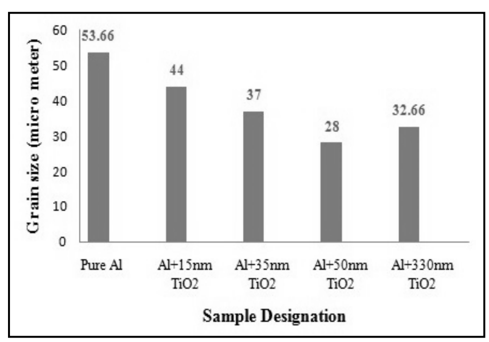


Fig. 8 Grain size variation of all the samples

From the above result, it is clear that the grain size refinement occurs with the addition of $TiO_2$ nanoparticles in the aluminium matrix because of the reduction in grain size from 53.66 microns to 28 microns. Due to the increased surface area of $TiO_2$ nanoparticles, grain sizes of the matrix get decreased. Hence the strength of the aluminium is increased with the $TiO_2$ nanoparticle addition. Also when the size of $TiO_2$ nanoparticle is increased from 15nm to 50nm, the grain size gets decreased from 44 microns to 28 microns resulting in the increase of strength. Hence the strength of the nanocomposites were increased as the size of $TiO_2$ nanoparticles increases in the aluminium matrix. But when 330nm $TiO_2$ particles were reinforced with the aluminium matrix, the grain size slightly increases to 32.66 microns indicating the slight reduction in the strength of the nanocomposites.

Variation of Rockwell hardness number for aluminium and aluminium matrix nanocomposites is shown in fig. 9. From the graph, it is clear that the Rockwell hardness number were improved with the addition of $TiO_2$ nanoparticles into the aluminium matrix. This is because of the presence of hard $TiO_2$ nanoparticles. This is to be expected since aluminium is a soft material and the $TiO_2$ nanoparticles being hard, contribute positively to the hardness of the nanocomposite.

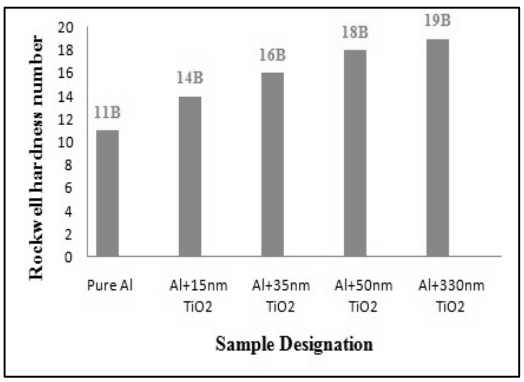


Fig. 9 Variation of Rockwell hardness number

It is seen that the hardness was increased with the addition of $TiO_2$ nanoparticles from sizes 15 nm to 330nm when reinforced into the aluminium matrix which means that the hardness was increased as the size of $TiO_2$ nanoparticles increases in the aluminium matrix. The improvement in the hardness value of the aluminium matrix nanocomposites compared with that of the pure aluminium indicates that $TiO_2$ nanoparticles have a great effect on the strengthening mechanism of aluminium matrix. This is due to the grain refinement of aluminium matrix which was already confirmed in the microstructure study, and the role of uniformly distributed nanoparticles which act as obstacles to the motion of dislocations according to Orowan mechanism [5].

Variation of nominal breaking stress, actual breaking stress and ultimate stress for aluminium with all the aluminium matrix nanocomposite samples are shown in figure 10, 11 and 12 respectively.

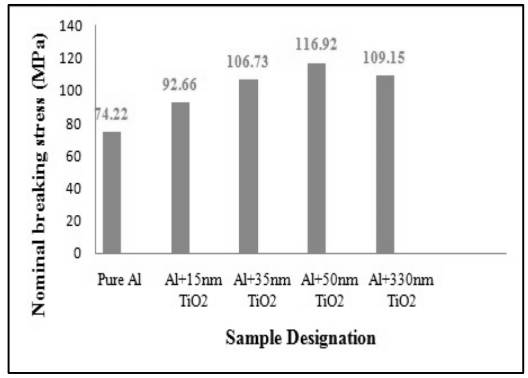


Fig. 10 Variation of Nominal breaking stress

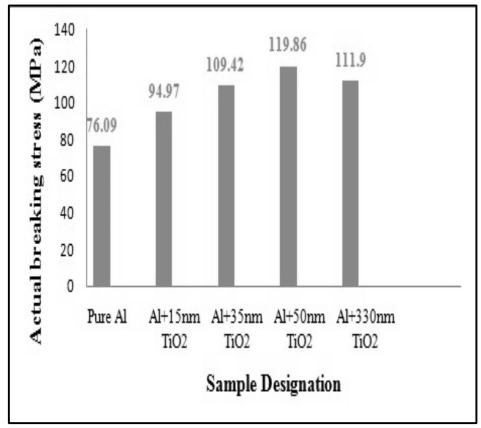


Fig. 11 Variation of Actual breaking stress

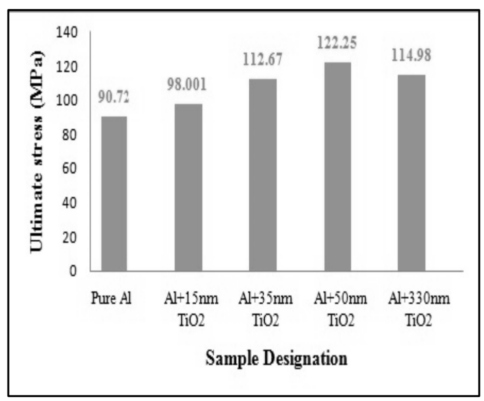


Fig. 12 Variation of Ultimate stress

From the above graphs, it is clear that the nominal breaking stress, actual breaking stress, and ultimate stress were improved with the addition of $TiO_2$ nanoparticles in the aluminium matrix. In this case, surface area of the reinforcement gets increased and grain sizes of the matrix get decreased. Hence the strength of aluminium is increased with the $TiO_2$ nanoparticle addition. Similarly nominal breaking stress, actual breaking stress and ultimate stress were increased with the addition of $TiO_2$ nanoparticles from sizes

15nm to 50nm and shows a slight decreasing effect for 330nm reinforced aluminium matrix composite. The tensile properties of the aluminium increases greatly up to the addition of 50nm sized $TiO_2$ particles and after that, the level of increasing in tensile properties gets reduced due to the clustering of $TiO_2$ reinforcement nanoparticles. As the size of $TiO_2$ nanoparticles in the aluminium matrix increases to 330nm, the particulates clustering becomes bigger and the possibility of crack arrest in the matrix material reduces and cracks thus propagate more easily in the nanocomposite, giving rise to the reduction in the strength for nanocomposite with 330nm sized $TiO_2$ particles [6]. It can be seen that the tensile properties of the nanocomposites are simultaneously improved because of the coupled effects of increase in grain boundary area due to grain refinement and the effective transfer of tensile load to the uniform distribution of $TiO_2$ nanoparticles in the aluminium matrix. Also, the improvement in the tensile properties is due to the grain refinement of aluminium matrix which was already confirmed in the microstructure study.

X-ray diffraction (XRD) pattern of aluminium with all the aluminium matrix nanocomposite samples are shown below from fig. 13 to fig. 17 respectively.

In fig.13, the diffraction peaks at 2θ values are the characteristic pattern of aluminium and are identified by matching the peak positions and intensities in XRD patterns to those in the JCPDS (Joint Committee on Powder Diffraction Standards) database. Hence the experimental XRD pattern of aluminium agrees with the JCPDS card no. [89-4037] indicating the presence of aluminium. From fig.14 to fig.17, the diffraction peaks at 2θ values indicates the XRD pattern of $TiO_2$ nanoparticles along with the XRD pattern of aluminium and are identified by comparing with those in the JCPDS database. Hence the experimental XRD pattern of $TiO_2$ nanoparticles agrees with the JCPDS card no. [21-1272] which shows the presence of the $TiO_2$ nanoparticles in the aluminium matrix.

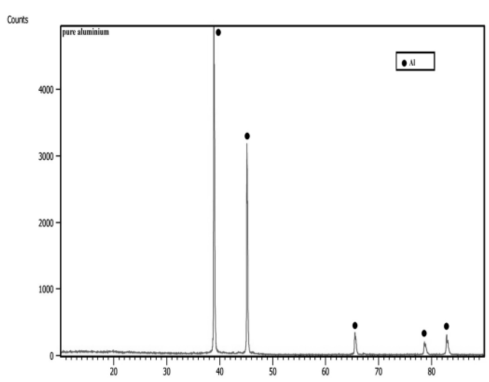


Fig. 13 XRD pattern of pure aluminium

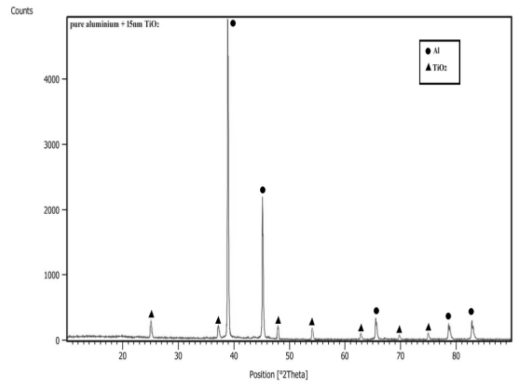


Fig. 14 XRD pattern of aluminium reinforced with 15nm sized $TiO_2$ articles

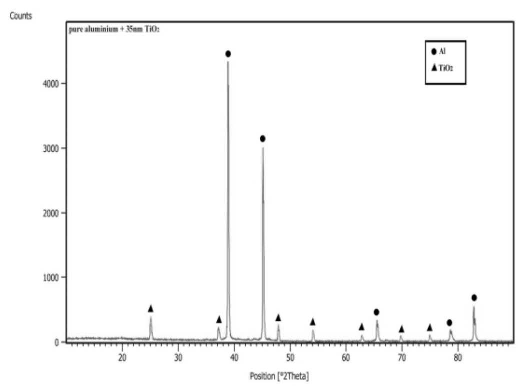


Fig. 15 XRD pattern of aluminium reinforced with 35nm sized $TiO_2$ particles

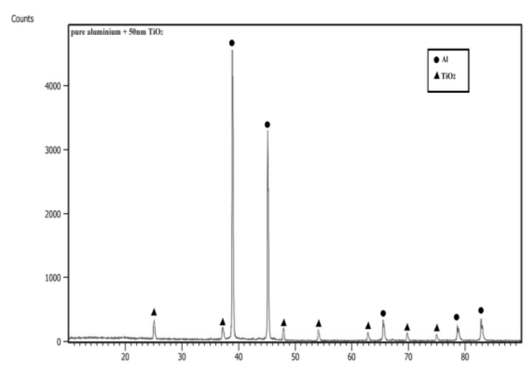


Fig. 16 XRD pattern of aluminium reinforced with 50nm sized $TiO_2$ particles

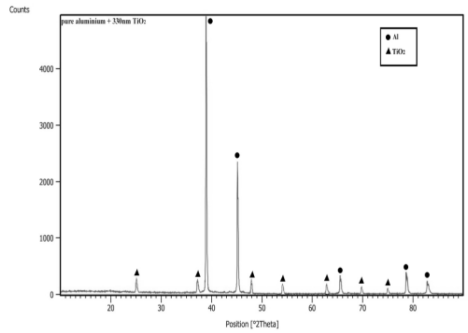


Fig. 17 XRD pattern of aluminium reinforced with 330nm sized $TiO_2$ particles

## V. CONCLUSIONS

A brief glance on the results obtained from this study showed a positive result to the addition of titanium dioxide nanoparticles in the aluminium matrix. Aluminium matrix nanocomposite samples have been successfully fabricated using powered stir casting method with uniform distribution of titanium dioxide nanoparticles. Hardness and tensile properties were improved with the addition of $TiO_2$ nanoparticles in the aluminium matrix. Hardness values were increased with the addition of $TiO_2$ nanoparticles from sizes 15nm to 330nm when reinforced into the aluminium matrix. Dispersion of $TiO_2$ nanoparticles in the aluminium matrix improves the hardness of the matrix material. Tensile properties were increased with the addition of $TiO_2$ nanoparticles from sizes 15nm to 50nm and as the size of $TiO_2$ nanoparticles changes from nanoscale to microscale, the tensile properties slightly reduced compared to that of nanocomposites. Microstructural evaluation confirmed that the aluminium grain size refinement is the major reason for the improvement in the mechanical properties of all the aluminium matrix nanocomposite samples fabricated. X-Ray Diffraction (XRD) results also confirmed the presence of $TiO_2$ nanoparticles in the aluminium matrix.

## VI. SCOPE FOR FUTURE WORK

The present investigation leaves a large scope to explore many other aspects related to metal matrix nanocomposites. Study of nanocomposite properties on the basis of different fabrication methods can be performed. Mechanical characterization such as compressive strength, impact strength and wear test can also be investigated. Different nanoparticles other than titanium dioxide nanoparticles can be incorporated into the aluminium matrix to produce metal matrix nanocomposites.

## REFERENCES

[1] Z. Amondarain, M. Arribas, J. L. Arana, G. A. Lopez., "Mechanical Properties and Phases Derived from $TiO_2$ Nanopowder Inoculation in Low Carbon Steel Matrix," Materials Transactions, Volume-54, No-10, 2013, pp. 1867 to 1876, The Japan Institute of Metals and Materials.

[2] Shubham Mathur and Alok Barnawal., "Effect of Process Parameter of Stir Casting on Metal Matrix Composites," International Journal of Science and Research, 2013, ISSN (Online): 2319-7064.

[3] S. Tahamtan, A. Halvaee, M. Emamy and M.S. Zabihi., "Fabrication of $Al/A_20_6$–$Al_2O_3$ nano/micro composite by combining ball milling and stir casting technology", Materials and Design 49, 2013, 347–359.

[4] Himanshu Kala, K.K.S Mer and Sandeep Kumar., "A Review on Mechanical and Tribological Behaviors of Stir Cast Aluminum Matrix Composites," Procedia Materials Science 6, 2014, 1951 – 1960.

[5] Reed-Hill RE, Abbaschian R., "Physical metallurgy principles", 3rded. Boston: PWS; 1994.

[6] Hamouda, A. M. S., Sulaiman S., Vijayaram, T. R., Sayuti, M. and Ahmad., "Processing and Characterisation of Particulate Reinforced Aluminium Silicon Matrix Composite", Journal of Achievements in Materials and Manufacturing Engineering, 2007, 25(2), 11-16.

[7] S. Gopalakrishnan and N. Murugan., "Production and wear characterisation of AA 6061 matrix titanium carbide particulate reinforced composite by enhanced stir casting method", Composites: Part B 43, 2012, 302–308.

[8] Muhammad Hayat Jokhio, Muhammad Ibrahim Panhwar and Mukhtiar Ali Unar., "Manufacturing of Aluminium Composite Material Using Stir Casting Process", Mehran University Research Journal of Engineering & Technology, Volume 30, No. 1, January 2011, ISSN:0254-7821.

[9] Mohsen Hajizamani and Hamidreza Baharvandi., "Fabrication and Studying the Mechanical Properties of A356 Alloy Reinforced with $Al_2O_3$-10% Vol. $ZrO_2$ Nanoparticles through Stir Casting", Advances in Materials Physics and Chemistry, 2011, 1, 26-30

# Optimization of Process Parameters in Milling of Aluminium 2014-T6 Alloy Using Grey Relation Analysis

Sony Thomas, Nadeera. M[2]

*Department of Mechanical Engineering, TKM College of Engineering, Kollam, Kerala, India*

[2]nadeeru94@gmail.com

***Abstract*: This experimental investigation was conducted to determine the effects of machining parameters on surface roughness and cutting forces in slot milling of A1uminium 2014-T6 under different lubrication conditions such as, FLOOD, MQL and also an external minimum quantity lubrication system was developed. Here the experiments are designed using Taguchi orthogonal array and nine experiments each under different lubrications .Then Taguchi based grey relation analysis is used to optimize the cutting parameters to have lowest surface roughness and cutting force among different combinations of speed, feed and depth of cut. After that the results are analyzed using analysis of variance which is used for identifying the factors significantly affecting the performance measures and developed a mathematical model using regression technique to predict performance measures (surface roughness, cutting force).And finally the results shows that MQL system has better surface finish and low cutting force than flood lubrication systems. It is true that this small reduction has enabled significant improvement in machinability index, so we can say that MQL machining is an alternative for both dry and flood systems.**

**Keywords: MQL, GRA**

## I. INTRODUCTION

The conventional types and methods of application of cutting fluid have been found to become less effective with the increase in cutting velocity and feed. The most common way of applying cutting fluids in machining process is by flood cooling in which the machining area is flooded with an abundant amount of cutting fluid. It is important to find a way to manufacture products using more sustainable methods and processes, which could minimize the use of cutting fluids in the machining operation and provide a healthy and safe working environment. The ideal way of performing manufacturing processes in this regard is by dry machining, which will eliminate completely, any use of cutting fluids. However, cutting fluids have their own advantages and positive effects which have to be assured in dry machining. Near-dry machining, which is also referred to as MQL (Minimum Quantity Lubrication), is a more realistic approach which is an intermediary stage between flood cooling and dry machining. [1].

The Paper has been organized as follows; Section B deals with the experimental details. Section C deals with the optimization of machining parameters. Section D deals with Statistical analysis. In Section E conformation test and Section F is the Conclusion part.

## II. EXPERIMENTAL DETAILS

The experiment is performed on 2014-T6 Aluminium alloy in the form of rectangular piece having 110 mm length, 100 width and 25 mm height. 2014-T6 Aluminium alloy was selected due to its emergent range applications in the field of space vehicles, aerospace application etc. The cutting tool insert for slot milling is uncoated carbide insert ( Sanvik R390-11T3-08E-NL-H13A). The different set of slot milling experiments are performed using a HSC linear 75, 3- axis verticalmillingIn this work, Taguchi method uses a special design of orthogonal array to design the experiment. According to the Taguchi method, a robust design and an $L_9$ orthogonal array are employed for the experimentation. Three machining parameters are considered as controlling factors - namely cutting speed, feed/tooth, depth of cut and each has three levels – namely low, medium, and high, denoted by 1, 2 and 3 respectively. Table 1 shows the cutting parameters and their levels considered for experimentation and Figure 1&2 shows block diagram external minimum quantity lubrication setup and photographic view.

Minimal quantity lubrication (MQL) machining, also known as near-dry machining (NDM), supplies very small quantities of lubricant to the machining zone. It was developed as an alternative to flood and internal high-pressure coolant supply to reduce metal working fluids consumption.

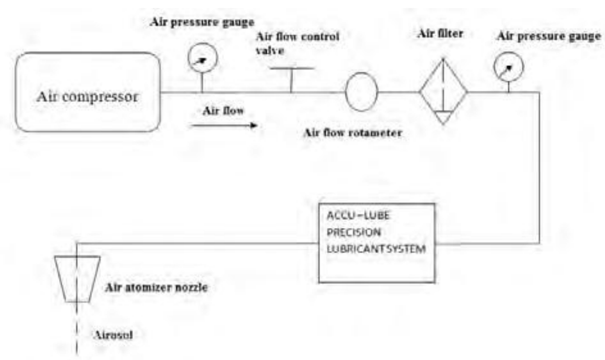


Figure 1: Block diagram of external MQL setup

In MQL machining, the cooling media is supplied as a mixture of air and an oil in the form of an aerosol (often referred to as the mist). An aerosol is a gaseous suspension of solid or liquid particles in air. In MQL machining aerosols are oil droplets dispersed in a jet of air. An idealized picture of MQL machining is shown in Fig. 2: small oil droplets carried by the air fly directly to the tool

TABLE 1: CUTTING PARAMETERS AND THEIR LEVELS

| Parameters | Units | Level 1 | Level 2 | Level 3 |
|---|---|---|---|---|
| Cutting speed(CS) | m/min | 700 | 800 | 850 |
| Feed/tooth($F_z$) | mm/tooth | 0.1 | 0.15 | 0.20 |
| Depth of cut (Doc) | mm | 0.6 | 1.2 | 1.8 |
| Type of lubrications: Flood, MQL(75ml/hr) | | | | |

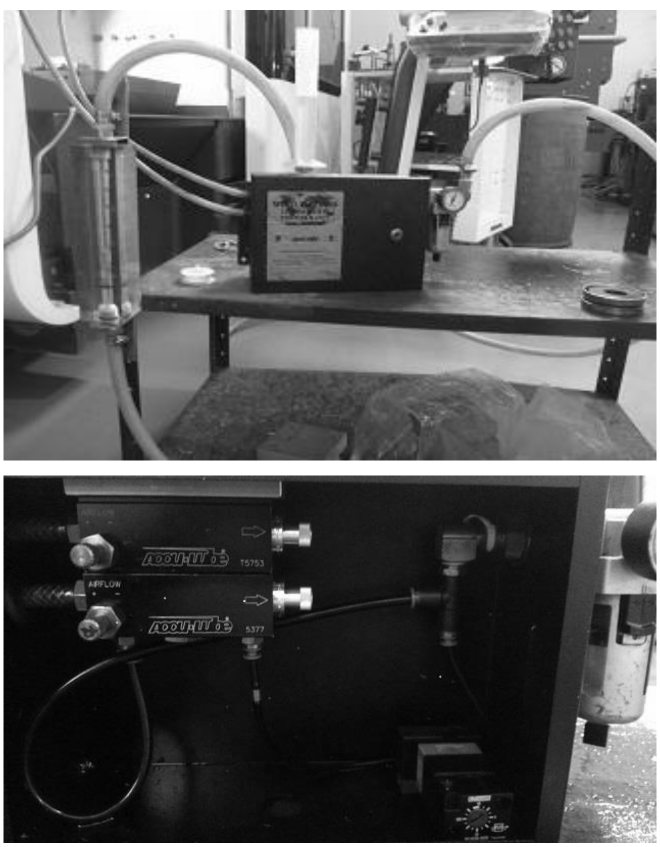

Figure 2: Photo graphic view of external MQL setup

working zone, providing the needed cooling and lubricating actions.

This lubrication system is used to deliver metered quantity aerosol mixture to tool work piece interface. With a small amount lubricant, tools last longer and parts come out cleaner. By eliminating flood coolant the impact on environment is minimized. Accu-Lube system didn't a provision to measure the amount of coolant dispensed. The amount of air flow through the device also couldn't be measured. Hence the Accu-Lube system was fitted with a beaker to measure the oil flow and a rotameter was connected to the inlet to measure the air flow. For three components measurement of cutting forces in X, Y and Z directions were recorded using a standard quartz dynamometer (Kistler 9257B) allowing measurements from−5 to 5 KN is shown in Fig.3.The Kistler dynamometer is connected to the charge amplifier and from the amplifier, it is connected to the Digital Acquisition Board (DAQ) and finally, it is connected to personal computer. The personal computer is equipped with software of Kistler Dynoware for data acquisition using cable that is provided in the Kistler dynamometer. During the milling operation, the cutting force produced will be detected by the sensors of the Kistler dynamometer and this cutting force signals will transmit to the amplifier. The amplifier will enlarge the signals and then transmitted to the DAQ board and then personal computer. With the assistance of the software of Kistler Dynoware. And the machined slot surface was measured at two different positions and the average ($R_a$) values are taken using Form Talysurf PGI 800 ,which has diamond stylus tip with accuracy of 2μm and resolution of 3.2 nm and the maximum transverse length 200mm and the pickup system used is phase grating laser interferometric.

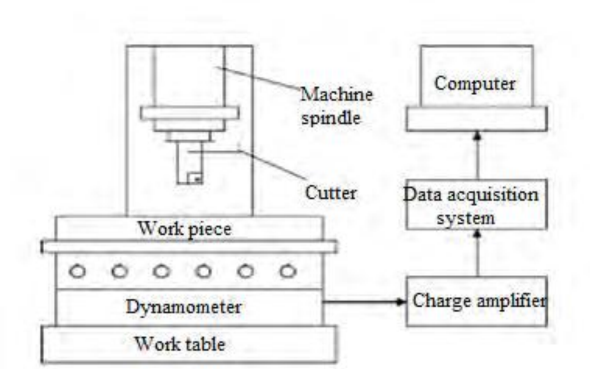


Fig 3: Systematic diagram for force measurement

In this work total 27 experiments are conducted under three different lubrication categories, and the observed response values are tabulated in Table 2.

TABLE 2: OBSERVATIONS OF AVERAGE SURFACE ROUGHNESS AND RESULTANT CUTTING FORCE FOR DRY AND MQL CONDITIONS

| Ex. no | CS | $F_Z$ | DOC | Avg $R_a$ Flood | Avg $R_a$ MQL | $F_c$ flood | $F_c$ (MQL) |
|---|---|---|---|---|---|---|---|
| 1 | 700 | 0.1 | 0.6 | 0.66 | 0.68 | 128.3 | 126.6 |
| 2 | 700 | 0.15 | 1.2 | 0.86 | 0.87 | 139.6 | 137.6 |
| 3 | 700 | 0.20 | 1.8 | 0.75 | 0.73 | 181.4 | 198.9 |
| 4 | 800 | 0.1 | 1.2 | 0.61 | 0.62 | 148. | 136.9 |
| 5 | 800 | 0.15 | 1.8 | 0.85 | 0.76 | 166. | 136.7 |
| 6 | 800 | 0.20 | 0.6 | 0.86 | 0.85 | 96.0 | 197.7 |
| 7 | 850 | 0.1 | 1.8 | 0.59 | 0.62 | 178. | 87.41 |
| 8 | 850 | 0.15 | 0.6 | 0.89 | 0.74 | 94.2 | 178.7 |
| 9 | 850 | 0.20 | 1.2 | 0.86 | 0.78 | 126.3 | 80.21 |

## III. .OPTIMIZATION

### *1. Grey relational analysis (GRA)*

By using multiple objective optimization (grey relation analysis) technique, used to found out the optimal set values of cutting parameters which minimize the both objective functions. In GRA higher grey relation grade is optimized level. And the general equations that are used as follows,

$$\text{Normalized value}=\frac{\text{Max } X_i^{(o)}k - \text{Mi}X_i^{(o)}k}{\text{Max } X_i^{(o)}k - \text{Min}X_i^{(o)}k} \tag{1}$$

where, $\text{Max } X_i^{(o)}k$ & $\text{Min}X_i^{(o)}k$ are the maximum and minimum value of response value and $\text{Mi}X_i^{(o)}k$ is current value of response value.

$$\text{GRC } (\varphi_i(k)) = \frac{\Delta_{min} + \delta\Delta_{max}}{\Delta_{oi}(k)+\delta\Delta_{max}} \tag{2}$$

Where GRC ($\varphi_i(k)$) is Grey relation coefficient, $\Delta_{min}$ & $\Delta_{max}$ are the maximum and minimum value of change, $\Delta_{oi}(k)$ is the current value of change and $\delta$ relational coefficient and its value is 0.5.

$$GRG\ (\gamma_i) = \frac{1}{n}\sum_{k=1}^{n}\varphi_i(k) \tag{3}$$

Where GRG ($\gamma_i$)grey relation grade and n is the number of response factor. Based on the above equations grey relation grade and response GRG for parameter levels were tabulated for both flood and MQL lubrication systems in Table 3, Table 4, Table 5, Table 6.

TABLE 3: GRG FOR FLOOD LUBRICATION SYSTEM

| Ex.no | Normalized value | | Grey coefficient | | Grey grade |
|---|---|---|---|---|---|
| | $R_a$ | $F_c$ | $R_a$ | $F_c$ | |
| 1 | 0.751 | 0.609 | 0.667 | 0.561 | 0.614 |
| 2 | 0.105 | 0.479 | 0.358 | 0.489 | 0.423 |
| 3 | 0.473 | 0 | 0.486 | 0.333 | 0.409 |
| 4 | 0.913 | 0.382 | 0.851 | 0.447 | 0.649 |
| 5 | 0.145 | 0.175 | 0.369 | 0.377 | 0.373 |
| 6 | 0.099 | 0.979 | 0.356 | 0.959 | 0.657 |
| 7 | 1 | 0.035 | 1 | 0.341 | 0.670 |
| 8 | 0 | 1 | 0.333 | 1 | 0.666 |
| 9 | 0.089 | 0.631 | 0.354 | 0.575 | 0.464 |
| Total mean G.R.G = 0.5927 | | | | | |

TABLE 4: RESPONSE GRG FOR PARAMETER LEVEL (FLOOD)

| Process Parameter | GREY RELATIONAL GRADE | | | | |
|---|---|---|---|---|---|
| | Level 1 | Level 2 | Level 3 | G.R.G | Rank |
| Cutting speed | 0.482 | 0.5596 | 0.6* | 0.118 | 3 |
| Feed/tooth | 0.6443* | 0.4873 | 0.51 | 0.157 | 2 |
| Depth of cut | 0.6456* | 0.512 | 0.484 | 0.1616 | 1 |
| Optimum levels* | | | | | |

TABLE 5: GRG FOR MQL LUBRICATION SYSTEM

| Ex.no | Normalized value | | Grey coefficient | | Grey grade |
|---|---|---|---|---|---|
| | $R_a$ | $F_c$ | $R_a$ | $F_c$ | |
| 1 | 0.741 | 0.608 | 0.658 | 0.560 | 0.690 |
| 2 | 0 | 0.515 | 0.333 | 0.507 | 0.420 |
| 3 | 0.544 | 0 | 0.523 | 0.333 | 0.428 |
| 4 | 0.983 | 0.523 | 0.927 | 0.511 | 0.739 |
| 5 | 0.415 | 0.010 | 0.460 | 0.335 | 0.397 |
| 6 | 0.076 | 0.939 | 0.351 | 0.891 | 0.627 |
| 7 | 1 | 0.169 | 1 | 0.375 | 0.687 |
| 8 | 0.5 | 1 | 0.5 | 1 | 0.75 |
| 9 | 0334 | 0.626 | 0.428 | 0.572 | 0.5 |
| Total mean G.R.G = 0.581 | | | | | |

TABLE 6: RESPONSE GRG FOR PARAMETER LEVEL (MQL)

| Process Parameter | GREY RELATIONAL GRADE | | | | |
|---|---|---|---|---|---|
| | Level 1 | Level 2 | Level 3 | G.R.G | Rank |
| Cutting speed | 0.5126 | 0.5858 | 0.645* | 0.1330 | 3 |
| Feed/tooth | 0.7053* | 0.5225 | 0.5163 | 0.189 | 1 |
| Depth of cut | 0.6870* | 0.553 | 0.5041 | 0.182 | 2 |
| Optimum levels* | | | | | |

## IV. STATISTICAL ANALYSIS

*1. Analysis of variance (ANOVA)*

ANOVA is useful for determining influence of any given input parameter from a series of experimental result by design of experiment for machining process and it can be used to interpret experimental data.

*2. Regression analysis*

Regression analysis is a statistical process for estimating the relationships among variables. It includes many techniques for modelling and analyzing several variables, when the focus is on the relationship between a dependent variable and one or more independent variables.

Analysis of variance & Regression equations for various lubrication systems were tabulated in Table 7 and Table 8 .

Table 7: Analysis of variance for Flood

| Source | DOF | S.S | M.S | F | %C |
|---|---|---|---|---|---|
| Cutting speed | 2 | 0.040 | 0.020105 | 0.0100 | 24.3 |
| Feed/tooth | 2 | 0.061 | 0.030916 | 0.0154 | 37.37 |
| Depth of cut | 2 | 0.063 | 0.031689 | 0.01584 | 38.31 |
| Error | 2 | - | - | - | - |
| Total fishers value = 0.04135564 | | | | | |

Regression equations are,

1) Surface roughness ($R_a$) = 0.421+0.000164 cutting speed +2.017Feed/tooth – 0.0644depth of cut

Optimized parameter levels- 3 ,1,1(cutting speed=850 ; feed =0.1 ; depth of cut = 0.6)

Predicted Surface roughness ($R_a$) = 0.7234 µm

**2**) Cutting force ($F_C$) = 186.1 – 0.1149 cutting speed -169.5 feed/tooth + 57.61 depth of cut

Predicted Cutting force ($F_C$) = 106.05 N

Table 8: Analysis of variance for MQL

| Source | DOF | S.S | M.S | F | %C |
|---|---|---|---|---|---|
| Cutting speed | 2 | 0.026 | 0.013312 | 0.00665 | 17.796 |
| Feed/tooth | 2 | 0.069 | 0.034588 | 0.01729 | 46.23 |
| Depth of cut | 2 | 0.053 | 0.029004 | 0.01345 | 35.62 |
| Error | 2 | - | - | - | - |
| Total fishers value = 0.037400399 | | | | | |

Regression equations are,

1)Surface roughness ($R_a$) = 0.797+0.000281 cutting speed +1.463Feed/tooth – 0.0442depth of cut

Optimized parameter levels - 3 ,1,1 ( cutting speed=850 ; feed =0.1 ; depth of cut = 0.6)

Predicted Surface roughness ($R_a$) = 0.67793 µm

2)Cutting force ($F_C$) = 197.3 – 0.1716 cutting speed -104.3 feed/tooth + 0.0442 depth of cut

Predicted Cutting force ($F_C$) = 87.858 N

## V. CONFIRMATION TEST

Once the optimal combination of process parameters and their levels are obtained the final step was to verify the predicted results with experimental value .The predicted values were compared with actual values for both flood and MQL lubrication systems were tabulated in Table 9.

Table 9: Comparison of predicted and actual values

| Cutting conditions | Predicted values | | Experimental values | |
|---|---|---|---|---|
| | $R_a$ (µm) | $F_c$ (N) | $R_a$ (µm) | $F_c$ (N) |
| Flood | 0.7234 | 106.05 | 0.701 | 106.01 |
| MQL | 0.67793 | 87.858 | 0.653 | 87.81 |

## VI. RESULTS AND DISCUSSION

Fig: 4-6 shows the main effect plot for both $R_a$ & Resultant cutting force. The result shows that with increase in cutting speed, there are continuous decreases in surface roughness and cutting force (i.e.; high G.R.G has low $R_a$ & cutting force). On the other hand as the feed increases both $R_a$ &$F_c$ values increases up to 0.15 feed/tooth and then slightly decreases, however with increase in depth of cut there is a continuous increase in both $R_a$&$F_c$. Optimum value of surface value was obtained at cutting speed 850 m/min (level 3), feed/tooth 0.1mm/tooth (level 1) and depth of cut 0.6 mm (level1).

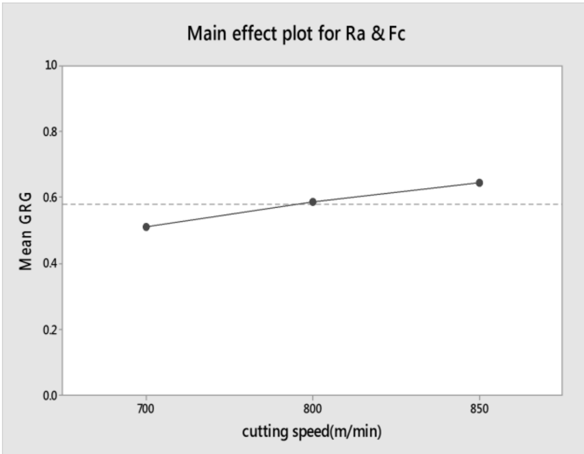


Fig.4: Cutting speed $V_s$ Mean GRG (MQL)

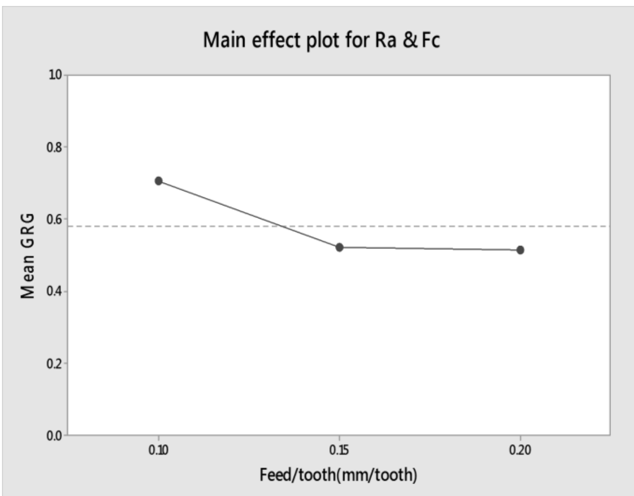


Fig.5: Feed/tooth $V_s$ Mean GRG (MQL)

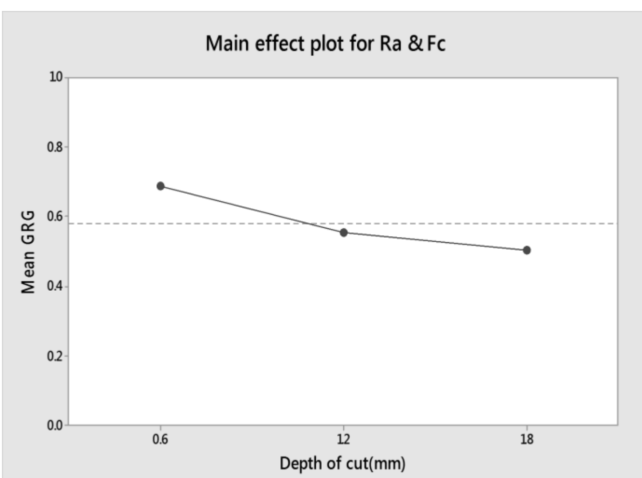


Fig.6: Depth of cut Vs Mean GRG (MQL)

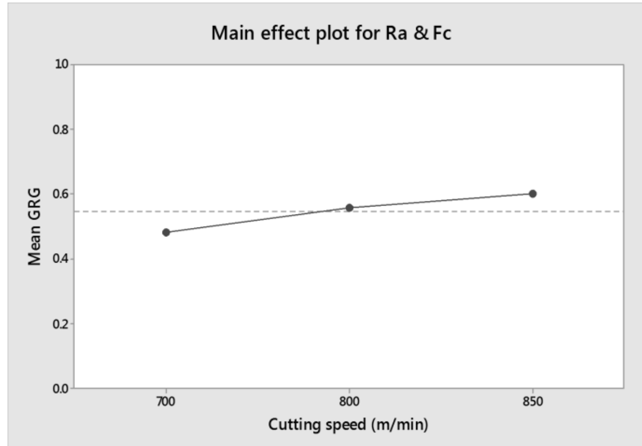


Fig.7: Cutting speed $V_s$ Mean GRG (FLOOD)

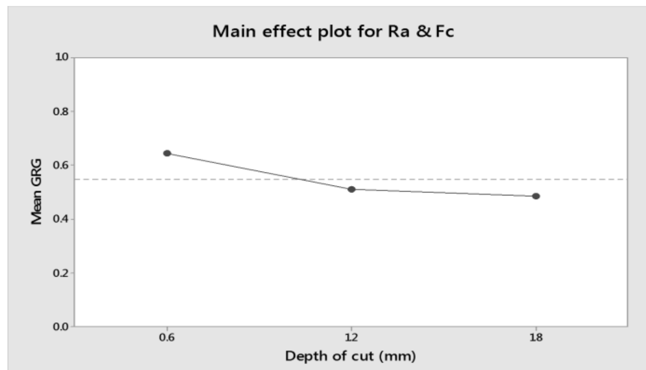


Fig 8: Depth of cut Vs Mean GRG (FLOOD)

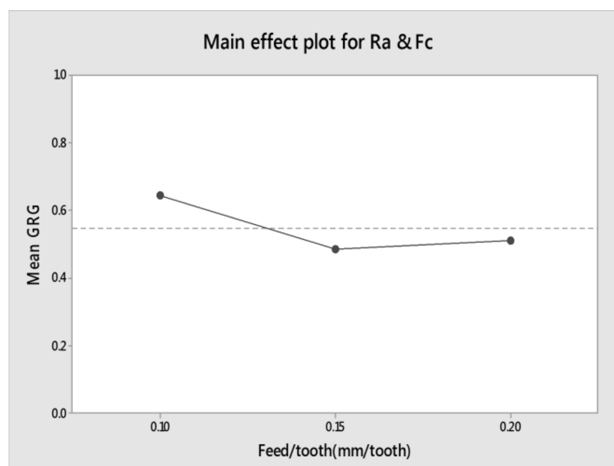


**Fig 9: Feed/tooth $V_s$ Mean GRG (FLOOD)**

Fig 7-9 shows the main effect plot for both $R_a$& Resultant cutting force. The result shows that with increase in cutting speed, there are a continuous decreases in surface roughness and cutting force (ie; high G.R.G has low $R_a$& cutting force). On the other hand as the feed increases both $R_a$&$F_c$ values increases up to 0.15 feed/tooth and then slightly decreases, however with increase in depth of cut there is a continuous increase in both $R_a$&$F_c$. Optimum value of surface value was obtained at cutting speed 850 m/min (level 3), feed/tooth 0.1mm/tooth (level 1) and depth of cut 0.6 mm (level 1).

## VII. CONCLUSIONS

The aim this work was to take advantage of the Taguchi method to perform optimization with small number of experiment and utilization of multiple regression analysis to obtain mathematical model which are a powerful tool to predict response for any of input parameters within the experimental domain.

Through ANOVA it was conformed that feed/tooth was the major significant factor followed by cutting speed and depth of cut. Cutting speed and depth of cut played an insignificant role in affecting both surface roughness and cutting force. This was true for minimum quantity lubrication and Flood lubrication system.

Through Taguchi based grey relation analysis; the optimum levels of cutting speed, feed/tooth and depth of cut is obtained as 850m/min,0.1feed/tooth,0.6mm respectively this was true for a all conditions of lubrication systems (flood, MQL(75ml/hr).The predicted surface roughness and cutting force at optimal condition for MQL(75ml/hr) is 0.67793 µm and 87.858N which was below than dry lubrication system. So it is true that this small reduction has enabled significant improvement in machinability indices. MQL has reduced the cutting force so we can say that MQL machining is an alternative for both flood and dry systems.

From the above experiments it shows that surface roughness and cutting force value is low in minimum quantity lubrication system when compared with flood lubrication system, Also its clear that while machining aluminium or its alloys coolant is necessary to get better surface finish.

## REFERENCES

[1] Sanjit Moshat , Saurav Datta , Asish Bandyopadhyay and Pradip Kumar Pal "Principal Component Analysis (PCA)-based Taguchi method is used to optimize CNC end milling process parameters" International Journal of Manufacturing Engineering, vol 13, no1 ,pp 360-372 ,2013.

[2] Pratyusha, Ashok kumar, Laxminarayana .P "optimization of cutting parameters using Taguchi methods and the experiments were conducted on AISI 304" International Journal of Manufacturing Engineering, vol 13, no1, pp 374-376, 2013.

[3] J.M.Vieira, A.R. Machado, E.O.Enugu " Performance of cutting fluids during face milling of steels" Journal of Materials Processing Technology , vol. 116, no. 2, pp. 244-251, 2001.

[4] Kedare S.B, Borse D.R, and Shahane P.T "Effect of minimum quantity lubrication (mql) on surface roughness of mild steel of 15hrc on universal milling machine" 3rd International Conference on Materials Processing and Characterization ,vol 6 , pp 150-153 ,2014.

[5] H.A.Kishawy, M.Dumitrescu, E.G. Ng, M.A. Elbestawi " Effect of coolant strategy on tool performance, chip morphology and surface quality during high-speed machining of A356 aluminum alloy" International Journal of Machine Tools & Manufacture , vol. 45, no. 2, pp. 219-227, 2005.

[6] Nilesh C Ghuge, Dhatrak V.K., Dr.AM.Mahalle, "Minimum Quantity Lubrication", National Symposium on engineering and Research, vol2, pp 55-60, 2009.

[7] N.Baskar,P.Asokan,G. Prabhaharan, R. Saravanan "optimization procedure based on the, optimization of machining parameters for milling operation" Journal of Materials Processing Technology , vol. 116, no. 2, pp. 214-219, 2004.

# Experimental Investigation on Hardfacing on EN 45 Steel Using Plasma Transferred Arc Welding

Sunod Kumar C[1], Nishath K[2]

*Department Mechanical Engineering, Government College of Engineering, Kannur, Kerala,India*

[1]Sunod57@gmail.com

[2]nishanth7783@gamil.com

***Abstract***— **In this current study, an experimental investigation has been carried out in order to explore the effect of hard-facing on EN45 spring steel using PTA Welding with Stellite12 as coating power. The study was initiated by conducting a chemical composition analysis on the substrate material to assess and ensure proportions of its chemical constituents. Suitable heat treatment processes has been provided at various occasion before and after the welding. PTA welding conducted based on Taguchi design of experiment. Micro–hardness test was performed using Vickers micro-hardness tester on the specimens and then wear test as per ASTM G99 standards. From the hardness test, it is observed that the hardness of the material improved and from wear test the substrate shows more wear resist than hardfaced sample even after the tempering process.**

**Keywords— hard facing, PTA welding, hardness, wear rate**

## I. INTRODUCTION

The relevance of surfacing in material engineering is to increase the service life, reduce its maintenance and replacement, and also reduce energy loss in machine operation. Surfacing is a process of depositing a filler metal on a substrate to impart desired properties to the surface that is not intrinsic to the underlying base metal [1]. There are four types of surfacing namely hard facing, build up, weld cladding, and buttering [1, 2]. Hard facing is a form of surfacing that is applied for the purpose of reducing wear and erosion of substrate. Build up refers to the addition of weld metal to a base metal surface for restoration of the component to the required dimensions. A weld clad is a relatively thick layer of filler metal applied to a base metal for the purpose of providing a corrosion-resistant layer. Buttering also involves the addition of one or more layers of weld metal to the face of the joint or surface to be welded. It differs from build-up in that the primary purpose of buttering is to satisfy some metallurgical consideration. It is used primarily for the joining of dissimilar base metals [2].

Surfacing is now widely used for the fabrication of engineering components used in chemical, fertilizer, nuclear power plants, food processing, petrochemical and other allied industries [3]. The primary objective of surfacing is to impart desirable properties to the surface of a substrate, or to conserve expensive materials by using only a relatively thin surface layer on a less expensive or abundant base metal. This results in considerable economic gains [2].

Hard facing is the process of depositing, by one of various welding techniques, a layer or layers of metal of specific properties on certain areas of metal parts that are exposed to wear. The welding processes employed for hard facing are oxy fuel welding (OFW), manual metal arc welding (MMAW), gas tungsten arc welding (GTAW), gas metal arc welding (GMAW), plasma transferred arc welding (PTAW) and submerged arc welding (SAW)[5].The relevance of hard facing are to increase service life of components and there by extend life time of engineering equipment efficiency [4].

Plasma Transferred Arc Welding is a thermal process for applying wear and corrosion resistant layers on surfaces of metallic materials. It is a versatile method of depositing high-quality metallurgical fused deposits on a wide range of base materials from carbon steel to exotics like non-mag super austenitic and nickel alloys. Soft alloys, medium and high hardness materials, and carbide composites can be used to achieve diverse properties such as improved mechanical strength, wear resistance, galling resistance, and corrosion resistance. PTA hardfacing has several significant advantages over traditional welding processes such as oxy-fuel (OFW) and gas tungsten arc (GTAW) welding. Such as it is easily automated, providing a high degree of reproducibility, allows precise metering of metallic powder feedstock, permits precise control of important weld parameters (powder feed rates, gas flow rates), produces deposits of a given alloy that are tougher and more corrosion resistant, provide a variety of deposits in thicknesses from 1.2 to 2.5 mm or higher and weld dilutions that can be controlled from 5-7% [5-8].

Stellite12 is a cobalt based alloy having high heat and corrosion resistance with excellent wear and abrasion resistant. Due to this quality this powder is used for this work. The present work is to investigate the effect of hardfacing on EN45 spring steel using plasma transferred arc welding; microhardness study; wear behaviour study

## II. PRINCIPLE

In PTA welding, two DC power supplies are used to primarily establish a non-transferred arc (pilot arc) between the tungsten electrode (-) and the anodic nozzle (+) and then a transferred arc between the tungsten electrode (-) and the workpiece (+).A pilot arc of high frequency device strikes the plasma gas flowing around the cathode, which is ionized at the electrode tip. When the transferred arc is ignited, the workpiece becomes part of the electrical circuit and the plasma arc is directed through the torch orifice into the workpiece and results in greater energy transfer to the work piece. The consumable used for PTA cladding is normally in the form of metallic powders. These powders are fed into the hot plasma through precise metering mechanisms in predetermined quantities. A powder carrier gas is used to deliver the powder to the work piece and to alter welding characteristics. The schematic diagram of plasma transferred arc welding is shown in Fig. 1

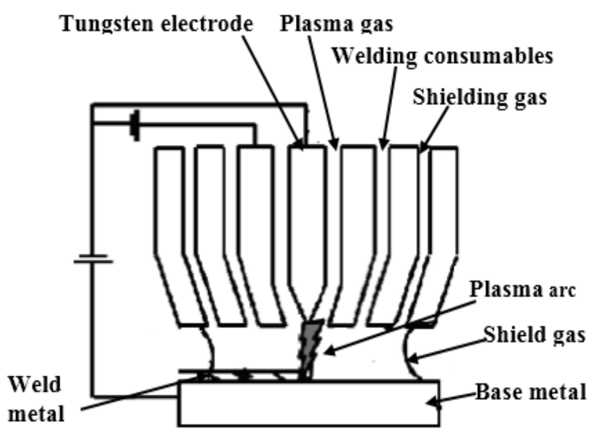


1 Fig. 1 Schematic diagram of PTA welding

2

## III. EXPERIMENTAL METHODOLOGY

### A. Chemical Analysis

Thechemical analysis of En 45 spring steel done for the confirmation of the material composition, used in this study is presented Table in 1.

TABLE. 1

CHEMICAL COMPOSITION OF EN 45

| Element | C | Si | Mn | S | P | Cr |
|---|---|---|---|---|---|---|
| Weight (%) | 0.589 | 1.623 | 0.963 | 0.015 | 0.021 | 1.26 |

The experimental procedure adopted for this work is shown in Fig.2

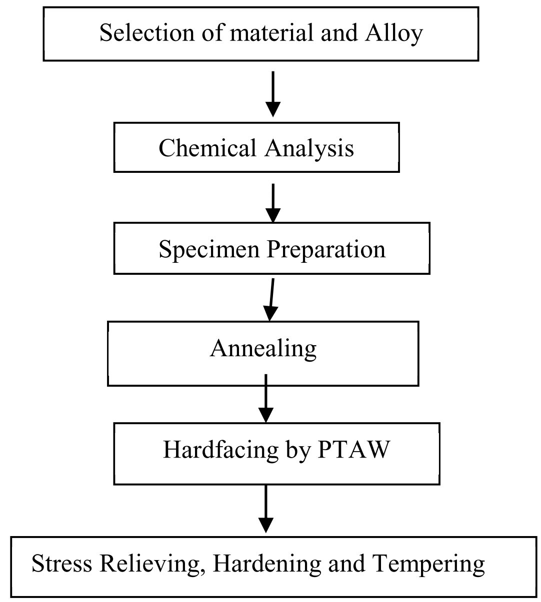


Fig. 2 Experimental procedure

### B. Specimen Preparation

For PTA welding the specimen of size 150mmx 120mm x16 mm is prepared from flat EN45 spring steel using conventional machining is show in Fig.3

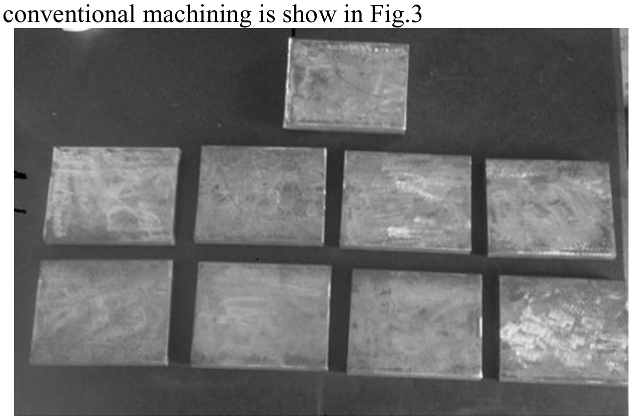

Fig. 3 Weld Specimens

### C. Annealing, Stress Relieving, hardening and Tempering

Suitable heat treatment like annealing, stress relieving, hardening and tempering done before and after the welding with proper heat treatment cycle

### D. Hardfacing

The PTA welding is conducted as per Taguchi design of experiment and L9 orthogonal array. The control parameters selected for the experiment is shown in Table.2 and keeping all other parameters constant like voltage, shielding gas flow rate, centre gas flow rate, plasma gas flow rate, nozzle to plate distance and number of layers. The PTAW system used for this work is shown in Fig.4. Stellite12 powder deposited onto the specimens of by hardfacing technique are given below. Initially, two waving beds were deposited on the specimen they adjust to each other and then above this two more waving beads were deposited .so total two layers made on the specimen surface. This procedure was performed all other specimens (for 9 sample) using the experimental design.

TABLE.II

CONTROL PARAMETERS AND LEVEL SETTINGS

| Control factors | Level 1 | Level 2 | Level 3 |
|---|---|---|---|
| Welding Current(A) | 150 | 165 | 180 |
| Welding Speed (mm/min.) | 125 | 325 | 525 |
| Feed Rate (mm/min.) | 6 | 8 | 10 |

Fig.4. PTA Welding system

*E. Hardness*

The micro-hardness tester used for this purpose was Mitutoyo micro hardness tester of Japan. The measurements on each specimen was carried out initially from the hardfaced area and progressed to various which is perpendicular to the welding direction and moved to base metal up to 10 mm. A Vickers indenter with load HV0.5 was used with a loading time 5 seconds to make indentation on the specimen. The micro-hardness values of were measured on the nine specimens zones along the center-line of the weld bead profile.

*F.* Wear

Dry sliding wear tests were conducted at room temperature (30°C) using a pin-on-disc type of machine as ASTM G99 standard. Cylindrical pins of 10 mm diameter were extracted from the hardfaced Specimen with the help of wire cut EDM. To ensure a constant surface finish, the hardfaced surface of each pin was carefully smoothened to a final average roughness. The disc was made of silicon carbide, with grit size of 125 µm and a hardness of 2500 HV. Generally, the hardness of disc material is higher than the hardness of specimen. Before the experiments, both the pin and the disc were carefully cleaned. The surface of the disc was placed with a silicon carbide. The lapping procedure was repeated after each test. The disc was installed in the machine chuck to slide against the mating pin which was mounted in the holder. Each test was performed on a new track on the disc.

The experiment were conducted at fixed parameter such as velocity 1 m/s, normal load 14.47N,distance 1000m and track diameter 80mm for all nine specimen The wear rate was calculated from the weight loss measurement and expressed in terms of volume loss per unit sliding distance as given below.

Wear Volume, $m^3$ = Weight loss/density

Wear rate, $m^3/m$=Wear Volume /Sliding distance

IV. RESULTS AND DISCUSSION

A. *Hardness*

The microhardness survey carried out in various zones of specimens hardfaced at 150 A and varying feed rate and welding speed is presented in the form of hardness profiles in Figures 5.1 .The survey was carried out over the specimens in three regions such as unaffected base metal (BM), heat-affected zone (HAZ), and hardfaced (HF). It is observed that the hardness value is increased in the hardfaced regions than that of base metal and hardness value in the heat affected region is gradually degreasing and same as base metal, this shows strong bond to base metal. The hardness value increase with increasing feed rate and welding speed. The average hardness improve for sample 1, 2 and 3 are 24.38%, 30.71% and31.41%.

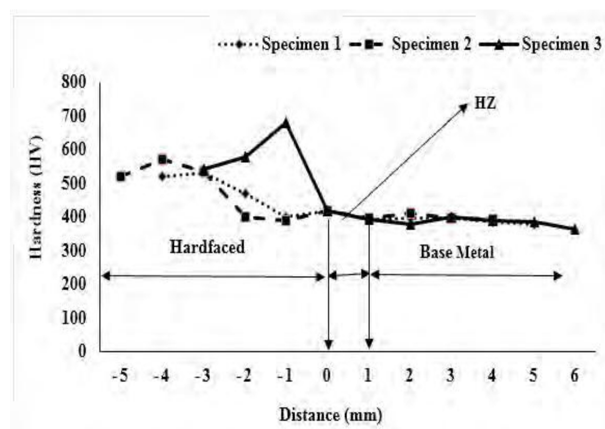


Fig.5.Micro-hardness distribution at 150A

The microhardness survey carried out in various zones of specimens hardfaced at 165 A is presented in the form of hardness profiles in Fig. 6 The survey was carried out over the specimens in three regions such as unaffected base metal (BM), heat-affected zone (HAZ), and hardfaced (HF). It is observed that the hardness value is increased in the hardfaced regions than that of base metal and the hardness value in the heat affected zone has little variation. The average hardness value improvement in percentage are 26.4%, 27.7% and16.8%.

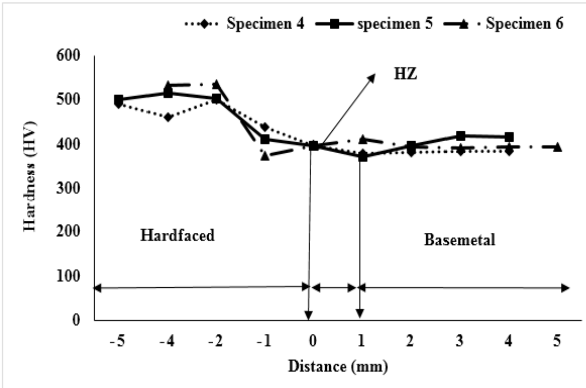


Fig.6 Micro-hardness distribution at 165A

The microhardness survey carried out in various zones of specimens hardfaced at 180A is presented in the form of hardness profiles in Figures 5.3 .The survey was carried out over the specimens in three regions such as unaffected base metal (BM), heat-affected zone (HAZ), and hardfaced (HF). It is observed that the hardness value is increased in the hardfaced regions than that of base metal and the hardness value in the heat affected zone is gradually decreasing (from 0 point) and same as base metal it means a strong bond with base metal. The average hardness improvement in percentage for sample 7, 8 and 9 are 16.5 %, 14.47 % and 10.67 %.

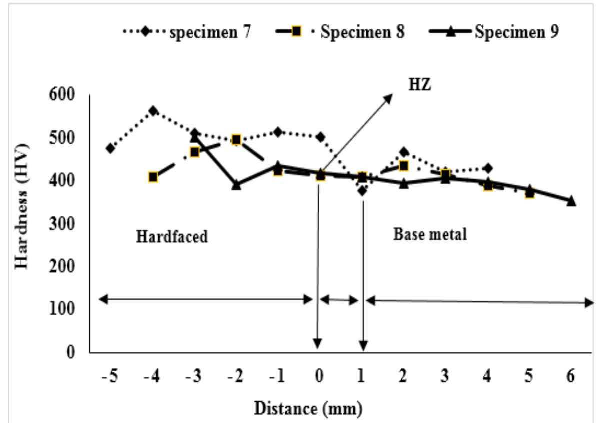


Fig.7.Micro-hardness distribution at 165A

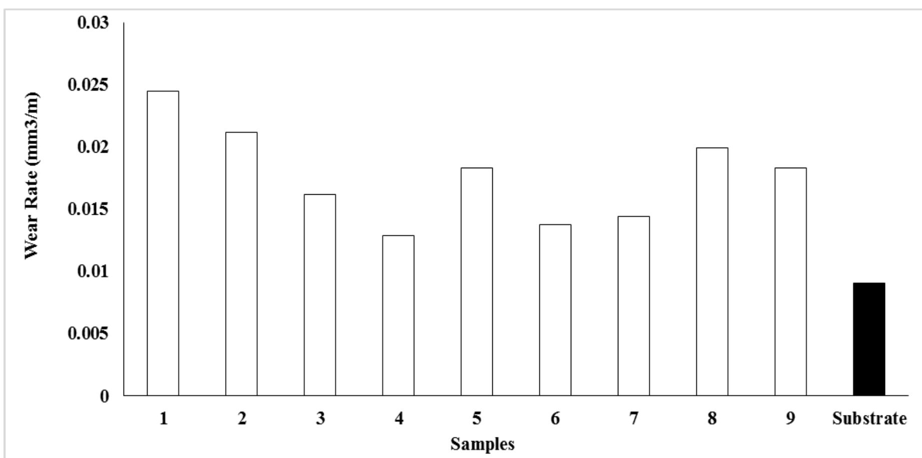


Fig.8 Wear rate of samples and substrate

B. *Wear*

The wear behavior hard-faced samples and substrate is given in Fig.8. From which sample 4 shows the good wear resistant with wear rate with 0.0088 $mm^3$/m, followed by sample 6 with 0.0009 $mm^3$/m and 0.00098 $mm^3$/m for sample 7. But while comparing with substrate the hardfaced sample are less wear resistant that shows stellite 12 is less wear resistant in room temperature or it may be due to the high hardness of substrate even after the tempering process.

1*) Wear Comparison of hardfaced and Substrate*: From Fig. 8 the wear is high at initial period and then increasing only with increase in time on hardfaced samples, but in substrate the wear rate to high at the initial period than that of hardfaced sample (up to 100 s) there after the wear of substrate is constant, it may be due to high hardness of substrate even after the tempering of material. So from it is clear that below 200s time period hardfaced sample shows less wear than the substrate. Fig.9 the hardfaced sample shows less wear than substrate during the same period of the test

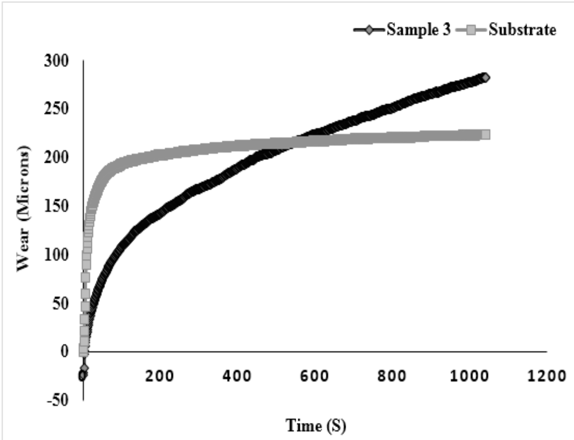


Fig.8 Wear versus time plot for hardfaced and substrate

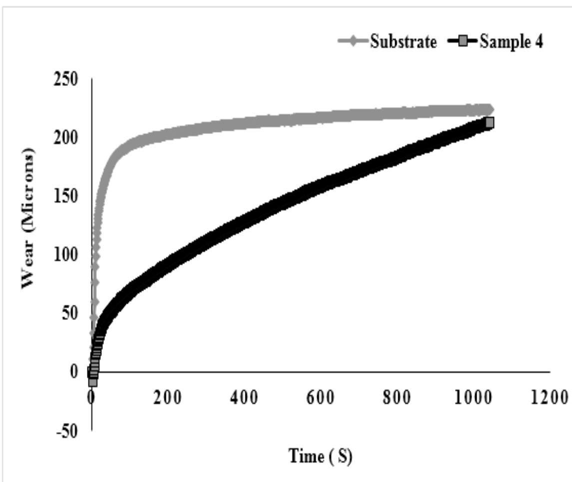


Fig.8 Wear versus time plot for hardfaced and substrate

## V. CONCLUSION

The stellite12 coated on EN 45 spring steel using plasma transferred arc welding and the following results are obtained from the current studies

- The hardness value is improved without affecting other mechanical properties and overall 21.1% percentage improvement in hardness value.
- From wear test result the hardfaced sample shows less wear resistant than the substrate ,it may be due to the high hardness of substrate even after the tempering process
- Stellite 12 is less wear resistant in room temperature


## ACKNOWLEDGMENT

The authors would like to thanks to TEQIP-II Government Engineering College Kannur for financial support and Vishnu heat treatment at Coimbatore for experimental work.


## REFERENCES


[1] Grainger S and Blunt J, Engineering Coatings and Design and Application, 2nd Ed., Abington Publishing U.S A.,1998

[2] R.Davis, Associates. Hardfacing, weld cladding and dissimilar metal joining in; ASM handbook – welding in: Brazing and Soldering, Vol.6.10thEd, ASM metal Park, OH, 1993, 699-823

[3] C S Ramachandran, V Balasubramanian , R Varahamoorthy, “Evaluation of Dry Sliding Wear Behaviour of Plasma Transferred Arc Hardfaced Stainless Steel”, Iron And Steel Research, 16(4): 49-54,2009

[4] Q.Y. Hou, J.S. Gao, F. Zhou “Microstructure and wear characteristics of cobalt-based alloy Deposited by plasma transferred arc weld surfacing”- Surface & Coatings Technology ,194, 238–243,20

[5] V Balasubrarnanian, A K Lakshminarayanan, R Varahamoorthy, S Babu, “Application of Response Surface Methodology to Prediction of Dilution in Plasma Transferred Arc Hardfacing of Stainless Steel on Carbon Steel”, Journal Of Iron And Steel Research International, 16(l): 44-53,2009

[6] S Mandel, S Kumar and LM Kukreja. “An Experimental Investigation and Analysis of PTAW Process,” Materials and Manufacturing Processes, 30: 1131–1137, 2015

[7] Víctor Vergara Díaz, Jair Carlos Dutra and Ana Sofia Climaco D' Oliveira, “Hardfacing by Plasma Transferred arc process” www.intechopen.com

[8] H.-J. Kim and Y. J. Kim, Wear and Corrosion Resistance of PTA Weld Surfaced Ni and Co Based Alloy Layers.- ISSN 0267–0844-Surface Engineering Vol. 15 No. 6,1999

[9] R. Choteborsky, P.Hrabe, M.Muller, J. Savkova, M. Jirka, ‘Abrasive wear of high chromium Fe-Cr-C hardfacing alloys’, Res. Agr. Eng., 54, (4): 192–198,2008

[10] Santiago Corujeira Gallo, Nazmul Alam, “Robert O'Donnell, In-situ precipitation of TiC upon PTA hardfacing with grey cast iron and titanium for enhanced wear resistance’, Surface and Coating technology ,63-68,2013

[11] Kirchgaßner, M., Badisch, E., Franek, “Behaviour of iron-based hardfacing alloys under abrasion & impact” Wear,Vol. 265(5-6), pp. 772-777,2008

# Microstructural, Mechanical and Wear Characteristics of Al-12.6Si-3Cu-(2-2.6 wt. %) Ni Piston Alloys

B. Sunil#1, V.R.Rajeev#1, S. Jose *

#Department of Mechanical Engineering, College of Engineering, Trivandrum, India

1sunil@cet.ac.in

*Department of Mechanical Engineering, TKM College of Engineering, Kollam, India

***Abstract*— Wear and friction characteristics of Al-Si-Cu-Ni piston alloys have significant importance in the field of automobile industry by considering the environmental and economic factors. The present study aims to investigate the effect of varying Ni weight percentage from 2 wt. % to 2.6 wt. % on the microstructural, physical and mechanical characteristics of the Al-12.6Si-3Cu-(2-2.6 wt. %) Ni piston alloys. Wear and friction characteristics of the Al-12.6Si-3Cu-(2-2.6 wt. %) Ni piston alloys were investigated at different sliding velocities (0.2-1 m/s) by using pin-on-disc tribometer under constant normal load of 30 N and sliding distance 500m. The microstructural observations showed that the needle like β eutectic silicon's are fragmented, spheroidized and evenly dispersed in the α-Al matrix after heat treatment under T6 conditions. It has been observed that the maximum hardness of 79 BHN obtained for Al-12.6Si-3Cu-2.3Ni Piston alloy. The maximum ultimate tensile strength of 230 MPa obtained for Al-12.6Si-3Cu-2.3Ni Piston alloy among the Al-12.6Si-3Cu-(2-2.6 wt. %) Ni piston alloys. Wear rate of Al-12.6Si-3Cu-(2-2.6 wt. %) Ni piston alloys decreases with the addition of 2.3 wt. % of Ni. A transition in the wear rate observed at a critical velocity of 0.6 m/s for the Al-12.6Si-2Cu-2 Ni and Al-12.6Si-3Cu-2.3Ni Piston alloys. But in the case of Al-12.6Si-3Cu-2.6Ni piston alloy the transition in wear occurs at critical velocity 0.4 m/s. However considerable decrease in the wear rate occurred by the addition of 2.3 wt. % of Ni and the minimum wear rate observed in the case of Al-12.6Si-3Cu-2.3Ni piston alloy in all the sliding conditions such as constant normal load 30N, constant sliding distance 500 m and sliding velocities in the range of 0.2-1 m/s.**

***Keywords*—Piston Alloys, Gravity casting, Wear rate, Coefficient of friction.**

## I. INTRODUCTION

Al-Si-Cu-Ni alloys are widely used in automobile industry for the production of piston and associated components due to its high strength to weight ratio, low density, good castability, low thermal expansion as well as high elevated temperature strength [1], [2]. Wear behaviour of such alloys have more significance in terms of economic and environmental factors [3]. In order to reduce the hydrocarbon emission it is required to reduce the crevice volume of internal combustion engines which leads to the requirement of stronger piston alloy with improved mechanical properties and wear characteristics. Addition of alloying element is one of the most important and practical methods to improve the elevated-temperature properties of Al–Si piston alloys, and many elements have been examined during the past decades[4]–[8].Ni has been known as the most important alloying element to improve the properties of Al-Si multicomponent piston alloy. Ni rich intermetallic phases formed by the addition of Ni on such alloys have significant role in the elevated temperature [4], [6]. The $Al_3Ni$, $Al_3CuNi$ and $Al_7Cu_4Ni$ phases have much bigger contributions to the elevated temperature properties of Al-Si piston alloys owing to their better thermal stability, mechanical properties, morphologies and distributions [6], [9].

In this study, attempts were made to investigate the effect of Ni addition on the microstructural, physical, mechanical, and wear characteristics of Al-12.6Si-3Cu-(2-2.6 wt. %) Ni piston alloys.

## II. EXPERIMENTAL DETAILS

### *A. Materials and preparation*

Al-12.6Si-3Cu-(2-2.6 wt. %) Ni piston alloys were prepared by using Al-6061 alloy, Al-50%Si master alloy, Al-50%Cu master alloy and Al-20%Ni master alloy.Table.1 describes the chemical composition of piston alloys used in this study.

TABLE VIII
CHEMICAL COMPOSITION OF AL-12.6SI-3CU-(2-2.6 WT. %) NI PISTON ALLOYS

| Piston Alloys | Si | Cu | Ni | Mg | Fe | Mg | Al (Balance) |
|---|---|---|---|---|---|---|---|
| | wt.% | | | | | | |
| **Alloy A** | **12.6** | **3** | **2** | **0.7** | **0.2** | **0.07** | **81.43** |
| **Alloy B** | **12.6** | **3** | **2.3** | **0.7** | **0.2** | **0.07** | **81.13** |
| **Alloy C** | **12.6** | **3** | **2.6** | **0.7** | **0.2** | **0.07** | **80.83** |

The gravity die casting technique was used to prepare the piston alloys. The melting process was carried out by using diesel fired tilting cast furnace .The preheated ingots were charged in to the furnace when the crucible attains a temperature of 700°C.The melting temperature was maintained at 750±5°C.The molten melt was continuously degased by bubbling Ar gas into the melt. The molten metal was poured at temperature of 720-730°C in to the open preheated metal mould and after solidification mould allows to water quenching.

### *B. Heat Treatment*

The T6 heat treatment process was carried out by using electrical muffle furnace. Solutionizing of the specimens were carried out at 450±5°C for 6 hrs. , followed by water quenching at a temperature of 20°C .After 15 minutes the specimens were removed and dried. The ageing or precipitation treatment carried out at a temperature of 180°C for 10hrs and the specimens were removed from the furnace and followed by air cooling [9].

### *C. Metallography*

Metallographic specimens were prepared by the normal polishing techniques. The specimens were polished with sand paper having grit size 320 to 2000, followed by fine polishing with diamond paste up to 0.25 microns on velvet cloth and then etched with Keller's reagent. The internal structure of cleaned and dried specimens inspected by using optical microscope.

### *D. Hardness test*

The hardness of samples were tested using Brinell Hardness Tester (INDENTEC). Samples with dimension 12mm x 12mm x12mm were cut from heat treated piston alloys. Surface of the samples were polished with 600 grit size SiC paper. The indentation was provided on the polished surface with a ball of diameter 2.5mm for a load of 62.5kg. Diameter of the impression was measured using a microscope with an accuracy of ±0.01mm.

### *E. Tensile test*

The tensile test of heat treated samples were performed by using Instron tensile testing machine in accordance with the ASTM E8M standard and each tensile test data was an average of three tensile specimens of accuracy. The dimensions of the specimens are given in figure. 1.

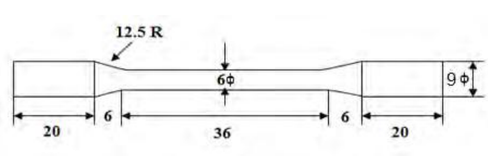


Fig. 1 Dimensions of Tensile Sample (All dimensions are in mm).

### *F. Wear test*

A pin-on-disc wear test rig was used to investigate the dry wear characteristics of Al-Si-Cu-Ni piston alloys in accordance with the ASTM G99-05 standards. A cylindrical pins of 6.0 mm diameter and length 30 mm cut from the heat treated samples was held on a rotating En 31 steel disc of diameter 200mm having a hardness of 60HRC. Both the pin and the counter body were polished flat with 600 grit SiC abrasive paper to a surface roughness of 0.35 and 0.27mm, respectively and then cleaned with acetone and dried before each sliding tests. All the tests were carried out using piston alloy pin with an applied load 30N and sliding velocity of 0.2–1 m/s range. The initial weight of the specimen was measured in a single pan electronic weighing machine (Zhimadzu) with least count of 0.01mg. After running through a sliding distance of 500m continuously as per the case, the specimens were removed, cleaned with acetone, dried and weighed to measure the weight loss due to wear. The difference in the weight of specimen before and after test was used as a measure of sliding wear. The frictional force was measured by using a load cell attached to the lever arm and the data acquisition system.

## III. Results and Discussion

### *A. Microstructural Analysis*

Fig.2 shows the as cast microstructure of Al-12.6Si-3Cu-(2-2.6 wt. %) Ni piston alloys. The average grain size varies with respect to the addition of Ni. The difference in the size and shape of different features are evident. The microstructure consists of α- aluminium dendritic halos with eutectic Si and complex intermetallic compounds segregated into the inter-dendritic regions. The features of the microstructures of the alloy in T6 condition undergo changes upon heat treatment. Microstructural observation showed that the secondary arm spacing is reduced for the heat treated alloys. Most of the intermetallic phases were partially dissolved and tend to spherodize, i.e., sharp corners have become rounded. The morphology change of the eutectic Si is obvious after heat treatment. The plate-like eutectic Si in the as cast condition is broken into small particles. That is, the Si particles break down into smaller fragments and become gradually spheroidized.

Alloy A

Alloy B

Alloy C

Fig. 2. Microstructure of Alloy A, Alloy B and Alloy C.

The changes in size and morphology of the discontinuous silicon phase are significant since they have a direct influence on the tensile properties [4].The massive rod like Si particles has been changed to a fine spherical shape besides the intermetallic phases distributing evenly along the grain boundaries. Further refinement in the grain size is also noticed after T6 heat treatment. The intermetallic phases are the main elevated-temperature strengthening phases in Al-Si-Cu-Ni piston alloys, especially Ni- rich phases [6]. At elevated temperature, the thermally stable Ni-rich phases could impose drag on boundaries and hinder the slide of α-Al grains. Therefore, Ni-rich phases can be called the main strengthening phases in Al-Si-Cu-Ni piston alloys at elevated temperature. Generally, the intermetallic phases found in these alloys are $Al_2Cu$, $Mg_2Si$, $Al_3CuNi$, $Al_7Cu_4Ni$, $Al_3Ni$ and $Al_5Cu_2Mg_8Si_6$ and so on [10].

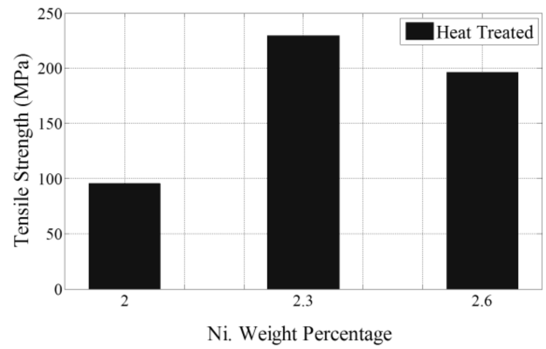


Fig. 3 Tensile Strength versus weight percentage of Ni for heat treated Al-Si-Cu-Ni (2-2.6 wt. %) Piston alloys.

*B. Tensile Characteristics.*

Fig.3 shows the tensile properties of the T6 samples. For the Alloy A, alloy B and alloy C samples in heat treated condition, the values of UTS are 96 MPa, 230 MPa and 197 MPa respectively. The ultimate tensile strength of Alloy B samples are more than 58 % and 14% than those for the Alloy A and Alloy C respectively. It can be observed that the ultimate tensile strength of Al-12.6Si-3Cu-(2-2.6) wt. %Ni piston alloys considerably improved by the addition of 2.3 wt. % of Ni.

*C. Physical Characteristics.*

Fig.4. Shows hardness values for all the piston alloys are increased after heat treatment and the hardness values of as cast Alloy A, Alloy B and Alloy C specimens are 35, 58 and 45BHN respectively. After heat treatment the hardness for the same are increased to 59, 79 and 63 BHN respectively. This indicates T6 heat treatment is effective in these casting methods for increasing the hardness. This hardening effect is due to the precipitation of $Al_2Cu$ and $Mg_2Si$ phases during heat treatment [9].

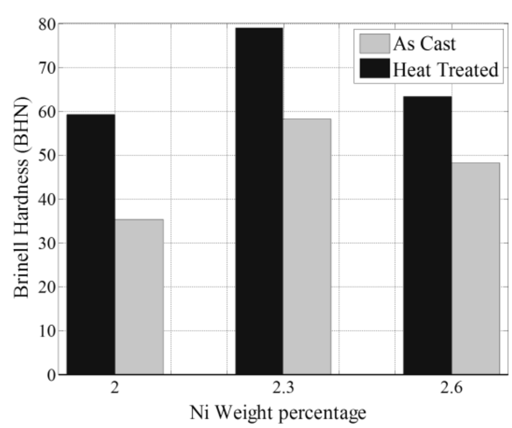


Fig. 4 Brinell hardness versus weight percentage of Ni for as cast and heat treated Al-12.6Si-3Cu-Ni (2-2.6 wt. %) Piston alloys.

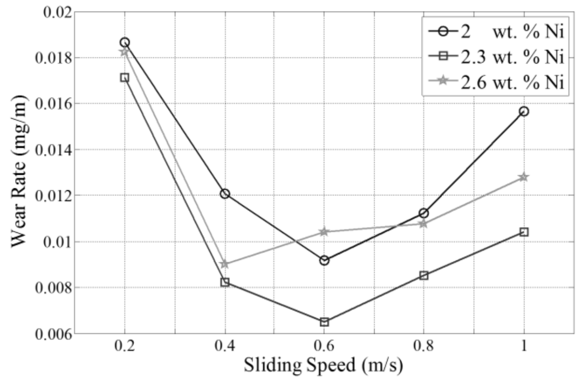


Fig. 5 Wear rate of Al-12.6Si-3Cu-Ni (2-2.6 wt. %) Piston alloy as a function of Sliding speed under the constant normal load of 30N and sliding distance of 500m.

*D. Wear and Friction Characteristics.*

*The effect of sliding velocity on wear rate:* Fig.5 shows the effect of sliding velocity on wear rate of the Al-12.6Si-3Cu-(2-2.6) wt. %Ni piston alloys against En 31 Steel counter surface under the constant normal load of 30N and sliding distance of 500m.It has been observed that the wear rate of Alloy A and Alloy B decreases with an increase of sliding velocity from 0.2 to 0.6 m/s. and a rapid increase observed beyond the sliding velocity of 0.6m/s. But in the case of Alloy C the wear rate decrease up to the sliding velocity of 0.4 m/s and increases beyond this velocity. Another aspect common to all the materials represented in Fig. 5 exhibited a transition from mild wear to severe wear beyond a critical value of sliding velocity. These results are in good agreement with the previous investigations of the same author [11].This transition behaviour of wear rate at the critical velocity is due to the formation and fracture of mechanically mixed layer (MML) on the sliding surface [12]–[14] .

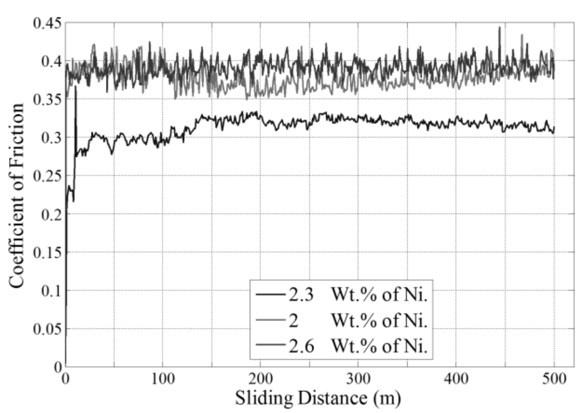


Fig. 6 Coefficient of Friction of Al-12.6Si-3Cu-Ni (2-2.6 wt. %) Piston alloys as a function of sliding distance under the constant normal load of 30N and sliding speed of 0.6 m/s.

*The effect of sliding velocity on the coefficient of friction*: Fig. 6 shows the effect of Ni weight percentage on the coefficient of friction of the Al-12.6Si-3Cu-Ni (2-2.6 wt. %) piston alloys as a function of sliding distance. It was observed that the coefficient of friction varies with the addition of Ni weight percentage. Alloy B exhibited the lowest coefficient of friction under the constant normal load of 30N and sliding velocity 0.6 m/s. In general, coefficient of friction is noted to be reduced due to addition of 2 to 2.3 wt. % of Ni among the Al-12.6Si-3Cu-Ni (2-2.6 wt. %) Piston alloys. Further addition of weight percentage of Ni from 2.3 to 2.6 wt. % in Al-12.6Si-3Cu-Ni (2-2.6 wt. %) Piston alloys the coefficient of friction was found to be increase [15].

Fig.7 shows the Coefficient of Friction of Alloy B as a function of sliding distance under the varying sliding speed (0.2 to1.0 m/s) and normal load of 30N.It is clear that the coefficient of friction decreases with the increase in the sliding speed and tends to increase beyond the critical velocity[16]. Alloy B observe the lowest average coefficient of friction of 0.29 at critical velocity 0.6 m/s.

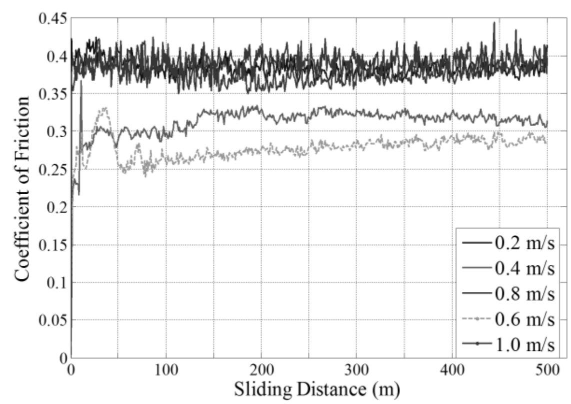


Fig. 7 Coefficient of Friction of Al-12.6Si-3Cu-2.3Ni Piston alloy as a function of sliding distance under the varying sliding speed (0.2 to1.0 m/s) and normal load of 30N.

## IV Conclusions

1) The plate like β-eutectic silicon are more fractured and spheroidized and evenly dispersed in the α-Aluminium dendritic haloes by the addition of Ni. The average grain size and degrees of fineness of β-eutectic silicon increased by the addition of 2.3 wt. % Ni in the Al-12.6Si-3Cu-Ni (2-2.6 wt. %) piston alloys. The difference in the size and shape of different features are evident.

2) A significant improvement in the ultimate tensile strength of Al-12.6Si-3Cu-Ni (2-2.6 wt. %) Piston alloys observed by the addition of Ni. Al-12.6Si-3Cu-2.3Ni piston alloy exhibited the maximum tensile strength of 236 MPa and is more than 58% and 14% that of Al-12.6Si-3Cu-2Ni and Al-12.6Si-3Cu-2.6Ni piston alloys respectively.

3) By the addition of Nickel on the Al-12.6Si-3Cu-Ni (2-2.6 wt. %) piston alloys improved the hardness. The maximum Brinell hardness of 58 and 79 observed for the Al-12.6Si-3Cu-2.3Ni Piston alloy in the as cast and heat treated conditions respectively among the Al-12.6Si-3Cu-Ni (2-2.6 wt. %) piston alloys.

4) A significant reduction in the wear rate obtained by the addition of 2.3 wt. % of Ni on the Al-12.6Si-3Cu-Ni (2-2.6 wt. %) Piston alloys. A transition in wear rate observed at critical velocity of 0.6 m/s.

5) Al-12.6Si-3Cu-2.3Ni Piston alloy experienced a lowest coefficient of friction in the means of Ni weight percentage and by varying the sliding velocity from 0.2 to 1 m/s.

## Acknowledgment

The authors are gratefully acknowledging the Centre for Engineering Research and Development (CERD), Kerala for awarding research fellowship for the first author.

## References

[1] R. X. Li, R. D. Li, Y. H. Zhao, L. Z. He, C. X. Li, H. R. Guan, and Z. Q. Hu, "Age-hardening behavior of cast Al – Si base alloy," vol. 58, pp. 2096–2101, 2004.

[2] M. M. Haque and M. A. Maleque, "Effect of process variables on structure and properties of aluminium – silicon piston alloy," *journal of materials processing technology*, vol. 77, pp. 122–128, 1998.

[3] H. Ye, "An Overview of the Development of Al-Si-Alloy Based Material for Engine Applications," vol. 12, no. June, pp. 288–297, 2003.

[4] Z. Qian, X. Liu, D. Zhao, and G. Zhang, "Effects of trace Mn addition on the elevated temperature tensile strength and microstructure of a low-iron Al – Si piston alloy," *Materials Letters*, vol. 62, pp. 2146–2149, 2008.

[5] A. M. H. A, A. Alrashdan, M. T. Hayajneh, and A. T. Mayyas, "Wear behavior of Al – Mg – Cu – based composites containing SiC particles," *Tribiology International*, vol. 42, no. 8, pp. 1230–1238, 2009.

[6] Y. Li, Y. Yang, Y. Wu, L. Wang, and X. Liu, "Quantitative comparison of three Ni-containing phases to the elevated-temperature properties of Al – Si piston alloys," *Materials Science & Engineering A*, vol. 527, no. 26, pp. 7132–7137, 2010.

[7] Y. Li, Y. Wu, Z. Qian, and X. Liu, "Effect of co-addition of RE , Fe and Mn on the microstructure and performance of A390 alloy," *Materials Science & Engineering*, vol. 527, pp. 146–149, 2009.

[8] N. A. Belov, D. G. Eskin, and N. N. Avxentieva, "Constituent phase diagrams of the Al – Cu – Fe – Mg – Ni – Si system and their application to the analysis of aluminium piston alloys," *Acta Materialia*, vol. 53, pp. 4709–4722, 2005.

[9] M. Zeren, "The effect of heat treatment on aluminium-based piston alloys," *Materials & Design*, vol. 28, pp. 2511–2517, 2007.

[10] Y. Yang, K. Yu, Y. Li, D. Zhao, and X. Liu, "Evolution of nickel-rich phases in Al – Si – Cu – Ni – Mg piston alloys with different Cu additions," *Journal of materials and design*, vol. 33, pp. 220–225, 2012.

[11] V. R. Rajeev, D. K. Dwivedi, and S. C. Jain, "Effect of load and reciprocating velocity on the transition from mild to severe wear behavior of Al – Si – SiC p composites in reciprocating conditions," *Materials and Design*, vol. 31, no. 10, pp. 4951–4959, 2010.

[12] B. Venkataraman and G. Sundararajan, "Correlation between the characteristics of the mechanically mixed layer and wear behaviour of aluminium , Al-7075 alloy and Al-MMCs," *Wear*, vol. 245, pp. 22–38, 2000.

[13] J. Clarke and A. D. Sarkar, "Topographical features observed in a scanning electron microscopy study of aluminium alloy surface in sliding wear," *Wear*, vol. 69, pp. 1–23, 1981.

[14] D. K. Dwivedi, T. S. Arjun, P. Thakur, H. Vaidya, and K. Singh, "Sliding wear and friction behaviour of Al – 18 % Si – 0 . 5 % Mg alloy," *journal of materials processing technology*, vol. 152, no. April, pp. 323–328, 2004.

[15] J. Kov, "Effect of composition on friction coefficient of Cu – graphite composites ˇ," *Wear*, vol. 265, pp. 417–421, 2008.

[16] C. Subramanian, "Some considerations resistant aluminium towards the design of a wear alloy," *Wear*, vol. 155, pp. 193–205, 1992.

# Dynamic Mechanical Behaviour of Carbon Fibre Based Composite Laminate Made of Micro rubber Blended Epoxy Matrix for Structural Applications

G.Vignesh[1], N.S.Tharunkrishna[2], C.Senthamaraikannan[3], R.Ramesh[4]

*Department of Mechanical Engineering*

*Sri Venkateswara College of Engineering, Sriperumbudur, Tamilnadu, India*

1vignesh4095@gmail.com

2tharun.krishna@gmail.com

3senthamarai@svce.ac.in

4rameshraja@svce.ac.in

*Abstract*— **The woven fabric carbon/epoxy composite is one of the commercially well recognized composite materials for structural applications like aerospace systems, automobiles and also in ship building industries. In the present investigation, dynamic mechanical behaviour of woven fabric carbon epoxy composite laminate fabricated by carboxyl terminated butadiene acrylonitrile rubber particles in epoxy matrix was studied by varying temperature. Three different weight fractions of rubber particle in epoxy matrix like 3%, 9% and 15% were considered. The composite plates were fabricated by hand layup method with 40% of fibre volume fraction. The Storage modulus, loss modulus and tan delta values were evaluated by conducting dynamic mechanical analysis for all the specimens. The results show that there is increase in damping parameter, tan delta value for increased rubber content in epoxy matrix. Damping parameter is increased to maximum of 24% for the addition of 15wt% rubber content in modified carbon epoxy composites. The storage modulus and loss modulus were also found to be increases with the increasing rubber content in epoxy matrix to a maximum of 44% and 36% respectively for the maximum rubber particulates 15wt.%.**

*Keywords*— **woven fabric carbon composites, micro rubber, damping parameter, storage modulus, loss modulus**

## I. Introduction

Woven fabric carbon epoxy composite were mostly used in structural applications due to their superior specific strength and specific stiffness ratio [1]. Laminated composite plates are used to fabricate aircraft structures in the aerospace industry, vehicle parts in the automotive industry, and in ship building industry. Michelle Leali Costa [2] et al studied the formation of rubber particles in epoxy matrix by carboxyl terminated process, they extended their study to analyse rubber modified carbon / epoxy laminates for aerospace field applications and concluded that they are most suitable for structural components of aerospace applications. Johnsen [3] et al proved that the brittleness of the epoxy can be reduced by adding reactive liquid rubber such as carboxyl terminated butadiene acrylonitrile copolymer, CTBN and thereby improving their toughness. Recent review on multi-functional composite materials reveals that tensile modulus; tensile strength and fracture toughness of epoxy considerably decreases with the addition of Carboxyl terminated butadiene acrylonitrile rubber (CTBN) particles [4]. Abu Baker et al [5] showed that the addition of liquid natural rubber in Kenaf fiber reinforced epoxy composites had improved mechanical properties like flexural modulus, flexural strength and fracture toughness. Li et al[6] experimentally showed that the impact strength of epoxy was improved significantly by adding mixture of rubber and nano clay in epoxy matrix. Kinloch et al [7] studied the cyclic fatigue behaviour of an epoxy polymer with micro rubber particles and concluded that the rubber modified epoxy shows better cyclic fatigue behaviour. There is limited experimental work in studying the material damping performance of micro rubber modified woven carbon epoxy composites. Experimentally, dynamic mechanical analysis (DMA) is very useful in studying the dynamic modulus and damping parameter of polymer over a range of temperature [8]. This paper presents our recent study on dynamic mechanical properties of carbon fibre /epoxy laminates by adding micro rubber particles in epoxy matrix by dynamic mechanical analysis. The epoxy was modified by adding different weight fractions of micro rubber particles and DMA tests were conducted on modified carbon epoxy laminate.

## II. Fabrication of Carbon Epoxy Composite Plates

The Neat carbon epoxy plate was fabricated by hand lay-up technique using woven carbon fabric of 600gsm with standard diglycidyl ether of bisphenol A (DGEBA) resin. The precision dam was used and four layers of woven carbon fiber are used for fabrication of composite plates to control the thickness of plates during fabrication. Fibre volume fraction of 40% and matrix volume fraction of 60% was preferred. Compression moulding machine was used for curing the composite plates with nominal pressure of 350 psi at room temperature for 24 hours. Figure 1 shows a schematic drawing of preparing carbon epoxy composites. After the curing process, the composite laminates are trimmed into uniform plates of size of 250 mm (length) × 250 mm (width) × 3 (thickness) mm as shown in Fig.2. Further to study the effect of micro rubber particles effect on dynamic mechanical properties, 20kg of Albipox 1000® containing 40 wt. % micro rubber particles in DGEBA resin of average size of 5 micrometer was obtained from Evonik industries AG, Germany. The same type of neat epoxy resin was applied to dilute the Albipox 1000® master batch down to a series of modified epoxy with various micro rubber contents: 3%, 9% and 15% weight fractions. Carbon Epoxy plates were fabricated with rubber particles of average size of 5µm with weight fractions of 3%, 9% and 15%. For fabricating, different weight fractions of micro rubber particle modified epoxy resin, procedure adopted by Manjunatha et al [9] was followed. Fabricated carbon/epoxy composite plates with different reinforcements are shown in Figure2. The matrix formulations of the samples are listed in Table 1. Optical microscope images of the epoxy mixed with different weight fractions of rubber is shown in Figure 3.

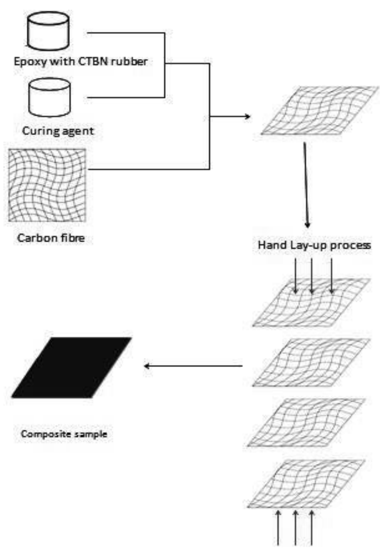


Fig. 1. Schematic diagram showing fabrication steps in composite plate

TABLE 1.

DIFFERENT RANGES OF WEIGHT CONTROL, CONSIDERED FOR BLENDING RUBBER IN CARBON EPOXY LAMINATES

| Material Code | Composition of epoxy and rubber by weight percentage (wt.%) | |
|---|---|---|
| | Epoxy | Rubber |
| CE | 100 | - |
| M3 | 97 | 3 |
| M9 | 91 | 9 |
| M15 | 85 | 15 |

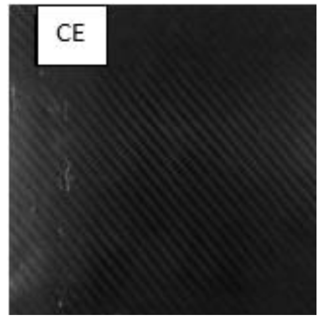


Dedicated Carbon Epoxy Plate

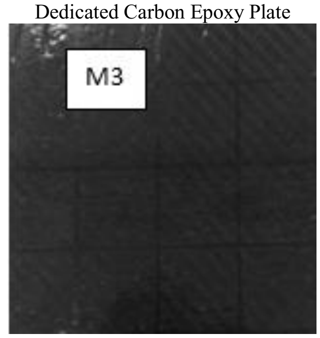


Carbon Epoxy plate fabricated with 3 % weight fraction rubber particles modified

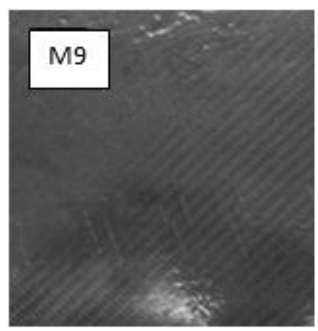


Carbon Epoxy plate fabricated with 9 % weight fraction rubber particles modified epoxy resin

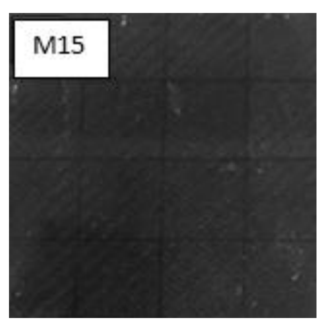


Carbon Epoxy plate fabricated with 15 % weight fraction rubber particles modified epoxy resin

Fig.2 Woven Carbon fabric composite plates with different weight percentage of CTBN rubber particle inclusions in epoxy matrix

## III. Dynamic Mechanical Analysis of CTBN modified carbon epoxy composites

Dynamic mechanical analysis was conducted using a dynamic mechanical analyzer (DMA Q800 V20.6 Build 24) shown in figure 3a, as per the ASTM Standard D4065 [10]. The samples with dimensions 35 mm long x 15 mm wide x 3 mm thick were tested from 20 to 180o C at a heating rate of 10 oC/ min and at frequency of 1.0 Hz. Three samples were used for conducting the experiments in three point bending mode as shown in figure 3b and results were discussed.

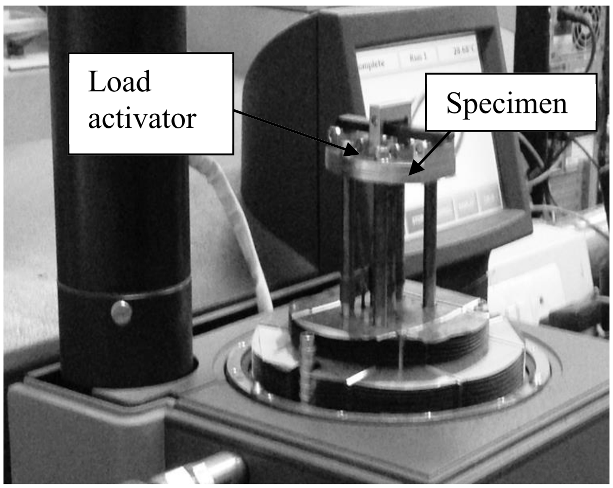


Fig. 3a Test setup used for DMA of carbon epoxy composites

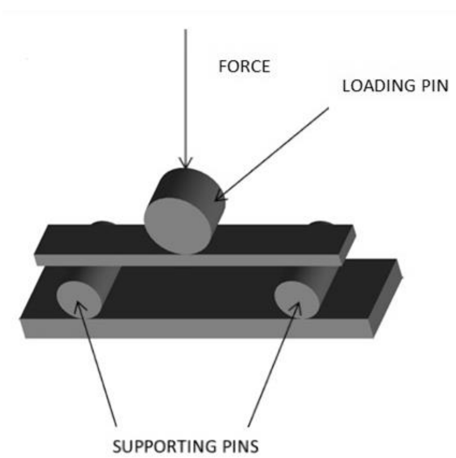


Fig. 3b Three point bending mode for DMA of epoxy composites

### A. *Storage modulus*

The variation of dynamic elastic modulus as a function of temperature for the micro rubber blended carbon epoxy laminates is given in Figure 4. The storage modulus curves of the modified and unmodified composites present three zones, a glassy region, an abrupt modulus decreasing region and the high temperature rubbery region. At the glassy region, storage modulus was measured and It was observed that storage modulus of all composites increases with the addition of 3 wt%, 9 wt% and 15 wt % of rubber particles, by 16%, 27% and 44% respectively.

Samples are subjected to tension-compression deformation mode as similar to three point bending mode at flexural test. Storage modulus will be increased when higher amount of stress transfer take place between fibre matrix interactions. This is due to effect of deformation of rubber particles inside the epoxy matrix. More loads can be taken up by the rubber particles if their weight content in the epoxy matrix increases. In the first phase, the rubber particles will deform within the matrix, in the second phase; this deformation will study as bulk deformation of matrix including the fibre. As there is increase in rubber content in each layer, this deformation pattern increases the rate of bulk deformation by providing more local individual particle deformation. Thereby increases the amount of elastic energy storage in the laminates. Distribution of more rubber particle in the matrix causes more amount of energy storage because of added flexibility to the epoxy matrix. Thus the deformation of the rubber particle is responsible for enhanced stress transfer. Additional deformation of adding rubber particle is supported by previous studies. Sprenger et al[11] reported that adding epoxidized rubber particle in the matrix, decreases the tensile and flexural modulus due to its additional deformation effect thereby increasing the plasticizing effect in the matrix. Kinloch [12] also confirms that the addition of rubber particle in the epoxy matrix enhances more energy absorbing capacity due to flexibility of rubber particles.

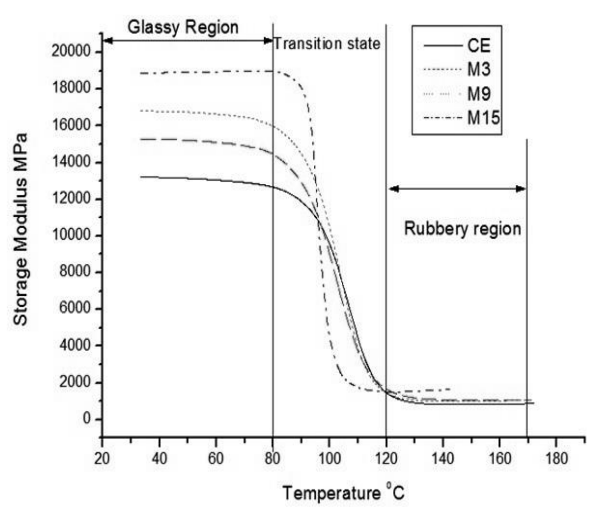


Fig.4 Effect of adding rubber particles on Storage modulus of Carbon epoxy composites

During transition state due to temperature rise, sudden collapse of bonding causes abrupt decrease in storage modulus. Addition of rubber particle influences more de-bonding in the epoxy network; it is clearly visible that M15 specimens show abrupt decrease in storage modulus value. M9 composite does not have abrupt change like M15 composites. In rubbery state, as further temperature increases more loosening of epoxy matrix causes increased mobility within the matrix and loses their close packing arrangement, thus decreases storage modulus for increasing temperature. This decreasing trend was almost common for all types of considered composites. Also addition of rubber particle in this state does not influence the storage modulus after 120oC. Increase in temperature causes dissolving of rubber particles within the epoxy matrix. For M15 laminate, more rubber particles causes dissolvement of more rubber content into epoxy, hence this laminate shows more storage modulus at high temperature range.

*B. Loss Modulus*

The effect of temperature on loss modulus of carbon epoxy composite by the addition of rubber particles is shown in figure 5. As discussed previously, laminates are subjected to cyclic load of 1Hz under three point bending mode. The loss modulus, E’’, is proportional to the lost or dissipated energy per cycle. At low temperatures up to 600C, viscous behaviour of rubber particles influences the loss modulus of the composite by increasing its viscoelastic property for increasing rubber weight concentrations, more the rubber particle more amount of energy dissipating capacity of the composites. In room temperature, loss modulus of M9 laminate was better than other considered rubber concentrations as shown in figure 6. Dissipation of energy at low temperature was very effective for this weight fraction. In transition region, the transition peak was found to become stronger for increasing rubber particle concentration. At this temperature, rubber particles exhibits pseudo plastic deformation, which further increases the energy dissipating capacity of composites. Further, comparison of loss modulus curves shows that the loss modulus peak or glass transition temperature (Tg) shifts towards lower temperature for M15 laminate due to the inclusion of more rubber particles in the epoxy matrix. It may be due to decrease in cross linking density of epoxy in the presence of rubber particles at this temperature. This happens because of dissolution of rubbery particles into epoxy matrix due to the increased temperature; hence increased free particle movement in the matrix. Bejoy Francis et al[13] also explains that there is increase in epoxy particle mobility with the inclusion of natural rubber particles. This is further confirmed by comparing the broadening and narrowing curve regions. Broadened curve can be seen for unmodified carbon epoxy composite. Curve become narrow for higher concentration rubber particle modified composite M15 than M3, this tendency is due to dissolution of more rubbery particles into epoxy matrix which in turn increases particle mobility. From the table 2, the loss modulus of M15 laminate is found to be the highest which is an indication of the improved energy dissipation, which could contribute to their better energy dissipating properties due to the above said reasons. There is a maximum increase of 36% in energy dissipating capability of carbon epoxy composites due to the addition of rubber particles in the epoxy matrix. Similar trend in loss modulus results was observed by Nishar Hameed et al [14], when incorporating polystyrene-co-acrylonitrile modified epoxy resin content in glass fiber reinforced composites. From the analysis of loss modulus curves it can be seen that 9wt % rubber particle added carbon epoxy laminate has higher Tg value and good loss modulus value at lower temperatures than 15wt%. This may be due the more cross linking effect of rubber into epoxy matrix when there is increase in weight concentration of rubber particles more than 9wt%.

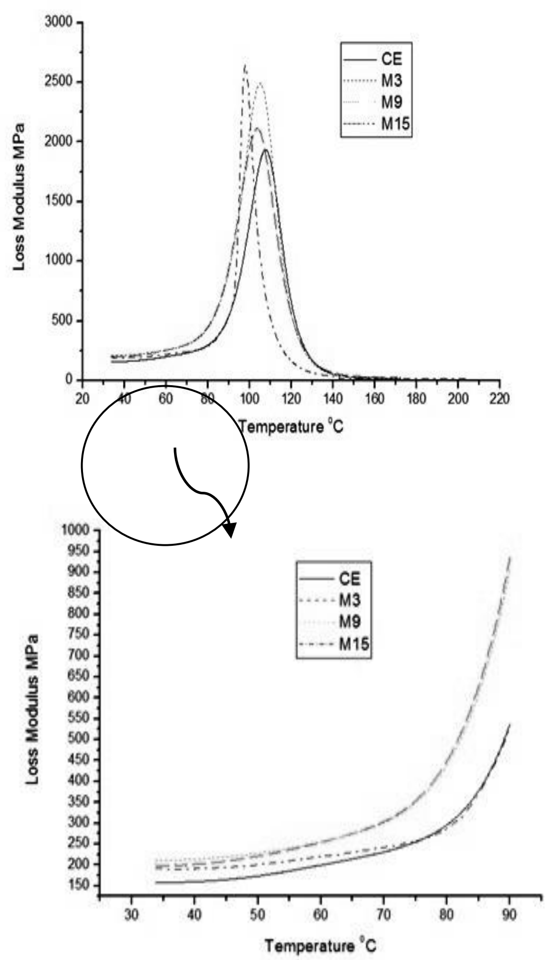


Fig. 5.Effect of rubber particles on loss modulus of carbon epoxy composite

TABLE 2 EFFECTS OF RUBBER PARTICLES ON DYNAMIC MECHANICAL PROPERTIES OF CARBON EPOXY COMPOSITES

| Material Code | | CE | M3 | M9 | M15 |
|---|---|---|---|---|---|
| **Parameters** | **Units** | | | | |
| **Storage Modulus** | **MPa** | 13116 | 15186 | 16720 | 18913 |
| **Loss Modulus** | **MPa** | 1930 | 2112 | 2487 | 2635 |
| **Damping factor** | **--** | 0.4175 | 0.4296 | 0.4919 | 0.5183 |
| **Glass Transition temperature** | **$^{o}$ C** | 101.3 | 111.62 | 114.8 | 112.83 |

### C. Damping factor

The magnitude of the damping factor (tan delta) is an indicative of the material damping present in polymer system and it gives balance between the elastic and viscous phase in a polymeric materials. Damping factor at glass transition temperature was extracted for each considered specimens and shown in figure 7 shows that damping factor increases with increase in rubber weight percentage; and reaches maximum value for 15 wt% rubber particles. Even though the increase in tan delta value is smaller for M3 specimens, damping factor increases considerably up to 24% for 15wt% rubber particles. As discussed in the previous section, the increasing trend in storage modulus and loss modulus of laminate for increased weight fraction of rubber particles, combinedly promotes higher damping factor.

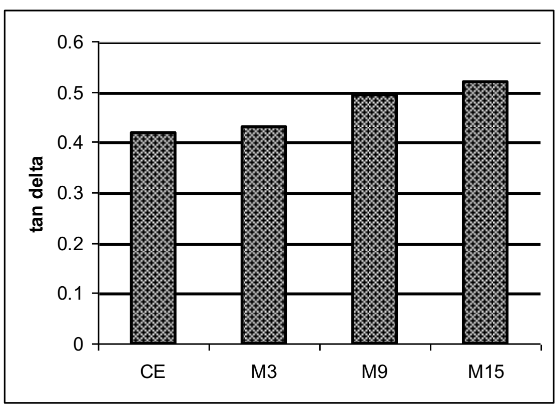


Fig. 7 Variation in damping factor values of carbon epoxy composites with addition of rubber particles

This is due to increase in domain size of epoxy matrix with the incorporation of rubber, which attributed to the coalescence of the dispersed rubber particles into the epoxy matrix at glass transition temperature Tg. This becomes more prominent in higher weight content as the dispersed rubber phase increases the viscosity as well as elasticity and in turn causes improved material damping property of the carbon composites.

## IV. CONCLUSIONS

Dynamic mechanical behaviour of woven fabric Carbon epoxy laminate was conducted with modified epoxy, blended with micro rubber particles as per standards. Dynamic mechanical test results shows that the addition of micro rubber particle in epoxy matrix in carbon laminate improves the material damping capacity of the composite. Storage modulus, Loss modulus and damping factor were increases with the increase in rubber particle concentration in epoxy matrix. Storage modulus was found to be increased due to the increased deformation of rubber particles for more weight fractions. This is due to increase rate of bulk deformation when rubber particle added to the epoxy matrix. Higher amount of energy storage and release is possible for composite due to increased deformation of matrix for same loading conditions. At lower temperature, energy absorbing capacity is better for increased weight content, thus 15wt% laminates have better storage modulus values. Carbon epoxy laminate with 9wt% rubber concentration exhibited high glass transition temperature and good loss modulus values at room temperature; hence M9 laminate is better among considered composites. There is no significant change in measured parameters above glass transition temperature for all considered weight fractions.

## REFERENCES

[1] Design and manufacture of textile composites, A. C. Long, CRC Press, 2005

[2] Michelle Leali Costaa, Mirabel Cerqueira Rezendea, Jane Maria Faulstich dPaivab, Edson Cocchieri Botelhoc , Structural Carbon/Epoxy Prepregs Properties Comparison by Thermal and Rheological Analyses, Polymer-Plastics Technology and Engineering, Volume 45, Issue 10, 2006.

[3] B.B. Johnsen, A.J. Kinloch, R.D. Mohammed, A.C. Taylor, Sprenger, Toughening mechanisms of nanoparticle-modified epoxy polymers, Polymer, Volume 48, [2], 2007, 530–541

[4] Ronald F. Gibson, A review of recent research on mechanics of multifunctional composite materials and structures, Composite, Volume 92, [12], 2010, 2793–2810.

[5] Abu Bakar, M, A Ahmad, S, Kuntjoro, Effect of Epoxidized Natural Rubber on Mechanical Properties of Epoxy Reinforced Kenaf Fibre Composites, Pertanika J. Sci. & Technol. 20 (1): 129 – 137 (2012)

[6] B. Li, X. Zhang, J. Gao, "Epoxy based Nano composites with fully exfoliated unmodified clay: mechanical and thermal properties," Journal of Nanoscience and Nanotechnology, vol. 10,no. 9, pp. 5864–5868, 2010.

[7] A.J. Kinloch, S.H. Lee, Taylor, Improving the fracture toughness and the cyclic-fatigue resistance of epoxy-polymer blends, Polymer, Volume 55, Issue 24, 2014, Pages 6325–6334.

[8] Laly A. Pothan , Sabu Thomas, G. Groeninckx, The role of fibre/matrix interactions on the dynamic mechanical properties of chemically modified banana fibre/polyester composites, Composites: Part A 37 (2006) 1260–1269.

[9] C.M. Manjunatha , Sprenger, A.C. Taylor, A.J. Kinloch, The Tensile Fatigue Behavior of a Glass-fiber Reinforced Plastic Composite Using a Hybrid-toughened Epoxy Matrix, Journal of Composite Materials August 2010, 44: 2095-2109

[10] ASTM D4065-01, Standard practice for plastics: dynamic mechanical properties: determination and report of procedures. West Conshohocken. PA. USA. American Society of Testing and Materials, 2004.

[11] Stephan Sprenger, Martin Heinz Kothmann, Volker Altstaedt, Carbon fiber-reinforced composites using an epoxy resin matrix modified with reactive liquid rubber and silica nanoparticles, Composites Science and Technology 105 (2014) 86–95.

[12] A.J. Kinloch, Toughening Epoxy Adhesives to Meet Today's Challenges, Materials Research Society Bulletin, vol. 28, 2003, 445-448.

[13] Bejoy Francis, Lakshmana Rao, R. Ramaswamy, Seno Jose, Sabu Thomas, Raju, Morphology, viscoelastic properties, and mechanical behavior of epoxy resin modified with hydroxyl-terminated poly(ether ether ketone) oligomer with pendent tert-butyl groups Polymer Engineering & Science, Volume 45,[12], 1548-2634.

[14] Nishar Hameed, P. A. Sreekumar, P. Selvin Thomas, P. Jyotishkumar, Sabu Thomas, Mechanical properties of poly(styrene-co-acrylonitrile)-modified epoxy resin/glass fiber composites, Journal of Applied Polymer Science, Volume 110, Issue 6, pages 3431–3438

# Experimental Investigation on Stacking Sequence Effects of Surface Treated Jute/Kenaf Hybrid Composite Laminates under Flexural Loading Condition

K. Rohit Krishna[1], N. Navin Kamesh[2], R Ramesh[3], R Murugan[4]

*Department of Mechanical Engineering, Sri Venkateswara College of Engineering, Pennalur, Sriperumbudur, Tamilnadu, India*

[1] Rohitkrishna.rocks@gmail.com
[2] navinkamesh24@gmail.com
[3] rameshraja@svce.ac.in
[4] muruga@svce.ac.in

***Abstract*— Natural fibre composite laminates are nowadays replacing the laminates with synthetic fibres in many structural applications such as aerospace, automobile, and in sports goods due to the advantages like environment friendly and recyclability. However the study of mechanical behaviors of natural fibre reinforced composites is very important in correct usage of these composite laminates for such specific applications. This paper aims in identifying the flexural properties of eight layered surface treated hybrid laminates made of Kenaf and Jute fibres. Surface treatment of fibre is made to improve the interfacial bonding between the fibre and resin and to reduce the moisture absorption. All laminates are fabricated using hand lay-up technique. Flexural tests were conducted for Kenaf and Jute hybrid laminates as per ASTM standard. Totally five trials were carried out for each type of laminate and the average values are reported and discussed.**

***Keywords*— stacking sequence, symmetric layering, asymmetric layering, flexural strength, flexural modulus**

## I. Introduction

In the last few decades, the volume and number of applications of polymer composite materials have grown rapidly. Composite materials consist of a matrix reinforced with fibres. Fibres are the principal constituents in a fibre reinforced composite material. They occupy the largest volume fraction in a composite laminate and share the major portion of the load acting on a composite structure. Proper selection of the type, volume fraction, length and orientation of fibre is very important. The usage of synthetic fibres like glass and carbon fibres in composite material causes many environment issues such as global warming and other environmental effects. This necessitates the search for the alternative and environmentally friendly material in the composite structures [1]. The use of natural fibre reinforced plastics represents attractive and suitable methods for replacing the synthetic fibres.

The natural fibre reinforced composites are considered as the smarter materials in recent technological advancements, since it offers robust mechanical properties [2]. It has procured the attention of industrialists and scientists for the application in automotive, aerospace, consumer goods, building and construction and for many other structural applications. Natural fibres offers higher benefits such as low cost, light weight, non abrasive, free from health hazard, higher resistance to fracture, biodegradable, recyclable, easier processing techniques, higher strength and stiffness and it contains acceptable specific strength properties.

Fibres in woven form offer many advantages in terms of manipulative requirements including dimensional stability, good conformability and deep draw shape ability. Compared with unwoven unidirectional composites, woven fabric composites provide more balanced properties, higher impact resistance, easier handling, and lower fabrication cost in specific for parts with complex shapes [3, 4].

## II. Fibre Treatment and Laminate Fabrication

### *A. Material*

In the present study, two types of natural fibres, Kenaf and Jute having different range of elastic modulus are preferred in fabric form for studying the effect of stacking sequence on mechanical properties. Kenaf fibre is the strongest among the natural fibres which provides good mechanical and thermal properties. Kenaf is a fast growing plant which is extracted from the stems of plants genus hibiscus, from the species named Hibiscus Cannabinus. In India, the availability of Kenaf fibre is enriched due to its increased usage in automotives and other applications. Jute fibre production takes place mainly in India, Bangladesh, China and Thailand.

The Jute composites can be very cost-effective material especially for construction industry (panels, false ceilings, partition boards etc.), packaging, automobile & railway coach interiors and storage devices.

The matrix phase in the composites serves two important functions that are, it holds the fibrous phase in the desired location and orientation, and under an applied force it deforms and distributes the stress to the high modulus fibrous constituent. The matrix used is a homogeneous mixture of Epoxy (LY556) and hardener (HY951) with the mixing ratio of 10:1. Epoxy resins are a class of thermoset materials used extensively in structural composite applications since they offer a unique combination of properties that are unattainable with other thermoset resins. Table I shows the mechanical properties of Jute, Kenaf natural fibres and epoxy matrix preferred for the present study.

TABLE I

PROPERTIES OF NATURAL FIBRES AND EPOXY MATRIX [5]

| **Physical Properties** | **Kenaf** | **Jute** | **Epoxy (LY556)** |
|---|---|---|---|
| Young's modulus (GPa) | 21-60 | 13-27 | 2.75-4.1 |
| Tensile strength (MPa) | 284-800 | 393-773 | 55-130 |
| Density (g/cc) | 1.4 | 1.3-1.45 | 1.15-1.2 |

### *B.* Surface Treatment of Natural Fibre

One of the major drawbacks encountered in embedding natural fibres into a polymer matrix is the lack of good interfacial adhesion between the two components, since the natural fibres are hydrophilic in nature contains free hydroxyl groups which results in poor properties in the final product [6]. Fibre - matrix interfacial adhesion can be improved with many chemical modifications of the fibre. One of the familiar and effective chemical modifications applied to natural fibre is alkaline treatment using sodium hydroxide (NaOH). Previous studies have shown that alkaline treatment is an effective process in removing impurities from the fibre, decreasing moisture absorption, enabling mechanical bonding and thereby improving matrix-reinforcement interaction and reported that 6% NaOH is the optimized one for the surface treatment of natural fibre [7-10].

Kenaf and Jute fibres are immersed in the 6% NaOH solution for two hours at room temperature and after immersion the treated fibres are rinsed with distilled water to remove the excess of sodium in them. The washed fibres are dried in sunlight for one day and it is dried in shade for three days. Post curing is done to remove surface moisture in the fibre by placing the fibre in the hot air oven at 50° C for 1 hr. In order to control the fibre volume fraction of different laminates during fabrication by hand layup technique, for very thin layer of low viscosity epoxy resin (GY 257) was sprayed over the natural fibre mat. So it is easy to handle and fabrication by hand layup techniques.

### *C.* Fabrication of Natural Composite Laminate using Hand Layup Method

Hand layup technique is followed for the fabrication of composite laminates [11, 12]. Kenaf and Jute fabrics were cut into pieces of 300 mm x 300 mm compatible with the mould used. The composite laminate was prepared by the impregnation of the fabric with the epoxy resin. The epoxy resin and hardener is mixed in the ratio of 10:1. In this study, the uniform fibre volume fraction of 0.3 is maintained for all types of laminates. Silicone spray is applied as the releasing agent which is coated in the top and the bottom layer of the material, which helps in easy removal of the material from the mould after curing. Roller is used to remove the entrapped air bubbles and to ensure uniform distribution of resin and the matrix. The casting is cured for 24 hours in compression moulding machine with nominal pressure of 2.5 MPa at room temperature. After the curing process, specimens of relevant dimension for mechanical property testing are cut using a diamond wheel cutter according to the dimensions specified by ASTM standard. The specimens are subjected to edge finishing using the emery sheet to obtain the uniform surface finish.

In the present investigation, six types of hybrid layer arrangements using Kenaf and Jute fibres are were considered. Three hybrid layer sequences are selected to achieve balanced property control along both the fibre plane and perpendicular to the fibre plane and layering sequence is symmetrical with reference to neutral axis of reference as shown in Fig.1. Next three hybrid layer sequences are considered asymmetrical with reference to neutral axis of reference with unbalanced property. For complete understanding purpose, two eight layered dedicated Jute and Kenaf laminates are also preferred. Fig.2 shows one of the Jute/Kenaf hybrid laminates fabricated by hand layup method.

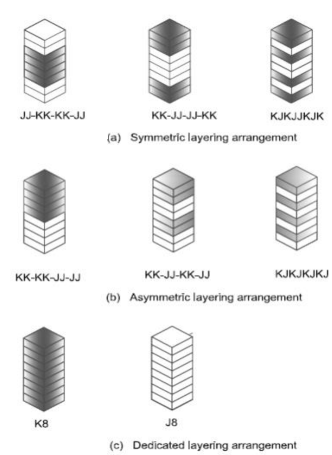


Fig.1 Layering arrangement of dedicated Jute, Kenaf and their hybrid laminates

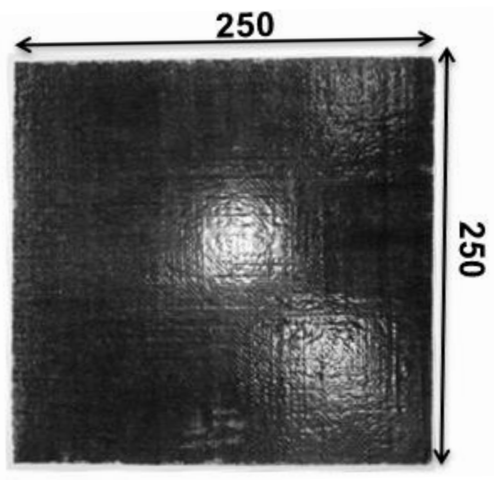


Fig.2 Image showing one of the Kenaf/Jute hybrid laminate fabricated by hand layup method

## III. TESTING OF LAMINATES BY FLEXURAL MODE

All types of laminates preferred were tested under three point bending mode to evaluate the flexural properties. Flexural test was performed as per ASTM D790 for all samples with a recommended span to depth ratio of 16:1 [13]. The size of the specimen is 126 mm × 12.5 mm × 9 mm. Fig. 3 shows the schematic diagram of the standard size for flexural test specimen as per ASTM D790 standard. The flexural test was conducted on closed loop servo hydraulic universal testing machine INSTRON with feed rate of 1.2 mm/min. Totally five trials were carried out for each type and the average results are reported and discussed. Fig.4 shows the image of flexural test conducted on one of the Jute/Kenaf hybrid composite specimen on universal testing machine.

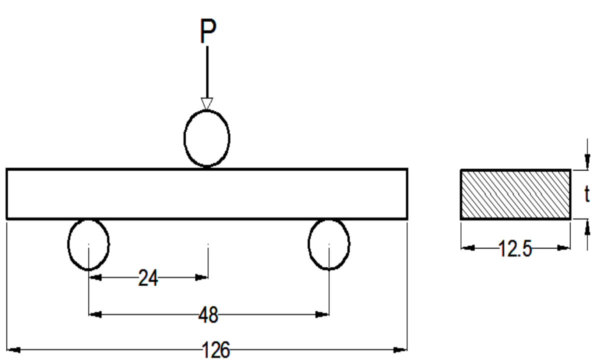


Fig.3 Schematic diagram showing the standard size for flexural test specimen

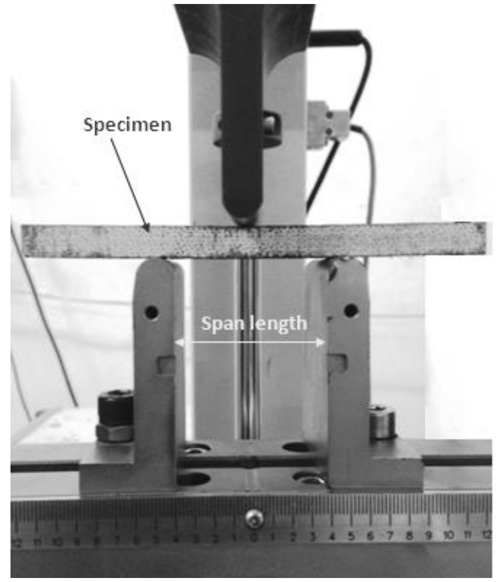


Fig.4 Image showing flexural test conducted for Jute/Kenaf hybrid composite specimens on INSTRON® machine

## IV. RESULTS AND DISCUSSION

The flexural strength of different Jute/Kenaf hybrid and dedicated layered composite laminates were evaluated. Hybridization of high modulus Kenaf fabrics with low modulus Jute fabric is expected to improve the mechanical properties. Table II shows the results obtained by performing flexural test on all types of hybrid and dedicated composite samples. The reported values are average values of test results conducted for five trials. There is considerable flexural strength variation between dedicated eight layered Jute and Kenaf fibre laminates as shown in Fig.5 [14]. Since Kenaf fibre possesses increased intrinsic strength than Jute fibre, the dedicated 8 layered Kenaf laminate showing higher flexural strength as expected.

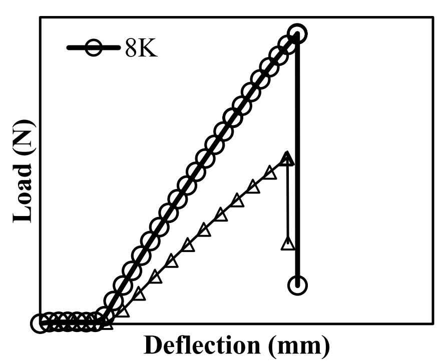


Fig.5. Load-Deflection plots of dedicated Jute and Kenaf laminates obtained from flexural test

*A. Symmetric hybrid Laminates plied by single and double alternative fibre layer control with respect to neutral axis of cross section*

Fig.6 shows the load - deflection plots of Kenaf-Jute Symmetric hybrid laminates plied by single and double alternative fibre layer control. In transverse bending the outer layer of composite beam plays important role. When Kenaf fibre plied in the outer layer, it offers very high resistance against bending load. From the Table II, it is observed that among the hybrid laminates plied with double alternative fibre layers, bending strength of KK-JJ-JJ-KK composite laminate is considerably higher than JJ-KK-KK-JJ laminate [15,16]. At the same time, hybrid laminate plied by single fibre layer alternatively, KJ-KJ-JK-JK, shows comparatively less increase in flexural strength.

TABLE II

EXPERIMENTALLY EVALUATED FLEXURAL PROPERTIES OF DEDICATED JUTE AND KENAF FIBRE LAMINATES AND THEIR HYBRID LAMINATES

| Layer Arrangement | Symbol Used → | Flexural Strength (MPa) | Flexural Modulus (GPa) |
|---|---|---|---|
| Symmetry | KK-JJ-JJ-KK | 81.5 | 6.99 |
| | JJ-KK-KK-JJ | 56.9 | 3.37 |
| | KJ-KJ-JK-JK | 64.1 | 3.76 |
| Asymmetry | KK-JJ-KK-JJ | 74.1 | 5.70 |
| | KK-KK-JJ-JJ | 61.2 | 3.78 |
| | KJ-KJ-KJ-KJ | 63.3 | 4.56 |
| Dedicated | 8K | 94.9 | 8.47 |
| | 8J | 50.9 | 5.34 |

As per the ASTM D790 standard, flexural modulus of various laminates were evaluated by considering the initial straight line portion of the load-deflection curves and reported in Table II. There is a considerable flexural modulus variation between hybrid laminates KK-JJ-JJ-KK and JJ-KK-KK-JJ. Hybrid layer arrangement, KK-JJ-JJ-KK, has flexural modulus value 52% higher than that of JJ-KK-KK-JJ arrangement as shown in Table II. Control of stacking sequence of natural fibres with two different elastic modulii resulted in laminates with different strength arrangement. Earlier experimental investigation conducted by Ary Subagia et al [17] stated that placing high stiffness fibre away from the neutral axis of the laminate and the low stiffness fibre at the neutral axis, will enhance the flexural modulus significantly and which also confirm the present characteristic study.

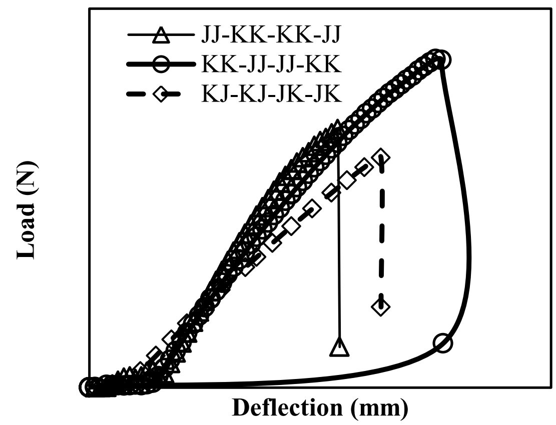


Fig.6. Load-Deflection plots of symmetric laminates plied by single and double alternative fibre layers obtained from flexural test

*B. Asymmetric hybrid Laminates plied by single and double alternative fibre layer control with respect to neutral axis of cross section*

Fig.7 shows the load-deflection plots of Kenaf-Jute asymmetric hybrid laminates plied by single and double alternative fibre layer control. From the Table 2, it is found that there is minimal variation in flexural strength among the asymmetric hybrid laminates plied with double alternative fibre layers, KK-JJ-KK-JJ and KK-KK-JJ-JJ. But, hybrid layer arrangement, KK-JJ-KK-JJ, has flexural modulus value 32% higher than that of KK-KK-JJ-JJ arrangement as shown in Table 2.

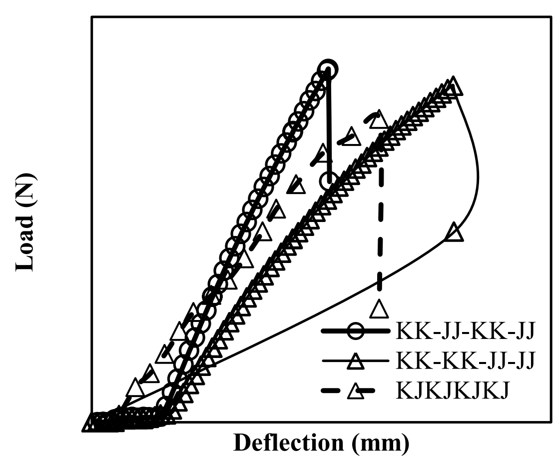


Fig.7. Load-Deflection plots of asymmetric laminates plied by single and double alternative fibre layers obtained from flexural test

Comparative result analysis on both symmetric and asymmetric layering arrangements revealed that double layered laminates with high modulus Kenaf fibre plied in the outer layer offered high strength and modulus. Double fibre layering arrangement offers accumulation of strength with increased combined strength and integrity along the thickness direction. Alternatively controlled fibre layering in terms of symmetry and asymmetry variation, exhibited merely similar flexural strength with marginal difference in flexural modulus of elasticity. This reveals the insignificant of single fibre layering over double fibre layering control.

## V. CONCLUSION

The influence of stacking sequence of Jute/Kenaf hybrid layered laminates on flexural properties was experimentally investigated for single and double alternative layer control. In hybrid laminates, different strength arrangement across the layers obtained by controlling with different fundamental modulus of natural fibre significantly modified the flexural behaviour. The experimental results showed that hybrid layering arrangement with higher modulus fibre plied as outer layer offer more resistance to bending load. Among all the hybrid laminates, layering sequence with double alternative layer control, KK-JJ-JJ-KK, has higher flexural strength and modulus than all other hybrid layering arrangements. Single fibre layering controls have exhibited same strength with marginal change in modulus value. Since Kenaf fibre possesses increased intrinsic strength than Jute fibre, the dedicated 8 layered Kenaf laminate, 8K, showing higher flexural strength as expected.

## REFERENCES


[1] Wambua, Paul, Ivens, Jan, Verpoest, and Ignaas, "Natural fibers: can they replace glass in fibre reinforced plastics," *Composite Science Technology*, vol.63, pp. 1259–1264, 2003.

[2] Zafeiropoulos NE, Williams DR, Baillie CA, and Matthews FL, "Engineering and characterization of the interface in flax fibre/polypropylene composite materials. Part 1. Development and investigation of surface treatments," *Composites; part A*, vol.33, pp.1083-93, 2002.

[3] Laly A Pothan, Petra Potschke, Rudiger Habler, and Sabu Thomas. "The static and dynamic Mechanical Properties of Banana and Glass Fibre Woven Fabric-Reinforced Polyester Composite," *Journal of Composite Materials*, vol. 39 (11): 1007-1025, 2005.

[4] Sabeel Ahmed K., Vijayarangan S. . "Tensile, flexural and interlaminar shear properties of woven jute and jute-glass fabric reinforced polyester composites," *Journal of Materials Processing Technology*, vol. 207, pp. 330-335, 2008.

[5] Mohanty, A. K., Misra, M., Drzal, L. T., Selke, S. E., Harte, B. R., and Hinrichsen, G, "*Natural fibres, biopolymers and biocomposites: An introduction*", (2005), CRC Press, London.

[6] Van de Weyenberg I, Chi Truong T, Vangrimde B, and Verpoest I, "Improving the properties of UD flax fibre reinforced composites by applying an alkaline fibre treatment,". *Composites: Part A* 2006;37:1368-76.

[7] Corrales F, Vilaseca F, Llop M, Girones J, Mendez JA, Mutje P. Chemical modification of jute fibres for the production of green composites. *J hazardous Mater*, vol.144, pp.730-735, 2007.

[8] Gassan Jochen, Bledzki Andrzej K. "Posiibilities for improving the mechanical properties of jute/epoxy composites by alkali treatment of fibres". Compos Sci Technol 1999;58:1303-9.

[9] V. Fiore, G. Di Bella, and A. Valenza, "The effect of alkaline treatment on mechanical properties of Kenaf fibers," *Composites: Part B*, vol.68, pp.14–21, 2015.

[10] Dipa Ray, B K Sarkar, A K Rana and N R Bose, "Effect of alkali treated Jute fibres on composite properties," *Bulletin of Material Science*, Vol. 24, No. 2, pp. 129–135, 2001.

[11] *ASM Hand book–Composites*, 2001, ASM International, The Material Information Company.

[12] Mallick. P. K, "*Fibre reinforced composites, materials and manufacturing and Design*". CRC Press, Taylor & Francis Group, 2008.

[13] *ASTM D790-03-Standard test method for flexural properties of unreinforced and electrical Insulating Materials*, Annual book of ASTM standards, Philadelphia.

[14] Vivek Mishra and Sandhyarani Biswas, "Physical and Mechanical Properties of Bi-directional Jute Fibre epoxy Composites," *Procedia Engineering*, vol.51, pp.561 – 566, 2013.

[15] Jarukumjorn Kasama and Suppakarn Nitinat, "Effect of glass fiber hybridization on properties of sisal fiber polypropylene composites," *Composites: Part B*, vol.40, pp.623–627, 2009.

[16] M. Ramesh, K.Palanikumar, and K. Hemachandra Reddy, "Mechanical property evaluation of sisal–jute–glass fiber reinforced polyester composites," *Composites: Part B*, vol.48, pp.1-9, 2013.

[17] Ary Subagia, IDG, Yonjig Kim, Leonard D Tijing, Cheol Sang Kim and Ho Kyong Shon, "Effect of stacking sequence on the flexural properties of hybrid composites reinforced with carbon and basalt fibres," *Composites: Part B*, pp. 251-258, 2014.

# Nonlinear Analysis of Adhesively Bonded Honeycomb Sandwich Structures

Rahul V R[1], R Ramesh kumar[2]

*Department of Mechanical Engineering*

*Sree Chitra Thirunal College of Engineering Thiruvananthapuram, Kerala, India*

[1]rahulvramakrishnan@gmail.com

[2]rameshkumar9446@gmail.com

***Abstract*— Generally, specification on the bond strength of adhesive joint is arrived at based on shear strength of the adhesive obtained by lap shear test. Then the design margin is assessed through structural test. Bond integrity is then ensured following NDT. In the present study, honeycomb core in the sandwich specimen of flatwise test is modelled as it is considering adhesive film layer of 0.1mm between the skin and core with nonlinear stress –strain relationship of the adhesive. The effect of filleting of adhesive with core is accounted by providing appropriate constraints along the free edge (periphery) of the adhesive film. The flatwise tensile load carrying capacity assessed by the nonlinear analysis is 20% more when compared to linear analysis. Comparison on the failure load obtained the test and analysis are 10400N and 12480N respectively. Present methodology can be considered as a more reliable and accurate yet a non-conservative approach suitable even when shelf life of adhesive reduces.**

***Keywords*—Honeycomb core, Nonlinear analysis, Bond strength, Flatwise tension test (FWT), Lap shear strength**

## I. INTRODUCTION

Adhesively bonded structures like stringer stiffened shells and honeycomb sandwich structures have wide applications in the area of Aerospace engineering where load bearing is mainly bending and compressive in nature as the conventional bolted joint makes the structure heavy and bulky [1-3]. In the case of minor debond observed in stringer stiffened construction, well known MCCI approach is followed to assess structural integrity for an anticipated onset of failure mode [4]. Sandwich structure consists of top and bottom composite skins that are bonded to honeycomb core using adhesive film following a curing process. In certain cases deviation in maintaining the storage condition of adhesive film at -20$^0$C, the shelf life as a measure of bond strength may reduce by as much as 20 to 30% within the expiry period of the adhesive film. Even for a realised sandwich product after several years of storage having bond integrity observed during NDT technique, prior to employ for service, it is necessary to conduct the test of coupons realizated at the time product delivery to ensure whether the lap shear strength meets the design specification. Once the bond strength as measured from a lap shear coupon is found to be low, it is necessary to access the integrity of the structure.

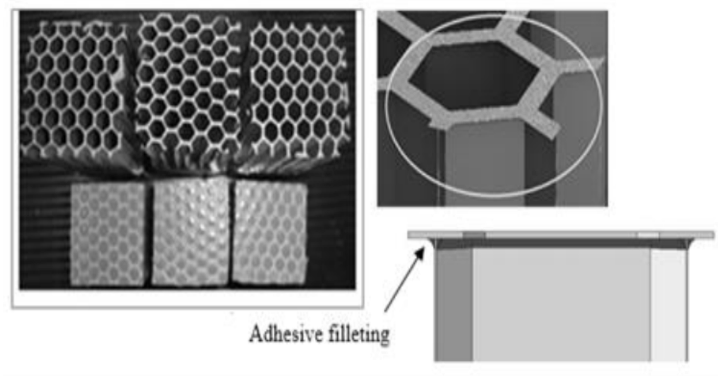


Fig. 1 Filleting around honeycomb core beyond foil thickness and the adherent plate (not to scale).

The intricacy in applying nonlinear approach is not only to model the adhesive filleting formed around a honeycomb cell during curing but also govern the path of debond (Fig.1). Though percentage of honeycomb core foil thickness is less than 5%, filleting area constitutes about 30% of the skin area of the sandwich panel. The surface area of the honeycomb core (from the model geometry for about 0.0508mm foil thickness) is 28.53mm$^2$ and surface area of the adhesive filleting from the modelling (where the area ranging between 400mm$^2$ to 480mm$^2$) is 473.54mm$^2$. Due to these difficulties assessment are being confined on the test data. Almost all the closed form and numerical studies do not consider the adhesive layer thickness.

The present work is aimed to study the nonlinear behaviour of adhesively bonded sandwich structure under pull out load corresponding to the test condition of FWT to assess the bond integrity [5]. For this purpose assembly of intricate model of skin, core and adhesive patch are made use of to compare the analysis results with test data.

## II. FINITE ELEMENT ANALYSIS OF HONEYCOMB SANDWICH SPECIMEN

The exploded view of skin – core - skin of FWT specimen of 40 x 40 x 30 mm is shown in Fig.2. In the present study, for the nonlinear analysis of FWT specimen under pull out load, full size of test specimen is modeled with minimum elemment size of 0.2mm using eight node quadratic brick element to accommodate 0.938mm of adhesive width (Fig.3). Further to study the effect of filleting for the entire model, a total number of one million elements are used.

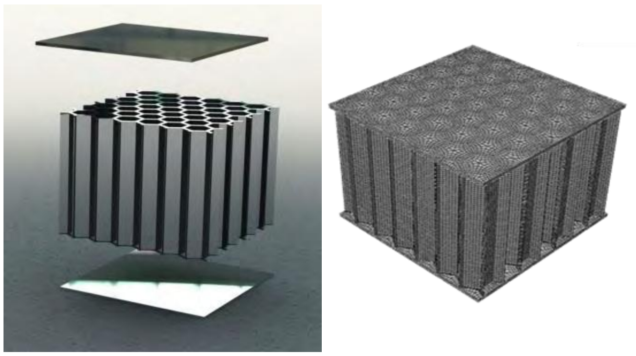

Fig. 2 Three dimensional model of the honeycomb sandwich FWT specimen

The element discretisation of the honeycomb sandwich assembly consists of aluminium skin, adhesive layer and the honeycomb core on the top side while for bottom side no adhesive layer is taken (Fig.2-3). Details of sub structural components are given in Table II.

*A.* Input data considered for Non-linear analysis

The material properties assigned for the skin, adhesive and honeycomb core for the FE analysis are given in Table I.

TABLE I
MATERIAL PROPERTIES OF HONEYCOMB SPECIMEN

| Material properties | |
|---|---|
| Modulus of the skin (AA 2014) and core (AA 5036) | - 70GPa |
| Yield Strength of Al skin | - 360MPa |
| Poison’s ratio for skin and core | - 0.3 |
| Lap hear strength of adhesive | - 20MPa |
| Flat wise Tensile Strength of specimen | - 6.7MPa |
| (average value of very large number of tested specimens) | |

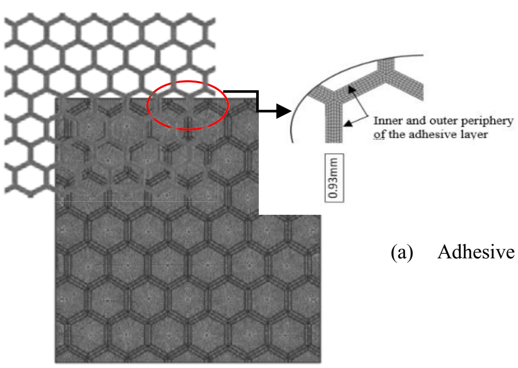


(a) Adhesive patch

Fig. 3 FE model of the adhesive layer and skin

*B.* Boundary condition and load

All the degrees of freedom are constrained at the bottom of the honeycomb core sandwich. In order to consider the effect filleting that provides strong integrity of adhesive with core even after skin separation, all degrees of freedom are constrained of the bottom nodes along the inner and outer periphery of all adhesive hexagonal patch modelled by the 3D brick element (Fig, 3a).

Pull out load up to 16000N corresponding 10MPa over 40 x 40 surface area (expected FWT value is 6.7MPa, Table I) is applied on the top skin surface and the auto load increment is considered.

The average nominal stress-strain relationship obtained from the test data for epoxy adhesive film taken for the analysis is given in Fig. 4. Only material nonlinearity of adhesive layer is considered while for the skin and core linear properties are taken.

Table II
Geometrical Details Required for Modeling

| Geometrical details of skin and core | |
|---|---|
| Length of the specimen | 40mm |
| Width of the specimen | 40mm |
| Skin thickness | 1mm |
| Cell size of the core | 6mm |
| Thickness of the core foil | 0.0508mm |
| Honey comb Core height | 30mm |
| Density of the core | 66 kg/m$^3$ |

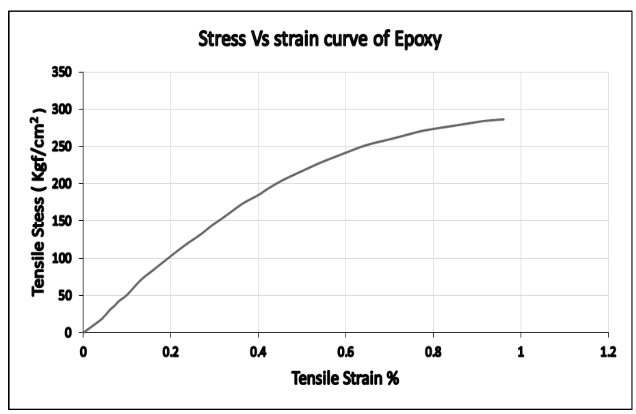


Fig. 4 Average values (three specimens) of film adhesive stress-strain variation.

The stress –strain variation of adhesive obtained by tension test (Figure 4) is converted into true stress and true plastic strains as per the ABAQUS user’s manual.

III. RESULTS AND DISCUSSION

The material nonlinear analysis (adhesive layer) results presented in figure.5 shows that up 8288N interfacial shear stress of the adhesive layer is found to be linear and is 16.5MPa as against the design specification shear strength value of 20MPa.

Beyond 8288N non linearity of the adhesive stress occurs. At around 12500N, converged value of shear stress is obtained as 19.35MPa as against the lap shear strength value of 20MPa. Just after this load, at 19.4MPa of the adhesive layer load becomes 16000N. Hence 12500N corresponding to 19.35MPa is assumed to be the failure load. Linear analysis result for 20MPa is evaluated as 10046N. It may be noted that actual adhesive strength may vary from 20MPa to 25MPa for different batch of adhesive film. The FWT value for 10046N (linear) for a surface of 40 x 40 mm is 6.3MPa (lower bound) while the upper bound value is 7.8 MPa respectively. The test value for the FWT is 6.7MPa. Present nonlinear analysis result for the failure load of 12500N yield a FWT value of 7.8MPa. Thus one can conclude that linear analysis prediction for the FWT specimen configuration considering adhesive layer of 0.1mm thickness gives a conservative value of 6.3MPa while a more reliable assessment considering material nonlinear property of adhesive gives an assessment of 7.8MPa for FWT value, even though test data is more close to linear adhesive property. This may be because rate of loading towards the ultimate failure load is quite faster.

It is very clear that 12480N is very close to the test data. Present study proposes an assumption that as soon as the nonlinear stress in the adhesive layer becomes nearly constant, load at the minimum strain, is taken as the ultimate failure load (Fig. 6-7).

## IV. Conclusions

3-D analyses of aluminium skinned honeycomb core sandwich FWT specimen of size 40 x 40 x 30 mm with honeycomb core modelled as it is and considering adhesive layer with effect of filleting with core as a geometrical input have been carried out to assess the critical load for a normal interfacial failure between skin and honeycomb core following the nonlinear analysis.

Linear analysis prediction for failure load of adhesively bonded honeycomb sandwich FWT specimen considering 0.1mm thick adhesive layer is 6.3MPa as a conservative estimate.

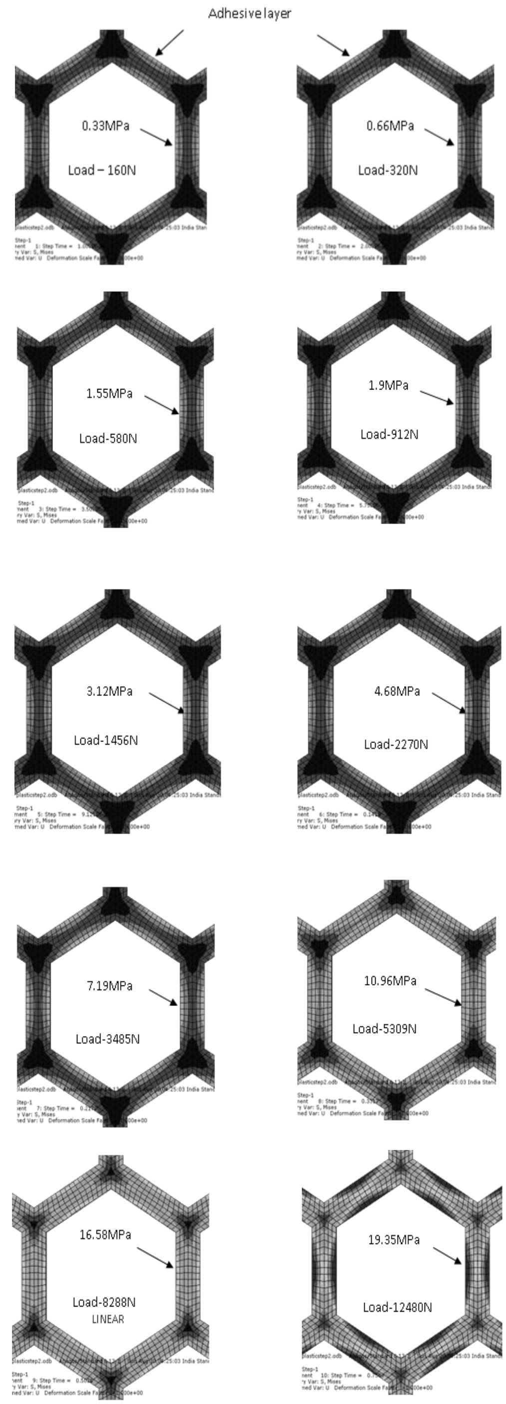


Fig. 5 Interfacial tensile stresses in the adhesive layer (nonlinear analysis).

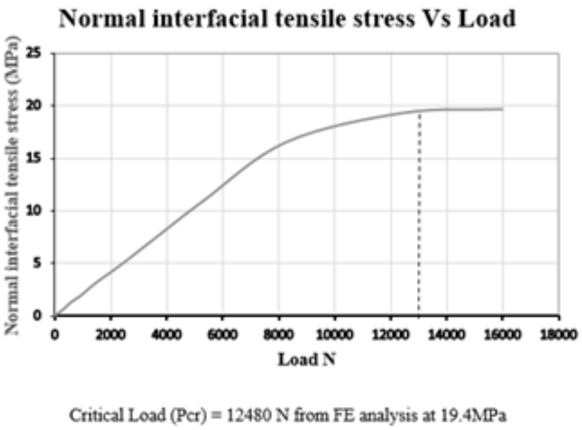


Fig. 6 Normal interfacial tensile stress in the adhesive layer

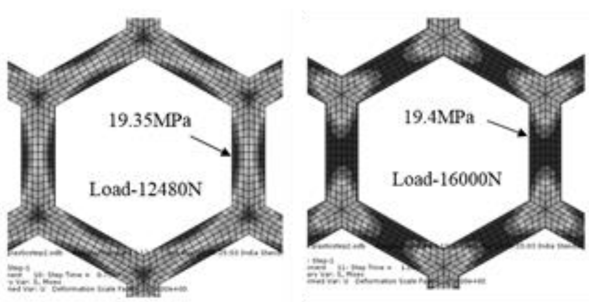


Fig. 7 Nonlinear effect on the adhesive layer

Nonlinear analysis prediction on the failure load is 12.5kN which corresponds to an FWT value of 7.8MPa while the test data on FWT is 6.7MPa.

Present study proposes an assumption that for a nearly constant nonlinear stress in the adhesive layer, critical failure can be obtained from FE analysis corresponding to the minimum strain.

## References

[1] S. Jose, R. Ramesh Kumar, G. Venkateswara Rao and P. Sriram, Studies on Mixed Mode Interlaminar Fracture Toughness of M55J/M18 Carbon/Epoxy Laminates, Advanced Composites Letters, Vol. 9(5), p.335, 2000.

[2] K.C. Gopalakrishnan, R. Ramesh Kumar, “Failure assessment of CFRP skinned honeycomb sandwich beam with delamination using cohesive zone model”, International Journal of Engineering Research and Applications, 1(3), 1040-1050,2011.

[3] K.C.Gopalakrishnan, R.Ramesh Kumar and S.Anil Lal , “Cohesive zone modelling of coupled buckling - debond growth in metallic honeycomb sandwich structure”, Journal of Sandwich structures and Materials, 14 (6), 679-693,2012.

[4] Ramesh Kumar R, Praveen K S and Venkateswara Rao (2003), “Assessment of Delamination Fracture Load of Stringer Stiffened Composite Panel”, AIAA Journal, 3: 551- 553

[5] ASTM Standard Test Method for Flat wise Tensile Strength of Sandwich construction C297/C297M-2004.

# Study of SiC Reinforced Functionally Graded Hyper-Eutectic Aluminium Composites

E. Jayakumar[#1], U. Manjunath Maiya[*2], S. RamakrishnaVikas[*], T.P.D. Rajan[#4],B.C. Pai [#] and Nagaraja[*]

[#] *CSIR- National Institute for Interdisciplinary Science and Technology,*
*Thiruvananthapuram, Kerala , India.*
[1] ejkumar@yahoo.com
[4] tpdrajan@rediffmail.com

[*] *Department of Mechanical and Manufacturing Engineering,*
*Manipal Institute of Technology, Manipal, India.*
[2]manjunath.maiya@gmail.com

***Abstract*— Functionally graded materials (FGM) are advanced class of inhomogeneous engineering materials with location specific properties, used economically and effectively in specific engineering applications. In functionally graded metal matrix composites (FGMMC) the variation of volume fraction of reinforcement leads to a continuously changing properties and a tailored microstructure. Liquid metal stir casting followed by the centrifugal casting was used for the production of A390 FGM composites. Silicon carbide particles (SiCp), of 23 m average particle size, and 10 wt% are used as ex-situ reinforcements. Higher density, ex-situ SiCp, diffuses towards the outer periphery of the FGM ring and in-situ primary silicon particles diffuses towards the inner periphery, giving a dual graded structure. While the less dense porosities, impurities and agglomerates accumulate towards the innermost periphery and they can be removed during machining. The mechanical characterisations are conducted in particle rich, transition and matrix rich regions. The microscopic image analysis at powder rich region shows a 64 % volume of SiCp. It is also found that the outer and the inner regions have better hardness, wear resistance and tensile properties compared to the transition region due to the high reinforcement concentrations.**

***Keywords*— Functionally Graded Material, A390, Silicon Carbide, Metal Matrix Composite, Centrifugal Casting, dual graded structure**

## I. INTRODUCTION

Metal matrix composites (MMCs) are widely used in transportation and infrastructure industries due to their better high specific modulus, strength and wear resistance properties over the conventional materials. Aluminum matrix composites (AMCs) possess higher wear resistance compared to aluminium alloys and are preferred over monolithic metals or alloys in specialized applications [1]. The properties of MMCs can be largely varied over a span by an appropriate selection of matrix, reinforcements, their volume fraction, morphology and distribution [2]. By a compositional gradient of one component to another along a certain direction, FGM's have the ability to obtain two conflicting properties in a single component enables its functionally specific applications economically [3]. Centrifugal casting is an economical and facile technique successfully utilized for processing FGMs among various available techniques [4]-[6]. Liquid stir casting method was used for MMC preparation. Then the FGM rings were produced by pouring the MMC melt into the rotating mould fitted to a vertical centrifugal casting machine. During the solidification, different regions were formed, depending on the density of reinforcement particles, matrix phases, melt temperature, metal viscosity, particle size, cooling rate and magnitude of centrifugal acceleration [7], [8]. The centrifugal force causes to position the lighter phases and particles towards the axis of rotation and the denser away from the axis of rotation. The different zones observed are namely; outer surface chilled zone, particle rich, transition and particle depleted/matrix rich zones. The size of different zones and its gradation inside the component depends mainly on the densities of the particle and matrix.

## II. MATERIALS AND METHODS

The A390, hyper eutectic cast aluminium alloy, was used for FGMMC preparation and its composition is given in the Table I. SiC particles of average particle size of 23 µm were used as reinforcements. SiCp properties along with alloy properties were listed in Table II. Before adding the SiC particles were cleaned, dried and preheated to 600°C for 3 hours.

For improving the wettability of SiC with alloy, before the addition, 1% Mg was added to the melt while the casting. The uniform addition of particles to a steady liquid vortex was done to ensure proper mixing and consistency of the MMC melt. Sufficient mechanical and hand stirring were also done before pouring. The melt at 760 °C is poured into metal mould, coated and preheated to 350 °C, which was rotating, at 1300 rpm, in vertical centrifugal casting machine.

Standard specimens are cut for mechanical characterisation. The standard T6 heat treatment procedures, solution treatment at 495 °C for 8 hours, quenching in warm water and artificially aging at 175 °C for 8 hours, were used for A390 FGMMC specimens. Alloy chemical compositions were found out by SPECTRO MAXX Optical Emission spectrometer. The DMRX Leica optical microscope was used to take microstructure. The volume fraction of the silicon carbide particles was measured by the Leica Qwin image analyser. The INDENTEC hardness tester was used for Brinell hardness measurements from the outer to the inner periphery of the specimens in both as-cast and heat treated conditions. Dry linear wear analyses were carried out in a DUCOM pin-on-disc tribometer.

TABLE I: COMPOSITION OF A390 ALLOY.

| Alloy details | Major alloying elements in percentages | | | | Minor alloying elements in percentages | | | Al in % |
|---|---|---|---|---|---|---|---|---|
| | Si | Mg | Cu | Fe | Zn | Mn | Ni | Al |
| A390 Standard | 16.0 to 18.0 | 0.45 to 0.65 | 4.0 to 5.0 | 1.3 | 0.1 | 0.10 | 0.10 | Bal. |
| A390 Ingot | 18.0 | 0.31 | 4.0 | 0.4 | 0.05 | 0.06 | 0.1 | 77.07 |

TABLE II : STANDARD PROPERTIES OF A390 ALLOY AND $SiC_P$

| Property | A 390 alloy | $SiC_P$ Particles |
|---|---|---|
| Density g/cm$^3$ | 2.73 | 3.2 |
| Melting Point °C | 650 (Approx.) | 2300 |
| Elastic Modulus GPa | 81.3 | 480 |
| Tensile Strength (T6 condition ) MPa | 320 | 250 |
| Percent Elongation % | 1 | Less than 1 |
| Hardness (T6 condition ) BHN | 120 | 120 |

Wear surface morphology was taken by Zeiss stereo microscope. INSTRON 1195 – 5500R series tensile tester was used for tensile testings of the heat treated specimens taken from inner and outer zones of the cast.

## III. RESULTS AND DISCUSSION

Figure 1 shows the microstructure of A390 alloy centrifugally cast ring without SiC addition. The micrographs were taken from the inner periphery to outer zones in a radial direction. Since, there were significant volume percentage of Si and Cu in the alloy, the volume of different phases formed were more and an effective diffusions were visible in the microstructure. It was observed that the grain size at the outer periphery was smaller in size than that of inner periphery. This was due to the pressure force generated, during the centrifugal casting process , by the molten melt which comes in contact with solidification edge. The solidification edge moves from the mould outer periphery towards inner regions, while the pressure force acts from inner to outer in an opposing radial direction producing a squeeze effect. In the inner regions more primary silicon phases of less density are concentrated due to the centrifugal effect and coarse matrix grains are found with copper and silicon aluminum eutectic phases.

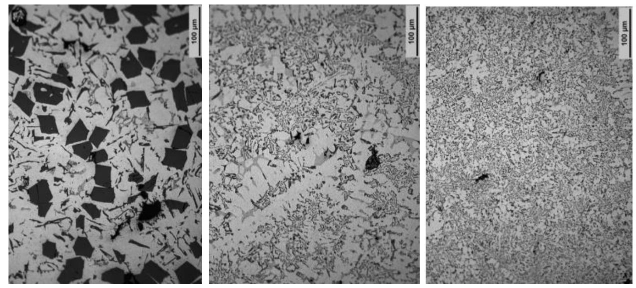

(a) (b) (c)

Figure 1: The micrographs of A390 alloy centrifugally cast ring taken from the inner periphery to the outer zones in a radial direction. (a) at inner ,(b)at Transition,(c) at outer zones.

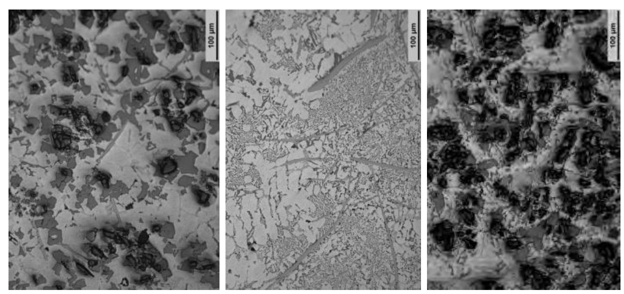

(a) (b) (c)

Figure 2: The micrographs of the A390-10 SiC FGMMC ring are taken from the inner periphery to the outer zones in a radial direction. (a) at inner, (b) at Transition, (c) at outer zones.

Figure 2 shows the graded distribution of SiC particles in A390-10 wt% SiC FGMMC ring at three specified regions, namely particle rich outer periphery, transition and matrix rich inner periphery respectively. The outer periphery of the casting shows a higher concentration of SiC particles than the inner and a clear transition region in between was also visible. The microstructural features of the matrix alloy also vary from outer to inner periphery. The grain size of the aluminium in particle enriched zone is very fine, which becomes coarser towards the interior. The presence of high volume fraction of SiC particles inhibits growth of primary aluminum and also the shear caused by movement of ceramic particles during solidification break the arms of dendrites to form fine structure [9].

The image analysis results depicted in Figure 3 shows that the outer periphery of 10 % SiC FGMMC ring contains a maximum of 64 vol. % SiCp followed by a gradual reduction to lower levels towards the inner periphery. In the transition zone, between 10 mm and 20 mm away from outer

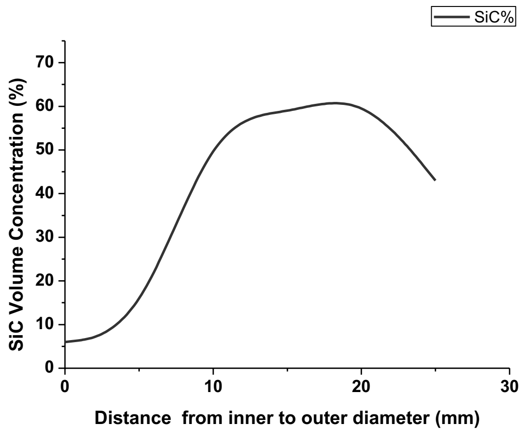


Figure 3: The volume fraction of the silicon carbide particles in A390-10 % SiC FGMMC ring from inner to outer periphery of the casting.

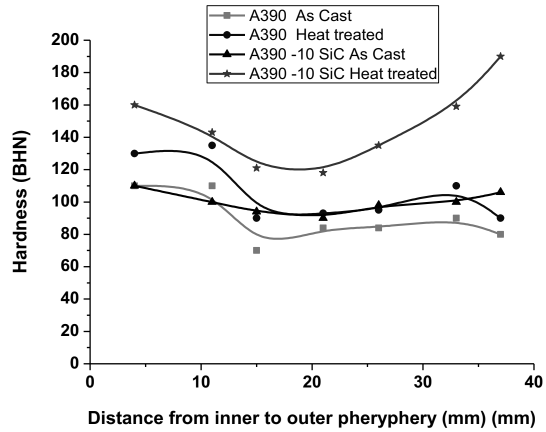


Figure 4: Brinell hardness values for the as-cast and T6 heat treated samples from inner to outer periphery of the FGM rings.

periphery, the reduction SiC volume percentage were steep and reaches a value below 10 vol. % near the inner periphery. In the inner regions more primary silicon phases were concentrated in coarse matrix grains with copper and silicon aluminum eutectic phases rather than SiC particles. The inner most periphery regions of the casting show the presence of gas porosity and few agglomerated particles. The agglomerates constituting partially wetted or non- wetted particles or both and gases having a lower overall density that were pushed towards the inner periphery by the centrifugal force. These can be easily removed from components while machining.

The variations of the Brinell hardness values in the as-cast and T6 heat treated samples from inner to outer zones of A390 FGM and A390-10 SiC FGMMC rings were shown in Figure 4. The curves clearly depicts that the hardness value varies in proportion to the volume fraction of the primary Si phase in both as cast and heat treated conditions for the A390 FGM ring. And the hardness value varies in proportion to the total volume fraction of Si phase and SiC particles in both as cast and heat treated conditions for the A390-10 SiC FGMMC ring. It was also found that the heat treated ones have far better hardness than that of as-cast ones. In A390 FGM ring the maximum hardness was observed in the inner regions due to the presence of primary silicon phases and a hardness of 110 BHN in the as cast condition was raised to 135 BHN after heat treatment. From the transition zone towards outer zone the hardness value slowly increases from a lower value to moderate and reaches a maximum then decreases towards the extreme outer periphery. This was due to the combined effect of grain refinement in the outer zones and the lesser presence of primary silicon phase in these regions.

The maximum hardness value in the particle rich zone was 106 BHN for 10% SiC FGMMC in as cast condition and raised to 190 BHN after the heat treatment. In the transition region the hardness value changes between 90-98 BHN in as-cast and 118-135 BHN in heat treated for 10% SiC FGMMC and the region of 15 to 25 mm away from the inner towards outer periphery. The region near the inner periphery shows high hardness of 160 BHN due to the presence primary silicon phases after heat treatment.

TABLE III
TENSILE TESTING FOR HEAT TREATED SAMPLES TAKEN FROM DIFFERENT LOCATIONS OF FGM CASTINGS

| Specimen Description | Tensile Test | |
|---|---|---|
| | UTS ( MPa ) | Yield strength (MPa) |
| A 390 FGM Outer | 295 | 178 |
| A 390 FGM Inner | 308 | 172 |
| A390-10SiC FGMMC Outer | 387 | 176 |
| A390-10SiC FGMMC Inner | 273 | 180 |

The ultimate tensile strength (UTS) value of 295 MPa and yield strength value of 178 MPa were obtained for the A390 FGM at the outer periphery. And for inner the values were 308 MPa and 172 MPa respectively. The higher values at the outer periphery are due to finer grain size and that at the inner are due to the large concentration of primary silicon. The UTS and yield strength values of A390-10%SiC FGMMC at outer were 387 MPa and 176 MPa and in inner periphery 273 MPa and 180 MPa respectively. All yield strength values and UTS values of A390 FGM and FGMMC, at inner and outer periphery, are comparable except the UTS value of A390-10 SiC FGMMC outer. This was due to the presence of high volume fraction of SiC.

The dry pin on disc wear tests were conducted with pins, of diameter 6mm and 30mm long, from inner and outer regions of A390 FGM. The test were conducted for inner, outer and transition regions of FGMMC castings. Figure 5 shows the wear rate versus load as a function of weight loss per metre. For A390 alloy the wear rate at outer periphery was higher when compared to the inner periphery, which was due to absence of primary silicon at the outer periphery and due to the fine grain size of aluminium. At the inner periphery wear was less due the presence of primary silicon phase and coarser grain size. At increased loads, the wear rate increases by a large amount.

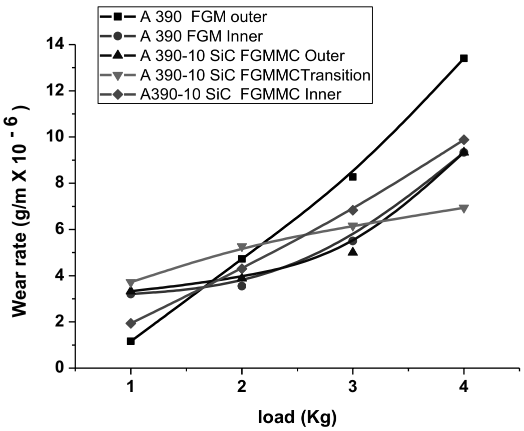


Figure 5: wear rate vs. load as a function of weight loss per meter for FGM alloy inner, outer pins, A390-10 SiC FGMMC inner, transition and outer heat treated pins.

A390-10% SiC FGMMC the wear rate at the outer periphery and the wear rate at the inner periphery of the A390 FGM ring was similar. The former was due to the presence of high volume fraction of SiC particles at the outer periphery, leading to higher wear resistance and the latter was due to the presence of high volume fraction of primary silicon in the inner of the FGM ring. In the transition region, lesser concentrations of primary silicon phases and SiC particles lowers the wear resistance causing more wear loss.

Figure 6 shows the coefficient of friction (μ) values as a function of loading. The frictional value increases as the load increases showing that the lesser wear resistance at higher loads for A390 FGM outer and A390-10 SiC FGMMC Transition heat treated wear pin samples. The microstructures taken from the respective regions clearly show that there were only aluminum matrix phase present in the region and neither primary silicon phase nor SiC particles present to protect matrix from more wear. The COF value fluctuates over the time period for the load applied due to the heterogeneous nature of the FGM. While the test was being carried out for A390-10SiC FGMMC outer more SiC

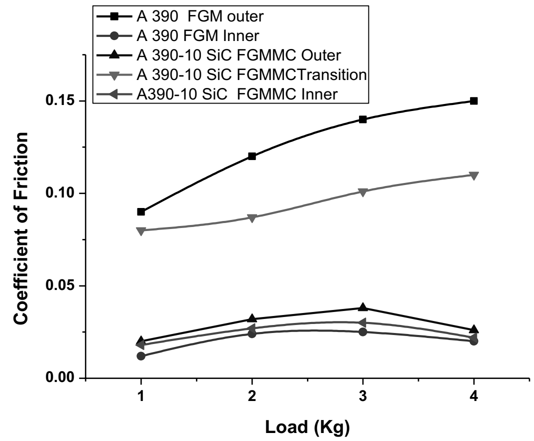


Figure 6 shows the coefficient of friction (μ) values as a function of loading for FGM alloy inner, outer pins, A390-10 SiC FGMMC inner, transition and outer heat treated pins.

particles were exposed to the disc, then both the wear and coefficient of friction will be less. For both A390 FGM inner and A390-10SiC FGMMC inner instead of SiC particles more and more primary Si phase will expose to the disc and will in turn reduce wear and friction. Even though the general trend was as the load applied increases the COF value will also increase due to the increase in resistance to the relative motion. The COF value dependent on the frictional force, which varies with the operating temperature, in the dry sliding test, as the temperature of the pin and disc increase substantially which in turn decreases the wear resistance of the pin and thus changing the value of the coefficient of friction.

Figure 7 shows the stereo micrographs of the surface morphology of the wear specimens at different loads. From stereo micrographs it was clear that for all specimens even at the maximum load of 4 kg only wear scratches were visible, indicating that the mild abrasive wear mechanism was responsible for the wear loss. At 1kg load the wear scars were fine and evenly spaced. As load increases more coarse deep scars were found in the specimens.

The weak interface bond between silicon particle and aluminium matrix at higher load and enhanced interface temperature is the main reason for the change in composite wear property under varying applied loads.The coarse wear scars at higher loads showing larger wear. It was seen that in A390- 10 % SiC FGMMC inner and outer pins the wear scars at all the load are fine indicating less wear due to the presence of reinforcement particles. The ex-situ added SiC and in-situ formed primary Si particles are very hard and do not wear off easily and quickly, thus imparting higher wear resistance to the component. Si particles were present in the inner pins causing similar wear rate with that of particle rich outer zone pins..

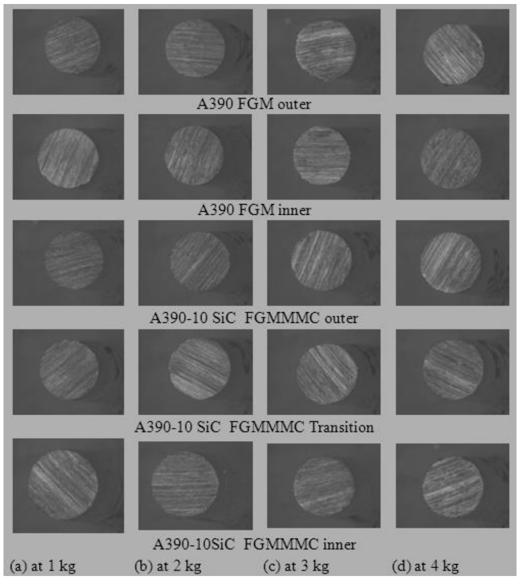


Figure 7. Stereo micrographs of the surface morphology of the wear specimens at different loads

## IV. Conclusions

A390 - 10 SiC FGMMC with 10 wt % SiCp particles, 23µm size, was successfully processed by the centrifugal casting. The functional gradation of SiCp particle distribution from outer to inner was revealed by the microstructure evaluation and image analysis. The hardness of different regions were largely depends upon the concentrations of SiC particles and primary silicon. The SiC rich outer zone and the Si rich inner region show lesser wear rate in comparison with the transition region. The variation of wear rate with respect to applied load is linear. The addition of SiC particle and heat treatment provide comparable improvements in the wear resistance. Also by the distribution of primary silicon phase in the A390 alloy by centrifugal force the wear and structural property can be effectively tailored. The study clearly depicts that the gradient nature of the structure and properties of the FGM rings can be controlled by particle addition as well as by phase distributions.

## Acknowledgment

The authors are grateful to the Director and Members of MSTD, CSIR-NIIST, Trivandrum for their support and help.

## References

[1] D. B. Miracle, "Metal matrix composites - From science to technological significance," Composites Science and Technology, vol. 65, no. 15-16, pp. 2526-2540, 2005.

[2] A. Mortenson and S. Suresh, "Functionally graded metals and metal-ceramic composites: Part 1 Processing," International Materials Reviews, vol. 40, no. 06, pp. 239-265, 1995.

[3] T. P. D. Rajan, R. M. Pillai and B. C. Pai, Indian Foundary Journal, vol. 49, no. 9, pp. 19-30, 2003.

[4] R. Rodriguez-Castro, R. C. Wetherhold and M. H. Kelestemur, "Microstructure and mechanical behavior of functionally graded Al A359/SiCp composite," Materials Science and Engineering: A, vol. 323, no. 1-2, pp. 445-456, 2002.

[5] Y. Watanabe, A. Kawamoto and K. Matsuda, "Particle size distributions in functionally graded materials fabricated by the centrifugal solid-particle method," Composites Science and Technology, vol. 62, no. 6, pp. 881-888, 2002.

[6] A. Halvaee and A. Talebi, "Effect of process variables on microstructure and segregation in centrifugal casting of C92200 alloy," Journal of Materials Processing Technology, vol. 118, no. 1-3, pp. 122-126, 2001.

[7] P. S. Robi, B. C. Pai, K. G. Satyanarayana, S. G. K. Pillai and P. P. Rao, "The role of surface treatments and magnesium additions on the dispersoid/matrix interface in cast Al-Si-Mg-15 wt.% SiCp composites," Materials Characterization, vol. 27, no. 1, pp. 11-18, 1991.

[8] J. Hashim, L. Looney and M. S. J. Hashmi, "The enhancement of wettability of SiC particles in cast aluminium matrix composites," Journal of Materials Processing Technology, vol. CXIX, no. 1-3, pp. 329-335, 2001.

[9] P. Rohatgi and R. Asthana, "The solidification of metal-matrix particulate composites," The Journal of the Minerals, Metals & Materials Society, vol. 43, no. 5, pp. 35-41, 1991.

# Numerical Study on the Effect of Supersonic Jet Impingement on Inclined Plate

Sarath.S.U[*1], Khalid Rashid[2], Deepak Kumar Agarwal[#3] and J.C.Pisharady[#4]

[*] *Mohamed Sathak A.J.College of Engineering, Chennai, Tamilnadu, India*

[1] sarathsu1990@gmail.com

[#] *Liquid Propulsion Systems Centre, I.S.R.O., Thiruvananthapuram, Kerala, India*

*Abstract* — **Supersonic impingement of plume over flat surface is characterized by complex flow phenomenon near the impingement surface. Flow structures created by the supersonic jets over the plates are often characterized by shock interactions, flow reversal, deflection and recirculation zones which strongly depend on the inclination of the plate with respect to plume axis. Also heat flux, pressure and temperature distribution over the plate varies with location of the plate with respect to the impinging jet. A detailed numerical (CFD) study is carried out to understand the flow behavior of supersonic jet impinging on flat plate.**

**Simulations are carried out for flow over a flat plate kept in front of a conical nozzle to obtain the plume characteristics. The simulation methodology used in the study is first validated with the published literature. Subsequently, detailed parametric study for the under-expanded supersonic jet impingement on a flat plate is carried out by varying the plate location and inclination of the plate. Impingement plate angle (θ) is varied between 0° & 60° and the nozzle-plate distance is varied in terms of non-dimensional parameters, i.e. L/D ratio in the axial direction and Y/D ratio in the radial direction, which ranges from 4 to 8 and 2 to 4 respectively. Extensive study of the flow impingement on the plate carried out. Study shows higher heat flux for the plate at 0° inclination which correspond to perpendicular to the nozzle axis. The impingement heat flux increases as the plate distance increases from the nozzle exit due to under expended plume.**

*Keywords*— **Jet impingement, Inclined plate, Heat flux, Computational fluid dynamics, Static temperature**

## I. Introduction

The problem of jet impingement in aerospace applications appears in the design of jet deflector, multistage rocket separation at higher attitude, rocket test-stand environment, and plume ducting system of canisterised missiles, space module attitude-control thrusters operation, and rocket plume impingement on spacecraft solar panels, among others. In this work main focus is given to impingement on flat plate surface.

Most of the former studies on jet impingement on a flat plate are concerned with the perpendicular impingement. By these studies, existence of stagnation bubbles came to be recognized as an important phenomenon. A stagnation bubble is a recirculation area that appears in the vicinity of the plate surface, affecting the pressure peaks on the plate surface and the stability of the jet. Such flow field contains many complex fluid dynamics phenomena. Flow structure created by the supersonic jets over the plates is often characterized by shock interactions, flow reversal, recirculating zones, nozzle-plate distance and strongly depends on the inclination of the plate. Empirically, it is known that local pressure and temperature peaks appear under certain conditions, and therefore analysis of the flow fields is important both from physical and engineering viewpoints. Inclined jet impingement exhibits more complex features than the perpendicular jet impingement. The maximum pressure on the inclined plate can be several times larger than that on the perpendicular plate because of the complex shock-shock interactions. Moreover, the stagnation bubble may disappear when the plate angle increases. Indeed, it is a great challenge to understand the physics of these flows and correctly predict the heat and pressure loads on the impingement plate.

The aim of the present work is to study the heat flux and temperature distribution over a flat plate. Numerical study for the under-expanded supersonic jet impingement on a flat plate is carried out by varying the plate location and inclination of the plate. Impingement plate angle (θ) is varied between 0º to 60º. Position of the Plate is varied in terms of non-dimensional parameters, i.e. L/D and Y/D ratios. L/D is the ratio of nozzle exit diameter to distance between nozzle exit and impingement plate in axial direction. Y/D is the ratio of nozzle exit diameter to distance between nozzle exit and impingement plate in radial direction. Extensive study of the flow impingement on the plate carried out. CFD analysis carried out using ANSYS FLUENT®.

## II. Simulation Methodology

For the complex nature of the supersonic jet impingement study, 2D and 3D computational simulation of the flow field is necessary, which may be either developing a code or by using conventional code. In the present study computation has been made to obtain the impinging flow using conventional software ANSYS FLUENT®.

### A. Validation Study

A validation study is carried out for the current numerical simulation and information from the existing works in this regards were used. For validation, model from [8] is simulated for the jet impinging on a vertical plate with the same boundary conditions given in the paper. The grid was made on the body with the given conditions reported on the journal. Fig. 1 shows the Mach number contour and time averaged surface pressure plots. From the above validation study it is evident that the impinging jet undergoes shock interaction with the flat plate surface. This leads to the creation of intermittent peak pressure regions along the length of the plate. The generated grid was used to obtain k-ε solution for axisymmetric case. For validation, simulation showed reasonably good result which is comparable to the value referred in [8].

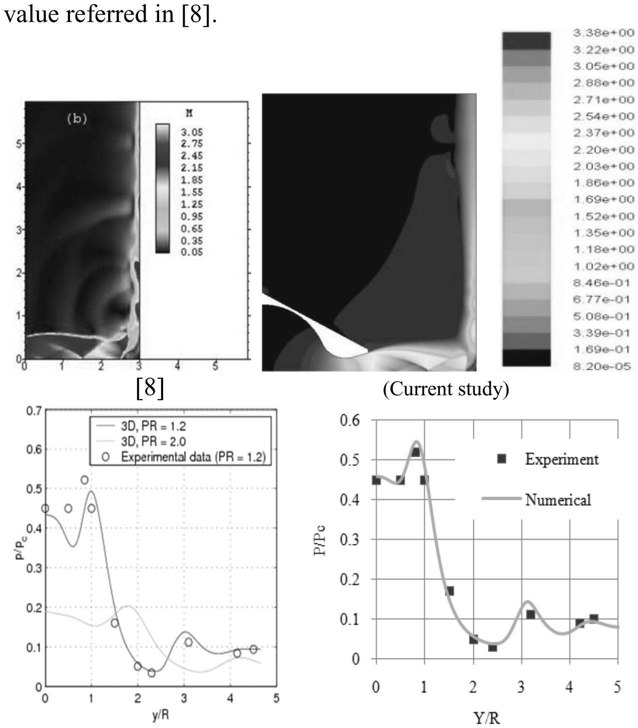


Fig. 1 Mach contours for PR = 1.2(top) and Time averaged surface pressure on the plate (bottom)

Further computation was made with vertical impinging flat plates. The results were not satisfactory indicating that k-ε computation is not suitable. Hence computation has been made with different turbulence models available in FLUENT i.e. k-Ɛ, k-ω and S-A. Finally k-ω SST model found to be more suitable for present work. The shear-stress transport (SST) k-ω model was developed to effectively blend the robust and accurate formulation of the k-ω model in the near-wall region with the free stream independence of the k-ω model in the far field.

## B. Computational Domain, Boundary and Initial Conditions

For the present work flow domain created using ANSYS GEOMETRY consists of different parts, which grouped into one part for meshing. With the knowledge of the grid generation on the validation part was imported for the grid generation for the actual cases. Based on the grid independence study and validation study 2-D and 3-D grids were created for vertical and inclined impingement plates respectively. Simulations are carried out to find peak heat flux changes with varying L/D and Y/D values (Table. 1 shows different L/D and Y/D values). For grid generation extensive use of edge sizing is employed. This is because; in some regions a finer mesh is needed for capturing the results. The grid generation for current work is carried out in two faces. In first face 2-D structured grid generation for vertical plate studies are carried out by using axisymmetric geometries and in the second face 3-D structured grids were created with symmetric geometries. After considering various factors the domain for 2-D studies was extended 20 times of the nozzle exit diameter in the axial direction and 15 times in the radial direction. For 3-D studies this was taken in the order of 12 times in axial and 10 times in the radial directions. Plate length is taken as 240 mm. A conical nozzle is used for the impinging jet source (inlet, throat and exit diameter are 20 mm, 4.7914 mm and 48 mm respectively). Fig. 2 shows the grid generated for computations.

TABLE I
DIFFERENT L/D AND Y/D VALUES

| Plate length (mm) | L/D | Y/D | | |
|---|---|---|---|---|
| 240 | 4 | 2 | 3 | 4 |
| 240 | 5 | 2 | 3 | 4 |
| 240 | 6 | 2 | 3 | 4 |
| 240 | 8 | 2 | 3 | 4 |

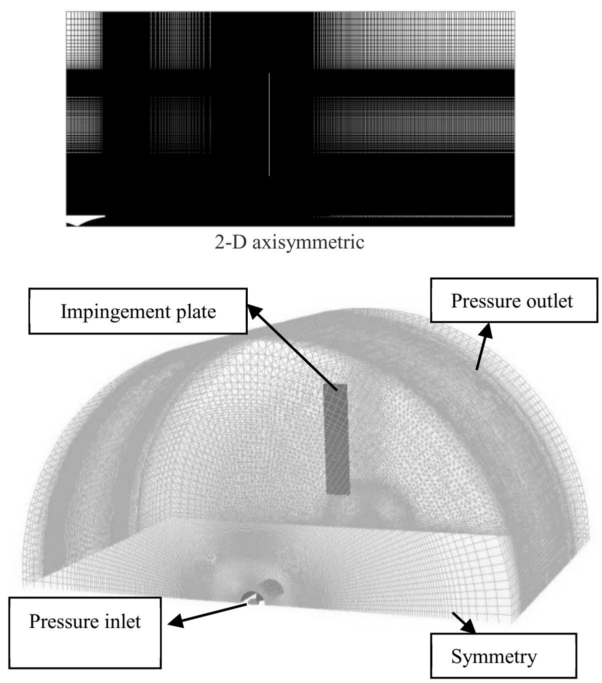


Fig. 2 Grid generated for 2-D (top) and 3-D (bottom) domains

4) *Initial Conditions:* Input parameters given are $P_c$ = 6.75 bar and $T_c$ = 3028.7 K. Outlet pressure is kept at 10 Pa for attaining the required simulation condition. The turbulence

intensity of 5% and viscosity ratio of 5 were fixed for all computations of present work. Plate temperature kept at 300 K. Gas properties like density, specific heat, thermal conductivity and viscosity plays vital role in flow simulation. For the present case, ideal gas condition was used. Since the flow considered here is depend on temperature, piecewise-linear input for specific heat, thermal conductivity and viscosity have been used as the values changes with temperature at different point in the flow field and these values are been taken from the NASA-CEA software.

## III. Results and Discussion

### *A. Plume Expansion Structure*

Understanding the plume expansion structure is important for an impinging flow study. For the current work the plume expansion structure is numerically simulated for a given set of inlet and outlet. Fig. 3 (a-b) shows the plate positions with varying L/D and different Y/D values.

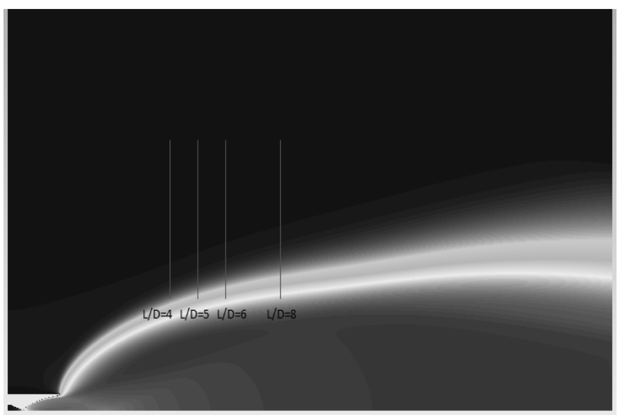


(a)

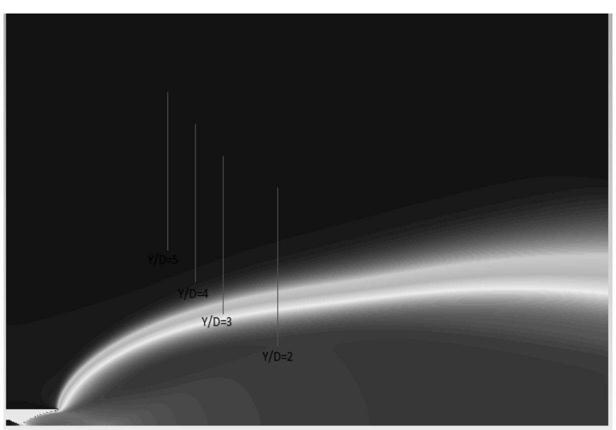


(b)

Fig.3 (a) Plume structure for different plate positions in the axial direction
(b) Plume structure for different plate positions in the radial direction

### *B. Effect on Heat Flux at Different Plate Positions (2-D Vertical Plate)*

From the plume expansion structure study it is understandable that as the position of the plat (steel plate) changes the area of exposure to the plume also change. By keeping this in mind different domains are created to analyse the change in Heat flux. The position of the plate is changed both in axial and radial directions. The change in axial distance is raging from L/D 4 to 8. The impingement plate position is changed in radial distance ranging from Y/D 2 to 4.

*1) Effect of Different L/D and Y/D Values:* From the numerical analysis following details were obtained. The results are for L/D = 4, 5, 6, 8 and Y/D = 2, 3, 4. Fig. 4 shows static temperature contour for 2-D axisymmetric cases.

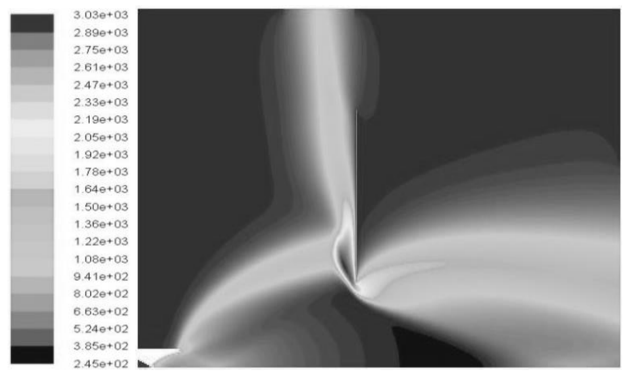


(a)

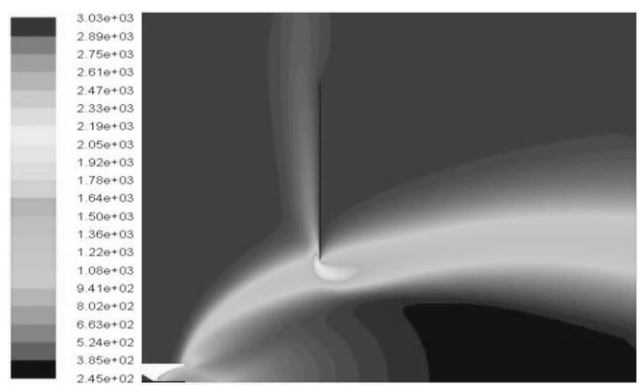


(b)

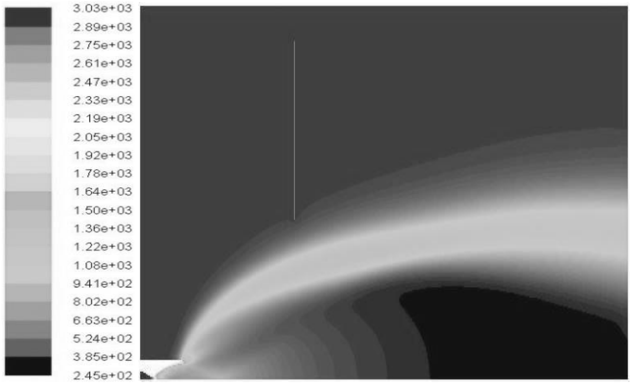


(c)

Fig. 4 Static Temperature contour for (a) L/D=8 Y/D=2 (b) L/D=6 Y/D=3 (c) L/D=5 Y/D=4

The following graphs are created by combing heat flux plot for various cases

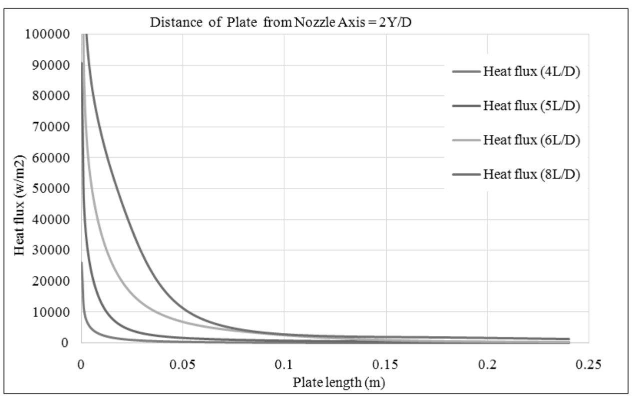


(a)

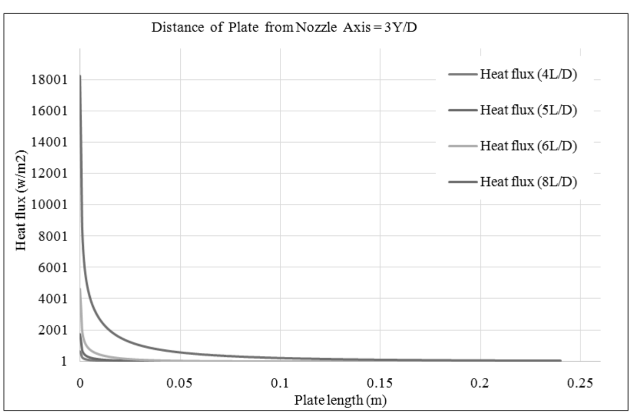


(b)

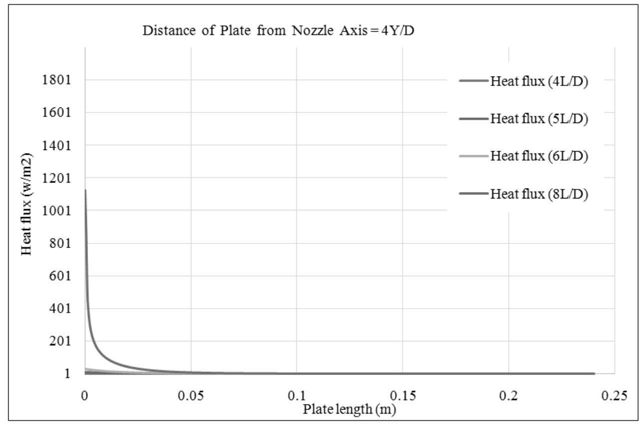


(c)

Fig. 5 Heat flux plot for different L/D at (a) 2 Y/D (b) 3 Y/D (c) 4 Y/D

From the above results it is evident that heat flux along the impingement plate is changing in each cases. From Fig.5 (a, b, c) we can understand that the heat flux is increasing when the distance between nozzle exit to impingement plate position,ie, L/D values increase from 4 to 8. Considering the increse in radial distance of the plate from nozzle axis, ie, increase in Y/D value from 2 to 4, follows a decrease in heat flux. This is happening because of the expansion of plume, ie, as the L/D value increases and vertical distance between the nozzle axis to plate decreases, the plate gets more exposed to the plume. This cause an increase in total heat flux over the impingement plates which are more exposed to the core flow region. To understand the changing heat flux along the impingement plate, heat flux values on a particular point (a point at 20 mm from bottom of the 240 mm plate) on the plate is ploted in Fig. 6 for better understanding.

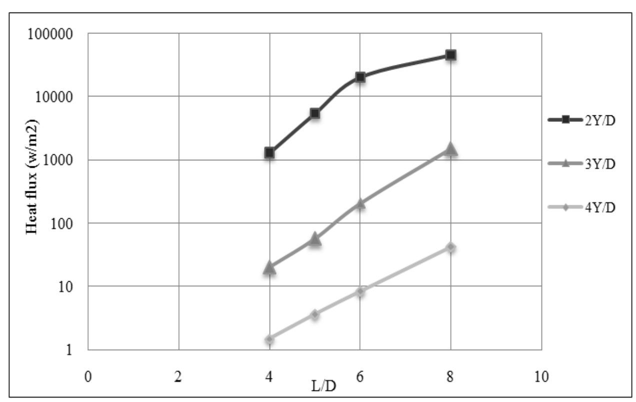


Fig. 6 Increase in heat flux

*C. Effect on Heat Flux due to Inclination of Flat Plate (3-D Domain)*

In the present work four different cases were analysed. The inclination angle 'θ' changed from 0º to 60º. For the analysis the domain around the plate is kept same, only the angle of flat plate were varied. The boundary conditions, solver settings and other parameters were kept same as in the 2-dimensional vertical plate study. The domain used here is extended twelve times in the axial direction and ten times in the vertical direction of the nozzle exit diameter. The grid around the plat contains tetrahedral element mesh where as other parts are generated with a hexahedral element mesh. The 3-dimensional domain contains approximately 5 million elements. Computational time needed for attaining acceptable convergence is high in this case. Around 3,500 iterations were carried out for each analysis which took around 12 hours with a parallel run on 8 core workstation.

Jet impingement on inclined flat plate shows the presence of recirculation zones near the impingement plate. The size and position of the recirculation zone is changing for each θ value.

Static temperature contour for various plate angles (θ) are shown in the Fig. 7. Presence of recirculation zones near the plates can affect the heat flux by creating a convective cooling effect. To understand the flow pattern near impingement plate, velocity vector for each case are shown in Fig. 8. Fig. 9 shows heat flux plot for various 'θ' values.

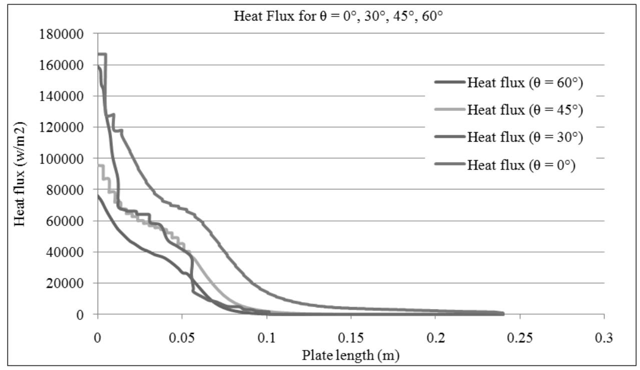


Fig. 9 Heat flux plot for various 'θ' values.

From the above heat flux plot it is evident that Heat flux along the impingement plate is decreasing as the plate inclination angle 'θ' changes from 0º, 30º, 45º and 60º respectively. Here the inclination angle 'θ' is changed in anticlockwise direction. As the plate inclination angle changes from 0° to 60°, plume exposed area on the impingement plate increases. This causes a decrease in heat flux, i.e., as the heat content of the plume remains same but exposed area is increasing, thus heat energy per unit area is decreasing.

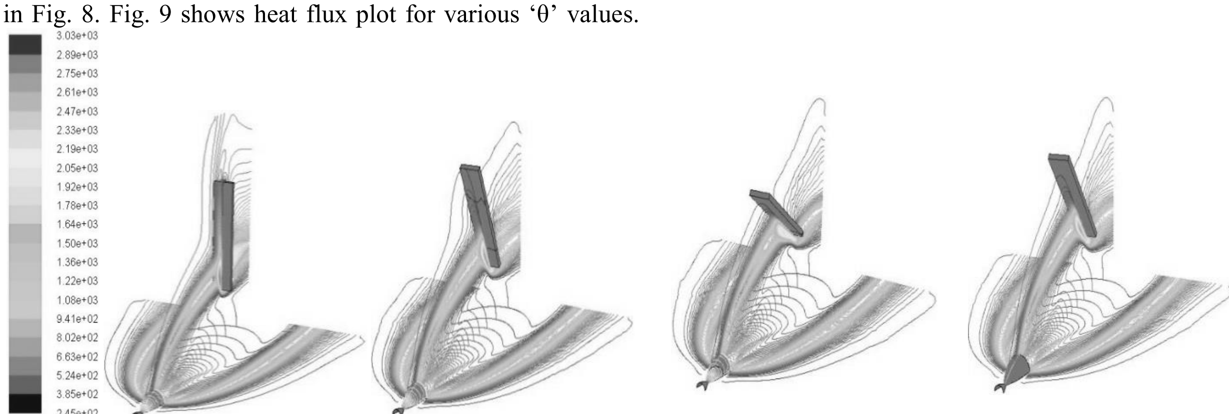


θ =45° θ =60$^0$

θ =0° θ =30°

Fig. 7 Static temperature contour

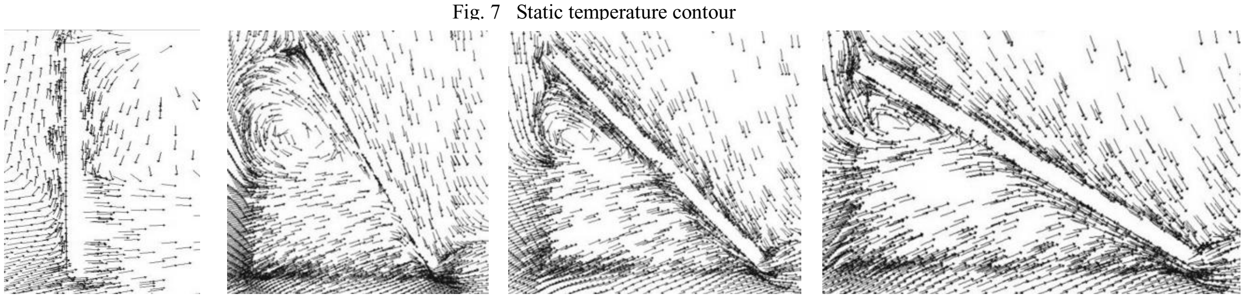

θ =0° θ =30° θ =45° θ =60°

Fig. 8 Velocity vector near the plate

*1) Plate Inclination Angle θ = 30°:* The recirculation zone is large in size and positioned near the upper middle region of the impinging plate. Recirculation zone will produce a convective cooling that will cause a drop in temperature in region where it is forming. Presence of large recirculation zone causes a temperature drop which eventually causes a drop in heat flux on the plate surface. Static temperature in recirculation zone for plate angle 30° is in between 362 K - 390 K whereas at the same point for plate angle 45° a lower temperature in between 445 K - 473 K is getting. This is the reason behind the sudden drop in heat flux on plate surface with 30°inclination.

*2) Plate Inclination Angle θ = 45°:* In this case the recirculation zone is small in size as compared to the 30° plate. The position of the recirculation zone shifts to the upper end of the plate. This causes a gradual drop in heat flux on the impingement plate.

*3) Plate Inclination Angle θ = 60°:* Compared to the other two cases recirculation zone formed here is smaller in size and positioned in the upper most region of the impingement plate. Thus the heat flux in this region is not affected as compared to the other two cases.

## IV. CONCLUSIONS

Computational study has been carried out for supersonic jet impingement on a flat plate. The effects of plate location and inclination angle on the heat flux are determined. Computational study includes jet impingement on vertical flat plate as well as inclined flat plate. 2-dimensional axisymmetric and three dimensional simulations using FLUENT® have been performed.

The following important observations are made from the results obtained through present study.

1. Mesh refinement near the impingement plate plays a major role in obtaining the flow features correctly.
2. Twelve different cases are used for 2-dimensional axisymmetric analysis. It was observed that heat flux generated by jet impingement on vertical flat plate depends on position of plate. As plate is moved away from the nozzle exit the area exposed to plume increases. More the plate exposed to impinging jet, higher the impingement heat flux.
3. Effect of plate inclination angle in heat flux is also analysed using 3-dimensional computational domain. Computations were carried out for four cases with different plate inclination angles ‘θ’ (θ = 0°, 30°, 45°, 60°) at L/D = 8 and Y/D = 2. It is noted that, as the plate angle increases, heat flux over the plate is decreasing.
4. Impingement on inclined plates generates a recirculation zone, which changes with the plate inclination angle. This phenomenon affects the heat flux on the plate. Large recirculation zone causes sudden drop in heat flux on the plate.


## ACKNOWLEDGMENT

I would like to mention my gratitude to Mr. Deepak Kumar Agarwal, Deputy Divisional Head, CHTD/TED, LPSC-ISRO, for his guidance and constantly rendered support.

I would like to extend my sincere gratitude to Mr. M.Jumma Khan, Associate Professor, Mohamed Sathak A.J.College of Engineering, Chennai, Tamilnadu, India.


## REFERENCES


[1] Lamont, P. J. and Hunt B. L., “The impingement of underexpanded, axisymmetric, jets on perpendicular and inclined flat plates,” *J. Fluid Mech.,* Vol. 100, Part 3, pp. 471-511, 1980.

[2] Kim, K. and Chang, K., “Three-Dimensional Structure of a Supersonic Jet Impinging on an Inclined Plate*,” Journal of Spacecraft and Rockets,* Vol. 31, No. 5, pp. 778-782, 1994.

[3] Nakai, Y., Fujimatsu, N. and Fujii, K., “Experimental Study of Underexpanded Supersonic Jet Impingement on an Inclined Flat Plate,” *AIAA Journal,* Vol. 44, No. 11, pp. 2691-2699, 2006.

[4] Fujii, K. Oyama, A., Tsuboi, N., Tsukada, M., Ouchi, H. and Hayashi, K., “Flow Field Analysis of Under-expanded Supersonic Jets Impinging on An Inclined Flat Plate –Analysis with PSP/Schlieren Images and CFD Simulations- ,” 2005 ASME Fluids Engineering Division Summer Meeting, FEDSM2005-77226, June 2005.

[5] Kansai McIlroy and Kozo Fujii., “Computational Analysis of Supersonic Under-expanded Jets Impinging on an Inclined Flat Plate” -Part I 37th AIAA Fluid Dynamics Conference and Exhibit AIAA 2007-3859 25 - 28 June 2007, Miami, FL.

[6] Malsur Dharavath and debases Chakraborty, “Numerical simulation of supersonic jet impingement on inclined plate”. *Defence science journal,* Vol.64 no.4, July 2013, pp. 355-362, DOI: 10.14429/DSJ.63.2545.

[7] Kalghatgi G. T. and Hunt B. L., “The Occurrence of Stagnation Bubbles in Supersonic Jet Impingement Flows, ”*Aeronautical Quarterly,* Vol. 26, pp. 169-185, 1976.

[8] Binu Pundirand and Manhar Dhanak., “Surface Pressure Fluctuations Due to an Impinging Supersonic Under expanded Jet”. 48th AIAA Aerospace Sciences Meeting Including the New Horizons Forum and Aerospace Exposition 4 - 7 January 2010, Rolando, Florida AIAA 2010-107.

[9] N. Zuckerman and N. Lior., *“Jet Impingement Heat Transfer: Physics, Correlations, and Numerical Modelling”*-Advances In Heat Transfer Vol. 39.

# Patient-Specific Simulation to Predict Thermal Distribution in Liver Cancer Treatment with RF Hyperthermia

Bibin Prasad[1], Jung Kyung Kim[2]

*Department of Mechanical Engineering, Graduate School, Kookmin University*
*Seoul 02707, Republic of Korea*

[1]bibinprasad@kookmin.ac.kr

[2]jkkim@kookmin.ac.kr

***Abstract*— Hyperthermia is a type of cancer treatment in which body tissue is exposed to higher temperatures to damage and kill cancer cells. Minimally invasive treatment of solid tumours, especially in the human organs, remains clinically challenging; despite a variety of treatment modalities are available. In the present study a non-invasive selective heating of tumour by sparing the normal cells was investigated with experimental and numerical approaches. A cylindrical tissue-mimicking tumour phantom gel was prepared for the selectivity test and a patient-specific simulation on real human anatomy model, which was reconstructed and segmented from computed tomography (CT) image was used to determine the thermal distribution in liver tumour during radiofrequency (RF) heating. An RF electrode at 13.56 MHz frequency was used as the heat source for the experiment and simulations were performed with the aid of the multiphysiscs simulation platform Sim4Life. Experimental results depict the selective heating of the tumour and the same was validated with that of simulations. A high temperature rise was achieved for the liver tumour from the patient-specific simulation which elucidated the high energy absorption of malignant tissue compared to the normal surrounding tissues and thereby regional heating of RF hyperthermia was demonstrated in a real human anatomy. The study also exhibits the effect of power modulation which can pave a way for effective treatment planning for clinical applications.**

***Keywords*— hyperthermia, selective heating, tumour, SAR, temperature, patient-specific simulation**

## I. INTRODUCTION

Hyperthermia is a type of cancer treatment in which body tissue is exposed to higher temperatures, from 39 to 44°C to damage and kill cancer cells. It is almost always used with other forms of cancer therapy, such as radiation therapy and chemotherapy [1]. Several methods of hyperthermia are currently under study, including local, regional, and whole-body hyperthermia. Many clinical trials and research studies are being conducted to evaluate the effectiveness of hyperthermia. However, the selective elevation of tumour cell temperature, while sparing the normal cells during hyperthermia heating, is a long-standing problem in oncology. Minimally invasive treatment of solid tumours, especially in the human organs, remains clinically challenging; despite a variety of treatment modalities are available. Invasive treatment modality has limitations of placing the probe or ultrasonic (US) beam in the target tissue for tumour ablation and monitoring and the treatment is more difficult when the tumour is surrounded by large blood vessels or organs. Non-invasive treatments have benefits such as minimal discomforts and trauma, short recovery time and no incisions.

Computer simulations exposed a new way of art in hyperthermia with theoretical methods for electromagnetic, ultrasound and heat transfer problems for estimating energy deposition and temperature distribution [1-14]. Three-dimensional computer simulation studies with the aid of finite differential time domain (FDTD) method showed deep heating regional hyperthermia by estimating the specific absorption rate (SAR) for prototype applicators and the same technique can be applied for human patient models for treatment planning [3]. For realistic treatment outcome in hyperthermia treatment, numerous computational studies on real human anatomy were performed and several significant findings were found out [1] [4-6]. Of that one was, in RF ablation the conventional single electrode technique requires careful choice of both excitation voltage and treatment time for treatment efficacy [4]. Hyperthermia treatment planning (HTP) becomes a strong optimizing tool in these days and there are many tools and techniques for that, review studies combining all showed that HTP has become an essential tool and plays a pivotal role for control, improvement and assessment of hyperthermia treatment quality [1]. Perfusion, electrical and thermal conductivity are important parameters to consider for effective treatment in hyperthermia and with the use of computational simulation models it was found that optimal combinations of thermal and electrical conductivity can partially negate the effect of perfusion [7]. Even though uncertainties are involved in the numerical simulations, experimental and comparative studies showed that it is possible to use numerical simulations to predict the energy absorption and temperature distribution from radio frequency fields [8].

In the present work, experimental and numerical study on a tissue mimicking tumour tissue and normal tissue phantom gel was conducted for the selective heating of RF hyperthermia and as a real application the study was further expanded to a patient-specific human anatomical model to determine the thermal distribution in the liver tumour and the surrounding organs for effective clinical treatment.

## II. Materials and Methods

### A. Tissue-mimicking Gel Phantom

The materials used for preparing the cylindrical gel phantom mainly include agar power with different concentration of NaCl [4] [8-11] [15]. For the normal gel 5 g agar power with 1 g NaCl and for the tumour gel 5 g agar powder with 3 g NaCl was used, so that phantoms with different dielectric properties can be obtained. A solution was prepared in 100 mL distilled water and then heated in an oven at a temperature of 130-150°C. The boiled sample was then poured into a plastic cylindrical mould and it was allowed to cool down for about 6 hours to solidify the agar gel phantom. The size of the cylindrical phantom was 100 mm height by 50 mm radius and a tumour phantom with a dimension of 30 mm was placed at the centre most part of the normal gel phantom for the experimental purpose.

### B. RF Experiment.

A newly developed RF generator (Union Medical Co., Uijeongbu-si, Gyeonggi-do, Republic of Korea) with an input power of 80 W and frequency of 13.56 MHz [16-20] was used for the experimental purpose. The prepared cylindrical phantom was placed in a water bed with a total size of 530 x 100 x 1190 $mm^3$ and an electrode including a water bolus of size 100 mm was placed at the top of the phantom as shown in Fig. 1(a). Fiber optic sensors were inserted inside the normal phantom and tumour phantom to estimate the temperature rise. After setting all impedance matching was checked in RF generator and the experiment was carried out for a time interval of 60 min.

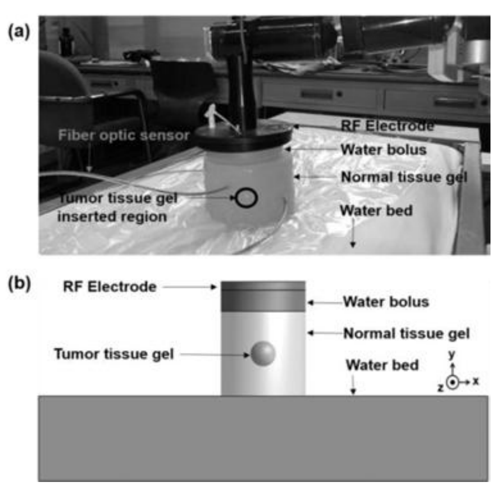


Fig. 4 (a) Experimental setup (b) 3D computational model for validating selective tumour heating in phantoms.

### C. Numerical Simulation

3D numerical simulations for validating the experimental results and executing the patient-specific simulations were performed with the aid of the multiphysics simulation platform Sim4Life (Schmid & Partner Engineering AG, Zurich, Switzerland). The electromagnetic (EM) and thermal simulations were employed by using the Electro Static approximation and Penne's bio-heat transfer equation. The governing equations are given as,

EM simulation,

$$\nabla(-\varepsilon\nabla\phi) = 0, \quad E = -\nabla\phi$$

$$SAR = \frac{\sigma}{2\rho}E^2$$

Thermal simulation,

$$\rho c\frac{\partial T}{\partial t} = \nabla\cdot(k\nabla T) + \rho_b c_b \omega_b (T - T_b) + Q_r + Q_m$$

where, $\varphi$ = electric potential, $E$ = electric field strength, $SAR$ = specific absorption rate, $\sigma$ = electrical conductivity, $\rho$ = mass density, $c$ = specific heat, $T$ = temperature, $t$ = time, $k$ = thermal conductivity, $Q_m$ = metabolic heat generation rate, $Q_r$ = regional heat generated by source, $\omega_b$ = perfusion rate and $\rho_b$, $c_b$ and $T_b$ correspond to the density, specific heat and temperature of blood, respectively.

Fig. 1(b) and Fig. 2 show the three dimensional physical models for the simulations. Fig. 1(b) consists of an RF electrode at the top with a water bolus just below the electrode, cylindrical phantom with tumour phantom inside, and water bed at the base. For the patient-specific simulation, CT images obtained from a cancer patient was reconstructed and segmented into solid parts using the Slicer program and exported as *.stl files for importing into Sim4Life. All imported solid parts were assembled together to form the computational model and the other settings such as electrode, water bolus and water bed were done as mentioned above to setup the computational domain as shown in Fig. 2.

Grid independent studies were conducted from coarser to finer meshes and finally an optimized gird of 1.489 M cells and 5.345 M cells were generated in the simple phantom and complex human anatomical models. A frequency of 13.56 MHz was set for the EM simulation and the energy absorbed during the EM simulation was exported and given as a user defined heat source for the thermal simulation. An input power of 80 W was given for the phantom simulation and it was varied from 80 – 180 W for the patient-specific simulation. For the thermal simulation, a convective boundary was used towards the background with an outside temperature of 25ºC and surface heat transfer coefficient of 5 $W/m^2{\cdot}K$ around the phantom and human models. The initial temperature of water bolus and water bed temperature were

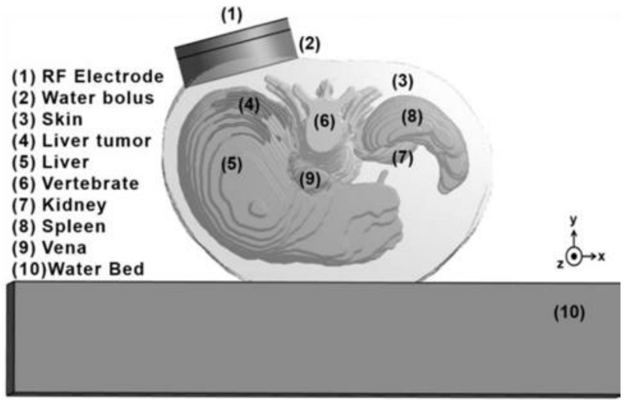


Fig. 2 Real human 3D anatomical model for patient-specific simulation

fixed as 25ºC and the others as 37ºC. The total duration was 60 min for both phantom and patient-specific simulations. The dielectric and thermophysical properties of the phantom and the real tumour in the patient-specific simulation were detailed in Table 1 [4] [8]. The properties for distilled water, human organs, vertebrate and blood vessels were taken from IT'IS Foundation [21] and the perfusion considered for the liver tumour was 111 mL/min/kg [4].

## III. Results and Discussion

Fig. 3 shows the temperature rise obtained during RF experiment at 80 W power and 13.56 MHz frequency in comparison with that of simulations. It was found from the fiber optic sensor readings that a temperature rise of 11.16 ºC and 17.91ºC was acquired for the normal and tumour gel phantoms, respectively. Fig. 4 illustrates the distribution of specific absorption rate (SAR) and temperature distribution at the cross section of the cylindrical phantom obtained from simulations. It is clear from the contours that a high energy absorption was calculated numerically from the EM simulation and a high temperature rise was obtained from thermal simulation in the tumour gel compared to that of the normal gel. The temperature rise obtained from experimental and simulation results are in very good agreement with each other as shown in Fig. 4 and hence the validation of the results was done. Microbiological studies proved that malignant tissues have high electrical conductivity in contrast to normal tissues, so there will be a high energy absorption in cancer cells than normal cells. From the tissue mimicking phantom experiment and simulation it is very evident that a high SAR and temperature profile was obtained in the tumour gel phantom and that can establish the selective heating principle in RF Hyperthermia. Since perfusion cannot be considered in the gel phantom experiments, studies on real human anatomy models can give more precise and accurate findings, which will be more relevant for clinical applications.

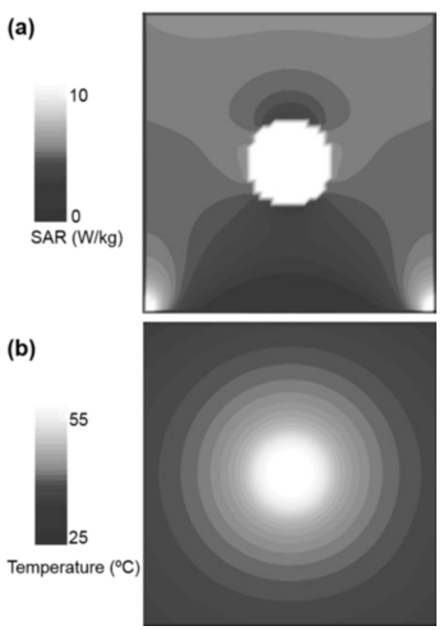


Fig. 3 (a) SAR distribution and (b) temperature distribution at the cross section of phantom

TABLE IX
Electric and Thermal Properties of Materials used for Simulation

| Materials | Electrical conductivity (S/m) | Density (kg/m$^3$) | Specific heat (J/kg/K) | Thermal conductivity (W/m/K) |
|---|---|---|---|---|
| Normal gel | 0.15 | 1000 | 4200 | 0.75 |
| Tumour gel | 2.97 | 1021 | 4200 | 0.498 |
| Liver tumour | 0.5 | 1079 | 3540 | 0.52 |

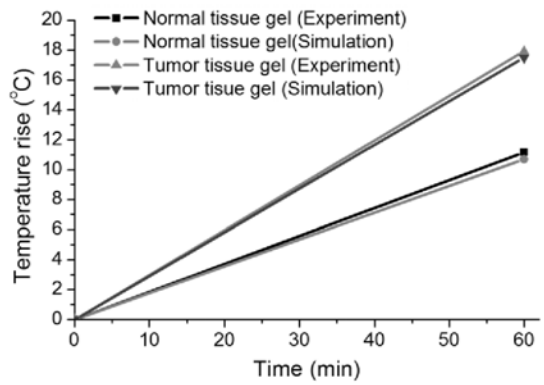


Fig. 4 Comparison of temperature rise obtained from experiment and simulation

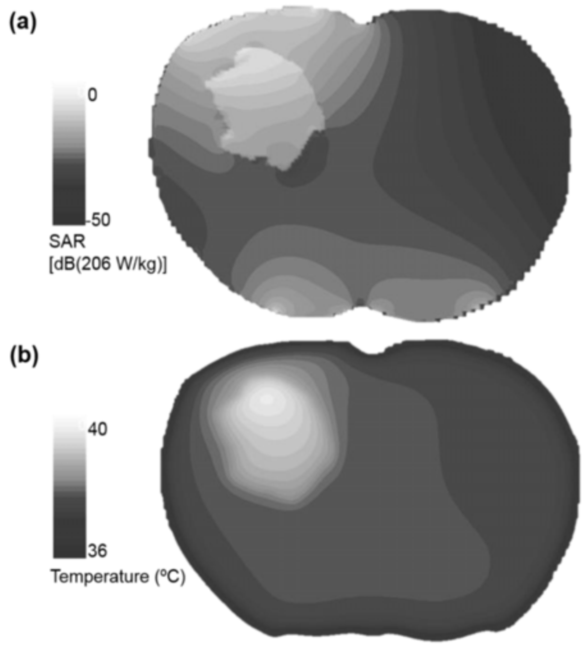


Fig. 5 (a) SAR distribution and (b) temperature distribution at the cross section of the human anatomical model

For the liver cancer treatment study, a patient-specific computational model was considered. Computations were carried out for six different input powers such as 80, 100, 120, 140, 160 and 180 W to determine its effect on heating the malignant and surrounding tissues. Fig. 5 shows the SAR (dB normalized to 206 W/kg) and temperature distribution in a real human anatomical model at 100 W power and 13.56 MHz frequency. It was evident from the contours that a high SAR and temperature rise was obtained in the liver tumour region compared to surrounding tissues and organs in the human anatomy which shows a better selective heating with high energy absorption and high temperature rise in the tumour region. Figs. 6 and 7 illustrate the percentage increment of SAR and temperature rise with respect to time

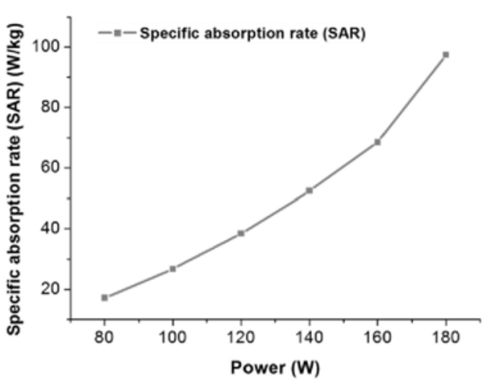


Fig. 6 SAR increment obtained in the liver tumour with respect to different input power.

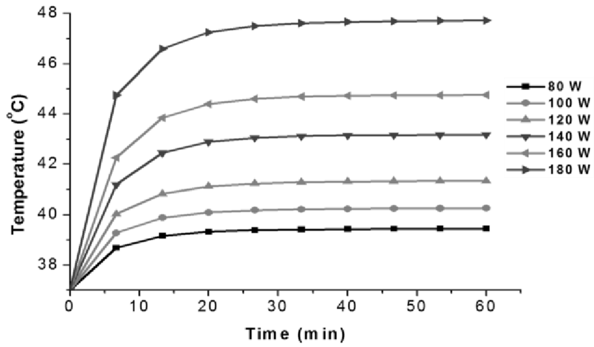


Fig. 7 Temperature rise obtained in liver tumour with respect to different input power

for different input powers in the liver tumour region. As we can see from the graph that there was an increase in SAR from 17.11 to 97.39 W/kg when the power was increased from 80 to 180 W which shows a high energy absorption in the liver tumour region with respect to an increasing power, correspondingly the temperature rise in the tumour was also increased gradually, even at a power of 80 W the temperature in the tumour reached above 39.5ºC and by 160 W it crossed a temperature above 44ºC, which is suitable enough to kill the cancerous cells, so the initial power can be set according to the temperature needed in the therapy. When the power was increased up to 180 W the temperature rise in the surrounding was found slightly high which may damage the surrounding normal tissues but the temperature rise in the nearby organs was only in a negligible range. In a real living human's case this issue can be rectified since continuous heating at a higher power is not needed and temperature rise can be controlled by changing the perfusion rate in the tumour and surrounding tissues, so that more effective treatment outputs can be achieved at a much lower power, which will be an added benefit in RF Hyperthermia compared to other Hyperthermia treatment techniques.

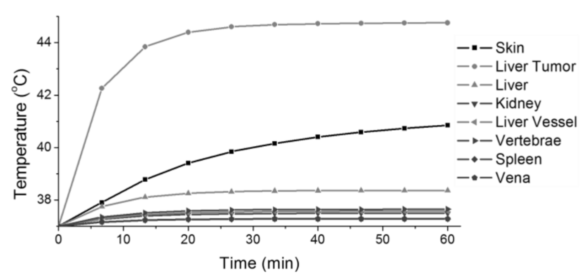


Fig.8 Temperature rise obtained in different organs with respect to irradiation time at 160 W

The graphical representation of temperature in Fig. 8 depicts the comparison of temperature rise obtained in the liver tumour in contrast to nearby organs at 160 W power and it shows that the temperature rise in the Liver tumour was over 44ºC followed by skin with 40.8ºC, normal liver with 38.3ºC and others in a range slightly above 37ºC which showcase an affordable temperature range for treatment. Even though a high heat transfer at the cross section of the human body may be expected due to conduction but the temperature upsurge obtained was not very higher than the initial temperature for the surrounding tissues and organs due to the difference in perfusion rate and thermophysical properties. Also, since the model is a realistic human anatomy with perfusion in contrast to a cylindrical tissue mimicking phantom without perfusion, the results obtained have more relevance to clinical outputs. Totally, from this study we found that the RF heating is a selective way for killing tumour by sparing the normal cells, hence this approach can be further developed by conducting experiments on animals and then to humans for establishing an advanced technique for cancer treatment.

## IV. CONCLUSIONS

Selective heating in RF Hyperthermia was successfully validated with experimental and computational simulations by using a tissue-mimicking tumour gel phantom which showcase that the temperature rise in tumour can be estimated based on its dielectric and thermophysical properties. Patient-specific simulation conducted in a real human anatomy by considering perfusion rate showed more precise details of energy absorption in the malignant tissues and surrounding normal tissues. The study displayed the effect of power modulation and it depicts that temperature in the tumour regions can be increased selectively with an increment in input power of heat source. The temperature rise obtained in the surrounding organs during heating were found to be in a negligible range which displayed an efficient regional heating of RF Hyperthermia. Overall, the study shows more realistic findings and reliable outputs which can be applied for clinical practices for improving effective treatment planning for liver cancer in real human patients.

## ACKNOWLEDGMENT

This research was supported by grants from the Industrial Core Technology Development Program (10047904) of the Korea Evaluation Institute of Industrial Technology (KEIT) and the Human Resources Development Program (20134010200580) of the Korea Institute of Energy Technology Evaluation and Planning (KETEP) funded by the Ministry of Trade, Industry and Energy, Republic of Korea. We thank SPEAG for providing a free license of Sim4Life used in this study. Bibin Prasad was funded by the Global Scholarship Program for Foreign Graduate Students at Kookmin University in Korea.

## REFERENCES

[1] Margarethus M. Paulides1, Paul R. Stauffer, Esra Neufeld, Paolo F. Maccarini, Adamos Kyriakou, Richard A.M. Canters1, Chris J. Diederich4, Jurriaan F. Bakker1 and Gerard C. Van Rhoon, "Simulation techniques in hyperthermia treatment planning", *Int J Hyperthermia*, vol. 29, pp. 346–357, May 2013

[2] John W Strohbehn and Robert B Roemer, "A Survey of Computer Simulations of Hyperthermia Treatments", *IEEE Transactions on Biomedical Engineering*, vol. 31, pp.136 – 149, Jan 1984

[3] Dennis Sullivan, "Three-Dimensional Computer Simulation in Deep Regional Hyperthermia Using the Finite-Difference Time-Domain Method", *IEEE transactions on microwave theory and techniques*, vol.38, pp.204-211, Feb 1990

[4] George Zorbas and Theodoros Samaras, "Simulation of radiofrequency ablation in real human anatomy", *Int J Hyperthermia*, vol. 30, pp.570–578,Nov 2014

[5] Earl Zastrow, Susan C Hagness and Barry D Van Veen, "3D computational study of non-invasive patient-specific microwave hyperthermia treatment of breast cancer" *Phys. Med. Biol,* vol.55, pp. 3611–3629, June 2010

[6] Matthew J Burfeindt, Earl Zastrow, Susan C Hagness,Barry D Van Veen and Joshua E Medow, "Microwave beamforming for non-invasive patient-specific hyperthermia treatment of pediatric brain cancer", *Phys. Med. Biol*, vol.56, pp. 2743–2754, April 2011

[7] Muneeb Ahmed, Zhengjun Liu, Stanley Humphries, and S. Nahum Goldberg, "Computer modeling of the combined effects of perfusion, electrical conductivity, and thermal conductivity on tissue heating patterns in radiofrequency tumor ablation", *Int. J. Hyperthermia*, vol.24, pp.577–588, Nov.2008

[8] Sukhoon Oh, Yeun-Chul Ryu, Giuseppe Carluccio, Christopher T. Sica, and Christopher M. Collins, "Measurement of SAR-Induced Temperature Increase in a Phantom and In Vivo with Comparison to Numerical Simulation" *Magnetic Resonance in Medicine*, vol.71, pp.1923–1931, June 2014

[9] Solazzo SA, Liu Z, Lobo SM, Ahmed M, Hines-Peralta AU, Lenkinski RE, "Radiofrequency ablation: Importance of background tissue electrical conductivity – An agar phantom and computer modeling study", *Radiology*, vol.236, pp.495–502, Aug 2005

[10] Mehrdad Javidi1, Morteza Heydari1, Mohammad Mahdi Attar, Mohammad Haghpanahi, Alireza Karimi1, Mahdi Navidbakhsh1, and Saeid Amanpour, "Cylindrical agar gel with fluid flow subjected to an alternating magnetic field during hyperthermia", *Int J Hyperthermia*, vol.31, pp.33–39, Dec.2015

[11] Madhuvanthi A. Kandadaia, Jason L. Raymondb, and George J. Shawa "Comparison of electrical conductivities of various brain phantom gels: Developing a 'Brain Gel Model'", *Mater Sci Eng C Mater Biol Appl*, vol.32, pp.2664-2667, Dec 2012

[12] R. B. Roemer and T. C. Cetas, "Applications of Bioheat Transfer Simulations in Hyperthermia1", *Cancer Research*, vol.44, pp. 4788-4798, Oct 1984.

[13] T. Voigt, H. Homann, U. Katscher, and O. Doesse "Patient-Individual Local SAR Determination: In Vivo Measurements and Numerical Validation", *Magnetic Resonance in Medicine*, vol.68, pp.1117-1126, Dec 2011.

[14] Vladimir V. Kosterev, Evgeny A. Kramer-Ageev, Vladimir N. Mazokhin, Gerard C. van Rhoon, & Johannes Crezee, "Development of a novel method to enhance the therapeutic effect on tumours by simultaneous action of radiation and heating", *Int J Hyperthermia*, vol.31, pp. 443–452, April 2015.

[15] Kao TJ, Saulnier GJ, Isaacson D, Szabo TL, Newell JC "A versatile high-permittivity phantom for EIT", IEEE Trans Biomed Eng 2008; vol.55, pp.2601–7, Nov 2008

[16] Marmor JB, Kozak D, Hahn GM "Effects of systemically administered bleomycin or adriamycin with local hyperthermia on primary tumor and lung metastases" *Cancer Treatment Reports*, vol.63, pp.1279-1290, Aug 1979.

[17] Bhudatt R. Paliwal, Frederic A. Gibbs, Albert L. Wiley, "Heating patterns induced by a 13.56 MHz radiofrequency generator in large phantoms and pig abdomen and thorax", *International Journal of Radiation Oncology Biology Physics,* vol. 8, pp. 857-864, May 1982.

[18] Jae Ho Kim, Eric W. Hahn and Sultan A. Ahmed, "Combination hyperthermia and radiation therapy for malignant melanoma", *Cancer*, vol. 50, pp. 478-482, Aug 1982.

[19] Herbst M, "13.56 MHz hyperthermia temperature distribution in phantoms, and clinical results of therapy", *Radiation Medicine,* vol. 3, pp. 99-106, June 1985

[20] Tanaka, Ryuichi M.D, Kim, Choong Hong,Yamada, Nobuhisa, Saito, Yoshiaki, "Radiofrequency Hyperthermia for Malignant Brain Tumours: Preliminary Results of Clinical Trials", *Neurosurgery*, vol.21, pp.478-483, Oct 1987.

[21] Hasgall PA, Di Gennaro F, Baumgartner C, Neufeld E, Gosselin MC, Payne D, Klingenböck A, Kuster N, "IT'IS Database for thermal and electromagnetic parameters of biological tissues," Version 2.6, January 13th, 2015. www.itis.ethz.ch/database.

# Analysis of Factors Affecting Cadaver Kidney Transplant Waiting Time in India Using ISM Approach

Pius Tom[1], K. Sunil Kumar[2]

*Department of Mechanical Engineering*
*College of Engineering Trivandrum, Kerala, India*
[1]tompiusk@gmail.com
[2]ksk_sunil@yahoo.com

***Abstract*— Kidney transplantation is one of the prominent treatment options available for patients suffering from kidney failure. It has been proven in the past that the process of transplantation engenders meliorated results compared to the alternative treatments available. In India, registering in the common waitlist for cadaver kidneys is one of the legalized forms of getting a kidney for transplantation. This paper examines the various factors affecting the waiting time to receive a cadaver kidney, in the Indian context. The influential relationships between various factors are analyzed through interpretive structural modelling (ISM) technique. A set of 19 factors affecting the waiting time are selected based on existing literature and expert opinion to serve as inputs to the model. The results from ISM approach shows that blood group, gender and geographic location as the key influential factors. The analysis of driving power versus dependence power shows geographic location as the factor with highest driving power to influence the cadaver kidney waiting time.**

***Keywords*— Transplantation, Cadaver Kidney, Waiting Time, Interpretive Structural Modelling (ISM), Driving power, Dependence power.**

## I. INTRODUCTION

Organ transplantation is one of the most complex medical process, which offers a second chance to live, by replacing the failed organ. Presently, there is huge gap between the demand and supply of organs in India. Organ donation can be through various programs likes living donation program or cadaver donation program. Cadaver donation means the organ donation from brain dead people. Cadaver kidney donations show a promising future to alleviate the demand-supply gap. This program is still in its nascent stage in India and offers a lot of room for improvement. Recent incidences on organ donation and successful transplantation amidst the odd factors like distance criteria have received wide attention among the public. Patients who want to receive a cadaver kidney are put in a common waitlist maintained by the state governments in India. Currently only few states like Tamil Nadu and Kerala have the central registry for cadaver transplant program. It is an alarming fact that about 3220 people are currently waiting for a cadaver Kidney in Tamil Nadu [1] and about 934 in Kerala [2]. While the supply stands around 235 for Tamil Nadu in 2013 [1] and 59 for Kerala in 2013 [2]. Examination of the past statistics of kidney donation shows a sluggish growth rate, which is incapable of satisfying the huge demand. This widening gap between demand and supply has resulted in a long cadaver kidney waiting list. Waiting for a transplant is equivalent to waiting for a second life and thus the time factor plays a crucial role in giving and taking life. It is to be also noted that the waiting time can significantly affect the post-transplant graft function as well [3]. Hence, it is vital to study the multiple factors affecting waiting time in a holistic manner.

## II. LITERATURE REVIEW

Waiting time to receive a kidney has always gained substantial research attention due to its evergreen social relevance. The equity of waiting times with respect to blood groups was examined [4]. They have found that limited number of cross-transplantation must be allowed to achieve equity, but only between specified blood types, based uniquely upon the blood mix of the given jurisdiction. The effect of waiting time on renal transplant outcome were studied [5]. They concluded that longer waiting times on dialysis negatively impact on post-transplant graft and patient survival. Also research was done to bring out the sub group and racial disparity in kidney paired donation (KPD) program [6]. They used simulation as their methodology to characterise the waiting time. Some others like [7] studied the role of dialysis facility chain status (affiliation, size, and ownership) on placement on the renal transplant waiting list. . They have addressed the various factors for placement on the renal transplant waiting list. Those factors included age, race, gender, ethnicity, insurance status, median household income, comorbidities (like diabetes, cardio vascular disease, cancer etc.), alcohol or drug dependence, geographical regions and staffing pattern. The various factors affecting cadaver kidney waiting time in the United States was studied [8]. This was a quantitative analysis and factors were primarily selected based on the U.S context. The present study makes a distinction by analysing the influential relationship between various factors affecting waiting time in the Indian context.

The study is presented section wise. The following section gives the methodology adopted for the study. Section IV identifies and explains the factors affecting cadaver kidney transplant waiting time in India. Section V provides an overview of ISM and section VI applies the approach of ISM to the present study of analysing the influential relationship between various factors affecting cadaver kidney waiting time in India. Section VII presents discussion on the results obtained. The study is concluded in section VIII.

## III. Methodology

The methodology involves study of various factors affecting cadaver kidney waiting time in India, through literature review and expert opinion. Later these factors are analysed using interpretive structural modelling for analysing the influential relationship among them. Finally the factors are clustered into various categories like autonomous factors, dependent factors, linkage factors and driving factors [14].

## IV. Factors Affecting Waiting Time to Receive a Cadaver Kidney

The following are the factors affecting waiting time to receive a cadaver kidney.

1) Age: As per [9], transplantation was inversely associated with age, with patients 18 to 34 years old having a 2.4-fold higher rate of transplantation than patients 50 to 65 years old. This means that age could be one of the determinants of how fast one can get a transplant. Also [8] listed age as one of the factors affecting waiting time to receive a cadaver Kidney.
2) Sensitization level of candidate: Sensitization here means Panel reactive antibody (PRA) sensitization which implies the presence of high antibody levels that react to foreign tissue. As per medical experts, sensitization is one of the factors capable of influencing the waiting time to receive a cadaver Kidney.
3) HLA match: HLA stands for human leukocyte antigen. It is actually a genetic marker located on the white blood cells. Transplant outcomes found to be better for better matched grafts and best for those with no (known) HLA antigen differences between the donor and recipient [10].Also [8] listed various types of HLA as the factors affecting waiting time to receive a cadaver Kidney
4) Brain death organ donation promotion campaigns: One of the important factors determining the waiting time is the cadaver organ availability. In India, the concept of brain death has not yet gained adequate momentum to significantly boost donation rate. Often doctors are hesitant to certify brain death due to their perceived fear of losing patient faith in them. Also, the lack of consent from families and relatives is another problem in recovering organs.
5) Extended criteria donor organs: These are donor organs of sub-standard quality. At present, this opportunity of increasing the cadaver organ supply is not properly utilized in India. But the inclusion of this factor in the allocation criteria can significantly reduce the waiting time, by increasing the transplant rate.
6) Cadaver transplant registration date: Currently in India, the registration date for the cadaver transplant is taken as the start date for waiting time. Previously, [8] had taken 'year listed for transplant' as one of the factors affecting waiting time.
7) Previous transplant history: Patients who are previously transplanted have a higher degree of sensitization and it may be difficult for them to find a suitable match. Prior transplantation was a factor affecting waiting time [8].
8) Dedicated medical staff (including nurses and doctors): This factor was taken for study as per expert opinion. Dedicated medical staff can do a lot of things ranging from identification of potential brain dead patients, seeking consent from the relatives of brain dead patients etc. to increase the supply of cadaver organs.
9) Presence of comorbid conditions: Patients having one or more additional disease conditions coexisting with the primary disorder are said to have comorbidities. Patients with comorbid conditions had significantly lower rates of transplantation than patients without one of the comorbid conditions [9].
10) Number of discarded Kidneys: A kidney lost is equivalent to a life lost. Kidneys are discarded primarily due to deterioration of quality. Quality problems can arise from a variety of sources like a) diseases of donor b) poor procurement and handling techniques c) exceeding cold ischemic time. The number of discarded kidneys can serve as a deterrent to higher number of transplants and less waiting time.
11) Cadaver kidney availability: Researchers had previously used patient to donor ratio as one of the factors affecting cadaver kidney waiting time in the United States [8]. The present study directly uses the kidney availability factor, since we are not dealing with quantitative analysis and are more interested in the influence relationship between various factors affecting cadaver kidney waiting time.
12) Cadaver waitlist arrival rate: Arrival rate is one of the well-known factors determining the waiting time for any queue. The same concept is applied here. Here we are dealing with patient arrival rate and not the cadaver organ arrival rate. As per [8]

wait list size is one of the factors affecting waiting time to cadaver kidney transplant.

13) Cadaver waitlist death rate: This is another dynamic factor capable of influencing the waiting time. Many patients die waiting without getting a cadaver organ. The death can also be associated with increased age or due to the presence of comorbid conditions.
14) Logistics available: it is a known medical fact that the cadaver kidneys are to be transplanted within the cold ischemic time. Logistics play a great role in achieving this goal. Thus a robust logistic network can increase the supply of cadaver kidneys by minimizing their wastage.
15) Blood group match: This factor is one the pre-requisites for kidney transplantation. In India, patients are waitlisted according to their blood group and zone of residence. Also it is the preliminary match required before progressing towards HLA typing and cross match. Researchers like [11] found that blood group could influence the chances of getting an HLA zero antigen mismatch kidney.
16) Geographic location: Researchers had shown the effect of geographic disparity in kidney allocation by portraying the transplant rate variation across different donor service areas [12]. This directly conveys the relationship between waiting time and geographic location
17) Allocation criteria used by the state government run organ registry: Allocation criteria refers to the combination of priority points set for various factors like waiting time, blood group match, HLA match etc. The change in the relative weights can affect the waiting time of a patient
18) Gender: Gender is not considered in India for the allocation of cadaver Kidneys. However, it can influence the waiting time to receive a transplant because of its interconnectivity with the factors like comorbid conditions, sensitization, physical and emotional health etc.
19) Physical and mental fitness of the candidate: Waiting for an organ demands requires physical and mental fitness. Issues like sensitization can cause emotional as well as physical health hazards to those waiting. Also general health is important for performing transplant surgery.

## V. ISM-AN OVERVIEW

Interpretive Structural Modelling (ISM) is a methodology used to identify the influence relationship among various factors, which define a problem or issue; it was firstly developed in 1970's [13].The following are the steps used in performing ISM.

- Identification of factors affecting cadaver kidney waiting time
- Establish contextual relationship between the factors using existing literature, additional literature and expert opinion.
- Develop the structural self-interaction matrix (SSIM)
  Let $X_{ij}$ represent the cell in the SSIM corresponding to factors 'i' and 'j'. Then if 'i' can influence 'j' and the reverse is not true, then write 'V' in $X_{ij}$. Similarly if 'j' can influence 'i' and the reverse is not true, then write 'A'. If both 'i and 'j' can influence each other, then write 'X'. If both 'i' and 'j' are unrelated then write 'O'.
- Develop the initial reachability matrix using the following relations. If the entry in cell (i, j) in SSIM is 'V', then $X_{ij}$ is replace by 1 and $X_{ji}$ is replaced by 0 in the initial reachability matrix. If the entry in cell (i, j) in SSIM is 'A', then $X_{ij}$ is replace by 0 and $X_{ji}$ is replaced by 1 in the initial reachability matrix. If the entry in cell (i, j) in SSIM is 'X', then $X_{ij}$ is replace by 1 and $X_{ji}$ is replaced by 1 in the initial reachability matrix. If the entry in cell (i, j) in SSIM is 'O', then $X_{ij}$ is replace by 0 and $X_{ji}$ is replaced by 0 in the initial reachability matrix.
- Develop the final reachability matrix from initial reachability matrix by considering transitivity. Sum the elements in the row and column to get driving power and dependence power respectively.
- Using the final reachability matrix, partition the factors into various levels. Whenever the reachability set is same as the intersection set, the corresponding factor is assigned top level. The factors already assigned a level are ignored in the future iterations.
- Using the information obtained from levels and final reachability matrix, create a digraph with node numbers and arrows. Remove the transitive links from diagraph and replace node numbers with corresponding factor labels to form the interpretive structural model
- Cluster the factors into driving, dependent, linkage and autonomous factors based on driving power and dependence power [14].

## VI. APPLICATION OF ISM TO THE CURRENT PROBLEM

The various factors affecting waiting time to cadaver kidney transplant are listed from one 1 to 19 in section IV. The contextual relationship between these factors is shown in Fig. 1, where the first row contains factor numbers from 19 to 2 and first column contains factor numbers from 1 to 18. The contextual relationship is marked for every two factors under consideration. For instance In Fig. 1, consider factor 1(age) and factor 19(physical and mental fitness), where factor 1 could influence factor 19 and the reverse is not true, hence the notation ‘V’ is given to denote the contextual relationship between these two factors. Similarly other contextual relations are marked with the help of additional literature and expert opinion. Fig. 2 represents the initial reachability matrix obtained by using the procedure stated in section V above. Fig. 3 represents the final reachability matrix after transitivity into the initial reachability matrix. The starred elements in Fig. 3 represents transitivity. The last row and last column of the final reachability matrix shows the dependence power and driving power respectively. Fig. 4 shows the identification of reachability set (list of factors which can be influenced by a factor), antecedent set (list of factors which can influence a factor), intersection set and finally the levels in the first iteration. The iterative process is repeated until all factors are assigned to some level. The summary of factors and levels assigned are shown in Table 1. Finally the interpretive structural model is developed using final reachability matrix and by removing any transitive links from diagraph. The final ISM based model developed is shown in Fig. 5. Also, the clustering of factors based on driver power and dependence power is shown in Fig. 6.

| | 19 | 18 | 17 | 16 | 15 | 14 | 13 | 12 | 11 | 10 | 9 | 8 | 7 | 6 | 5 | 4 | 3 | 2 |
|---|---|---|---|---|---|---|---|---|---|---|---|---|---|---|---|---|---|---|
| 1 | V | O | V | O | O | O | V | O | O | O | V | O | O | O | O | O | O | V |
| 2 | V | A | V | A | O | O | V | O | O | O | A | O | X | O | O | O | A | |
| 3 | O | A | V | A | A | O | O | O | O | O | V | O | V | O | O | O | | |
| 4 | O | O | O | O | O | O | O | O | V | V | O | X | O | O | O | | | |
| 5 | O | O | V | O | O | O | O | O | X | V | O | O | O | O | | | | |
| 6 | O | O | X | A | O | O | O | O | O | O | O | O | O | | | | | |
| 7 | X | A | A | A | A | A | A | A | A | A | A | A | | | | | | |
| 8 | O | O | O | O | O | O | O | O | V | V | O | | | | | | | |
| 9 | V | A | V | O | O | O | V | O | O | O | | | | | | | | |
| 10 | O | O | O | O | O | A | V | O | X | | | | | | | | | |
| 11 | O | O | O | A | O | A | V | O | | | | | | | | | | |
| 12 | O | O | O | A | O | O | O | | | | | | | | | | | |
| 13 | A | O | O | A | O | O | | | | | | | | | | | | |
| 14 | O | O | O | A | O | | | | | | | | | | | | | |
| 15 | O | O | V | O | | | | | | | | | | | | | | |
| 16 | O | O | V | | | | | | | | | | | | | | | |
| 17 | O | O | | | | | | | | | | | | | | | | |
| 18 | V | | | | | | | | | | | | | | | | | |

Fig. 5 SSIM for factors affecting waiting time to receive a cadaver kidney

| | 1 | 2 | 3 | 4 | 5 | 6 | 7 | 8 | 9 | 10 | 11 | 12 | 13 | 14 | 15 | 16 | 17 | 18 | 19 |
|---|---|---|---|---|---|---|---|---|---|---|---|---|---|---|---|---|---|---|---|
| 1 | 1 | 1 | 0 | 0 | 0 | 0 | 0 | 0 | 1 | 0 | 0 | 0 | 1 | 0 | 0 | 0 | 1 | 0 | 1 |
| 2 | 0 | 1 | 0 | 0 | 0 | 0 | 1 | 0 | 0 | 0 | 0 | 0 | 1 | 0 | 0 | 0 | 1 | 0 | 1 |
| 3 | 0 | 1 | 1 | 0 | 0 | 0 | 1 | 0 | 1 | 0 | 0 | 0 | 0 | 0 | 0 | 0 | 1 | 0 | 0 |
| 4 | 0 | 0 | 0 | 1 | 0 | 0 | 0 | 1 | 0 | 1 | 1 | 0 | 0 | 0 | 0 | 0 | 0 | 0 | 0 |
| 5 | 0 | 0 | 0 | 0 | 1 | 0 | 0 | 0 | 0 | 1 | 1 | 0 | 0 | 0 | 0 | 0 | 1 | 0 | 0 |
| 6 | 0 | 0 | 0 | 0 | 0 | 1 | 0 | 0 | 0 | 0 | 0 | 0 | 0 | 0 | 0 | 0 | 1 | 0 | 0 |
| 7 | 0 | 1 | 0 | 0 | 0 | 0 | 1 | 0 | 0 | 0 | 0 | 0 | 0 | 0 | 0 | 0 | 0 | 0 | 1 |
| 8 | 0 | 0 | 0 | 1 | 0 | 0 | 1 | 1 | 0 | 1 | 1 | 0 | 0 | 0 | 0 | 0 | 0 | 0 | 0 |
| 9 | 0 | 1 | 0 | 0 | 0 | 0 | 1 | 0 | 1 | 0 | 0 | 0 | 1 | 0 | 0 | 0 | 1 | 0 | 1 |
| 10 | 0 | 0 | 0 | 0 | 0 | 0 | 1 | 0 | 0 | 1 | 1 | 0 | 1 | 0 | 0 | 0 | 0 | 0 | 0 |
| 11 | 0 | 0 | 0 | 0 | 1 | 0 | 1 | 0 | 0 | 1 | 1 | 0 | 1 | 0 | 0 | 0 | 0 | 0 | 0 |
| 12 | 0 | 0 | 0 | 0 | 0 | 0 | 1 | 0 | 0 | 0 | 0 | 1 | 0 | 0 | 0 | 0 | 0 | 0 | 0 |
| 13 | 0 | 0 | 0 | 0 | 0 | 0 | 1 | 0 | 0 | 0 | 0 | 0 | 1 | 0 | 0 | 0 | 0 | 0 | 0 |
| 14 | 0 | 0 | 0 | 0 | 0 | 0 | 1 | 0 | 0 | 1 | 1 | 0 | 0 | 1 | 0 | 0 | 0 | 0 | 0 |
| 15 | 0 | 0 | 1 | 0 | 0 | 0 | 1 | 0 | 0 | 0 | 0 | 0 | 0 | 0 | 1 | 0 | 1 | 0 | 0 |
| 16 | 0 | 1 | 1 | 0 | 0 | 1 | 1 | 0 | 0 | 0 | 1 | 1 | 1 | 1 | 0 | 1 | 1 | 0 | 0 |
| 17 | 0 | 0 | 0 | 0 | 0 | 1 | 1 | 0 | 0 | 0 | 0 | 0 | 0 | 0 | 0 | 0 | 1 | 0 | 0 |
| 18 | 0 | 1 | 1 | 0 | 0 | 0 | 1 | 0 | 1 | 0 | 0 | 0 | 0 | 0 | 0 | 0 | 0 | 1 | 1 |
| 19 | 0 | 0 | 0 | 0 | 0 | 0 | 1 | 0 | 0 | 0 | 0 | 0 | 1 | 0 | 0 | 0 | 0 | 0 | 1 |

Fig. 2 Initial reachability matrix for factors affecting waiting time to receive a cadaver kidney.

| | 1 | 2 | 3 | 4 | 5 | 6 | 7 | 8 | 9 | 10 | 11 | 12 | 13 | 14 | 15 | 16 | 17 | 18 | 19 | sum |
|---|---|---|---|---|---|---|---|---|---|---|---|---|---|---|---|---|---|---|---|---|
| 1 | 1 | 1 | 0 | 0 | 0 | 1* | 1* | 0 | 1 | 0 | 0 | 0 | 1 | 0 | 0 | 0 | 1 | 0 | 1 | 8 |
| 2 | 0 | 1 | 0 | 0 | 0 | 1* | 1 | 0 | 0 | 0 | 0 | 0 | 1 | 0 | 0 | 0 | 1 | 0 | 1 | 6 |
| 3 | 0 | 1 | 1 | 0 | 0 | 1* | 1 | 0 | 1 | 0 | 0 | 0 | 1* | 0 | 0 | 0 | 1 | 0 | 1* | 8 |
| 4 | 0 | 0 | 0 | 1 | 1* | 0 | 1* | 1 | 0 | 1 | 1 | 0 | 1* | 0 | 0 | 0 | 0 | 0 | 0 | 7 |
| 5 | 0 | 0 | 0 | 0 | 1 | 1* | 1* | 0 | 0 | 1 | 1 | 0 | 1* | 0 | 0 | 0 | 1 | 0 | 0 | 7 |
| 6 | 0 | 0 | 0 | 0 | 0 | 1 | 1* | 0 | 0 | 0 | 0 | 0 | 0 | 0 | 0 | 0 | 1 | 0 | 0 | 3 |
| 7 | 0 | 1 | 0 | 0 | 0 | 0 | 1 | 0 | 0 | 0 | 0 | 0 | 1* | 0 | 0 | 0 | 1* | 0 | 1 | 5 |
| 8 | 0 | 1* | 0 | 1 | 1* | 0 | 1 | 1 | 0 | 1 | 1 | 0 | 1* | 0 | 0 | 0 | 0 | 0 | 1* | 9 |
| 9 | 0 | 1 | 0 | 0 | 0 | 1* | 1 | 0 | 1 | 0 | 0 | 0 | 1 | 0 | 0 | 0 | 1 | 0 | 1 | 7 |
| 10 | 0 | 1* | 0 | 0 | 1* | 0 | 1 | 0 | 0 | 1 | 1 | 0 | 1 | 0 | 0 | 0 | 0 | 0 | 1* | 7 |
| 11 | 0 | 1* | 0 | 0 | 1 | 0 | 1 | 0 | 0 | 1 | 1 | 0 | 1 | 0 | 0 | 0 | 1* | 0 | 1* | 8 |
| 12 | 0 | 1* | 0 | 0 | 0 | 0 | 1 | 0 | 0 | 0 | 0 | 1 | 0 | 0 | 0 | 0 | 0 | 0 | 1* | 4 |
| 13 | 0 | 1* | 0 | 0 | 0 | 0 | 1 | 0 | 0 | 0 | 0 | 0 | 1 | 0 | 0 | 0 | 0 | 0 | 1* | 4 |
| 14 | 0 | 1* | 0 | 0 | 1* | 0 | 1 | 0 | 0 | 1 | 1 | 0 | 1* | 1 | 0 | 0 | 0 | 0 | 1* | 8 |
| 15 | 0 | 1* | 1 | 0 | 0 | 1* | 1 | 0 | 1* | 0 | 0 | 0 | 0 | 0 | 1 | 0 | 1 | 0 | 1* | 8 |
| 16 | 0 | 1 | 1 | 0 | 1* | 1 | 1 | 0 | 1* | 1* | 1 | 1 | 1 | 1 | 0 | 1 | 1 | 0 | 1* | 14 |
| 17 | 0 | 1* | 0 | 0 | 0 | 1 | 1 | 0 | 0 | 0 | 0 | 0 | 0 | 0 | 0 | 0 | 1 | 0 | 1* | 5 |
| 18 | 0 | 1 | 1 | 0 | 0 | 0 | 1 | 0 | 1 | 0 | 0 | 0 | 1* | 0 | 0 | 0 | 1* | 1 | 1 | 8 |
| 19 | 0 | 1* | 0 | 0 | 0 | 0 | 1 | 0 | 0 | 0 | 0 | 0 | 1 | 0 | 0 | 0 | 0 | 0 | 1 | 4 |
| sum | 1 | 16 | 4 | 2 | 7 | 9 | 19 | 2 | 6 | 7 | 7 | 2 | 15 | 2 | 1 | 1 | 12 | 1 | 16 | |

Fig. 3 Final reachability matrix for factors affecting waiting time to receive a cadaver kidney

| factors | reachability set | antecedent set | intersection set | level |
|---|---|---|---|---|
| 1 | 1,2,6,7,9,13,17,19 | 1 | 1 | |
| 2 | 2,6,7,13,17,19 | 1,2,3,7,8,9,10,11,12,13, 14,15,16,17,18,19 | 2,7,13,17,19 | |
| 3 | 2,3,6,7,9,13,17,19 | 3,16,15,18 | 3 | |
| 4 | 4,5,7,8,10,11,13 | 4,8 | 4,8 | |
| 5 | 5,6,7,10,11,13,17 | 5,4,8,10,11,14,16 | 5,10,11 | |
| 6 | 6,7,17 | 1,2,3,5,6,9,15,16,17 | 6,17 | |
| 7 | 2,7,13,17,19 | 1,2,3,4,5,6,7,8,9,10,11,1 2,13,14,15,16,17, 18,19 | 2,7,13,17,19 | 1 |
| 8 | 2,4,5,7,8,10,11,13, | 4,8 | 4,8 | |
| 9 | 2,6,7,9, 13,17,19 | 1,3,9,15,16,18 | 9 | |
| 10 | 2,5,7,10,11,13,19 | 4,5,8,10,11,14,16 | 5,10,11 | |
| 11 | 2,5,7,10,11,13,17, | 4,5,8,10,11,14,16 | 5,10,11 | |
| 12 | 2,7,12,19 | 12,16 | 12 | |
| 13 | 2,7,13,19 | 1,2,3,4,5,7,8,9,10,11,13, 14,16,18,19 | 2,7,13,19 | 1 |
| 14 | 2,5,7,10,11,13,14, | 14,16 | 14 | |
| 15 | 2,3,6,7,9,15,17,19 | 15 | 15 | |
| 16 | 2,3,5,6,7,9,10,11,1 2,13,14,16,17,19 | 16 | 16 | |
| 17 | 2,6,7,17,19 | 1,2,3,5,6,7,9,11,15,16,1 | 2,6,7,17 | |
| 18 | 2,3,7,9,13,17,18,1 | 18 | 18 | |
| 19 | 2,7,13,19 | 1,2,3,7,8,9,10,11,12,13, 14,15,16,17,18,19 | 2,7,13,19 | 1 |

Fig. 4 Level partitioning (first iteration) for various factors affecting waiting time to receive a cadaver kidney

## VII. RESULTS AND DISCUSSION

The interpretive structural modelling was successfully applied to the complex problem of factors affecting waiting time to the cadaver kidney transplant program, with reference to the Indian context. The ISM based model brings out the influence relationship among various factors affecting cadaver kidney waiting time. Fig. 5 highlights that geographic location, blood group and gender occupies the base of the ISM pyramid. These are also the driving factors as shown in Fig. 6. These are the factors having the highest influence on the waiting time to receive a cadaver kidney transplant in India. These factors influence almost all other factors and any effort towards the management of waiting time, should start with a key focus on these factors.The greater influence of geographic location on the waiting time is practically reflected as a higher variance in the average waiting time across different geographical zones in the Indian states of Kerala and Tamil Nadu. Thus the results of the study underline the significance of waiting time management from the geographic location point of view, as it is the factor with highest driving power as seen in Fig. 6. Kidneys should be treated like a national resource and geographic location should not be a major determinant of waiting time to receive a cadaver kidney. Factors like blood group and gender are having eight times strong driving power than dependence power. It is highly undesirable that patients from a particular geographic location or patients with a particular blood group, have to wait longer compared to others. In light of the results in this study, it is advisable to rethink about the ability of the current cadaver kidney allocation policies used in India, in granting equal access to kidney transplantation.

TABLE I
SUMMARY OF LEVELS AND FACTORS

| Level | Factors affecting waiting time |
|---|---|
| First | a) Physical and mental fitness of the candidate (F19) |
| | b) Waiting list death rate (F13) |
| | c) Previous transplant history (F7) |
| Second | a) Allocation criteria for cadaver Kidneys (F17) |
| | b) Transplant registration date (F6). |
| Third | a) Extended criteria donor organs (F5) |
| | b) PRA sensitization (F2) |
| Fourth | a) Waiting list arrival rate (F12) |
| | b) Comorbid conditions (F9) |
| | c) Number of discarded kidneys (F10) |
| | d) Cadaver kidneys available (F11) |
| Fifth | a) Age (F1) |
| | b) HLA (F3) |
| | c) Brain death organ donation promotions (F4) |
| | d) Dedicated medical staff (F8) |
| | e) Logistics available (F14) |
| Sixth | a) Geographic Location (F16) |
| | b) Blood group (F15) |
| | c) Gender (F18) |

Factors like age, dedicated medical staff, brain death organ donation promotion campaigns, logistics and HLA occupy the next level from bottom. It should be noted that, dedicated medical staff could play a major role in the Indian context. Identification of potential brain dead donors is entirely vested in the hands of medical professionals.

Factors like previous transplant history, physical and mental health and waitlist death rate occupied the top of the ISM model. These factors are also highly dependent factors as seen from Fig. 6. Any effort targeting on these factors to analyse waiting time would require an in depth study of other factors which influence them.

Factors like waiting list arrival rate, extended criteria donor organs, number of discarded kidneys etc. are classified as autonomous factors, as these are having weak driving power and dependence power. These factors stand disconnected in the waiting time analysis. There are no linkage factors identified in Fig. 6, which means that none of the factors are having high driving power and dependence power. Thus factors with high driving power can be confidently addressed as it does not create any feedback effect on themselves.

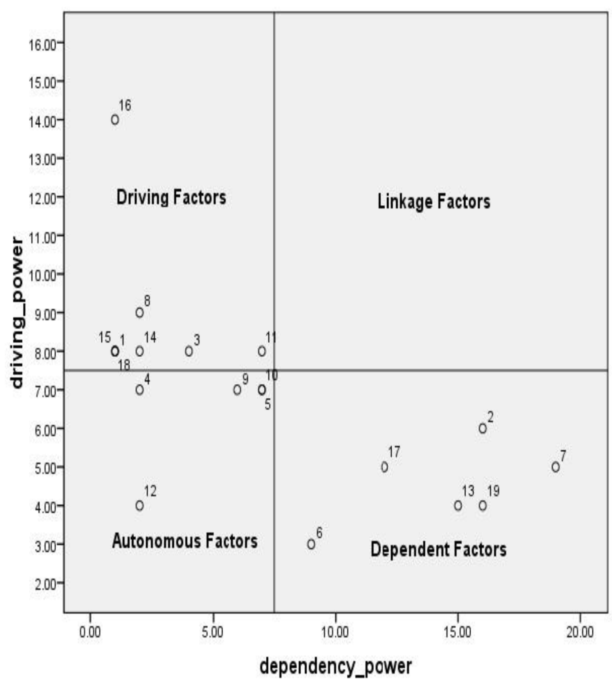


Fig. 6 Clustering of factors based on driving power and dependence power

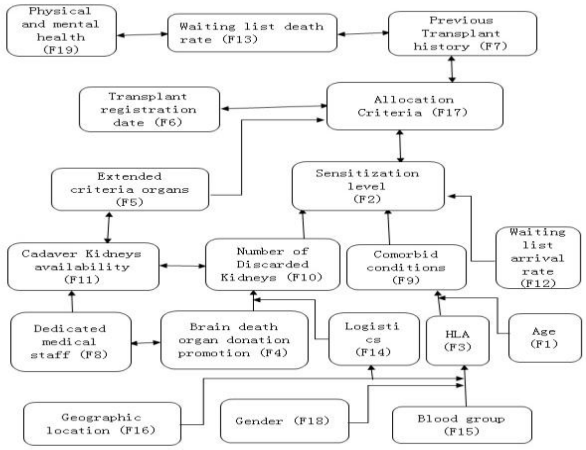


Fig. 5 ISM based model for factors affecting waiting time to cadaver kidney transplant

## VII. CONCLUSION

This paper examined the various factors affecting the waiting time to receive a cadaver kidney, in the Indian context. The influential relationships between various factors are analyzed through interpretive structural modelling (ISM) technique. A set of 19 factors affecting the waiting time were selected based on existing literature and expert opinion to serve as inputs to the model. The results from ISM approach shows that blood group, gender and geographic location as the key influential factors.

It should be noted that the model should be interpreted as a flexible one and does not give a hard and fast rule governing the input factors ([15], [16]). The model should not be misunderstood that any major modifications made with respect to factors like geographic location, blood group and gender alone will result in drastic changes to the amount of waiting time for various patient classes. The model just gives a guideline of the influence relationships of various factors affecting the waiting time to receive a cadaver kidney.

Future researchers could develop models incorporating the relative strength of influence between various factors affecting waiting time to receive a cadaver kidney. Also more number of factors could be selected and different approaches could be used for analyzing the problem.

## REFERENCES


[1] TNOS, 'Tamil Nadu Organ Sharing Registry – Share Organs Save Lives', *tnos.org*.

[2] KNOS, 'Kerala Organ Sharing Registry – Share Organs Save Lives', *knos.org*.

[3] P. J. Morris, R. J. Johnson, S. V. Fuggle, M. A. Belger, and J. D. Briggs, "Analysis of factors that affect outcome of primary cadaveric renal transplantation in the UK," *The Lancet*, vol. 354, no. 9185, pp. 1147–1152, Oct. 1999.

[4] D. Stanford, J. Lee, N. Chandok and V. McAlister, "A queuing model to address waiting time inconsistency in solid-organ transplantation," *Operations Research for Health Care*, vol. 3, no. 1, pp. 40-45, 2014.

[5] H.-U. Meier-Kriesche, F. K. Port, A. O. Ojo, S. M. Rudich, J. A. Hanson, D. M. Cibrik, A. B. Leichtman, and B. Kaplan, "Effect of waiting time on renal transplant outcome," *Kidney International*, vol. 58, no. 3, pp. 1311–1317, Sep. 2000.

[6] D. L. Segev, S. E. Gentry, J. K. Melancon, and R. A. Montgomery, "Characterization of Waiting Times in a Simulation of Kidney Paired Donation," *American Journal of Transplantation*, vol. 5, no. 10, pp. 2448–2455, Oct. 2005

[7] Y. Zhang, M. Thamer, O. Kshirsagar, D. Cotter and M. Schlesinger, "Dialysis Chains and Placement on the Waiting List for a Cadaveric Kidney Transplant," *Transplantation*, vol. 98, no. 5, pp. 543-551, 2014.

[8] F. P. Sanfilippo, "Factors affecting the waiting time of cadaveric kidney transplant candidates in the United States," *JAMA: The Journal of the American Medical Association*, vol. 267, no. 2, pp. 247–252, Jan. 1992.

[9] S. Satayathum, R. L. Pisoni, K. P. Mccullough, R. M. Merion, B. Wikström, N. Levin, K. Chen, R. A. Wolfe, D. A. Goodkin, L. Piera, Y. Asano, K. Kurokawa, S. Fukuhara, P. J. Held, And F. K. Port, "Kidney transplantation and wait-listing rates from the international Dialysis Outcomes and Practice Patterns Study (DOPPS)," *Kidney International*, vol. 68, no. 1, pp. 330–337, Jul. 2005.

[10] J. M. Cecka, "HLA matching for organ transplantation… Why not?" *International Journal of Immunogenetics*, vol. 37, no. 5, pp. 323–327, Sep. 2010.

[11] C. F. Bryan, W. S. Cherikh, Y. Cheng, M. I. Aeder, N. A. Muruve, P. W. Nelson, C. F. Shield, B. A. Warady, and F. T. Winklhofer, "ABO blood group influences a candidate's likelihood of receiving an HLA zero antigen mismatch kidney," *Clinical Transplantation*, vol. 18, no. s12, pp. 55–60, Aug. 2004.

[12] A. Davis, S. Mehrotra, J. Friedewald, M. Daskin, A. Skaro, M. Abecassis and D. Ladner, "Improving Geographic Equity in Kidney Transplantation Using Alternative Kidney Sharing and Optimization Modeling," *Medical Decision Making*, vol. 35, no.6, pp. , 1-11, Nov. 2014.

[13] J. N. Warfield, "Developing Interconnection Matrices in Structural Modeling," *IEEE Transactions on Systems, Man, and Cybernetics*, vol. SMC-4, no. 1, pp. 81–87, 1974.

[14] A. Mandal and S. G. Deshmukh, "Vendor Selection Using Interpretive Structural Modelling (ISM)," *International Journal of Operations & Production Management*, vol. 14, no. 6, pp. 52–59, Jun. 1994.

[15] G. G. Lendaris, "Structural Modeling a Tutorial Guide," *IEEE Transactions on Systems, Man, and Cybernetics*, vol. 10, no. 12, pp. 807–840, 1980.

[16] D. W. Malone, "An introduction to the application of interpretive structural modeling," *Proceedings of the IEEE*, vol. 63, no. 3, pp. 397–404, 1975.

# Heat Transfer Enhancement in a Tube Heat Exchanger Using $Al_2O_3$/Water Nanofluid and Perforated Helical Screw Tape Inserts with and without Wings

Venkitaraj K.P.[1], Gopu R[2]

*Department of Mechanical Engineering*

*College of Engineering, Adoor, Kerala,India*

[1] kpvraj @gmail.com

[2] grgopu @gmail.com

*Abstract*— **This paper deals with experimental investigation of heat transfer and pressure drop characteristics of $Al_2O_3$/water nanofluid in the flow through a circular tube fitted with perforated helical screw tape inserts with and without wings of three different twist ratio 1.2, 1.7 and 2.5. The study has been performed under constant heat flux condition for the Reynolds number ranging from 950 to 5000. Tests have been carried out on plain tube and tube fitted with inserts using water and $Al_2O_3$/water nanofluid of 0.1 % volume concentration. The results showed that Nusselt number increases with decrease in twist ratio and $Al_2O_3$/water nanofluid showed better heat transfer enhancement than water with very less rise in friction factor. The usage of insert increases the heat transfer since the swirl flow induces turbulence near the tube wall and also there is increase in the residence time of the fluid in the tube. Even though the inserts create pressure drop, while considering the thermal performance factor, the suggested compound technique of insert and nanofluid has higher thermal performance factor than plain tube.**

***Keywords*— Nanofluid, Helical screw tape insert, Thermal performance factor, Nusselt number, Friction factor**

## I. Introduction

The design of a heat exchanger is effective when it makes the device compact and achieve maximum heat transfer rate using minimum pumping power. The need to increase the thermal performance of the heat exchanger led to the development and use of many techniques termed as heat transfer augmentation techniques. In general, heat transfer augmentation methods are classified into three broad categories: active, passive and compound techniques. Active method involves the use of some external power input, passive techniques generally make modifications in surface or geometry with the help of additional devices and compound technique is a combination of different methods. The passive techniques require no external power supplies which make them popular and effective. Thus researchers have been looking for devices to enhance the mixing, swirling and turbulence intensity of the fluid flow to obtain higher value of heat transfer. These researches led to new types of swirl flow generators. Among them, twisted tape (TT) is one of the main inserts which can improve heat transfer rate. The important factors related to twisted tapes are it increases the turbulence of the flow, higher tangential velocity near the tube walls, more mixing of fluid, the fin effect of twisted tapes which increases heat conduction area. Helical screw tape insert is another variation of twisted tape which is effective. Smith Eiamsa-ard et al [1] conducted an experimental study on a circular tube fitted with helical insert and used hot air as the fluid. The result shows that the increase in heat transfer and friction factor is due to the swirling motion induced by the helical screw tape insert. P.Sivashanmugam et al. [2] experimentally investigated heat transfer and friction factor characteristics of water in laminar flow through a circular tube fitted with regularly spaced helical screw-tape inserts and presented the effective performance of the insert. Suhas V. Patil et al [3] showed that helical screw tape inserts are more effective than the twisted tapes in a square duct.

Low performance of conventional fluids like water led to different fluid additives for different properties. This led to the development of nanofluids, coined by S.U.S Choi et al [4]. They are suspension of metallic nanoparticles (1 to 100 nm) in conventional heat transfer fluids. In nanofluids, the particle size is very small and also they are in small volume fraction, thus the problems such as clogging and pressure drop increase become insignificant in case of nanofluids. Since heat transfer takes place at the surface of the particle, relative large surface area of nanoparticles provide a greater advantage. Also, low inertia leads to little erosion of the pipes. Wen [5] studied about $Al_2O_3$/water nanofluid and reported an increase in heat transfer coefficient with Reynolds number and nanoparticles concentration. S. Suresh, K.P.Venkitaraj et al [6] made comparative study on the thermal performance of helical screw tape inserts using $Al_2O_3$/water and CuO/water nanofluids. The results showed the effectiveness of helical screw tape inserts and also

CuO/water nanofluids gave better heat transfer than $Al_2O_3$/water nanofluid.

The most desired type of insert is the one which yields excellent heat transfer with minimum pressure drop. Modifications for helical screw tape insert aren't found reported extensively. This experimental investigation reports the thermal performance of perforated helical screw tape inserts with and without wings and $Al_2O_3$/water nanofluid by studying the heat transfer and pressure drop characteristics of this compound technique.

## II. Experimental Setup

The experimental set up (Fig. 1) consists of a test section, calming section, pump, cooling unit and a fluid reservoir. The calming section and the test section are provided for a length of 1000 mm and are made of copper tube of 10 mm inner diameter and 1 mm thickness. The tube is wounded by nichrome heating coil of resistance 103 Ω for heating the tube. There are 5 temperature measuring points located in the axial positions (at distance 150, 300, 500, 700 and 900mm from inlet) for measuring the wall temperature. The temperature probes used are RTD PT100. Two RTDs are used for measuring the fluid in and fluid out temperatures and the remaining 5 measures the wall temperatures. Pressure tapings are made for connecting a U- tube mercury manometer just before the inlet of test section and just after the test section. Electricity is passed on to the test section through the terminals of the heating coil. Using a dimmerstat the required amount of power can be supplied. A peristaltic pump is used to circulate the fluid. It has flow rate ranging from 332.5 ml/min to 3430 ml/min. The fluid after passing through the heated test section flows through a riser section and then through the air cooled cooling unit and is collected in the reservoir.

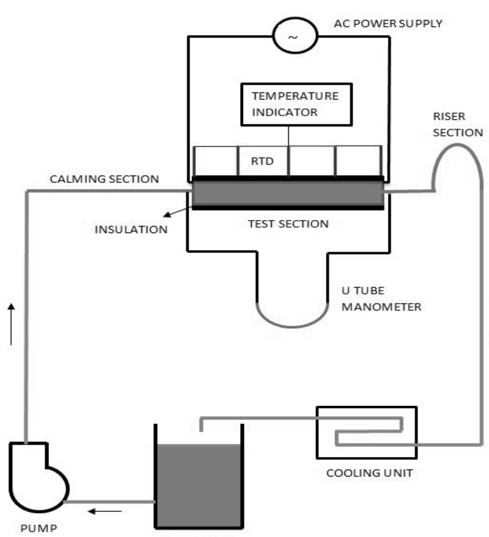


Fig. 1 Schematic diagram of the experimental setup

## III. Details of Insert

The helical screw tape inserts were made by winding uniformly a copper strip of 3.5 mm width over a 2.5 mm brass rod. Three inserts having twist ratio 1.2, 1.7 and 2.5 were made. For an insert the twist ratio, Y is defined as the ratio of length of one twist (pitch, P) to the diameter of the twist (D). Then the three inserts were modified by creating holes of 1.5 mm. Furthermore, a cut was made on the edge between two holes and the cut was tilted at an angle of 45°. These modifications created perforated helical screw tape inserts with wings.

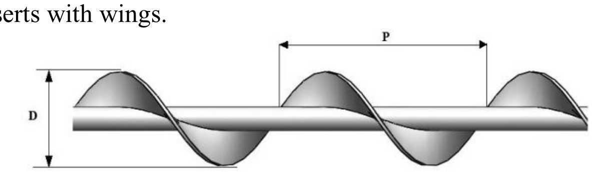


Fig. 2 Geometrical configurations of helical screw tape insert

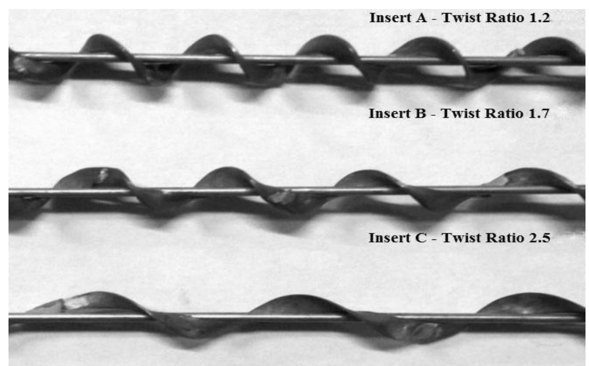


Fig. 3 Helical screw tape inserts before modifications

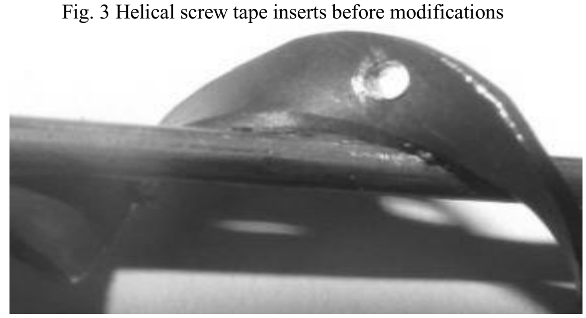

Fig. 4 View of a section of the perforated insert

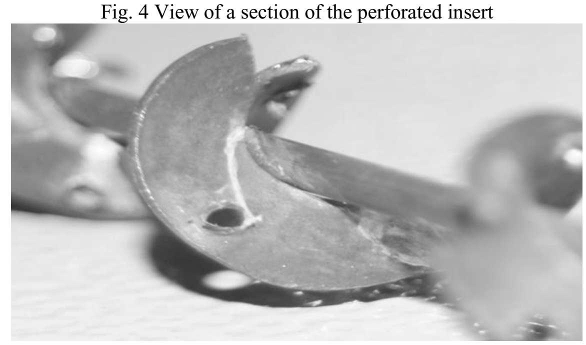

Fig. 5 Isometric view of a section of a perforated insert with wings

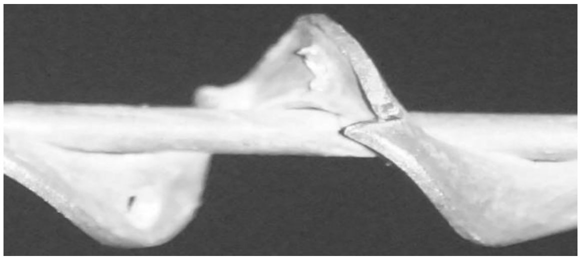

Fig. 6 Top view of a section of the perforated insert with wing

## IV. NANOFLUID PROPERTIES AND PREPARATION

Aluminium oxide nanoparticles purchased from Alfa Aesar was used for nanofluid preparation. The company specified the product as Alumina ($Al_2O_3$), NanoDur 99.5%, APS = 40-50 nm, SA= 32-40 $m^2$/g, MW= 101.96. $Al_2O_3$/water nanofluid of 0.1 volume concentration was prepared by dispersing the required amount of nanoparticles in deionized water and ultrasonic vibrator was used to obtain a stable suspension.

The density of nanofluid was determined using Pak and Cho's equation [7].

$$\rho_{nf} = \phi\rho_s + (1-\phi)\rho \quad (1)$$

The thermal conductivity of the nanofluid was determined using Maxwell's model [8] for volume fraction less than one.

$$\frac{k_{nf}}{k} = \frac{k_s + 2k + 2\phi(k_s - k)}{k_s + 2k - \phi(k_s - k)} \quad (2)$$

The specific heat of the nanofluid is calculated using Xuan and Roetzel's equation [9]

$$(\rho C_p)_{nf} = (1-\phi)(\rho C_p) + \phi(\rho C_p)_s \quad (3)$$

The measurement of viscosity of the nanofluid was done using Brookfield Rotational Viscometer (model: DV2TLVCJ0) supplied by Brookfield Engineering Laboratories.

## V. EXPERIMENTAL PROCEDURE

The peristaltic pump was switched on and the flow rate to the test section was maintained by adjusting the speed of rotation of the pump. With the help of an auto transformer, a constant heat flux was set by adjusting the electrical voltage. The steady state was reached within 1 hour initially. The required temperature readings of fluid and wall temperatures are noted. Ammeter and voltmeter readings gave the input power. The pressure drop was measured with the help of U-tube manometer. Next the flow rate was varied by adjusting the pump speed. After the first run steady state was achieved within half an hour. Experiments were conducted for plain tube, and subsequently by inserting the helical screw tape inserts using water and nanofluid.

## VI. DATA REDUCTION

Total heat produced by the electrical winding is

$$Q_e = V \times I \quad (4)$$

Considering a loss of 5 %, the actual value of heat produced is

$$Q_1 = 0.95 \times Q_e \quad (5)$$

Total heat absorbed by the fluid is

$$Q_2 = m\, C_p(T_{out} - T_{in}) \quad (6)$$

Average value of heat transfer

$$Q = (Q_1 + Q_2)/2 \quad (7)$$

Heat flux

$$q = Q/\pi DL \quad (8)$$

The average heat transfer coefficient

$$h = q / (T_{wavg} - T_{favg}) \quad (9)$$

The average Nusselt Number

$$Nu = hD / k \quad (10)$$

The local heat transfer coefficient

$$h_x = q / (T_{wx} - T_{fx}) \quad (11)$$

The local fluid temperature

$$T_{fx} = T_{fin} + (qs_x / \rho C_p A v) \quad (12)$$

The local Nusselt Number

$$Nu = h_x D / k \quad (13)$$

The pressure drop across the section is

$$\Delta P = (\rho_m - \rho_w)\, g\, h \quad (14)$$

The friction factor

$$f = 2\Delta PD / \rho v^2 L \quad (15)$$

Thermal performance factor is the ratio of Nusselt number for tube with insert to that of the plain tube at the same level of pumping power. Usui and Sano [10] performed performance evaluation analysis for the same pumping power for laminar flow and turbulent flow and proposed the following equations,

For laminar flow

$$\eta = \frac{\frac{Nu}{Nu_{pt}}}{\left(\frac{f}{f_{pt}}\right)^{0.1666}} \quad (16)$$

For turbulent flow

$$\eta = \frac{\frac{Nu}{Nu_{pt}}}{\left(\frac{f}{f_{pt}}\right)^{0.3333}} \quad (17)$$

## VII. RESULTS AND DISCUSSION

### *A. Experimental Validation*

For validating the experimental setup, experiments were conducted in plain tube using water in at constant heat flux boundary condition. In the laminar flow range the experimental data was compared with Shah Equation [11]. The Reynolds number used for validation is 989.54

$$Nu = 1.953(RePrD/x)^{0.3333} \text{ for } RePrD/x \geqslant 33.33 \quad (18)$$

In turbulent flow, the data was compared with Gnielinskis equation [12]

$$Nu = \frac{\epsilon/2\,(Re - 1000)Pr}{1 + 12.7\left(\frac{\epsilon}{2}\right)^{0.5}\left(Pr^{\frac{2}{3}} - 1\right)} \quad (19)$$

where $\varepsilon = 1 / (1.58\ln Re - 3.82)^2$

The experimental friction factor was compared with Hagen Poiseuille equation in laminar flow

$$f = 64/Re \quad (20)$$

and Blasius equation in turbulent flow

$$f = 0.316 / Re^{0.25} \quad (21)$$

From the figures 7, 8, 9 and 10 it can be seen that theoretical and experimental values showed a good agreement.

*B. Heat Transfer Study*

Experiments were conducted on the plain tube with water and aluminium oxide nanofluid of 0.1 % volume concentration before trying out the inserts. Nusselt number increased with increase in Reynolds number for both fluids, also $Al_2O_3$/water nanofluid gave higher Nusselt number than water. There is an average increase of 6.7 % in Nusselt number when nanofluid is used instead of water.

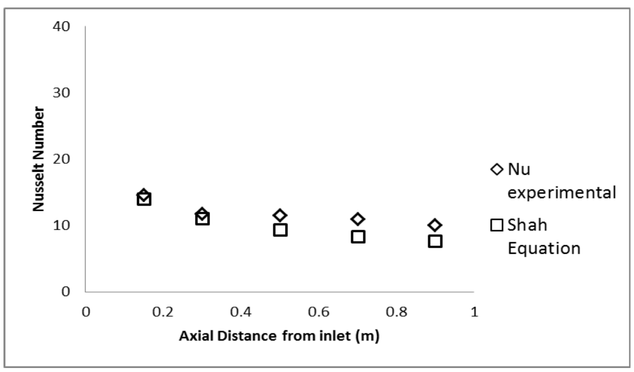


Fig. 7 Comparison of experimental Nusselt number with Shah´s equation

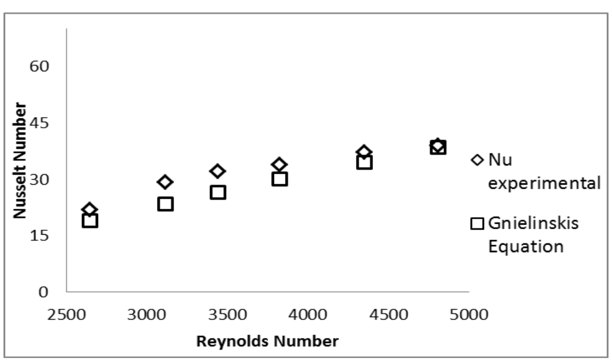


Fig. 8 Comparison of experimental Nusselt number with Gnielinskis equation

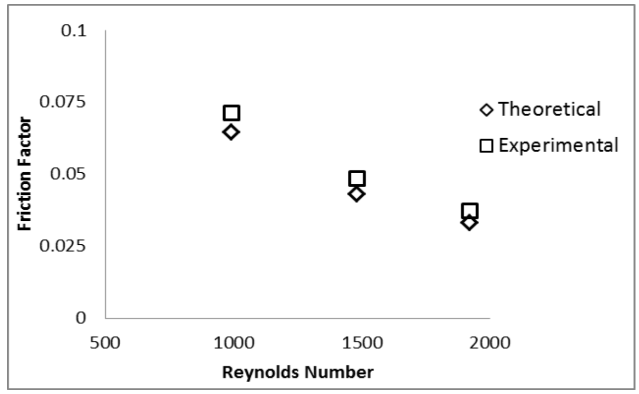


Fig. 9 Friction factor vs. Reynolds number in plain tube in laminar flow

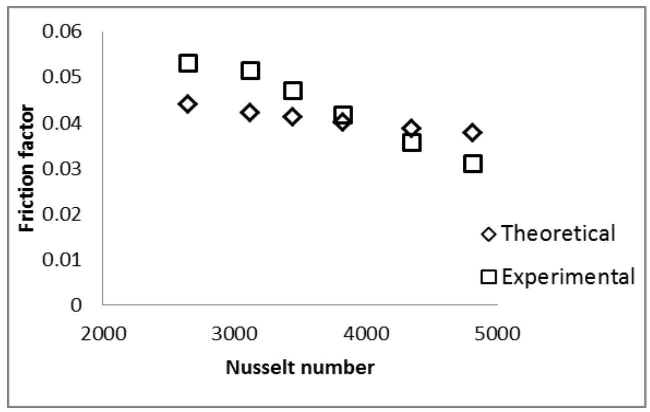


Fig. 10 Friction factor vs. Reynolds number in plain tube in turbulent flow

The results also suggest that there is no considerable difference in friction factor between water and $Al_2O_3$/water nanofluid. Higher thermal conductivity of the nanofluid and Brownian motion of the nanoparticles provides this enhancement in heat transfer than water.

With the usage of insert, there is increase in heat transfer for both the fluids. All the three inserts gave enhancement in heat transfer. The increase in Nusselt number decreases increase in twist ratio. Comparing with the plain tube with water as test fluid, the average value of enhancement for the perforated insert without wings of twist ratio 1.2, 1.7 and 2.5 are 238%, 210% and 178% respectively. When used with the nanofluid, the heat transfer enhancement for the inserts of twist ratio 1.2, 1.7 and 2.5 are 343%, 218% and 187 % respectively. After providing wings to the insert an additional average enhancement of 13 % was obtained. Higher tangential velocity near the tube walls, mixing of fluid and turbulence in flow due to the presence of wings and holes provides this enhancement in heat transfer.

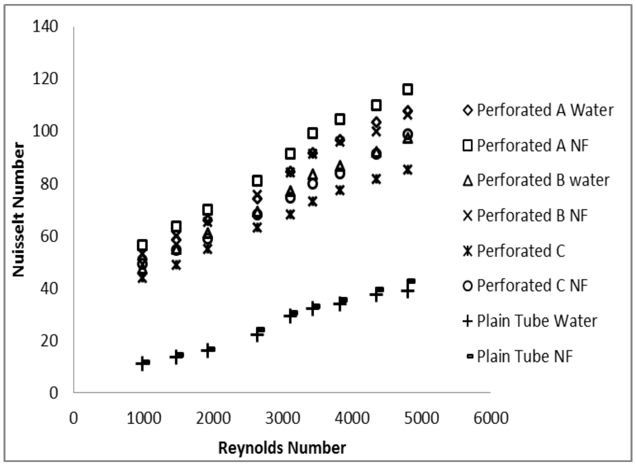


Fig. 11 Nusselt number vs. Reynolds number for inserts without wings

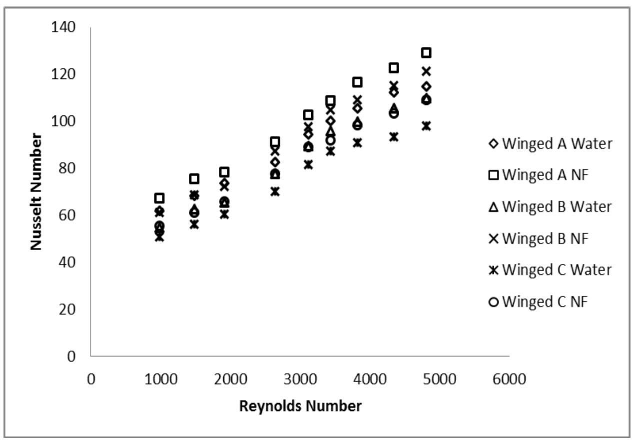


Fig. 12 Nusselt number vs. Reynolds number for inserts with wings

*C. Pressure Drop Study*

With the addition of the insert to the tube, there is increase in the pressure drop than plain tube due to the increase of contact area and more resistance to the flow. The value of friction factor got decreased with increase in twist ratio. Comparing the two test fluids used, water and $Al_2O_3$/water nanofluid, there was no significant difference in the pressure drop created.

Comparing with the plain tube, the average increase in friction factor for the perforated insert without wings of twist ratio 1.2, 1.7 and 2.5 are 29, 25 and 18 times respectively. After providing wings to the insert an additional average increase of 20% was seen.

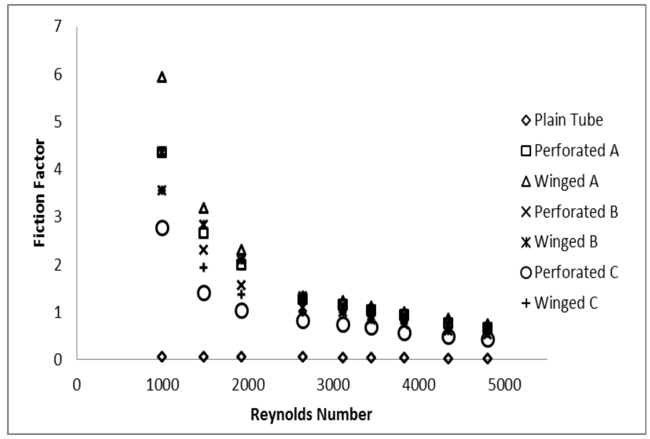


Fig. 13 Friction factor vs. Reynolds number for inserts

*D. Evaluation of Thermal Performance*

Even though the usage of insert show high enhancement in the heat transfer, the increase in the pressure drop is a demerit. The technique becomes effective when it has a thermal performance factor greater than one. It can be seen that the value of thermal performance factor value decreased with increase in Reynolds number. It can be also seen that the value of thermal performance factor decreased with increase in twist ratio. This is due to the stronger turbulence generated by the insert with smallest twist ratio. Laminar flow region showed higher values in thermal performance factor than turbulent flow range. Its reason can be that the increase pressure loss with Reynolds number could not be compensated with the increase in heat transfer. The results obtained show that in each twist ratio, the perforated insert with wings when used along with water and nanofluid has good thermal performance factor in laminar and turbulent flow than the perforated insert without wings.

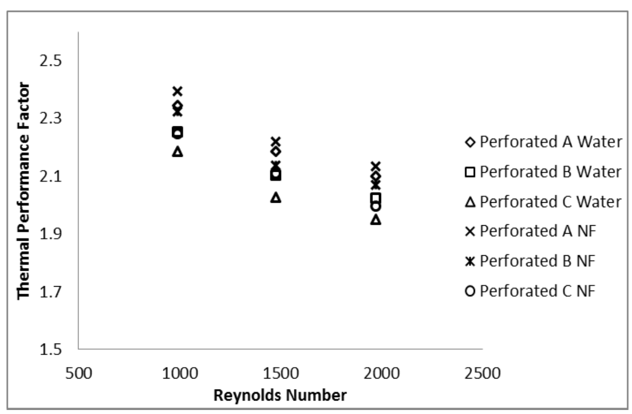


Fig. 14 Thermal performance factor in laminar flow for inserts without wings

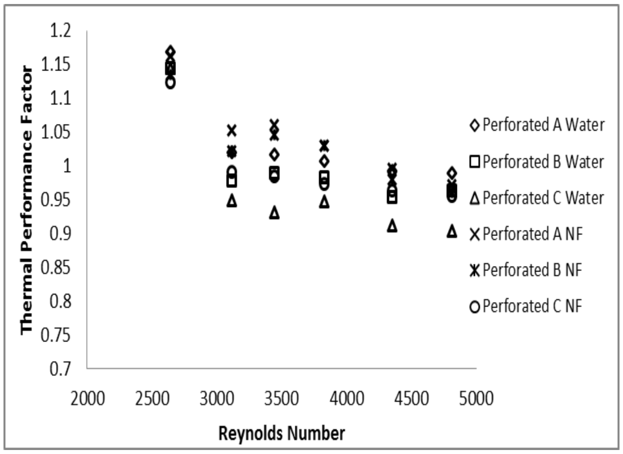


Fig. 15 Thermal performance factor in turbulent flow for inserts without wings

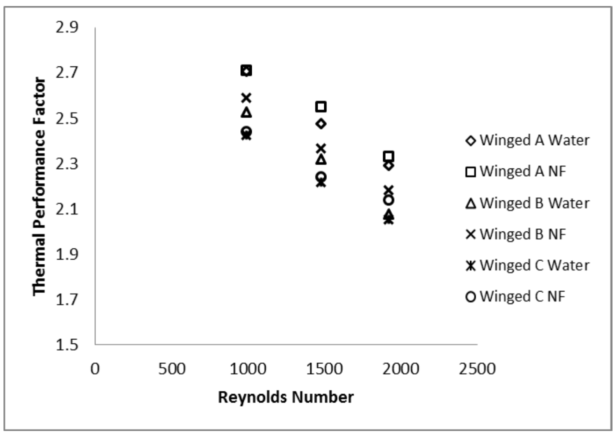


Fig. 16 Thermal performance factor in laminar flow for inserts with wings

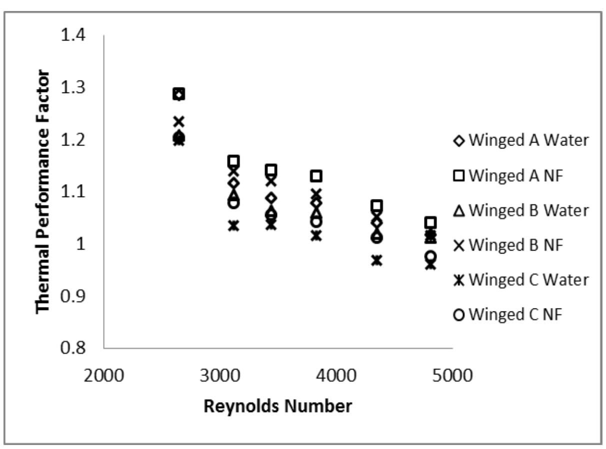


Fig. 17 Thermal performance factor in turbulent flow for inserts with wings

## VIII. Conclusions

An experimental investigation was done into the compound technique created using perforated helical screw tape insert with wings and $Al_2O_3$/water nanofluid. The study was done on a copper pipe of 10 mm inner diameter and 1000 mm length at constant heat flux boundary condition. The value of Nusselt number increases and friction factor decreases with increase in Reynolds number for both fluids with and without insert. Nusselt number and friction factor increases with decrease in twist ratio. $Al_2O_3$/water nanofluid gave higher Nusselt number than water. When the perforated insert was provided with wings, it showed better thermal performance factor than the insert without wings. The combination of perforated helical screw tape insert with wings of twist ratio 1.2 along with $Al_2O_3$/water nanofluid gave the best thermal performance factor for all Reynolds number among different combinations.


## Acknowledgement

The authors would like to extend their thanks to Central Gov. of India for the financial support under grant by TEQIP Phase II to this work and to Department of Mechanical Engineering, College of Engineering Adoor, Kerala.


## References


[1] Smith Eiamsa-ard, Yuttana Ploychay, Somchai Sripattanapipat and Pongjet Promvong, "An experimental study of heat transfer and friction factor characteristics in a circular tube fitted with a helical tape", Proceedings of the 18th Conference of Mechanical Engineering Network of Thailand (2004) International Journal of Scientific and Research Publications, Volume 4, Issue 4, April 2014.

[2] P. Sivashanmugam , S. Suresh, "Experimental studies on heat transfer and friction factor characteristics of laminar flow through a circular tube fitted with regularly spaced helical screw-tape inserts", Elsevier Experimental Thermal and Fluid Science 31 (2007)301–308

[3] Suhas V. Patil , P. V.Vijay Babu, Heat Transfer Augmentation in a Circular tube and Square duct Fitted with Swirl Flow Generators: A Review International Journal of Chemical Engineering and Applications, Vol. 2 , No. 5 (2011) 326-331

[4] S.U.S. Choi, Enhancing thermal conductivity of fluids with nanoparticles, in: D.A. Signer, H.P. Wang (Eds.), Developments Applications of Non-Newtonian Flows, FED-vol. 231/MD-vol. 66, ASME, New York, NY, USA, 1995, pp. 99–105.

[5] Dongsheng Wen, Yulong Ding, "Experimental investigation into convective heat transfer of nanofluids at the entrance region under laminar flow conditions", International Journal of Heat and Mass Transfer 47 (2004) 5181– 5188

[6] S. Suresh , K.P. Venkitaraj, P. Selvakumar , "Comparative study on thermal performance of helical screw tape inserts in laminar flow using $Al_2O_3$/water and CuO/water nanofluids", Elsevier Superlattices and Microstructures 49 (2011) 608–622

[7] B.C. Pak, Y. Cho, "Hydrodynamic and heat transfer study of dispersed fluids with submicron metallic oxide particle", Experimental Heat Transfer 11 (1998) 151–170.

[8] J.C. Maxwell, Treatise on Electricity and Magnetism, Dover, New York, 1954.

[9] H. Usui, Y. Sano, K. Iwashita, A. Isozaki, “Enhancement of heat transfer by a combination of internally grooved rough tube and twisted tape”, International Chemical Engineering 26 (1) (1996) 97–104.

[10] Y. Xuan, W. Roetzel, “Conceptions for heat transfer correlation of nanofluids”, International Journal of Heat and Mass Transfer 43 (2000) 3701–3707.

[11] R.K. Shah, “Thermal entry length solutions for the circular tube and parallel plates”, in: Proceedings of Third National Heat Mass Transfer Conference, Indian Institute of Technology, Bombay, 1975, pp 11-75.

[12] V. Gnielinski, “New equations for heat and mass transfer in turbulent pipe and channel flow”, Int. Chem. Eng. 16 (1976) 359–368.

# Performance Studies on a Vapour Compression System Using Nanolubricants

Aswin Mohan[#1], Subramani N[*2], Jose Prakash M[$3]

[#]*Department of Mechanical Engineering, Sree Buddha College of Engineering, Alapuzha, Kerala, India*
[1]aswinmohan88@gmail.com

[*]*Department of Mechanical Engineering, ACE College of Engineering, Trivandrum, Kerala, India*
[2]npskalyan@gmail.com

[$]*Department of Mechanical Engineering, TKM College of Engineering, Kollam, Kerala, India*
[3]jpmmech@yahoo.co.in

***Abstract* - In the face of imminent energy resource crunch there is need for developing refrigeration and air conditioning systems which are energy efficient. The performance of a vapour compression refrigeration system can be improved by adding nanoparticles to the lubricant and refrigerant. This paper deals with the experimental study on a vapour compression refrigeration system with different nanolubricants and nanorefrigerants and the results were theoretically verified. It is found that the freezing capacity is higher and the power consumption reduces by 28 % when Polyoil-ester (POE) oil is replaced by a mixture of mineral oil and cupric oxide nanoparticles. It is also found that the increase in actual coefficient of performance is 37% and the enhancement factor in the evaporator is 1.54, when nanorefrigerant is used instead of pure refrigerant.**

***Keywords*- Nanorefrigerants, nanolubricants, enhancement factor, freezing capacity, COP**

## I. INTRODUCTION

Present day mankind depends heavily on refrigeration for daily needs and these cover a wide range of applications such as food processing, preservation and transport, comfort cooling, commercial and industrial air conditioning, manufacturing etc. Refrigeration systems consume a substantial amount of energy. Taking for instance supermarket refrigeration systems as an example, they can account for up to 50-80% of the total energy consumption. The energy efficiency is a prime mover in reducing energy consumption and global warming emissions. In respect to this new technologies to conserve energy are under continuous development.

The rapid advances in nanotechnology have lead to emerging of new generation heat transfer fluids called nanofluids. Nanofluid is a mixture of host/base fluid and nano-sized particles having size in the range 1 to100 nm. The nanoparticles usually used for the preparation of nanofluids are metal, metal oxide and carbon nanotube(CNT) and they have higher thermal conductivity than the base fluids. Nanofluids have the following characteristics compared to the normal solid liquid suspensions i) higher heat transfer between the particles and fluids due to the high surface area of the particles ii) better dispersion stability with predominant Brownian motion iii) reduces particle clogging iv) reduced pumping power as compared to base fluid to obtain equivalent heat transfer (Choi SUS,1995). Keblinski et al. (2005) conducted studies on nanofluids and found that there is a significant increase in the thermal conductivity of nanofluids compared to the base fluid. They also found that addition of nanoparticles results in significant increase in the critical heat flux.

Recently researchers used nanoparticles in refrigeration systems in order to improve its performance. The nanoparticles can be added to the lubricant used in the compressor and also to the refrigerant. Nanolubricant is a type of nanofluid which is prepared by adding nanoparticles to the lubricant. Nanorefrigerant is another kind of nanofluid in which nanoparticles are dispersed in the refrigerant. In a refrigeration system where the refrigerant comes into contact with the lubricant, the nanorefrigerant will be a mixture of refrigerant, lubricant and nanoparticles. The advantages of adding nanoparticles to the refrigeration system are manifold (i) Addition of nanoparticles to the lubricant improves tribological characteristics of the lubricant, so that there is improvements in the performance of the compressor. (ii)addition of nanoparticles to the refrigerants improves the thermo physical and heat transfer characteristics of the refrigerant which in turn results in the enhancement in the refrigerating effect(iii) presence of nanoparticles in the refrigeration system enhances the solubility between the lubricant and refrigerant and returns more lubricant oil back to the compressor(Wang et al,2003). Bi et al. (2007, 2008) conducted studies on a domestic refrigerator using nanorefrigerants. In their studies R134a was used the refrigerant, and a mixture of mineral oil $TiO_2$ was used as the lubricant. They found that the refrigeration system with the nanorefrigerant worked normally and efficiently and the energy consumption reduces by 21.2% compared to R134a/POE oil system and later they reported that there is remarkable reduction in the power consumption and significant improvement in freezing capacity. Jwo et al. (2009) carried out studies on a refrigeration system replacing R-134a and polyester oil with a hydrocarbon and mineral oil.

Their studies show that the optimum value of mass fraction of $Al_2O_3$ nanoparticles is 0.1 % and the power consumption is reduced by about 2.4%, and the coefficient of performance is increased by 4.4%. Peng et al. (2010) conducted experimental studies on nucleate pool boiling heat transfer characteristics of refrigerant/oil mixture with diamond nanoparticles. The refrigerant used is R113 and the oil is VG68. They found out that the nucleate pool boiling heat transfer coefficient of R113/oil mixture with diamond nanoparticles is larger than the R113/oil mixture. A correlation was proposed for predicting the nucleate pool boiling heat transfer coefficient of refrigerant/oil mixture with nanoparticles. Henderson et al. (2010) conducted an experimental study on the flow boiling heat transfer of R134a based nanofluids in a horizontal tube and found excellent dispersion of CuO nanoparticle with R134a and POE oil. It is reported that the heat transfer coefficient increases by more than 100% over baseline R134a/POE oil case. Bobbo et al. (2010) conducted studies on the influence of dispersion of single wall carbon nanohorns (SWCNH) and $TiO_2$ on the tribological properties of POE oil. Studies were carried at different temperatures and reported that the tribological behavior of the base lubricant can either be improved or worsened by adding nanoparticles. Bi et al. (2011) conducted an experimental study on the performance of a domestic refrigerator using $TiO_2$-R600a nanorefrigerant as working fluid and reported that the system worked normally and efficiently and the energy consumption reduces by 9.6%. The purpose of this article is to report the results obtained from the experimental studies on a vapour compression system. In the present study the refrigerant selected is R134a, because it one of the most widely used alternate refrigerant in lots of countries, though its global warming up potential is high. The lubricants used are POE oil and SUNINSO 3GS mineral oil and both are miscible with R134a (Wang et al, 2003). The nanoparticles used are $Al_2O_3$ and CuO.

## II. EXPERIMENTAL SETUP

A refrigeration test rig which consists of a compressor, air-cooled condenser, thermostatic expansion valve and an evaporator was designed and fabricated. The compressor used is a hermetically sealed reciprocating compressor. The evaporator is in the form of a cylindrical spiral coil and is completely immersed in water (cooling load). A serpentine coil finned tube heat exchanger is used as the condenser and it is cooled using a fan. Both evaporator and condenser are made of copper. Bourdon tube pressure gauges are used to measure the pressures at salient points of the refrigeration system. T- Type thermocouples (36 SWG) are used to measure the temperature at the various locations. The thermocouples were calibrated using a constant temperature bath (JulaboF25). The temperature data was acquired using a temperature scanner and the power consumption of the compressor is measured using a digital energy meter. The experimental setup used for the present study is shown in Figure 1.

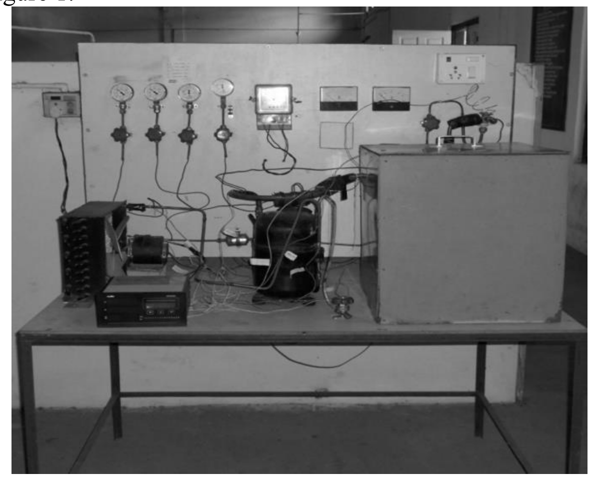

*Fig. 1. Photograph of the experimental set up*

Before charging the test rig with the refrigerant, the system was checked thoroughly for leaks. Leak testing was carried out by charging the system with nitrogen gas at a pressure of 200 Psi. After the leak test the system was properly evacuated using a vacuum pump. The compressor was filled with nanolubricant and the system was charged with the refrigerant.

## III. PREPARATION OF NANOLUBRICANT

Preparation of nanolubricant and nanorefrigerant is the first step in the experimental studies. Nanolubricants and nanorefrigerants are nanofluids and they are not simply liquid-solid mixtures. Special requirements are even, stable and durable suspension, negligible agglomeration of particles, and no chemical change of the fluid. The nanolubricant can be prepared by dispersing nanoparticles in to the lubricant using an ultrasonic agitator. Nanorefrigerants can be prepared in two ways. In the case refrigerants like R113 which is in the liquid state at room temperature and atmospheric pressure, the nanoparticles can be directly dispersed in the refrigerant using an ultrasonic agitator. In the case of refrigerants like R134a which is not in the liquid state at room temperature and pressure, the nanoparticles can be dispersed in the lubricating oil using an ultrasonic agitator and this nanolubricant is filled in the hermetic compressor. The refrigerant will carry traces of nanolubricant which contains nanoparticles. The refrigerant used for the present study is R134a and the nanoparticles are dispersed in the lubricant. The nanoparticles used are aluminium oxide and cupric oxide. The average particle size of both aluminium oxide and cupric oxide nanoparticles (manufactured by Sigma Aldrich) is less than 50nm and the mass fraction of nanoparticles used for the preparation of the nanolubricant is 0.06%. An ultrasonic vibrator (Micro clean 102, Oscar Ultrasonics) is used for the uniform dispersion of the nanoparticles and it took about 24 hours of agitation to achieve the same. Experimental observation shows that the stable dispersion of alumina and cupric oxide nanoparticles can be kept for more than 3 days without coagulation or deposition. Here the working fluid will be a mixture of refrigerant and small amounts of lubricant and nanoparticles and here after this mixture will be referred as nanorefrigerant.

## IV. THEORETICAL ANALYSIS

In order to estimate the heat transfer coefficient in the refrigerant side of the evaporator the thermophysical properties of the nanorefrigerant have to be calculated. The thermophysical properties of the nanorefrigerant are calculated in two steps, firstly thermophysical properties of the nanoparticles oil mixture are calculated and this data is used to calculate the properties of nanorefrigerant.

### *A. Calculation of Thermophysical Properties of Nanolubricant*

The following correlations are used to calculate the thermo physical properties of nanolubricant

Specific heat (Cp) of nanolubricant (Pak. B.C., Cho. Y.I. (1998)), $Cp_{n,o} = (1-\psi_n)\, Cp_o + \psi_n\, Cp_n$ (1)

Where subscript n,o = nanoparticle and oil

Thermal conductivity (K) nanolubricant, (Hamilton. R.L., Crosser. O.K., (1962))

$$K_{n,o} = K_o[(K_n+2K_o- 2\psi_n(K_o-K_n)) / (K_n+2K_o+ \psi_n (K_o-K_n))] \tag{2}$$

Viscosity of nanolubricant (Brinkman. H.C., (1952)),

$$\mu_{n,o} = \mu_o [1 / (1- \psi_n)^{2.5}] \tag{3}$$

Density of nanolubricant, $\rho_{n,o} = (1- \psi_n)\, \rho_o + \psi_n\, \rho_n$, (4)

Volume fraction of nanoparticle in the nanoparticle-oil suspension,

$$\psi_n = \omega_n \rho_o / [\omega_n\rho_o + (1-\omega_n)\rho_n] \tag{5}$$

Mass fraction in the nanoparticle oil suspension,

$$\omega_n = m_n/(m_n+m_o) \tag{6}$$

### B. *Calculation of thermo-physical properties nanorefrigerant*

Specific heat of the nanorefrigerants (Jensen. M.K., Jackman. D.L., (1984))

$$Cp_{r,n,o,f} = (1-X_{n,o})\, Cp_{r,f} + X_{n,o}Cp_{n,o}, \tag{7}$$

Where subscript r,n,o = refrigerant, nanoparticle and oil

Viscosity of the nanorefrigerants (Kedzierski. M.A., Kaul. M.P., (1993))

$$\mu_{r,n,o,f} = \exp (X_{n,o}\ln\mu_{n,o} + (1-Xn,o)\ln\mu_{r,f}), \tag{8}$$

Thermal conductivity of the nanorefrigerants (Baustian et.al, (1988))

$$K_{r,n,o,f} = K_{r,f}(1-X_{n,o}) + (K_{n,o}X_{n,o}) - (0.72X_{n,o} (1- X_{n,o})(K_{n,o}- K_{r,f})), \tag{9}$$

Density of the nanorefrigerants

$$\rho_{r,n,o,f} = [(X_{n,o}/\rho_{n,o}) + ((1-X_{n,o})/ \rho_{r,f})]^{-1} \tag{10}$$

Nanoparticle/oil suspension concentration,

$$X_{n,o} = m_{n,o} / (m_{n,o} + m_r) \tag{11}$$

### C. *Calculation of heat flux and heat transfer coefficient in the refrigerant side of the evaporator*

The heat flux (q) is calculated from the formula proposed by Hao Peng et. Al, (2010)

$$\Delta T_b = \frac{C_{sf} h_{fg}}{C_{p,r,n,o,f}} \left[ \frac{q}{\mu_{r,n,o,f} h_{fg}} \sqrt{\frac{\sigma_{r,n,o}}{g\left(\rho_{r,n,o,f} - \rho_{r,g}\right)}} \right]^{0.33} \left[ \frac{C_{p,r,n,o,f}\, \mu_{r,n,o,f}}{K_{r,n,o,f}} \right]^{n} \tag{12}$$

Where $h_{fg}$ =latent heat of vaporization, $\rho$ = Density, $\mu$ =Viscosity

$$\Delta T_b = T_w - T_{sat} \text{ , where, T = Temperature} \tag{13}$$

Surface tension of nanorefrigerants

$$\sigma_{r,n,o}= \sigma_r + (\sigma_{n,o} - \sigma_r)\, X_{n,o}^{0.5} \tag{14}$$

(Jensen. M.K., Jackman. D.L., (1984))

$$\mathbf{C_{sf}} = \exp (-8.062-1.789\omega_n+ 2.786X_{n,o}) \quad \text{and} \quad n = 1.085 \tag{15}$$

The boiling heat transfer coefficient of refrigerant/oil mixture with nano particles,

$$h_{r,n,o} = q / \Delta T_b \tag{16}$$

The value of heat transfer coefficient without nanoparticles is calculated using the boiling correlations for conventional refrigerants

The energy enhancement factor (E.F) is calculated using the equation $E.F = h_{r,n,o} / h_{r,o}$ (17)

where subscript r,o = refrigerant and oil

Figure 2 shows the pressure enthalpy diagram of an ideal vapour compression refrigeration system. Here process 1-2 is the compression process in the compressor, 2-3 is the condensation process, 3-4 is the expansion process in the expansion device and 4-1 is the evaporation process.

The theoretical C.O.P is calculated using the equation $C.O.P_{th}= (h_1 - h_4) / (h_2 - h_1)$ (18)

$h_1$ – enthalpy of refrigerant at the inlet of the compressor

$h_2$ – enthalpy of refrigerant at the outlet of the compressor

$h_4$ – enthalpy of refrigerant at the inlet of the evaporator

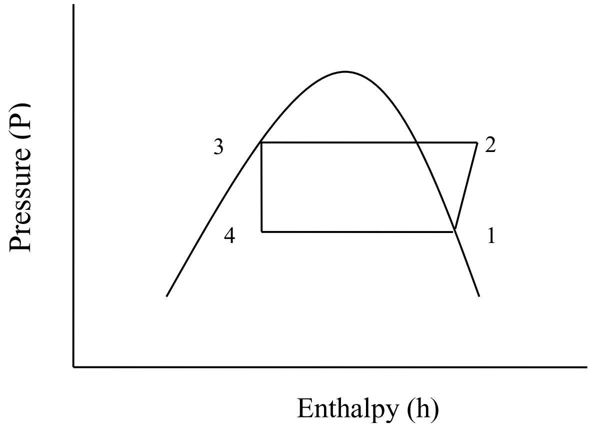


*Fig. 2. Pressure enthalpy diagram of the vapour compression cycle*

The values of the enthalpy are taken from refrigerant tables. The actual C.O.P is calculated using relation

$$C.O.P_{act} = \text{cooling load / power input} \quad (19)$$

## V. RESULTS AND DISCUSSION

In the present study the refrigerant selected is R134a, because it one of the most widely used alternate refrigerant in lots of countries, though its global warming up potential is high. Four cases have been considered i.e. the hermetic compressor filled with i) pure POE oil ii) SUNISO 3GS oil (mineral oil) and iii) SUNISO 3GS+ alumina nanoparticles and iv) SUNISO 3GS+ CuO nanoparticles. In the first two cases the working fluid is a mixture of refrigerant and small amount of lubricant and in the second and third cases the working fluid is a mixture of refrigerant and small amounts of lubricant and nanoparticles (nanorefrigerant). The lubricants POE oil and SUNINSO 3GS mineral oil with nanoparticles are miscible with R134a (Wang et al, 2003). The amount of lubricant /nanolubricant filled in the compressor is same and the mass fraction of nanoparticles added in the lubricant is 0.06%. In all the four cases the refrigeration system is charged with the same amount of refrigerants.

Theoretical analysis shows that the enhancement factor in the evaporator with alumina nanorefrigerant and cupric oxide nanorefrigerant are 1.5338 and 1.5449 respectively. That means the heat transfer coefficient in the evaporator increases by 53% with alumina nanorefrigerant and 54% with cupric oxide nanorefrigerant compared to pure R134a. The value of heat transfer coefficient without nanoparticles is calculated using the boiling correlations for conventional refrigerants and its value is found to be 1612 $Wm^{-2}K^{-1}$. Peng et.al (2010) have reported that the value of energy enhance factor is in the range 1.17 – 1.63.

The cooling load temperature – time history is shown in figure 3 and the freezing capacity for the four cases is shown in figure 4.

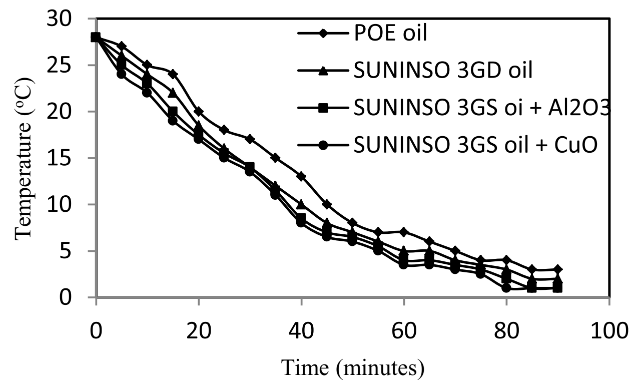


*Fig. 3: Temperature-Time history*

In all the cases the condenser pressure is 1.2 MPa (180 Psi) and the evaporator pressure is 0.2 MPa (30 Psi). No appreciable pressure drops due to friction were observed in the condenser and evaporator. From the figures 3 and 4 it is clear that, the time required for reducing cooling load temperature from 28°C to 1°C is least for SUNISO 3GS oil + CuO nanorefrigerant the and its value is found to be 80 minutes. The corresponding value for pure POE oil+ pure refrigerant is 110 minutes i.e. the time required for reducing the cooling load temperature decreases by 27 % if SUNISO 3GS oil + CuO nanorefrigerant is used instead of POE oil+ pure refrigerant.

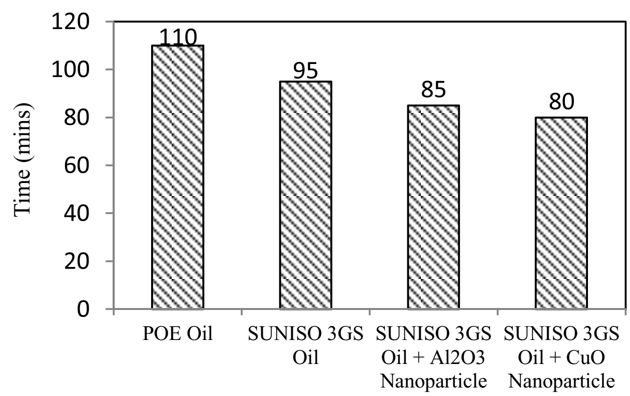


*Fig.4 Effect of nanoparticles on the freezing Capacity*

The time required for the same reduction in cooling load temperature for SUNISO 3GS oil + alumina nanorefrigerant is 85 minutes. This enhancement in freezing capacity with nanorefrigerant is due to the fact that the nanoparticle present in the refrigerant enhances the heat transfer rate in the refrigerant side of the evaporator.

Figure 5 shows reduction in the refrigerant temperature while the refrigerant passes through the condenser of the refrigeration system. Temperature drop of the refrigerant is more with nanorefrigerant when compared to the cases without nanoparticles. The temperature of the refrigerant at the inlet of the condenser is in the range 85 – 80°C.

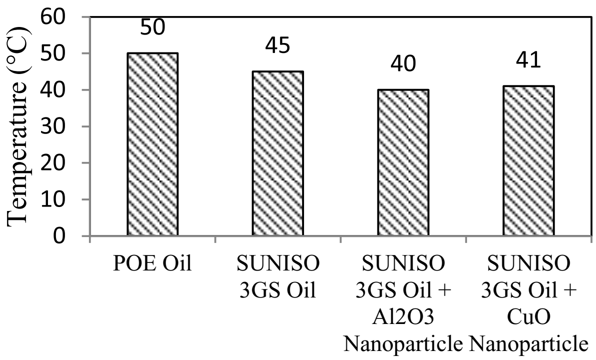


*Fig.5 Reduction in temperature of the refrigerant in the condenser*

The saturation temperature of R134a corresponding to the condenser pressure of 1.2 MPa is 46.3°C. In the case of SUNISO 3GS+$Al_2O_3$ nanorefrigerant and with SUNISO 3GS+CuO nanorefrigerant the temperature at the exit of the condenser is 40°C and 39°C respectively and the sub-cooling obtained 6.3°C and 7.3°C respectively. In fact there is no sub-cooling when POE oil+ pure refrigerant is used as the working fluid. The enhanced heat transfer rate in the condenser is due to the presence of nanoparticles in the refrigerant.

Figure 6 shows the comparison of power consumption of the compressor.

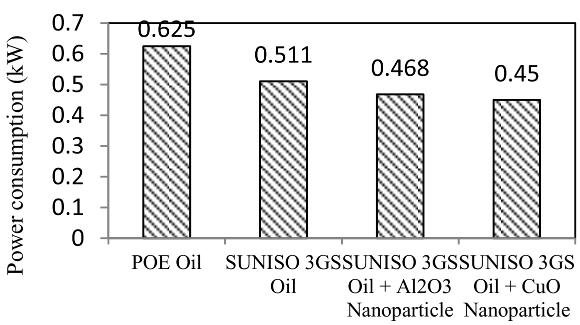


*Fig.6. Comparison of power consumption*

The reduction in power consumption is 18% if the SUNISO 3GS is used instead of POE oil. The reduction in power consumption with SUNISO 3GS +CuO nanolubricant is 28% and the corresponding value with SUNISO 3GS+$Al_2O_3$ nanolubricant is 25%. Bi et al (2007) reported that for a refrigeration system using R134a as refrigerant the power consumption can be reduced by 26.1 % if mineral oil with $TiO_2$ nanoparticles is used instead of POE oil. The reduction in power consumption can be attributed to the friction reduction and anti-wear characteristics of nanoparticles in the lubricant. The studies on tribological properties with and without nanoparticles show that the friction coefficient with nanoparticles is less than that without nanoparticles, as reported by Wu et.al (2006).

Figure 7 shows the coefficient of performance (COP) calculated using the experimental data and temperatures at the salient points of the refrigeration system are shown in table 1.

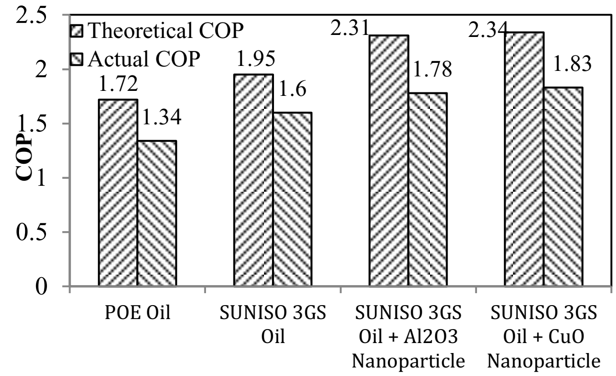


*Fig.7 Comparison of Coefficient of Performance (COP) for the four cases.*

The actual COP is calculated using the cooling load and the power input (energy meter reading). The theoretical values are also shown for comparison. For the calculation of theoretical COP the enthalpy values at the salient points are taken from P-h chart for R134a. It is clear from the histogram shown below that the SUNISO 3GS + CuO nanorefrigerant has the highest COP when compared to the other cases. The advantages of adding nanoparticle to the refrigeration system is manifold.

TABLE 1: TEMPERATURES AT SALIENT POINTS

| Quantity | POE Oil (°C) | SUNISO 3GS oil (°C) | SUNISO 3GS oil with $Al_2O_3$ (°C) | SUNISO 3GS oil with CuO (°C) |
|---|---|---|---|---|
| Temperature at the inlet to the compressor | 19 | 19 | 10 | 9 |
| Temperature at the inlet to the condenser | 85 | 82 | 80 | 80 |
| Temperature at the outlet of the condenser | 50 | 45 | 40 | 39 |
| Temperature at the inlet to the evaporator | -6 | -7 | -6 | -5 |

It reduces the power consumption of the compressor and increases heat transfer in the condenser and evaporator which in turn results in increase COP. The coefficient of performance of the refrigeration system increases by 37% when cupric oxide nanolubricant is used instead of POE oil.

## VI. CONCLUSIONS

Extensive experimental studies have been carried out to evaluate the performance of a vapour compression refrigeration system with different lubricants, nanolubricants and nanorefrigerants. The conclusions derived out of the present study are(i) The R134a /mineral oil/nanoparticles worked normally and efficiently (ii) Freezing capacity of the refrigeration system is higher with SUNISO 3GS + CuO nanorefrigerant compared to system with SUNISO 3GS + alumina nanorefrigerant and POE oil + pure refrigerant(iii) The power consumption of the compressor reduces by 28%, when CuO nanolubricant is used in the compressor instead of conventional POE oil (iv) The coefficient of performance of the refrigeration system increases by 37% with SUNISO 3GS + CuO nanorefrigerant compared to pure POE oil+pure refrigerant. v) the energy enhancement factor in the evaporator with cupric oxide nanorefrigerant is 1.5449.

## REFERENCES

[1] Baustian. J.J., Pate. M.B., Bergles. A.E., Measuring the concentration of a flowing oil–refrigerant mixture, instrument test facility and initial results. ASHRAE Trans. 94167–177, 1988.

[2] Bi. S., Guo. K., Liu. Z., Performance of a domestic refrigerator using TiO2- R600a nano refrigerant as working fluid. Energy Convers. and Manag. 52733-737, 2011.

[3] Bi. S., Shi. L., Zhang. L., Performance study of a domestic refrigerator using R134a/mineral oil/nano- TiO2 as working fluid, Int. Conf.on Refrig. Beijing, 2007.

[4] Bi. S., Shi. L., Zhang. L., Application of nanoparticles in domestic refrigerators. Appl. Therm. Eng. 28, 1834-1843, 2008.

[5] Bobbo. S., Fedel. L., Fabrizio. M., Barison. S., Battison. S., Pagura. C., Influence of nanoparticles dispersion in POE oils on lubricity and R134a solubility. Int. J. of Refrig. 33, 1180-1186, 2010.

[6] Brinkman. H. C., The viscosity of concentrated suspensions and solution. The J. of Chem. Phys. 20, 571–581, 1952.

[7] Hamilton. R.L., Crosser. O.K., Thermal conductivity of heterogeneous two-component systems. Ind. and Eng. Chem. Fundam. 187–191, 1962.

[8] Jensen. M.K., Jackman. D.L., Prediction of nucleate pool boiling heat transfer coefficients of refrigerant–oil mixtures, Int. J. Heat Transf.106184–190, 1984.

[9] Jwo. S.S., Jeng. L.Y., Teng. T.P., Chang. H., Effect of nano lubricant on the performance of Hydrocarbon refrigerant system, J. Vac. Sci. Techno. B, 27(3), 1473-1477, 2009.

[10] Keblinski. P., Jeffrey. A.E., David. G.C., Nanofluids for thermal transport. Mater. Today, 836-44, 2005.

[11] Kedzierski. M.A., Kaul. M.P., Horizontal nucleate flow boiling heat transfer coefficient measurements and visual observations for R12, R134a, and R134a/ester lubricant mixtures. Int. Proc. of the 6th Int. Symp. on Transp. Phenom. in Therm. Eng. 1111–116, 1993.

[12] Kristen. H., Young. G. P., Liping. L., Anthony. M. J., Flow boiling heat transfer of R134a based nano fluids in a horizontal tube. Int. J. Heat and mass transf. 53, 944-951, 2010.

[13] Pak. B. C., Cho. Y. I., Hydrodynamic and heat transfer study of dispersed fluids with submicron metallic oxide particles. Exp. Heat Transf., 11, 151–170, 1998.

[14] Peng. H. P., Ding. G., Hu. H., *Jiang*. W., Zhuang. D., Wang. K., Nucleate pool boiling heat transfer characteristics of refrigerant/oil mixture with diamond nanoparticles. Int. J. Refrig. 3, 347-358, 2010.

[15] Wu. Y.Y., Tsui. W.C., Liu. T.C.,. Experimental analysis of tribological properties of lubricating oils with nanoparticles additives. Wear, 262, 819-825, 2006.

# Experimental Studies on the Effect of Surfactants on Thermophysical Properties of Nanofluids

*Sajin Mathew Varghese[1], T. S. Krishna Kumar[2], Manu M*
*Department of Mechanical Engineering*
*TKM College of Engineering,Kollam, Kerala, India*

[1]sajinmv91@gmail.com
[2]krishnakumarts@gmail.com

***Abstract*- The technology advancement in nanotechnology has enabled nanosized particles to be dispersed in a base fluid. This new generation fluids is known as nanofluids. Producing a stable nanofluid with improved thermophysical properties is a challenge. Surfactant plays an important role in dispersing the nanoparticles into the basefluid and improving the stability of nanofluids. In the present work, different nanofluids are prepared by sonication process and the effect of surfactants on thermophysical properties such as thermal conductivity, viscosity and stability are studied. Surfactants such as Polyvinylpyrrolidone (PVP), Sodium dodecylbenzenesulfonate (SDBS) and Gum arabic (GA) are used. The effect of various concentrations of these surfactants on alumina and titanium dioxide nanofluids of different particle sizes are investigated. The base fluids used are de-mineralized water and ethylene glycol. GA, PVP and SDBS surfactants are used in alumina/ethylene glycol nanofluids (0.5% volume fraction) of size 13nm and 50nm. Thermophysical property changes corresponding to different volume concentrations of surfactants ranging from 0.1 to 2% are studied. PVP and SDBS surfactants are used in titanium dioxide/ demineralized water - ethylene glycol mixture nanofluids (0.2% volume fraction) with nanoparticle sizes 21nm and 40nm. Results showed that surfactant plays an important role in dispersing nanoparticles into the base fluid and improving the thermal conductivity and stability of nanofluids. Non-ionic surfactant PVP shows better positive effects than anionic surfactants SDBS and GA. The highest thermal conductivities were obtained at 1% volume fraction of surfactant for alumina nanofluids and 0.3% volume fraction for titanium dioxide nanofluids. The viscosity also increases with increase in surfactant concentration.***

***Keywords*-Nanofluids; Surfactants; Thermal conductivity; Stability; Viscosity.**

## I. INTRODUCTION

Nanofluids are engineered colloidal suspensions of nanoparticles in a basefluid. The size of nanoparticles vary from 1-100 nm. All physical mechanisms have a critical length scale, below which the physical properties of materials are changed. Nanoparticles exhibit properties that are considerably different from those of conventional solids.The enhanced thermal conductivity of nanofluids is mainly due to Brownian motion of particles, molecular level layering of the liquid and the effect of nanoparticle clustering. The thermal conductivity of nanofluids has a good corresponding relation with the stability of nanofluids. Better the dispersion behaviour, higher will be the thermal conductivity.

Surfactants used in nanofluids are also called dispersants. Dispersants consists of a hydrophobic tail portion, and a hydrophilic polar head group. Surfactant helps to modify the hydrophobic surface of nanoparticles into hydrophilic surface and thereby improving the stability of nanofluids. Addition of surfactants will create a repulsive force between the suspended particles and helps to increase the stability of nanofluids.The disadvantage of surfactants is for applications above $60^0$C.The bonding between surfactant and nanoparticles can be damaged which results in sedimentation of nanoparticles and deteriorates the stability of nanofluids.

Viscosity is an important flow property of fluids. Viscosity describes the internal resistance of a fluid to flow and it is an important property for all thermal applications involving fluids. Hence viscosity is as important as thermal conductivity in engineering systems involving fluid flow.

Yu et al. [9] at prepared stable ethylene glycol based copper nanofluids with PVP as surfactant and found an improvement in the stability of copper nanofluids. Peng et al.[10] investigated the effect of surfactants on nucleate pool boiling heat transfer of refrigerant- based nanofluids, and found that adding surfactant could enhance the heat transfer of copper nanofluids. Zhou et al. [11] experimentally investigated the thermal conductivity of several of several common surfactant solutions, concluding that the thermal conductivities of surfactant solutions reach a stable ratio after a certain concentration X. Wang et al.[12] found that the thermal conductivity had a good corresponding relation with the stability of nanofluids, the better dispersion behavior, the higher will be the thermal conductivity.

## II. . EXPERIMENTAL PROCEDURE

### *A. . Preparation of nanofluids*

Two-step method was employed for the preparation of nanofluids. This method is the most widely used method for preparing nanofluids. Nanoparticles, nanofibers, nanotubes, or other nanomaterials used in this method are first produced as dry powders by chemical or physical methods.

Then, the nanosized powder will be dispersed into a fluid in the second processing step with the help of intensive magnetic force agitation, ultrasonic agitation, high-shear mixing and homogenizing.

In this work, ultrasonic agitation is used for nanoparticle dispersion. The thermophysical properties of these nanofluids without adding surfactants are measured. Alumina nanoparticles of sizes 13nm and 50nm were used for the preparation of alumina nanofluids. Titanium dioxide of sizes 21nm and 40nm were used for the preparation of titanium dioxide nanofluid. The first step in this experiment is the preparation of nanofluid. The mixture of nanoparticles and base fluid was continuously agitated in a high frequency sonicator at maximum frequency. Sonicator is mainly utilized to crack the agglomeration and clusters formed inside the bulk of nanofluids. Alumina nanofluid of 0.5% volume fraction and titanium dioxide nanofluid of 0.2% volume fraction were prepared by this method.

The next step in this work is the preparation of nanofluids with the inclusion of surfactants. GA, PVP, and SDBS surfactants were used for the preparation of alumina nanofluid. PVP and SDBS surfactants were used for the preparation of titanium dioxide nanofluid. Nanofluids with surfactants were prepared initially by adding surfactant into the base fluid and is agitated or stirred for a few minutes. Then the nanoparticles were added into this surfactant solution in an ultrasonic environment and is agitated using a sonicator. GA, PVP, and SDBS surfactant concentration ranging from 0.1% to 2% volume fractions were used for the preparation of alumina nanofluids. PVP and SDBS surfactant concentration ranging from 0.1% to 0.5% volume fraction were used for the preparation of titanium dioxide nanofluids.


Fig. 1.Apparatus for the preparation of nanofluid

## III. . MEASUREMENTS

### A. *Thermal conductivity*

It is the most important property that can be investigated to prove the heat transfer enhancement of a prepared nanofluid. In nanofluids, particle aggregation plays an important role in the thermal conductivity enhancement. Transient method is used in the present study. Thermal conductivity enhancement in nanofluids also depends on many parameters such as particle size, shape, concentration, addition of surfactants and basefluids.

The thermal conductivity of the prepared nanofluids were measured using a KD2 PRO thermal conductivity probe .This instrument works on the classical transient hot wire method which is the most widely used technique in measurement of thermal conductivity of liquids in general and nanofluids in particular.In this method, a thin metallic wire is used both as a line heat source and a temperature sensor. The wire is surrounded by the liquid whose thermal conductivity is to be measured. The wire is then heated by sending current through it. The higher the thermal conductivity of the surrounding liquid, the lower will be the temperature rise of the wire. This principle is used to measure the thermal conductivity of the liquid.

### B. *Viscosity*

It is a measure of the resistance of a fluid to deform under shear stress. Viscosity is due to the friction between neighboring particles in a fluid that are moving at different velocities. Viscosity decreases with increase in temperatures. A liquid's viscosity depends on the size and shape of its particles and the attractions between the particles.The viscosity measurements for the nanofluids were carried out using a Cone/Plate Rheometer (Viscometer). The resistance to the rotation of the cone produces a torque that is proportional to the shear stress in the fluid.This reading is easily converted to absolute centipoises units. The stationary plate forms the bottom of a sample cup which can be removed, filled with 0.5 ml to 2.0 ml of sample fluid (depending on cone in use), and remounted without disturbing the calibration. The sample cup is jacketed and has tube fittings for connection to a constant temperature circulating bath. The temperature of the sample was kept constant during the measurement process by circulating mineral oil through the jacketing of the cup of the instrument. A constant temperature bath/ circulator was used to circulate the fluid.

### C. *Stability*

Stability of nanofluids was studied by visual comparison. The time taken for visible settling was noted as a measure of stability. The settlement in the samples of nanofluid which is prepared with and without surfactants is compared. A nanofluid sample with same concentration of PVP, GA and

SDBS surfactants are prepared and is kept stationary for a fixed period of time and the stability is inspected by observation method. Stability of alumina/EG nanofluid with and without surfactants were visually inspected after 8 days of preparation and that of titanium dioxide after 10 days.

## IV. . RESULTS AND DISCUSSION

### *A. Effect of surfactants on thermal conductivity of nanofluids*

For analyzing the effect of surfactants on thermal conductivity of alumina/EG nanofluids of different particle sizes, nanofluids of 0.5% volume fraction suspension was prepared with surfactants. Fig 2, 3 and 4 shows the effect of SDBS,PVP and GA surfactants on the thermal conductivity of alumina/EG nanofluids.

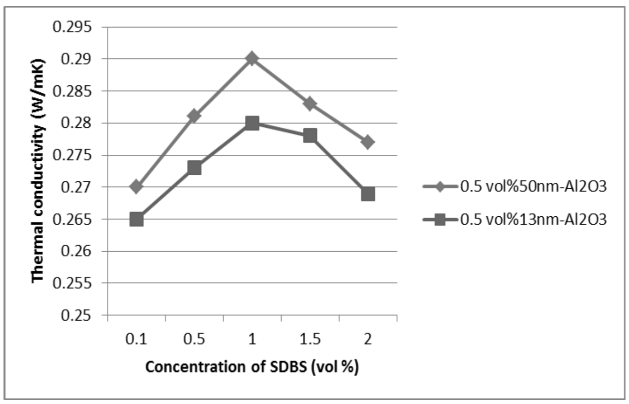


Fig.2.Thermal conductivity of Alumina/EG nanofluids with SDBS surfactant at different volume fractions.

In Fig.2 with addition of SDBS surfactants on 50nm $Al_2O_3$ nanofluid, the thermal conductivity was found to be increased at lower concentrations. At 1% volume fraction of SDBS addition, the thermal conductivity was found to be increased by 9.5%. Up to this amount of addition of surfactants, the thermal conductivity was found to be increased and beyond this concentration the thermal conductivity was found to be decreased. The same change was found in the case of 13nm $Al_2O_3$ nanofluid. At 1% volume fraction addition of surfactant, the thermal conductivity was increased by 7.6%.

The reduction in the thermal conductivity during higher concentrations are due to the fact that supersaturated adsorption arises and played a role in flocculation, which will weaken the heat transfer between particles[15]. Another reason is that at high surfactant concentrations, the heat transfer area becomes narrower as high volume fraction surfactants result in more surfactant molecules adsorbed on the particle surface. It is observed that the highest thermal conductivity occurs at an optimal concentration of surfactants.

With addition of PVP surfactant, the maximum enhancement was obtained at 1% volume fraction of PVP for alumina nanofluid of 50nm. Alumina nanofluid of 13nm requires only 0.5% volume fraction of PVP to attain maximum enhancement. More concentration of PVP surfactants were required to attain maximum thermal conductivity enhancement for alumina nanofluid of 50nm than that with 13nm.

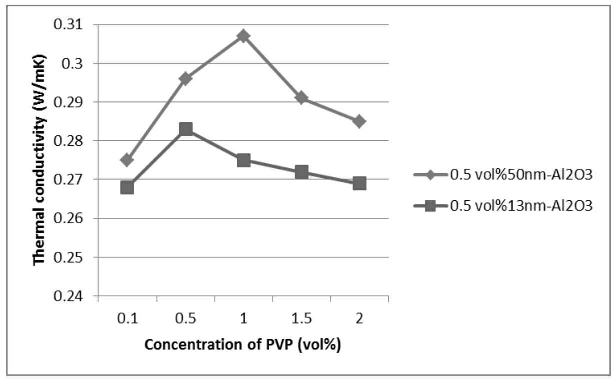


Fig. 3.Thermal conductivity of alumina/EG nanofluids with PVP Surfactant at different volume fractions

With GA surfactant, the maximum thermal conductivity enhancement was obtained at 1% volume fraction of GA surfactant for nanofluids of both 50nm and 13nm size.Thermal conductivity enhancement of 9.5% and 8% was obtained for alumina nanofluids of 50nm and 13nm respectively.

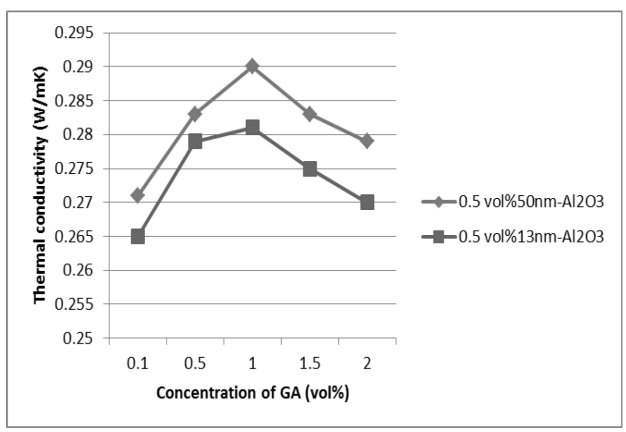


Fig. 4.Thermal conductivity of alumina/EG nanofluids with GA surfactantat different volume fractions

With all surfactants the maximum thermal conductivity was found for alumina nanofluids of 50nm size. Alumina nanofluid with PVP surfactant shows the highest thermal conductivity when compared to that of alumina nanofluid with GA and SDBS surfactant and less amount of PVP surfactant were required to attain highest thermal conductivity for alumina nanofluid of 13nm size. For alumina nanofluids with SDBS and GA surfactants, the maximum thermal conductivity enhancement was observed at same concentration of surfactants. Maximum thermal conductivity enhancement was obtained at optimum concentration of surfactants in nanofluids.

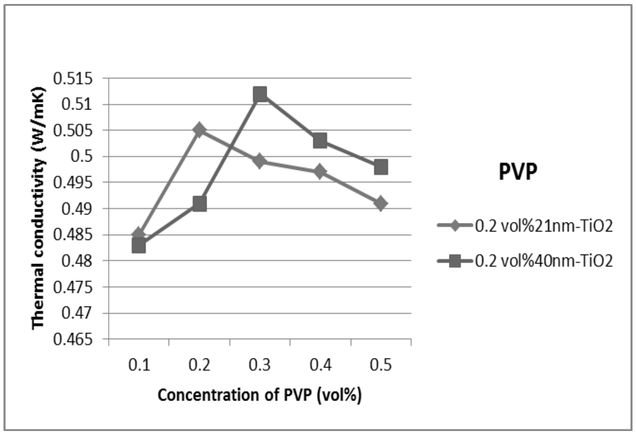


Fig. 5. Thermal conductivity of titanium dioxide nanofluids with PVP Surfactant at different volume fractions

Titanium dioxide nanofluid of 0.2% volume fraction with water/ethylene glycol (60:40) mixture as base fluid was prepared for the study. Fig.5 shows the effect of different concentration of PVP surfactants on titanium dioxide nanofluid. In $TiO_2$ nanofluid of 21nm size, the maximum thermal conductivity enhancement was obtained on the addition of 0.2% volume fraction of PVP surfactant. Thermal conductivity enhancement of 7.2% was obtained at this volume fraction. On the addition of surfactant above this volume the thermal conductivity is found to be decreased. This decrease in thermal conductivity is found as a result of addition of excess surfactant concentration than actually needed to stabilize the nanofluids

For $TiO_2$ nanofluid of 40nm size, the maximum thermal conductivity enhancement was observed at 0.3% volume fraction of PVP surfactant. An enhancement of 9% was obtained for this volume. The highest thermal conductivity enhancement is obtained at a surfactant concentration higher than that needed for titanium dioxide nanofluid of 21nm size. This may be due to the fact that more PVP surfactant is needed to stabilize titanium dioxide nanofluid of 40 nm size than that of 21nm size since aggregation rate is more for nanofluid of 40nm size.

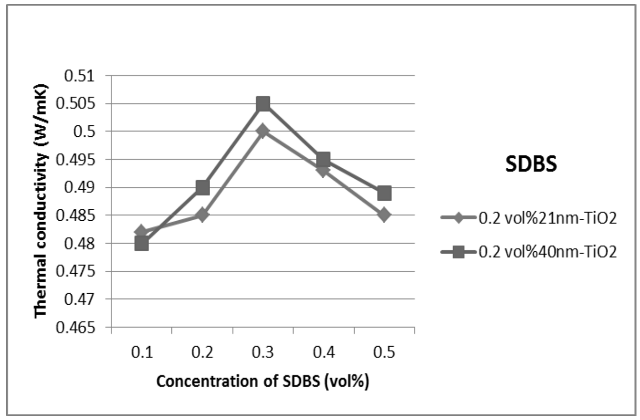


Fig. 6. Thermal conductivity of titanium dioxide nanofluids with SDBS Surfactant at different volume fractions

$TiO_2$ nanofluid of 21nm size shows maximum thermal conductivity enhancement on addition of 0.3% volume fraction of SDBS surfactant. At this volume the thermal conductivity enhancement was about 6.1%. On further addition of surfactant the thermal conductivity was found to be decreasing. For $TiO_2$ nanofluid of 40nm size also the thermal conductivity enhancement was maximum at 0.3% volume fraction of SDBS surfactant. The thermal conductivity enhancement was about 7.6%. With SDBS surfactant the maximum thermal conductivity enhancement was found for titanium dioxide nanoparticle of 40nm size when compared to 21nm sized nanofluid.

*B. Effect of surfactants on viscosity of nanofluids*

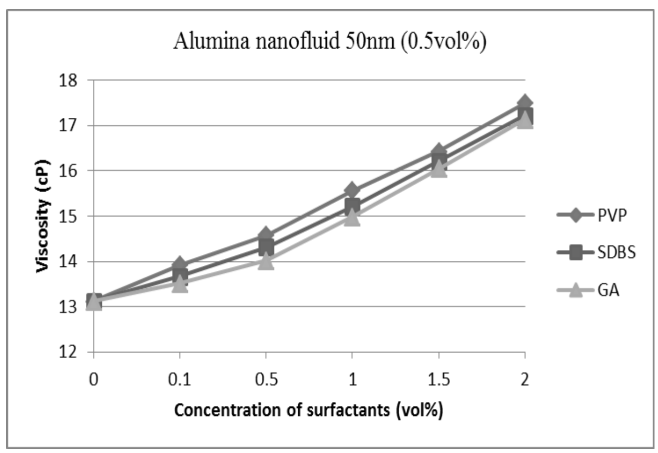


Fig. 7. Comparison of surfactants on viscosity of alumina/EG nanofluid of 50nm size

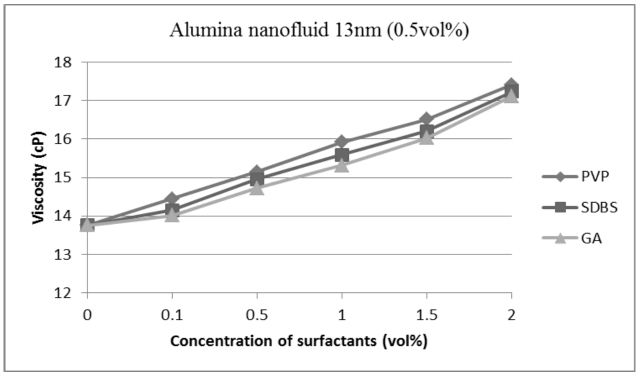


Fig. 8 . Comparison of surfactants on viscosity of alumina/EG nanofluid of 13nm size

For alumina nanofluids of both 13nm and 50nm size, the viscosity increases with increase in surfactant concentration. Fig.7 and Fig.8 shows the effect of surfactants on viscosity of alumina nanofluids. Of all surfactants used, PVP surfactant shows maximum viscosity while GA is of least viscosity. For alumina nanofluid of 50nm and 13nm size, PVP surfactant of 2% volume fraction gives the maximum viscosity.

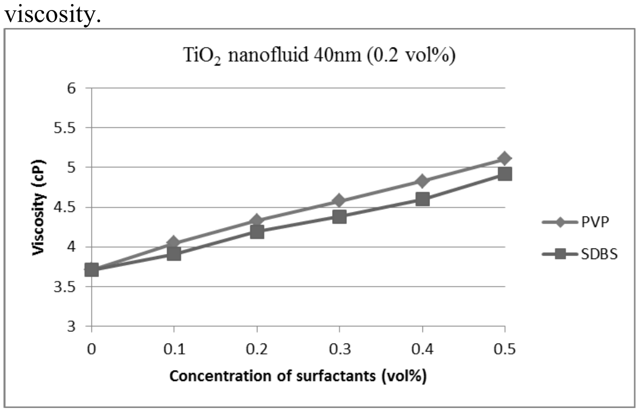


Fig. 9. Comparison of surfactants on viscosity of titanium dioxide nanofluid of 40nm size

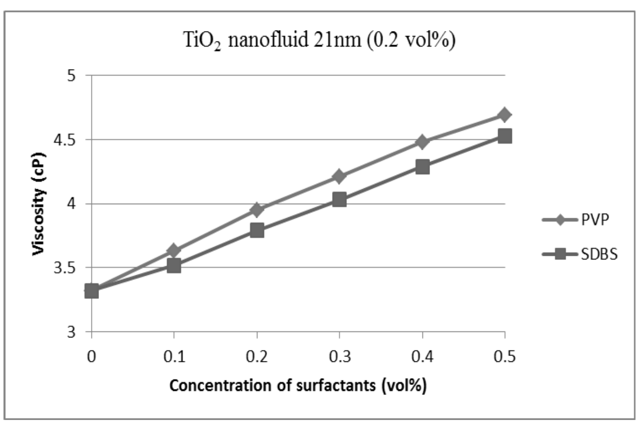


Fig. 10. Comparison of surfactants on viscosity of titanium dioxide nanofluid of 21nm size

For titanium dioxide nanofluids of both 21 and 40nm size, the viscosity increases with increase in surfactant concentration. Titanium dioxide nanofluid with PVP surfactant shows higher viscosity than that with SDBS surfactant. Titanium dioxide nanofluid with 0.5% volume fraction of PVP surfactant have the maximum viscosity for both 40nm and 21nm size.

### *C. Effect of surfactants on stability of nanofluids*

Stability of nanofluids was studied by visual comparison. The time taken for visible settling was noted as a measure of stability. The stability inspection was carried out after 8 days of preparation of alumina nanofluids with and without surfactants. For titanium dioxide nanofluids, the inspection was after 10 days. Nanofluids with surfactants are found to be more stable than that without surfactants. Stability of alumina and titanium dioxide nanofluids of different particle sizes are studied with and without surfactants. Nanofluids with PVP surfactants are more stable than that of SDBS and GA surfactants. Addition of SDBS surfactants above optimum concentration gives a negative effect on the stability of alumina nanofluids, while high concentration of PVP and GA surfactant doesn't deteriorated the stability of alumina nanofluids. The deterioration of stability of alumina nanofluid at high SDBS surfactant concentration is due to supersaturated adsorption.

Addition of PVP and SDBS surfactants helps to improve the stability of titanium dioxide nanofluids of particle size 21nm and 40nm. Titanium dioxide nanofluids with PVP surfactant are found to be more stable than that with SDBS surfactant. Nanofluids with large particle size are found to be settled earlier than that of nanofluids with smaller particle size.

## V. CONCLUSION

In the present work, experiments were conducted to measure the effect of surfactants on thermophysical properties of nanofluids. It was found that the addition of surfactants on nanofluids helps to increase the thermal conductivity and stability. The highest thermal conductivity enhancement is obtained at an optimum surfactant concentration. Excess of surfactant result in reduction in thermal conductivity and stability.

Nanofluids with PVP surfactant shows higher thermal conductivity and stability than that of SDBS surfactants. It was observed that the enhancement with surfactants were highest for nanofluid with larger particle size. This is due to the fact that more agglomeration is found for nanofluids with larger particle size. Optimum concentration of surfactants is the amount of surfactants that is required to stabilize the nanofluids. Addition of surfactants above optimum concentration gives a negative effect on the thermal conductivity of nanofluids. The reduction in the thermal conductivity during higher concentrations are due to the fact that supersaturated adsorption arises and played a role in flocculation, which will weaken the heat transfer between particles. Another reason is that at high surfactant concentrations, the heat transfer area becomes narrower as high fraction surfactants result in more surfactant molecules adsorbed on the particle surface [15]. The viscosity of nanofluids is found to be increased with increase in surfactant concentration. Nanofluids with PVP surfactants are more viscous when compared to GA and SDBS.

Non-ionic surfactant PVP is more effective than anionic surfactant SDBS in dispersion of titanium dioxide and alumina nanofluids. High concentration of SDBS surfactant deteriorated the stability of alumina nanofluids while suspension with high concentration of PVP doesn't deteriorated the stability. For nanofluids with large particle size, high concentration of PVP surfactants is required to get the highest thermal conductivity.

## ACKNOWLEDGEMENT

This project was supported by TKM College of Engineering and TEQIP-II.

## REFERENCES

[1] Das, S. K, Putra N, & Roetzel, W, *Pool boiling characteristics of nano-fluids*, International Journal of Heat and Mass Transfer, Vol.46, pp.851-862, 2003.

[2] Buongiorno, J, *Convective transport in nanofluids*, Journal of Heat Transfer,Vol.128, pp.240–250, 2006.

[3] Sang Hyun Kim, Sun Rock Choi, Dongsik Kim, *Thermal Conductivity of MetalOxide Nanofluids:Particle Size Dependence*, Journal of Heat Transfer, Vol.129, pp.298-307, 2007.

[4] Alexander Hays Charles, P.Marsh Jorge Alvarado Ryan Franks,*The Effect of Nanoparticle Agglomeration on Enhanced Nanofluidic Thermal Conductivity*, International Refrigeration and Air Conditioning, Vol.7, pp. 227-232, 2008.

[5] Abu-Nada,*Effects of Variable Viscosity and Thermal Conductivity of $Al_2O_3$- Water Nanofluid on Heat Transfer Enhancement in Natural Convection*, Int. J. Heat Fluid Flow, Vol.30, pp.679–690, 2009.

[6] L.Yang, K.Du, X.S.Zhang, *Preparation and stability of alumina nanoparticle suspension of ammonia water solution*, Appl. Therm.Eng, Volume.31, pp.3643-3647,2010.

[7] C.T Nguyen, F.Desgranges, H.AngueMinsta, *Temperature and particle-size dependent viscosity data for water-based nanofluids*, Internatiomal Journal of Heat and Fluid Flow, Vol.28, pp.1492-1506,2010.

[8] Tun-Ping Teng, Yi-Hsuan Hung, Tun-ChienTeng,*The effect of alumina/water nanofluid particle size on thermal conductivity*.Applied Thermal Engineering, Vol.30, pp.2213-2218, 2010.

[9] W.Yu, H.Xie,*Investigation of thermal transport properties of ethelene glycol based nanofluid containing copper nanoparticles*, Powder technology, Vol.197, pp.218-211, 2010.

[10] H. Peng, G. Ding, *Effect of surfactant additives on nucleate pool boiling heat transfer of refrigerant-based nanofluid*, Exp. Therm. Fluid Sci, Vol.35, pp.960-970, 2011.

[11] M.Z. Zhou, G.D.Xia, *Analysis of factors involving thermal conductivity and viscosity in different kinds of surfactant solutions,* Exp. Thermal Fluid Science, Volume. 36, pp.22-29, 2012.

[12] X. Wang, D. Zhu,*Investigation of pH and SDBS on enhancement of thermal conductivity in nanofluids*, Chem.Lett, Vol.470, pp. 107-111, 2012.

[13] Faris Mohammed Ali ,W.Mahmood Mat Yunus and ZainalAbidinTalib,*Study of the effect of particles size and volume fraction concentration on the thermal conductivity of $Al_2O_3$nanofluids*, International journal of physical sciences, 8(28), pp.1442-1457, 2013.

[14] Aklilu Tesfamichael Baheta and Abraham D.Woldeyohannes, *Effect of particle size on effective thermal conductivity of nanofluids*, Asian journal of scientific research, 6(2), pp. 339-345, 2013.

[15] Guodong Xia, Huanming Jiang, Effects of surfactant on the stability and thermal conductivity of $Al2O_3$/de-ionized water nanofluids, International Journal of Thermal Sciences, Vol.84, pp.118-124, 2014.

# Presurgical Numerical Analysis of Bone Cement Injection and Curing in Vertebroplasty

Abdul Rahoof A R[1], Shamnadh M[2], Dileep P N[3]

*Department of Mechanical Engineering, TKM College of Engineering, Kollam, Kerala, India*

[1]rahoofar1991@gmail.com
[2]shamnadhm@gmail.com
[3]dileepkollam@yahoo.com

***Abstract*—Vertebroplasty is a non-surgical procedure that has been widely accepted for the treatment of vertebral osteoporotic compression fractures. During the treatment, liquid bone cement gets injected into the affected vertebral body and therein cures to a solid. In order to investigate the treatment and the impact of injected bone cement, an integrated modelling and simulation framework was developed. The framework includes (i) the generation of good computational model of the vertebra from the CT images, (ii) computational fluid dynamics (CFD) simulations of bone cement injection into the trabecular structure and (iii) finite element (FE) analysis of the subsequent bone cement curing. This paper initiates an intensive research on Vertebroplasty by numerical investigations.**

***Keywords*— Osteoporosis; Bone cement; Vertebroplasty; Computational Fluid Dynamics; Finite Element Analysis**

## I. Introduction

Osteoporosis is a progressive bone disease that is characterized by a decrease in bone mass and density which can lead to an increased risk of fracture. In osteoporosis, the bone mineral density (BMD) is reduced, bone micro-architecture deteriorates, and the amount and variety of proteins in bone are altered [1]. The prevalence of osteoporosis is increasing significantly with the aging population. According to incomplete statistics, there are currently nearly 200 million osteoporotic patients in the world. The most serious complication caused by osteoporosis is the osteoporotic fracture (also known as brittle fractures). The spinal fractures caused due to osteoporosis are called as vertebral compression fractures (VCF). Since spine is rich in cancellous bone, mild violence can cause vertebral compression fractures. A vertebral compression fracture occurs when the bones of the spine breaks due to trauma. Usually the trauma necessary to break the healthy vertebra is quite large. In certain circumstances, however, such as in elderly people and in people with osteoporosis, these same bones can break with little or no force. The vertebrae most commonly getting broken are those in the lower back. Even though vertebroplasty is a well-accepted procedure, it may be accompanied by risks of complications caused by the treatment procedure itself or by the utilization of specific injectable biomaterials. Regarding the treatment of vertebroplasty, a possible complication is cement leakage into unwanted regions of the vertebra. Furthermore, treated vertebral bodies exhibit an altered mechanical behaviour due to different mechanical properties of the biomaterial compared to human cancellous bone. This leads to different load distributions which may affect the treated vertebra itself but also adjacent vertebral bodies [2]. There are different classes of injectable biomaterials used in vertebroplasty. However, acrylic bone cements play the most important role. This class of materials is a bio-compatible but non resorbable polymer based on polymethylmethacrylate (PMMA) [3]. The application of acrylic bone cements within the scope of vertebroplasty can provoke further complications. Firstly, risk of thermal necrosis exists due to the exothermic chemical reaction which leads to a heat production and heating of the material. Moreover, release of remaining monomer caused by an incomplete chemical reaction may have a toxic impact on human tissue [4]. Besides in vivo and in vitro measurement techniques, the process of vertebroplasty is subject of intensive research by numerical investigations. Generally, the overall procedure can be structured into three parts: the injection process during the operation, the curing process of bone cement inside the human body, and finally the long term behaviour of treated vertebrae. The injection process, which, from a physical point of view, is a fluid-dynamics problem, can be numerically examined using different computational methods. Moreover, the curing of bone cement inside the human body, has been rarely investigated by numerical analyses. As mentioned earlier, the curing process of bone cements is accompanied by chemical shrinkage and an exothermic reaction, which leads to heating of the material and the vertebral body. The impact of bone cement shrinkage on the residual stresses of bone has, for example, can also be numerically investigated. The aim of this paper is to present a numerical simulation which take into account the curing process itself and the temperature evolution during bone cement curing.

## II. MATERIALS AND METHODS

### *A. Geometric Modeling of Vertebra*

The geometry of L3 vertebra is of complex in nature. CT images have to be processed to extract necessary geometric data in order to generate a geometric model of the vertebra [5][6]. The program ScanIP (Simpleware Software, Castle Street, United Kingdom) was used to process the CT images (95 slices) and derive the geometry for the model (Fig 1).

In order to create an accurate three-dimensional geometric model of lumbar vertebra L3, it is essential to discern regions containing bone tissue. Thus, image segmentation has to be done by setting threshold values of CT number for bone tissue. The pixels having CT numbers in the threshold range were treated as bone tissue and collected in a segmentation mask. In the next step of geometric modeling of the vertebra, three-dimensional surface mesh is created on the basis of generated 3D surface model and exported into the Ansys neutral format file. The surface mesh consists of triangular surface elements that form the outer surface of vertebra, where the triangles share common sides and vertices.

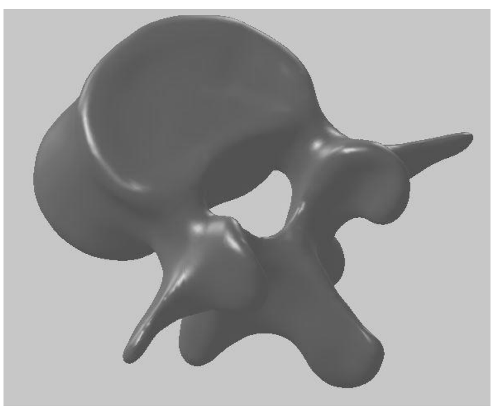

*Fig 1: 3D Model of the Vertebra*

### *B. FE Analysis of Osteoporotic Vertebra*

Finite element analysis (static structural) is carried out on an L3 vertebra by simulating osteoporotic conditions, to find out the stresses generated in the vertebra during various normal physiological activities, the site of maximum stress concentration and the trend of stress variations in the cortical and cancellous region of the bone. Here the structural analysis is carried out by using Ansys 14.5.

Since there are many factors throughout the human life that pathologically weaken the structural strength of the vertebrae and put them at the risk of fracture. Undoubtedly, osteoporosis comprises the most common cause of this weakness and fragility. So the reduction in the strength of vertebra is simulated by the reduction in the elastic moduli of the both cancellous (by 66%) and cortical bone region (by 33%) [7]. In this study the bone material is considered to be an isotropic material. The material properties of the vertebra are depicted in the Table 1 [8].

The model is subjected to 5 loading cases which simulate the basic physiological activities named standing, flexion, extension, rotation and walking. Standing was simulated by a follower load of 500N. For simulating flexion, a load of 1175N and a flexion bending moment of 7.5 Nm was used. While for extension and rotation a follower load of 500N and a corresponding moment of 7.5 Nm were used. Walking was simulated with a follower load of 650N and a torsion moment of 7.5 Nm. These force values were converted to pressure values based on area on vertebral body and articular facets. The lower end plate and region is constrained in XYZ directions under all loading conditions [7]. Here the vertebral body is only taken for the analysis. About 85% of the total pressure acting on the vertebra is taken by the vertebral body whereas the remaining 15% is taken by the facets. So the pressure acting on the vertebral body is more predominant compared to facets [7].

TABLE 1: MATERIAL PROPERTIES OF THE VERTEBRA

| | Elastic modulus of normal vertebra (MPa) | Elastic modulus of osteoprotic vertebra (MPa) | Poisson's Ratio |
|---|---|---|---|
| Cortical Region | 12000 | 8040 | 0.30 |
| Cancellous Region | 100 | 34 | 0.315 |

### *C. CFD Simulation of Injection Phase*

The CFD simulation of the injection phase is carried out using Ansys Fluent 14.5. For this purpose, multispecies flow is considered. Here a small crack is randomly created inside the cancellous bone of the generated 3D model of the L3 vertebra, in order to simulate osteoporotic compression fracture. The generated fracture is of A1 type [7]. It is to this crack the bone cement is being injected. Initially the crack is completely filled with bone marrow. The ambient temperature of bone cement is assumed to be $20^0$C prior to injection. The boundaries of the computational domain to the trabecular bone is referred to as "bone". Fluid flow through this boundary is also not permitted. Additionally to the boundary conditions, initial conditions have to be defined for the computational domain. To adopt the natural environment inside human body, the initial temperature is set to $37^0$C and a pressure of 1 bar is present. Moreover, the initial velocity of bone marrow is set as 0 mm/s, thus no initial fluid flow is expected. Also, it is assumed that the crack doesn't contain any bone cement in the initial state.

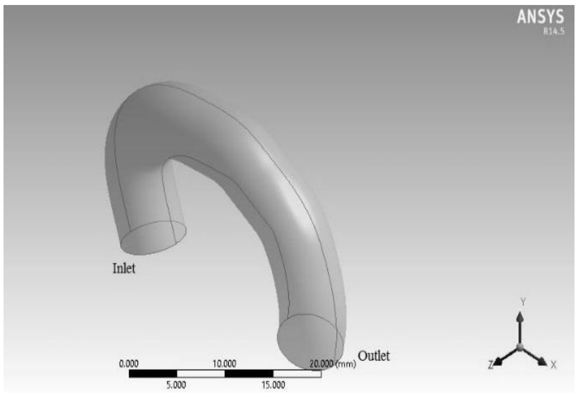


*Fig 2: 3D Fluid domain for CFD analysis*

The boundary conditions and the material properties for the CFD analysis are summarized in the Table 2 and Table 3 [8][9][10].

TABLE 2: BOUNDARY CONDITIONS FOR CFD MODEL

| | Inlet | Outlet |
|---|---|---|
| Pressure | Zero grad | 1 bar |
| Velocity | 2.5mm/sec | Zero grad |
| Temperature | $20^0$C | Zero grad |

TABLE 3: MATERIAL PROPERTIES FOR CFD MODEL

| | Bone cement | Bone marrow |
|---|---|---|
| Kinematic Viscosity | 300 Pa.s | $4 \times 10^{-4}$ m$^2$/s |
| Density | 1.48 g/cm$^3$ | 1.2 g/cm$^3$ |
| Specific heat capacity | 1.2 kJ/kg K | 2 kJ/kg K |
| Thermal conductivity | 0.25 W/mK | 0.34 W/mK |
| Surface Tension | 0.03W/mK | 0.03W/mK |

In our test case, the injection was supposed to stop at simulation time of 20 seconds Here the viscosity of the bone cement is assumed to be a constant [10].

*D. FE Simulation of Bone Cement Curing*

Subsequently to the injection simulation, the curing of bone cement inside the trabecular structure is investigated by finite element simulations.

*1) Thermal Analysis*

The thermal analysis is carried out using Ansys 14.5. The resulting FE-mesh consists of approximately 46,789 tetrahedral elements. The bone cement distribution is transferred to the FE mesh. The setting of bone cement inside the trabecular structure is an exothermic reaction. That is, the change of bone cement from the fluid phase to the solid phase results in the generation of a large amount of heat [3][4]. Thermal analysis helps to find out the distribution of temperature within the cancellous bone during the exothermic reaction occurring due to setting of bone cement. Here we have defined the temperature at the bone and bone cement interface with respect to time. The temperature evolution characteristics of Simplex bone cement is used for this (Fig 3). The maximum temperature of simplex bone cement is $77^0$C and the setting time is around 500 seconds [9][10]. This analysis helps to figure out those portions on the vertebral body which are exposed to temperature more than the critical limit.

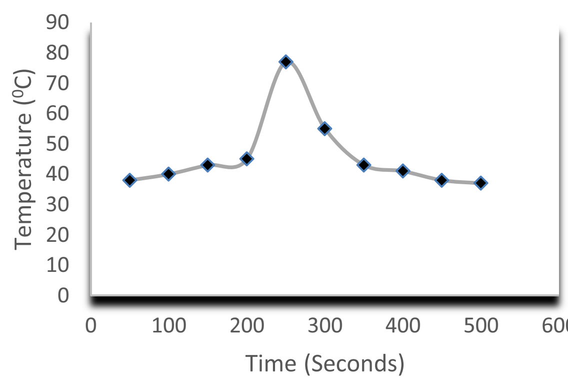


*Fig 3: Temperature evolution profile*

TABLE 4: MATERIAL PROPERTIES FOR THERMAL ANALYSIS

| | Cortical Bone | Cancellous Bone | Bone Cement |
|---|---|---|---|
| Elastic Modulus (MPa) | 8040 | 34 | 2760 |
| Poisson's Ratio | 0.30 | 0.315 | 0.40 |
| Coefficient of thermal expansion (/$^0$C) | $8.5 \times 10^{-5}$ | $5.8 \times 10^{-5}$ | $72.2 \times 10^{-6}$ |

In addition to this temperature evolution curve, material properties are specified for the thermal analysis. The material properties used for the analysis are tabulated in Table 4 [8][9][10]. The temperature evolution curve helps to provide boundary condition which varies respect to time.

*2) Structural Analysis*

Subsequent to the transient thermal analysis, the results of transient thermal analysis are coupled with structural analysis solver of the Ansys 14.5 to investigate the thermal stress induced on the vertebral body due to the exothermic reaction. The thermal stress developed on the vertebral body as a result of the exothermic reaction can lead to adjacent fracture on the vertebra. This analysis helps to predict the possibility of further fractures on the future. The boundary conditions and material properties from the transient thermal analysis is coupled to the structural analysis.

## III. RESULTS AND DISCUSSION

### *A. FE Analysis of Osteoporotic Vertebra*

After applying the loading and boundary conditions on the meshed model, the solution is obtained by running the solver. User defined result (Von Mises stress) is obtained after running the solver, that is the value of stresses generated at each elements. The results obtained under various loading conditions are given below (Fig 4 and Fig 5).

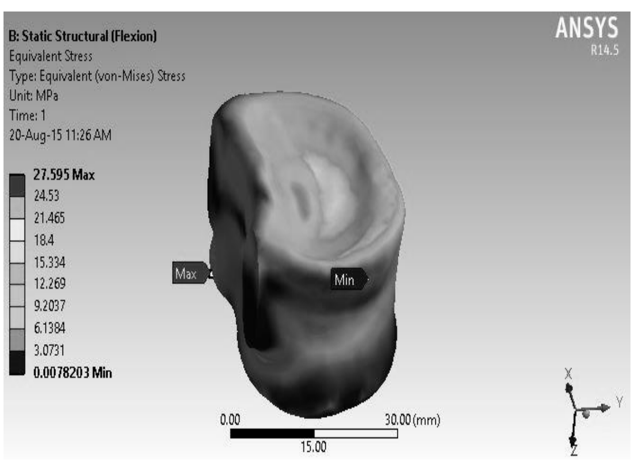


*Fig 4: Stress during Flexion condition*

From the stress distribution diagram for every loading condition, it is clear that the maximum stress is concentrated in the area near the pedicle and the maximum stress is generated during flexion condition

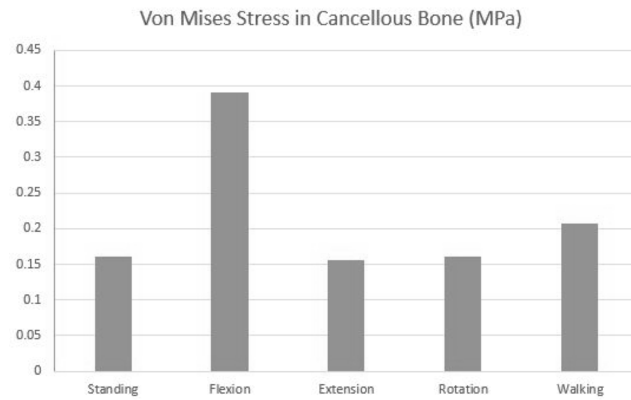


*Fig 5: Stress Variation in Cancellous Bone*

### *B. CFD Simulation of Injection Phase*

The CFD simulation enables us to obtain the distribution of the bone cement with time within the crack and thereby helps to find out the injection time. The bone cement distribution, velocity variations of different layers and the temperature variation of the bone cement during injection are evaluated. The results of temperature and cement distribution were passed to the FE-model. The distribution of the bone cement with in the crack with respect to time is showed on the Fig 6. The Variation of temperature of the bone cement during flow is depicted on Fig 7.

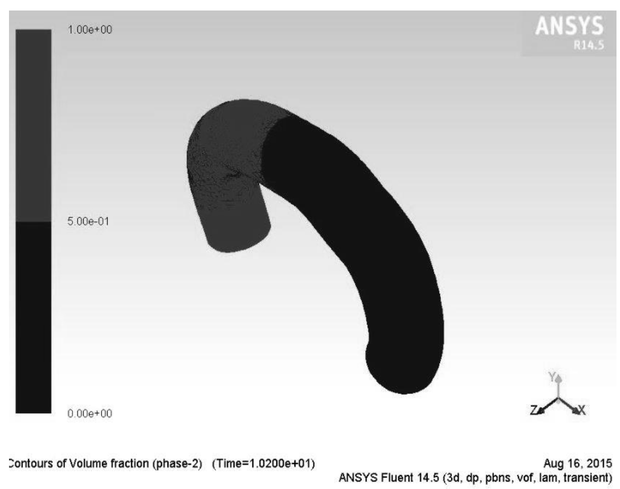


*Fig 6: Bone cement distribution*

One of the major complication of vertebroplasty is the leakage of cement into the spinal canal which occurs as a result of excessive cement injection and unknown injection time [2].This proposed method will enables us to determine the injection time and volume of bone cement required to fill the cavity even before the surgery using the CT images of the vertebra. In this particular case the injection time was 19.87 seconds and the volume of fluid required to completely fill the crack was 1884 $mm^3$. Furthermore the temperature variation of the bone cement during the flow can be evaluated and can be transferred to FE analysis in order to find out the thermal stress inducing in the vertebral body due to the temperature variation occurring during injection.

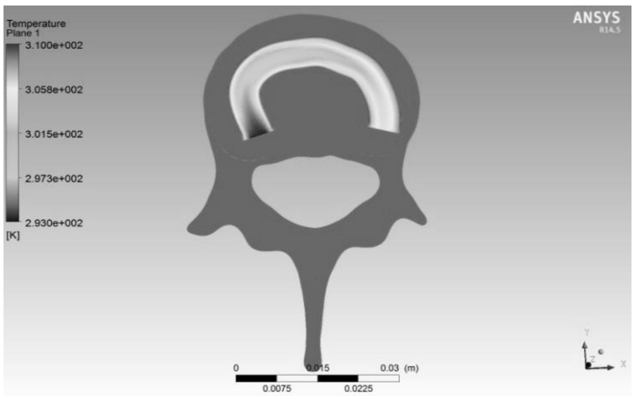


*Fig 7: Temperature distribution contour*

*C. Thermal Analysis*

The results of the thermal analysis reveal the variation of temperature within the vertebral body with respect to time. The temperature variation occurs due to the exothermic reaction during the bone cement setting. The variation of temperature within the vertebral body during the cement setting reaction is shown in the Fig 8.

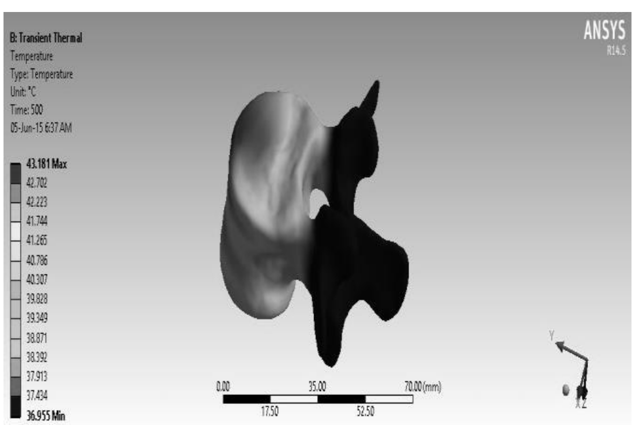


*Fig 8: Temperature distribution after 500 seconds*

*D. Structural Analysis*

The structural analysis shows the variation of stress induced in the vertebra, as the result of the exothermic reaction during the bone cement setting. The stress distribution in the vertebra is shown in Fig 9.

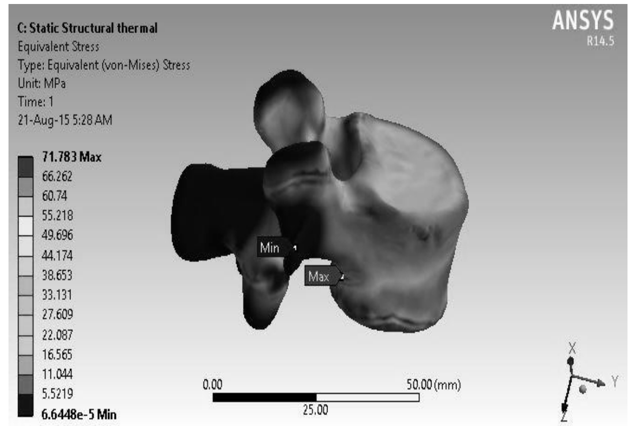


*Fig 9: Von Mises stress on the vertebra*

From the stress distribution diagram it is clear that the maximum stress is generated in the area below the pedicle and the stress generated is much more when compared to the stress induced on the vertebra during the normal conditions. The maximum stress generated in cancellous bone of the vertebra is depicted below with graph to study the effect of heat evolution occurring on the vertebra due to bone cement setting (Fig 10).

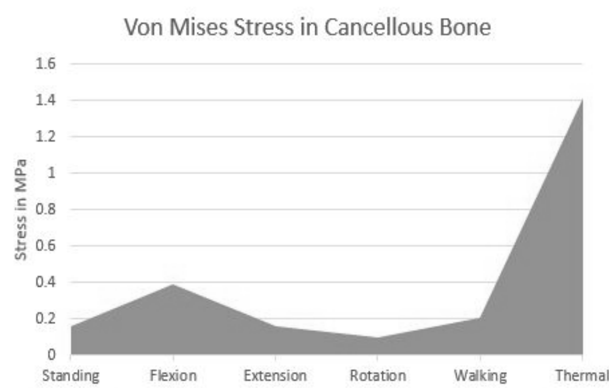


*Fig 10: Von Mises stress in Cancellous Bone*

Thermal damage to the intraosseous neural tissue caused by cement polymerization cannot be ruled out as a potential mechanism for pain relief after vertebroplasty. In addition, the exothermic reaction from the bone cement may cause thermal damage to surrounding tissue [3][4]. The human mesenchymal cells can withstand upto temperature of $58^0$C. When the bone cells are exposed to a temperature more than $58^0$C for a period more than 150 seconds, the cells undergo damage and it gets dead [11]. These phenomenon is the prime cause for the pain relief during vertebroplasty. These thermal analysis helps to figure out those portions on the cell which undergo degradation. Moreover, these results can be coupled with structural analysis to find out the residual stress inducing on the vertebral body.

Under the normal conditions of physiological activities, the maximum stress induced on the cortical bone is 22.2 MPa which occurs during the extension condition. At the same time, the stress induced on the cortical bone during the exothermic reaction is 71.183 MPa which is much more when compared to the normal conditions.

Under the normal conditions of physiological activities, the maximum stress induced on the cancellous bone is 0.414 MPa which occurs during the extension condition. At the same time, the stress induced on the cancellous bone during the exothermic reaction is 1.4 MPa which is much more when compared to the normal conditions. Hence we can clearly predict the possibility of further fracture inside the vertebral body.

## IV. CONCLUSION

In this paper, a computational framework for the simulation of bone cement injection and curing processes related to the surgical treatment of vertebroplasty was presented. The framework includes the generation of 3D-computer models based on patient specific data obtained from CT imaging, CFD-simulations of bone cement injection into trabecular structures and thermo-mechanically coupled FE-simulations of bone cement curing. The CFD-simulation of the injection process revealed reasonable filling patterns and the thermal analysis revealed the thermal distribution with in the vertebral body which can be utilized for finding out the induced stresses on the bone.

From the FE analysis of osteoporotic vertebra, it is clear that the maximum stress is generated in the cortical as well as the cancellous region of the vertebra, during the flexion motion. So among those five physiological motions, flexion is more vulnerable for initiating fracture in the vertebra. The CFD simulation of the bone cement injection is carried out to visualize the flow and distribution of the bone cement with in the crack. One of the major complication of vertebroplasty is the leakage of cement into the spinal canal which occurs as a result of excessive cement injection and unknown injection time. This proposed method will enables us to determine the injection time and volume of bone cement required to fill the cavity even before the surgery using the CT images of the vertebra. In this particular case the injection time is 19.87 seconds and the volume of fluid required to completely fill the crack was 1884 $mm^3$. Furthermore the temperature variation of the bone cement during the flow was evaluated and is transferred to FE analysis inorder to find out the thermal stress inducing in the vertebral body due to the temperature variation occurring during injection. The thermal analysis helps to figure out those portions on the cell which undergo degradation. The structural analysis gives the residual stress on the vertebra, which can be used to predict the possibility of further cracks.

In our future work it is intended to carry out the same procedure for different commercially available bone cements in order make a comparative study of the different bone cements. By carrying out experiments, we can identify the flow properties of the bone cements during injection phase and can be used for obtaining the input parameters and boundary conditions for the simulation and analysis. Moreover, the viscosity of the bone cements shows slight variations with respect to the variation in temperature. This can also be considered for the future works. The study can be extended to mark those regions of the vertebra which undergo degradation due to the thermal effect. If the CT image of an augmented vertebra is available, the distribution of the cement in vertebra can be clearly defined for the study. In this study an arbitrarily defined cement distribution was assumed. Also study can be made by incorporating the anisotropic properties of the bone by deriving the material property of various region of vertebra from its grey scale value in CT image. Thus a patient specific study can be made.

## REFERENCES


[1] P. MC Donnell, P. E. MC Hugh.,"Vertebral Osteoporosis and Trabecular Bone Quality", Annals of Biomedical Engineering, Vol. 35, No. 2, February 2007.

[2] ] Lih-Hui Chen, Po-Liang Lai, Wen-Jer Chen., "Current Status of Vertebroplasty for Osteoporotic Compression Fracture" Chang Gung Medical Journal 34 (2011) 352-359.

[3] William Lavelle., "Vertebroplasty and Kyphoplasty", Anesthesiology Clin, pp: 913928, 2007.

[4] Isador H. Lieberman., "Vertebroplasty and kyphoplasty: filler materials", The Spine Journal, pp: 305316, 2005.

[5] M.A. TYNDYK., "Generation of a _nite element model of the thoracolumbar spine", Acta of Bioengineering and Biomechanics, Vol. 9, No. 1, 2007.

[6] Andre Lupi., "Reverse engineering applied to a lumbar vertebra", Malta Medical Journal, Volume 20, Issue 04, December 2007.

[7] Antonius Rohlmaann et al.,"A probabilistic finite element analysis of the stresses in the augmented vertebral body after vertebroplasty", Spine journal (2010) 19: 1585-1595

[8] Marta Kurutz,"Finite Element Modelling of Human Lumbar Spine", ISBN: 978-953-307-123-7, InTech, 2010.

[9] Ralf Landgraf, Jorn Ihlemann, Sebastian Kolmeder et al.,"Modelling and simulation of acrylic bone cement injection and curing within the framework of vertebroplasty", Sciences Indexed, 27 March 2014.

[10] S. Kolmeder, A. Lion .,"Characterisation and modelling rheological properties of acrylic bone cement during application", Mechanics Research Communications 48 (2013) 93 -99.

[11] Yannis Reissis,Elena Garcia Gareta et al .,"The effect of temperature on the viability of human mesenchymal stem cells", Stem Cell Research and Therapy: 2013.

# Experimental Studies on Forced Convection Heat Transfer Characteristics of Al2O3- water based Nanofluid in Turbulent Regime

Manu. M[1], Krishnakumar T. S[2], Sajin Mathew Varghese

*Department of Mechanical Engineering*

*TKM College of Engineering, Kollam, Kerala, India*

[1]manumurali777@gmail.com

[2]krishnakumarts@gmail.com

***Abstract*— Enhancing heat transfer in equipments used in energy, electronics and transportation industries is an important area getting attention these days. Maxwell introduced the concept of mixed fluids to improve heat transfer characteristics, but they created problems like sedimentation, increased pressure drop and erosion. Nanofluids are fluids which has nano sized particles suspended in base fluids like water, ethylene glycol, oils etc. and improves heat transfer characteristics of base fluids. In the present work, an experimental set up is designed and fabricated to study forced convection heat transfer of nanofluids in turbulent flow regime. Flow is studied under constant heat flux conditions and temperature is measured using thermocouples. Forced convection heat transfer coefficient is estimated experimentally for Aluminium Oxide ($Al_2O_3$/water, size 13nm) based nanofluids. Nanofluids of various volume fractions are made and Reynolds number is varied from 4000 to 10000. Nanofluids showed enhanced heat transfer compared to demineralised water and this enhancement increased with Reynolds number and volume fraction for the case of $Al_2O_3$ – water nanofluid.**

***Keywords*— nanofluids, nano, forced convection, turbulent flow, $Al_2O_3$**

## I. Introduction

Maxwell introduced the concept of mixture fluids which is the technique of adding thermally superior metallic particles in conventional base fluids like water, oil etc. By this technique microsized and millimetre sized particles where suspended in conventional cooling fluids (that time nano technology was not even conceptualised). The major problem with such suspensions is the rapid settling of these particles. If the fluid is kept circulating, millimetre- or micrometre-sized particles would wear out pipes, pumps, and bearings. Also, such particles are not applicable to microsystems because they can clog micro channels. These conventional solid - fluid suspensions are not practical because of the significantly greater pressure drop and pumping power.

Choi [1] in 1995 first coined the term nanofluids, it was him who first successfully suspended nanoparticles in fluids and used for heat transfer enhancement at the Advanced Fluids Program at Argonne National Laboratory (ANL) USA. He was in charge of increasing heat transfer characteristics of micro channel heat exchangers. Getting inspired from Maxwell model he tried to suspend nanoparticles in fluids, which does not increase the pressure drop and he was successful in making stable nanofluids.

Experiment on convective heat transfer of nanofluids (γ-$Al_2O_3$/water and $TiO_2$/water) under turbulent flow conditions was performed by Pak & Cho in 1998. In their study, even though the Nusselt number (*Nu*) was found to increase with increasing nanoparticle volume fraction and Reynolds number (*Re*), the heat transfer coefficient (*h*) of nanofluids decreased after a particular load of nanoparticles. Xuan and Roetzel[3] proposed the following general function for the Nusselt number:

$$Nu = f\,[Re, Pr, \Phi, \text{particle shape, flow geometry}]$$

Where Re - Reynolds number, Pr - Prandl number, Φ is volume fraction, particle shape varies from sperical to modified shapes and flow geometry is the shape of flow passage . Another possible method of formulation suggested by Xuan and Roetzel is by postulating that the ratio of the heat transfer coefficients of the nanofluid and base fluid is proportional to the ratio of the respective thermal conductivities of the nanofluid and base fluid raised to some power. Buongiorno[12] analytically developed a two-component four-equation nonhomogeneous equilibrium model for mass, momentum, and heat transfer in nanofluids. He concluded that only Brownian diffusion (the random motion of nanoparticles within the base fluid) which results from continuous collision between nanoparticles and the molecules of the base fluid and the thermophoresis (diffusion of particles under the effect of a temperature gradient) are important slip mechanisms in nanofluids. SadikKakaç[8] has given a comprehensive review of heat transfer in nanofluids,it seriously discuss each paper available to explain convection in nano fluids. Many studies have been conducted using nano particle suspensions ([2-5],[8–11]) and many interpretations of result is seen in literature, the limitation of nano fluids is its small size itself, no competent technology is available to observe or compute what happens at such small size.Even though many papers are available both supporting and contradicting the unusual increase of heat transfer in nanofluids, the mechanism quoted are just theoretical models. Also there are variation in the results given by each paper.

## II. EXPERIMENTAL SETUP

In order to find out the heat transfer coefficient for a fluid passing through a circular pipe, an experimental setup is designed [15].

### *A. Experimental Setup*

From [15] it is evident that as the temperature difference between pipe material and bulk temperature of fluid increases, the uncertainty error also decreases, so an average temperature difference of 15$^{o}$C is assumed and rest of the design have been based on this assumption. The Reynolds number is varied from 4000 to 10000. Estimation of all properties have been done based on pure water and using Dittus Boelter equations as reference

The experimental set up is in the form of a loop made of stainless steel grade 306 (in many set ups copper pipe is used but due to higher thermal conductivity of copper, axial heat transfer loss was significant). Test section has a length of 1metre and inner diameter of 9mm. Test section is taken short due to larger (L/D) ratio which is enough for fully developed turbulent flow. Also an entry length of 36cm was given according to 40*D ( D = inner diameter).

The heater was designed based on maximum amount of heating required. A nichrome wire with resistance 6.828 Ω per metre length was heated using passing current and produces a constant heat flux condition along the test section. A total of 61 ohm resistance wire is wound over the one metre long test section. Porcelain beads are used to give electrical insulation between nichrome wire and test section tube. Three layers of asbestos rope is wound over the heater as insulator to prevent heat leakage to surrounding and to obtain a constant heat flux condition along the test section. It is ensured that the insulation thickness is more than the critical thickness of insulation to make insulation more effective. An autotransformer is used to control voltage across the test section and accordingly heating is controlled.

A thorough analysis of the temperature at each point is required which is given by several T type thermocouples. Eight thermocouples are connected on surface of heating test section. For calculation purposes average of the pipe wall temperature is used. Two thermocouples are inserted inside the pipe to measure the inlet and outlet temperature of the fluid. These thermocouples were calibrated using Julabo F 25-HP constant temperature bath.

A self-priming regenerative type centrifugal pump of 0.5 hp power and with a maximum head of 14 m working in 240V, 50 Hz, AC supply is used to pump the nanofluid through the test section. It has a maximum output of 750 liters per hour. It was ensured that it works in the Reynolds number range which we require. A globe valve is used to control the flow rate in Reynolds number range 4000 to 10000. The Reynolds number is limited to 10000 due to technical limitations. As Reynolds number increases the temperature difference of fluid reduces, which according to uncertainty error analysis increases the error, otherwise we should go for a higher capacity heater (DC heater) which is very costly or by using transformer of higher capacity.

Since study is conducted using nanofluids which is very costly nanofluid should be reused if an option is available, so only way is to make the experimental set up in the form of a loop, i.e. the fluid coming from heater should be cooled and reused. Condenser is used to cool the nanofluid back to the initial temperature. For each flow rate, the cooling load will also be varying. Condenser is designed based on maximum cooling load.

The following assumptions are made while doing experiment. The experiment is conducted at fully developed turbulent flow regime. The test section is assumed to be of constant heat flux type. Negligible heat loss is considered in the radial and lateral directions of the test section. Measurements are taken after steady state conditions are achieved. Due to extremely small dimension, it has been suggested that nano particles may be considered to behave more like a fluid (Xuan and Roetzel, 2000). By assuming negligible motion slip between the particles and the continuous phase, the nanofluids may be considered as a conventional single-phase fluid (Pak and Cho, 1998; Xuan and Roetzel,2000).

### *B. Preparation of nanofluid*

Preparation of nanofluid is the first key step in experimental studies with nanofluids. Nanofluids are not simply liquid - solid mixtures. Some special requirements are essential, like even and stable suspension, negligible agglomeration of particles, no chemical change of fluid etc. A measured volume of nanoparticles is added into the beaker containing measured volume of distilled water. The volume fraction is determined as the ratio of the volume of the nanoparticles to the total volume, where the total volume is the sum of the volume of the base fluid and the volume of nanoparticles. Mass was measured using weighing balance which can measure a minimum of 1mg. The beaker is placed in a controlled chamber where it is agitated for 4-5 hours using ultrasonic agitator. Mass of nanopowder added, is find out from the volume fraction

$$\emptyset = (\boldsymbol{m_p}/\boldsymbol{\rho_p}) \,/\, (\boldsymbol{m_p}/\boldsymbol{\rho_p} + \boldsymbol{m_f}/\boldsymbol{\rho_f})$$

Where,

$\emptyset$ = volume fraction

$m_p$ = mass of nano particle

$\rho_p$ = Density of particle

$\rho_f$ = Density of fluid

$m_f$ = mass of fluid

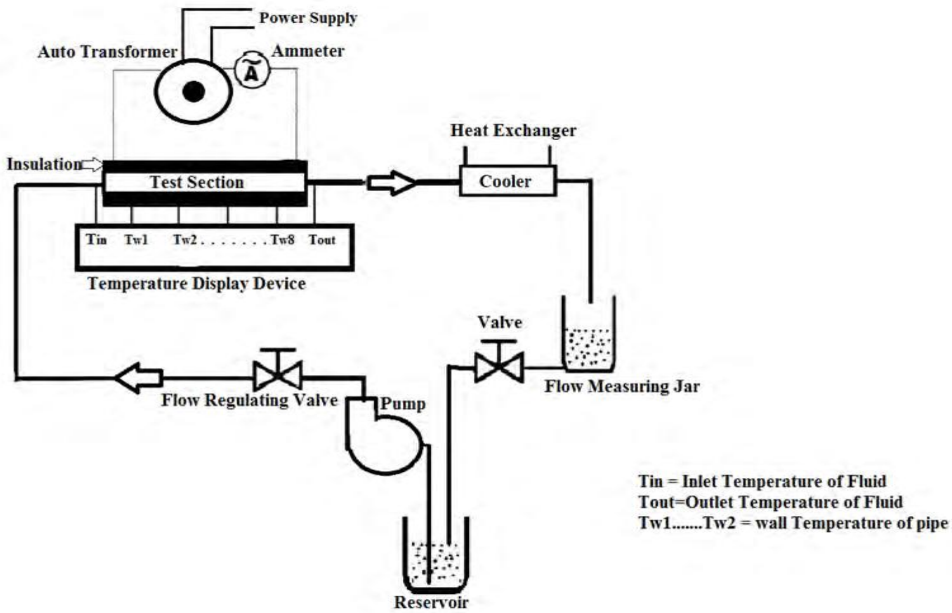


Fig.1.Lay out Diagram of experimental set up

The nanoparticle used in the study is $Al_2O_3$ (13nm) having density – 1.06g/mL and surface area 85- 115 $m^2$/g. Size of the particles have been confirmed by the TEM by the manufacturer itself.

The purpose of the agitation is to break down or de-agglomerate clustered nanoparticles, facilitate even particledistribution, minimize nanoparticle sedimentation after some duration of time. The nanoparticles remains suspended for a period of 1-2 hrs. (for the case of $Al_2O_3$nano particles), after which settling begins to occur. $Al_2O_3$ - water nanofluids are prepared with volume fractions 0.1%, 0.2% and 0.3%. A minimum quantity of base fluid (2.5ltrs) was used to ensure proper flow inside the circular tube. Further studies are required for the effect of surfactants and pH on the stability of nanofluids.

*C. Properties of nanofluid*

Even though nanofluids can be considered as single phase fluids (Xuan and Roetzel, 2000), their properties shows some variation from base fluid. From literature so many models are available to derive their properties, some resembling to Maxwell model. Nano fluids are suspended with metal oxide particles which contribute some of their properties to the bulk fluid and acting like a different fluid. For the fluid density increases, Specific heat decreases, viscosity increases and Thermal conductivity increases

*1. Density :*

The density of prepared nanofluid is calculated using the formula given by Maxwell for mixtures

$$\rho nf = \emptyset \rho p + (1 - \emptyset)\rho f$$

Where ρnf, ρp, ρf are densities of nanofluids, nano particles and base fluid. Φ is volume fraction taken.

2. Specific Heat:

The specific heat of nanofluids is calculated using the following volume fractioned-based mixture rule (Pak & Cho, 1998 )

$$Cp(nf) = [\emptyset \rho_p Cp_p + (1 - \emptyset)\, \rho_f Cp_f] / \rho_{nf}$$

Where $Cp_{nf}$, $Cp_f$, $Cp_p$ are the specific heat of nanofluid, base fluid and the nanoparticles.

*3. Viscosity:*

The viscosity of nanofluid can be determined from Batchelor's model given by Batchelor, (Batchelor, 1977)

$$\mu(nf) = \mu_f (1 + 2.5\emptyset + 6.2\emptyset^2 )$$

Where, $\mu(nf)$ is the nanofluid viscosity and $\mu_f$ is the base fluid viscosity.

*4. Thermal conductivity:*

The Maxwell model is used for the determination of effective thermal conductivity of nanofluids $k_{nf}$ which is given by Maxwell.

$$k_{nf} = [k_f(k_p + 2k_f + 2\emptyset(k_p - k_f))] / [k_p + 2k_f - \emptyset(k_p - k_f)]$$

Where $k_{nf}$ ,$k_f$ and $k_p$ are the thermal conductivities of the nanofluid, base liquid and the nanoparticles respectively, ∅ is the volume fraction of nanoparticles. The effect of temperature on properties of nano fluids has not been considered as temperature change in our experiment is kept low.

*D. Uncertainity errors*

Calibration of the thermocouples was done using a calibration bath. Before measuring the heat transfer coefficient of nanofluids, the experimental system was calibrated with demineralized water. The total uncertainty for the measurements of the heat transfer coefficient can be estimated from the following equation.[15]

$$\frac{\omega_h}{h} = \sqrt{\left(\frac{\omega_q}{q}\right)^2 + \left(\frac{\omega_{\Delta T}}{\Delta T}\right)^2}$$

$$\frac{\omega_{Nu}}{Nu} = \sqrt{\left(\frac{\omega_h}{h}\right)^2 + \left(\frac{\omega_d}{d}\right)^2}$$

The thermocouples were calibrated. The accuracy of the heat flux calculated was 4.14%. The accuracy of the flow rate measured was within 3%. The accuracy of the tube diameter was less than ±0.2mm.

The uncertainty of the measured heat transfer coefficient and Nusselt number were estimated to be 4.35% and 5.14% respectively.

Validation was done using Dittus - Boelter equation using demineralized water as shown in Fig.2.Both theoretical and experimental values were showing good agreement

$$Nu = 0.023Re^{0.8}Pr^{0.3}$$

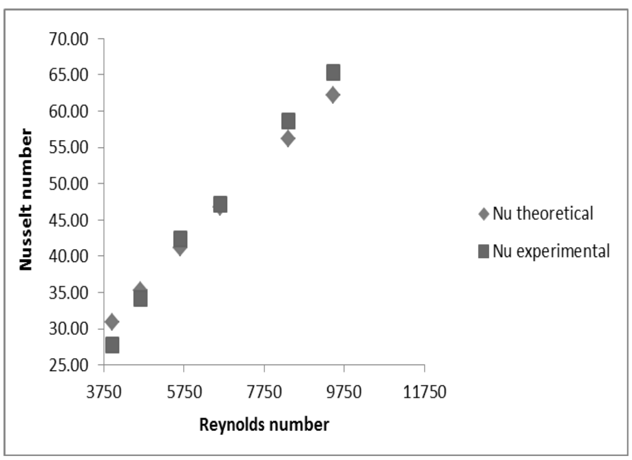


Fig 2 Variation of Nusselt number with Reynolds number

## III. RESULTS AND DISCUSSION

The experiments are conducted with demineralised water and $Al_2O_3$ based nanofluids at different volume fractions (0.1%, 0.2% and 0.3%). Convective heat transfer coefficients for different samples are calculated using the experimental readings at different flow velocities. The results well establishes an enhancement in the convective heat transfer characteristics of the nanofluid compared to the base fluid. Also there is an enhancement in the heat transfer properties with particle volume fraction up to the 0.3%.

The experimental data are compared with other correlations available for the case of nanofluids in the turbulent region for Reynolds number from 4000 to 10000. The experimental results are discussed below.

Fig.3. shows variation of convective heat transfer coefficient with Reynolds number for demineralized water and different percentage particle volume fractions of the $Al_2O_3$–water nanofluid. It is evident that there is an enhancement in the heat transfer coefficient with respect to the flow velocity for all the samples compared to water. The specific surface area of $Al_2O_3$ nano particle is 85-115m$^2$/g (from manufacturer data) which is a clear indication of increase of heat transfer. From calculation total surface area of alumina available at test section for heat transfer is 25.9m$^2$ (at 0.1% volume fraction) and 78m$^2$ (at 0.3% volume fraction). This much area of solid suspension will be interacting with the water inside test section, which causes enhance in heat transfer as thermal conductivity of $Al_2O_3$ is higher than that of water. The results obtained is in fair agreement with that reported by Pak and Cho[2].

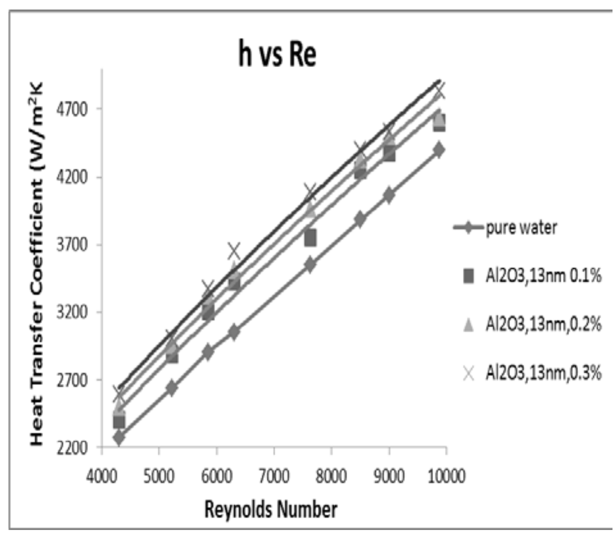


Fig.3. Heat transfer coefficient vs Reynolds number for $Al_2O_3$, 13nm for volume fraction 0.1%,0.2% and 0.3%.

Fig.4. shows the variation of heat transfer enhancement ratio with volume fraction for various Reynolds number of $Al_2O_3$ -water nanofluid. It is not necessary that heat transfer always enhances with increase in Reynolds number. There is an optimum point at which heat transfer enhances the maximum and then drops, which can be attributed to the settling of agglomerated $Al_2O_3$ nano particles with increasing volume fraction. In this case the maximum enhancement is shown for Reynolds number of 5852.This will hinder the use of nanofluids for long term use.

Even though use of surfactants and controlling the pH value[7],[8] are recommended for increasing stability of nanofluids, their practical implementation requires further studies.

In literature review it is seen that many correlations were postulated both analytically and empirically for Nusselt number in terms of Reynolds number and Prandtl Number.

Most of the correlations suggested for the nanofluids are specific to the nanofluid used and were modified version of the Dittus Boelter equations. In the present study experimental

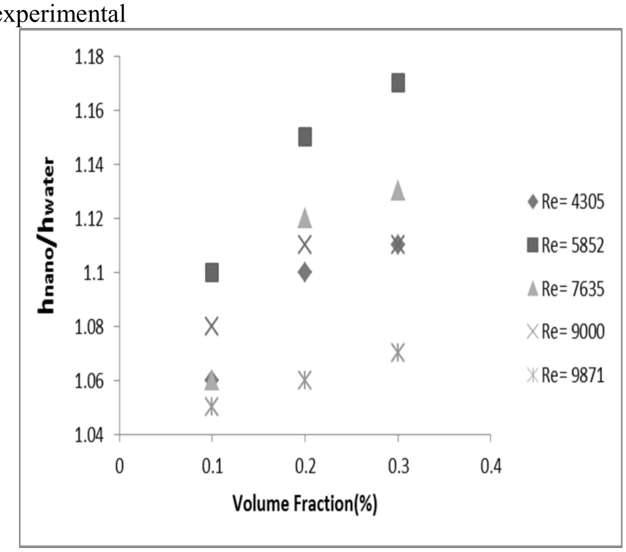


Fig.4. Heat transfer coefficient ratio vs volume fraction for $Al_2O_3$, 13nm for different Reynolds number.

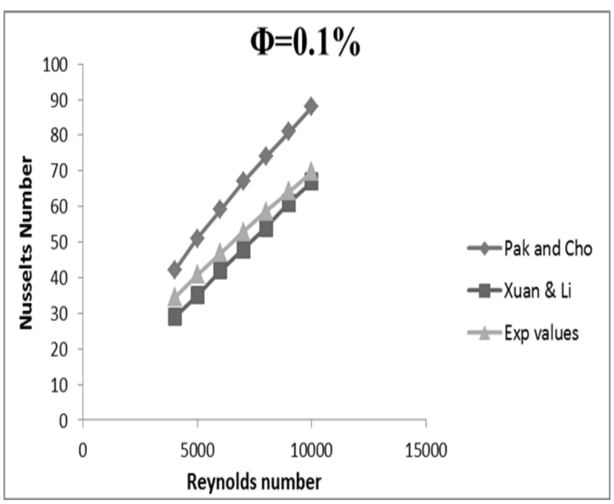


(a)

Nusselt number is compared with two correlations of Pak and Cho[2] and Xuan & Li [4] as shown in Fig.5.

Pak and Cho: $Nu = 0.021Re^{0.8}Pr^{0.3}$

Xuan & Li: $Nu = 0.0059(1+7.628\ \Phi^{0.6886}\ Pep^{0.001})\ Re^{0.9238}\ Pr^{0.4}$

The results are more confirming with the results of Xuan and Li correlation. As the Reynolds number increased the line moves more towards the Xuan and Li values. Pak and Cho used a colloidal alumina which may be considered more stable than nanofluids prepared with two step method. This can be reason for variation of experimental result from Pak and Cho correlation.

## IV. Conclusions

In the present work, experiments were conducted to measure the convective heat transfer coefficient of nanofluids in the turbulent flow regime. It was found that there is an increase in

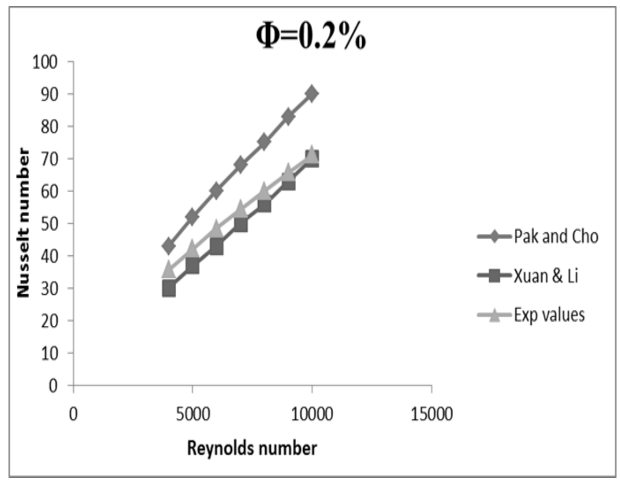


(b)

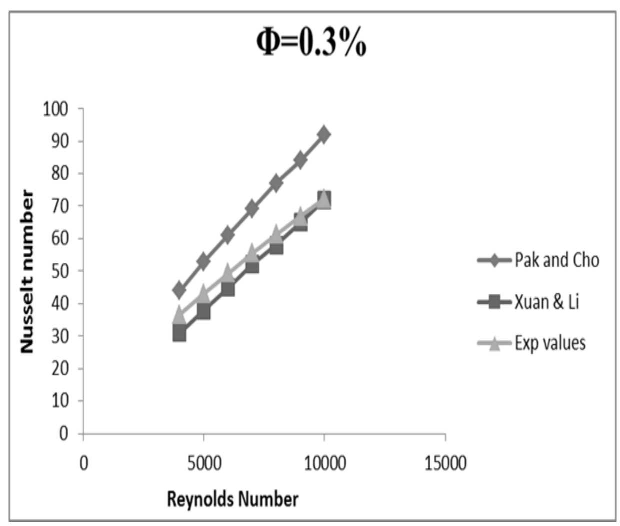


(c)

Fig.5.Graph showing comparison of experimental values with with other correlations for various volume fractions a) 0.1% b)0.2% c)0.3%.

the convective heat transfer when $Al_2O_3$– water nanofluids was used instead of demineralized water. This enhancement increases with increase in the flow velocity and particle volume fraction. Along with the enhanced effective thermal conductivity and viscosity of the nanofluids, the migration and the random movement of nanoparticles and the resulting disturbance of the boundary layer may be the reasons for such an increase in the heat transfer coefficients of nanofluids. Other possible reasons may be thermal dispersion, Brownian diffusion, particle- particle collisions and enhanced surface area of heat transfer. Further investigations are needed for a better understanding of the underlying mechanisms for enhanced heat transfer characteristics of nanofluids.

Showing a significant increase in heat transfer, nanofluids are a good replacement for conventional fluids. With increase in volume fraction, heat transfer enhancement also increases for $Al_2O_3$. A maximum increase of 17% enhancement is seen for $Al_2O_3$ water nano fluid for a Reynolds number of 5852 at a volume fraction of 0.3% volume fraction.

Further studies are required to find the effect of size of nanoparticles, shape, and higher Reynolds number on heat transfer rate and to develop more accurate mathematical models to simulate the mechanisms in nano fluid heat transfer.

## ACKNOWLEDGMENT

This work was supported by the TKM College of Engineering and TEQIP II.

## REFERENCES

[1] Choi.S., *Enhancing Thermal Conductivity of Fluids with Nanoparticles, in Developments and Applications of Non Newtonian Flows*, ASME,FED-Vol 231/MD-Vol.66, pp 99-105, 1995

[2] Pak B.C., and Cho Y, *Hydrodynamic and Heat Transfer Study of Dispersed Fluids with submicron Metallic Oxide Particles* , Exp. Heat Transfer,11,pp. 151-170, 1998.

[3] XuanY, Roetzel W., *Conceptions for heat transfer correlation of nanofluids*. Int. J. Heat Mass Transfer 43, 3701–3707, 2000.

[4] XuanY and Li Q, *Investigations on Convective heat transfer and flow features in Nano fluids*, Journal of Heat Transfer, 125,,PP. 151- 155, 2003.

[5] Maiga et al, *Heat Transfer Behaviors of Nanofluids in Uniformly Heated Tube,Supperlattices Microstruct*,35,pp.280 -289,2004.
Xiang-Qi Wang, Arun SMujumdar, *Heat transfer characteristics of nanofluids: a review*, International Journal of Thermal Sciences 46 pp.1–19, 2007.

[6] Sarit K. Das, Stephen U. S. Choi, Wenhua Yu, T. Pradeep, *Nanofluids-Science and Technology*, John Wiley & Sons, Inc. , 2008.

[7] SadikKakaç, AnchasaPramuanjaroenkij,, *Review of convective heat transfer enhancement with nanofluids*, International Journal of Heat and Mass Transfer 52 3187–3197, 2009.

[8] Sidi El Be´cayeMaiga ,Samy Joseph Palm, Cong Tam Nguyen, Gilles Roy, NicolasGalanis. *Heat transfer enhancement by using nanofluids in forced convection flows*. International Journal of Heat and Fluid Flow 26 (2005) 530–546, 2005.

[9] Ulzie Rea, Tom McKrell, Lin-wen Hu, Jacopo Buongiorno, *Laminar convective heat transfer and viscous pressure loss of alumina–water and zirconia–water nanofluids*. International Journal of Heat and Mass Transfer 52 2042–2048, 2009.

[10] Wesley Williams, Jacopo Buongiorno. *Experimental Investigation of Turbulent Convective Heat Transfer and Pressure Loss of Alumina/Water and Zirconia/Water Nanoparticle Colloids (Nanofluids) in Horizontal Tubes*.Journal of Heat Transfer Vol. 130 / 042412-1.

[11] J. Buongiorno , *A non-homogeneous equilibrium model for convective transport in flowing nanofluids*, in: The Proceedings of HT2005, SanFrancisco, CA., 2005.

[12] KyoSikHwang, SeokPil Jang. Stephen U.S.Choi, *Flow and convective heat transfer characteristics of water based Al2O3 nanofluids in fully developed laminar flow regime*, International journal of Heat and Mass Transfer 52193 – 199, 2009.

[13] J E Julia, L Hernandez, R Martinez Cuenca, T Hibiki, R Mondragon,C Segarra, J C Jarque, *Measurement and modelling of forced convective heat transfer coefficient and pressure drop of* $Al_2O_3$ *and* $SiO_2$ *water nanofluids*, Journal of Physics: Conference Series 395,012038(2012).

[14] Holman J.P., *Experimental Methods in Engineering*, McGraw Hill Companies Inc., New York , 2007

# Experimental Study on the Effects of Surfactants on Formation of Refrigerant Hydrates

Abdul Azeez P. A[1], Yaseer M , Mohamed Iqbal Pallipurath [3]

*Department of Mechanical Engineering, TKM College of Engineering,Kollam, Kerala, India*

[1]abdulazeez350@gmail.com

[3]mohamediqbalp@gmail.com

***Abstract-*** **This work presents an experimental study which is intended to understand the effects of surfactants on formation of Clathrate hydrates in R22/liquid-water system. The experiments were performed by fabricating a laboratory scale, isobaric hydrate forming reactor made of transparent acrylic cylinder for the ease of visual inspection. The surfactants used in this study were Gum acacia, Cetylpyridinium chloride (CPC) and Benzalkonium chloride. Notable increases in induction temperature and hydrate formation rate were simultaneously observed by the addition of CPC to the aqueous solution at optimum concentration. Neither the rate of hydrate formation nor induction temperature exhibited appreciable improvement on using gum acacia and Benzalkonium chloride. Based on the observations it is concluded that surfactant CPC has better effect on R22 clathrate hydrate formation compared to Gum acacia and Benzalkonium chloride.**

***Keyword—*** **Hydrate, Cool Storage, Surfactants, Induction Time, Formation Temperature**

## I. INTRODUCTION

The word “clathrate” from the Greek word “khlatron” meaning barrier, indicates crystalline inclusion compounds in which small guest atoms or molecules are physically trapped by three dimensionally shaped cavities formed by three dimensional assemblies of hydrogen atoms. These compounds are called clathrate hydrates when these compounds contain water and gas hydrates when the enclosed molecules are gases. Gas hydrates are ice like crystalline compounds in which two or more gas molecules are housed in a cage of water molecules under high pressure and low temperature conditions. They appear like ice but form at elevated temperatures well above ice point. These solid crystals are formed when water along with low molecular weight slightly polar gas molecules are exposed to appropriate pressure and temperature conditions. At low temperature and moderate pressure hydrogen bonded water molecules form cage like structure with cavities that need to be filled with hydrate forming gas molecules (guest molecule)

to stabilize the crystal structure. Without the support of the trapped molecules, the lattice structure of hydrates would collapse into conventional ice crystal structure or liquid water. The formation and decomposition of clathrate hydrates are first order phase transitions, not chemical reactions.

The many facets of Gas hydrate technology, which has captured the attention of many researchers worldwide, are cool storage, gas transportation, marine $CO_2$ sequestration, desalination of sea water, and gas separation [1]. The present problem faced by gas hydrate technology

is how to improve hydrate formation rate, storage capacity, improve hydrate formation temperature and so on. This paper describes the experimental studies of the effect of different surfactants on R22 hydrate formation and dissociation conditions and summarizes the same.

*A. Action principle of surfactant on gas hydrate formation*

Gas hydrate formation conditions can be improved by increasing solubility of guest gas molecules in water. This can be done either by increasing the pressure of hydrate reactor or by adding surfactant to water prior to hydrate formation. Surfactant that is added to the gas hydrate system at a particular concentration reduces the gas water interfacial tension, which can decrease the interphase diffusion resistance and increase the solubility of gas molecules in the solution.[2] Due to this, contacting area of gas-liquid increases to generate hydrate crystal molecules and shorten induction time of hydrate formation.

The experimental results on hydrate formation show that the addition of surfactants does not increase hydrate formation conditions anymore if its concentration exceeds a certain value. Beyond a certain concentration surfactant molecules may get adsorbed on the hydrate particles and inhibit further growth at higher concentrations. This optimum concentration can be determined experimentally by performing the experiment with selected concentrations of surfactants. The particular concentration that gives highest possible hydrate formation temperature and lowest induction time at constant pressure can be taken as the optimum concentration of that particular surfactant. The different kinds of surfactants used in experiment are Cetylpyridinium chloride, Benzalkonium chloride and Gum acacia. CPC and BZK belong to cationic surfactant family while gum acacia is a non-ionic natural surfactant obtained from tree acacia.

## II. EXPERIMENTAL APPARATUS

The experimental setup comprises of an isobaric hydrate reactor made of transparent acrylic cylinder, magnetic stirring system, constant temperature bath, pressure gauge, and K-type thermocouple. Through the transparent apparatus hydrate formation and dissociation could be monitored directly. Figure.1 illustrates schematic of experiment test section where R22 hydrate formation take place.

The thickness required for the acrylic cylinder is calculated using the relation of thick cylinders,

$$t = \frac{PD}{\frac{Su}{2} - 1.2P}$$

Where,

t= Thickness of acrylic cylinder.
P= Pressure inside the apparatus.
D= Outer diameter of cylinder.
$S_u$=Ultimate strength of acrylic cylinder (70Mpa).

The maximum pressure the apparatus can withstand is found to be 38bar. Taking into account the safety considerations, maximum of 6bar is introduced in the apparatus of volume 0.28 litres. A magnetic stirring device actuated by permanent magnet was set to run at constant RPM (400-500) during experiment.

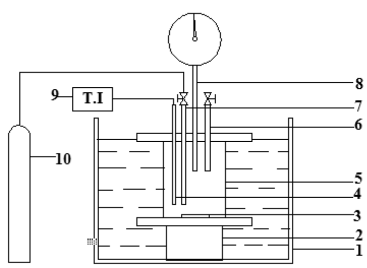


Fig.1 experiment set up for gas hydrate formation.

1-constant temperature bath, 2-magnetic stirrer, 3-stirrer bar, 4-thermo couple, 5-hydrate reactor, 6-ball valve, 7-pin valve, 8-pressure gauge, 9-temperature indicator, 10-R22 container.

The hydrate formation temperature was determined by immersing the hydrate reactor inside the constant temperature bath after filling the same with predetermined quantity of water (150ml) and charging with R22 gas to required pressure level. The formation temperature was determined by a K-type thermocouple. Its range was -100$^o$C to 400$^o$C with an error band of -0.2$^o$C.Pressure inside the reactor was measured by a commercial pressure gauge with range 0 to *500psi* and error band of.02bar.

Dissociation conditions were investigated by placing the apparatus outside the constant temperature bath (room temperature) and observing corresponding thermocouple and pressure gauge reading.

## III. RESULTS AND DISCUSSION

### *A. Experiments to find out optimum concentration of surfactants.*

Figure.2-5 shows concentration-temperature relation of R22 hydrate formation for three different surfactants at constant pressure 3bar. The concentration that provides highest possible hydrate formation temperature and least induction time is taken as optimum concentration of that particular surfactant.

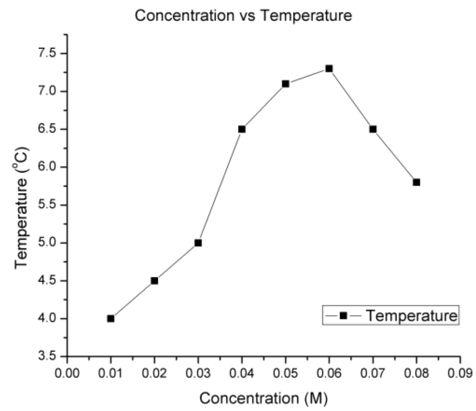


Fig.2. Concentration-temperature plot of R-22 hydrate in aqueous CPC solution.

Optimum concentration=.06M

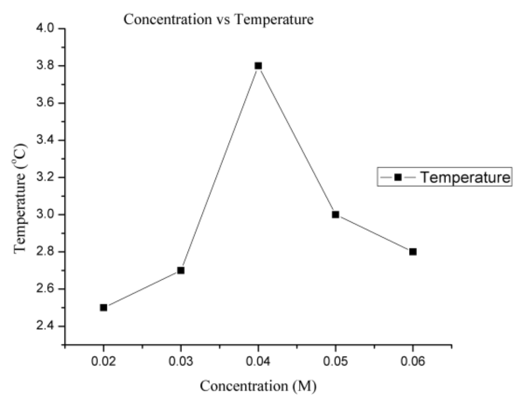


Figs .3 Concentration-temperature plot of R-22 hydrate in aqueous BZK solution.

Optimum concentration =0.04M

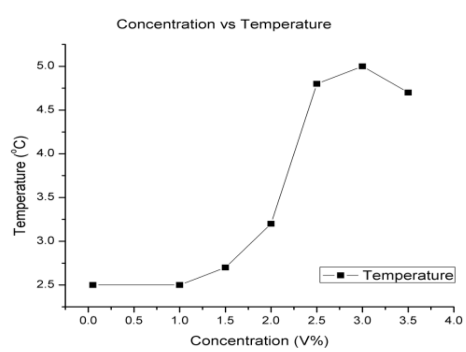


Fig.4 Concentration-temperature plot of R-22 hydrate in aqueous Gum acacia solution.

Optimum concentration=3V% of solution.

*B. Effects of surfactants on R22 hydrate formation and dissociation conditions.*

*1) Effect on R22 hydrate formation temperature:*

Figure shows comparison of effect of surfactants and pure water on R22hydrate formation pressure-temperature relation. At lower pressure CPC exhibited better result on hydrate formation temperature compared to rest of the additives and pure water. On increasing the pressure it is noted that temperature difference of R22 hydrate formation between pure water and aqueous solution of CPC got reduced. In aqueous CPC solution R-22 hydrate formed at 1 bar pressure and 4oC. At 2bar pressure hydrate formation temperature raised by 3.8oC in aqueous CPC solution. For pressure range of 2 to 5 bar aqueous CPC solution exhibited an average improvement of 3.4oC, but the effects of BZK and Gum acacia were not appreciable compared to CPC.

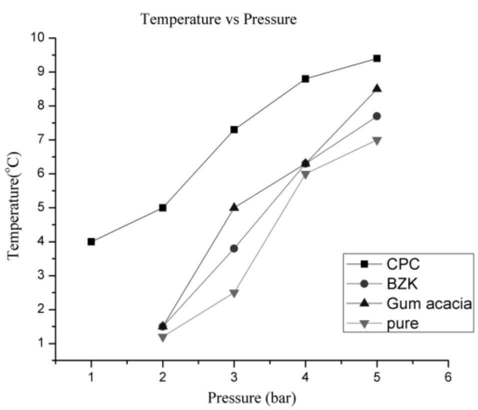


Fig.5 Pressure-temperature plot for R-22 hydrate formation

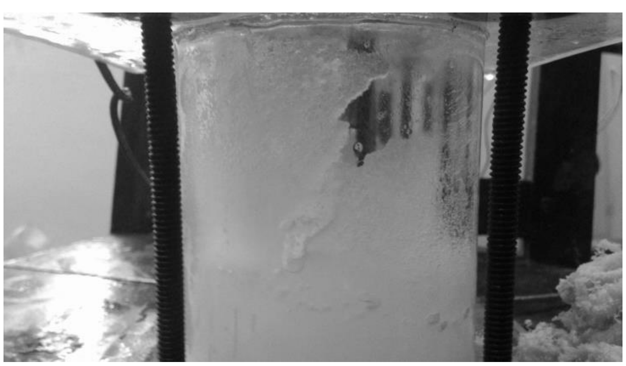

Fig.6 R22 Hydrate

*2) .Effect on induction time of R22 hydrate:*

Figure shows comparison of effect of surfactants and pure water on R22 hydrate induction time.An induction period refers total time required for hydrate formation. Results from the study shows that addition of CPC additive exhibited considerable reduction in induction time at lower pressure, on increasing the pressure its effect on induction time reduced. At 5 bar pressure the effect of CPC on induction time was negligible. Additives BZK and Gum acacia increased the induction time by an average of 15 and 8 minutes respectively. For a pressure range of 2 to 5 bar CPC exhibited an average reduction of 6 minutes on induction time.

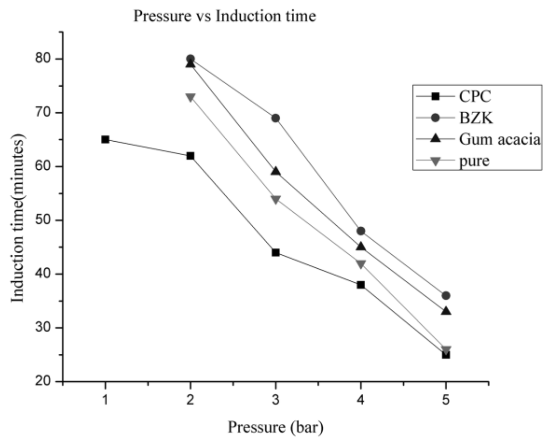


Fig.7 Pressure-induction time plot for R-22 hydrate.

*3) Effect on dissociation starting temperature:*

Figure shows comparison of effect of surfactants and pure water on R22 hydrate dissociation starting temperature.

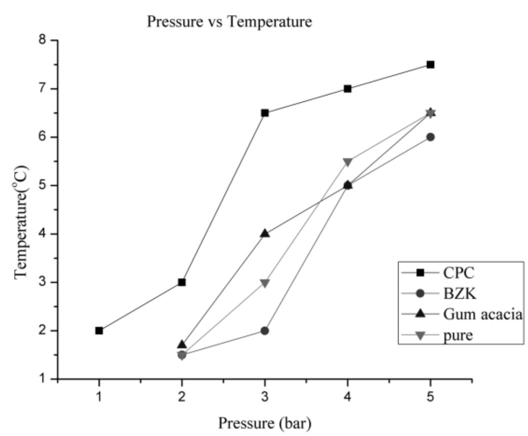


Fig.8 Pressure-dissociation starting temperature plot for R22 hydrate

Hydrate dissociation usually starts at a temperature close to that of hydrate formation. This is an endothermic process and considered as cool releasing period of refrigerant hydrate. From the graph it is observed that there is a positive shift in dissociation starting temperature for CPC, while BZK and Gum acacia exhibited negligible change for the same. The increase in dissociation starting temperature for CPC is due to corresponding increase in hydrate formation temperature.

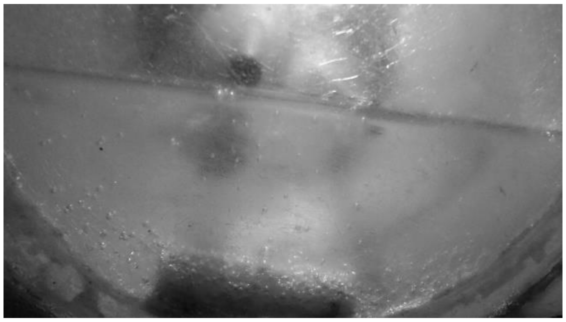

Fig.9 R22 Hydrate Dissociation

*4) Effect on dissociation time:*

Figure shows comparison of effect of surfactants and pure water on R22 hydrate dissociation completion time. Total dissociation time is the time required for complete dissociation of refrigerant hydrate. Significance of this time period is that during this period hydrate can provide cooling effect to the surrounding since it is an endothermic process. From the analysis of data it is found that change in pressure exhibited negligible effect on dissociation completion time for all the three additives. However beyond 3bar pressure all additives reduced dissociation completion time compared to pure R22 gas hydrate.

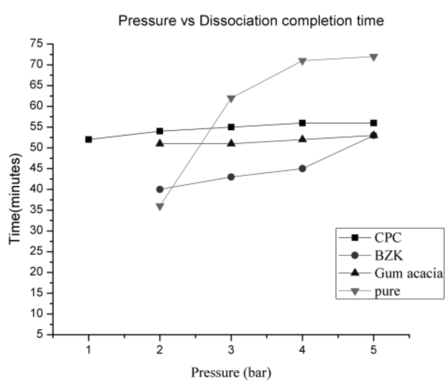


Figure.10 Plot for Pressure-dissociation completion time for R22 hydrate

At 2bar pressure few quantity of R22 hydrate was formed in pure water so it took lesser time to dissociate. Surfactants also acted as anti-agglomerating agents, tearing up the hydrate particles and dispersing it throughout the water. So its surface area got increased compared to R22 hydrate in pure water simultaneously reducing total dissociation time.

## IV. CONCLUSION

Experimental observation of hydrate formation from R22 in contact with aqueous solutions of CPC, BZK and Gum acacia was performed. Optimum concentration of surfactants was determined. From the experimental observations it is found that surfactant CPC has better effect on R22 hydrate formation compared to BZK and Gum acacia. At 2 bar pressure CPC improved hydrate formation temperature from 1.2°C to 5°C and reduced induction time from 72 minutes to 62 minutes. An extensive research is still required to find a surfactant which form hydrates at atmospheric conditions and which is environmentally compatible.

## REFERENCES

[1] Xiaolin Wang, Mike Dennis, and Liangzhuo Hou, “Clathrate hydrate technology for cold storage in air conditioning systems,” Renewable and Sustainable Energy Reviews vol.36, pp.34–51, 2009.

[2] Naoki Ando, yuikuwabara, and yasuhikoh.Mori, “Surfactant effects on hydrate formation in a nunstirred gas/liquid system: An experimental study using methane and micelle-forming surfactants,” Chemical Engineering Science vol.73, pp.79–85, 2012.

[3] Moon-Kyoon Chun, and Huen Lee, “Phase equilibria of R22 ($CHClF_2$) hydrate system in the presence of sucrose, glucose and lactic acid,” Fluid Phase Equilibria vol.51, pp. 361–370, 1998.

[4] Shi Cai Sun and Chang-Ling Li, “Hydrate phase equilibria of the guest mixtures containing $CO_2$, $N_2$ and tetrahydrofuran,” fluid phase equilibria vol. 185, pp. 101–109, 2014.

[5] Jinping Li, Kaihua Guo, Deqing Liang, and Ruzhu Wang, “Experiments on fast nucleation and growth of HCFC141b gas hydrate in static water columns”, International Journal of Refrigeration vol.27, pp.932–939, 2004.

[6] Jinping Li and Deqing Liang, “The influence of additives and metal rods on the nucleation and growth of gas hydrates,” Journal of Colloid and Interface Science vol.283, pp.223–230, 2005.

[7] Tomohiro Ogawa and Tomonari Ito, “Development of a novel hydrate-based refrigeration system: A preliminary overview,” Applied Thermal Engineering vol.26, pp. 2157–2167, 2006.

[8] Yuehong Bi, Tingwei Guo, Liang Zhang, and Hua Zhang Lingen Chen, “Experimental study on cool release process of gas-hydrate with additives,” Energy and Buildings vol. 41, pp.120–124, 2009.

[9] Wu Qiang, Zhang Qiang, and Zhang Baoyong, “Influence of super-absorbent polymer on the growth rate of gas hydrate,” Safety Science vol.50, pp.865–868, (2011).

[10] Fatemeh Nikbakht, Amir Abaas Izadpanah, “Modeling of hydrate formation conditions for refrigerant r-134a, r-141b and r-152a using the cpa equation of state and obtaining the kihara potential parameters for these refrigerants,” international journal of refrigeration vol. 35, pp. 1914-1920, 2012.

[11] Minwei Sun, and Abbas Firoozabadi, “Gas hydrate powder formation – Ultimate solution in natural gas flow assurance,” Fuel vol., pp.146, 1–5, 2014.

[12] Maryam Karamoddin, Farshad Varaminian, and Maryam Daraee,” Kinetic study on the process of

CHClF2 (R22) hydrate formation in the presence of SDS surfactant based on chemical affinity," Journal of Natural Gas Science and Engineering vol.19, pp. 46-51, 2014.
[13] Xiaolin Wang, Mike Dennis, and Liangzhuo Ho, "Clathrate hydrate technology for cold storage in air conditioning systems," Renewable and Sustainable Energy Reviews vol.36, pp.34–51, 2014.
[14] Imen Chatti, and Anthony Delahaye, "Benefits and drawbacks of clathrate hydrates: a review of their areas of interest," Energy Conversion and Management vol.46, pp.1333–1343, 2005.
[15] Yuan Dai, Xiaoxia Zhong, and Xin Jiang, "Experiment of New Additives Effect on Gas Hydrate Formation," Energy and Power Engineering vol.6, pp.133-141, 2014.
[16] Abdullah abbas kendoush, Khalid A, Joudi, and Najim Abid Jassim,"The growth rate of gas hydrate from refrigerant R12" experimental and thermal fluid science vol.30, pp.643-651, 2006.

# Experimental Investigation on the Effect of Bio-additives on Refrigerant Hydrate Formation

Yaseer M. [1], Mohamed Iqbal Pallipurath [2], Abdul Azeez P A

*Department of Mechanical Engineering, TKM College of Engineering*
*Kollam, Kerala, India*
[1]yaseer.yas@gmail.com
[2]mohamediqbalp@gmail.com

***Abstract-*** **Cool storage technology can be used for shifting electrical demand from peak hours to off-peak hours by storing cool thermal energy required to meet the cooling load of a building. Refrigerant hydrates, ice–like crystalline compounds formed when refrigerant guest molecules are trapped in the cage like structure formed by host water molecules, are promising phase change materials for cold storage because of their large fusion heat. The exothermic formation and endothermic dissociation nature of hydrates can be used effectively for cool storage and release. The major challenge in the realisation of hydrate based refrigeration system is that, the hydrates are formed at high pressures and low temperatures (5-12$^0$C) with large induction/formation time. Additives can improve hydrate formation pressure and temperature conditions and reduce induction time. Chemical surfactants like Sodium dodecyl sulfate (SDS) as additives reduced the induction time and improved formation-dissociation conditions. Bio-additives, produced from plants or animals, are gaining popularity over chemical additives due to their non-toxic nature, environmental compatibility and biodegradability. The effects of bio-additives like Methyl ester sulfonate (MES), Coco-glucoside and gum tragacanth on R-134a refrigerant hydrate formation and dissociation processes are studied here through experimental means.**

***Keywords*****— Refrigerant hydrates; Chemical surfactants; Bio-additives; Induction time; Methyl ester sulfonate (MES); Coco-glucoside; Gum tragacanth.**

## I. INTRODUCTION

The growing demand for air conditioning and high consumption of electrical energy by air-conditioning and refrigeration processes during peak usage periods, especially in summer season, have encouraged researchers to look for more economical and efficient air conditioning systems [1-3]. Cool storage technology is a promising solution for these problems. The term cool storage refers to adding cold thermal energy to any storage medium and removing it for use when required [3]. The technology has wide applications like air conditioning in buildings, factories, vehicles, cold storage transport etc. Refrigerant hydrates can be considered to be an ideal cool storage medium as compared to conventional mediums like ice, eutectics, paraffin waxes etc., due to their large cold storage capacity (270-430kJ/kg) and high cold storage efficiency (formation temperature above freezing point of water) [3].

Clathrates are open crystalline structure of host molecule, usually water; enclosing molecules of other compound, usually gas [1-4]. The host molecules are held together by hydrogen bonds while Van der waals force holds the guest molecules in the cage, which indicates that the formation and decomposition of gas hydrates are phase transitions, not chemical reactions [3-4]. The term "clathrate" is derived from the Greek word khlatron which means barrier [4]. Gas hydrates exist in three different structures based on the type of cavities formed by the host molecule-SI, SII, S-H [3-4]. R-134a gas is used in this study, form SII hydrates with a hydrate fusion heat of 358kJ/kg [3].

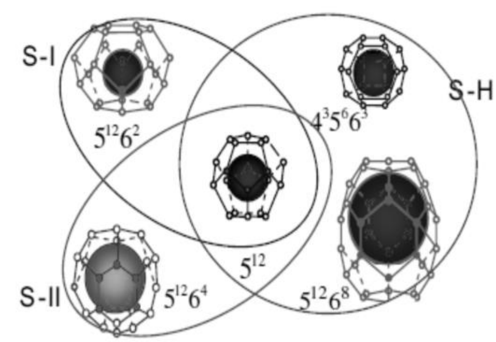


Fig. 1 Types of hydrate structures and their cage arrangements [3]

Clathrates or Gas hydrates were discovered by Sir Humphrey Davy in 1810 [4]. Hydrate based cold storage medium was first proposed by Tomlinson in 1982 [4]. Researchers first studied the cold storage characteristics of CFC and HCFC hydrates, later shifted their attention to HFC hydrates and other alternatives like TBAB. F. Isobe and Y. H. Mori [5] reported that, the degree of supercooling before the inception of gas hydrate formation with R-134a was found to be reduced by the addition of powdery alumina or zinc or a surfactant to the water, while addition of Pseudomonas Fluorescens, a strain of ice-nucleating bacteria showed no effect. Jinping Li et al. [6] reported that, a properly placed metal rod combined with proper amount of SDS considerably promoted the hydrate formation speed and reduced the nucleation time for HCFC141b hydrates. In 2006, he found that the addition of nano-copper suspensions enhanced the heat and mass transfer process of R-134a hydrate formation, reducing the induction time for formation of hydrate [7]. Imen chatti et al. [4] reviewed the benefits of clathrates-as an energy source (naturally occulting methane hydrates in deep sea or permafrost regions), for marine carbon- dioxide sequestration (solution for global warming), as a gas separation process, for natural gas storage and transportation and cool storage applications; and its disadvantage-pipeline plugging. Ogawa et al. [8] put forward a conceptual design of a hydrate based refrigeration system, shown in fig 2. The higher efficiency of this system was due to high heat of formation/dissociation of hydrates than phase change latent heat of fluorocarbons and isothermal compression (a part of heat generated is absorbed by water). A thermodynamic analysis of the system was done and a simulation of its operation was performed and a COP of 8 which is higher than conventional refrigeration systems were obtained. A laboratory model was created by him and it worked continuously.

Ni Liu et al. [9] investigated the effect of additives like SDS, Tetrahydrofuran (THF) and their mixture on $CO_2$ hydrate formation. He concluded that, with SDS, hydrate could form rapidly and the induction time of hydrate formation was reduced, while THF showed no effect. However, the mixture of SDS and THF promoted the hydrate formation rate considerably, and large amount of hydrates were formed. Yuehong Bi et al. [1] confirmed from his experimental studies that the cool release processes of R141b gas hydrate were quicker than the corresponding cool storage processes. He also concluded that the cold energy release rate

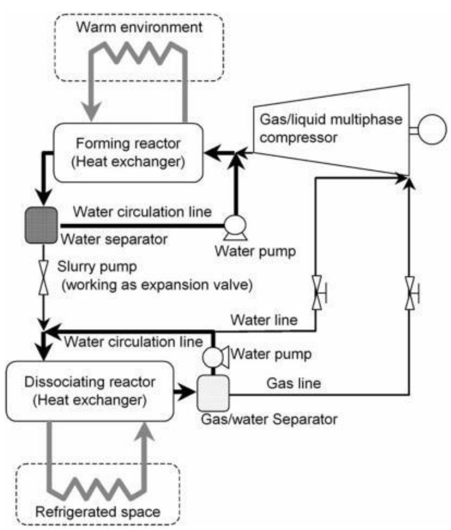


Fig. 2 Conceptual design of hydrate-based refrigeration system [6]

of the cool storage system was increased by adding reasonable proportions of additives like Calcium hypochlorite or benzenesulfonic acid sodium salt. Rudy Rogers et al. [10] reported that microbial cell-wall materials inhibited hydrate formation, although biosurfactants produced by those cells promote hydrate formation. He also suggested that the memory effect may be dissipated if subjected to sufficient stresses of time, elevated temperature, vigorous mechanical energy, or combinations thereof. Jianghong Wu et al. [11] studied R134a hydrate's potential in cool storage by means of alcohol additives. He found that 1.34% of alcohol substantially accelerated the cool storage rate. Amit Arora [12] studied the effects of biosurfactants such as Rhamnolipid, Surfactin, Snomax, Emulsan, Phospholipids, Hydroxystearic acid etc., on Gas Hydrate formation. All the surfactants reduced the induction time considerably, among them Surfactin was the most effective which reduced induction time by 71%. Stirring and presence of magnetic field also reduced the induction time and increased the hydrate formation rate considerably [3].

Most of the additives studied previously were chemical surfactants, except a few such as Rhamnolipids and Surfactin [12]. Rebello et al. [13] gave a detailed description of the toxic nature of chemical surfactants, how they affect soil, plants, microbial world, aquatic system and higher vertebrates. Due to their toxic nature and low biodegradability, chemical surfactants are now replaced by a bio-additives or green surfactants. This paper analyses the effects of bio-additives, generally green surfactants like MES, Coco–glucoside and Gum tragacanth on R-134a hydrate formation and dissociation.

### *A. Green surfactants*

Green surfactants are defined as bio-based amphiphilic molecules obtained from nature or synthesised from renewable raw materials like triglycerides, carbohydrates sources or organic acids, by their chemical modifications-hydrogenation, hydrolysis, trans-etherification- yielding various surfactants or their precursors including fatty acids, methyl esters, fatty alcohols, methyl ester sulfonate, fatty acid anhydrides, fatty amines and alkyl polyglucosides or by utilising the biotic community (plants, microbes, yeast etc.) yielding biosurfactants [13]. As the precursors are not petrochemical products as in the case of chemical surfactants, $CO_2$ emission is less at the time of manufacturing. They have several advantages over chemical surfactants like higher biodegradability, lower toxicity, better environmental compatibility, high selectivity and specific activity at extreme temperatures and higher foaming ability.

The surfactants added to a hydrate system reduce the surface tension and the gas–water interfacial tension thereby decreasing the diffusion resistance. The gas-liquid contact area is increased and hence the chance of hydrate nucleation is increased. The induction time is shortened and hydrate formation efficiency is improved.

Surfactants can be divided into anionic, cationic, amphoteric and non-ionic surfactants. Mostly anionic and non-ionic surfactants are used for promoting natural gas hydrate formation [14].

The surfactants used in this study and their details are given below:

1. Methyl Ester Sulfonate: It is an anionic surfactant derived from palm oil, and has a molecular weight of 414g/mol. Chemical formula is $RCH(SO_3Na)COOCH_3$ where R stands for alkyl group with 16-18 carbon atoms. Supplier is Wilmar Indonesia.
2. Coco-Glucoside: It is a non-ionic surfactant derived from coconut oil and fruit sugars, and has a molecular weight of 320.42g/mol. Chemical formula is $C_{16}H_{32}O_6$. Supplier is Chemspark India Pvt. Ltd.
3. Gum Tragacanth: It is an anionic surfactant derived from Astragalus plant, and has a molecular weight of 840kDa. Supplier is Nice Chemicals Pvt. Ltd., India.

## II. EXPERIMENTAL SYSTEM AND EXPERIMENTAL PROCESS

The experimental system mainly consists of a constant temperature bath, part of a vapour compression refrigeration system; and a hydrate forming apparatus made of transparent acrylic cylinder of 100x100x10mm size and acrylic plates at top and bottom, of size 150x150x10mm. The plates were fastened to the cylinder by means of adhesives and bolts. The hydrate formation and dissociation takes place in this apparatus. Fig. 3 shows schematic diagram of the experimental system. The effect of MES was studied in an apparatus having volume $0.785x10^{-3}m^3$ and the other two in an apparatus of volume $0.282x10^{-3}m^3$. Maximum pressure that the apparatus could withstand was 26bar; the studies were limited to only 5bar. A pressure gauge and a K type thermocouple were attached to the cylinder to measure the inside pressure and temperature. Gas feeding line and air removing line attached to the cylinder were regulated by means of valves. Magnetic agitator around 500rpm was specially built and used intermittently to ensure proper mixing of surfactant solution.

The apparatus was initially tested for leakage. Then it was filled with 200ml of water and pressurized with R-134a gas and cooled slowly by immersing in the temperature bath maintained at $1^0C$. Time for each degree fall in temperature was noted. Hydrate formation was visualised and the corresponding temperature and the total time for formation (induction time) were noted. A small rise in temperature of $1\text{-}1.5^0C$ was observed at the time of hydrate formation and later the temperature remained almost constant till the formation was complete. A drastic reduction in pressure was also observed. The apparatus was then kept outside and the temperature gradually increased inside the apparatus. Hydrate dissociation was visualised and corresponding temperature (dissociation starting temperature) was noted.

The time for dissociation was found to be increased compared to the time required without additive. The dissociation completion temperature and the time for dissociation were also noted. Pressure inside the apparatus also increased during dissociation. Experiment was repeated by varying pressure (1-5bar).

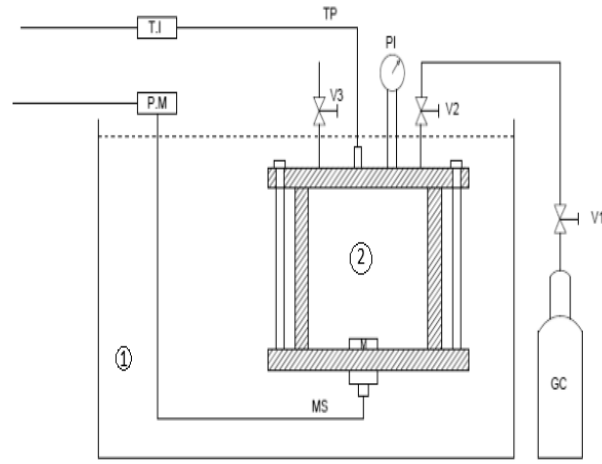


Fig. 3 Schematic diagram of experimental setup: 1. Constant water temperature bath; 2. Acrylic apparatus; GC: R-134a gas cylinder; PI: Pressure indicator; TP: Thermocouple probe; TI: Temperature indicator; V-Valves; MS: Magnetic stirrer

The experiment was repeated taking 200ml of MES solution and optimum concentration was found at a moderate pressure of 3bar. Readings were also taken by varying pressure with the optimum concentration solution. Apparatus was cleaned properly after each experiment. Same procedures were repeated with Coco-glucoside and Gum tragacanth, but the volume of water taken was 150ml.

## III. EXPERIMENTAL RESULTS AND DISCUSSION

### *A. MES as additive*

0.08 MES solution gave highest formation temperature-$7.2^0C$ and minimum induction time of 49minutes at 3bar and this was taken as the optimum concentration of MES for further studies.

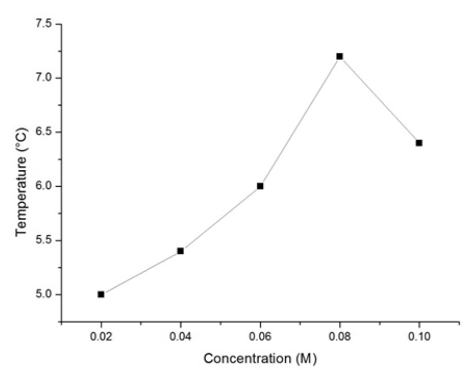


Fig. 4 Concentration-Temperature plot for R-134a hydrate formation with MES at 3bar

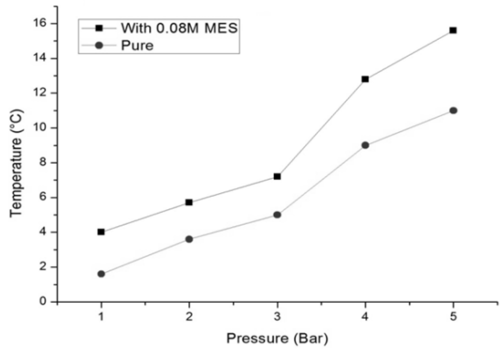


Fig. 5 P-T relation for R-134a hydrates formation with and without MES

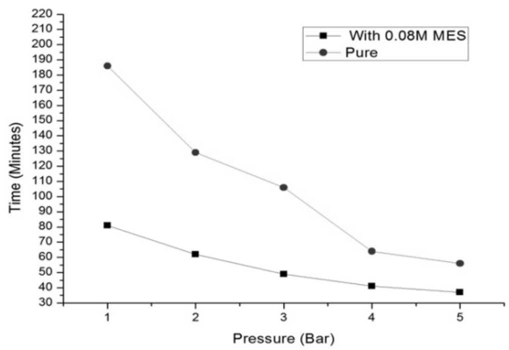


Fig. 6 Pressure-Time relation for R-134a hydrates formation with MES

Hydrates were formed at a higher temperature in the presence on MES-an average of $3^0$C rise. The increase was more at high pressure due to the combined effect of pressure and MES. The average induction time, 108 minutes, decreased by 50% in the presence of MES. The decrease was more prominent at lower pressures. A similar rise was observed in hydrate dissociation starting and completion temperatures, $2.8^0$C and $2.6^0$C respectively, in the presence of MES. The average dissociation time also increased from 74 minutes to 80minutes.

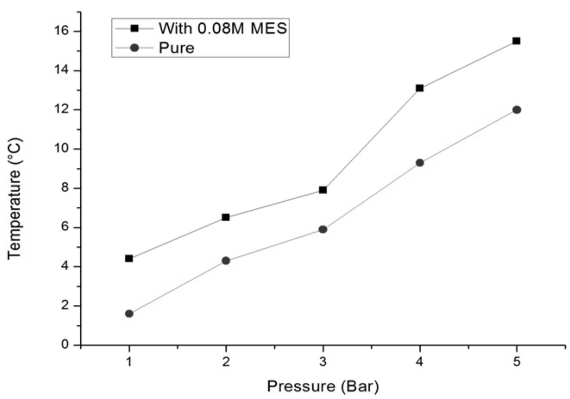


Fig. 7 P-T relation for R-134a hydrates dissociation starting with MES

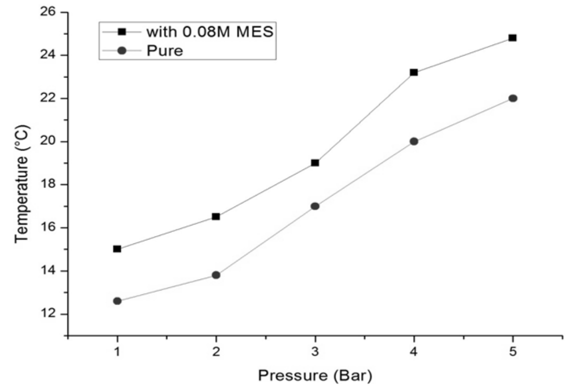


Fig.8 P-T relation for R-134a hydrates dissociation completion with MES

### B. *Coco-glucoside and Gum tragacanth as additives*

*C.* Coco-glucoside promoted R-134a hydrate formation while Gum tragacanth had a small inhibiting effect. The concentrations which gave maximum formation temperature and minimum induction time at 3bar, in the studied range, were 0.04M ($5.5^0$C and 81minutes) and 0.075mM ($2.8^0$C and 128 minutes) respectively.

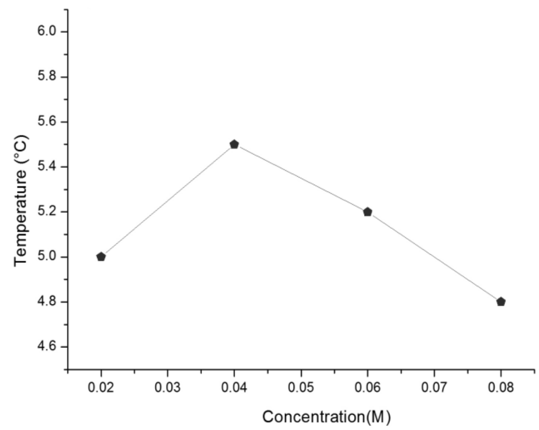


Fig. 9 Concentration-Temperature plot for R-134a hydrate formation with Coco-glucoside at 3bar

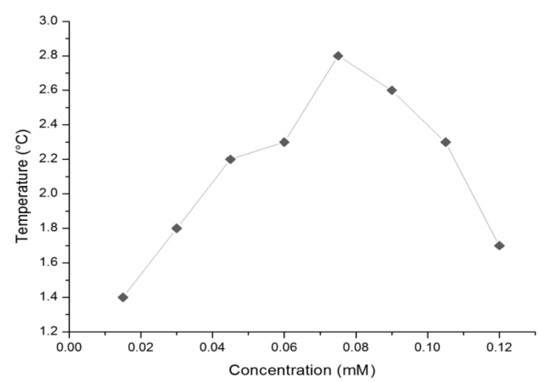


Fig. 10 Concentration-Temperature plot for R-134a hydrate formation with Gum tragacanth at 3bar

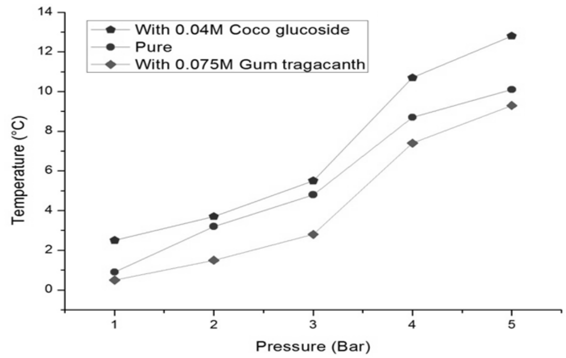


Fig. 11 P-T relation for R-134a hydrates formation with Coco-glucoside and Gum tragacanth

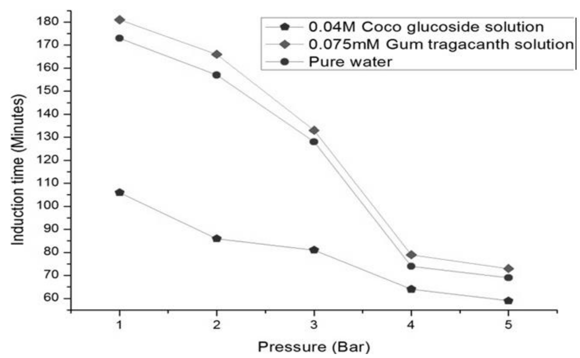


Fig. 12 Pressure-Time relation for R-134a hydrates formation with Coco-glucoside and Gum tragacanth

An average of 1.5$^0$C improvement in formation temperature and 34% reduction in induction time (120minutes to 79minutes) was observed with Coco-glucoside. Formation temperature was reduced by 1.24$^0$C and the induction time increased by 4% (126minutes) with Gum tragacanth. An average of 1$^0$C rise in hydrate formation temperature was observed with Coco-glucoside and 1.3$^0$C fall with Gum tragacanth. The average cool release time was 62, 69 and 59 minutes respectively for water, Coco-glucoside and Gum tragacanth solutions.

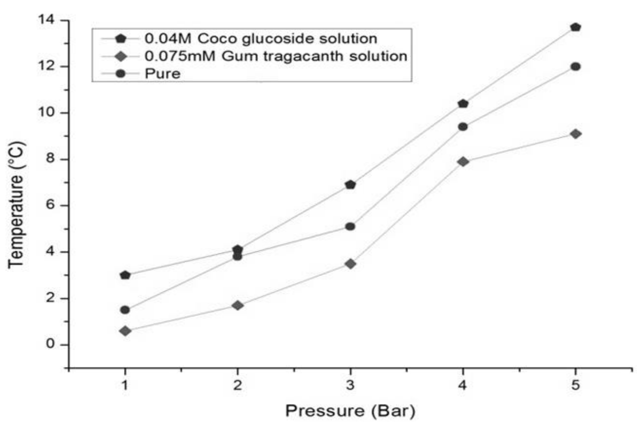


Fig. 13 P-T relation for R-134a hydrates dissociation starting with Coco-glucoside and Gum tragacanth

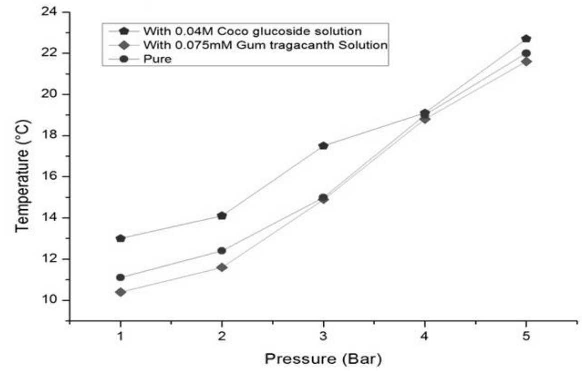


Fig.8 P-T relation for R-134a hydrates dissociation completion with Coco-glucoside and gum tragacanth

## IV. Conclusions

The cold stored during low load conditions, at night, can be released when the load is high preventing overloading problems. Additives can increase hydrate formation rate and reduce induction time. The effect of bio-additives like MES, Coco-glucoside and Gum tragacanth; which are environment friendly with high biodegradability, on R134a hydrate formation were studied experimentally. The former two had a promoting effect and the later had an inhibiting effect. The optimum concentration of first two additives was 0.08M and 0.04M respectively. An average of 3$^0$C and 1.5$^0$C rise in formation temperature with 50% and 34% reduction of induction time was observed with the two additives. Similar rise was observed in hydrate dissociation starting and completion temperatures along with the dissociation time. Among the two, MES had better promoting effect. An extensive research is required to find an additive which form hydrates at atmospheric conditions and which is environmentally compatible. The high cost and low commercial availability of bio-additives hinder their extensive usage.

## Acknowledgment

The authors are grateful to TKM college of Engineering for providing the lab facilities at the college to carry out the experiments.

## References

[1] Yuehong Bi, Tingwei Guo, Liang Zhang, Hua Zhang,and Lingen Chen, "Experimental study on cool release process of gas-hydrate with additives," *Energy and Buildings*, vol. 41, pp. 120–124, 2009.

[2] E. Oró, A. de Gracia, A. Castell, M.M. Farid, L.F. Cabeza, "Review on phase change materials (PCMs) for cold thermal energy storage applications," *Applied Energy*, vol. 99, pp. 513–533, 2012.

[3] Gang Li, Yunho Hwang, and Reinhard Radermacher, "Review of cold storage materials for air conditioning application," *International Journal of Refrigeration*, pp. 1-25, 2012.

[4] Imen Chatti, Anthony Delahay., Laurence Fournaison, and Jean-Pierre Petitet, "Benefits and drawbacks of clathrate hydrates: a review of their areas of interest," *Energy Conversion and Management*, vol. 46, pp. 1333–1343, 2005.

[5] F. Isobe and Y. H. Mori, "Formation of gas hydrate or ice by direct-contact evaporation of CFC alternatives," *Int. J. Refrig.*, Vo1. 15, No. 3, pp. 137-142, 1991.

[6] Jinping Li, Kaihua Guo, Deqing Liang and Ruzhu Wang, "Experiments on fast nucleation and growth of HCFC141b gas hydrate in static water columns," *International Journal of Refrigeration*, Vol. 27, pp. 932–939, 2004.

[7] Jinping Li, Deqing Liang, Kaihua Guo, Ruzhu Wang, and Shuanshi Fan, "Formation and dissociation of HFC134a gas hydrate in nano-copper suspension," *Energy Conversion and Management*, Vol. 47, pp. 201–210, 2006.

[8] Tomohiro Ogawa, Tomonari Ito, Kenji Watanabe, Ken-ichi Tahara, Ryuzo Hiraoka, Jun-ichi Ochiai, Ryo Ohmura, and Yasuhiko H. Mori, "Development of a novel hydrate-based refrigeration system: A preliminary overview," *Applied Thermal Engineering*, vol. 26, pp. 2157–2167, 2006.

[9] Ni Liu, Guoqing Gong, Daoping Liu and Yingming Xie, "Effects of additives on carbon dioxide hydrate formation," in *Proceedings of the 6th International Conference on Gas Hydrates*, Vancouver, British Columbia, Canada, 2008.

[10] Rudy Rogers, James Radich and Shangmin Xiong, "The multiple roles of microbes in the formation, dissociation and stability of seafloor gas hydrates," *Proceedings of the 7th International Conference on Gas Hydrates*, Edinburgh, Scotland, United Kingdom, 2011.

[11] Jianghong Wua, and Shiping Wang, "Research on cool storage and release characteristics of R134a gas hydrate with additive," *Energy and Buildings*, vol. 45, pp. 99–105, 2012.

[12] Amit Arora, Swaranjit Singh Cameotra, Rajnish Kumar, Pushpendra Kumar, and Chandrajit Balomajumder, "Effects of Biosurfactants on Gas Hydrates," *Petroleum & Environmental Biotechnology*, vol. 5: 170, 2014.

[13] Sharrel Rebello, Aju K. Asok, Sathish Mundayoor, and M. S. Jisha, "Surfactants: toxicity, remediation and green surfactants," *Environmental Chemistry Letters*, vol. 12, pp. 275-287, 2014.

[14] Yuan Dai, Xiaoxia Zhong, Xin Jiang, and Shuli Wang, "Experiment of new additives effect on gas hydrate formation," *Energy and Power Engineering*, vol. 6, pp. 133-141, 2014.

# Numerical and Experimental Studies on Electronic Cooling by Jet Impingement

Arun Jacob*1, Shafi K A#2, Jose Prakash.M#3

* Department of Mechanical Engineering, MES College of Engineering, Kollam, Kerala. India

1arunjacobcool@gmail.com

# Department of Mechanical Engineering, T.K.M College of Engineering ,Kollam, Kerala, India.

2shafika.tkm@gmail.com

3jpmmech@yahoo.co.in

*Abstract*— **In the present century effective cooling of electronic equipment has emerged as a challenging and constraining problem. In the present work the effectiveness and feasibility of jet impingement were studied numerically and experimentally. The various geometrical parameters such as jet diameter (D), jet to target spacing (Z) and ratio of jet spacing to jet diameter (Z/D) were studied. The values of Reynolds number considered are in the range 7000 to 42000. The results obtained from numerical studies are validated by conducting experimental studies. From the studies the optimum value of Z/D is obtained at 5. A correlation is proposed for Nusselt number in term of Reynolds number and is valid for air as cooling medium**

*Keywords*—**Ratio of jet diameter to jet spacing (Z/D), CFD, Reynolds number, heat transfer enhancement, turbulence model.**

## I. INTRODUCTION

Now a day we require smaller, faster and reliable electronic components. Therefore the demand for high powered electronics has been increased that lead to high heat flux. We have to remove these heat fluxes to avoid failure. The traditional cooling techniques such as heat sink heat sink with fan have reached their limits. Jet impingement cooling is one of the very efficient solutions of cooling hot objects in industrial processes as it produces a very high heat transfer rate through forced convection. Jet impingement is widely used in industrial applications such as drying of food products, textiles, films and paper processing of some metals and glass, cooling of turbine blades etc. due to their high heat removal rates with low pressure drop. Over the past 30 years, experimental and numerical investigations of flow and heat transfer characteristics under jet impingement remain a very dynamic research area. The effects of jet diameter, jet-to-surface spacing, Reynolds number, Nusselt number, etc. on flow and heat transfer have been studied by both numerically and experimentally.

Most industrial application jets are concerned with turbulence flow in the downstream of a nozzle. Modeling of turbulence flow is the greatest challenge for rapidly and accurately predicting impinging heat transfer under a single round jet over the past years ,no single mode has been universally accepted therefore research are going on to develop various turbulence model for the prediction of impingement flow and heat transfer.

Due to many industrial applications of impinging jet extensive prior research has been conducted to understand their flow and heat transfer characteristics. Liu et al. [1] investigated experimentally a convective heat transfer by using impingement of circular liquid jet in laminar and turbulent flow conditions for different Prantl number Baughn et al. [2] studied the heat transfer and fluid flow for impinging jets by investigating experimentally the entrainment effects of jets for circular jet. The result from this research have been summarized by Jambunathan and Viskanta et al. [3,4]. Lytle and Webb [5] carried out an experimental study to investigate the effect of Prandl number and jet to plate spacing for stagnation point Nusselt number. Garinella in a review paper presented a detailed discussion of heat transfer and flow fields in confined jet impingement [6]. The flow and heat transfer characteristics of laminar imp-inging rectangular slot jet were investigated by Sezai and Mohammed [7]. The effect of jet velocity profiles on the flow and thermal fields of laminar confined and swirling jet were investigated by Shuja et al. [8]. H.G.Lee [9] investigated numerically the unsteady two-dimensional fluid flow and heat transfer in the confined impinging slot jet for different Reynold numbers of 50-500 and different height ratios of 2-5.It is found that the unsteadiness gives a big impact on the flow and the temperature fields and as a result the pressure coefficient, skin friction and Nusselt number in the unsteady region show different characteristics from coefficient those in the steady region. Yahya Erkan Akansu [10] studied experimentally the effects of inclination of an impinging of two dimensional slot jets on the heat transfer from a flat plate. It showed that as the inclination angle increases, the location of the maximum heat transfer shifts towards the uphill side of the plate and the value of the maximum Nusselt number gradually increases at lower jet -to-plate spacing. Juan et.al [11] conducted experimental research on heat transfer of confined air jet with tiny size

## II. EXPERIMENTAL SETUP

### A. Experimental system

Experiments have been conducted to see the effect of the various parameters on the heat transfer coefficient. The key parameters determining the heat transfer characteristics of a single jet impingement jet are the diameter of the nozzle, spacing between the jet and the target, Reynolds number and the ratio of jet spacing to diameter of the jet (Z/D).

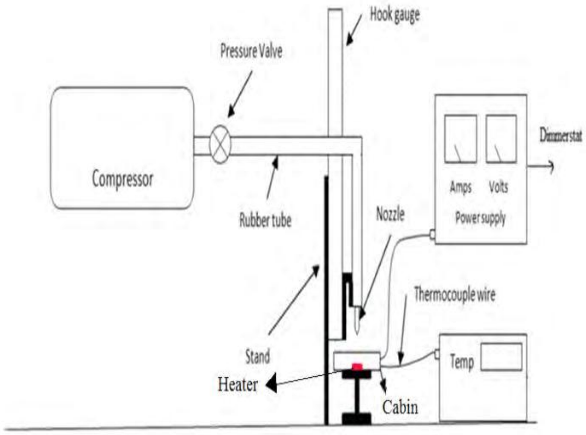


Fig. 1 Schematic of Experimental Setup

The schematic of the experimental setup is shown in Fig.1. The cooling medium is air and the same is supplied from a reciprocating compressor. The thermal environment of the microprocessor is simulated using a copper plate of size 5cm X 5cm X 1cm with a heater placed underneath. The cabinet is made of aluminium and its dimensions are 45cm X 40cm X 15cm and one of the smaller sides is open. The power input to the heater is varied using a dimmerstat and the voltage and current are measured using voltmeter and ammeter respectively. T- type thermocouples (36 SWG) were used to measure the temperature at various locations.). The temperature data were acquired using a temperature scanner. The jet to target spacing is adjusted using a hook gauge. The flow rate of air is measured using an orifice meter.

*B. Experimental Procedure*

Prior to experimental measurements the thermocouples were calibrated using a constant temperature bath (JulaboF25). Experiments have been conducted by varying the nozzle diameter, nozzle to plate spacing, jet spacing to diameter ratio and the Reynolds number.

## III. Numerical analysis

*A. Geometry and Boundary Conditions*

The computational domain considered for the present study is shown in fig. 2. It consists of an enclosure which has the same dimensions as that of the cabinet used in the experimental studies and one of the smaller sides of it is open. The copper plate which has the same dimensions as that of a typical computer processor (5cm X 5cm X 1cm) is placed at the centre of the bottom surface of the enclosure. A tube having diameter same as that of jet is protruding in to the enclosure and positioned in such a way that the jet impinges on the centre of the top surface of the copper plate. The thickness of the enclosure is not considered adiabatic boundary condition is applied to all walls except the top one.

Heat flux boundary condition is applied to the bottom surface of the copper plate. Mass flow boundary condition is applied to the inlet of the tube and temperature of air entering is 300. The flow is assumed to be steady, incompressible and three dimensional over the entire computational domain. K.

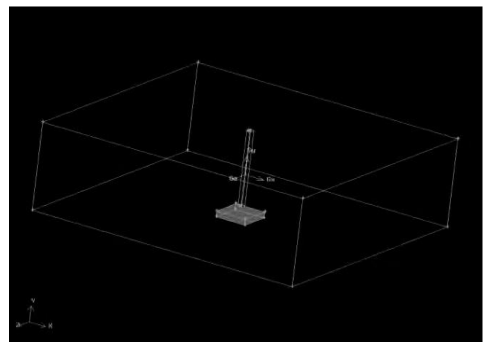

Fig. *2* The computational domain/model

*B. Numerical Procedure*

The computational domain is modeled using the help of GAMBIT 2.3.16 software and the same is meshed using Tet/hybrid elements. The number of elements is about 20 lakhs. No slip condition is applied to the wall surfaces. Fig.3 shows the computational domain with mesh.

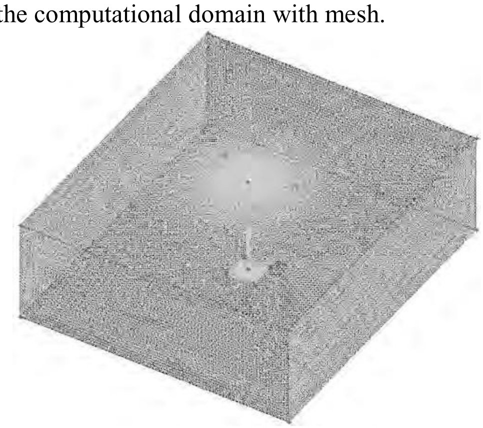

Fig. 3 The computational domain with mesh

C. Analysis

The software used for analysis is FLUENT 6.3.26. The turbulence model used is SST (k- ε) model which is found to be the best among available turbulence models for this type of flow configurations. The interfaces are coupled together by using the grid interface tool. The solver used is pressure base segregates solver. The materials selected for the enclosure, chip and tube are aluminium, copper and brass respectively and the coolant medium is air.

Analysis have been conducted to see the effect of Reynolds number (Re), jet spacing to jet diameter (Z/D) ratio on cooling effectiveness.

## IV. RESULT AND DISCUSSION

Numerical investigations have been carried out on jet impingement cooling for its effectiveness. The results are validated by conducting experiments.

### A. *Effect of Z/D ratio on Heat Transfer*

Fig.4 shows the variation of temperature at the top surface of the copper plate. The heat flux at the bottom of the copper plate is 12000 W/$m^{2.}$ The results obtained from numerical and experimental studies are shown for comparison. Here the diameter of the jet is 2 mm and the velocity of flow of air is taken as 300 m/s. There is only marginal difference in the values of temperature obtained from the studies. It is observed that the temperature is minimum when the Z/D ratio is 5

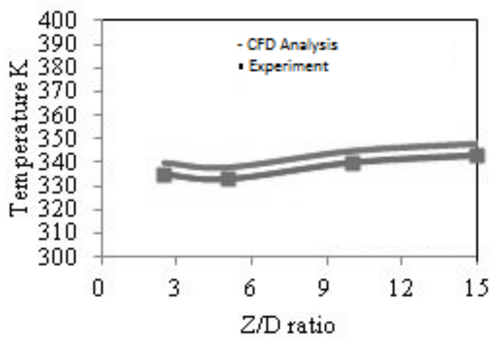


Fig. 4 Shows variations of temperature on the top surface of the heat sink. Diameter of the jet is 2 mm

Higher heat transfer is observed for lower Z/D ratio because of reduction in impingement surface area. In case of higher Z/D ratio there is a higher momentum exchange between impinging fluid and surrounding fluid due to this the jet diameter becomes border and spreads over more surface area. In case of low Z/D ratio the same amount of fluid spreads over lesser surface area causing a higher heat transfer rate. If the Z/D ratio is very low it will prevent the free flow of jet.

Fig.5 Shows variations of Nusselt number at the bottom surface of the heat sink with Z/D ratio. Here the heat flux is 12000 W/$m^2$ and the diameter of the jet is 2mm. It is clear from the graph that the Nusselt number increases and then decreases with Z/D ratio. The maximum Nusselt number is obtained for the Z/D ratio is 5. The Reynolds number corresponding to this graph is above 20000. The results explained below are for the optimum Z/D ratio.

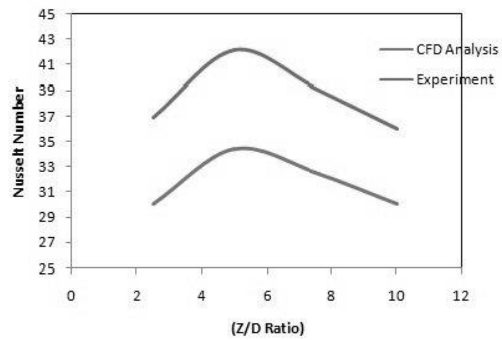


Fig. 5 Shows variations of Nusselt number on top surface of the heat sink with Z/D ratio. Diameter of the jet is 2mm.

### B. *Effect of Reynolds Number on Temperature*

Fig.6 illustrates the temperature variations at the top surface of heat sink with Z/D ratio 5, diameter 1mm and heat flux is 12000 W/$m^2$ .These temperature contour plots shows that for higher Reynolds number the average temperature of the top surface are lowered due to localized cooling. It is also observed that top portion of flat plate below the nozzle area is cooled intensively with respect to other area. Minimum temperature at the stagnation point and maximum temperature are observed around the impingement zone due to mixing of flow. It is observed that if the Reynolds number is more than 20000 the chip can be maintained at the safe temperature limit.

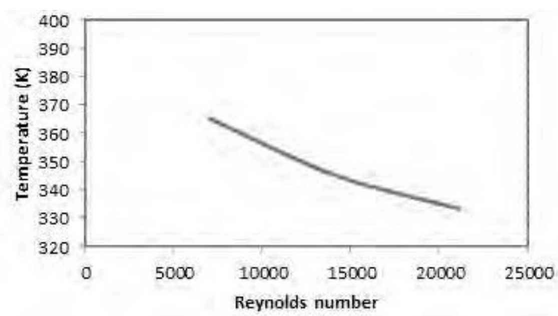


Fig. 6 Shows the variations of the temperature on the top surface of heat sink with Reynolds number. Diameter of the jet = 1mm

Fig.7 illustrates the temperature distribution on the top surface of heat sink with Z/D ratio 5, heat flux 12000W/$m^2$ and the jet diameter 2 mm. It is observed that if the Reynolds number is more than 19000 the chip can be maintained at the safe temperature limit. For the same Reynolds number the temperature reduces by 15$^o$C if a 1mm diameter jet is used instead of 2mm diameter jet. It can be observed that for the same Reynolds numbers the volume flow rate of air increases by 100 percentages when the jet diameter is doubled.

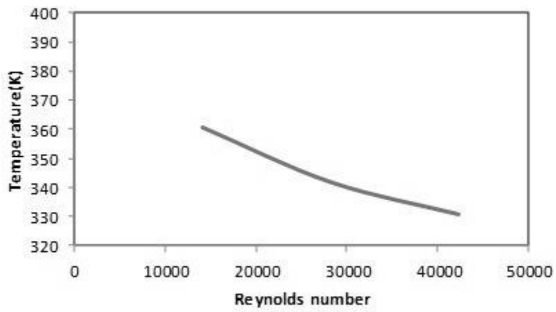


Fig. 7Shows the variations of the temperature at the bottom surface of heat sink with Reynolds number Diameter of the jet = 2mm

Fig.8 illustrate the variations of temperature at the top surface of the heat sink with heat inputs 20 W, 30 W and 50 W. It can be observed that if the heat input is more than 30 W the flow velocity required is very high for effective localized cooling.

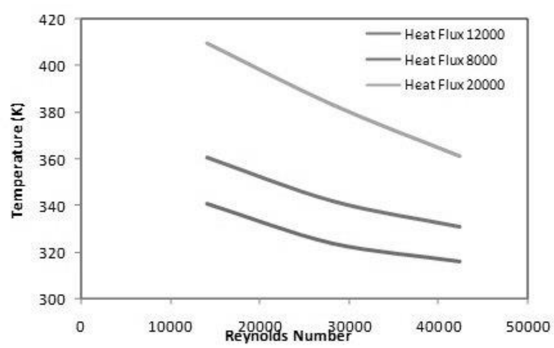


Fig. 8 Shows the variations of the temperature at the bottom surface of heat sink with Reynolds number Diameter of the jet = 2mm

## *C. Effect of Reynolds Number on Heat Transfer Coefficient*

Fig.9 illustrate the variations of the heat transfer coefficient at the top surface of heat sink with various Reynolds number with heat flux 12000 W/m$^2$ and the jet diameter 1 mm. The average heat transfer coefficient increases by 114 percentages if the Reynolds number is increased from 7000 to 21000.

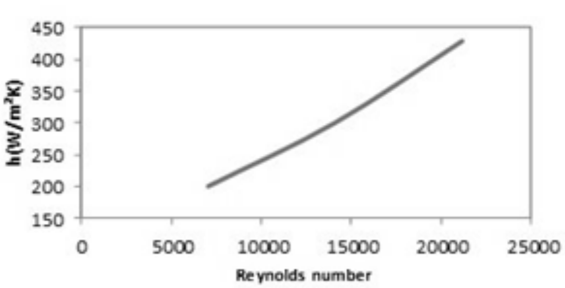


Fig. 9 shows the variations of the heat transfer coefficient at the top surface of heat sink with Reynolds number. Diameter of the jet = 1mm

Fig.10 illustrates the heat transfer coefficient variation on the top surface of heat sink with different Reynolds number. Heat flux is 12000 W/m$^2$and the diameter of the jet is 2 mm. The average heat transfer coefficient corresponding to a Reynolds number of 14000 is 215 W/m$^2$K and increases by 114 percentage if the Reynolds number is increased from 14000 to 42000

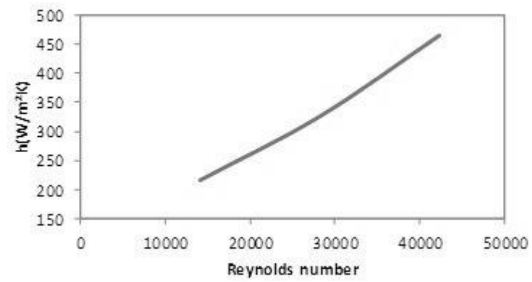


Fig10 shows the variations of the heat transfer coefficient at the top surface of heat sink with Reynolds number. Diameter of the jet = 2mm.

## *D. Effect of Nusselt Number with Reynolds Number*

Fig.11 illustrate shows the variations of the average Nusselt number at the top surface of heat sink with Reynolds number. The diameter of the jet is 1 mm. The Nusselt number corresponding to a Reynolds number of 7000 is 7.38 and corresponding value for Reynolds number of 14000 is 15.81.

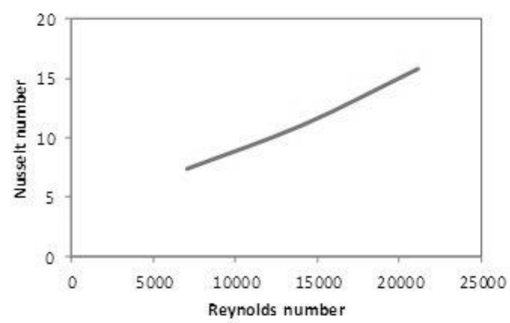


Fig. 11 shows the variations of the Nusselt number at the top surface of heat sink with Reynolds number. Diameter of the jet = 1mm.

Fig.12 illustrates variations of the average Nusselt Number at the top surface of heat sink with different Reynolds number and jet diameter 2 mm. The Nusselt number corresponding to a Reynolds number of 14000 is 15.9 and corresponding value for Reynolds number of 42000 is 34.37.

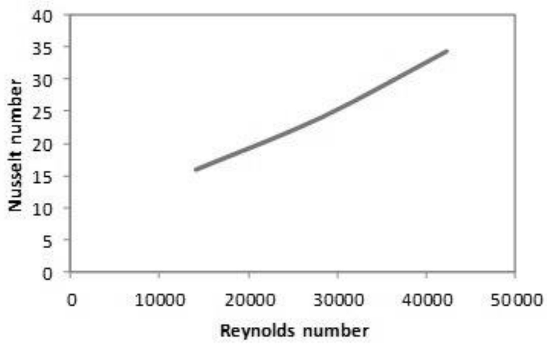


Fig. 12 shows the variations of the Nusselt number at the top surface of heat sink with Reynolds number. Diameter of the jet = 2mm

The Nusselt number increases from 7.38 to 34.37 by increasing the Reynolds number from 7000 to 42000 at Z/D = 5. The average heat transfer coefficient increases with increase in Reynolds number at a given Z/D ratio. At higher Reynolds number, turbulence level increases and along with this spread of jet also increases. The net amount of fluid that comes out of the jet is also higher for higher Reynolds number which causes better heat transfer performance.

## V. CORRELATION

A correlation is proposed for Nusselt number in terms of Reynolds number and this is valid for air as the cooling medium. This correlation is based on the numerical experiments. The Nusselt number is calculated based on the average value of heat transfer coefficient and the heat transfer coefficient (h) is estimated using the correlation

$$h = q/ (Tw - Ti)$$

here q is the heat flux, $T_w$ is the average wall temperature and $T_j$ is the temperature of jet.

The correlation is $Nu = 0.034Re^{0.69}$ and this is independent of the diameter of the jet and is applicable to air as the cooling medium. The correlation can be used in the range of Reynolds number 7000 to 42000. A similar correlation in the form $Nu = 0.0409Re^{0.5}$ was proposed by Juan et al (2005)

## VI. CONCLUSION

An experimental and numerical simulation investigation of heat transfer due to confined and single impinging circular jet for diameters 1mm Reynolds number 7000 to 21000 and 2mm diameter with Reynolds number varying from 14000 to 42000 with varying Z/D ratio from 2 to 10. Optimum Z/D ratio is found to be 5. Numerical predictions based on k-e turbulence model show good agreement with experimental results. The cooling using impingement jets are more efficient than forced flow over plate. With the increase in Reynolds number thermal boundary layer on the bottom wall becomes thinner which will enhance the heat transfer rate. Decrease in Z/D ratio increases the heat transfer. Peak Nusselt number is obtained at the stagnation point which results in higher heat transfer. A correlation is proposed for Nusselt number in terms of Reynolds number and it is applicable for air as the jet cooling medium.

The investigations can be carried out using dielectric fluids as the cooling medium. The investigations may be extended for the case of multiple jets to investigate the effect of the parameters Reynolds number and Z/D ratio. Different nozzle geometries can also be tried to find the effectiveness of cooling. The effect of jet impingement angle can also be studied by varying the angle of jet impingement with surface plate.

## ACKNOWLEDGEMENT

This work was supported by the CFD Lab of Mechanical Engineering Department, TKM College of Engineering.

## REFERENCES


[1] X. Liu, V.J.H. Lienvard, J.S. Lombara, "*Convective heat transfer by impingement of circular liquid jets*", J. Heat Transfer 113 (1991) 571 – 582.

[2] J.W. Baughn, A.E. Hechanova, X. Yan, *"An experimental study of entrainment effects on the heat transfer from a flat surface to a heated circular impinging jet"*, J. Heat Transfer 113 (1991) 1023 - 1025.

[3] K Jambunathan, E. Lai, M.A. Moss, B.L. Button, "*A review of heat transfer data for single circular jet impingement"*, Int.J.Heat Fluid Flow 13 (1992)106 - 115.

[4] R. Viskanta, "*Heat transfer to impinging isothermal gas and flame jets"*. Exp. Therm. Fluid Sci.6 (1993) 111-134.

[5] D. Lytle, B.W. Webb, "*Air jet impingement heat transfer at low nozzle-plate spacing's"*, Int. J.Heat Mass Transfer 37 (1994) 1687 - 1697.

[6] S.V. Garimella, "*Heat transfer & flow fields in confined jet impingement"*, Ann. Rev. Heat Transfer 11 (1999) 413 - 494 (Chapter-7).

[7] 7. I. Sezai, A.A. Mohamed, "*Three dimensional simulations of laminar rectangular impinging jets, flow structure and heat transfer"*, ASME J. Heat Transfer- 121(1999) 50 - 56.

[8] S.Z. Shuja, B.S. Yilbas, M. Rashid, "*Confined swirling jet impingement onto an adiabatic wall"*, Int. J. Heat Mass Transfer 46 (2003) 2947 - 2955.

[9] H.G. Lee, H.S. Yoon, M.Y. H, "*A numerical investigation on the fluid flow and heat transfer in the confined impinging slot jet in the low Reynolds number region for different channel heights"*, International Journal of Heat and Mass Transfer 51 (2008) 4055 - 4068.

[10] Yahya Erkan Akansu, Mustafa Sarioglu , Kemal Kuvvet B, TahirYavuz, "*Flow field and heat transfer characteristics in an oblique slot jet impinging on a flat plate"*, International Communications in Heat and Mass Transfer 35 (2008) 873 - 880.

# Numerical Study of Jet Impingement Cooling on Modified Flat Plate

Arun Jose Tom[1], Leena R, M. Jose Prakash, Shakir Mohammed Illias

*Department of Mechanical Engineering*

*TKM college of Engineering, Kollam, Kerala, India*

[1]arunjosetom7777@gmail.com

***Abstract-*** **Impinging jets provide an effective and flexible way to transfer thermal energy in various industrial applications. This paper presents the numerical investigation of the convective heat transfer on the rib-roughened wall impinged by a single circular air jet. Four rows of transverse ribs were arranged in the wall-jet zone downstream from the impinging jet stagnation. The heat transfer distribution was studied numerically by varying three different rib shapes (square ribs, triangular ribs and semi-circular ribs) with jet Z/D=1 and Reynolds number 6000. The model is created using ANSYS software. Numerical simulations were performed using CFD software package ANSYS 14.5 FLUENT. The computations are validated against available experimental data. Results shows that the rib-roughened wall decreases the convective heat transfer in the ribbed region compared to the smooth flat wall using the single jet. Among the three rib configurations, the semi-circular shaped rib shows higher heat transfer rate in the wall jet region.**

***Keywords—*** **Single circular jet; Jet impingement; Heat transfer enhancement; Rib-roughened surface; CFD**

## I. INTRODUCTION

The existing method of heat removal from compact electronic devices are known to be deficient as the growing technology demands more power and accordingly better cooling techniques with time. Impinging jets can be used as a satisfactory method for thermal management of electronic devices with limited space and volume. Impinging jets has been widely used for applications where high heat and mass transfer rates are required. The thin boundary layer is formed due to the collision of the fluid with the wall surface. Due to its simple design and low cost, jet impingement has been applied in a wide variety of practical applications that aim to achieve intense heating, cooling or drying rates. Few industrial processes which employ impinging jets are drying of food products, textiles, films and papers, processing of some metals and glass, cooling of gas turbine blades and outer wall of the combustion chamber, cooling of electronic equipment, etc.

D.Lytle et al. [1] has considered the local heat transfer characteristics of air jet impingement at nozzle-plate spacing of less than one nozzle diameter. The Reynolds number is varied from 3600 to 27600 at Z/D =0.1 to 6. A stagnation point minimum surrounded by an inner and outer peak in the local heat transfer was observed for nozzle-plate spacing less than *Z/**D*** = 0.25. It was seen that the outer peak, which was due to shear induced increases in turbulence, moved radially outward for larger nozzle-plate spacing and larger Reynolds number flows. Lance Fisher [2] conducted a numerical study to investigate the heat transfer to an axisymmetric circular impinging air jet using the k-ϵ turbulence model.

Mirko Bovo et al. [3] have studied the different turbulence models (k-ϵ, k-ω and V2F), different grid densities, grid topology, varying Reynolds number (10000 to 30000) and inlet velocity profile (uniform flow and fully developed flow). Gardon and Akfirat [4] studied the effect of turbulence on the heat transfer between two-dimensional jet and flat plate. Vadiraj Katti et al. [5] conducted an experimental investigation to study the effect of jet-to plate spacing and Reynolds number on the local heat transfer distribution to normally impinging submerged circular air jet on a smooth and flat surface.

N. Zuckerman et al. [6] deals with the applications, physics of the flow and heat transfer phenomena, available empirical correlations and values they predict, and numerical simulation techniques and results of impinging jet devices for heat transfer. The relative strengths and drawbacks of the k–ϵ, k–ω, Reynolds stress model, algebraic stress models, shear stress transport and V2F turbulence models for impinging jet flow and heat transfer are compared. Lei Tan et al. [7] has consider the convective heat transfer on the rib-roughened wall with three typical rib configurations, including orthogonal ribs, V-shaped ribs and inverted V-shaped ribs. Among three rib configurations, the inverted V-shaped rib seems to be advantageous on the convective heat transfer enhancement.

Vadiraj Katti et al. [8] has conducted an experimental investigation to study the effect of jet to plate spacing and low Reynolds number on the local heat transfer distribution. N. K. Chougule et.al [9] has studied the numerical simulation of the 4x4 pin fin heat sink with single jet and 3x3 multi air jet impingement. It is observed that multi-jet impingement showed higher heat transfer enhancement than single jet impingement on pin fin heat sink.

V.Katti and Prabhu [10] reported an experimental investigation of heat transfer enhancement in turbulent jet impingement with axisymmetric detached ribs. It is found that contrary to a smooth surface, there is a continuous increase in Nusselt number from a stagnation point. They investigated the effect of rib width, rib height, pitch between ribs, and clearance under the ribs, jet-to-plate spacing, and location of first rib from a stagnation point.

M. Behnia et al. [11] has studied the ability of computational fluid dynamics to accurately and economically predict the heat transfer rate in an impinging jet situation, strongly relevant to industrial applications. Gau and Lee [12] made an investigation on the impingement cooling flow structure and heat transfer along rib-roughened surface which was made from parallel rectangular ribs attached to a heated wall. It was found that in some situations the heat transfer along the rib roughened wall was indeed significantly enhanced. Miyake et al. [13] investigated the impinging jet heat transfer from rib-roughened flat surfaces and presented some optimum conditions (i.e. rib height, shape, pitch, jet-to-plate distance, etc.) for the maximum heat transfer. Gau and Lee [14] reported that the presence of triangular surface corrugations permitted a significant increase of the local heat transfer coefficient. Hansen and Webb [15] have studied the effect of the modified surface on the average heat transfer between impinging circular jet and the flat plate.

The paper describes a numerical investigation of heat transfer on modified surface using single impinging jet. Three rib shapes, including square shaped ribs, triangular shaped ribs and semi-circular shaped ribs, were considered to investigate numerically the effects of rib-roughened surfaces on the jet impingement heat transfer behaviours under jet-to-target spacing of 1 nozzle diameter. The numerical computation in this study is performed using ANSYS FLUENT14.5 .The validation of the models is carried out by comparing the numerical results with experimental data available from D.Lytle et.al [1].

## II. NUMERICAL ANALYSIS

Numerical studies have been carried out to understand the fundamental mechanisms of heat transfer in jet impingement cooling with the modification of the surface. The package used for the present study is the Finite Volume Method software ANSYS Fluent.

### *A. Geometry and Boundary Condition*

A 3D impinging jet configuration is modeled as shown in Fig.1. The model considered for the analysis is a copper plate 60mm x 60mm x 6mm dimensions. The jet is injected vertically down from a circular nozzle and it impinges on the top surface of the wall of the copper plate. The solution domain is filled with stagnant air. The three dimensional Navier-Stokes and energy equations with the standard turbulence model are solved using CFD software which is combined with continuity and momentum equations to simulate thermal and turbulence flow fields. The turbulence model used is k-ϵ model which is found to work the best for this flow configuration and is also chosen due to its simplicity, computational economy and wide acceptability.

The flow is assumed to be steady, incompressible and three dimensional. The buoyancy and radiation heat transfer effects are neglected and thermo physical properties of the fluid such as density, specific heat and thermal conductivity are assumed to be constant.

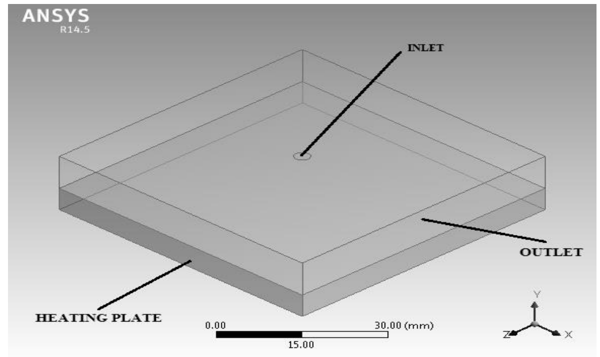


Fig.1 The computational of jet impingement

The square rib has a size of 1mmx1mmx60mm.The triangular and the semi-circular rib have the same volume as the square rib. The schematic diagrams of the computational domain for different rib shapes are shown in the following Fig.2.

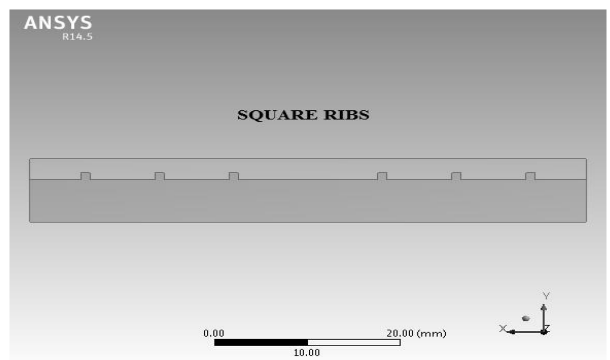


(a) Square ribs

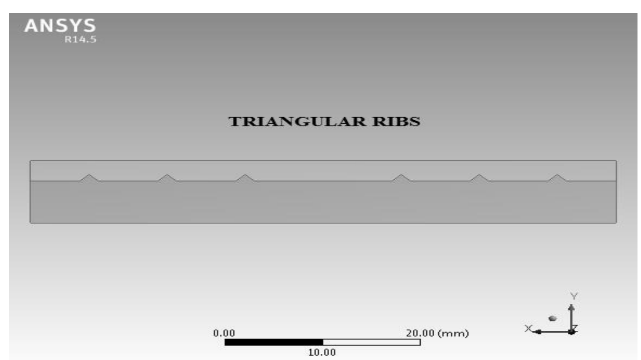


(b) Triangular ribs

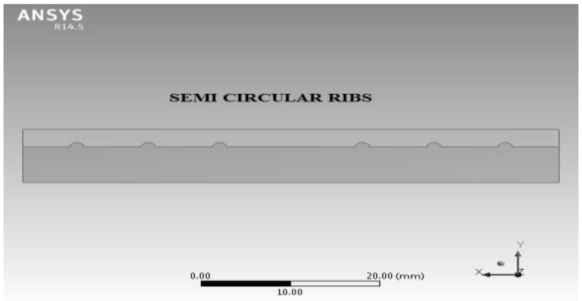


(c) Semi-circular ribs

Fig.2 Computational domain for different ribs

The bottom wall of domain is considered to be bottom surface of heat sink base. It is assumed that heat is generated inside heat sink base at uniform rate and can be represented by a constant heat flux from the bottom surface of the heat sink. Air flow at high velocity passes through a circular jet with diameter D=3mm, vertically impinging on the target plate of 60mm x 60mm with 6mm thickness. The jet after impingement will exit from opening. The target plate was kept at constant heat flux of 5000W/m$^2$ and all other walls are adiabatic.

*B. Analysis*

An unstructured mesh was used for the current problem. Computational domain contains around 400000 elements. Local inflation is done under the fluid domain with appropriate number of inflation layers. The schematic diagram of the mesh domain is shown in the following Fig.3.

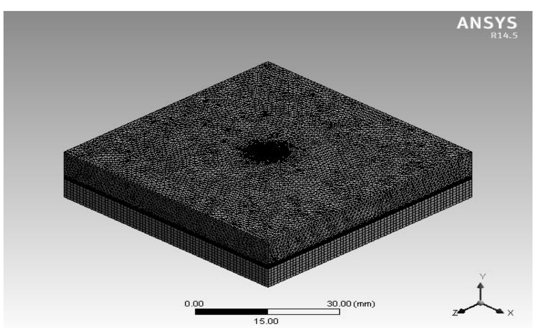


Fig.3 Mesh domain

Grid independency on heat transfer characteristics is checked by changing the element size from 1 lakhs to 4.5 lakhs which follows that about 3.5 lakhs was good enough for present analysis from view point of accuracy and computational time. The numerical simulations are carried out using the Ansys Fluent 14.5 version. The simulation type is steady state condition. Higher order discretization scheme is used for the pressure, momentum, turbulence kinetic energy, specific dissipation rate and the energy. In the fluid domain the inlet boundary condition is specified the measured velocity and static temperature (300K) of the flow were specified at the inlet of the nozzle. No-slip condition was applied to the wall surface. In fluid domain there is also opening boundary condition in which flow regime is subsonic, relative pressure is 0 Pa with the details of operating temperature (300K) and the turbulence intensity of 5%. In solid domain the constant heat flux 5000W/m$^2$ was given at the base of heat sink and the sides of heat sink base plate are adiabatic.

*C. Solver*

Second order discretization scheme is used for the pressure, momentum, turbulence kinetic energy, specific dissipation rate, and the energy. Flow, turbulence, and energy equations have been solved. The standard SIMPLE algorithm is adopted for the pressure-velocity coupling.

## III. RESULTS AND DISCUSSION

*A. Mesh Independent Study*

To ensure that the results are independent of the computational grid, grid sensitivity analysis is carried out. Generally, the accuracy of the solution and the time required for the solution are dependent on mesh refinement.

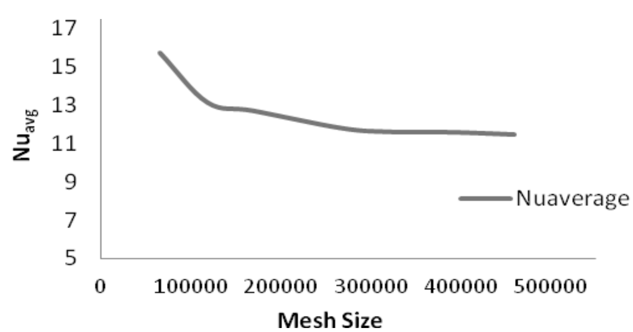


Fig.4 Variation of Average Nusselt number with No. of elements

The optimum grid is searched to have the appropriate run-time and enough accuracy. Figure 4 shows the results of a typical grid independence study for the case of Re=6000 and Z/D=1. A close examination of the plots reveals that grid distribution in excess of 400000 does not produce any significant change in average Nusselt number. So this grid distribution is used for further computations of this case.

*B. Validation of Numerical Results*

Numerical simulation was validated using the experimental results obtained from the previous work done by Lytle and Webb [1] is shown in Fig.5

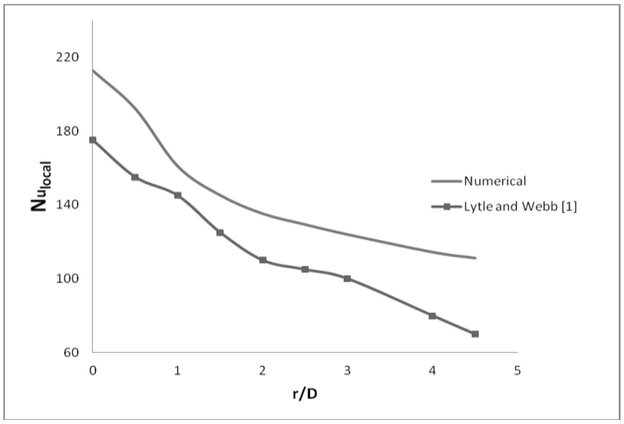


Fig.5 Variation of Local Nusselt number with radial distance (r) for Re=23000, Z/D=6, D=10mm

The numerical results are in good agreement with the experimental one. The selected k-ϵ model over-predicts the value of Nusselt number in the stagnation region than the wall jet region.

*C. Effect of Ribs and Rib Shapes*

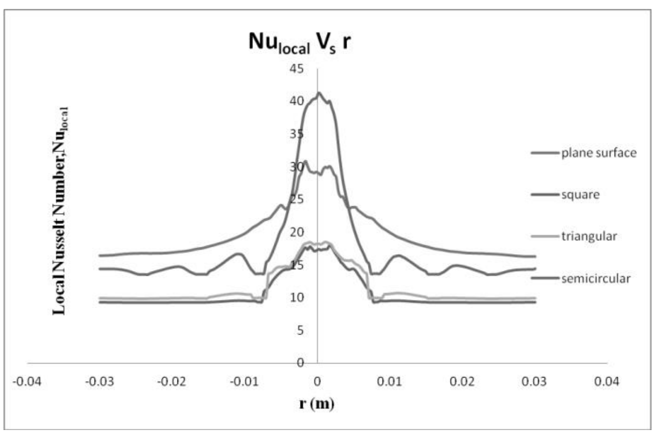


Fig.6 Variation of local Nusselt number with different shapes of ribs at Re=6000 and Z/D=1

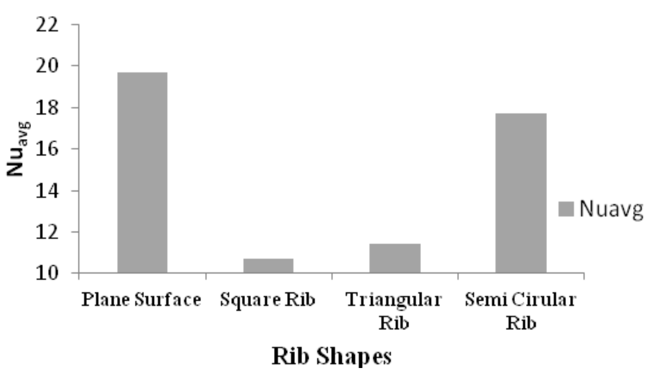


Fig.7 Variation of Average Nusselt number with different shapes of ribs at Re=6000 and Z/D=1

Fig.6 and 7 shows the variation of local and average Nusselt number variations using ribs with different shapes. The results show that the rib-roughened wall decreases the convective heat transfer in the ribbed region by comparison with the smooth wall under the same jet Reynolds number. This is due to the lack of fluid over the ribbed region and also the use of a single nozzle. Most of the fluid comes out from the nozzle is deviated in between the first two ribs. Stagnation Nusselt number is highest for semi-circular ribs due to increased turbulence developed in the stagnation region. Heat transfer enhancement by using array of jet is more effective for ribs. Among three rib shapes, the semi-circular rib seems to be advantageous on the convective heat transfer enhancement, especially at lower jet-to-target spacing. This is due to the low flow resistance provided by the semi-circular rib in the wall jet region. The square shaped ribs deviate most of the wall jet fluid in the upward direction, so there is a shortage of fluid contact with the wall jet region at larger radial distances.

The ribs on the impinging target provide stronger convective heat transfer in the wall-jet region due to the breakage of boundary layer. The ribs on the impinging target surface do provide convective heat transfer enhancements in the wall-jet zone, but this achievement is at the expense of pressure drop inside the channel. The rib roughened wall is more effective at low Z/D and for multiple nozzles. In the current model, lack of fluid in the wall jet region occurs due to a single nozzle with a smaller diameter. Nozzle with larger diameter or using multiple nozzles provides more amount of fluid in the wall jet region. The velocity contours corresponding to different rib shapes are shown in Fig.7.

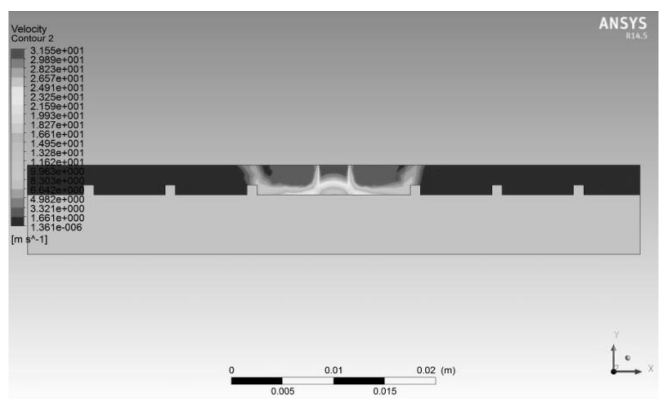


(a)

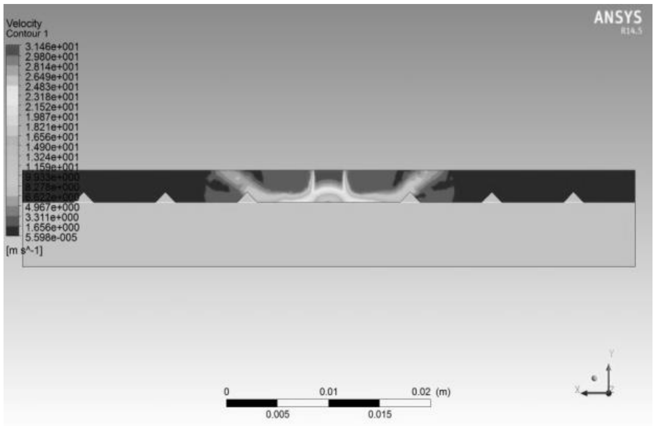


(b)

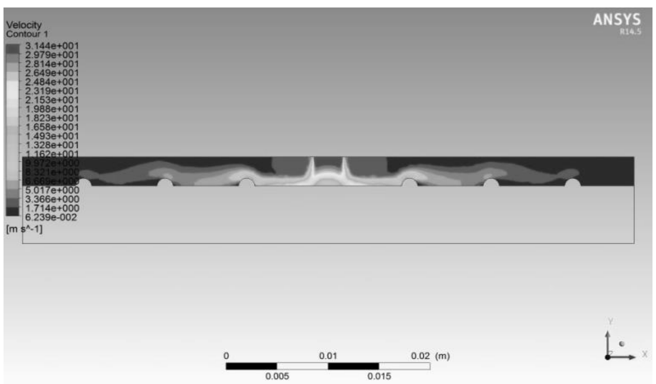


(c)

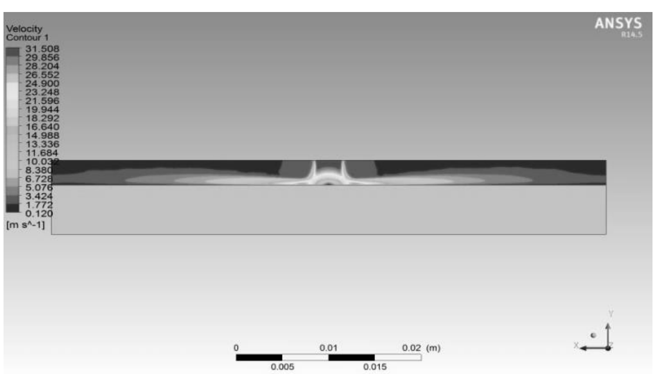


(d)

Fig.8 Velocity contours for different rib shapes at Re=6000 and Z/D=1 (a) Square (b) Triangular (c) Semi-circular (d) plane surface

The temperature contours corresponding to different rib shapes are shown in Fig.8.

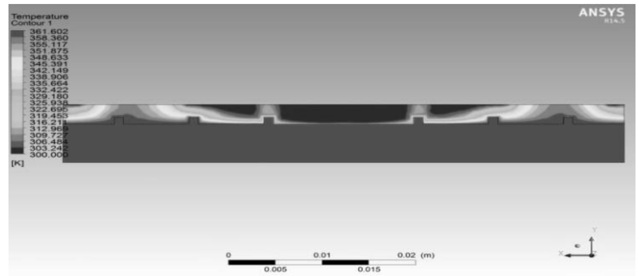


(a)

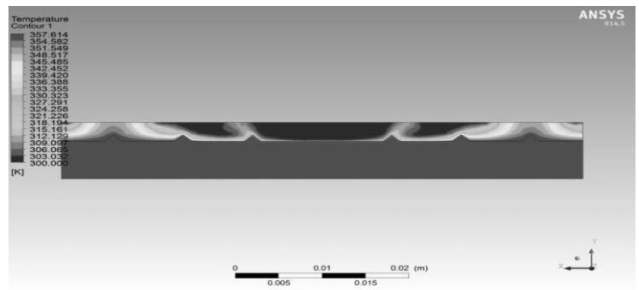


(b)

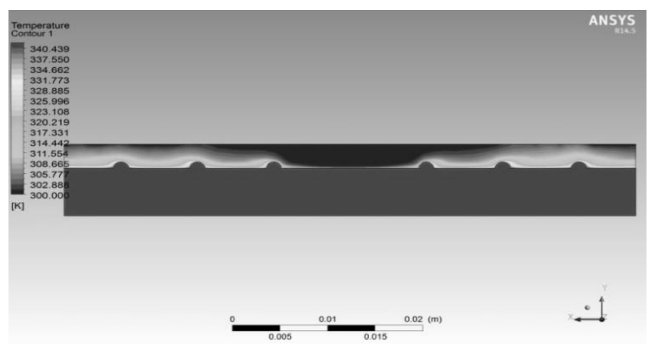


(c)

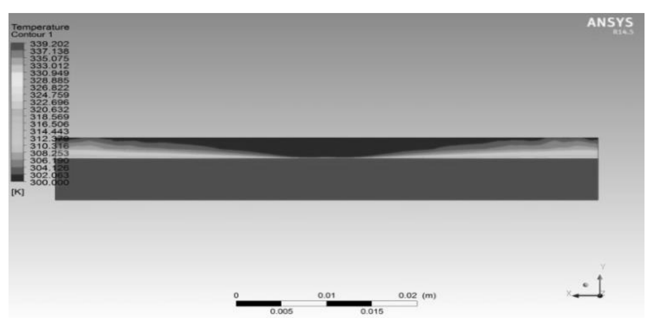


(d)

Fig.9 Temperature contours for different rib shapes at Re=6000 and Z/D=1 (a) Square (b) Triangular (c) Semi-circular (d) plane surface

## IV. CONCLUSION

The present work investigated heat transfer characteristics within an impingement model of single jet at a constant Reynolds number and Z/D ratio. The rib-roughened wall decreases the convective heat transfer in the ribbed region by comparison with the smooth wall under the same jet Reynolds number due to the lack of fluid over the ribbed region and also the use of a single nozzle. Among three rib shapes, the semi-circular rib shows higher value of average heat transfer due to the low flow resistance provided by the semi-circular rib in the wall jet region. The rib roughened wall is more effective for multiple nozzles.

## ACKNOWLEDGMENT

This study was supported by TEQIP II

## REFERENCES

[1] D. Lytle, B.W.Webb (1994) Air Jet Impingement Heat Transfer at Low Nozzle-Plate Spacing's. Int.J.Heat Mass Transfer 37, No.12, 1687-1697

[2] Lance Fisher (2001) A Numerical Investigation of Jet Impingement on a Heated Flat Plate, ME 513, 3-20

[3] Mirko Bovo, Sassan Etemad, Lars Davidson,2009, On the Numerical Modelling of Impinging Jet Heat Transfer, Int.Symp.on Convective Heat and Mass Transfer in Sustainable Energy

[4] Robert Gardon, J. Cahit Akfirat (1965) The Role Turbulence in Determining the Heat Transfer Characteristics of Impinging Jets, Int.J.Heat Mass Transfer 8.1261-1272

[5] Vadiraj Katti,S.V.Prabhu (2011) Experimental Study and Theoretical Analysis of Local Heat Transfer Distribution Between Smooth Flat Surface and Impinging Air Jet from a Circular Straight Pipe Nozzle, International Journal of Thermal Sciences 48,602-617

[6] N.Zuckerman, N.Lior (2006) Jet Impingement Heat Transfer: Physics, Correlations, and Numerical Modelling, Advances in Heat Transfer 39, 565-631

[7] Lei Tan, Jing-Zhou Zhang, Hua-Sheng Xu (2014) Jet Impingement on a Rib-Roughened Wall inside Semi-Confined Channel, International Journal of Thermal Sciences 86, 210-218

[8] Vadiraj V.Katti, S.Nagesh Yasaswy, S.V. Prabhu (2011) Local Heat Transfer Distribution Between Smooth and Flat Surface and Impinging Air Jet from a Circular Nozzle at Low Reynolds Numbers, Heat Mass Transfer 47, 237-244

[9] N.K.Chougule, G.V.Parishwad, C.M.Sewatkar (2012) Numerical Analysis of Pin Fin Heat Sink with a Single and Multi Air Jet Impingement Condition, International Journal of Engineering and Innovative Technology 1, Issue 3, 44-50

[10] V. Katti, S.V. Prabhu (2008) Heat transfer enhancement on a flat surface with axisymmetric detached ribs by normal impingement of circular jet, Int. J. Heat Fluid Flow 29, 1279-1294.

[11] M.Behnia, S.Parneix, P.Durbin (1997) Accurate Modelling of Impinging Jet Heat Transfer, Centre for Turbulence Research, Annual Research Briefs, pp.149-164

[12] C. Gau, C.C. Lee, (1992) Impingement cooling flow structure and heat transfer along rib-roughened walls, Int. J. Heat Mass Transfer 35, 3009-3020.

[13] G. Miyake, M. Hirata, N. Kasagi (1994) Heat transfer characteristics of an axisymmetric jet impinging on a wall with concentric roughness elements, Exp. Heat Transfer 7, 121-141.

[14] C. Gau, I.C. Lee (2000) Flow and impingement cooling heat transfer along triangular rib-roughened walls, Int. J. Heat Mass Transfer 43, 4405-4418.

[15] Hansen, L.G., Webb, B.W (1993) Air jet impingement heat transfer from modified surfaces. Int. J. Heat Mass Transfer 36, 989–997.

# Numerical Simulation of Loud Speaker Driven Thermoacoustic Refrigeration System

Jaison George varghese[1], Mathew Skaria, K. K. Abdul Rasheed, K. A. Shafi,. S. Kasthurirangan

*Department of Mechanical Engineering*
*TKM college of engineering, Kollam, Kerala, India*
[1]jaisonvrgh@gmail.com

***Abstract*— Numerical study was carried out to find out the performance of a thermo acoustic refrigerator. It has a stack which is subjected to pressure oscillations and as a result of these pressure oscillations one end of the stack is cooled to a temperature below ambient temperature and the other end is heated to a temperature higher than that of ambient.**

**The numerical simulation is done using 'ANSYS FLUENT 15'.A three dimensional model consisting of a pressure inlet, stack and a buffer is modelled and meshed using the software. Pressure based simulations were carried out. A used defined function is used as sound wave at pressure inlet. Isothermal boundary conditions where used for the stack plates. Outer surfaces are treated as adiabatic walls. A temperature of 300 kelvin was used as initialization. The gas used for simulation process is helium. Simulation studies were carried out for various mean operating pressures. With an increase in mean operating pressure the degree of cooling obtained also increases.**

***Keywords*— Thermo acoustics; acoustic cryo cooler; Acoustic stack; Buffer; CFD simulation**

## I. INTRODUCTION

Thermoacoustics means interactions between sound and heat. The conversion from one form of energy to another is done in thermoacoustic systems. When acoustic vibrations are used to generate cooling power, such a system is a thermoacoustic refrigerator system. Conversely a system which converts heat input into useful pressure oscillations can be regarded as a thermoacoustic engine system.

Thermoacostic refrigerator consists mainly of a loudspeaker attached to an acoustic resonator filled with a working fluid. In the resonator, a spiral shaped stackalong with two heat exchangers, are used. The loudspeaker sustains an acoustic standing wave in the working fluid. The acoustic standing wave displaces the gas in the channels of the stack while compressing and expanding. The thermal interaction between the oscillating working fluid and the surface of the stack generates an acoustic heat pumping. The heat exchangers exchange heat with the surroundings, at the cold and hot sides of the stack. A detailed explanation of the way thermoacoustic coolers work is given by Swift [1] and Wheatly et al. [2].

In this paper a 3D numerical analysis of a loud speaker driven thermoacoustic refrigerator (TAR) is done on ANSYS FLUENT for different operating pressures. The analysis is carried out to find out the variation in performance of a thermoacoustic refrigerator with mean operating pressures inside TAR. A temperature of 252 K was obtained at cold heat exchanger at a mean operating pressure of 30 bar.

## II. NUMERICAL FORMULATION

CFD modelling leads to the better understanding of the physical phenomena. It allows insight into fluid behaviour which normally cannot be studied experimentally. We have used ANSYS 15 for geometric modelling, meshing and analysis.

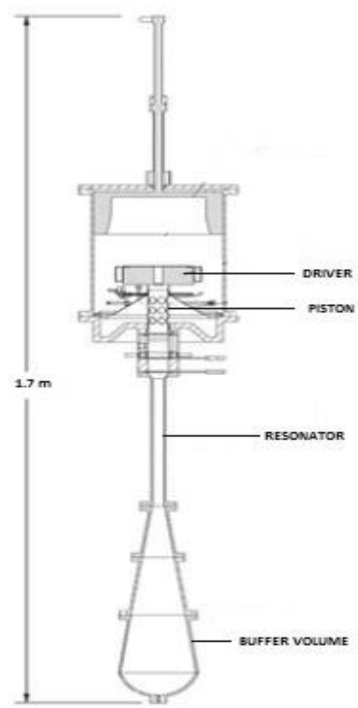


**Fig 1 Schematic Diagram Showing a Thermoacoustic Refrigerator Assembly (TAR)**

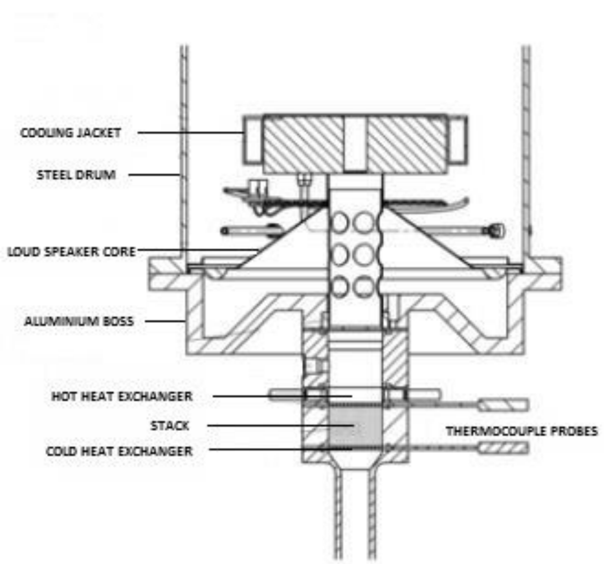


**Fig 2 Schematic diagram showing driver end, stack and heatexchanger positions of TAR assembly**

(Courtesy: Development of low cost loud speaker driven thermo acoustic Refrigerator,Luke Zoontjens, Carl Q. Howard, Anthony C. Zander and Ben S. Cazzolato,9-11 November 2005, Busselton, Western Australia,Proceedings of ACOUSTICS 2005[3] )

A standing wave thermoacoustic refrigerator (TAR) has been designed. The schematic diagram of the setup is shown in Figure 1 and 2. The system consists of a loud speaker, a stack, a cold and hot heat exchanger a resonator and a buffer. The loud speaker is the source for pressure oscillations.

In the present problem, Three Dimensional numerical simulation of air flow through in Thermo-Acoustic Refrigerator is carried out. Pressure based simulation studies were done.The Turbulent Flow Model is employed to study the variation of flow and thermal parameters.

The geometry is drawn using workbench 15.The stack used is spiral Mylar stack having 0.01mm thickness and the space between each subsequent layers is separated by using spacers which is 0.3 mm thick. We modelled the fluid space between the stack as well as resonator instead of the solid walls and stack. So the geometry is a single fluid body with only a single part. Geometry drawn on workbench is shown in figure 3. The meshing for the Three Dimensional model developed is done using Mesh generator of ANSYS 15.The number of elements present in the mesh is 52111. The number of nodes present after mesh is 64431.Figure 4 shows the mesh obtained after the mesh generation process. The analysis was done using FLUENT 15. Pressure based solver was used and transient formulation was done. Turbulence modelling is done using k-epsilon equation and energy equation is kept on. A time step size of 0.00001 was used for calculations. This time step size ensures that convergence at every subsequent iterations [5].

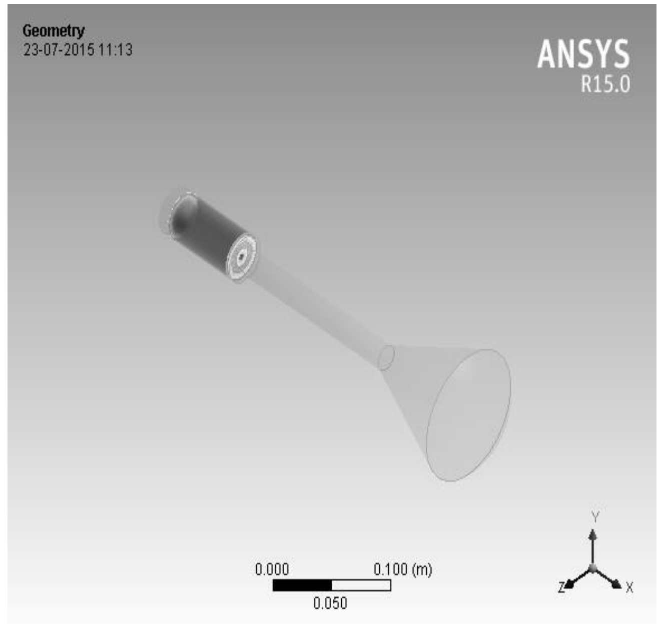


**Fig 3 Geometry of TAR Modelled Using ANSYS WORKBENCH 15**

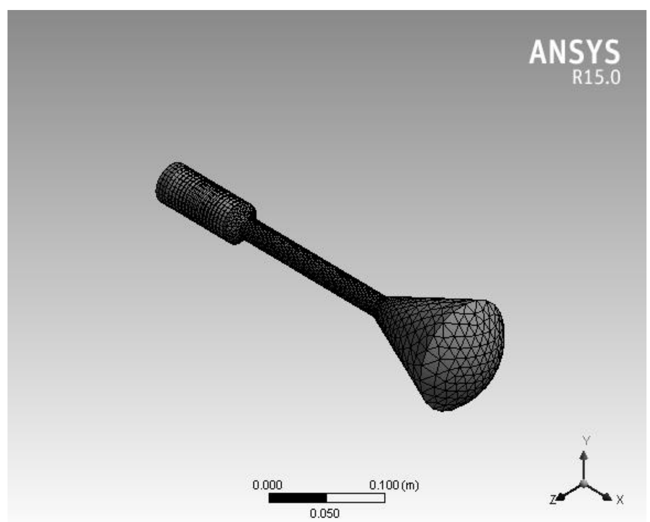


**Fig 4 Mesh Generated Using ANSYS 15**

## III. RESULTS AND DISCUSSION

For CFD simulation, a spiral stack is used. A user designed function is developed for a frequency of 400 Hz and is given as pressure input at pressure inlet. The parameter which was varied and studied is mean operating pressure. An initial temperature of 300 K is assigned to the system. Results obtained include graphs plotted for weighted average total temperature on the cold side of the stack versus number of iterations and also contours for total temperature across the stack. CFD simulations were carried out for mean operating pressures ranging from 2 bar to 30 bars and optimum mean operating pressure has been found out. The weighted average total temperature on cold side of stack versus number of iterations for a mean pressure of 4 bar is shown in figure 5. Temperature profile across the stack for the same mean operating pressure is shown in figure 6.

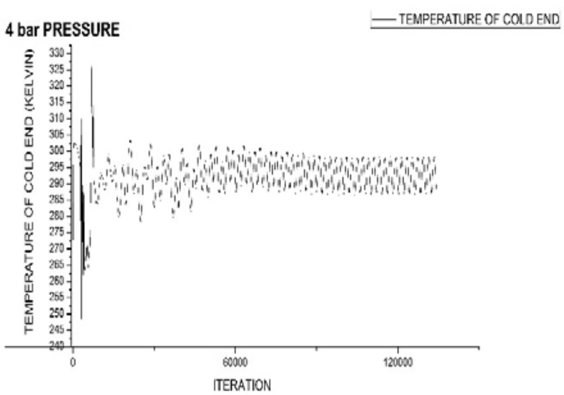


**Fig 5 Temperature of Cold End VS Iteration for 4 bar Operating Pressure**

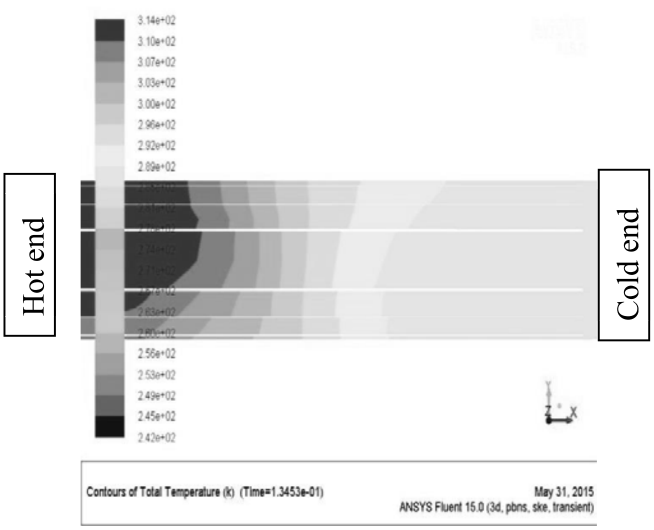


**Fig 6 Contours of Temperature Distribution across Stack for 4 bar Operating Pressure**

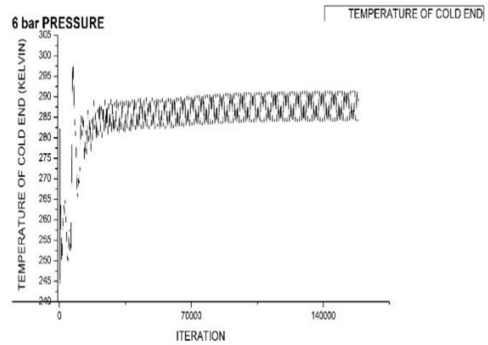


**Fig 7 Temperature of Cold End VS Iteration for 6 bar Operating Pressure**

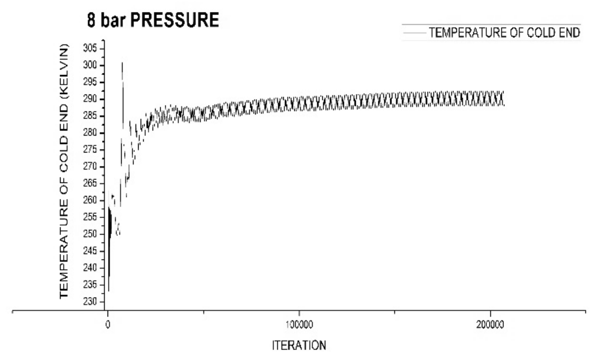


**Fig 8 Temperature of Cold End VS Iteration for 8 bar Operating Pressure**

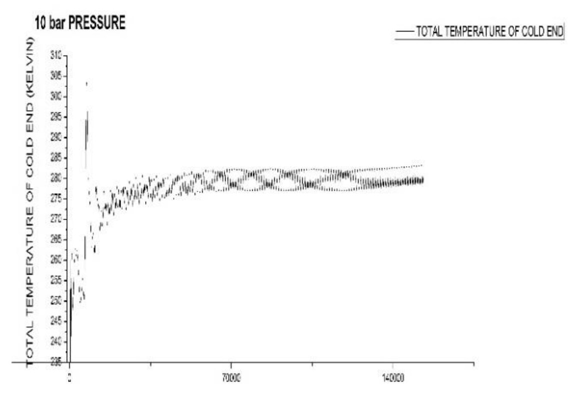


**Fig 9 Temperature of Cold End VS Iteration for 10 bar Operating Pressure**

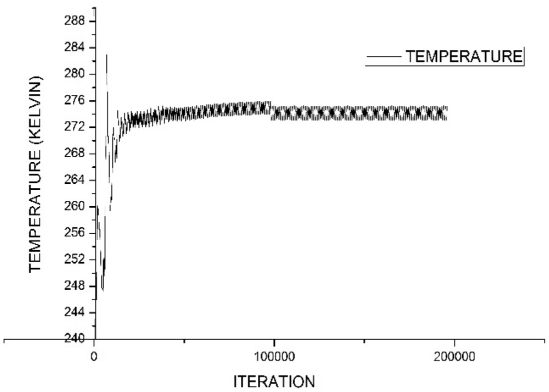


Fig 10 Temperature of Cold End VS Iteration for 20 bar Operating Pressure

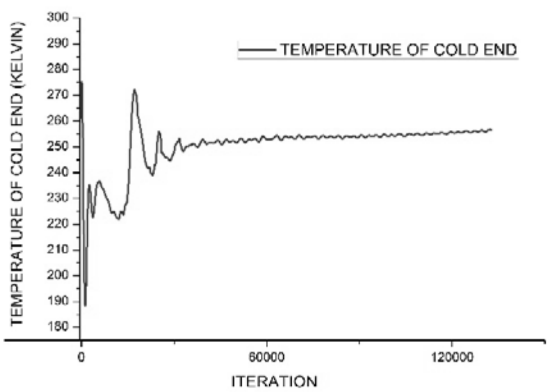


Fig 11 Temperature of Cold End VS Iteration for 30 bar Operating Pressure

| Mean operating pressure (bar) | Average temperature of cold end of stack (k) | Temperature fluctuation range |
|---|---|---|
| 2 | 294 | 300-280 |
| 4 | 291 | 296-285 |
| 6 | 286 | 290-281 |
| 8 | 284 | 287-279 |
| 10 | 279 | 283-276 |
| 20 | 272 | 274-271 |
| 30 | 252 | 252-251 |

Table 1 Variation in average temperature of cold end of stack and temperature fluctuation range for various mean operating pressures

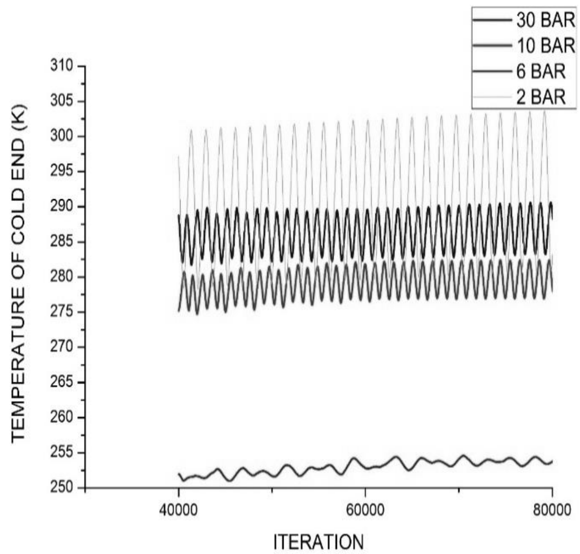


Fig 12 Comparison of Cold End Temperatures at Various Mean Operating Pressures

By analysing the comparison plot we noticed two major changes that take place with an increase in mean operating pressure.

The first one is that with an increase in mean operating pressure, there is an increase in temperature drop at the cold end of the stack of TAR. This was be explained by Olson and Swift [4]. They proposed that acoustic power and cooling power are functions of mean pressure, the sound velocity, and the cross-sectional area of the stack. Thus cooling power and acoustic power are directly proportional to the mean operating pressure and hence with an increase in mean operating pressure the temperature drop at the cold end of the stack decreases.

The second observation is that with an increase in mean operating pressure the temperature fluctuations goes on reducing after system attaining a steady state. That is, at 2 bar mean operating pressure the cold end temperature fluctuates between 300 K and 280 K. For 4 bar it is between 296 K and 285 K, while for 6 bar the fluctuations are between 290 K and 281 K. For 8 bar mean operating pressure the cold end stack temperatures fluctuates between 287K and 279 K and for 10 bar it is between 283 K and 273 K. For 20 bar the temperature limits are between 274 K and 271 K and finally for 30 bar mean operating pressure the temperature fluctuations ranges between 252 K and 251 K.

The reason for reduction in temperature fluctuation is that as pressure increases, molecules come closer and the mean free path between them is reduced and hence the pressure oscillations have to travel less to transfer heat from one molecule to another. As a result of this heat is transferred in a shorter time from one molecule to another than at lower mean operating pressures. Hence there is only less time for the dissipation of heat into the surrounding. Thus the temperature of molecule does not very much at high pressures. This explains why the thermo acoustic refrigerator works well at higher mean operating pressures and have very low performance at lower operating pressures.

## IV. CONCLUSION

1. With an increase in mean operating pressure, there is an increase in temperature drop at the cold end of the stack of TAR. A temperature drop as large as 48 K was observed at 30 bar mean operating pressure.
2. With an increase in mean operating pressure the temperature fluctuations goes on reducing after system attaining a steady state. This explains why the thermo acoustic refrigerator works well at higher mean operating pressures and have very low performance at lower operating pressures.

## REFERENCES


[1] Swift GW,1988 Thermoacoustic engines. J Acoust Soc Am;84:1146–1180.

[2] Wheatley JC, Hofler T, Swift GW, Migliori A. Understanding some simple phenomena in thermoacoustics with applications to acoustical heat engines. Am J Phys 1985;53:147–62.

[3] Luke Zoontjens, Carl Q. Howard, Anthony C. Zander and Ben S. Cazzolato, Development of low cost loud speaker driven thermo acoustic Refrigerator, Busselton, Western Australia,Proceedings of ACOUSTICS 2005 November 2005,9-11

[4] Olson JR, Swift GW,1994 Similitude in thermoacoustic. J Acoust Soc Am;95:1405–12.

[5] Tijani MEH, Zeegers JCH, de Waele ATAM, Design of thermoacoustic refrigerators.2002,Cryogenics. . J Appl Phys;10:786-795.

[6] Garrett SL,1991, Thermoacoustic life science refrigerator. NASA Report, No. LS-10114

[7] Hofler TJ. Thermoacoustic refrigerator design and performance. Ph.D. dissertation, Physics Department, University of California at San Diego, 1986.

[8] Garrett SL, Adeff JA, Hofler TJ. Thermoacoustic refrigerator for space applications. J Thermophys Heat Transfer 1993;7:595–9.

[9] Oberst H. Eine Methode zur Erzeugung extrem starker stehender Schallwellen in Luft Akustische Zeits 1940;5:27–36;English translation: Beranek LL. Method for Producing Extremely Strong Standing Sound Waves in Air. J Acoust Soc Am 1940;12:308–400.

[10] Wetzel M, Herman C. Experimental study of thermoacoustic effects on a single plate. Part I: Temperature fields. Heat Mass Transfer 2000;36:7; Wetzel M, Herman C. Part II: Heat transfer. Heat Mass Transfer 1999;35:433–42.

[11] Jeromen, A. (2003). A simplified thermoacoustic engine demonstration. American Journal of Physics, 71(5), 496-499.

[12] Luo, E. C., Dai, W., Zhang, Y., & Ling, H. (2006). Experimental investigation of a thermoacoustic-stirling refrigerator driven by a thermoacoustic-stirling heat engine. Ultrasonics, 44(Supplement 1), e1531-e1533.

# An Investigation on Enhanced Heat Transfer Characteristics of Nanofluids

Sanukrishna.S.S

*Department of Mechanical Engineering,*

*Sree Chitra Thirunal College of Engineering, Pappanamcode, Thiruvananthapuram, Kerala, India.*

sanukrishna@sctce.ac.in

***Abstract-*** **Nanofluids are new class of heat transfer fluids developed by suspending nano sized (1-100nm) solid particles in liquids. They have higher thermal conductivity and single phase heat transfer coefficients than their base fluids. Numbers of models are available in the literature to estimate the thermalconductivity and heat transfer coefficient of nanofluids. In the present study, experimental verification of enhanced thermal conductivity has been conducted. A theoretical investigation have been carried out on a double pipe, counter flow heat exchanger using Cu-Water nanofluid to study the effect of nanofluids on the effectiveness of the heat exchanger and it is found that the heat exchanger effectiveness can be increased by 19% at a volume fraction of 5%. All these reveal the potentials of nanofluids. Recent researches have indicated that substitution of conventional coolants by nanofluids in thermal transport phenomena appears promising.**

**Key words- Nanofluids, Nanofluids; nanoparticles; thermal conductivity, Heat transfer coefficient; effectiveness.**

## I. INTRODUCTION

Ultra high performance cooling is one of the most vital needs of many industrial technologies. However, inherently poor thermal characteristics of usual engineering fluids are a primary limitation in developing energy efficient cooling systems. To overcome this limitation, a new class of heat transfer fluids was developed by suspending nanoparticles in these fluids. A very small amount of nanoparticles, when uniformly dispersed and stably suspended in these fluids, can provide dramatic improvements in the thermal properties of the fluids. Nanofluids is the term coined by Choi [1] to describe this new class of nanotechnology-based heat transfer fluids that exhibit superior thermal properties compared to those of their host fluids or micro sized particle fluid suspensions.

## II. APPLICATIONS OF NANOFLUIDS

Researches on a variety of nanofluids applications is under way. Nanofluids find most of their applications in thermal management of industrial and consumer products.
Efficient cooling is vital to realizing the functions and long-term reliability of a variety of industrial and consumer products and there are tribological and biomedical applications. Nanofluids can be used in broad range of engineering applications due to their improved heat transfer and energy efficiency.

### *A. Cooling Applications*

*1)Crystal Silicon Mirror Cooling:* One of the first applications of research inthe field of nanofluids is for developing an advanced cooling technology to cool crystal silicon mirrors used in high-intensity x-ray sources (Lee and Choi,1996). Because an x-ray beam creates tremendous heat as it bounces off a mirror, cooling rates of 2000 to 3000 W/cm2 should be achievable with the advanced cooling technology.

*2)Electronics Cooling:* Chien et al. (2003) were probably the first to show experimentally that the thermal performance of heat pipes can be enhanced by nearly a factor of 2 when nanofluids are used. They used water-based nanofluids containing17-nm gold nanoparticles as the working fluid in a disk-shaped miniature heat pipe (DMHP).

*3)Vehicle Cooling:*In automobile arena, nanofluids have potential application as engine coolant, automatic transmission fluid, brake fluid, gear lubrication, engine oil and greases. Tzeng et al. (2005) were probably the first to apply nanofluid research in cooling a real-world automatic power transmission system. Application of nanofluid in the car radiator has been studied experimentally by various researchers [2]. Heat transfer enhancement of about 45% compared to water has been recorded.

*4)Transformer Cooling*: The power generation industry is interested in transformer cooling application of nanofluids for reducing transformer size and weight. Xuan andLi (2000) and Yu et al. (2007) have demonstrated that the heat transfer properties of transformer oils can be improved by using nanoparticle additives.

*5)Space and Nuclear Systems Cooling:* You et al. (2003) and Vassallo et al. (2004) have discovered the unprecedented phenomenon that nanofluids can double or triple the CHF in pool boiling. Kim et al. (2006) found that the high surface wettability caused by nanoparticle deposition can explain this remarkable thermal properties of nanofluids. The Massachusetts Institute of Technology has established an interdisciplinary center for nanofluid technology for the nuclear energy industry. Currently, they are evaluating the potential impact of the use of nanofluids on the safety, neutronic, and economic performance of nuclear systems.

*6)Defense Applications:* A number of military devices and systems, such as high powered military electronics, military vehicle components, radars, and lasers, require high-heat-flux cooling, to the level of thousands of W/cm2. At this level, cooling with conventional heat transfer fluids is difficult. Some specific examples of potential military applications include power electronics and directed-energy weapons cooling. Nanofluids also provide advanced cooling technology for military vehicles, submarines, and high-power laser diodes.

*7) Tribological Applications:*Nanofluid technology can help develop better oils and lubricants. Recent nanofluid activity involves the use of nanoparticles in lubricants to enhance tribological properties of lubricants, such as load-carrying capacity and antiwear and friction-reducing properties between moving mechanical components. In lubrication application it has been reported that surface-modified nanoparticles stably dispersed in mineral oils are very effective in reducing wear and enhancing load-carrying capacity (Que et al., 1997).

*8) Biomedical Applications:* Nanofluids are now being developed for medical applications, including cancer therapy. Traditional cancer treatment methods have significant side effects. Iron-based nanoparticles can be used as delivery vehicles for drugs or radiation without damaging nearby healthy tissue by guiding the particles up the bloodstream to a tumor with magnets. Nanofluids could also be used for safer surgery by cooling around the surgical region, thereby enhancing a patient's chance of survival and reducing the risk of organ damage.

## III. THERMAL CONDUCTIVITY AND HEAT TRANSFER COEFFICIENTOF NANOFLUIDS.

### *A.Thermal conductivity.*

Thermal conductivity of conventional fluids can be explained by simple heat transfer equations. Currently there is no reliable theory to predict the anomalous increase in thermal conductivity of nanofluids. However there exist several empirical correlations to calculate the apparent conductivity of two phase mixtures. A brief description of the various models is given in table 1.

### *B.Heat transfer coefficient*

The nanofluids have higher heat transfer coefficient and the increase appears to go beyond the mere thermal-conductivity effect, and cannot be predicted by traditional pure fluid correlations such as Dittus-Boelter's. The abnormal single-phase convective heat-transfer coefficient increase relative to the base fluid has been investigated by several researchers. Some of the prominent correlations have been shown in table 2.

## IV. EXPERIMENTAL DETERMINATION OF THERMAL CONDUCTIVITY OF NANOFLUIDS.

The one-dimensional, steady-state parallel-plate method has been employed to measure the thermal conductivity of CuO-Distilled Water and $Al_2O_3$-Distilled Water nanofluids at different particle mass fractions.

### *A. Preparation of nanofluids*

Preparation of nanofluids is the key step in experimental studies with nanofluids. Nanofluids are not simply liquid-solid mixtures. Some special requirements are essential, eg: even and stable suspension, negligible agglomeration, better dispersion, no chemical reaction etc.Commercially available nanoparticles of copper oxide and aluminium oxide with size <50nm and having density 1.25 g/cc and 0.26 g/cc respectively and distilled water as base fluid were used for preparing nanofluids. Ultrasonic agitation (using ultrasonic vibrator at a frequency of 34 KHz) method was used, with an agitation time of one hour. The nanoparticles remains suspended for a period of 1-2 days, after which settling begins to occur. Even when settling occurs, the particles can be redistributed by agitation of the nanofluid .CuO-Distilled water and $Al_2O_3$-Distilled water nanofluid samples of various mass fractions (1wt% – 3wt %) were prepared for performing experiments.

### *B Experimental set-up.*

The apparatus works according to the guarded hot plate principle. This plate is to reduce lateral heat losses and to most nearly secure a one-dimensional heat flow. The samples to be tested are filled in the liquid chambers. To make the heat flow in one dimensional, the central plate heater (Nichrome strip type sandwitched between mica sheets) is surrounded by a guard heater (Nichrome strip type sand witched between mica sheets), which is heated separately. By varying the input power, the temperature can be varied. Temperature at the required interfaces is measured by connecting the corresponding thermocouples to the PC based data acquisition system. Knowing the heat input to the central plate, the temperature difference across the container, its thickness and area of heat transfer, the thermal conductivity *k* of the fluid can be calculated using the 1-D conduction equation.

$$k = \frac{QL}{A\Delta T}$$

Where, A is the heat transfer area in $m^2$, L the thickness of specimen column in m, Q is the heat flux in W.
Base line tests were conducted with distilled water at different temperatures and thermal conductivity of distilled

water at a steady state temperature of was found to be 0.63W $m^{-1}K^{-1}$.

Then the experiments were conducted with CuO/Distilled water with 1wt% and 3wt% particle concentrations and $Al_2O_3$/ Distilled water at a particle concentration of 3wt% to investigate the influence of dosing levels of nanoparticles in the effective thermaconductivity of nanofluids. Observations were taken at a steady state temperature of $32^0C$.

The main sources of uncertainties are error due to the measurement of temperature by thermo couples, the combined uncertainty of the data logger and variation of line voltage, current etc.

Fig 1. Experimental set-up

## V. ANALYSIS OF EFFECT OF NANOFLUIDS IN HEAT EXCHANGER EFFECTIVENESS.

A theoretical investigation has been carried out to find out the effect of nanofluids on the effectiveness of heat exchangers. For the analysis, a double pipe heat exchanger with the hot fluid (in this case water) flowing through the inner tube and the cold fluid (in this case nano fluids) through the annulus is considered. The flow is assumed to be counter flow type. The specifications of the heat exchanger considered are shown in table3.

In this present study two cases have been considered. In the first case a water to water heat exchanger is considered i.e. both hot and cold fluids are water. In the second case the cold side water is replaced by Cu-water nanofluid. In the first case Dittus-Boelter correlation for pure fluids is used for the calculation of heattransfer coefficient at the cold side and hot side of the heat exchanger. For the second case, cold side heattransfer coefficient is calculated by the correlation proposed by Vasu et al. For the estimation of thermal conductivity of nanofluid, the calculation scheme proposed by Jang and Choi is used. Because Jang and choi model is successful in estimating the thermalconductivity of nanofluids.

Neglecting the conduction resistance offered by the wall of the inner pipe, overall heattransfer coefficient was calculated using the following relation.

BLE III
SPECIFICATIONS OF HEAT EXCHANGER

| | |
|---|---|
| Inner pipe diameter | 6 cm |
| Outer pipe diameter | 10 cm |
| Length of the heat exchanger | 5 m |
| Mass flow rate through inner pipe | 550 kg/hr |
| Mass flow rate through annulus | 1300 kg/hr |
| Hot fluid inlet temperature | $94^0C$ |
| Cold fluid inlet temperature | $27^0C$ |

$$U = \frac{1}{\left[\left(\frac{1}{h_1}\right)+\left(\frac{1}{h_2}\right)\right]}$$

Where, $h_1$ = hot side heattransfer coefficient and $h_2$=cold side heattransfer coefficient.

The effectiveness of the heat exchanger is calculated using the following expression.

$$\in = \frac{\left[1-e^{\left[-N(1-C)\right]}\right]}{\left[1-Ce^{\left[-N(1-C)\right]}\right]}$$

Where, N= Number of Transfer Units.

## VI. RESULTS AND DISCUSSION

From the experiment, it is seen that addition of copper oxide and aluminium oxide nanoparticles improves the effective thermal conductivity of the nano fluid and in all cases the thermal conductivity increases almost linearly with volume fraction. There is an increased thermal conductivity for copper oxide –water nanofluid than aluminium oxide-water nanofluid.

TABLE I
THERMAL CONDUCTIVITY MODELS

| Investigator | Models ($k_{eff}/k_{bf}$) | Comments |
|---|---|---|
| Maxwell [4] | $\frac{k_{eff}}{k_{bf}}=\frac{k_p+2k_{bf}-2(k_{bf}-k_p)\phi}{k_p+2k_{bf}+\phi(k_{bf}-k_p)\phi}$ | Relates the thermal conductivity of spherical particle, base fluid and solid volume fraction. Where $K_{eff}$, and $k_{bf}$ are the effective and base fluid thermal conductivities,φ is particle volume fraction. |
| Hamilton and Crosser [5] | $\frac{k_{eff}}{k_{bf}}=\frac{k_p+(n-1)k_{bf}-(n-1)(k_{bf}-k_p)\phi}{k_p+(n-1)k_{bf}+(k_{bf}-k_p)\phi}$ | for non-spherical particles, $kp/kb$ > 100, $n$ is an empirical shape factor ($n = 3/\psi$, $\psi$ is the sphericity) |
| Yu and Choi [6] | $\frac{k_{eff}}{k_{bf}}=\frac{k_{pe}+2k_{bf}+2(k_{pe}-k_{bf})(1+\beta)^3\phi}{k_{pe}+2k_{bf}-(k_{pe}-k_{bf})(1+\beta)^3\phi}$ | a modified Maxwell and Hamilton–Crosser model, $K_{pe}$ is the modified thermal conductivity of particle. |
| Jang and Choi [7] | $k_{eff}=k_{bf}(1-\phi)+\beta k_{particle}\phi+C_1\frac{d_{bf}}{d_{nano}}k_{bf}\,\mathrm{Re}^2{}_{d_{nano}}\,\mathrm{Pr}\,\varphi$ | Four modes: collisons between fluid molecules, thermal diffusion of nanoparticles, collisons between nanoparticles due to Brownian motion and thermal interaction of dynamic nanoparticles withbase fluid molecules |

TABLE II
CORRELATIONS OF HEATTRANSFER COEFFICIENT

| Investigator | Correlations | Comments |
|---|---|---|
| Pak and Cho [8] | $Nu_{nf}=0.021(\mathrm{Re}_b)^{0.8}(\mathrm{Pr}_b)^{0.5}$ | for $Al_2O_3$–water nanofluid |
| Xuan and Li [9] | $Nu_{nf}=0.0059\left[1+7.6286\phi^{0.6886}\left(\mathrm{Re}_b\,\mathrm{Pr}_b\frac{d_b}{D}\right)^{0.001}\right]\mathrm{Re}_b^{0.9238}\,\mathrm{Pr}_b^{0.4}$ | for Cu-water nanofluid. Where, $\mathrm{Re}_b$ , $\mathrm{Pr}_b$ and $d_b$ are the Nusselt number, Reynolds number and Prandtl number of base fluid and diameter of base fluid respectively. D is the tube diameter. |
| Vasu et al [10] | $Nu=0.0256(\mathrm{Re}_{nf})^{0.8}(\mathrm{Pr}_{nf})^{0.4}$ | for $Al_2O_3$-Water |
| | $Nu=0.027(\mathrm{Re}_{nf})^{0.8}(\mathrm{Pr}_{nf})^{0.4}$ | for Cu-water adopted the 'single phase fluid' approach |

For copper oxide nanofluids, there is an increase in thermal conductivity of 27.9% compared to the base fluid at a volume fraction of 3% and for aluminium oxide 7.46% enhancement is observed, which could be attributed to the individual enhancement of the thermo physical properties offered by them. The variations are shown in Fig 2and3. Among various analytical models, Jang and Choi model [6] predicts the highest values of thermal conductivity and the model predictions are in line with theexperimental results From the theoretical analysis, it was observed that the addition of nanoparticles to the heat exchanger fluid increases the effectiveness of the heat exchanger; this enhancement is a direct function of concentration of the nanoparticles used in the base fluid.

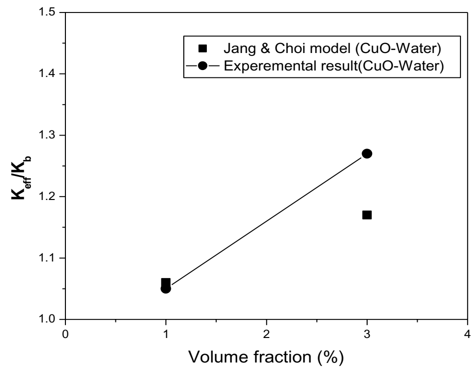


Fig 2: Effect of volume fraction on effective thermal conductivity of CuO -water nanofluid.

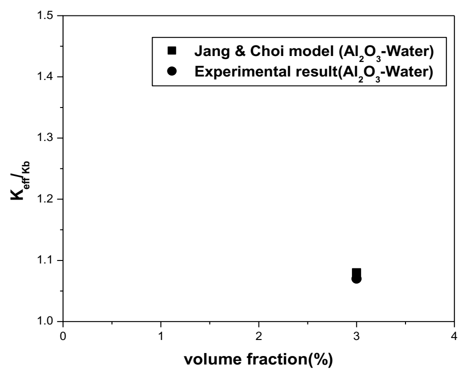


Fig 3: Effect of volume fraction on effective thermal conductivity of $Al_2O_3$-water nanofluid

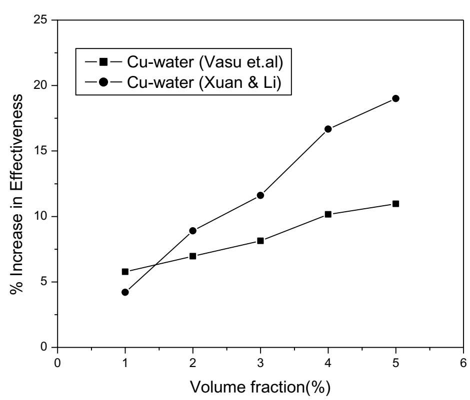


Fig 4: Percentage increase in effectiveness of the heat exchanger using Cu-Water nanofluid

From the investigation, it has been observed that by using nanofluids as the heat transfer fluid in a double pipe counter flow heat exchanger, the effectiveness of the heat exchanger is been enhanced. .In the case of Cu–water nanofluid, at a mass fraction of 5wt%, the effectiveness increases by 19% (shown in fig.4). Higher concentrations of nanoparticles, though would produced much improved effectiveness and are prone to larger agglomeration and sedimentation of particles over continued use.

## VII. CONCLUSIONS

The potentials behind the new generation heat transfer fluid have been discussed. The thermal conductivity of fluids can be increased by adding nanosized particles. Experiments were conducted to verify the effect of nanoparticles on the thermal conductivity of suspensions. It is observed that addition of 3wt% of CuO nanoparticles to water enhances the thermal conductivity by 27.9%. The increase in thermal conductivity is 7.46% with the addition of 3wt% of$Al_2O_3$ nanoparticles to distilled water. The effectiveness of heat exchangers can be increased by using nanoluids and the increase in effectiveness of the heat exchanger is found to be 19% when using Cu-Water nanofluid at 5wt% particle concentration.

## REFERENCES

[1] Eastman, J. A., Choi, S. U. S., Li, S., Yu, W. and Thomson, L. J. Anomalously increased effective thermal c1onductivities of ethylene glycol based nanofluids containing copper nanoparticles. Applied Physics Letters, 2001. 78:pp 718-720.

[2] S.H. Hashemabadi, M. Seifi Jamnani, S.M. Hoseini ,Improving the cooling performance of automobile radiator with $Al_2O_3$/water nanofluid, Applied Thermal Engineering,Volume 31, Issue 10, pp 1833–1838.

[3] R. Saidur, K.Y. Leong, H.A. Mohammad, Renewable and Sustainable Energy Reviews, Volume 15, Issue 3,2011, Pages 1646-1668

[4] Maxwell, J. C. *Treatise on electricity and magnetism*. Oxford: Clarendon Press., 1873.

[5] Hamilton, R. L., and O. K. Crosser . *Thermal conductivity of heterogeneous two component systems. Industrial & Engineering Chemistry Fundamentals*,1962 1: 187-191.

[6] [Yu, W., and S. U. S. Choi . *The role of interfacial layers in the enhanced thermal conductivity of nanofluids: A renovated Maxwell model*. Journal of NanoparticleResearch,2003 pp167-171.

[7] Jang, S. P., and Choi, S. U. S. . *Role of Brownian motion in the enhanced thermalconductivity of nanofluids*. Applied Physics Letters, 2004 84: pp 4316-4318.

[8] Pak, B. C., and Cho, Y., "Hydrodynamic *and Heat Transfer Study of Dispersed Fluids with Submicron Metallic Oxide Particles*, Exp. Heat Transfer, 1998,11, pp. (151–170)

[9] Xuan , Y , Q.Li .*Investigation on convective heat transfer and flow features of Nanofluids*. ASME trans. Journal of Heat transfer, 2003 pp 151-155.

[10] V.Vasu,K.Rama Krishna, ACS Kumar,,*Analytical prediction of thermo physical properties of fluids embedded with nano structured materials*.Int.J.nanopartles, 2008 Vol I.

[11] Xuan, Y., and Li, Q. *Heat transfer enhancement of nano-fluids*. Int. J. Heat FluidFlow ,2000 21: pp58–64.

[12] Das, S. K., Putra, N., Thiesen, P., and Roetzel, W..*Temperature dependence of thermal conductivity enhancement for nanofluids*. ASME J. Heat Trans.,2003 125: pp567–574.

# Experimental Investigations on Tube in Tube Helical and Conical Heat Exchangers

M.Kiran Kumar[1], C.M.Abhijith[2], Sheeba A[3]

*Department of Mechanical Engineering*

*TKM college of Engineering, Kollam, Kerala, India*

[1]kiran8247@gmail.com

[2]tomeabhijith@gmail.com

[3]sheebajameel100@gmail.com

***Abstract*— The complex fluid-dynamic inside curved pipe heat exchangers gives them important advantages over the performance of straight tubes in terms of area/volume ratio and enhancement of heat transfer and mass transfer coefficient. In the present study an experimental investigation on heat transfer and frictional characteristics in a non-previously implemented cone shaped double tube helical coil heat exchanger is reported for various Reynolds numbers. The purpose of this article is to compare the heat transfer in cone shaped helical coil and simple helical coil. The pitch, base radius of coil and length of both the coils are kept same for comparative analysis. The calculations have been performed for the steady state condition and experiments were conducted for different flow rates in laminar flow regime. Overall heat transfer coefficients were calculated and heat transfer coefficients in the inner and outer tube were determined using Wilson plots. It was observed that the heat transfer rate, overall heat transfer coefficient and convective heat transfer coefficient for the cone shaped helical coil is more than that for the simple helical coil. It was found that the heat transfer rates are 1.01 to 1.2 times more for the cone shaped helical coil than that of simple helical coil.**

**Keywords – Helical coil, helical cone coil, heat exchanger, heat transfer, friction factor**

## I. INTRODUCTION

Helical coils have been long and widely used as heat exchangers in power, petrochemical, HVAC, chemical and many other industrial processes. Helical and spiral coils are known to have better heat and mass transfer compared to straight tubes, the reason for that is the formation of a secondary flow superimposed on the primary flow, known as Dean Vortex. Extensive research on numerical and experimental investigations in simple helical coils was carried out by different researchers in laminar and turbulent flow regime. However flow through the cone shaped helical coils is still under exploration.

Dravid *et al.* [1] numerically investigated the effect of secondary flow on laminar flow heat transfer in helically coiled tubes both in the fully developed region and in the thermal entrance region. The results obtained from predictions were validated with those obtained from experiments in the range in which they overlapped. A correlation for the asymptotic Nusselt numbers, Nu, was proposed as follows:

$$Nu = \left(0.65\sqrt{De} + 0.76\right)Pr^{0.175} \qquad (1)$$

Where Nu is the Nusselt number, De is the Dean number varied from50 to 200, and Pr is the Prandtl number in the range 5 to 175. Yang *et al.* [2] presented a numerical model to study the fully developed laminar convective heat transfer in a helical double pipe having a finite pitch. The effects of the Dean number, torsion, and the Prandtl number on the laminar convective heat transfer were discussed. The laminar flow of fluid was subjected to be hydrodynamically and thermally fully developed with uniform wall temperature. The temperature gradient increased on one side of the pipe wall and decreased on the other side with increasing torsion. In the case of a fluid with a large Prandtl number, the Nusselt number was significantly decreased as torsion increased, but in the case of a fluid with a small Prandtl number, the Nusselt number declined slightly as the torsion increased.

Rennie and Raghavan [3] simulated the heat transfer characteristics in a two-turn tube-in-tube helical coil heat exchanger. Various tube-to-tube ratios and Dean numbers for laminar flow in both annulus and in-tube were examined. The temperature profiles were predicted using a computational fluid dynamics package PHEONICS 3.3. The results showed that the flow in the inner tube at the high tube-to-tube ratios was the limiting factor for the overall heat transfer coefficient. This dependency was reduced at the smaller tube-to-tube ratio, where the influence of the annulus flow was increased. In all cases, as other parameters were kept constant, increasing whether the tube Dean numbers or annulus Dean numbers resulted in an increase in the overall heat transfer coefficient.

Jayakumar *et al.* [4] presented a CFD model to evaluate the effects of coil parameters: pitch circle diameter, tube pitch and pipe diameter. Analysis with heat transfer to water flowing through a helical coil is carried out using CFD package FLUENT version 6.3. Analysis has been carried out both for the constant wall temperature and constant wall heat flux boundary conditions. Nusselt number on the outer side of the coil is found to be the highest among all other points at a specified cross-section, while that at the inner side of the coil is the lowest. The coil pitch is found to have significance only in the developing section of heat transfer and the average Nusselt number is not affected by the coil pitch. The developed correlations for Nusselt number are applicable to either of the boundary conditions

Naphon and Suwagrai [5] studied the Effect of curvature ratios on the heat transfer in the horizontal spirally coiled tubes both experimentally and numerically. They have found that due to the centrifugal force, the Nusselt number and pressure drop obtained from the spirally coiled tube are 1.49 - 1.50 times higher than those from the straight tube, respectively. Acharya *et al.* [6] numerically studied steady heat transfer enhancement in coiled-tube heat exchangers due to chaotic particle paths in steady, laminar flow. The velocity vectors and temperatures fields were discussed. A series of correlations of the spatially varying local and constant bulk Nusselt number were presented. Chen and Zhang [7] studied the combined effects of rotation, curvature, and heating/cooling on the flow pattern, friction factor, temperature distribution, and Nusselt number. Yan Ke *et al.* [8] have investigated the helical cone tube bundles both numerically and still some foregoing experiments. The authors found that the cone angle has a significant effect on enhancing the heat transfer coefficient. Pitch has nearly no effect on the heat transfer. Heat transfer enhancement mainly taken place near the outer surface.

Ge Pei-qi *et al.* [9] investigated the heat transfer characteristic of conical spiral tube bundle with numerical simulation method. He found that the cone angle and cross section have major effect on heat transfer through the conical coil and helical pitch has little influence on heat transfer enhancement. Heat transfer coefficient of circular section of conical tube is larger than the elliptical section in condition that the area of the cross section is kept constant. Daniel Florez *et al*. [10] conducted experimental and CFD study of single phase cone-shaped helical coiled heat exchanger. They Proposed a correlation for Nusselt number in the Reynolds number range of 4300 to 18600 and Prandtl number range of 2 to 6 as follows:

$$Nu = 0.00797\ \mathrm{Re}^{0.82}\ \mathrm{Pr}^{0.4} \qquad (2)$$

Numerical simulations were performed using ANSYS FLUENT 12.1 software. An appreciable inclination of the velocity vector components in the secondary flow was observed for the cone-shaped helical coils, although velocity contours are similar to the formers, with the particles of the fluid near the outer wall going faster due to the unbalance in centrifugal forces. M. M. Abo Elazm *et al*. [11] studied the effect of changing the taper angle (curvature ratio) on the heat transfer characteristics of the coil. The coil exit temperature increases with taper angle and that was attributed to the increase in both coil area and the Dean number.

## II. GEOMETRY OF CONE SHAPED HELICAL COIL

Both the helical and helical cone coil heat exchangers are made from seamless copper tubing of outer diameters 9.5mm and 15.9mm. Both tubes have a thickness of 0.8mm and axial length of 2.96m. The bottom radius of curvature and axial pitch of both the heat exchangers are kept constant. Helical coil has 2 turns and helical cone coil has 2.55 turns. The cone angle of helical cone coil is $72^0$. Experiments were performed with the axis of both coils in vertical direction.

## III. EXPERIMENTAL SET UP

### *A. Experimental Facility*

The material used to construct the helical coil and helical cone coil is copper tubing. Both the double tube coils are made by winding straight tube- in- tube structure on wooden patterns. While bending of copper tubes, very fine salt was filled in the inner and annular spaces in order to maintain the concentricity of tubes as well as smoothness on inner surfaces. After bending it was washed away with water. The care was taken to preserve the circular cross section of the coil during the bending process and distortion was kept at minimum. The care was taken to maintain the constant pitch for both the coils while bending. The end connections soldered at copper tube ends. Axes of both the coils were kept in vertical direction. Inner tubes of both the heat exchangers were provided with straight entry and exit hydrodynamic lengths. Both lengths were attached tangentially to the inner coil. The end connections were such that the entry and exit from the annular tube of both the double tube heat exchangers through $90^0$ bends. In order to prevent the heat loss to the surroundings one layer of poly urethane foam insulation followed by another layer of asbestos rope insulation were provided.

A schematic diagram of the experimental apparatus of cone shaped helical coil heat exchanger is shown in Fig. 1. The test section is a cone shaped double tube helical coil heat exchanger. In both the heat exchangers, hot water flow through inner tube and cold water through annulus. Also counter flow configurations were used for both. The hot water is entered from bottom of the coil and exited from the top. Similarly cold water entered from top of the coil and exited from the bottom. A constant head water heater of 5 kW and 12 litre capacity was used to provide hot water supply to the test coils. Cold tap water was used for the cold fluid in the annulus. The outlets of both the inner and annular flow are directly fed to atmosphere. Flow rates of hot and cold fluid streams are measured by using stop watches and collecting tanks at the outlets.

T type thermocouples of $0.1^0$C accuracy were used to for measurement of the inlet and outlet temperatures of inner and annular tubes for both the heat exchangers. Differential U tube manometers were used to measure the pressure difference between the inlet and outlet of inner and annular tubes. Flow rates through inner and annular tubes are varied by flow control valves.

### *B. Experimental Procedure*

Experiments were performed for various flow rates of both hot water and cold water entering the test section. The hot water flows though the inner tube and cold water flows through the annulus with constant flow rate. The inlet hot water temperatures were adjusted at desired level by using electric heaters controlled by temperature

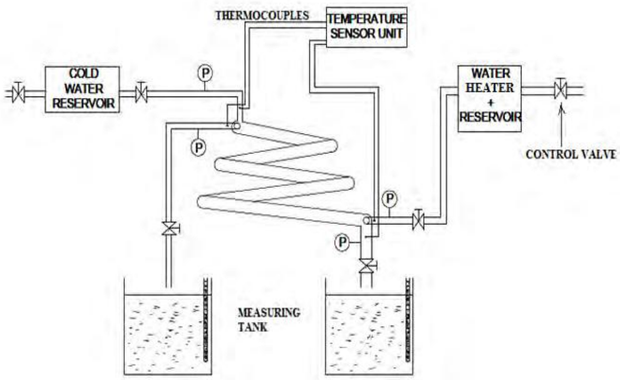


Fig.1 Schematic diagram of experimental apparatus

controller while the inlet temperature of cold water is kept constant. The system was allowed to reach steady state before any data was recorded. The flow rates were controlled by adjusting the valve and measured by using collecting tanks and stop watches.

In this experimental work heat transfer coefficients and heat transfer rates were based on the measured temperature data. The overall heat transfer coefficient, $U_o$ and heat transfer rate, q is calculated from equations as below

Overall Heat transfer coefficient, Uo:

$$U_o = q / (A_o \Delta T_{LM}) \text{ W/m}^2\text{K} \quad (1)$$

Where, q is the heat transfer rate, $A_o$ is the outer surface area of the inner tube, $\Delta T_{LM}$ is the Log Mean Temperature Difference. The overall heat transfer surface area was determined based on the tube diameter and it is given as $\pi L d_o$.

$$\Delta T_{LM} = (\Delta T1-\Delta T2) / \ln(\Delta T1/\Delta T2) \quad (2)$$

Where, $\Delta T_1$ is the temperature difference between the hot inlet and cold outlet streams and $\Delta T_2$ is the temperature difference between the cold inlet and hot outlet streams.

Hot water Heat Transfer Rate:

$$q_h = m_h.Cp_{,h}.(Tin\text{-}Tout)_h \quad (3)$$

Cold water Heat Transfer Rate:

$$q_c = m_c.Cp_{,c}\ (Tout\text{-}Tin)_c \quad (4)$$

The physical properties of water are taken at average temperature:

$$T_{mean} = (T_{in} + T_{out}) / 2 \quad (5)$$

Where $T_{in}$ and $T_{out}$ are the inlet and outlet temperatures respectively for the hot and cold fluid streams. Heat transfer coefficients were calculated for both the inner and outer tubes. The inner and outer heat transfer coefficients are usually obtained from the overall thermal resistance consisting of three resistances in series: the convective resistance in the inner surface, the conductance resistance of the pipe wall and the convective resistance on the outer surface by the following equation:

$$\frac{1}{U_o} = \frac{A_o}{A_i h_i} + \frac{A_o \ln(d_o/d_i)}{2\pi k L} + \frac{1}{h_o} \quad (6)$$

Where $d_o$ is the outer diameter of the tube, $d_i$ is the inner diameter of the tube, $k$ is the thermal conductivity of the wall and $L$ is the length of the tube. Heat transfer coefficients for the outer tube, ho, and for the inner tube, hi, were calculated using traditional Wilson plot technique, as in [12]. For the calculation of inner heat transfer coefficient, the mass flow rate in the annulus side was kept constant and assumed that the annulus heat transfer coefficient is constant. The inner heat transfer coefficient was assumed to behave in the following manner with the fluid velocity in the inner tube, $u_i$

$$h_i = C u_i^n \quad (7)$$

Eq. (7) was placed into Eq. (6) and the values for the constant, $C$ and the exponent, $n$ were determined through curve fitting. The inner and outer heat transfer coefficients could then be calculated. This procedure was repeated for each outer tube flow rate.

Nusselt number for the inner tube flow ($Nu_i$)

$$Nu_i = h_i\, d_i / k \quad \text{W/m}^2\text{K} \quad (8)$$

Where $Nu_i$ is the Inner Nusselt Number, k is the thermal conductivity of water and $d_i$ is the inner diameter of the coil.

Friction factor ($f$):

$$f = \frac{\Delta P}{\rho (u^2/2)(\frac{L}{d})} \quad (9)$$

Where ΔP is the difference in pressure between inlet and exit of the inner flow, $u$ is the mean velocity of the flow and d is the diameter of tube.

## IV. RESULTS AND DISCUSSION

The results obtained from the experimental investigation of helical and cone shaped helical coil heat exchangers operated at various operating conditions are studied in detail and presented.

### A. Thermal Performance:

The thermal performance of helical and cone shaped helical coil heat exchanger is evaluated on the basis of heat transfer rates, overall heat transfer coefficients and Nusselt numbers. The inner flow rate is varying between 300 ml/min to 900 ml/min and at the same time flow rate through the annulus is kept constant. The tests are conducted only for counter flow configuration.

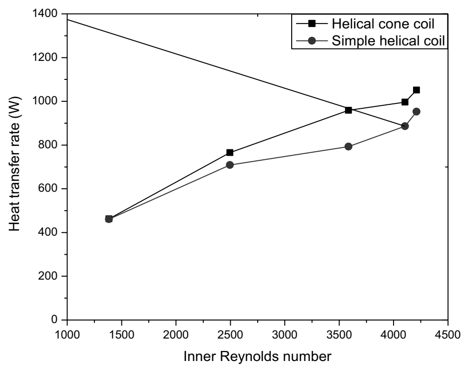


Fig. 2 Variation of heat transfer rate with inner Reynolds

The variation of heat transfer rate, Q with inner Reynolds number is shown in Fig. 2. In the laminar region as Re increases the secondary developed in the fluid goes on increasing which enhances the heat transfer. This is in tune with the findings of Rennie *et al*. [3]. It is seen that the values for heat transfer rate for cone shaped coil are on higher side as compared with the simple helical coil.

The variation of overall heat transfer coefficient with inner Reynolds number is indicated in Fig. 3. The values for the cone shaped helical coil are higher as compared with the simple helical coil. In cone shaped helical coil there is an increase in number of turns and curvature ratio. Varying the curvature ratio for the same coil would vary the Dean number and the heat transfer. Re is calculated from the equation considering curvature ratio, δ for the coil.

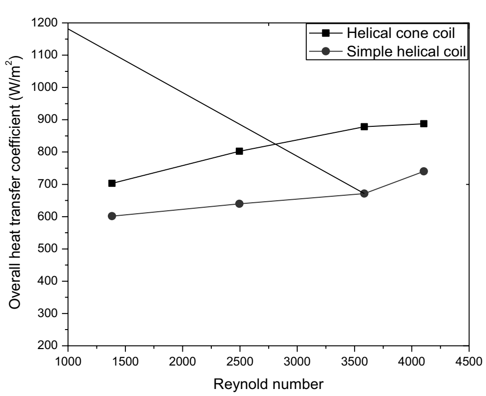


Fig. 3 Variation of overall heat transfer coefficient with inner Reynolds number

$$Re_{cr} = 20000\ \delta^{0.32} \qquad (10)$$

Fig. 4 indicates the variation of inner Nusselt number (Nu) with inner Reynolds number. The Nusselt number which is directly proportional to convective heat transfer coefficient increases as Reynolds number increases. This is in tune with the findings of Yan Ke *et al. and* Ge Pei-qi *et al.* [8,11]. It is clearly found that the Nusselt number for cone shaped helical coil is higher than that of the simple helical coil. In the case of cone shaped helical coil curvature ratio varies along the length of the coil. The heat transfer coefficient and Nusselt number were found to increase with increasing the taper angle of the helical cone coil and that was attributed to the increase in the curvature ratio and thus Dean Number.

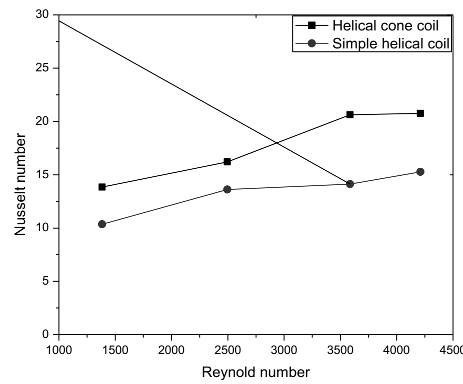


Fig. 4 Variation of Nusselt number with Reynolds number

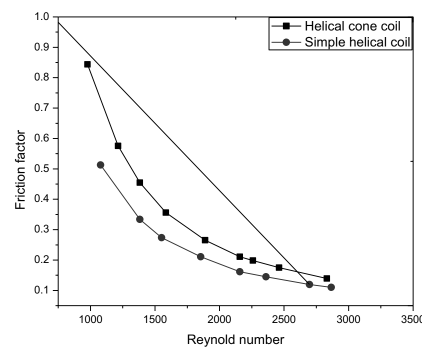


Fig. 5 Variation of Friction factor with Reynolds number

### *B. Friction factor*

Fig. 5 gives the variation of friction factor, *f* with the Reynolds number. Even though heat transfer rate in the conical coil heat exchanger is higher than the simple helical coil the pressure drop is more. The friction factor decreases with fluid flow rate in the laminar region. The values for the same are on higher side for cone shaped helical coil as compared with that of simple helical coil. The center of the axial fluid flow offsets to the outer surface of the tube, and the secondary fluid flow is complicated. The centrifugal forces caused by the pipe curvature results in loss of energy.

## V. CONCLUSION

In this work, the experimental evaluation of cone shaped helical coil heat exchanger is carried out. The overall conclusions related to the comparative analysis between the cone shaped coil and simple helical coil are presented. The mass flow rate in the inner tube and the annulus were both varied and the counter flow configuration was tested. It was observed that the overall heat transfer coefficient increases with increase in the inner coiled tube flow rate for a constant flow rate in the annulus region. It is found that the inner Nusselt number and heat transfer rate increases when the fluid flow rate increases and friction factor decreases with the flow rate. It is found that the inner Nusselt number, convective heat transfer coefficient, overall heat transfer coefficient and friction factor are higher in case of conical coil than that of simple helical coil. It was found that the heat transfer rates are 1.01 to 1.2 times and friction factors are 1.2 to 1.6 times more for the cone shaped helical coil than that of simple helical coil.

## REFERENCES

[1] Dravid AN, Smith KA, Merrill EW, Brain PLT. Effect of secondary fluid on laminar flow heat transfer in helically coiled tubes. *AIChE J*, 1971, 17:1114–22.

[2] Yang G, Dong F, Ebadian MA. Laminar forced convection in a helicoidal pipe with finite pitch. *Int J Heat Mass Transfer,* 1995, 38:853–62.

[3] Rennie TJ, Raghavan GSV. Laminar parallel flow in a tube-in-tube helical heat exchanger, *AIC 2002 Meeting CSAE/SCGR Program, Saskatoon, Saskatchwan*: July, 2002, 14-17

[4] Jayakumar J.S. , S.M. Mahajania, J.C. Mandala, Kannan N. Iyer, P.K. Vijayan. CFD analysis of single-phase flows inside helically coiled tubes. *Computers and Chemical Engineering* 34 , 2010 430–446

[5] Naphon P, Suwagrai J. Effect of curvature ratios on the heat transfer and flow developments in the horizontal spirally coiled tubes, *International Journal of Heat and Mass Transfer*, 2007, 50(3-4), 444-451.

[6] Acharya N, Sen M, Chang HC, "Analysis of heat transfer enhancement in coiled-tube heat exchangers", *Int J Heat Mass Transfer*, 2001, 44:3189–99.

[7] Chen H, Zhang B, "Fluid flow and mixed convection heat transfer in a rotating curved pipe" *Int J Therm Sci*, 2003, 42:1047–59

[8] Yan Ke, Ge Pei-qi, Su Yan-cai, Meng Hai-tao. Numerical simulation on heat transfer characteristic of conical spiral tube bundle. *Applied Thermal Engineering* 31, 2011, 284-292

[9] Ge Pei-qi *et al.,* "Numerical simulation on heat transfer characteristic of conical spiral tube bundle", *Applied Thermal Engineering* 31, 2011, 284-292.

[10] Daniel Florez-Orregoa, Walter Ariasa, Diego Lopeza and Hector Velasqueza. "Experimental and CFD study of a single phase cone-shaped helical coiled heat exchanger: an empirical correlation". *Proceedings of Ecos 2012 - The 25th International Conference on Efficiency, Cost, Optimization, Simulation And nvironmental Impact of Energy Systems June 26-29, 2012, Perugia, Italy*

[11] M. M. Abo elazm, A. M. Ragheb, A. F. Elsafty, M. A. Teamah, "Numerical investigation for the heat transfer enhancement in helical cone coils over ordinary helical coils ", *Journal of Engineering Science and Technology* ,Vol. 8, No. 1, 2013, 1 - 15

[12] J. W. Rose, "Heat-transfer coefficients, Wilson plots and accuracy of thermal measurements", *Experimental Thermal and Fluid Science*, 28, 2004, 77-86

# Performance Analysis of Automotive Muffler Using CFD

L. S. Telmasre[1], A. P. Tadamalle [2]

*Department of Mechanical Engineering, Sinhgad college of Engineering, Pune, India.*

[1]lokeshstelmasre14@gmail.com

[2]aptadmalle.scoe@sinhgad.edu

***Abstract* - A muffler is an important part of the engine system used in exhaust system to reduce noise level. This study aims to estimate transmission loss of muffler by varying geometry parameters. It was revealed that the exhaust gas noise level depend upon number of perforated holes, diameter of the perforated pipes and its diameters in last chamber. The performance of the muffler is assessed by analyzing pressure variation, exhaust gas flow pattern, velocity contours, velocity streamlines and transmission loss. The RANS method is used to obtain transmission loss and pressure distribution using sinusoidal pressure wave. The modeling of muffler is done by using modeling software and performance parameters are estimated using Star CCM+ software. This study helps to reduce noise pollution. The results obtained from analysis software are in good agreement with the analytical results.**

***Keywords*- Muffler, CFD, Expansion Chamber, Transmission loss, Pressure distribution.**

## I. INTRODUCTION

The major contributors for noise generated by a vehicle are pressure wave noise, mechanical noise, vibration induced noise and transmission noise. These all noises generated by an automobile do not pass through the exhaust system. The major portion of the total noise generated by the vehicle pass through the muffler. The sole purpose of an automotive muffler is to reduce engine exhaust gas noise level. The Muffler used in the exhaust system are classified into two types based on its operating mechanism either reactive or absorptive type of muffler. The reactive muffler use the phenomenon of destructive interference to reduce the noise. This reduction is due to the internal reflections and change in geometry or area discontinuity of the muffler. Whereas, in case of absorptive type silencers reduction in the noise level depends on fibrous or porous material absorptive properties. Further the sound energy is reduced and converted into heat in the absorptive material.

The high pressure waves are generated due to repeated opening and closing of exhaust valve and consequently these gases enter into the exhaust system. When the exhaust gas passes through the muffler the transmission loss and backpressure induced in the muffler plays significant role in the reduction of noise level. Hence to access the performance of any muffler the transmission loss and backpressure can consider. The transmission loss (dB) variation is responsible for the damping the noise level. Transmission loss does not vary with respect to noise source. In this study, acoustic and flow characteristic of a perforated reactive muffler were analyzed.

Muffler is the most important element of a engine exhaust gas system. The performance of the muffler is assessed by studying variations in pressure, exhaust gas flow pattern, velocity contours, velocity streamlines and transmission loss across the Muffler. The RANS method is employed to estimate performance parameters using sinusoidal pressure wave.

## II. LITERATURE REVIEW

The principal of muffler design and advantages of various types of mufflers has been discussed by Potente et. al. for design purpose [1]. The effect of varying number of perforations on transmission loss and back pressure which are most important parameters are studied by K. Suganeswaran et. al. to estimate performance of the muffler [2]. The performance characteristics, i.e. noise reduction capability of the muffler has been tested and compared with that of the conventional muffler has discussed by M. Rahman et al for design of muffler of stationary engine [3]. The current techniques of measuring transmission loss has been discussed by Z. Tao and A. F. Seybert. Study focused on two methods mostly used are two load method and two source method [4]. Modern CAE tools to optimize overall system design balancing parameters like noise and transmission loss are studied by Shitalkumar Ramesh Shah et al [5]. The CFD analysis on flow through muffler to obtain the effect of pressure and velocity inlet input estimated by Pradyumna Saripalli and K. Sankaranarayana. To simulate the field by numerical method with Cosmos Flow and analyses the effect which the internal flow field has on the performance of the muffler found out [6].

From extensive literature survey, limited study has been found on the effect of varying muffler geometry parameters as diameter of perforated pipe and diameter of perforations on transmission loss.

## III. METHODOLOGY

Several numerical methods are widely used for either modeling or optimizing the performance parameters. The

Taguchi method is one of the methods effectively used for optimizing performance parameters to achieve desired quality in the muffler without increasing the cost of experimentation. The Taguchi L8 orthogonal array design matrix is used for study the effect of parameters on performance of the muffler. Eight set of mufflers are created with different geometries for analysis. The input process parameters and corresponding responses are presented in Table I.

TABLE I

| Set. No. | No of holes on baffle | No. of pipes in third chamber | pipe diameter ( mm) | Dia. of perforations ( mm) |
|---|---|---|---|---|
| 1 | 2 | 2 | 25 | 2.5 |
| 2 | 2 | 4 | 29 | 3 |
| 3 | 4 | 2 | 20 | 2 |
| 4 | 4 | 2 | 25 | 2.5 |
| 5 | 4 | 1 | 29 | 3 |
| 6 | 6 | 2 | 29 | 3 |
| 7 | 6 | 2 | 20 | 2 |
| 8 | 4 | 4 | 25 | 2.5 |

## IV. CFD ANALYSIS

To estimate the performance parameters of the muffler analysis is done by using Star CCM+ software. Air is fluid so to carry out analysis use of CFD is necessary. CFD is a branch of fluid mechanics that uses numerical analysis and algorithms to solve and analyze problems that involve fluid flows

### A. *Muffler Modeling*

The performance parameters of the muffler is estimated by considering transmission loss, flow pattern, velocity contours and pressure distribution. The 3D model have been created using CATIA modeling software.

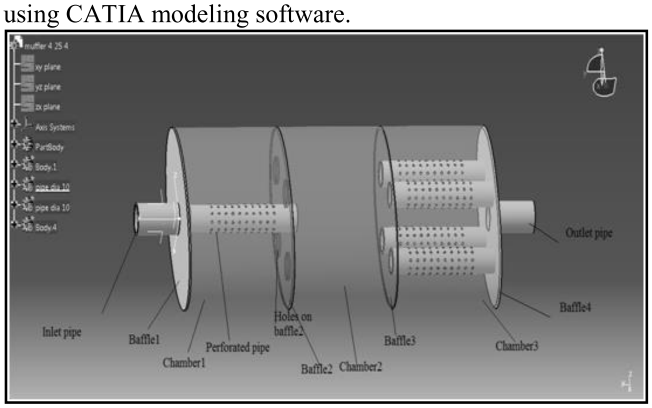


Fig. 1- Geometric model of reactive muffler

The Fig. 1 shows the geometric model of reactive muffler (set 8) of length of 360 mm. The entire model is divided into three chambers of length 120 mm having different constructional features. First chamber has perforated inlet pipe extended up to second chamber which discharge gas into second chamber. These perforations located on pipes allow to percolate exhaust gas into the first chamber.

The second baffle of muffler has four holes on it to pass and spread exhaust gas into second chamber. Third chamber has four perforated pipes which spread exhaust gas into the chamber. The spread waves of same amplitude collide with each other they create destructive interference causes cancellation of wave and thus noise gets reduced. The muffler construction consist of four baffles arrangement placed equidistant and parallel to each other.

### B. *Computational Meshing*

Geometry of muffler is divided into number of parts for meshing. Hexahedra trimmer volume mesh type of meshing is preferred for analysis, since it provides better results and less number of elements as compared to other types.

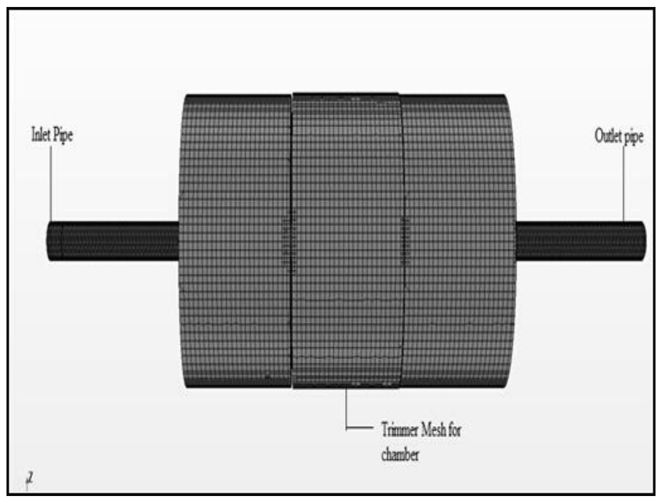


Fig.2- Mesh model of muffler

The reduction in number of meshing elements causes reduction in computational time and less memory for the same model.

The muffler volume is divided into 449990 number of elements with mesh size of 5 mm is shown in Fig. 2 of set 8. Uniform meshing has been observed at the outer plane surface but at the change in geometry inside the muffler there is formation of dense meshing it is known as prism layer mesh.

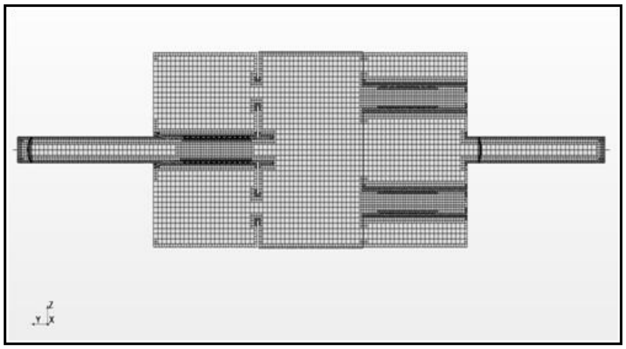

Fig. 3- Cut section of muffler mesh model

*C. Turbulent Model*

All physical phenomena involved in the exhaust flow are highly related with the turbulent flow nature of rapid change of turbulent kinetic energy generation.. Therefore, it is very significant which turbulence model is selected for the simulation of the flow patterns in exhaust system. There are many turbulent model used in CFD such as k-epsilon, k-omega, Shear stress transport depends on their applicability for specific work.

In this work K- epsilon turbulent model is selected for simulating mean flow characteristics for turbulent flow conditions in Star CCM+ software for validating results. It is a two equation model which gives a general description of turbulence by means of two transport equations (PDEs). Two equation model is :

$$\frac{\partial(\rho k)}{\partial t} + \frac{\partial(\rho K u_i)}{\partial x_i} = \frac{\delta}{\delta x_j}\left[\frac{\delta k \mu_t}{\sigma_k\, \delta x_j}\right] + 2\mu_t\ E_{ij}E_{ij} - \rho\epsilon$$

Where,

$u_i$ - Velocity of component in corresponding direction

$E_{ij}$ - Component of rate of deformation

$\mu_t$ - Eddy viscosity

$\sigma_k$ - Adjustable constant

The first transported variable determines the energy in the turbulence and is called turbulent kinetic energy (k). The second transported variable is the turbulent dissipation (Ɛ ) which determines the rate of dissipation of the kinetic energy. In K epsilon model, kinetic energy gets dissipated in flow. .

*D. Inlet and outlet Boundary conditions*

The inlet and outlet boundary conditions govern fluid flow control across the muffler chamber. Its inlet conditions, outlet conditions, wall surface conditions and initial conditions need to be defined when the fluid dynamics of the reactive muffler performed. At the inlet pipe of muffler sinusoidal pressure wave of 7000 Pa is given as a input pressure wave at velocity of 33 m/s and at outlet atmospheric pressure is considered.

## V. Experimental Setup

The transmission loss is measured by using experimental setup available at ARAI, Pune. The experiments are conducted on the muffler fabricated based on the optimum transmission loss results obtained from CFD analysis

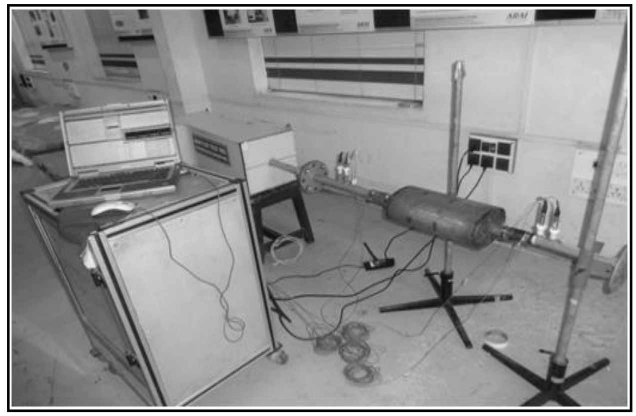

Fig. 4- Experimental setup ( Courtesy- ARAI)

The muffler model is fabricated by using the parameters stated against set 8 given in Table I. The experimental setup used for conducting experiments is shown in Fig 4 available at Automotive Research Association of India (ARAI), Pune. The set up used for testing consist of data acquisition system, FFT analyzer, one way speaker, two microphones at the inlet and outlet of the muffler. Random noise source is given as input to the muffler and the data recorded by microphone is converted into frequency domain using FFT analyzer.

Transmission loss is a characteristic parameter which governs the performance of muffler. Transmission loss is the difference between the sound level at inlet and outlet of the muffler pipe. The selection of suitable muffler is based on transmission loss also transmission loss does not depend upon the source of noise.

Table II – Transmission loss obtained from different set of model

| Set No. | Transmission Loss (dB) | Set No | Transmissio n Loss (dB) |
|---|---|---|---|
| 1 | 38 | 5 | 35 |
| 2 | 28 | 6 | 33 |
| 3 | 34 | 7 | 41 |
| 4 | 37 | 8 | 42 |

The CFD analysis results shows different behavior at different frequencies as flue gas passes through the chambers. This is due to change in number of holes on baffle, variation in the diameter of perforated holes and perforated pipe. The transmission loss results obtained from all geometry depicts that the model 8 has better transmission loss as compared to remaining models. Comparison of transmission loss at frequency 1080 Hz shown in Table II

## IV. RESULTS AND DISCUSSION

### A. Pressure Distribution

Fig 5 shows the inside pressure distribution of muffler and non uniform pressure distribution of – 1000 Pa to + 3000 Pa is observed in the first chamber as compared to other chambers however in third chamber the negligible pressure variation of -200 Pa to + 300 Pa reported. The red region is observed inside the muffler at first chamber that indicates that stagnation point of fluid flow. Pressure inside the muffler varies from -3000 pa to 3000 pa.

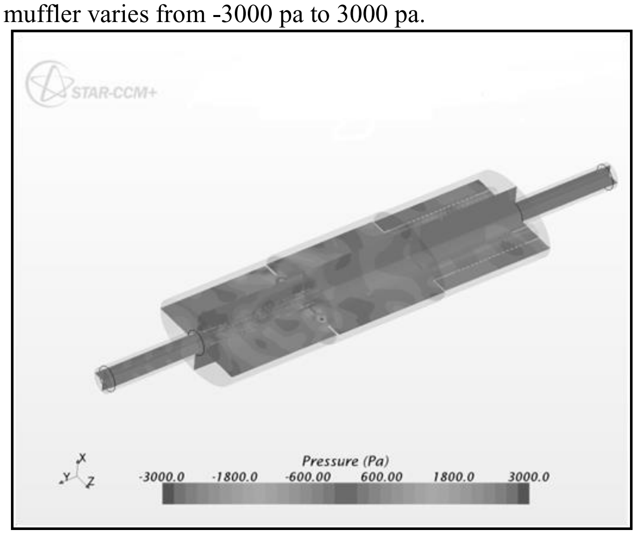


Fig. 5- Pressure distribution of muffler

### B. Velocity Streamlines and Velocity vectors

Fig 6 and Fig 7 shows the velocity streamlines and velocity contours.

The central chamber depicts greater turbulence as compared to other chambers. Streamlines confirms variation in velocity between 5 - 32 m/s. Velocity contours shows the nature of flow of exhaust gas. Velocity of contours varies from 2m/s to 32 m/s. Due to small opening of perforations on the perforated pipes contours comes out with high velocity.

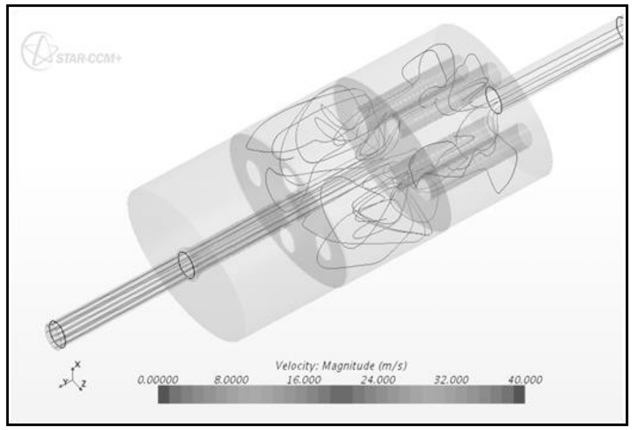


Fig. 6- Velocity Streamlines

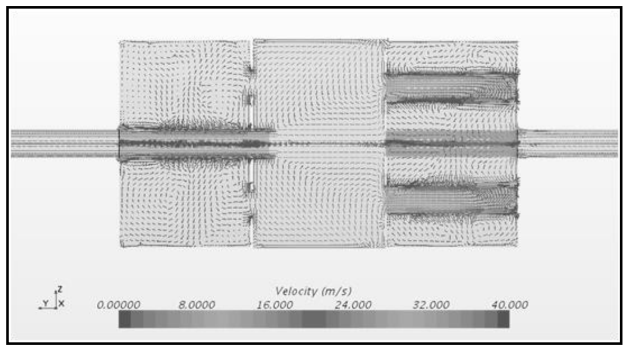


Fig. 7- Velocity Contours

Fig. 8 shows the comparison of transmission loss of all 8 models and from above graph it depicts that model 8 has better transmission loss compared with others. So it is considered as the suitable model for fabrication. Fig 9 shows the comparison of analytical and experimental results of transmission loss results are compared by using a plot of transmission loss verses frequency. The comparison of analytical and experimental

The Fig 8 shows the transmission loss varies randomly up to frequency of 500 Hz. The maximum transmission loss fluctuation is observed in the range of 1100 Hz to 1400 Hz across the muffler. The significant fluctuations in transmission loss are found after 1400 Hz. The minimum transmission loss of 27 dB has been found for model 2 at 1180 Hz. It has been also found that maximum transmission loss of 43 dB for model 8 at 1180 Hz whereas transmission loss of 38 dB is reported between 500 - 600 Hz for the model 8.

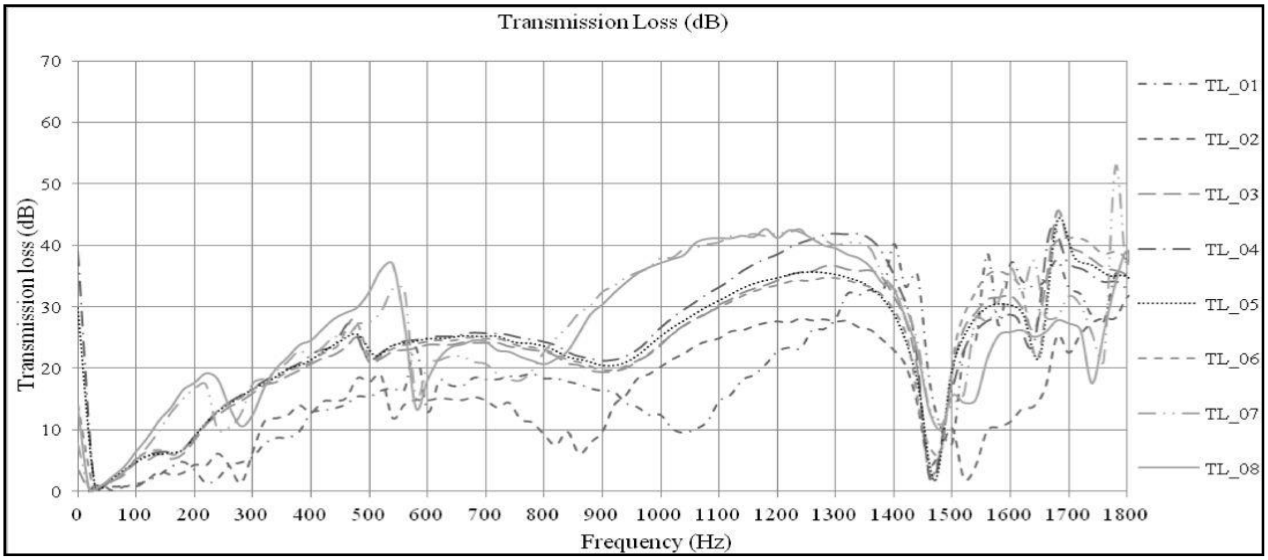


Fig. 8- Comparison of Transmission Loss results

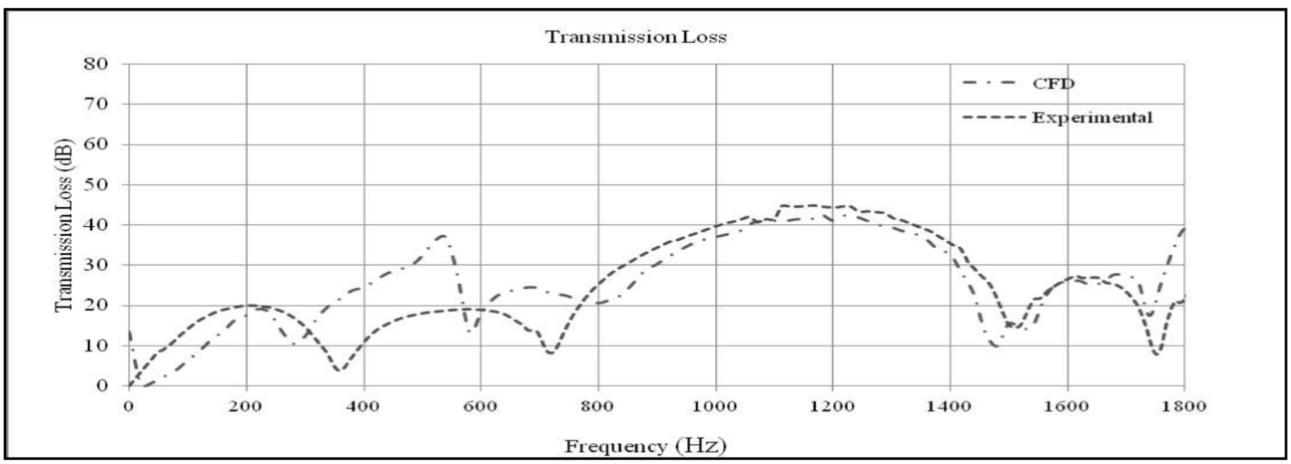


Fig. 9- Comparison of analytical and experimental results of transmission loss

Analytical and experimental results are in close agreement with each other. In starting frequencies some variations between experimental and CFD results has been observed. This is due to baffles which creates disturbance at baffles. The experimental results gives the 45 dB transmission loss at 1180 Hz which is better than 42 dB of analytical results.

## IV. CONCLUSIONS

The performance of the muffler is assessed by varying pressure, exhaust gas flow pattern, velocity contours, velocity streamlines and transmission loss across muffler. The following conclusions are drawn from the study. The streamline examination reveals that highest turbulence in second chamber whereas lowest turbulence in third chamber. The velocity contours depicts as diameter of the holes increases with decreases the magnitude of velocity of vectors. CFD analysis of automotive muffler confirms that the pressure distribution in the first chamber is randomly distributed as compared to the chambers located towards exit side. The pressure variation across the length of the muffler decreases from inlet to the exit side. The model 8 having two holes on baffles, four pipes in third chamber and 2.5 mm diameter perforated holes gives the optimum transmission loss of 45 dB. The models having four perforated pipes in third chamber has more transmission loss as comparing to models having single and two perforated pipe in third chamber.

ACKNOWLEDGMENT

The authors acknowledge ARAI, Pune for providing experimental facility to conduct experiments and Continuum Techonologies LLP, Pune for providing technical support.

REFERENCES

[1] Yunshi Yao, Shaodong Wei, Jinpeng Zhao, Shibin Chen, Zhongxu Feng and Jinxi Yue " Experiment and CFD Analysis of Reactive Muffler" *Research Journal of Applied Sciences, Engineering and Technology*, 3282-3288, 2013

[2] Potente, Daniel "General Design Principles for an Automotive Muffler" in *Proceedings of Acoustics* November 2005, pp 9-11.

[3] Pradyumna Saripalli, K. Sankaranarayana, "CFD Analysis on Flow Through a Resistance Muffler of LCV Diesel Engine" *International Journal of Science, Technology and Society*, 3(4): 162-175, June 6, 2015

[4] K.Suganeswaran ,Dr. R.Parameshwaran, S.Amirthamani , D.Palanimohan "Design and Optimization of Muffler for Manufacturing" *International Journal of Innovative Research in Science, Engineering and Technology*, Volume 3, Special Issue 4, April 2014

[5] M. Rahman, T. Sharmin, A F M E. Hassan, and M. Al Nur, "Design And Construction Of A Muffler For Engine Exhaust Noise Reduction" in *proceedings of the International Conference on Mechanical Engineering* 2005 December 2005, 28- 30.

[6] Shital Shah, Saisankaranarayana K, Kalyankumar S. Hatti, Prof. D. G.Thombare, "A Practical Approach towards Muffler Design, Development and Prototype Validation" SAE International 2010

[7] M. L. Munjal, "Automotive Noise – The Indian Scene In 2004" *proceedings of Acoustic* 2004, 3-5 November 2004, Gold Coast , Austraila

[8] M.Rajasekhar Reddy, Dr K.Madhava Reddy ,"Design and Optimization of Exhaust Muffler in Automobiles" *International Journal Of Engineering Research and Applications* Vol. 2, Issue 5, September- October 2012, pp.395-398

[9] Jianmin Xu and Shuiting Zhou, "Analysis of Flow Field for Automotive Exhaust System Based on Computational Fluid Dynamics", *The Open Mechanical Engineering Journal,* 2014, 8, 587-593.

[10] Deepak Rana, Felix Regin and Mohan Makana, "Analysis of Flow Induced Noise in a Passenger Car Exhaust System - An Experimental and Numerical Approach", SAE 2011-01-1528 dated 7/17/2011

[11] Zeynep Parlar, Şengül Ari, Rıfat Yilmaz, Erdem Özdemir, and Arda Kahraman 'Acoustic and Flow Field Analysis of a Perforated Muffler Design' *World Academy of Science, Engineering and Technology* Vol:7 2013-03-27

# Air Cooled Solar Driven Silica gel + Water Adsorption Chiller

Ankush K. Jaiswal[#1], Sourav Mitra[#2], Kandadai Srinivasan[#3], Srinivasa S. Murthy[*4], Pradip Dutta[#*5]

[#] *Department of Mechanical Engineering, Indian Institute of Science Bangalore, India*

[1]ankush@mecheng.iisc.ernet.in

[2]sourav@mecheng.iisc.ernet.in

[3]mecks@hotmail.com

[*]*Interdisciplinary Center for Energy Research, Indian Institute of Science Bangalore, India*

[4]ssmurthy@iitm.ac.in

[5]pradip@mecheng.iisc.ernet.in

***Abstract*— Silica-gel + water vapor adsorption chiller is most suitable pair with source temperature less than 100 C wherein non-concentrated type solar energy can be utilized. The conventional water cooled adsorption systems require large amount of makeup water making them unattractive for regions where soft "heat exchange" grade water is unavailable. Present work simulates the performance of air cooled solar driven single-stage silica gel + water adsorption chiller. The effect of diurnal variation of solar irradiance and ambient air temperature is investigated. To evaluate the seasonal performance, two extreme weather month: April and December is selected for Bangalore, India. It is found that the cooling capacity and COP during December is marginally higher than that in April, even though maximum hot water temperature achieved is 95 C and 70 C in April and December respectively.**

***Keywords*—Adsorption, Chiller, Silica gel, Solar, Dry Cooled**

## I. Introduction

A lot of effort has been made to find an alternative to the conventional vapor compression refrigeration cycle (VCRS) due to global warming potential and ozone layer depletion associated with working fluids (CFC's and HFC's). The adsorption based system is one of the alternatives to these conventional cycles. The major advantage of these cycles is use of low grade thermal energy for compression. Silica-gel + water vapor is found to be good adsorbent and adsorbate pair due to the utilization of low grade thermal energy (<100°C) and the environmentally benign working fluid [1]. There have been various studies to investigate the performance of single stage silica gel + water adsorption chiller such as: effect of cycle and switching time [1], water inlet temperatures and mass flow rate [2], heat and mass recovery [3]. The majority of the studies are performed with constant hot water inlet temperature. However, constant hot water temperature when solar is used as heat source due to diurnal and seasonal variation of solar irradiance and ambient air temperature. Some studies have been performed to evaluate the performance of solar driven adsorption chiller with China [4], Japan [5] and Middle East [6] meteorological data. However, all of the above mentioned systems employ cooling tower thereby maintaining near constant heat rejection temperature. Recently, the performance of dry cooled two-stage adsorption chiller with constant source temperature has been investigated by Mitra *et al.* [7]. However, the study of dry cooled adsorption chiller coupled with solar energy as heat source hasn't been performed. The present work simulates the performance of solar driven dry cooled adsorption chiller for Bangalore, India conditions [8]. The simulation is performed for April and December month to evaluate the seasonal performance of chiller which is expected to change due to combined effect of irradiance and ambient temperature variation.

Fig. 2 shows the schematic of the air cooled solar adsorption chiller. The system consist of two adsorber beds, air cooled condenser, evaporator, water-air heat exchanger, solar collector, various pumps and valves. Evacuated tube collector is selected in this study. The adsorption cycle comprises of four processes namely: adsorption, desorption, pre-cooling and pre-heating (also known as switching process). During adsorption the adsorber bed connects to evaporator, while during desorption it gets connected to the condenser. During switching period the beds are isolated from both evaporator and condenser by closing the vapour valves. Fig. 2 shows the timing scheme adopted. Hot water flows through the bed during desorption and pre-heating process, while cold water flows during adsorption and pre-cooling process. The adsorption/desorption and pre-heating/pre-cooling time in this study are 1100 and 100 second respectively. The adsorber beds comprise of 93 kg of regular density (RD) type silica gel with particle radius of 0.8 mm. The diurnal variation of solar irradiance and ambient air temperature is coupled with the transient heat and mass transfer model of the adsorption chiller to evaluate the system performance under these variations. A constant chilled water inlet temperature of 16°C is assumed. The heat transfer to the adsorber beds, evaporator and condenser are estimated using LMTD method and the adsorption kinetics is modeled using linear driving force (LDF) model. The modelling equations of all heat exchanger are as given by Mitra *et al.* [9]. Simulation is performed in MATLAB® 2010 platform, and the fluid properties are calculated with REFPROP [10] and MATLAB® coupling.

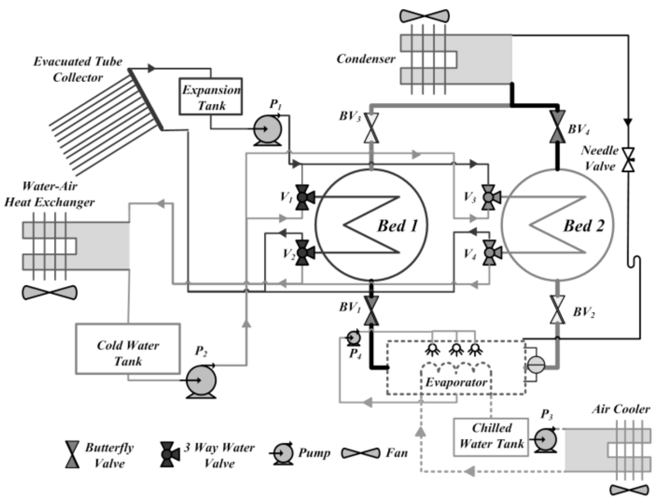


Fig. 1 Schematic of air cooled solar adsorption chiller

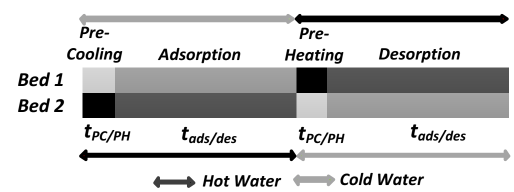


Fig. 2 Cycle Timing

## II. Modelling and Methodology

The energy balance of solar collector is represented by Eq. (1). The term on left hand side represents the sensible heating of the solar field. The first term on the right side is solar energy absorbed by the collector and the second term being the amount of energy gain by hot water. The collector water outlet temperature is calculated by using Eq. (2).

$$\left(MC_p\right)_{sf,eff}\frac{dT_{sf}}{dt}=\eta_{sf}I(t)A_{sf}+\dot{m}_{sf,w}C_{p,w}\left(T_{sf,w,in}-T_{sf,w,\text{out}}\right) \tag{1}$$

$$T_{sf,w,\text{out}}=T_{sf}+\left(T_{sf,w,in}-T_{sf}\right)\exp\left[\frac{-(UA)_{sf}}{\dot{m}_{sf,w}C_{p,w}}\right] \tag{2}$$

2-pass (U-type) evacuated tubular solar collector efficiency [11] is used, and shown in Eq. (3).

$$\eta_{sf}=a_o-a_1\frac{T_{\text{sf},w,\text{in}}-T_{amb}(t)}{I_0} \tag{3}$$

The transient solar irradiance value from sunrise to sunset is calculated by Eq. (4) [5].

$$I(t)=I_{\text{c,max}}\sin\left(\frac{\pi(\text{t}-\text{t}_{sunrise})}{\text{t}_{sunset}-\text{t}_{sunrise}}\right) \tag{4}$$

The irradiance received at collector comprises of direct, diffuse and reflected component as shown in Eq. (5) [12].

$$I_{\text{c}}=I_{\text{b}}\cos\theta+I_d+I_r \tag{5}$$

Perez diffuse irradiance model is utilized to calculate the diffuse radiation [13]. The solar azimuth and zenith angles are calculated by using flat plate PV module in System Advisor Model (SAM) [14]. The value of a and b are maximum of 0 and cosine of incident angle, 0.087 and cosine of solar zenith angle respectively.

$$\cos\theta=\sin\theta_{sun}\cos\left(\gamma-\gamma_{sun}\right)\sin\beta+\cos\theta_{sun}\cos\beta \tag{6}$$

$$I_d=I_{dh}\left[0.5\left(1-\text{F}_1\right)\left(1+\cos\beta\right)+\text{F}_1\,a/b+\text{F}_2\sin\beta\right] \tag{7}$$

$$I_r=0.5\rho_{sur}\left[I_{gh}\left(1-\cos\beta\right)\right] \tag{8}$$

Eq. (9) is used to calculate the ambient air temperature [5], where the value of ζ is 1. The values of maximum irradiance, maximum and minimum ambient air temperatures, sunrise and sunset times considered for months of December and April and are shown in table I.

$$T_{amb}(t)=\frac{T_{amb,\max}+T_{amb,\min}}{2}+\left(\frac{T_{amb,\max}-T_{amb,\min}}{2}\right)\sin\left(\frac{\pi(\text{t}-\text{t}_{sunrise}-\zeta)}{2(\text{t}_{sunset}-\text{t}_{sunrise})}\right) \tag{9}$$

TABLE I
Location Data

| Parameter | April | December |
|---|---|---|
| $I_{c,max}(W/m^2)$ | 909 | 813 |
| $t_{sunrise}(hr)$ | 6.08 | 6.33 |
| $t_{sunset}(hr)$ | 18.32 | 17.56 |
| $T_{amb,max}$(°C) | 33.3 | 25.6 |
| $T_{amb,min}$(°C) | 22.7 | 16.6 |

LDF model (Eq. 10) is used to model adsorption kinetics and Tòth equation [15] is utilized to calculate the equilibrium mass fraction (Eq. 11):

$$\frac{d\phi}{dt} = \frac{15D_{so}\exp\left(-E_a/RT\right)}{R_p^2}\left(\phi^* - \phi\right) \tag{10}$$

$$\phi^* = \frac{K_o \exp\left(\Delta H_{ads}/RT\right) p}{\left[1 + \left\{\frac{K_o}{\phi_\infty}\exp\left(\Delta H_{ads}/RT\right) p\right\}^{t_1}\right]^{1/t_1}} \tag{11}$$

Energy balance of evaporator is shown in Eq. (12). The LHS is the rate change in the sensible energy content of evaporator, which includes the thermal mass of water and metal tubes. The first and second terms on the RHS are latent heat required to evaporate water (refrigerant) and the cooling gained by water respectively.

$$\left(MC_p\right)_{\text{evap},eff}\frac{dT_{evap}}{dt} = -\lambda M_{sil}\frac{d\phi_{ads}}{dt}h_{fg}(\text{p}_{evap}) + \dot{m}_{\text{ch},w}C_{p,w}\left(T_{\text{ch},w,\text{in}} - T_{ch,w,out}\right) \tag{12}$$

During adsorption/desorption the value of λ is 1, while it is 0 during pre-cooling/pre-heating mode. The chilled water outlet temperature is calculated by using Eq. (13).

$$T_{ch,w,out} = T_{evap} + \left(T_{\text{ch},w,\text{in}} - T_{evap}\right)\exp\left[\frac{-(UA)_{evap}}{\dot{m}_{\text{ch},w}C_{p,w}}\right] \tag{13}$$

The mass balance of refrigerant (water) is represented by Eq. (14).

$$\frac{dM_{ref}}{dt} = -M_{sil}\left[\frac{d\phi_{ads}}{dt} + \frac{d\phi_{des}}{dt}\right] \tag{14}$$

The energy balance for the condenser is analogous to the evaporator as represented in Eq. (15). LHS is the rate of change in the sensible energy content of condenser. The first and second terms on the RHS are latent heat released due to condensation of water and the heat taken away by ambient air respectively.

$$\left(MC_p\right)_{\text{con},eff}\frac{dT_{con}}{dt} = -\lambda M_{sil}\frac{d\phi_{des}}{dt}h_{fg}(\text{p}_{con}) + \dot{m}_{\text{air,con}}C_{p,\text{air}}\left(T_{\text{air,con,in}} - T_{\text{air,con,}out}\right) \tag{15}$$

The ambient air outlet temperature is calculated by using Eq. (16).

$$T_{air,con,out} = T_{con} + \left(T_{air,in} - T_{con}\right)exp\left[\frac{-(UA)_{con}}{\dot{m}_{air,con}C_{p,air}}\right] \tag{16}$$

The energy balance of adsorber is represented by Eq. (17). The LHS of Eq. (17) is the rate of change in the energy content of adsorber which consists of thermal mass of silica gel and metal mass of the heat exchanger embedded in it. The first term on the RHS represents the heat of adsorption whereas the second term denotes the sensible cooling of the bed.

$$\left[\left(MC_p\right)_{\text{ads},eff} + M_{sil}\phi_{ads}C_{p,w}\right]\frac{dT_{ads}}{dt} = \lambda M_{sil}\frac{d\phi_{ads}}{dt}\Delta H_{ads} + \dot{m}_{\text{cw,ad}}C_{p,w}\left(T_{\text{cw,ad,in}} - T_{cw,\text{ad},out}\right) \tag{17}$$

The cooling water outlet temperature is calculated in Eq.

$$T_{cw,\text{ad},out} = T_{ads} + \left(T_{\text{cw,ad,in}} - T_{ads}\right)\exp\left[\frac{-(UA)_{evap}}{\dot{m}_{\text{cw,ad}}C_{p,w}}\right] \tag{18}$$

The adsorber cooling water rejects heat to the water-air heat exchanger. And the temperature of cooling water inlet to the adsorber is calculated by using Eq. (19).

$$T_{cw,ad,in} = T_{cw,ad,out} - \varepsilon_{air-wHX}\frac{\dot{m}_{air,HX}C_{p,air}}{\dot{m}_{cw,ad}C_{p,w}}\left(T_{cw,ad,out} - T_{air,in}\right) \tag{19}$$

Analogously, the energy balance during desorption is represented by Eq. (20) and the outlet temperature of hot water is given by Eq. (21).

$$\left[\left(MC_p\right)_{\text{ads},eff} + M_{sil}\phi_{des}C_{p,w}\right]\frac{dT_{des}}{dt} = \lambda M_{sil}\frac{d\phi_{des}}{dt}\Delta H_{ads} + \dot{m}_{\text{hw}}C_{p,w}\left(T_{\text{hw,in}} - T_{hw,out}\right) \tag{20}$$

$$T_{hw,out} = T_{des} + \left(T_{hw,\text{in}} - T_{des}\right)\exp\left[\frac{-(UA)_{des}}{\dot{m}_{\text{hw}}C_{p,w}}\right] \tag{21}$$

At the beginning of simulation, the temperature of evaporator, condenser, adsorber, desorber and solar collector are taken as ambient temperature corresponding to the sunrise time of the respective month, however, the simulation is performed for multiple days, and the converged results are shown in this work.

The cycle averaged performance parameters such as: cooling capacity, COP and solar COP, which is the ratio of cooling generated to the incident solar energy, are calculated using Eq. (22-24) respectively.

$$CACC = \frac{\int_{t_{cycle,start}}^{t_{cycle,end}} \dot{m}_{\mathrm{ch},w} C_{p,w} \left( T_{\mathrm{ch},w,\mathrm{in}} - T_{ch,w,out} \right) dt}{t_{cycle}} \tag{22}$$

$$COP = \frac{\int_{t_{cycle,start}}^{t_{cycle,end}} \dot{m}_{\mathrm{ch},w} C_{p,w} \left( T_{\mathrm{ch},w,\mathrm{in}} - T_{ch,w,out} \right) dt}{\int_{t_{cycle,start}}^{t_{cycle,end}} \dot{m}_{\mathrm{hw}} C_{p,w} \left( T_{\mathrm{hw,in}} - T_{hw,out} \right) dt} \tag{23}$$

$$COP_{sol} = \frac{\int_{t_{cycle,start}}^{t_{cycle,\mathrm{end}}} \dot{m}_{\mathrm{ch},w} C_{p,w} \left( T_{\mathrm{ch},w,\mathrm{in}} - T_{ch,w,out} \right) dt}{\int_{t_{cycle,start}}^{t_{cycle,end}} I(t) A_{sf} \, dt} \tag{24}$$

The daily averaged performance indicators such as: daily average cooling capacity (*DACC*), daily average coefficient of performance (*DACOP*) and daily average solar coefficient of performance ($DACOP_{sf}$) are as follows:

$$DACC = \frac{\int_{t_{cycle,start}}^{N_{cycle} t_{cycle,end}} \dot{m}_{\mathrm{ch},w} C_{p,w} \left( T_{\mathrm{ch},w,\mathrm{in}} - T_{ch,w,out} \right) dt}{N_{cycle} t_{cycle}} \tag{25}$$

$$DACOP = \frac{\int_{t_{cycle,start}}^{N_{cycle} t_{cycle,end}} \dot{m}_{\mathrm{ch},w} C_{p,w} \left( T_{\mathrm{ch},w,\mathrm{in}} - T_{ch,w,out} \right) dt}{\int_{t_{cycle,start}}^{N_{cycle} t_{cycle,end}} \dot{m}_{\mathrm{hw}} C_{p,w} \left( T_{\mathrm{hw,in}} - T_{hw,out} \right) dt} \tag{26}$$

$$DACOP_{sf} = \frac{\int_{t_{cycle,start}}^{N_{cycle} t_{cycle,\mathrm{end}}} \dot{m}_{\mathrm{ch},w} C_{p,w} \left( T_{\mathrm{ch},w,\mathrm{in}} - T_{ch,w,out} \right) dt}{\int_{t_{cycle,start}}^{N_{cycle} t_{cycle,end}} I(t) A_{sf} \, dt} \tag{27}$$

## III. Results And Discussion

*Table II shows the all input parameters used in the simulation.*

TABLE II
INPUT DETAILS

| Parameter | Value | Parameter | Value |
|---|---|---|---|
| $T_{ch,in}$ | 16°C | $a_o$ | 0.45 |
| $(MC_p)_{evap}$ | 376 kJ/K | $a_1$ | 1.1 W/m$^2$K |
| $(MC_p)_{con}$ | 130 kJ/K | $\beta$ | 25$^o$ |
| $(MC_p)_{ads}$ | 195 kJ/K | $\gamma$ | 180$^o$ |
| $(MC_p)_{sf}$ | 667 kJ/K | $\rho_{sur}$ | 0.2 |
| $(UA)_{evap}$ | 5 kW/K | $F_1$ | 0.5 |
| $(UA)_{con}$ | 4.95 kW/K | $F_2$ | 0.15 |
| $(UA)_{bed}$ | 4.2 kW/K | $A_{sf}$ | 60 m$^2$ |
| $(UA)_{sf}$ | 22.2 kW/K | $D_{so}$ | 2.54×10$^{-4}$ m$^2$/s |
| $\dot{m}_{ch,w}$ | 0.68 kg/s | $E_a$ | 4.2×10$^4$ J/mol |
| $\dot{m}_{air,con}$ | 1.2 kg/s | $R_p$ | 0.8 mm |
| $\dot{m}_{hw}$ | 1.2 kg/s | $M_{sil}$ | 93 kg |
| $\dot{m}_{cw,ad}$ | 1.2 kg/s | $\Delta H_{ads}$ | 2693 kJ/Kg |
| $\dot{m}_{sf,w}$ | 1.2 kg/s | $I_0$ | 800 W/m$^2$ |
| $\dot{m}_{air,HX}$ | 2.65 kg/s | $\varepsilon_{air\text{-}wHX}$ | 75 % |

The irradiance and the ambient air temperature variation with time for April and December are shown in Fig. 3. The large value of tilt angle (12° surplus to the latitude of Bangalore, India) is the major reason for the comparatively higher irradiance value in the December; however it also leads to marginal reduction in the irradiance received in April.

Fig. 4 shows the temperature and uptake history curves results for the April month. The variation of mean hot water temperature is similar to the irradiance variation. The maximum hot water temperature attains the values of 95°C around 1:20 p.m. (Fig. 4a); while the irradiance is maximum value around 12:10 p.m. (Fig. 3). The thermal capacitance of solar collector and the adsorption system is the major reason for the observed lag. The bed temperature during adsorption varies in the range of 35–45°C (Fig. 4a), which is significantly higher than the ambient air temperature ranging between 26–33°C (Fig. 3). The major reason for this being the use of water as intermediate heat transfer fluid between the bed and air. The condenser temperature depends on the change in uptake during desorption and the ambient air inlet temperature. The condenser temperature varies in the range of 27–36°C (Fig. 4b). The difference in the condenser and air temperature is larger at afternoon due to higher heat load on condenser arising from higher desorption. The minimum evaporator temperature attained is 10.5°C. As seen from Fig. 4c) absolute uptake of the bed initially increases for a short duration (6–8 a.m.); then decreases, attains minimum at about 2 p.m. and then starts increasing beyond this. The reason for this phenomenon becomes apparent from Fig. 4d). The start-up phase (up to 7 a.m.) is marked by finite change in uptake during adsorption with negligible change in uptake during desorption. This leads to increase in the absolute value of uptake. Afterwards (7 a.m. to 2 p.m.), with rise in the hot water temperature, the net change in uptake during desorption increases and surpasses that during adsorption. This results in decrease in absolute value of uptake. After 2p.m. this variation reverses due to decrease in hot water temperature. The value of uptake varies in the range of 0.042–0.21 whereas maximum net change in uptake during adsorption and desorption for this month are 0.051 and 0.057 respectively.

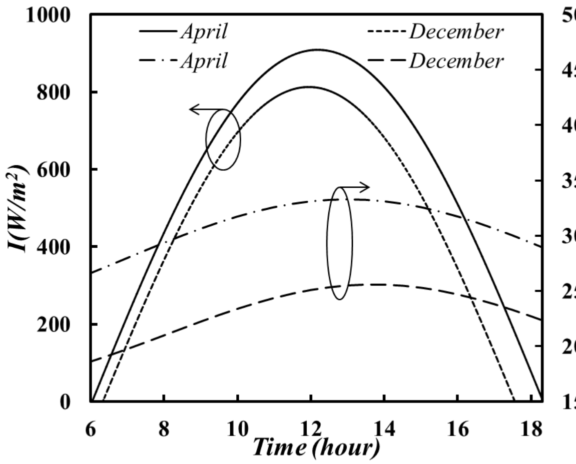


Fig. 3 Diurnal variation of Irradiance (left ordinate) and ambient air temperature (right ordinate)

The temperature and uptake history curves for the month of December are shown in Fig. 5. The variations are similar to that of April however, the absolute values are different. The maximum hot water temperature attained is 70°C (Fig. 5a), which is approximately 25°C lower compared to that in April. Further, this maximum occurs at around 2 p.m. denoting a longer response time in December compared to April. This may be attributed to the lower ambient temperature and irradiance in December (Fig. 3). Lower ambient temperature leads to lower bed temperature during adsorption (28–36°C) and condenser temperature (20–28°C as seen in Fig. 5b) which is significantly lower compared to April.

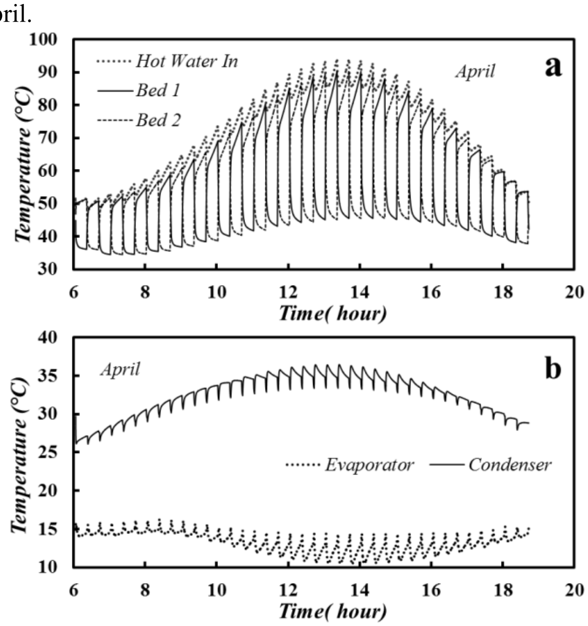


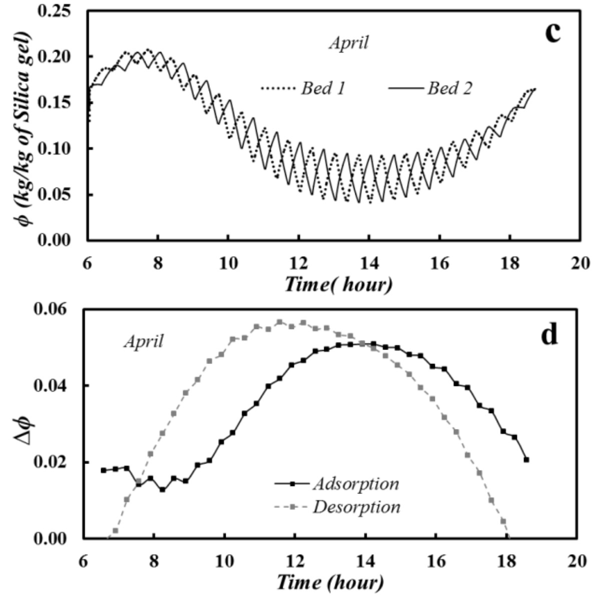


Fig. 4 Temperature variation of : a) hot water and adsorber beds b) condenser and evaporator; c) uptake variation d) net change in uptake during adsorption/desorption in April

The minimum evaporator temperature achieved is 11°C (Fig. 5b), which is similar to that observed in April. The absolute value of uptake and the net change in uptake during adsorption/desorption is similar to that of April. However, the range of absolute value of uptake varies in the range of 0.1–0.3 (Fig. 5c), which is significantly larger than for the month of April. Furthermore, the maximum net change in uptake during adsorption and desorption are 0.053 and 0.063 respectively, which is marginally larger than the April value.

The cooling capacity generated is proportional to the change in uptake during adsorption, and the amount of heat required is proportional to the change in uptake during desorption.

Hence, the COP depends on the ratio of net change in uptake during adsorption to that during desorption. Fig. 6 shows the variation of cooling capacity throughout the day for April and December. It can be seen that the cooling capacity closely follows the net change in uptake due to adsorption (Fig. 4d and 5d). Fig. 7 depicts the COP and solar COP curves for April and December. During the start-up phase the ratio of uptake due to adsorption to that of desorption is inflated due to reasons explained earlier. This inflates the COP as seen from Fig. 7. Immediately after this period there is a significant rise in net uptake due to desorption without any gain in net uptake due to adsorption. This causes the COP to decrease sharply and a minimum is observed. Subsequently, the net change in uptake due to adsorption keeps on increasing along causing the increase in COP. During the evening period, the net change in uptake due to desorption diminishes due to drop in hot water temperature causing the COP to inflate in this period.

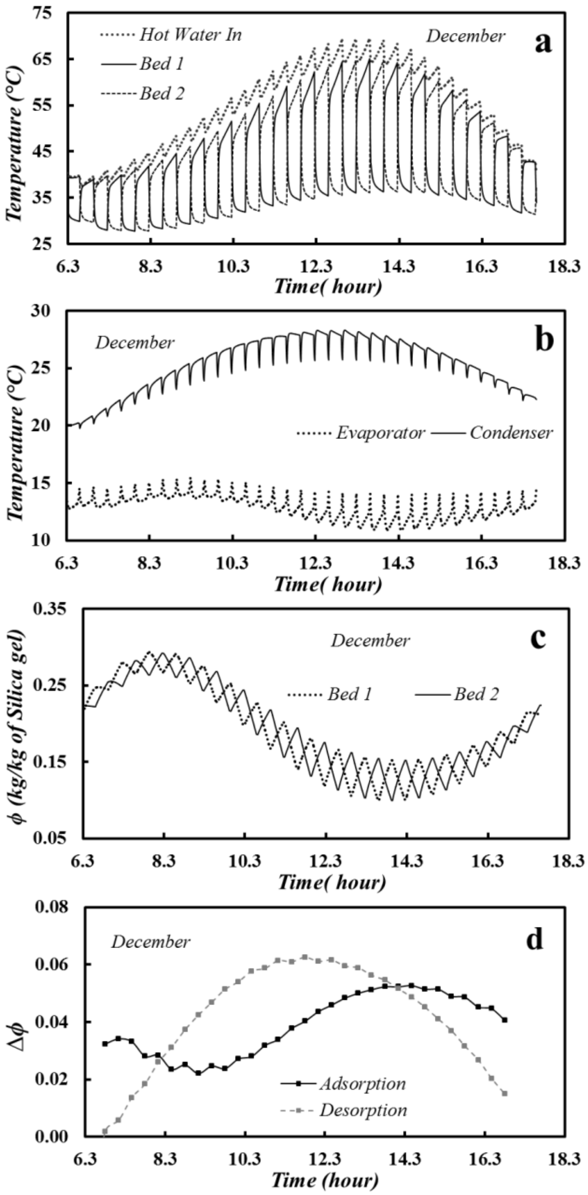


Fig. 5 Temperature variation of : a) hot water and adsorber beds b) condenser and evaporator; c) uptake variation d) net change in uptake during adsorption/desorption in December

The solar COP varies similar to that of *COP*; however the absolute values are lower because of the collector efficiency. It is interesting to note that the daily averaged values namely *DACC, DACOP* and $DACOP_{sol}$ are significantly larger in the December compared to April, as shown in table III. This shows that the cooler ambient conditions have a much more significant effect on system performance than the decrease in hot water temperature in December.

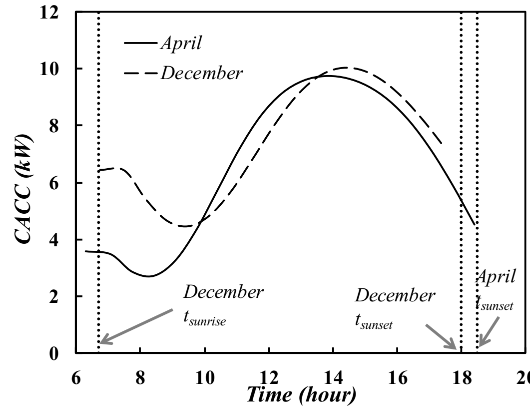


Fig. 6 Cycle average cooling capacity (*CACC*) vs. time

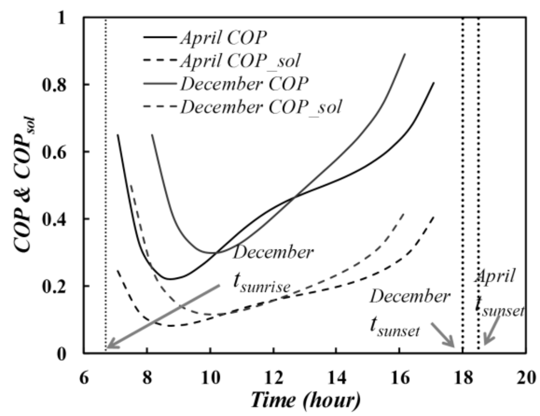


Fig. 7 *COP* and $COP_{sol}$ *vs.* time

TABLE III
DAILY AVERAGED PARAMETERS

| | *DACC(kW)* | *DACOP* | $DACOP_{sol}$ |
|---|---|---|---|
| **April** | 6.50 | 0.49 | 0.19 |
| **December** | 7.38 | 0.58 | 0.24 |

## IV. CONCLUSIONS

The air cooled solar driven adsorption chiller with Bangalore, India meteorological data is simulated for April and December. The diurnal variation of cooling capacity is found to be dependent on net change in uptake due to adsorption whereas the COP depends on ratio of net change in uptake due to adsorption to that of desorption. It is also found that the condenser and hot water temperature in December (maximum 28°C and 70°C respectively) is significantly lower than April (maximum 36°C and 95°C respectively) owing to lower irradiance and ambient air temperature. However, the daily averaged cooling capacity and COP in December is significantly higher than the April depicting the sensitivity of system performance towards condenser temperature.

## ACKNOWLEDGMENT

The work reported in this paper is supported by the grant and aid from the Department of Science and Technology, Government of India.

## REFERENCES

[1] H.T.Chua, K.C. Ng, A. Malek, T. Kashiwagi, A. Akisawa, B.B. Saha, 1999. "*Modeling the performance of two-bed, sillica gel-water adsorption chillers*". International Journal of Refrigeration, 22, October, pp. 194–204

[2] B.B. Saha, E.C. Boelman, T. Kashiwagi, 1995 "*Computer simulation of a silica gel-water adsorption refrigeration cycle – the influence of operating conditions on cooling output and COP*". ASHRAE Trans Res, 101(2), pp. 348–357

[3] R.Z. Wang, 2001. "*Performance improvement of adsorption cooling by heat and mass recovery operation*". International Journal of Refrigeration, 24, December, pp. 605–611

[4] Z.S. Lu, R.Z. Wang, Z.Z. Xia, X.R. Lu, C.B. Yang, Y.C. Ma, G.B. Ma, 2013 "*Study of a novel solar adsorption cooling system and a solar absorption cooling system with new CPC collectors" Renewable Energy*, 50, pp. 299-306

[5] A.K.C. Alam, B.B. Saha, A. Akisawa, 2013. "*Adsorption cooling driven by solar collector: A case study for Tokyo solar data*". Applied Thermal Engineering, 50, September, pp. 1603–1609

[6] I. I. El-Sharkawy, M. H. Abdel, B.B. Saha, 2014. "*Potential application of solar powered adsorption cooling systems in the Middle East*". Applied Energy, 126, March, pp. 235–245

[7] S.Mitra, P. Kumar, K. Srinivasan, P. Dutta, 2015. "*Performance evaluation of a two-stage silica gel + water adsorption based cooling-cum desalination system*". International Journal of Refrigeration, June (In Press)

[8] Weather Data Sources, *Energy Plus Energy Simulation Software*, available at http://apps1.eere.energy.gov/buildings/energyplus/weatherdata_about.cfm

[9] S.Mitra, P. Kumar, K. Srinivasan, P. Dutta, 2014. "*Simulation study of a two-stage adsorber system*". Applied Thermal Engineering, 72(2), November, pp. 283–288

[10] E. W. Lemmon, M. L. Huber, M. O. McLinden, 2010. *NIST Standard Reference Data Base 23: Reference Fluid Thermodynamic and Transport Properties—REFPROP*, Version 9.0, National Institute of Standards and Technology, Standard Reference Data Program, Gaithersburg,

[11] X.Q. Zhai, R.Z. Wang, 2010. "*Experimental investigation and performance analysis on a solar adsorption cooling system with/without heat storage*". Applied Energy, 87, October, pp. 824–835

[12] A. Dobos, 2013. "*PVWatts Version 1 Technical Reference*". NREL/TP-6A20-60272.

[13] R. Perez, R. Seals, P. Ineichen, R. Stewart, D. Menicucci, 1987. "*A new simplified version of the perez diffuse irradiance model for tilted surfaces*". Solar Energy, 39, pp. 221-231

[14] System Advisor Model Version 2013.1.15 (SAM 2013.1.15). *National Renewable Energy Laboratory*, Golden, CO, Accessed October 11, 2013, https://sam.nrel.gov/content/downloads

[15] H. T. Chua, K. C. Ng, A. Chakraborty, N. M. Oo, and M. A. Othman, 2002. "*Adsorption Characteristics of Silica Gel + Water Systems*". Journal of Chemical and Engineering Data, 47(5), pp. 1177-1181.

# Theoritical Investigation on Traveling Wave Thermoacoustic Prime mover


Rizwan Rasheed[#1], K.K.Abdul Rasheed[*]

[#] *TKM Institute of Technology, Kollam, Kerala, India*

[1]rizwanrashd@gmail.com

[*]*TKM College of Engineering, Kollam, Kerala, India*



***Abstract-*** **Thermoacoustic prime mover (TAPM) converts heat energy into acoustic energy and they serve as the ideal choice for driving the Pulse Tube Refrigerator replacing the conventional compressors. The development of thermoacoustic systems has become the focus of the recent research due to the absence of moving parts, construction simplicity, reasonable efficiency, and the use of environmental friendly working fluids. The present work involves the analysis of a small travelling wave TAPM using CFDandDeltaEC.**



**Key words: Thermoacoustic prime mover, Traveling Wave, Computational Fluid Dynamics,DeltaEC**


## I. INTRODUCTION

The thermoacoustic prime mover (TAPM) is an attractive alternative as a pressure wave generator to drive Pulse Tube Refrigerators. The important advantages of using such a drive is that there are no moving components and it can be driven by low grade energy such as fuel, gas, solar energy, waste heat etc. The numerical modeling of a thermoacoustic prime mover can be carried out by several methods. We have used procedures of CFD for the simulation of the engine.

## II. CFD MODELLING

In order to investigate the effects of various operating parameters on a travelling wave thermoacoustic prime mover (TWTAPM), CFD simulation was carried out. CFD simulation gives a better insight into fluid behavior which normally cannot be studied experimentally.

The CFD simulation involves the solution of the governing equations of momentum, continuity and energy in the computational domain ofthermoacoustic prime mover(TAPM)for the given working fluid. Several CFD codes are available and we have used the commercial CFD package Fluent 6.3.26 for the present analysis along with Gambit 2.3.16 for the modeling and meshing of the geometry.

### *A. Development of CFD Model*

The schematic of the TWTAPM is shown in the Figures 1.The system consists of looped tube, resonant tube, heat exchangers, buffer and regenerator.

The regenerator is a porous medium with high thermal conductivity characteristics in order to create the temperature gradient necessary for thermoacoustic oscillations. This engine uses a hollow cylinder filled with steel meshes cut into circles stacked on top of one another.

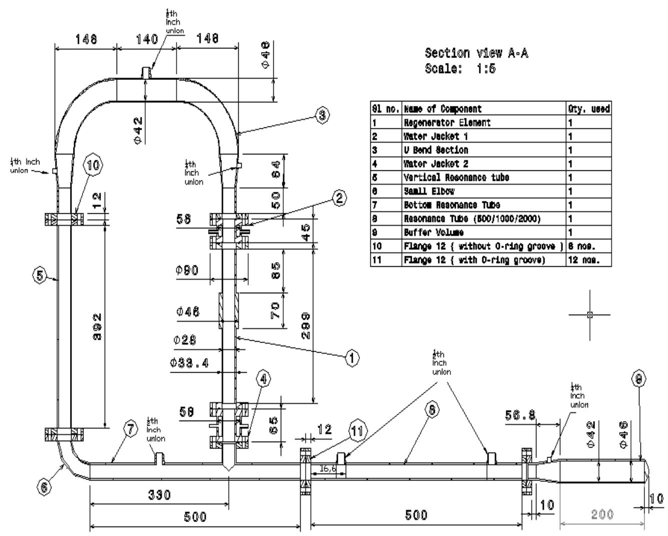


Figure.1 Schematic of TWTAPM with dimensions

The computational domain of the TWTAPM is shown in Figure 2. It was modeled and meshed using Gambit2.3.16. The TWTAPM has a resonator length of 1m and regenerator length of 85mm. The grid is built using quadrilateral pave cells, with a total cell count approximately50,000. Figure 3 shows a closer view of the meshed regenerator area.

Of all the boundary conditions, the regenerator is most critical. The regenerator is set with appropriate temperature gradient using user defined function over the length of the regenerator. All other surfaces are modeled as adiabatic walls. The entire system was modeled without buffer.

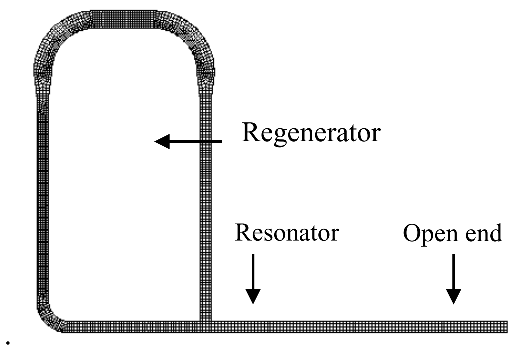


Fig.2.Computational domain for the Travelling Wave thermoacoustic Engine

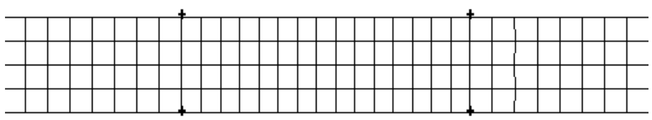

Fig.3 Section of the CFD Grid

With the above boundary conditions, the models were solved in Fluent6.3.26.The simulation is divided into two parts; first, a steady state simulation to find the initial condition of a pressure disturbance, and second, a transient simulation which goes from the initial state to stabilized pressure oscillations. In both cases, the gas is modeled as an ideal gas. This equation of state is used to obtain the temperature dependence of the density. The k-ε model was used to account for the turbulence as it is valid for a wide range of flows. The discretization for all flow variables is chosen to be of second order for increased accuracy. Pressure is discretized with the PRESTO! Scheme for increased accuracy of flow in porous media.

The simulation has been carried out at different pressures with helium as the working fluid for resonator length of 1m.Figure4shows the typical result of the development of oscillations for Helium. Figure5shows the zone of stable oscillations for the same gas.

*B. Simulation Using DeltaEC*

Design Environment for Low-Amplitude thermoAcoustic Energy Conversion (DeltaEC) is a computer program that can calculate details of how thermoacoustic equipment performs, or can help the user to design equipment to achieve desired performance. DeltaEC numerically integrates in one spatial dimension using a low-amplitude, acoustic approximation and sinusoidal time dependence. It integrates the wave equation and some-times other equations such as the energy equation, in a gas (or a very compressible, thermodynamically active liquid), in a geometry given by the user as a sequence of segments such as ducts, compliances, transducers, and thermoacoustic stacks or regenerators.

.

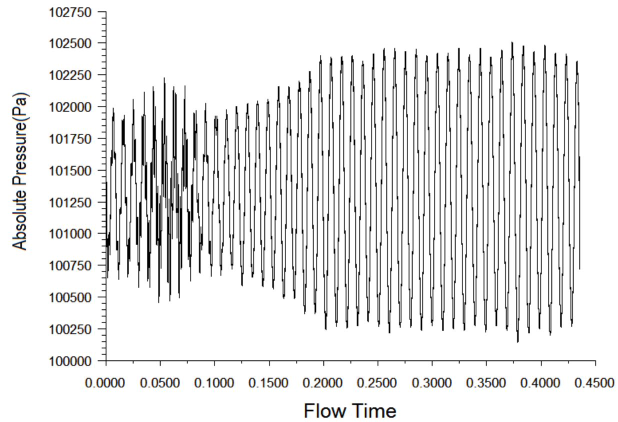


Fig.4 Development of oscillations in the TWTAPM for Helium with the resonator length of 1m at an operating pressure of 1bar

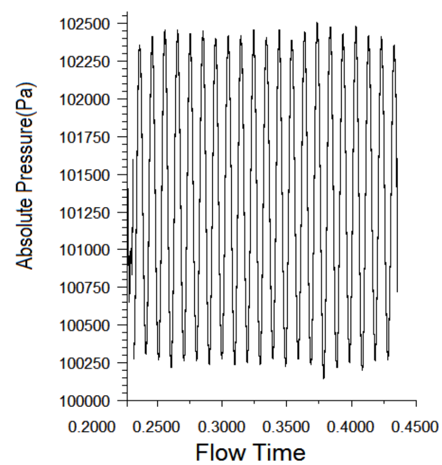


Fig.5 Pressure wave form under stable oscillation TWTAPM for Helium with the resonator length of 1mat an operating pressure of 1 bar

III. RESULTS AND DISCUSSION

*A. Effect of Working Fluid*

The simulation results for different working fluids of Ar, He and $N_2$ for an operating pressure of 2bar and temperature gradient of 300K were compared. The simulation confirms that the working fluid in the system is an important parameter in deciding the frequency and pressure amplitudes in the travelling wave system Figure 6 indicates that Ar is the fluid with the highest pressure amplitude and lowest frequency (28Hz), while He is the one with the highest frequency (100 Hz), but with lower pressure amplitude. The molecular weight and the velocity of sound in the medium are the reasons for changes in frequency and pressure amplitude [1]

TABLE 1 COMPARISON OF THE OPERATING FREQUENCY OBTAINED BY CFD AND DELTAEC

| Workingfluid | Operating pressure (MPa) | Frequency(Hz) (CFD) | Frequency(Hz) (DeltaEC) |
|---|---|---|---|
| He | 0.1 | 100 | 98 |
| | 0.2 | 90 | 97 |
| Ar | 0.1 | 28 | 25 |
| | 0.2 | 30 | 28 |
| $N_2$ | 0.1 | 40 | 37 |
| | 0.2 | 30 | 29 |

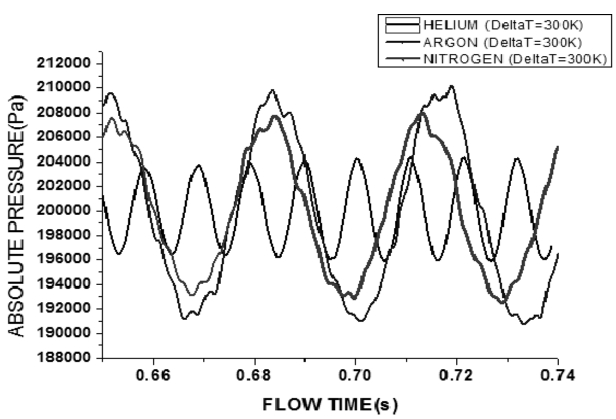


Fig.6 Comparison of oscillations in He, Ar&$N_2$ at same operating parameters

*B. Effect of Temperature Gradient*

The temperature gradient across the stack is a critical parameter in the operation of a thermo-acoustic system. The effect of variation of ΔT across the stack for He gas at the operating pressure of 1 bar is shown in Figure7. Increase in ΔT leads to increase in pressure amplitude with minor changes in frequency

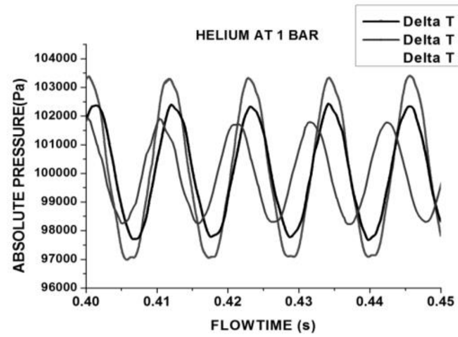


Fig.7 Comparison of oscillations in He for different temperatures

*C Effect of Operating Pressure*

The operating pressure is another important parameter of the thermo-acoustic system. In order to study its effects keeping all other parameters constant analysis of $N_2$ gas was done at different operating pressures of 1 bar and 2 bars. As shown in the Figure 8 its evident frequency and pressure amplitude increased with increase in operating pressure.

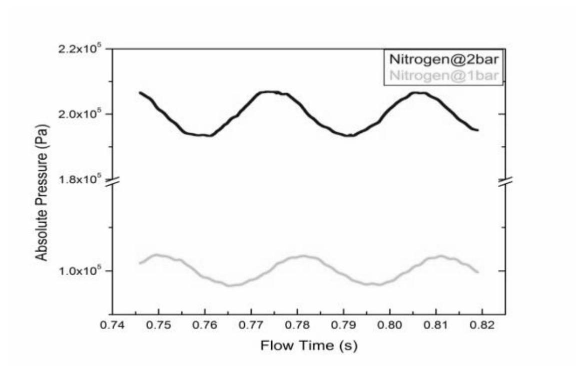


Figure.8Comparison of oscillations in N at different operating pressures

The contour plots of temperature profiles for a TWTAPM with $N_2$ as the working fluid and an operating pressure of 1 bar and temperature gradient of 300K over the entire domain and the regenerator region has been shown in the Figure 8.

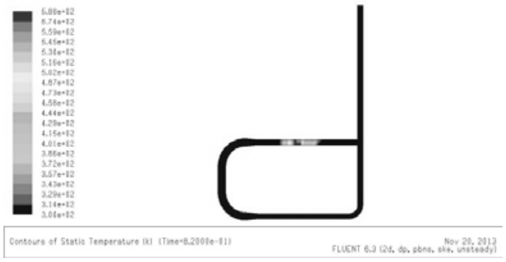


Figure.8 Contour plots of temperature profile over the entire domain

## IV. CONCLUSION

The simulation studies on TWTAPM was carried out on the system with different working fluids and different operating parametersby CFD and compared with DeltaEC.The studies indicates that forTWTAPM, the working fluid always plays a vital role in deciding the operating frequency and the pressure amplitude. In the system argon shows the lowest frequency with the highest amplitude for all the working fluids investigated, the operating pressure increases the pressure amplitude along with minor changes in frequency. For travelling wave thermoacoustic prime mover, increase in ΔT across the regenerator leads to increase in the pressure amplitude.

## REFERENCES

[1] Mathew Skaria , K.K. Abdul Rasheed , K.A. Shafi , S. Kasthurirengan, UpendraBehera, Simulation studies on the performance of thermoacoustic prime moversand refrigerator, Computers & Fluids 111 (2015) 127–136

[2] Hao XH, Ju YL, Behera U, Kasthurirengan S. Influence of working fluidon theperformance of standing wave thermoacoustic prime mover.Cryogenics2011;51:559–61.

[3] Nijeholt JAL, Tijani MEH, Spoelstra S. Simulation of a traveling-wavethermoacoustic engine using computational fluid dynamics. J Acoust. Soc Am.2005;118(4):2265–70

[4] Zink, F., Vippermann, J., Scheaefer, L., "CFD simulation of Thermoacoustic Cooling", *Intl. J. Heat and Mass Transfer* Vol. 53, pp. 3940-3946 (2010).

[5] Swift G.W., "Thermoacoustic engines", J Acoust Soc Am Vol. 84 pp 1146-80. (1988)

# A Novel Thermal Fluid Based on $Ti_3SiC_2$ MAX phase Ternary Carbide

K. V. Mahesh[#], T. S. Krishnakumar[*], A. Peer Mohamed[#], M. Jose Prakash[*], S. Ananthakumar[1#]

[#]*Functional Materials Section, Materials Science and Technology Division,*
*CSIR-National Institute for Interdisciplinary Science and Technology (CSIR-NIIST),*
*Trivandrum, Kerala, India*
[1]ananthakuamr70@ gmail·com

[*]*Department of Mechanical Engineering,*
*TKM College of Engineering, Kollam, Kerala, India*

***Abstract-*** **The reliability and durability of mechanical and electronic devices are negatively affected by the uncontrolled heat generation during operation. Nanofluids are usually employed to carry away the heat in such situations. Herein, we report the formulation of a novel multifunctional nanofluid with enhanced thermal conductivity and controlled viscosity via dispersion of $Ti_3SiC_2$ MAX phase nanosheets in base fluids such as propylene glycol, ethylene glycol and mineral oil. A highly stable nanofluid thus obtained was then subjected to thermal fluid properties evaluation. It was observed that the newly developed fluids show enhanced thermal conductivities and controlled viscosity properties.**

*Keywords—* **MAX phase, $Ti_3SiC_2$, thermal fluids, thermal conductivity**

## I. INTRODUCTION

Management of heat is critically important in various fields such as electronics, automobiles, solar cells, medical, food industries and nuclear plants [1-3]. The considerably large heat production during operation deteriorates the performance of the electrical and engine components used in these fields and consume more energy. The miniaturization and efficiency improvement of the functioning components in such areas demand good control of heat. Heat transfer fluids play a significant role in this context. The need for energy conservation added importance to these fluids. Conventional heat transfer fluid included mineral oil, white/paraffinic oils, silicones, water, ethylene/ propylene glycols, etc. Thermal conductivity, viscosity and pumpability are the primary parameters that determine the quality and performance of a heat transfer fluid. Over the years, many attempts were reported to enhance the performance of conventional heat transfer fluids. Adding metallic particle into classical fluids was initially regarded as a promising method to improve the thermal conductivity [4, 5]. However clogging in microchannels and poor stability of those fluids prepared with micron sized particle made this process practically unviable [2, 6]. The advent of nanofluids successfully surpassed these demerits. A nanofluid is a kind of novel engineering fluid consisting of high thermal conducting nanoparticles dispersed in base fluids such as ethylene glycol, propylene glycol, water, oil, etc. Research on nanofluids has been going on for more than 15 years. Over the years, ceramic nanoparticles such as oxides, carbides, and nitrides, metal nanoparticles, carbon nanotubes, etc. are explored to improve the thermal conductivity of base fluids. An enhancement of 40% in thermal conductivity was reported by Eastman et al. with Cu nanoparticles dispersed in ethylene glycol. The high thermal conductivity and low density of carbon nanomaterials such as CNTs also attracted the attention of many researchers [7-10]. However, the non-reactive surfaces, intrinsic Van der Waals forces and very high aspect ratios cause severe aggregation of CNTs and precipitate to the bottom and make it less stable dispersion.

Surfactants were introduced to such systems to overcome this drawback. But on the other hand, surfactants will deteriorate the thermal properties of CNTs. It will cause foaming on heating and also increase the thermal resistance between CNTs and fluid. Xie et al. introduced functionalization of CNTs to avoid the use of surfactants. Metal nanoparticles decorated CNTs are also reported [11].

The advent of graphene catches the attention of researchers towards exploring graphene and its analogues 2D materials for heat transfer fluids. Recent advances in layered materials enable large scale synthesis of various two-dimensional (2D) materials. Two-dimensional materials can be good choices as nanofillers in heat transfer fluids, due to the high surface area they have available for heat transfer. Many attempts were reported with graphene, graphene oxide and metal oxide modified graphene as fillers in heat transfer fluids [12, 13]. Successive to this, Ajayan et al. reported boron nitride nanosheets as active filler for thermal fluids [14, 15].

In this work, we have proposed a novel layered materials $Ti_3SiC_2$ as active filler for thermal fluids. $Ti_3SiC_2$ belongs to the MAX phase family of ternary carbides. MAX phase is the general name of ternary carbides/nitrides having the general formula Mn+1AXn where M is an early transition metal, A element belongs to group IIIA, or IVA and X is either carbon and/or nitrogen) [16, 17]. These types of materials possess layered structure in which MX layers are alternate with A layer. This type of materials known for their dual nature of both ceramic and metals [18]. They are thermally and electrically conducting like metals. At the same time, they possess the properties of ceramic such as high-temperature stability, high toughness, wear resistance, etc. $Ti_3SiC_2$ possess a high thermal conductivity of 37-40W/mK [19]. The material is also known for its self-lubricating properties owing to its nanolayered characteristics. These exotic properties make $Ti_3SiC_2$ as a promising candidate for thermal fluids. In the present work, we have dispersed nanosheets of $Ti_3SiC_2$ in the base fluids such as propylene glycol, ethylene glycol and mineral oil by micromechanical milling technique and important thermal fluid properties such as thermal conductivity and viscosity were analysed and reported.

## II. MATERIALS AND METHODS

$Ti_3SiC_2$ (3-ONE-2 LLC, USA), Propylene glycol (Merck India ltd), Ethylene glycol (Merck India ltd), Mineral Oil (Suniso 3gs) etc. were used as the raw materials for the preparation of thermal fluids. Ultra-Fine mortar grinder (Retsch-RM 200, Germany) was used for micromechanical milling. This instrument is working on pressure-friction principle. Typically required amount of of bulk $Ti_3SiC_2$ was added to about 100 mL of base fluid and subjected to micromechanical milling for 12h. The resultant dispersion was then separated by centrifugation to get stable dispersions.

*Characterization*

The composition/phase purity of the bulk Ti3SiC2 was analysed by Powder X-ray diffraction (XRD) studies and is recorded using X'Pert Pro, Philips X-ray diffractometer with a monochromator on the diffraction beam side (Cu Kα radiation, λ=0.154 nm). The structural characteristics of bulk $Ti_3SiC_2$ and nanosheets obtained after micromechanical milling were Scanning electron microscopy (SEM) CILAS EVO18 special edition operated at 20kV. Particle size measurements of the thermal fluids were conducted at room temperature by Dynamic Light Scattering (DLS) using Malvern Zetasizer 3000HSA. The rheological properties of the nanofluids with temperature were studied using cup and cone Anton Paar rheometer. The thermal conductivity of the nanofluid was analysed using KD2 Pro (Decagon Devices, USA) Thermal properties analyser which is working by transient hot wire technique. Thermal conductivity was measured by immersing KS-1 probe having diameter of 1.2mm and length of 6cm in the nanofluid. The probe consists of a needle with heater and temperature sensor inside. Prior to the measurements, the probe was calibrated using glycerol, the standard fluid. Thermal conductivity up to 50°C was measured above which free convection affect the measurement due low viscosity of the fluid at high temperatures.

## III. RESULTS AND DISCUSSION

The as procured $Ti_3SiC_2$ powder was analysed by XRD to ensure the phase purity. The result is depicted Fig. 1. It is well clear that the sample containing mainly $Ti_3SiC_2$ along with small amount of TiC which is very difficult to avoid. The spectrum is analysed by X'pert high score plus software and it reveals that the XRD spectrum of samples contains all the corresponding peaks of $Ti_3SiC_2$ according to the JCPDS file no. 00-048-1826.

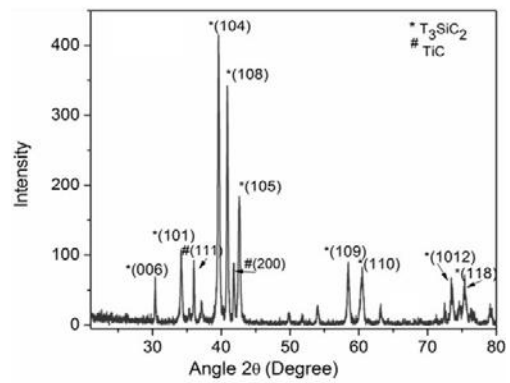


Fig.1 Powder X-ray Diffraction spectra of as received $Ti_3SiC_2$

The morphological feature of the as received $Ti_3SiC_2$ was analysed by Scanning election microscopy (SEM). The microstructure clearly shows the nanolayered structure of $Ti_3SiC_2$. The corresponding SEM image is given as Fig. 2

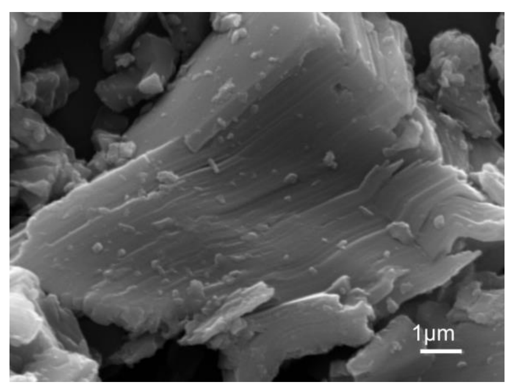


Fig.2 Scanning Electron Microscopy image showing the nanolayered characteristics of bulk $Ti_3SiC_2$

For converting the bulk $Ti_3SiC_2$ in to ultrathin nanosheets, a micromechanical milling was performed. The milling was carried out using Retsch Ultra-Fine mortar grinder in different base fluids. The fluids after milling centrifuged at 8000rpm for 10 minutes to obtain stable nanofluid dispersions. Initially the milling was performed with varying the milling time in order to study the role of milling time on exfoliation and dispersion stability of the nanofluids. In typical experiment, 1g $Ti_3SiC_2$ was milled for 2h, 4h, 6h, 8h and 12 h followed by centrifugation at 8000 rpm. The photographs of the dispersions after 1 week shelf life in given in Fig. 3. It is observed that the exfoliation and extent of dispersion is more with increasing milling time. The photographs clearly show this difference.

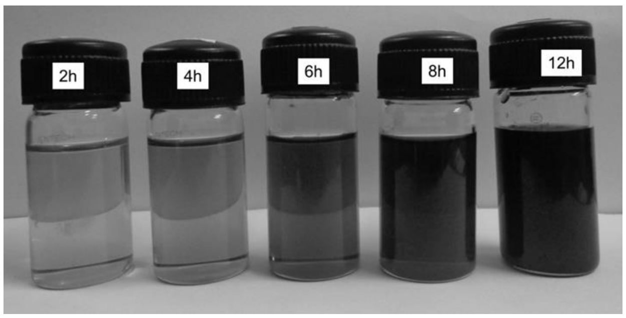


Fig. 3 Photographs showing the stability and extent of exfoliation with respect to milling time.

The particle size of the dispersions in different base fluids was measured by Malvern Zetasizer. The results are depicted in fig 4. It was seen that irrespective of type of base fluid the diameter of the nanosheets are about 90-95 nm. Since DLS technique all the particle as perfect spheres, we can assume that the nanosheets in the present system may have lateral dimension of about 90 nm with few nm thickness. The nanosheets of $Ti_3SiC_2$ are highly stable and can withstand for several months without the use of any surfactants. This suggests that these nanosheets can be used for making nanofluids for various purposes.

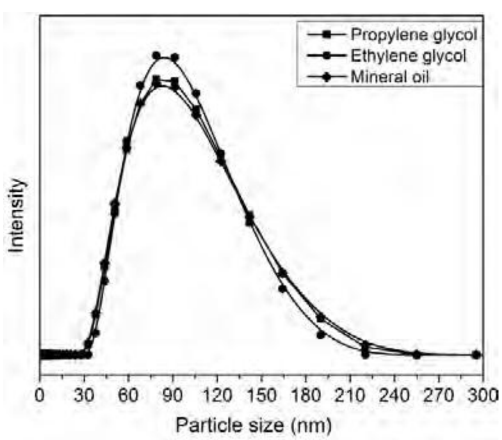


Fig.4. Particle size analysis of $Ti_3SiC_2$ nanosheets in different base fluids

The structural features of the $Ti_3SiC_2$ nanosheets in nanofluids are studied with help of SEM images which are given in Fig. 5. It is well clear from the SEM images that the bulk nanolayered structure of $Ti_3SiC_2$ (Fig. 2) was changed to deformed flakes upon milling and ultrasonication. The bulk layers were extracted and separated as individual layers.

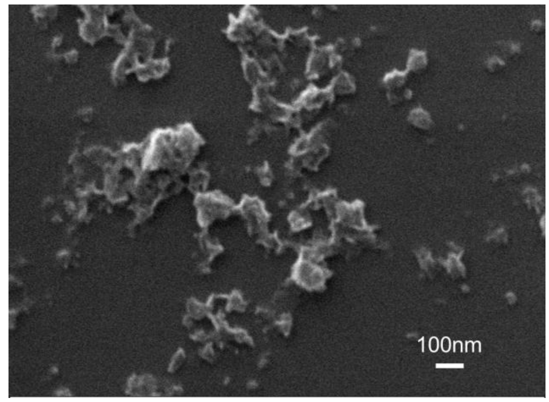


Fig.5. Scanning electron microscopy image of the $Ti_3SiC_2$ nanosheets in propylene glycol based thermal fluid after micromechanical milling

The higher thermal conductivity of nanofluids, when compared to the thermal conductivity of base fluid, is the major driving force for research in heat transfer nanofluids. Heat transfer using fluids is a complex phenomenon, and various factors such as fluid stability, interface and morphology of the dispersed particles, composition, viscosity, and surface charge influence the observed results. The nanofluid viscosity too plays an important role in the performance of nanofluids. The thickness of boundary layer and the onset of turbulence are influenced by nanofluid viscosity. Hence, an appropriate process condition for preparation of nanofluids must be identified on the basis of variation of thermal conductivity as well as viscosity with process variables. The major process variable in the present work is the concentration of exfoliated $Ti_3SiC_2$.

The viscosity of different nanofluids with respect to the amount of $Ti_3SiC_2$ nanosheets are depicted in Fig. 6. It is well evident from the figure that nanolayered characteristics of $Ti_3SiC_2$ play an important role in controlling the viscosity. It is observed from the viscosity curves that the presence of exfoliated $Ti_3SiC_2$ nanolayers reduces the viscosity of the base fluids. Usually, the addition of fillers in base fluid causes an increase in viscosity that will adversely affect the fluid properties.

In ethylene glycol (EG), propylene glycol (PG) and mineral oil (MO) systems, the base oil is showing a shear thickening behavior or in other words, the viscosity of the fluid is increasing with increase in shear rate. After the small increase in viscosity with the shear rate, it became constant with further increase in shear rate. This nature is retained in MAX phase nanofluids derived from the base oil also. In PG and EG systems, the addition of $Ti_3SiC_2$ lowered the viscosity of the systems. In the case of MO, the viscosity was retained. This is because of the nanolayered nature of $Ti_3SiC_2$. Usually, hard ceramic fillers tend to increase the viscosity because of the formation of agglomerates and their increased friction with the wall of the container. In this case, the nanolayered $Ti_3SiC_2$ is a low friction material and it shear over the surface easily which in turn aids the smooth flow of the liquid. In other words, $Ti_3SiC_2$ reduces the friction between the walls of the container and the nanofluids. This results in the reduction of viscosity. The decrease is viscosity is more prominent when the system is containing more $Ti_3SiC_2$. This is very good sign for using $Ti_3SiC_2$ nanosheets as a functional filler for developing thermal fluids. As we know, thermal conductivity will increase with an increase in filler content.

Since viscosity is not enhancing with increase in filler loading we can load more $Ti_3SiC_2$ in base fluid without losing its flowability. This is an added advantage since the increase in viscosity will decrease the effective thermal conductivity values as well as flow characteristics of the fluid. These nanofluids are stabilized in the carrier fluid without any surfactant. The surfactants can decrease the thermal conductivity of the nanofluids since surfactants introduce defects at the interfaces.

The thermal conductivity of the nanofluids was measured by KD2 Pro Thermal conductivity analyser. The results are summarized in Table 1. It is seen that the thermal conductivity is increasing with increasing the filler content. The increase in filler content will lead to dynamic Brownian motion of the particles. This fast particle movement will increase the thermal conductivity.

As we seen earlier, the viscosity of the fluid is decreasing with the amount of nanosheets. This will aid enhanced particle movement that in turn increased the thermal conductivity. There is an enhancement of ~ 40-50 % in nanofluids produced by 12 milling. Enhancement in thermal conductivity with increase in the $Ti_3SiC_2$ concentration in base oil indicates the formation of percolation channels for thermal conduction by ultrathin nanosheets of $Ti_3SiC_2$. The increase in nanofluid thermal conductivity with filler content indicates the role of Brownian motion in the enhancement of thermal conductivity.

The Brownian motion causes micro convection that in turn influences thermal conductivity enhancement in nanofluids through both increases in thermal energy and decrease in viscosity, both of which contribute to enhancement in Brownian velocity of nanoparticles [20]. Brownian velocity is inversely proportional to both viscosity and particle size. Hence, the increase in Brownian velocity contributes to enhancement in thermal conductivity of nanofluids. Thus it can be concluded that the Nanofluids developed in the present study is suitable for several heat transfer applications.

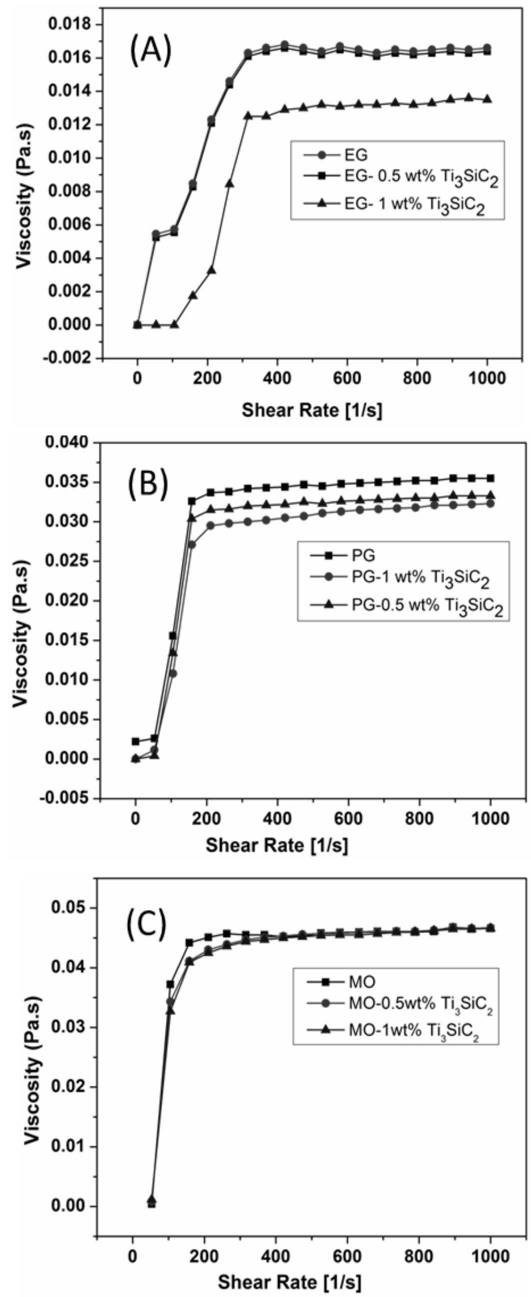


Fig. 6 Viscosity of the different nanofluids with respect to filler loading (A) Ethylene glycol, (B) Propylene glycol and (C) Mineral oil

TABLE 1 THERMAL CONDUCTIVITY OF THE NANOFLUIDS

| Sample name | Thermal conductivity (W/mK) | % enhancement in thermal conductivity |
|---|---|---|
| Propylene glycol (PG) | 0.207 | - |
| PG- 0.5 wt% $Ti_3SiC_2$ | 0.248 | 20 |
| PG - 1 wt% $Ti_3SiC_2$ | 0.288 | 39 |
| Ethylene glycol (EG) | 0.255 | - |
| EG - 0.5 wt% $Ti_3SiC_2$ | 0.301 | 18 |
| EG - 1 wt% $Ti_3SiC_2$ | 0.351 | 37 |
| Mineral oil (MO) | 0.117 | - |
| MO- 0.5 wt% $Ti_3SiC_2$ | 0.142 | 21 |
| MO- 1 wt% $Ti_3SiC_2$ | 0.175 | 49 |

## CONCLUSIONS

In the present work, feasibility of utilizing the nanolayered $Ti_3SiC_2$ as active filler for high performing thermal fluids was attempted. It was observed that the nanolayered $Ti_3SiC_2$ transformed into ultrathin layers by micromechanical milling and form a very stable suspensions. In the present work three types of base fluids namely propylene glycol, ethylene glycol and mineral oil were selected. The material is compatible with all the three base fluids. The nanolayered $Ti_3SiC_2$ resulted in decrease in viscosity with increase in filler loading which is an added advantage since the reduction in viscosity will improve the pumpabilty of the thermal fluid. The newly developed thermal fluids show an enhancement of thermal conductivity of ~40-50% with a filler loading of 1 wt%.

## ACKNOWLEDGMENT

The authors are thankful to the Director, CSIR- National Institute for Interdisciplinary Science and Technology for providing the necessary lab facilities. Authors also thank Dept. of Mechanical Engineering, TKM college of Engineering, Kollam for thermal properties measurements. K.V. Mahesh acknowledges CSIR, Govt. of India for Senior Research Fellowship.

## REFERENCES

[1] V. W. Kaufui and L. Omar De,"Applications of Nanofluids: Current and Future", *Advances in Mechanical Engineering*, 2010, 2010, 1-11.

[2] S. S. Thadathil, K. Asha, A. P. Mohamed, U. S. Hareesh and G. Swapankumar,"Synthesis and characterization of cerium oxide based nanofluids: An efficient coolant in heat transport applications", *Chemical Engineering Journal*, 2014, 255, 282-289.

[3] K. S. Suganthi and K. S. Rajan,"Improved transient heat transfer performance of ZnO-propylene glycol nanofluids for energy management", *Energy Conversion and Management*, 2015, 96, 115-123.

[4] G. Prasad, S. S. Naik, A. Komel, S. Srinath, K. A. Kishore, Y. P. Setty and S. Shirish,"Stable colloidal copper nanoparticles for a nanofluid: Production and application", *Colloids and Surfaces A: Physicochemical and Engineering Aspects*, 2104, 441, 589597.

[5] S. B. Subelia, N. Patrick and J. B. Bernard,"Physicochemical Properties of Oil-Based Nanofluids Containing Hybrid Structures of Silver Nanoparticles Supported on Silica", *Industrial & Engineering Chemistry Research*, 2011, 50, 3071-3077.

[6] S. S. Thadathil, K. Asha, S. Lakshmi Narayan and G. Swapankumar,"Facile synthetic strategy of oleophilic zirconia nanoparticles allows preparation of highly stable thermo-conductive coolant", *RSC Advances*, 2014, 4, 28020-28028.

[7] S. S. J. Aravind, B. Prathab, B. Tessy Theres, R. K. Sabareesh, D. Sumitesh and S. Ramaprabhu,"Investigation of Structural Stability, Dispersion, Viscosity, and Conductive Heat Transfer Properties of Functionalized Carbon Nanotube Based Nanofluids", *The Journal of Physical Chemistry C*, 2011, 115, 16737-16744.

[8] X. Huaqing and C. Lifei,"Review on the Preparation and Thermal Performances of Carbon Nanotube Contained Nanofluids", *Journal of Chemical & Engineering Data*, 2011, 56, 1030-1041.

[9] V. Kumaresan and R. Velraj,"Experimental investigation of the thermo-physical properties of waterâ€“ethylene glycol mixture based CNT nanofluids", *Thermochimica Acta*, 2012, 545, 180186.

[10] C. Lifei and X. Huaqing,"Silicon oil based multiwalled carbon nanotubes nanofluid with optimized thermal conductivity enhancement", *Colloids and Surfaces A: Physicochemical and Engineering Aspects*, 2009, 352, 136-140.

[11] J. Neetu and S. Ramaprabhu,"Synthesis and Thermal Conductivity of Copper Nanoparticle Decorated Multiwalled Carbon Nanotubes Based Nanofluids", *The Journal of Physical Chemistry C*, 2008, 112, 9315-9319.

[12] P. M. Sudeep, J. Taha-Tijerina, P. M. Ajayan, T. N. Narayanan and M. R. Anantharaman,"Nanofluids based on fluorinated graphene oxide for efficient thermal management", *RSC Advances*, 2014, 4, 24887-24892.

[13] B. Tessy Theres and S. Ramaprabhu,"Investigation of thermal and electrical conductivity of graphene based nanofluids", *Journal of Applied Physics*, 2010, 108, 124308.

[14] Z. Chunyi, X. Yibin, B. Yoshio and G. Dmitri,"Highly thermo-conductive fluid with boron nitride nanofillers", *ACS nano*, 2011, 5, 6571-6577.

[15] T.-T. Jaime, N. N. Tharangattu, G. Guanhui, R. Matthew, A. T. Dmitri, P. Matteo and M. A. Pulickel,"Electrically insulating thermal nano-oils using 2D fillers", *ACS nano*, 2012, 6, 1214-1220.

[16] W. M. Barsoum,"The MN+1AXN phases: A new class of solids", *Progress in Solid State Chemistry*, 2000, 28, 201281.

[17] M. W. Barsoum and T. El-Raghy,"The MAX Phases: Unique New Carbide and Nitride Materials: Ternary ceramics turn out to be surprisingly soft and machinable, yet also heat-tolerant, strong and lightweight", *American Scientist*, 2001, 89, 334-343.

[18] M. W. Barsoum and M. Radovic, in *Annual Review of Materials Research, Vol 41*, eds. D. R. Clarke and P. Fratzl, vol. 41, pp. 195-227.

[19] M. W. Barsoum, T. El-Raghy, C. J. Rawn, W. D. Porter, H. Wang, E. A. Payzant and C. R. Hubbard,"Thermal properties of Ti3SiC2", *Journal of Physics and Chemistry of Solids*, 1999, 60, 429-439.

[20] S. M. S. Murshed and C. A. N. d. Castro,"Predicting the Thermal Conductivity of Nanofluidsa" Effect of Brownian Motion of Nanoparticles", *Journal of Nanofluids*, 2012, 1, 180185.

# Numerical Investigation on the Effect of air Jet Velocity in Co-Axial Air-Water Jet Impingement Quenching of Hot Steel Plate

Amjith T John[1], Leena R[2]

*Department of Mechanical Engineering, TKM College of Engineering, Kollam, Kerala, India*

[1]amjithtjohn@gmail.com

[2]leenakalidas@gmail.com

***Abstract*— Jet impingement cooling is an attractive cooling mechanism of achieving high heat transfer rates in controlled cooling. The microstructure and mechanical properties of steel plates can be highly modified by controlled cooling. When water impinges on the hot plate the vapour produced deflects the liquid from the plate therefore liquid-plate contact decreases. Liquid-plate contact and thereby the heat transfer can be enhanced by using co-axial air water jet system. In this work a transient multiphase simulation of water and co-axial air-water jet system is done. The effect of air jet velocity in heat transfer was studied. Maximum cooling rate and maximum heat flux at the stagnation point was increased about 41.7% and 45.9% when the co-axial air jet velocity becomes 6 m/s than the case in which only water is used (co-axial air jet velocity is 0 m/s).**

*Keywords*—**Jet Impingement Quenching, Co-axial Jet, VOF model, Transient simulation, Multiphase.**

## I. INTRODUCTION

Quenching is needed for ensuring very high cooling rate. In manufacturing industries, quenching can be used for cooling moulds (glass-maker industry) or controlling the structure of the steel alloys. Structure and thus mechanical properties of steel alloys are conditioned by the cooling rate of the product. It is thus of primary importance to control this cooling rate and its homogeneity to obtain steels with good and homogeneous mechanical properties. This cooling is usually ensured by quenching of the hot moving strip by many subcooled water jets.

During the cooling process of a steel recrystallization occurs at temperature below 723°C (996K). The mechanical properties of the specimen depend upon the grain structure and the grain structure depends on the cooling rate. As the cooling rate increases grain structure becomes finer; hence mechanical properties improve.

Water jet impingement quenching systems are widely used in steel industries; especially in hot rolling mills. Fig. 1 shows schematic representation of a typical run out table. After hot rolling process the temperature of the plate will be about 850°C. Inorder to get steel plate with better mechanical properties steel must be cooled rapidly upto 500°C and then allowed to cool in atmosphere. The cooling process in this temperature range has a pivotal role in determining the properties of steel.

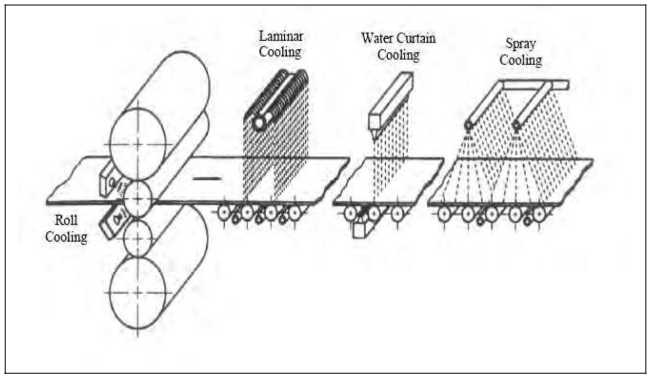


Fig. 1 Schematic *of a cooling system in a runout table (Yongjun Zao,2005).*

Since the metal part temperature is much higher than the saturation temperature of the liquid at atmospheric pressure, heat transfer occurs by boiling. Boiling is a two-phase heat transfer process in which heat is transferred by phase change processes. Numerical simulation on transient water jet impingement quenching is rare. In this work transient numerical simulation of water jet quenching is done. Inorder to enhance the cooling rate a co-axial air jet is introduced and the effect of velocity of air jet in the cooling process is studied.

Few studies of jet cooling at thermal conditions encountered in steel hot rolling mills have been reported in the literature. N. Zuckerman and N. Lior et al. [1] done a comprehensive review on the applications, physics of the flow and heat transfer phenomena, available empirical correlations and values they predict, and also numerical simulation techniques and results of impinging jet devices for heat transfer are described. They reviewed that co-axial air jets increased Nu at stagnation point by up to 25% for higher H/D (9<H/D<16). Yongjunzao [2] experimentally investigated the cooling of a hot steel plate by an impingement water jet and revealed that maximum cooling rate is obtained at stagnation zone and is increased by increase in velocity. Maximum cooling rate was quickly reached at a certain time after the water jet impinging on the surface.

Nitin Karwa et al. [3].experimentally investigated the quenching process and revealed the effect of hydrodynamics during quenching process and explained the rewetting phenomenon during the quenching process. They observed that boiling is not happening in the wetted region even if the heat flux in the wetted region is high enough to cause boiling. Md Lokman Hosain et al. [4] did steady and transient numerical simulation on jet impingement cooling of hot steel plate with temperature below the boiling point to understand the convection heat transfer phenomenon using VOF model. S.Hardt et al [5]. done numerical simulation of film boiling process using VOF model in fluent. In addition, a two-dimensional film boiling problem was considered that has been analyzed by other authors based on the VOF and the level-set technique. Good agreement between the numerical and the analytical results was found for the Stefan problems Dong-Liang Sun et al[6] proposed a vapour–liquid phase change model using the volume-of-fluid (VOF) method in FLUENT. They verified the phase change model by one-dimensional Stefan problem and two-dimensional boiling problem

Numerical simulation on transient quenching process is conducted to study the effect of heat transfer in co-axial air -water jet . Numerical studies are done using VOF model in ANSYS FLUENT 14.5.

## II. MODELLING

The modelling of the geometry is done in ANSYS 14.5 design Modeller. The fluid domain had length 200 mm; the distance from the upper surface of plate to the co-axial nozzle is taken as 66 mm (11 D, where D is the diameter of water nozzle). Length of co-axial air water jet is fixed at 50 mm.

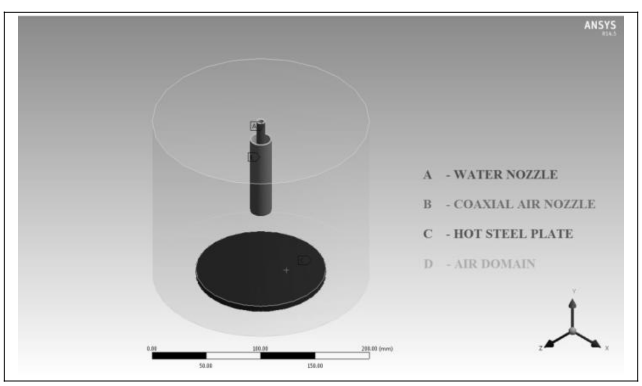


Fig. 2 3D model of the computational domain

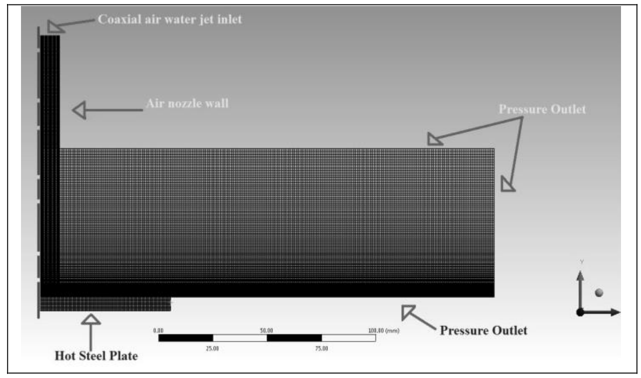


Fig.3 Mesh of the Computational Domain

The steel plate is modelled as a solid domain having radius 60 mm and thickness 6 mm. In order to reduce computational effort the problem is modelled as 2D axisymmetric .The material properties of the solid plate is given as that of steel. Fine quadrilateral mesh is used for meshing the geometry.

Initial temperature of the plate is taken as 1123K. Temperature of air jet and water jet at inlet is taken as 300K. Velocity of water jet at inlet is taken as 0.5 m/s and co-axial air jet velocity is varied as 0, 2, 4, and 6 m/s.

## III. RESULTS AND DISCUSSION

A transient multiphase simulation of water and co-axial air-water jet impingement quenching is done. The phase change of water is simulated using volume-of-fluid (VOF) method in fluent.

When water impinges on a surface with temperature above the boiling point of water; water vapour will be formed. This water vapour has low thermal conductivity and reduces the water-surface contact thereby the heat transfer also reduces. So inorder to avoid this difficulty a co-axial air jet is provided; which pushes the water layer towards the plate surface and thereby water-plate contact is increased considerably. Also due to the presence of the air jet a portion of vapour condenses; therefore the height of water film above the plate surface increases; this leads to an increase in heat transfer.

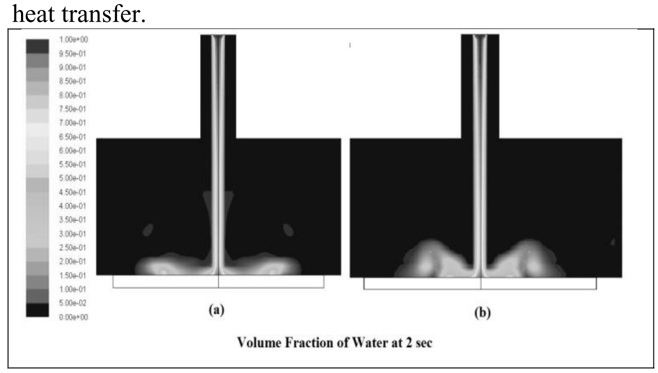


Fig. 4 volume fraction of water at 2 sec

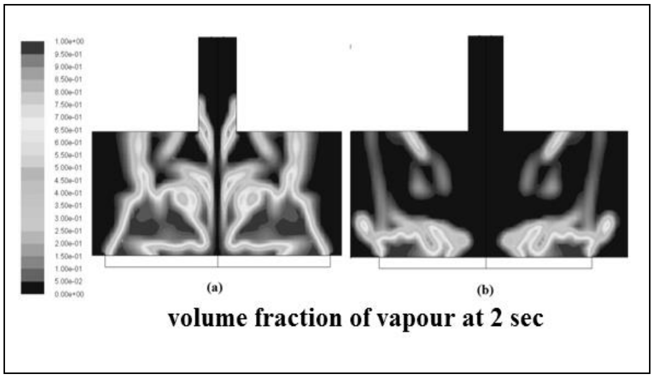


Fig. 5 volume fraction of vapour at 2 sec

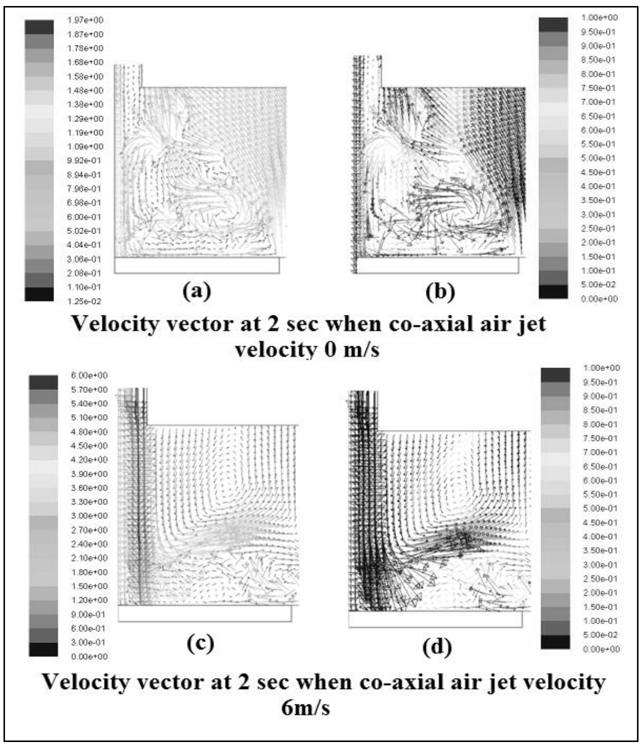


Fig. 6 Velocity vectors when air jet velocity in co-axial air-water system is 0 m/s and 6 m/s.

Fig. 4 shows the volume fraction of water at 2 sec. Fig. 4.a shows the volume fraction of water when co-axial air jet velocity is 0 m/s, and Fig. 4.b shows the volume fraction of water when the co-axial air jet velocity is 6 m/s. Fig. 5.a and Fig. 5.b show the volume fraction of vapour when co-axial air jet velocity is 0 m/s and 6 m/s respectively. From the Fig. 4.a and fig.4.b shows that the height of the water layer is more near the jet impingement region when the co-axial air jet velocity is 6 m/s. Due to the presence of this excess amount of water heat transfer near the impingement region is increased considerably.

From the Fig.5.a and fig.5.b shows that more amount of vapour is produced when the co-axial air jet velocity is 0 m/s fig. 5. a and this vapour produced affects the flow of water jet. But in the case of co-axial air jet with velocity 6 m/s; less amount of vapour is produced and co-axial air jet pushes the vapour formed outwards hence vapour produced doesn't affect the flow of water jet.

Fig 6.a and fig.6.b shows the velocity vector by magnitude and volume fraction of vapour when co-axial air jet velocity is 0 m/s. From the figure it's clear that the vapour formed affects the flow of water jet and also spreads the water layer over the surface. Due to the spreading of water there is a decrease in thickness of water film due to this reason less amount of heat is transferred. From Fig.6.c and fig.6.d the effect of co-axial air jet can be easily understood. Due to the presence of air jet the vapour formed will not interfere with the water jet and the air jet pushes the water layer towards the plate; also a portion of vapour generated is condensed due to the presence of air jet. Thus the height of water layer near the surface is increased which leads to an increase in heat transfer.

*A. Cooling Curve at Different Radial Distances*

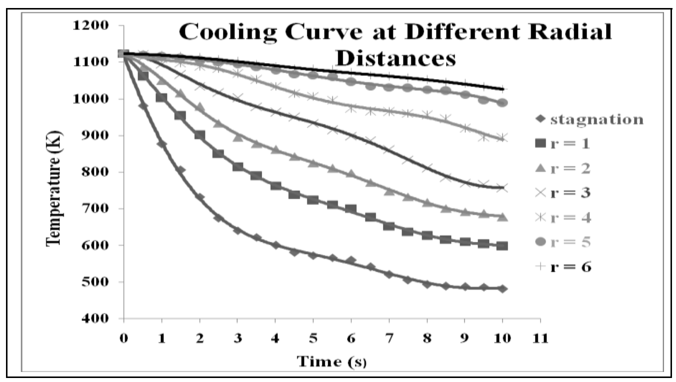


Fig. 7 cooling curve at different radial distances when co-axial air jet with air velocity 0 m/s

Fig.7 shows cooling curve at different radial distances at 1, 2, 3, 4, 5, 6 cm from the centre point of stagnation region when air jet velocity 0 m/s is used. The temperature at the stagnation drops suddenly and becomes 208°C (481 K) after 10 sec. In a steel producing industry controlled cooling of steel plate is done upto 500°C in order to control the microstrucral and hardness properties. In this case the temperature at stagnation is reduced below 500°C (773 K) within 2 sec. Temperature at radial distance 1 cm, 2cm, and 3cm drops below 500°C at 4, 6.5 and 9.5 sec respectively. At the regions at radial distance greater than 3cm temperature drops in much slower rate.

The cooling curve at radial distances 1, 2, 3, 4, 5 and 6 cm from the centre point of stagnation region when co-axial air-water jet with air jet velocity 6 m/s is shown in Fig.8. The temperature at the stagnation drops in much faster than the previous case. The temperature at stagnation point becomes 139°C( 412 K ) at 10sec. Temperature at stagnation becomes less than 500°C within 1 sec. Temperature at radial distance 1cm, 2cm and 3 cm becomes lower than 500°C within 3.5,5 and 10 sec respectively. An important observation is that cooling rate is considerably lower than water jet quenching as the radial distance from the stagnation point.

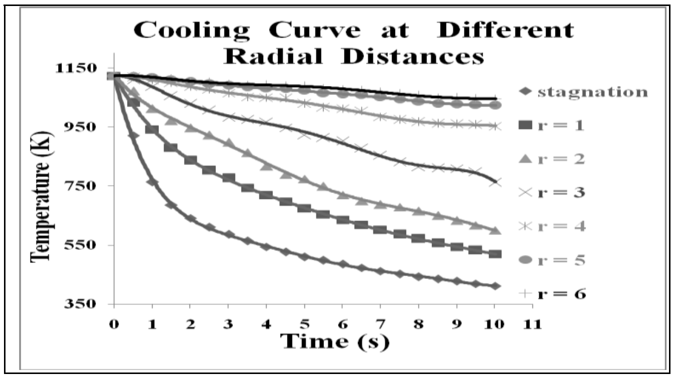


Fig. 8 cooling curve at different radial distances when co-axial air jet with air velocity 6 m/s.

The cooling curve at radial distances 1, 2, 3, 4, 5 and 6 cm from the centre point of stagnation region when co-axial air-water jet with air jet velocity 6 m/s is shown in Fig.8. The temperature at the stagnation drops in much faster than the previous case. The temperature at stagnation point becomes 139°C( 412 K ) at 10sec. Temperature at stagnation becomes less than 500°C within 1 sec. Temperature at radial distance 1cm, 2cm and 3 cm becomes lower than 500°C within 3.5,5 and 10 sec respectively. Graph shows that cooling rate is considerably lower than water jet quenching as the radial distance from the stagnation point

*B. Effect of Air Jet Velocity In Cooling Rate*

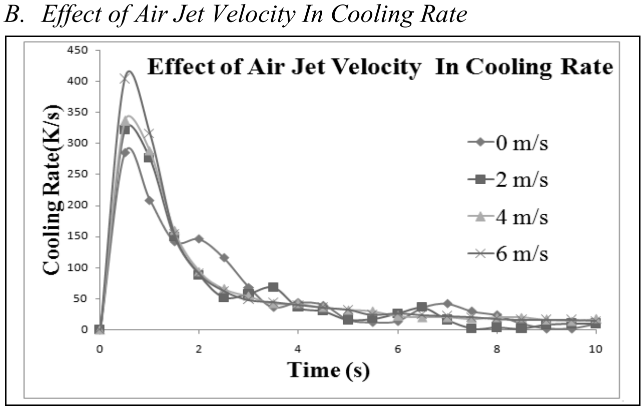


Fig. 9 Effect of Air Velocity in Cooling Rate at stagnation point.

Maximum cooling rate is obtained at the stagnation point. So the cooling rate at stagnation is taken for comparison. Fig.9 shows the change in cooling rate during quenching. At air jet velocity 0 m/s maximum cooling rate 285.12 K/s is obtained. The change in cooling rate is not occurred in a smooth fashion. When the air jet velocity becomes 2 m/s maximum cooling rate becomes 322 K/s. The variations in cooling rate become much smoother than the previous case. When the velocity becomes 4m/s change in cooling rate becomes much smoother and the maximum cooling rate becomes 336 K/s. When the velocity of air jet becomes 6 m/s the maximum cooling rate becomes 404 K/s.

Fig.10 shows the variation of maximum cooling rate at stagnation point for different air jet velocity. As the air velocity increases cooling rate also increases. Maximum cooling rate obtained for water jet (air jet velocity = 0) is 285.12 K/s, When the velocity of air jet becomes 2 m/s maximum cooling rate becomes 322 K/s that means improvement in maximum cooling rate is about 12.93 %. When the velocity of air jet becomes 4 m/s maximum cooling rate becomes 336 K/s. That means improvement in maximum cooling rate is about 17.85 % than water jet. When the velocity of air jet becomes 6 m/s maximum cooling rate becomes 404 K/s. That means improvement in maximum cooling rate is about 41.7%.

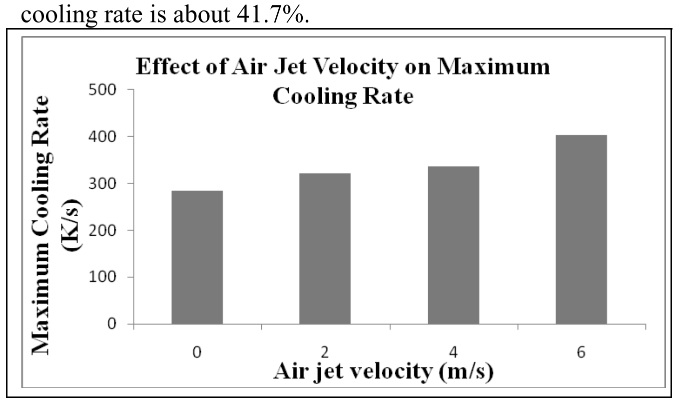


Fig. 10 Effect of Air Velocity in Maximum Cooling rate at stagnation point

Maximum heat flux is obtained at the stagnation point so a variation in heat flux at stagnation is taken for comparison. Fig.11 shows the change in heat flux during the quenching process. Maximum heat flux obtained at stagnation point at air velocity 0 m/s is 3.16 MW/m² and the cooling curve shows large variation.

Maximum heat flux becomes 3.7 MW/m² when the air velocity equals to 2 m/s and the curve becomes smoother. Maximum cooling rate at stagnation becomes 3.84 MW/m² when the air jet velocity becomes 4 m/s. When the air jet velocity becomes 6 m/s maximum heat flux obtained becomes 4.45 MW/m² and the curve becomes smoother than the previous cases

*C. Effect of Air Velocity in Heatflux*

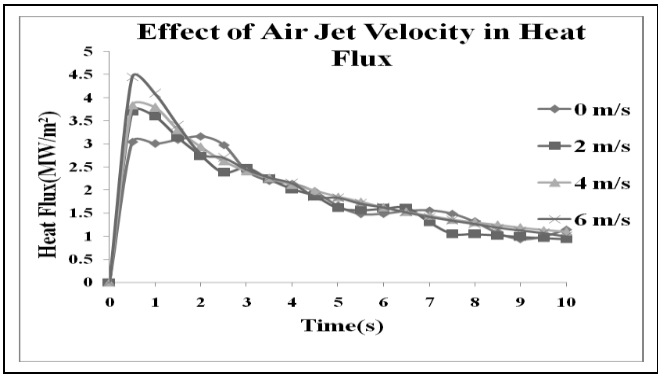


Fig. 11 Effect of Air Velocity in Heat flux at stagnation point

.

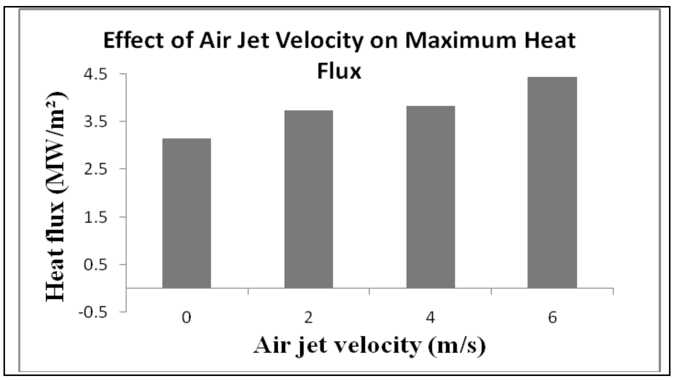


Fig. 12 Effect of Air Velocity in Maximum Heat flux at stagnation point

Fig.12 shows variation of maximum heat flux at stagnation point for different air jet velocity is shown. For water jet maximum heat flux obtained is 3.16 MW/m². When the air jet velocity becomes 2m/s; heat flux obtained at stagnation becomes 3.71 MW/m² Increase in heat flux is about 21.94%. Similarly an increase of about 25.9% and 45.9% increase in heat flux are obtained while using air jet with 4 and 6 m/s velocity respectively

## IV. CONCLUSIONS

Numerical analysis is carried out to study the effect of air jet velocity in a co-axial air-water jet impingement system for quenching. In this analysis air velocity of the co-axial air-water jet is varied from 2, 4, 6 m/s and effect of variation are studied and compared with water jet. Maximum cooling rate and maximum value of heat transfer increases as air-jet velocity is increased. Increase in maximum cooling rate about 12.93%, 17.85% and 41.7% is obtained with air jet velocity 2, 4 and 6 m/s respectively when compared with water jet. Percentage increase of maximum heat flux of 21.94 %, 25.9 %and 45.9 % is obtained for an air jet velocity of 2, 4 and 6 m/s when compared with water jet.

## ACKNOWLEDGMENT

This work is supported by TEQIP

## REFERENCES

[1] N. Zuckerman and N. Lior , "Jet Impingement Heat Transfer: Physics, Correlations, and Numerical Modeling". Advances in Heat Transfer vol. 39, ISSN 0065-2717(2006).

[2] Yongjun Zhao, " The cooling of a hot steel plate by impinging water jet".Thesis report (2005),University of Wallongong F. Scarpa a , G. Tagliafico b , L.A. Tagliafico," Control optimization in experiments for the heat transfer assessment of saturated packed bed regenerators", International Journal Of Heat and Mass Transfer55(2012)6944

[3] Nitin Karwa," Experimental sstudy of water jet impingement cooling of hot steelplate",Thesis report (2012)

[4] Md Lokman Hosaina, Rebei Bel Fdhila, Anders Daneryda , " Multi-Jet Impingement Cooling of a Hot Flat Steel Plate". Energy Procedia 61 ( 2014 ) 1835 – 1839

[5] S. Hardt , F. Wondra" Evaporation model for interfacial flows based on a continuum-field representation of the source terms" Journal of Computational Physics 227 (2008) 5871–5895

[6] Dong-Liang Sun , Jin-Liang Xu , Li Wang Development of a vapour–liquid phase change model for volume-of-fluid method in FLUENT International Communications in Heat and Mass Transfer 39 (2012) 1101–1106

[7] M.H. Yuan , Y.H. Yang, T.S. Li, Z.H. Hu, " Numerical simulation of film boiling on a sphere with a volume of fluid interface tracking method". International Journal of Heat and Mass Transfer 51 (2008) 1646–1657

[8] M. Molana and S. Banooni, , " Investigation of heat transfer processes involved liquid impingement jets: a review". Brazilian Journal of Chemical Engineering, Vol. 30, No. 03, pp. 413 - 435, July - September, 2013

[9] M. Gradeck a, A. Kouachi , M. Lebouche , F. Volle , D. Maillet , J.L. BoreanJ. Xu , J. Tian , T.J. Lu , H.P. Hodson"Boiling curves in relation to quenching of a high temperature moving surface with liquid jet impingement". International journal of heat and mass transfer 52 (2009) 1094-1104.

# System level Thermal analysis of Power Amplifier module in FloTHERM CFD code

Anu N Vincent[1], Sabu Sebastian M, O R Nandagopan

*Naval Physical and Oceanographic Laboratory, Kochi, Kerala, India*

[1]anvincent@npol.drdo.in

***Abstract*—This paper discusses thermal analysis of the power amplifier module using computational fluid dynamic software FloTHERM considering an ambient temperature of 30$^0$C with varying air velocities i.e. 0.5m/s, 1m/s, 1.5 m/s, 2m/s, 3m/s, 4m/s, and 5m/s. The critical operation of the power amplifier module at an ambient temperature of 55$^0$C was also studied which ensured its operation at extremely adverse thermal environment onboard platform.**

***Keywords*— CFD, Electronic cooling, FloTHERM, Forced convection, system level thermal analysis**

## I. Introduction

Electronic packaging of military electronic enclosures which is prone to harsh environmental conditions has to qualify the JSS 55555 [1] standards put forward by the end user before getting installed on the platform. According to statistics almost 55% of electronic component failures are due to thermal failure. Figure1 shows the schematic representation of failure in electronic components.

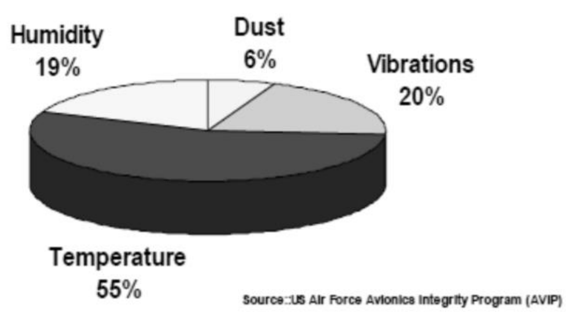


Fig. 1 Schematic representation of failure in Electronic components

The maximum permissible limit for junction temperature for MIL standard components is 125$^0$C. Most of the electronic enclosures for military applications are air cooled since air is abundantly present and is the cheapest method of cooling. Thermal design of electronic enclosures should take into account the varying ambient temperatures the component withstands during operation. The maximum ambient temperature in which the military electronic enclosures should operate is 55$^0$C. For closed loop forced air cooled enclosures in practical scenario, in many instances, specified air supply will be limited from the platform due to other mission operations. The design should be conservative about 15% at this juncture. The thermal characterization study is conducted during the design phase to facilitate reduction in failures during installation.

In this paper, thermal analysis of a power amplifier module with an overall dimension of 135mm (W) X 6U (H) X 360mm (D) and mass of 7Kg shown in Figure 2 is conducted which has its application in naval systems. The total heat dissipation of the power amplifier module is about 130W. The main heat generating components inside a power amplifier module are the MOSFETs with a heat flux of 8.33 W/cm$^2$ and the power transformer with a heat flux of 0.448 W/cm$^2$. The heat load distribution inside the module is given in Table I. The heat loads of components are calculated considering its continuous operation.

TABLE X
HEAT DISSIPATING COMPONENTS OF POWER AMPLIFIER MODULE

| Sl No | Component | Heat Dissipation |
|---|---|---|
| 1 | MOSFET 1 ( mos1) | 20W |
| 2 | MOSFET2 (mos 2) | 20W |
| 3 | MOSFET3 (mos 3) | 20W |
| 4 | MOSFET4 (mos 4) | 20W |
| 5 | Power Transformer | 50W |

The MOSFETs are attached to the convective cooled aluminium plate fin heat sink of dimension 352 mm (W) X 222mm (H) X 20mm (t) with a total of 52 number of fins. The MOSFETs are powered by a printed circuit board attached to it. In order to reduce the thermal contact resistance, thermal grease is applied in between the MOSFETs and the heat sink. Heat is transferred from these MOSFETs to heat sink and from this heat sink it is transferred to ambient air i.e. combined conductive and convective heat transfer. Other components inside the module are EMI filter transformer and current regulating devices. Top plate and bottom plate of power amplifier module are having 14% perforation for allowing airflow inside the power amplifier module.

In the system-level analysis, the larger components like enclosure, shelf and fans are included in detail but the smaller parts like semi-conductors are neglected [2]. The numerical analysis was conducted in computational fluid dynamic code FloTHERM [3] considering its normal working ambient temperature of $30^0$C with varying air flow rates i.e. 0.5m/s, 1m/s, 1.5 m/s, 2m/s which in turn depends upon the availability of chilled air from the platform. Another case study was conducted with an ambient temperature of $55^0$C simulating the working of power amplifier module in critical conditions.

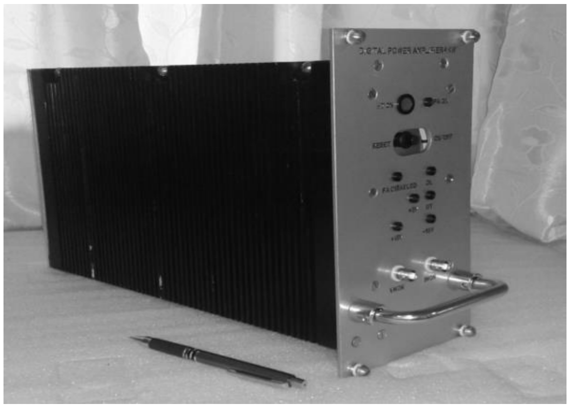

Fig. 2 Power Amplifier Module

## II. CFD SIMULATION APPROACH

### *A. Basic Assumptions*

Three-dimensional, steady state turbulent air convection in the electronic enclosure was assumed. The Reynolds number taken based on the flow inlet velocity. Constant properties of air were assumed in all computational domain .Buoyancy effect was included. Contributions from radiation were ignored. The fins were modelled as rectangular fin instead of actual trapezoidal fin.

### *B. Computational Domain*

To generate the system resistance curve a numerical wind tunnel is simulated in FloTHERM. The side of the computational domain was same as that of the test section i.e. the power amplifier module, However the domain size extended in the flow direction both at the entry and exit. Figure 3 shows the numerical wind tunnel replicated in FloTHERM.

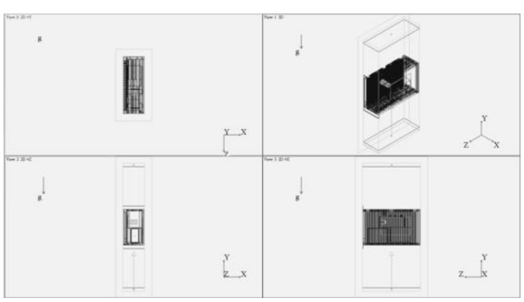

Fig. 3 Numerical Wind Tunnel

### *C. Governing Equations*

The field variables that FloTHERM solves are u, v and w, the velocity resolutes in cartesian coordinate directions x, y and z, p, the pressure, T, the temperature of the fluid and solid materials. These variables are functions of x, y, z and time. The differential equations that these field variables satisfy are referred to as conservation equations. u, v and w satisfy the momentum conservation equations in the three coordinate directions. Temperature satisfies the conservation equation of thermal energy. The pressure does not itself satisfy a conservation equation, but is derived from the equation of continuity which is a statement in differential form of the conservation of mass. The governing equations are solved for the steady state incompressible flow of Newtonian fluid i.e. air at $30^0$C and $55^0$C of temperature respectively for its normal operation and critical operation.

$$\frac{\partial(\rho u)}{\partial x}+\frac{\partial(\rho v)}{\partial y}+\frac{\partial(\rho w)}{\partial z}=0 \text{ ............ } (1)$$

$$\frac{\partial(\rho u)}{\partial t}+div(\rho u\boldsymbol{u})=-\frac{\partial p}{\partial x}+div(\mu\ grad\ u)+S_{M_x} \text{ ..... } (2)$$

$$\frac{\partial(\rho v)}{\partial t}+div(\rho v\boldsymbol{u})=-\frac{\partial p}{\partial y}+div(\mu\ grad\ v)+S_{M_y} \text{....... } (3)$$

$$\frac{\partial(\rho w)}{\partial t}+div(\rho w\boldsymbol{u})=-\frac{\partial p}{\partial z}+div(\mu\ grad\ w)+S_{M_z} \text{ ... } (4)$$

$$\frac{\partial(\rho i)}{\partial t}+div(\rho i\boldsymbol{u})=-p\ div\ \boldsymbol{u}+div(k\ grad\ T)+\emptyset+S_i \text{ .. } (5)$$

Where $S_{M_x}, S_{M_y}, S_{M_z},\ S_i$ represent the Source terms

### *D. Boundary Conditions*

One to one geometry creation is done in FloMCAD module of FloTHERM CFD code. Figure 4 shows the physical model in FloTHERM. A free boundary of constant pressure through which air can flow on all surfaces of the solution domain is considered. Air flow simulated from bottom to top of the module. Flow is simulated by modeling fixed volume smartpart in FLOTHERM.

Gravity is on in the negative Y-direction. Heat transfer coefficient is calculated based on the empirical equation

$$Nu= 0.664 * Re^{0.5} * Pr^{0.33}$$

Figure 5 and Figure 6 show variation of Nusselt number with Reynolds number for various flow velocities of 0.5m/s, 1m/s, 2m/s, 3m/s, 4m/s and

5m/s at an ambient temperature of 30$^0$C and 55$^0$C respectively.

*E. Turbulence Model*

The default turbulent model of FloTHERM CFD code is the algebraic turbulence model. It is the computationally least expensive one since no extra equations are solved in addition to continuity, momentum and energy equations. However, in order to rely on the results that the algebraic model gives, it should be validated with higher order turbulence models. The LVEL K-ε model is used as a test case. The temperature distributions and velocity fields are compared.

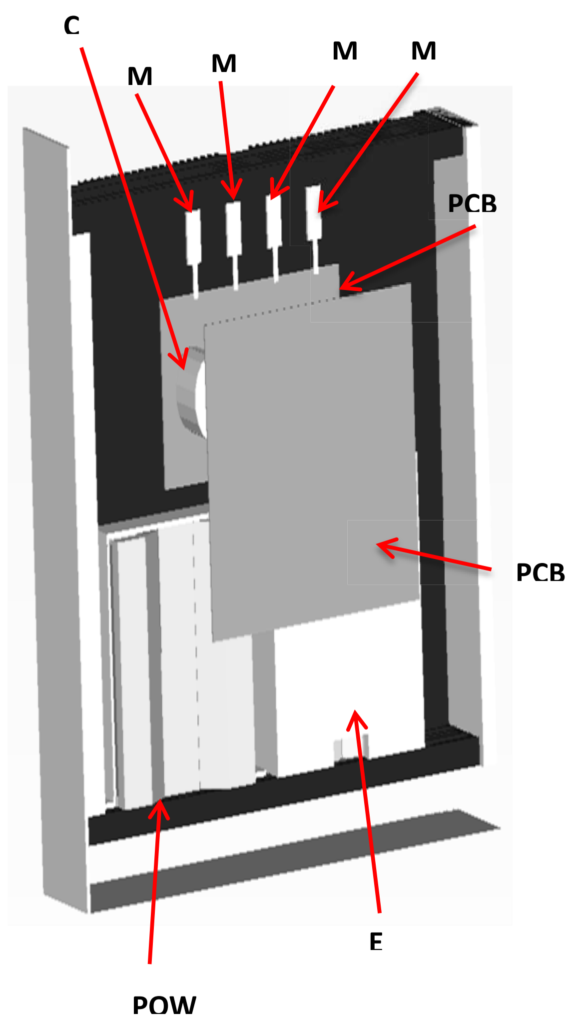


Fig. 4 Modeling in FloTHERM (Sectioned View)

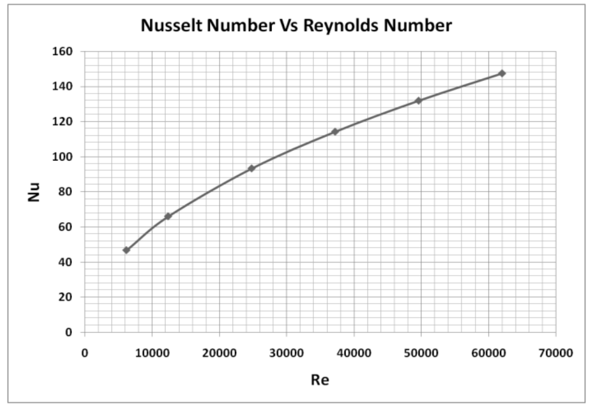


Fig. 5 Variation of Nu Vs Re at an ambient temperature of 30$^0$C

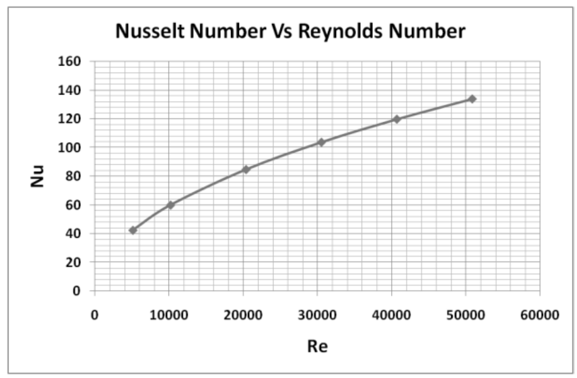


Fig. 6 Variation of Nu Vs Re at an ambient temperature of 55$^0$C

*F. Grid Independence*

FloTHERM uses simple Cartesian grid meshing. Local grids are incorporated wherever necessary in order to capture accurate values. Grid independence study conducted inorder to ensure the authenticity of values generated from FloTHERM CFD code. Table 2 shows the value of variation of mosfet temperature with the change of total number of cells. From Case 2 onwards the values are steady and the same can be taken for further analysis since lesser number of cells will reduce the computational time. Total number of cells are 14, 50,440.

TABLE XI
HEAT DISSIPATING COMPONENTS OF POWER AMPLIFIER MODULE

| Case Study | X Grids | YGrids | Z Grids | Total No of Cells | Reference as MOSFET Temperature |
|---|---|---|---|---|---|
| Case1 | 69 | 52 | 155 | 5,56,140 | 84.12 |
| Case2 | 108 | 85 | 158 | 14,50,440 | 85.33 |
| Case3 | 125 | 85 | 158 | 16,78,750 | 85.26 |
| Case4 | 102 | 80 | 323 | 26,35,680 | 85.399 |

## III. Results and Discussion

### *A. System Impedance curve of the power amplifier module*

Fig 6 shows the system impedance curve of the power amplifier module. The fans to the power amplifier module are selected based on this input. The fan characteristic curve will be plotted along with this system impedance curve to determine the operating point of fan.

### *B. Case 1: Power Amplifier Module at an ambient temperature of $30^0C$*

Figure 7 and Figure 8 show temperature distribution on power amplifier module at an ambient temperature of $30^0$C when the inlet air velocity is at 5m/s. The maximum temperature noticed at the MOSFET's of the power amplifier module. The middle MOSFET show the maximum temperature of 42.5 $^0$C. Figure 9 shows velocity profile inside the power amplifier module when the inlet velocity of air is about 5m/s.

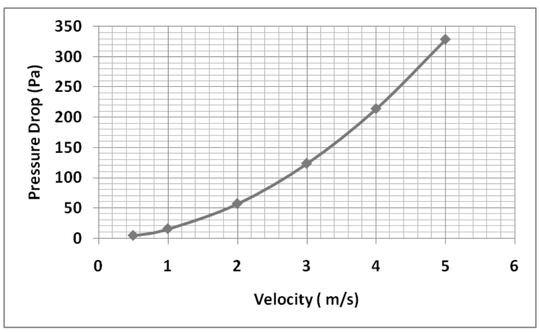


Fig. 6 System Impedance curve of the power amplifier module

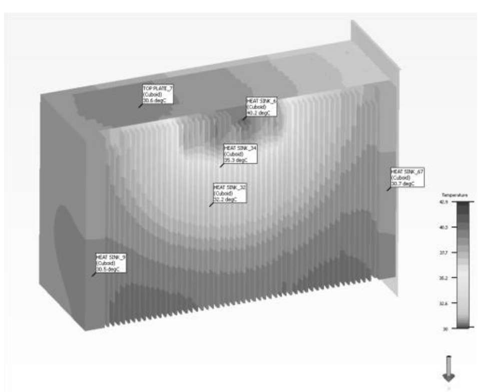

Fig. 7 Temperature profile at an ambient temperature of $30^0$C

Figure 10 shows the variation of temperatures with varying air velocities for MOSFET's and Power Transformer. The maximum temperature noted is 79.3 $^0$C for MOSFET 2 at an ambient of $55^0$C and air velocity of 0.5m/s.

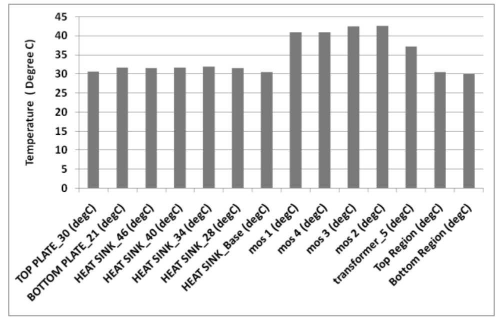


Fig. 8 Temperature distribution of components at $30^0$C ambient

Fig. 9 Velocity profile inside power amplifier module

### A. Case 2: Power Amplifier Module at an ambient temperature of 55 $^0$C

The junction temperature of the MOSFET 2 calculated is $81.7^0$C given $\theta_{jc}$ is 0.12 °CW [4]. Maximum permissible operating junction temperature of the MOSFET is 125 $^0$C which means the component is safe even at $55^0$C at an air velocity of 0.5m/s.

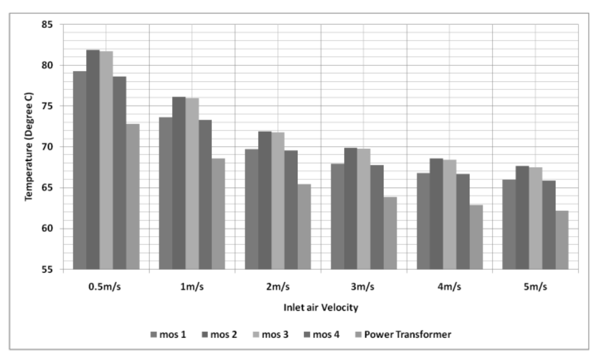


Fig. 10 Variation of MOSFET and Power Transformer temperatures with air velocities

## IV. Conclusions

System level thermal analysis of power amplifier module was carried out using commercial CFD code FloTHERM. Numerical wind tunnel was simulated which aided in getting the system impedance curve of the power amplifier module. The study was conducted at two ambient temperatures, one at the normal operating temperature of the module and other at the critical operating temperature of the module. Maximum surface temperatures of the heat generating components noted and were found within permissible limits as given according to manufacturer's specification. At an ambient temperature of $55^0$C the module will safely operate at an air velocity of 3m/s or above.

## Acknowledgment

Authors would like to express their gratitude to Director NPOL for his support and encouragement for completing this paper. The authors also gratefully acknowledge Shri Krishnakumar P, Sc 'D' Power Electronics division of NPOL for giving necessary inputs for doing the thermal analysis. The authors would also like to thank Shri Roni Francis, Sc 'E' of Engineering group, NPOL and Dr Anand Raj Hariharan, Associate professor, ASIET, kalady for timely review & relevant inputs.

## References

[1] Joint Services Specification On Environmental Test Methods For Electronic And Electircal Eqipment JSS 55555: 2000 Revision No.2.

[2] Jongsun Park, Yunhee Park and Yong Woo Kim, "Thermal Design and Verification of Telecommunication Equipment", 21st IEEE SEMI-THERM Symposium, 2005.

[3] FloTHERM V 9.3, Mentor graphics, help and product manual.

[4] IXYS Power MOSFET product manual.

# Author Index

**T**



**U**



**V**



**Y**